

Syntheses and Functional Studies of Advanced Porous Materials (APMs): A Promising Platform for Aquatic Pollutant Remediation and Energy Applications

A Thesis

Submitted in Partial Fulfillment of the Requirements for the
Degree of

Doctor of Philosophy

by

Yogeshwar D. More

Reg. ID: 20153360



Indian Institute of Science Education and Research (IISER), Pune

2022

Dedicated to...

‘मममा-पप्पा’



Indian Institute of Science Education and Research (IISER), Pune

Certificate

It is hereby certified that the work described in this thesis entitled “*Syntheses and Functional Studies of Advanced Porous Materials (APMs): A Promising Platform for Aquatic Pollutant Remediation and Energy Applications*” submitted by *Mr. Yogeshwar D. More* was carried out by the candidate, under my supervision. The work presented here or any part of it has not been included in any other thesis submitted previously for the award of any degree or diploma from any other university or institution.

A handwritten signature in blue ink, appearing to read "Sujit K. Ghosh", with a horizontal line underneath.

Date: 10.11.2022

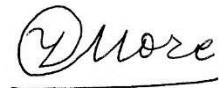
Dr. Sujit K. Ghosh
Research Supervisor

Email: sghosh@iiserpune.ac.in

Contact No.: +91(20)25908076

Declaration

I declare that this written submission represents my ideas in my own words and wherever other's ideas have been included; I have adequately cited and referenced the original sources. I also declare that I have adhered to all principles of academic honesty and integrity and have not misrepresented or fabricated or falsified any idea/ data/ fact/ source in my submission. I understand that violation of the above will cause for disciplinary action by the Institute and can also evoke penal action from the sources which have thus not been properly cited or from whom proper permission has not been taken when needed.



Date: 10.11.2022

Yogeshwar D. More

Reg. ID: 20153360

Acknowledgement

First and foremost, this has been vibrant and scintillating journey and I would like to take advantage of this wonderful and memorable occasion to express my gratitude to my loved ones, including my parents, friends, mentors, the administration at IISER, and family members, for their unwavering support throughout my doctoral studies. I would like to dedicate this fruitful outcome to **Mummy-Papa** (the best parental duo), **Sangram-Nilesh-Tejas** (the ever supportive power house), **Vaibhav-Suwarna** (supportive siblings), **Adv. Bhimrao Shinde** (the moral support), **Sharad, Girish, Ganesh, Gaurav, Bhushan, Samraj and Bhavin** (friends for life) and **Mentors**.

For the past several years, in fact a period over a *Quinquennial*, as my PhD advisor, **Prof. Sujit K. Ghosh** has helped shape me into a well-rounded scholar, and I would like to take this moment to express my sincere thanks to him. For the advancement of scientific aptitude and temperament, he has been a devoted guide and a persistent source of enthusiasm. It has been a privilege to learn from him as a mentor. In my opinion, his encouraging direction was a major factor in my being able to successfully plan and carry out a number of research projects. Thank you for trusting in me, for always seeing the bright side of things, and for always being an encouraging supervisor. In particular, I wishes to take advantage of this opportunity to thank **Prof. Satishchandra Ogale**, a member of the Research Advisory Committee (RAC) and my PhD mentor, for all the invaluable guidance, enthusiasm, and patience he has shown me over the course of the past several years as I have worked to become a well-rounded researcher. He has been a dedicated educator and a consistent source of motivation, instilling the disciplined work ethic crucial to developing one's scientific skills and temperament. It's been a privilege to have him as a mentor and work with him. A number of my research projects would not have been as fruitful without his insightful guidance. Sir, thank you for your confidence in me, your positive outlook, and, most of all, for being such a supportive role model.

I would like to thank Prof. K. N. Ganesh, the former director of IISER Pune, and Prof. J. B. Udgaonkar, the current director, for creating such a stimulating environment for research and enforcing necessary regulations. In addition, I owe a great debt of gratitude to the members of my research advisory committee (RAC), specifically Drs.

Avinash Kumbhar (SPPU, Pune) and Shabana Khan (IISER, Pune) for the invaluable feedback they provided during our annual RAC meetings. I would like to extend my gratitude to the chemistry department's current chair Prof. Nirmalya ballav, and to the department's former chairs, Prof. H. N. Gopi, Prof. M. Jayakannan, for creating a stimulating research environment and making themselves available to answer my many queries. Thanks to everyone who assisted me in my studies and research, but especially to Prof. Jin-Chong Tan (Oxford University, UK), Dr. Mandar M. Shirolkar (Symbiosis International University), and **Dr. Samraj Mollick** (Indian Institute of Science, Bangalore) (University of Oxford, UK).

Being a part of the "Microporous Materials Lab" has provided me with invaluable experience, and I am grateful to everyone who has worked there in the past and who continues to work there today. I would like to express my gratitude to Sanjog Nagarkar, Avishek Karmakar, Samraj Mollick, Sreenu Bhanoth, Shilpa Sonar, Prateek Agrawal, Subhajit Dutta, Sumanta Let, Writakshi Mandal, Sahel Fajal, Debanjan Mahato, Gourab Kumar Dam, Satyam Saurabh, Priyanshu Chandra, Arkendu Roy, Depanjan Majumder, Kishalay Biswas, and Dibyanjan Sahoo. To everyone who has made significant contributions, provided assistance, or made the lab a welcoming place to work, thank you.

In particular, I want to express my gratitude to Sanjog and Abhijeet, who introduced me to the lab, and to the other lab members who provided me with invaluable advice and encouragement as I began my PhD studies. I would like to express my gratitude to a number of retirees who have offered me advice and support. It was a pleasure to work with everyone here, and I feel like I gained a lot of knowledge and insight from the experience. In addition to the invaluable guidance they have given me, I've also had the good fortune to form close friendships with each of them. I would also like to thank everyone currently working in my lab for their contributions to making this experience what it has been so far. Samraj was the person in my cohort with whom I spent the most time in the lab; ours was a long, memorable partnership in which we shared highs and lows and pushed each other to reach our full potential, and I count myself fortunate to have had such a friend and cohort member. I owe so much to him for his invaluable support and the insights he has provided to my studies. Satyam, Subahjit, and Dipanjan are three junior colleagues who have worked closely with me for a long time, and I

appreciate their dedication, enthusiasm, and punctuality.

For a long course to run smoothly, both administrative and technical support are essential. **I am extremely thankful to Prof Satishchandra Ogale, Prof./Dr. Jahnavi Kedare, Prof. Girish Ratnaparkhi, Prof. Bhas Bapat, Prof. Ram G. Bhat, Prof. Sanjeev Galande, Prof. Sunil Mukhi and Prof. Jayant Udgaonkar for timely and equivocal support.** I would like to thank Anuradha and Dr. Umeshreddy Kacherki for the all the help from library services; the technical staff at the institute, including Parveen Nasa, Ravinder Malothu, Mahesh Jadhav, Nilesh Dumbre, Anil Jadhav, Yatish, Ganesh Dimbar, Suresh Prajapat, Sandeep Kanade, Nitin Dalvi, Megha, and Deepali; and the administrative staff, including As well, I would like to express my appreciation to IISER Pune, where I was awarded a research fellowship. Several of my research and review articles have been published by the following organizations: John Wiley & Sons (Wiley-VCH), the American Chemical Society (ACS), the Royal Society of Chemistry (RSC), and Elsevier.

I am thankful to all of the professors and lecturers who have helped me grow and develop over the years. In addition, I would like to express my gratitude to Dr. Dhiraj Bhatia for all of his help and encouragement throughout my time at college and university. I owe a great debt of gratitude to the faculty and staff at K.T.H.M. College (K.R.T. Arts, B.H. Commerce, and A.M. Science College) in Nashik (University of Pune), particularly Dr. Madhukar N. Jachak, Dr. Raghunath Toche, Dr. Vishwas Gaikwad, Dr. Nitin Gaikwad, Dr. Niranjana Patil, Dr. Madhukar Shinde, and Baban Padwal sir.

I appreciate everyone who has been there for me throughout the years. I would like to give special thanks to my good friends Avinash, Bhavin, and Ganesh, who have been there for me through the ups and downs of the last six years with their unwavering encouragement and insightful tea and coffee conversations. I would like to express my gratitude to everyone who has ever worked in the departmental labs, both past and present, for their unfailing patience and kindness in granting us unfettered use of the UV-vis and fluorescence spectrometers. I appreciate everyone in my class and hope the best for them in the future. Moreover, I would like to thank my many campus pals, including Sachin Batar, Sachin Nalawade, Avinas Warankar, Bhavin Uttakar, Ganesh Shinde, Rakesh Pant, Rakesh Gaur, Rishabh Gupta, and Aniruddha. A debt of gratitude is also due to my mentors, Drs. Sanjog Nagarkar, Dinesh Mullangi, and Abhijeet. In

addition, I am pleased to give a shout-out to the "Resonance" cricket team at my alma mater and wish them the best of luck in the future. I would like to extend my gratitude to the other members of my B.Sc. class—Raju, Girish, Sagar, Vikas, Suraj, Amol, Pavan, Rohan, and Bhushan—for their unwavering moral and intellectual support, and everyone who has been a part of this amazing adventure filled with lessons.

Finally, I can affirm to phrase; "**All is Well That Ends Well**"

Grateful - Yogeshwar Dnyaneshwar More.

Contents

1	Introduction	
1.1	Metal-Organic Frameworks (MOFs)	1.1
1.2	Applications of Ionic MOFs (iMOFs)	1.14
1.3	Porous Materials for Energy Applications	1.22
1.4	Thesis Overview at a Glance	1.28
1.7	References	1.29

Part-I: Functional Anionic MOFs for Environmental Applications

2.	Superior Uranium Extraction from Seawater by Trap Grafted Anionic Metal-organic Frameworks	
2.1	Introduction	2.1
2.2	Experimental	2.3
2.3	Results and discussion	2.8
2.4	Conclusions	2.15
2.5	Appendix section	2.16
2.6	References	2.73

3.	Efficient Recognition and Capture of Specific Toxic Organic Pollutants Using Water-Stable Highly Luminescent Anionic Metal-organic framework	
3.1	Introduction	3.1
3.2	Experimental	3.6
3.3	Results and discussion	3.10
3.4	Conclusions	3.25
3.5	Appendix section	3.27
3.6	References	3.50

Part-II: Advanced Porous Materials for Energy Applications

4.	Highly Stable and End-Group Tuneable Metal-organic Framework / polymer composite for Superior Triboelectric Nanogenerator Application	
4.1	Introduction	4.1

4.2	Experimental	4.5
4.3	Results and discussion	4.8
4.4	Conclusions	4.20
4.5	Appendix section	4.21
4.6	References	4.60

5. Surface Feature Tuned Metal-organic Polyhedra for Triboelectric Nanogenerator: Self-Powered Sensors for Wearable Electronics

5.1	Introduction	5.1
5.2	Experimental	5.9
5.3	Results and discussion	5.12
5.4	Conclusions	5.20
5.5	Appendix section	5.22
5.6	References	5.47

6. Summary and Perspectives 6.1

Attachments: Rights, Permissions and License Agreements

Synopsis

In the work comprised here, we sought to elucidate the design principles influencing the formation of stable ‘O and N-donor’ linker-based MOFs by deploying linkers with higher denticity. Polydentate linkers; carboxylate-based linkers additionally bearing N-donor sites have been used in the synthesis, offering diverse alternatives to building functional MOFs are being explored. Thus, the primary motivation for this thesis work is to design, synthesize, and perform functional studies on a few ambidentate (N and O-donor) linker-based anionic Metal-organic frameworks (MOFs) and relevant porous materials in the fields of energy, the environment, and industrially relevant applications, which include selective recognition, capture, and efficient remediation of toxic aquatic pollutants, as well as application-oriented utilization in the field. Metal-organic frameworks have come to be the most important subset of functional porous materials owing to their several advantages over traditional porous materials. MOFs, being crystalline solids made up of organic ligands held together in an ordered manner by metal nodes, have evolved as a distinct class of porous materials and are being explored for a variety of applications, including gas storage, separation, hazardous oxo-ion remediation, ion-conduction, catalysis, and so on.

Development of advanced porous materials (APMs), including MOFs, Metal-organic Polyhedra (MOP), and others, has progressed fast during the last two decades, particularly in the fields of energy and environmental applications. This is attributed to features that enable tunable architectures and alter chemical or physical properties on demand at the molecular level. MOFs have recently attracted attention for the difficult task of selective, efficient remediation of environmentally hazardous contaminants such as hazardous oxo-ions, organic medical and pharmaceutical pollutants, as well as separation of important light hydrocarbons and greenhouse gases, which has sparked widespread global concern and requires further investigation. Generally, MOFs are classified into ionic and neutral frameworks depending upon the residual charge on the framework backbone. Distinct terminal donor groups have been employed for the synthesis of MOFs such as N-heterocyclic aromatic rings, carboxylates, phosphonates, sulfonates, etc. Among them, neutral N-donor-based ligands possess several advantages compared to other donating groups, and they can facilitate the formation of ionic MOFs with counter anions or cations free inside the pores. Whereas the counter cations can act as the extra-framework functionalities for anionic MOFs, the organic building blocks can also be custom-designed via pre-or post-synthetic functionalization to introduce desired functional groups. Although anionic MOFs have been employed for several applications like catalysis, sensing, ion-conduction etc., their utility toward extremely challenging priority chemical sequestration and selective aquatic pollutant remediation is still to be explored relatively. In this context, one of the prime objectives of this thesis work is functional studies of anionic MOFs toward selective

separation of the aforementioned constituents. To accomplish this, attempts were made to design and synthesize several functional anionic MOFs with both different inorganic and organic anions inside the pores as extra-framework functionalities. Such linkers facilitate the formation of anionic frameworks coupled with extra functionality through exchangeable uncoordinated cations within the porous cavity of the framework. Design strategies were centered on building compounds that were specifically targeted for the remediation of hazardous pollutants, including heavy metal oxo-cations, radioactive species (via surrogate cations), antibiotics and pesticides via ion-exchange pathways, and compounds with polar sites for the adsorption of hydrocarbons and greenhouse gases. Furthermore, responding to emerging demand for wearable electronics, self-powered sensors, and e-skin with compatible and flexible/ dynamic devices has resulted in rapid advancements in Triboelectric Nanogenerators (TENG) related technologies that use MOFs as a versatile platform. MOFs have acquired precedence in latter years as low, medium, and high power mechanical (or any translational) energy harvesting devices and have been explored recently for the conversion of mechanical energy into electricity by means of Nanogenerators (NG), utilizing the virtue of being a multifunctional, tunable platform, thus extending the applications of a TENG. In this respect, we sought to comprehend the in-depth design concepts affecting NG and developed a simple, unique, reusable, and flexible NG composed of MOFs and MOPs capable of successfully harvesting irregular mechanical energy. The mechanics of the TENG were thoroughly explored and demonstrated. Advanced tunability and stabilization strategies enabled outcomes to validate the advantages of APMs in a diverse range of applications.

Chapter 1. Introduction

An overview of MOFs and their scope in terms of structural diversity and approach is provided in the introduction. It has been suggested that selecting building blocks and metal nodes judiciously is important for creating functional MOFs. In particular, the potential for stable "O and N-donor" linker-based MOFs is provided, and the contributions of various types of organic ligands in the construction of MOFs have been thoroughly examined. Additionally, a thorough discussion of MOF classification based on structural variety (MOF generations) and residual framework charge (ionic and neutral) is provided. Additionally, various approaches for synthesising ionic MOFs have been thoroughly covered. An overview of the wide applications of ionic MOFs has been presented, particularly in the areas of uranium sequestration and toxic aquatic pollutant remediation. The importance of on-demand uranium extraction from seawater (UES) in mitigating growing sustainable energy needs while overcoming high salinity and low concentration barriers has been thoroughly researched and demonstrated in this context. Additionally, the issue of hazardous and toxic pollutants contaminating water has been extensively discussed. A brief state-of-the-art overview has been provided since the current work's main focus is the use of anionic MOFs for

energy and environmental applications. The methods for creating anionic MOFs and the functions of cations have been briefly discussed because one of the most crucial things to consider is how the functional cations inside of them can be altered. Additionally, the maiden report on the improvement and tuning of MOF-based composites aimed for TENG applications through rational and methodical alterations in organic ligand chemistry is detailed here. This was done while purposefully maintaining identical conditions in view of isoreticularity of frameworks, dimensions of thus formed composites, and fabrication method. The current discussion makes an effort to establish a logical and mechanical understanding of the electronic effects attributed to functionalities that have been substituted for ligands (such as halogen substitution) and greatly improve the triboelectric characteristics of MOF composites. In the light of aforementioned work and its nature, the dissertation is divided into two parts or sections that are themed on environmental applications and energy applications simultaneously.

References:

1) Luminescent Metal-Organic Frameworks as Chemical Sensors (Book Chapter).

Y. D. More, S. Fajal, S. Dutta, Sujit K. Ghosh, *CRC Press*, **2022**. (*Accepted; In Press*)

2) Ionic Metal-Organic Frameworks (iMOFs): Progress and Prospects as Ionic Functional Materials.

S. Dutta,[†] **Y. D. More**,[†] S. Fajal, W. Mandal, G. K. Dam, S. K. Ghosh.

Chem. Commun. **2022**, DOI: 10.1039/D2CC05131A.

Part-I: Functional Anionic MOFs for Environmental Applications

It is a prevailing fact that we are in an era of energy crisis and sustaining the world's energy supply in the face of increased energy demand while considering the environmental hazards posed by fossil fuels remains a challenging endeavor. An uninterrupted, reliable, and clean energy supply continues to be a major challenge that mankind is facing today. According to the International Atomic Energy Agency (IAEA), nuclear power will remain among the few existing reliable energy sources in the future. Since nuclear technologies could provide energy for generations to come, uranium recovery from unconventional sources such as natural seawater has gained cutting-edge research interest. However, as nuclear technologies advance with increasing demand for uranium, the gap between uranium supply and demand has become more glaring simultaneously. This is because the world's known geological deposits of uranium are finite and will be depleted within the next couple of decades. In view of the aforementioned daunting situation, uranium strewn and rationed in the oceans is gaining scientific attention. The ocean stores 4.5 billion tons of uranium, which is equivalent to a nearly endless uranium supply. Therefore, uranium extraction from seawater (UES) is desperately needed to make nuclear energy a sustainably long-lasting energy source. The recovery of uranium from seawater is widely acknowledged to be one of seven chemical separations that are projected to have a substantial impact and repulse on our

society. However, meeting the UES in a timely manner through the development of uranium adsorbents is still a formidable challenge. In this section, we devoted our effort toward pore-engineering of stable anionic MOFs via deployment of Lewis basic site functionalized ligand and swapping different functional uncoordinated cations inside the pore. This section of the thesis is divided into two Chapters, Chapter-2 and Chapter-3. In Chapter-2, we established the effectiveness of a novel anionic metal-organic framework (iMOF-1A) adorned with rare Lewis basic pyrazinic sites as a uranyl-specific trap serving as a robust ion exchange material for selective uranium extraction. While in Chapter-3, selective and rapid identification of hazardous aquatic pollutants, i.e., of antibiotics and pesticides in aqueous solution, besides Paraquat capture, is carried out by delving into the particular fluorescence quenching mechanism of a recently created highly luminous, electronically rich, porous metal-organic framework (iMOF-4A). The iMOF-4A demonstrated a specific, substantial quenching response in the presence of electron-deficient antibiotics like Nitrofurantoin (NFT) and Nitrofurazone (NFZ), as well as herbicides like Paraquat (PQ) in water.

Chapter 2. Superior Uranium Extraction from Seawater by Trap Grafted Anionic Metal-organic Frameworks

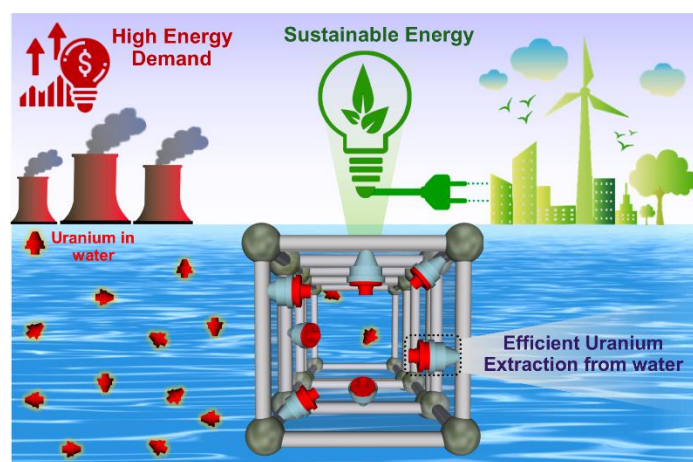
On-demand uranium extraction from seawater (UES), often known as uranium mining, is one method that has the potential to meet the rising need for environmentally friendly sources of energy. However, due to the extremely low concentration of uranium in saltwater and the high salinity of seawater, selective uranium recovery from seawater has continued to be a significant difficulty. In this study, we demonstrated a novel anionic metal-organic framework called iMOF-1A. It is adorned with a rare Lewis basic pyrazinic nitrogen site called Pyz-N. This site functions as a uranyl-specific nanopocket that serves as a robust ion exchange material for uranium extraction. Additionally, the intrinsic ionic characteristics of this material help to minimize leaching. The ionic adsorbents were able to sequester 99.8% of the uranium in just 120 minutes (from 20,000 ppb to 24 ppb). Additionally, they were able to adsorb extraordinarily large amounts of uranium, including 1336.8 mg g⁻¹ and 625.6 mg g⁻¹ from uranium spiked deionized water and artificial seawater, respectively, with a very high distribution coefficient, $K_d^U > 0$. The material achieves the UES standard of 6.0 mg g⁻¹ in just 18 days, in contrast to the 30-day limit of UES, and it harvests 9.38 mg g⁻¹ in 30 days from natural seawater that has not been contaminated in any way. It has a very high enrichment index of 5754 in comparison to the previously well-known outstanding uranium adsorbents. Isothermal titration calorimetry (ITC) studies demonstrated the precise quantification of detailed thermodynamic parameters of adsorption on MOF in the liquid phase. These parameters, which had previously been unknown in uranium sorption experiments, were demonstrated by the precise quantification of detailed thermodynamic parameters of adsorption on MOF in the liquid phase. Infrared nearfield nanospectroscopy (nano-FTIR) and tip-force microscopy (TFM) techniques enabled chemical

elucidation of the host-guest interaction at the atomic level in sub-micron crystals. Additionally, these techniques demonstrated the occurrence of capture events throughout the MOF single crystals in addition to on their surfaces. An existing mechanistic insight has been uncovered as a result of the synergistic combination of extensive experimental and computational studies. These studies directly reveal the ultrahigh selectivity for uranium capture from seawater.

(Manuscript under revision)

Superior Uranium Extraction from Seawater by Trap Grafted Anionic Metal-organic Frameworks.

Y. D. More,[†] S. mollick,[†] S. Saurabh, S. Fajal, M. Tricarico, S. Dutta, W. Mandal, J, -C. Tan and S. K. Ghosh.



Chapter 3. Efficient Recognition and Capture of Specific Toxic Organic Pollutants Using Water-Stable Highly Luminescent Anionic Metal-organic framework

Newly developed antibiotics and pesticides are two examples of anthropogenic wastes that have contributed to water pollution through their misuse or inappropriate application. Because of the serious consequences for human health, the detection (identification) of antibiotics and pesticides in wastewater must be carried out promptly and selectively. A promising sensory material for the detection of antibiotics and pesticides in water is still sought for practical reasons. Ionic metal-organic frameworks (iMOFs) are an innovative class of porous materials that may be useful for the detection of aqueous micropollutants. We investigated the fluorescence quenching process of a newly developed very bright, electrically rich, porous metal-organic framework in order to detect antibiotics and pesticides in aqueous solution (iMOF-4A). In the presence of electron-deficient antibiotics like Nitrofurantoin (NFT), Nitrofurazone (NFZ) and herbicides like Paraquat (PQ) in water, the iMOF-4A showed a particular, considerable quenching response. Both NFT and NFZ were detected at detection limits of 6.68 ppm and 7.18 ppm, respectively,

demonstrating the iMOF-4A's exceptional sensitivity. However, they were among the best-performing bright MOF-based sensing materials with PQ detection limits of 1.79 ppm. The selectivity analysis study showed that iMOF-4A was exceptionally selective since its fluorescence detection performance was not significantly affected by the presence of the many different antibiotics and pesticides that were present at the time of the study. Furthermore, it may be regenerated for ongoing usage without appreciable loss of functionality following a detection test. In addition, time-resolved photoluminescence lifespan decay analyses and density functional theory were used to provide light on the in-depth mechanistic investigation of iMOF-4A's detecting skills (DFT). These studies point to two mechanisms, photo-induced electron transfer (PET) besides fluorescence resonance energy transfer (FRET), as the causes of selective quenching of emission. Additionally, an isothermal titration calorimetry (ITC) investigations was conducted to show that iMOF-4A can pick up low concentrations of electron-deficient antibiotics from a model of hospital wastewater. An iMOF-4A-based mixed-matrix membrane has been designed and implemented to reproduce real-time antibiotic detection in water.

(Manuscript under refinement)

Efficient Recognition and Capture of Specific Toxic Organic Pollutants Using Water-Stable Highly Luminescent Anionic Metal-organic framework

Y.D. More, S. Fajal, D. Majumdar, S. Mollick, S. Dutta, M.M. Shirolkar, S. Saurabh, W. Mandal, S. K. Ghosh.

Part-II: Advanced Porous Materials for Energy Applications

Fossil fuels are used as an energy source on a global scale, which harms the environment and reduces their supply for future generations. As a result, there has been a greater reliance on renewable energy sources. While wind and solar energy have likely received the most attention, mechanical energy and other sources have received less. Historically, energy from mechanical (vibrational, translational...) motions such as human motion, wind, and tidal energy (water currents) has been largely wasted and ignored. Fortunately, the scientific community is starting to recognise alternative energy sources as part of the solution to the world's escalating energy-related problems. Mechanical energy conversion technologies have advanced significantly over the last ten years, particularly in the fields of wearable electronics, high-precision sensors, portable high-voltage sources, and distributed micro/nano-power sources. At the heart of this advancement are Triboelectric Nanogenerators (TENGs), which rely on the idea of charge separation achieved by relative motion between two disparate materials in close proximity—the process is expressed by the widely understood phenomena of friction. The "triboelectric series" depicts the differences in materials' ability to transfer or absorb electrons when they are in close proximity to one another. To achieve maximum power output, materials further apart in this series are

used as partners in a TENG device. The ability of the design to facilitate charge transfer is heavily influenced by how the device is configured. This section is split into two Chapters, 4 and 5. We used a highly stable MOF in Chapter 4 for a repeatable, robust, and tuneable application in the domain of Triboelectric Nanogenerators (TENG), whereas in Chapter 5, we used a chemically stable, solution processable, and hydrophobicity tuned series of MOPs blended by Polymer composites as a maiden example for on-demand self-powered energy devices, highlighting a maiden example in the domain of MOP derived TENGs with efficient power output.

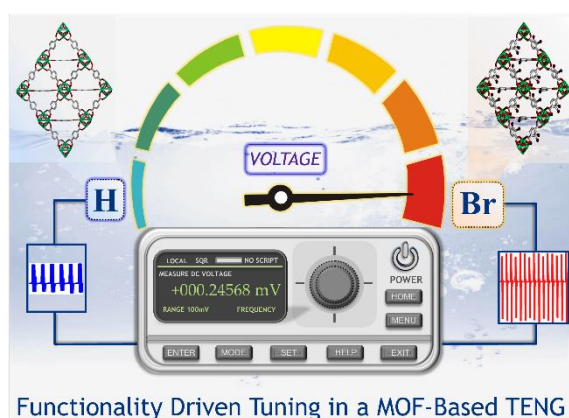
Chapter 4. Highly Stable and End-Group Tuneable Metal-organic Framework / polymer composite for Superior Triboelectric Nanogenerator Application

This Chapter presented the maiden example of functional group (end group) tuned triboelectric output from MOF-Polymer composite. On-demand harvesting of operating power from the dynamic work environment is appealing for self-powered unattended electronics and electro-mechanics. Dynamic workplaces can be utilized to provide this power. This category includes the intriguing triboelectric Nanogenerator (TENG). It harvests mechanical energy lost in various workplaces. A typical TENG device uses two flexible, triboelectric series materials to separate charge carriers in response to mechanical energy stimuli. TENGs still lack performance tunability, modulatory electronic effects of constituents, and stability features for adverse and ambient working environments. Essentially, TENGs fail to meet these practical demands despite their flyweight-compactness, cost efficiency, high output, and variety of device materials. In this regard, Metal-organic frameworks (MOFs) is a choice of material that can optimise energy conversion due to their molecular tunability. We investigated the underexplored MOF subfamily UiO-66(Zr) (UiO: University of Oslo) to determine how synthetic tuning affects TENG output. UiO-66-X/PVDF (PVDF: Polyvinylidene difluoride) composites for TENG output amplification are designed and tuned using a prototype hybridization method that tunes organic ligand chemistry in isostructural Zr-MOFs. UiO-66-X/PVDF composites (X = H and Br) had excellent aquatic, thermal, and TENG power properties in addition to their MOF properties. Its underlying mechanism was studied. A functionalized 1,4-benzenedicarboxylic acid (H₂BDC) linker tuned MOF electron withdrawing (EW) effect. Surface roughness and composite potential seemingly improved. The UiO-66-Br encased in a PVDF matrix's resulted into significant charge augmentation causing higher TENG performance due to increased electrification. Computational mechanistic studies support observations. Energy harvesters use contact electrification and electrostatic induction. Its durability and vertical contact-separation mode allow it to recover wasted energy. Functionalized TENG-2 provided 110.41 V_{p-p} output open circuit voltage and when compared to non-functionalized TENG-1 and PVDF film, this improved output of TENG-2 upto 2.92 and 14.12 times, respectively. The research includes a first-of-its-kind example of

ligand-mediated functional group-driven performance tuning of TENG and a mechanistic understanding achieved through strategic use of isostructural MOFs that use high-performance UiO-66/PVDF composites, by rationally comparing and correlating observations bound results, since functional group or halogen group is only embedded or modulated, hence such a halogen mediated alteration is expected to tune or alter the result.

Reference:

Y. D. More, S. Saurabh, S. Mollick, S. K. Singh, S. Dutta, S. Fajal, A. Prathamshetti, M. M. Shirolkar, S. Panchal, M. Wable, S. Ogale, S. K. Ghosh, *Adv. Mater. Interfaces* **2022**, 2201713.



Chapter 5. Surface Feature Tuned Metal-organic Polyhedra for Triboelectric Nanogenerator: Self-Powered Sensors for Wearable Electronics

In one of our notable works mentioned herein, we deployed our previously published series of Metal-organic Polyhedra (MOPs)¹³, namely IPMOP-n (n = I, II, III, IV, i.e., IPMOP-A, IPMOP-PA, IPMOP-IL, IPMOP-V), for strategic application in Triboelectric Nanogenerators (TENG) due to its incremental hydrophobicity and its subsequent effect on triboelectric output in this Chapter. This was a novel discovery about the charge building process at the interface of polymer/MOP composites. Because of their miscibility in various organic solvents, crystalline porous materials such as MOP show significant potential for a wide range of applications and are suited for solution processing. Despite the fact that MOPs and MOFs have similar intrinsic porosities and physicochemical properties, the utilization of carboxylate MOPs is limited due to a lack of chemical stability. To take advantage of the benefits of their combined properties, a series of cages known for their a priori methodology for fabricating chemically resistant carboxylate MOPs via outer-surface functionalization were used in conjunction with a blend of suitable compositing polymers to stabilize MOP systems with weak metal-ligand bonds. These MOPs were carefully selected for their stability characteristics, which include resilience to a wide pH range,

stability in extremely acidic conditions, and in oxidizing and reducing media, which has been minimized by tuneable hydrophobic shielding. Molecular modelling studies back up these conclusions. A prototype method for chemically stable MOPs is described, in which the shift from an unstable to a chemically ultra-stable phase was accomplished by undertaking a fast gram-scale synthesis at room temperature (within seconds). These MOPs were rationally used in the manufacture of MOP/PVDF composites at various blending concentrations, and they were produced into flexible thin films using drop-casting, doctor blading, and electrospinning processes. All of these films were moulded into tiny, light-weight, and compact TENG devices. Because of the steady increase in hydrophobicity caused by shielding by alkyl and aryl groups, the devices displayed triboelectric output at very low optimal concentrations in the order of IPMOPs, as IPMOP-A, IPMOP-V, IPMOP-PA, and IPMOP-IL. A simultaneous increase in power density was seen at 201.66 mW/m², 552.8 mW/m², 1095.5 mW/m², and 513 mW/m². The chosen devices, namely IPMOP-IL/PVDF@5%, were then submitted to real-time tests, yielding stability, recyclability, and exceptional application display in power storage in batteries and capacitors, real-time LED, and mobile and medium-range electronic charging. In addition to being the maiden report in the cage-based TENG realm with such exceptional electric output attributes, the materials solution processability facilitates the generation of foldable self-charging devices as well as lighter and more durable self-powered goods (outfits).

(Manuscript under refinement)

Surface Feature Tuned Metal-organic Polyhedra for Triboelectric Nanogenerator: Self-Powered Sensors for Wearable Electronics

Y.D. More, S. Mollick, S. Saurabh, S. Dutta, A. Shetty, M.M. Shirolkar, S. B. Ogale, S. K. Ghosh.

Chapter 6. Summary and Perspectives

In conclusion, there has been presented a brief overview of the insights gained through the cautious application of anionic MOFs and various functional porous materials in aqueous pollutant remediation and energy-related applications. The systematic design, synthesis, and functional research of anionic MOFs are the main objectives of this work since they hold the greatest promise for resolving difficult environmental pollution concerns and reducing the necessity for sustainable energy. The role of counter cations (both inorganic and organic cations) in pore-engineered and trap-grafted functional anionic MOFs to steer the structure-property correlation for specific purposes has been reviewed. The results of this thesis's research into anionic MOFs for rapid sensing, efficient capture, and consequent sequestration of aqueous and environmental pollutants, as well as novel approaches to device fabrication and structure property correlation for energy application, have been discussed in light of the state-of-the-art investigations. Next-generation ionic materials could be developed in the near future to address important

industrial and environmental concerns, and studies based on functional MOFs and porous materials for sustainable energy-environment applications and water pollution remediation could pave the way.

Abbreviations

Anal.	Analysis / Unit / Test / Compound
AFM	Atomic Force Microscopy
Calc.	Calculated
CCDC	Cambridge Crystallographic Data Centre
DMF	N,N'-dimethylformamide
DCM	Dichloromethane
EtOH	Ethanol
EDX	Energy Dispersive X-ray Analysis
FE-SEM	Field Emission Scanning Electron Microscopy
FTIR	Fourier transform infra-red spectroscopy
g	Gram
ICP-AES	Inductively Coupled Plasma Atomic Emission Spectroscopy
ICP-MS	Inductively Coupled Plasma Mass Spectroscopy
iMOF	Ionic Metal Organic Framework
IPMOP-A	IISER Pune Metal-organic Polyhedra-Alanine
IPMOP-IL	IISER Pune Metal-organic Polyhedra-Iso-Leucine
IPMOP-PA	IISER Pune Metal-organic Polyhedra-Phenyl Alanine
IPMOP-V	IISER Pune Metal-organic Polyhedra-Valine
ITC	Isothermal Titration Calorimetry
KPFM	Kelvin Probe Force Microscopy
MeOH	Methanol
MOP	Metal-organic Polyhedra
mg	Milligram
min	Minutes
mL	Milliliter
mM	Millimolar
mmol	Millimoles
mW	Milliwatt

MOF	Metal-Organic Framework
MeCN	Acetonitrile
cMOF	Cationic Metal-Organic Framework
iMOF	Ionic Metal-Organic Framework
NG	Nanogenerator
NMR	Nuclear Magnetic Resonance
Nano-FTIR	Infrared Nearfield Nanospectroscopy
PCP	Porous Coordination Polymer
PXRD	Powder X-Ray Diffraction
RT	Room Temperature
SCXRD	Single-Crystal X-Ray Diffraction
TENG	Triboelectric Nanogenerator
TGA	Thermogravimetric Analysis
TFM	Tip-Force Microscopy
UV	Ultraviolet
V	Voltage
V_{avg}	Average Voltage
V_p	Peak Voltage
V_{p-p}	Peak to Peak Voltage
V_{rms}	Root Mean Square Voltage
W	Watt

Research Publications

(† - indicates equal contribution, publications arranged in descending order of publication date)

Included in Thesis:

1. Highly Stable and End-Group Tuneable Metal-organic Framework UiO-66/PVDF Composite for Superior Triboelectric Nanogenerator Application.
Yogeshwar D. More, Satyam Saurabh, Samraj Mollick, Sachin Kumar Singh, Subhajit Dutta, Sahel Fajal, Anil Prathamshetti, Mandar M. Shirolkar, Suresh Panchal, Minal Wable, Satishchandra Ogale, and Sujit K. Ghosh.
Adv. Mater. Interfaces **2022**, 2201713.
2. Luminescent Metal-Organic Frameworks as Chemical Sensors (Book Chapter).
Yogeshwar D. More, Sahel Fajal, Subhajit Dutta and Sujit K. Ghosh.
CRC Press, **2022**.
3. Ionic Metal-Organic Frameworks (iMOFs): Progress and Prospects as Ionic Functional Materials. Subhajit Dutta,† **Yogeshwar D. More**,† Sahel Fajal, Writakshi Mandal, Gourab K. Dam and Sujit K. Ghosh.
Chem. Commun. **2022** (DOI: 10.1039/D2CC05131A).
4. Trap Grafting in Anionic MOF for Superior Uranium Extraction from Seawater.
Yogeshwar D. More, Samraj Mollick, Satyam Saurabh, Sahel Fajal, Michele Tricarico, Subhajit Dutta, Mandar M. Shirolkar, Writakshi Mandal, Jin-Chong Tan and Sujit K. Ghosh.
(Manuscript under revision)
5. Efficient Recognition and Capture of Specific Toxic Organic Pollutants Using Water-Stable Highly Luminescent Anionic Metal-organic framework.
Yogeshwar D. More, Sahel Fajal, Dipanjan Majumdar, Samraj Mollick, Satyam Saurabh, Subhajit Dutta, Mandar M. Shirolkar, Writakshi Mandal, and Sujit K. Ghosh.
(Manuscript under refinement).
6. Surface Feature Tuned Metal-organic Polyhedra for Triboelectric Nanogenerator: Self-Powered Sensors for Wearable Electronics.
Yogeshwar D. More, Samraj Mollick, Satyam Saurabh, Sahel Fajal, Michele Tricarico, Subhajit Dutta, Mandar M. Shirolkar, Jin-Chong Tan, Satishchandra Ogale and Sujit K. Ghosh.
(Manuscript under refinement)

Not Included in Thesis:

7. Benchmark Uranium Extraction from Seawater using an Ionic Macroporous Metal-organic Framework.
Samraj Mollick, Satyam Saurabh,† **Yogeshwar D. More**, † Sahel Fajal, Mandar M. Shirolkar,

- Writakshi Mandala and Sujit K. Ghosh.
Energy Environ. Sci., **2022**, *15*, 3462–3469.
8. Trap Inlaid Cationic Hybrid Composite Material for Efficient Segregation of Toxic Chemicals from Water.
Sahel Fajal, Writakshi Mandal, Samraj Mollick,[†] **Yogeshwar D. More**,[†] Arun Torris, Satyam Saurabh, Mandar M. Shirolkar, and Sujit K. Ghosh.
Angew. Chem.Int. Ed. **2022**, *61*, e2022033.
9. Selective and Sensitive Recognition of Specific Types of Toxic Organic Pollutants with a Chemically Stable Highly Luminescent Porous Organic Polymer (POP).
Writakshi Mandal, Sahel Fajal, Partha Samanta, Subhajit Dutta, Mandar M. Shirolkar, **Yogeshwar D. More**, and Sujit K. Ghosh.
ACS Appl. Polym. Mater. **2022**. (DOI: 10.1021/acsapm.2c01538)
10. Unveiling the Impact of Diverse Morphology of Ionic Porous Organic Polymers with Mechanistic Insight on the Ultrafast and Selective Removal of Toxic Pollutants from Water.
Writakshi Mandal, Sahel Fajal, Samraj Mollick, Mandar M. Shirolkar, **Yogeshwar D. More**, Satyam Saurabh, Debanjan Mahato, and Sujit K. Ghosh.
ACS Appl. Mater. Interfaces **2022**, *14*, 20042–20052.
11. Unfolding the Role of Building Units of MOFs with Mechanistic Insight Towards Selective Metal Ions Detection in Water.
Sahel Fajal,[†] Writakshi Mandal,[†] Dipanjan Majumder, Mandar M. Shirolkar, **Yogeshwar D. More**, and Sujit K. Ghosh.
Chem. Eur. J. **2022**, *28*, e2021041.
12. Post-synthetically modified metal–organic frameworks for sensing and capture of water pollutants.
Soumya Mukherjee,[†] Subhajit Dutta,[†] **Yogeshwar D. More**, Sahel Fajal and Sujit K. Ghosh.
Dalton Trans., **2021**, *50*, 17832–17850.
13. Hydrophobic Shielding of Outer Surface: Enhancing the Chemical Stability of Metal–organic Polyhedra.
Samraj Mollick, Soumya Mukherjee, Dongwook Kim, Zhiwei Qiao, Aamod V. Desai, Rajat Saha, **Yogeshwar D. More**, Jianwen Jiang, Myoung Soo Lah and Sujit K. Ghosh.
Angew. Chem. Int. Ed. **2019**, *58*, 1041–1045.
14. A luminescent cationic MOF for bimodal recognition of chromium and arsenic based oxo-anions in water.
Subhajit Dutta, Sumanta Let, Mandar M. Shirolkar, Aamod V. Desai, Partha Samanta, Sahel Fajal, **Yogeshwar D. More** and Sujit K. Ghosh.

- Dalton Trans.*, **2021**, *50*, 10133-10141.
15. A silver nanoparticle-anchored UiO-66(Zr) metal-organic framework (MOF)-based capacitive H₂S gas sensor
Sandeep G. Surya,[†] Sreenu Bhanoth,[†] Sanjit M. Majhi, **Yogeshwar D. More**, V. Mani Tejaa and Karumbaiah N. Chappanda.
CrystEngComm, **2019**, *21*, 7303–7312.
16. A Bifunctional Metal–Organic Framework: Striking CO₂-Selective Sorption Features along with Guest-Induced Tuning of Luminescence.
Soumya Mukherjee, Aamod V. Desai, **Yogeshwar D. More**, Arif I. Inamdar and Sujit K. Ghosh.
ChemPlusChem, **2016**, *81*, 702–707.
17. Seed Power: Natural Seed and Electrospun Poly(vinyl difluoride) (PVDF) Nanofiber Based Triboelectric Nanogenerators with High Output Power Density.
Sachin Kumar Singh,[†] Piyush Kumar,[‡] Rushikesh Magdum,[‡] Utkarsh Khandelwal,[‡] Swati Deswal,[†] **Yogeshwar More**,[†] Subas Muduli,[‡] Ramamoorthy Boomishankar,[†] Sagar Pandit,^{*,§} and Satishchandra Ogale*.
ACS Appl. Bio Mater. **2019**, *2*, 3164.
18. Unveiling the Metal-node Mediated Triboelectric Output Tuning and Mechanistic Relevance in Isostructural series of iMOFs.
Yogeshwar D. More, Samraj Mollick,[†] Satyam Saurabh,[†] Subhajit Dutta, Mandar M. Shirolkar, Satishchandra Ogale and Sujit K. Ghosh.
(Manuscript under refinement)
19. Unveiling the Metal-node Mediated Triboelectric Output Tuning and Mechanistic Relevance in Isostructural series of iMOFs.
Yogeshwar D. More, Samraj Mollick,[†] Satyam Saurabh,[†] Subhajit Dutta, Mandar M. Shirolkar, Satishchandra Ogale and Sujit K. Ghosh.
(Manuscript under refinement)
20. A Lewis Basic Sites Endowed Ultramicroporous Anionic MOF for Dual Adsorption Selectivity Performance.
Yogeshwar D. More, Samraj Mollick,[†] Subhajit Dutta, [†] Soumya Mukherjee, Mandar M. Shirolkar, Satishchandra Ogale and Sujit K. Ghosh.
(Manuscript under refinement)
21. Selectivity Driven Adsorptive Separation of C₂H₂ across an Isoreticular Family of Anionic MOFs
Yogeshwar D. More, Samraj Mollick,[†] Subhajit Dutta, [†] Mandar M. Shirolkar, Satishchandra Ogale and Sujit K. Ghosh. *(Manuscript under refinement)*

Rights and Permissions

Chapter 1:

Minor portion / figure of it reprinted (adapted) with permission from a) *Chem. Commun.* **2022**, 58, 13676., <https://doi.org/10.1039/D2CC05131A>. Copyright: © 2022 Royal Society of Chemistry; b) *J. Am. Chem. Soc.* **2009**, 131, 8376. <https://doi.org/10.1021/ja902972w>. Copyright: © 2009, American Chemical Society. c) *Angew.Chem.Int.Ed.* **2019**, 58, 1041. <https://doi.org/10.1002/anie.201811037>. Copyright © 2019 Wiley-VCH Verlag GmbH & Co. KGaA, Weinheim. d) *Adv. Mater. Interfaces* **2022**, 2201713. <https://doi.org/10.1002/admi.202201713>. Copyright: © 2022 Wiley-VCH GmbH. e) *Angew.Chem.Int.Ed.* **2016**, 55, 7811. <https://doi.org/10.1002/anie.201600185>. Copyright: © 2016 WILEY-VCH Verlag GmbH & Co. KGaA, Weinheim.

Chapter 4:

Reprinted (adapted) with permission from *Adv. Mater. Interfaces* **2022**, 2201713. <https://doi.org/10.1002/admi.202201713>. Copyright: © 2022 Wiley-VCH GmbH.

Chapter 5:

Minor portion / figure of it reprinted (adapted) with permission from *Angew.Chem.Int.Ed.* **2019**, 58, 1041. <https://doi.org/10.1002/anie.201811037>. Copyright: © 2019 Wiley-VCH Verlag GmbH & Co. KGaA, Weinheim.

*Electronic copy of thesis contains all the rights and permissions / license agreement files compiled at the end of thesis.

Thesis Chapters...

Chapter 1

Introduction

1. Introduction

1.1 Metal-organic frameworks (MOFs):

In the past few decades, the field of porous materials has experienced a parabolic boom throughout the scientific community as a result of its vast applicability across a range of fields and spectrum of applications. The reason for this surge is due to the fact that porous materials demonstrated potential that enables them for being deployed in variety of fields.¹ Amongst its sub-classes, metal-organic frameworks (MOFs) or porous coordination polymers (PCPs) have emerged as a new research hotspot due to their enormous potential as next-generation inorganic-organic hybrid materials. This is due to the fact that MOFs and PCPs are both porous coordination polymers can be made of from numerous plausible combinations of ligands and metal ions that are chosen in regards with their desired applications.² MOFs are solid-state porous crystalline materials that include the possibility for voids. They are made from bi- or multi-dentate organic struts that stretch indefinitely via metal nodes in a periodic way to form a framework structure (Figure 1.1). In most cases, the solvent molecules, counter ions, and unreacted ligands will continue to occupy the vacant space that is included within the framework after the synthesis process has been completed.³ According to the size of the pore-aperture, MOFs can be broadly categorised into three groups: ultramicroporous MOFs (pore size 0.7 nm), microporous MOFs (pore size 2 nm), and mesoporous MOFs (pore size > 2 nm). The freedom to design and create MOFs on demand, using a wide variety of organic ligands and metal cations as building blocks, is a significant advantage.

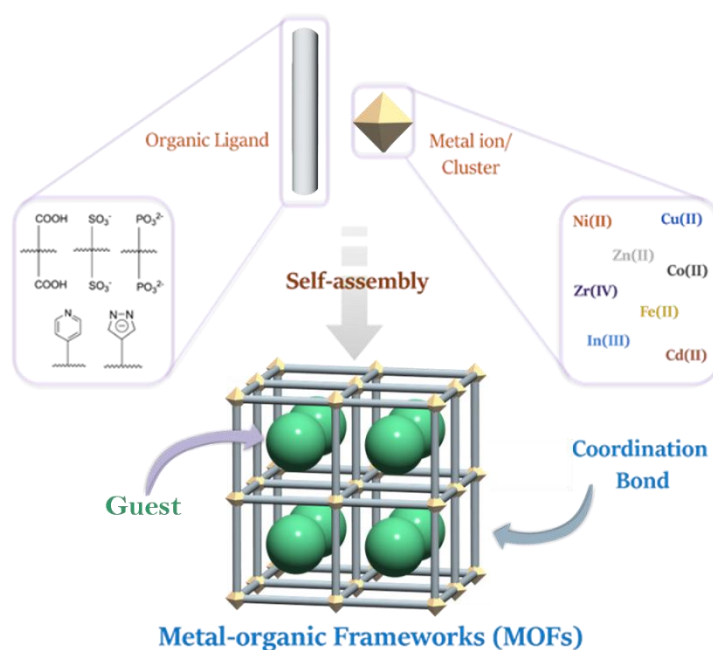


Figure 1.1 Schematic representation illustrating general protocol to synthesize metal-organic frameworks (MOFs).

Likelihood of limitless permutations of networked structures that have been demonstrated to be industry leaders and choice of materials for material scientists in a variety of domains, including gas adsorption, sensing, ion conduction, catalysis, environmental pollutant capture, drug-delivery, and others. The freedom to design and create MOFs on demand, using a wide variety of organic ligands and metal cations as building blocks, is of a significant advantage.⁴⁻⁸

1.1.1 Components of MOFs:

In most cases, several varieties of organic ligand systems and 3d transition metal cations are required to successfully construct MOFs. The 3d transition metal cations are the favored choice besides 4d transition metal cations (ex. Zr(IV)). The selection of these first row transition metal cations has unquestionably become vital as a result of the variety of benefits that they offer. For instance, Fe(II) can impart magnetic properties, while Zn(II) or Cd(II) [d^{10} cations] can impart fluorescence capabilities in the system. On the other hand, the incorporation of particular metal ions, such as the Zn(II) cation (for dynamic coordination sphere) and the Cu(II) cation (for Jahn-Teller distortion), has shown some promise in the development of dynamic MOFs, whereas 4d transition metal ions such as Zr(IV) offer excellent chemical and water stability features.⁹⁻¹⁴ In the quest to create novel materials, achieving chemical stability has emerged as a significant obstacle. This is true not only in terms of the synthesis of compounds, but also in terms of their subsequent application in real time. When it comes to MOFs, the framework stability is closely associated with the strength of the metal-ligand bond. This highlights the necessity of making an informed choice of the metal cations during the design and synthesis of MOFs.¹⁵⁻¹⁸ On the other hand, the library of organic ligands is made up of a wide variety of functionalities, both in terms of the nature of the terminal binding moieties and the nature of the core or backbone of the organic ligands themselves.¹⁹⁻²¹

Organic ligands can be divided into two broad categories: (a) oxygen-donor ligands, such as carboxylates (R-COOH), sulfonates (R-SO₃H), phosphonates (R-PO(OH)₂), and so on; and (ii) nitrogen-donor ligands, which contain N-heterocyclic aromatic groups as terminal binding units (pyridine, imidazole, triazole, adenine, pyrazine etc.). Because of their potent ability to bind with the majority of metal cations, carboxylate-based ligands have been used for the synthesis of the majority of MOFs ever since the invention of MOFs. This is why MOFs are called metal-organic frameworks. On the other hand, despite the fact that N-donor ligands are frequently used as the co-ligand in conjunction with carboxylate-terminal linkers, the field of standalone MOFs constructed from N-donor ligands has not been thoroughly researched.²²⁻²⁵ In addition, N-donor ligands can be divided into two broad categories, namely (i) neutral ligands and (ii) ionic

ligands, according to the charge that they carry. Because of their higher pK_a values, ionic N-donor linkers with N-heterocyclic aromatic groups like pyrazolate, imidazolate, tetrazolate, etc. are able to form strong coordination bonds with the metal center, which in turn imparts a higher resistance to hydrolysis. In most cases, neutral N-donor moieties have been utilized for the synthesis of cationic MOFs. These neutral N-donor moieties, which include imidazole, pyridine, triazole, and others, are then used as co-ligands to either increase the porosity of the MOF or provide additional functional sites. N-donor ligand-based MOFs are catching up with potential solutions in a number of fields, despite the fact that O-donor ligand-based MOFs are becoming more popular in the field of MOF and have been studied for a number of applications. This is despite the fact that N-donor ligand-based MOFs are catching up.

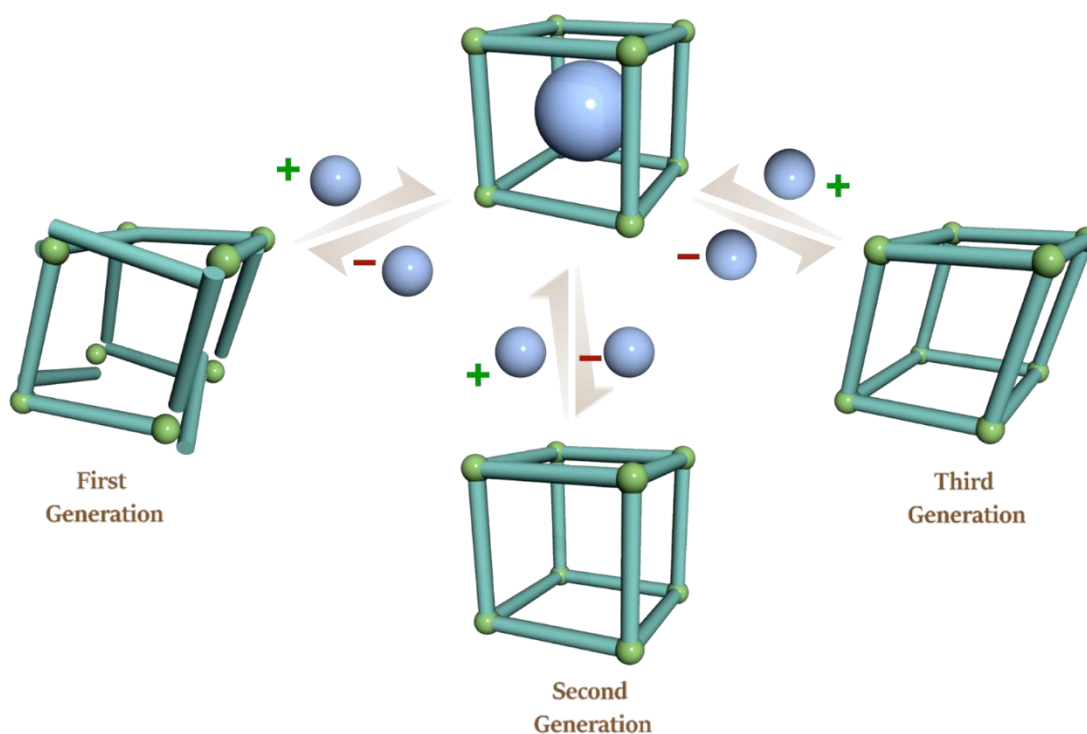


Figure 1.2 Classification MOFs by their generation evolution; outcome after the evacuation of guest molecules.

1.1.2 Types of MOFs:

1.1.2.1 Classification of MOFs Based on Structural Aspect:

The removal or desolvation of occluded guest (solvent or solute) from the voids of the MOF is known to, in most cases, result in a change in the structural rigidity of the MOF. On the basis of this, MOFs can be

grouped in a broad way into three generations (Figure 1.2).²⁶ When the solvent molecules are removed from the first generation of metal-organic frameworks (MOFs), it is well known that the framework completely disintegrates. After the elimination of guests, the MOFs of the second generation are recognized for being robust and maintaining their structural integrity. The third generation of MOFs are known as the dynamic MOFs because they are able to change their structural rigidity when a guest is removed from the system and can return to their early phase when an antagonistic stimulus is applied to MOFs.

1.1.2.2 Classification of MOFs Rendered by Charge: Neutral MOFs and Ionic-MOFs:

Aside from their structures, metal-organic frameworks (MOFs) are typically divided into two categories: neutral MOFs and ionic MOFs. These categories are determined by the residual charge of the framework backbone (Figure 1.3).²⁷⁻²⁸ When it comes to neutral MOFs, the positive charge of the metal center is typically neutralized by a variety of charge-balancing moieties, like negatively charged coordinating linkers or the negative charge of the counter anions. In other words, the positive charge of the metal center is compensated.

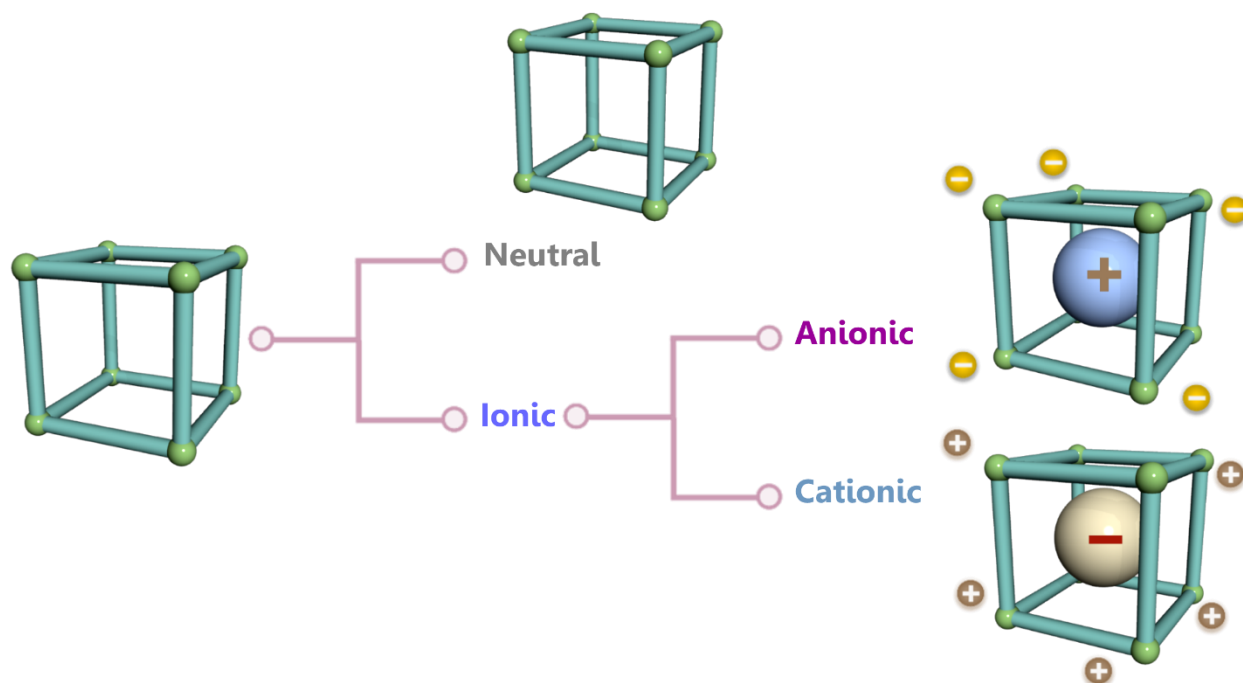


Figure 1.3 Classification of MOFs on the basis of the charge of the framework backbone.

On the other hand, the framework backbone of ionic MOFs (iMOFs) has a residual unbalanced charge (positive or negative), which results in either cationic or anionic frameworks with some additional

framework counter-ions. The construction of ionic or neutral MOFs can be accomplished through the use of a variety of methods, and the synthetic procedures are steered by the underlying principles of coordination chemistry. These fundamentals explicitly emphasize the substantial role that is played by the selection of organic linkers and metal ions in MOF synthesis.

1.1.2.2a Neutral MOFs:

A clear predominance of published electronically neutral MOFs has been seen in the MOF literature. This type of MOF has positive charges on its metal center that are completely balanced through coordinating moieties, because then the MOF is considered to be electronically neutral. In scenarios like these, the electronic charge is neutralized by anionic linkers (chiefly carboxylate-based ligands) or negatively charged counter anions of the metal salts that are coordinated to a central metal ion (Figure 1.4a).²⁹⁻³¹

1.1.2.2b Ionic MOFs:

In most cases, the formation of ionic MOFs is caused by the existence of an unbalanced framework charge. As a result, these MOFs need additional framework ions, which can either be negative or positive, in order to keep the overall charge balanced or neutral. Ionic MOFs can be split into two categories: anionic and cationic MOFs, depending on the type of residual charge that is carried by the framework backbone. The uncoordinated anions that are found inside the voids of cationic MOFs act to balance the framework backbone's net positive charge, which is generated by the cationic MOF's positive charge.

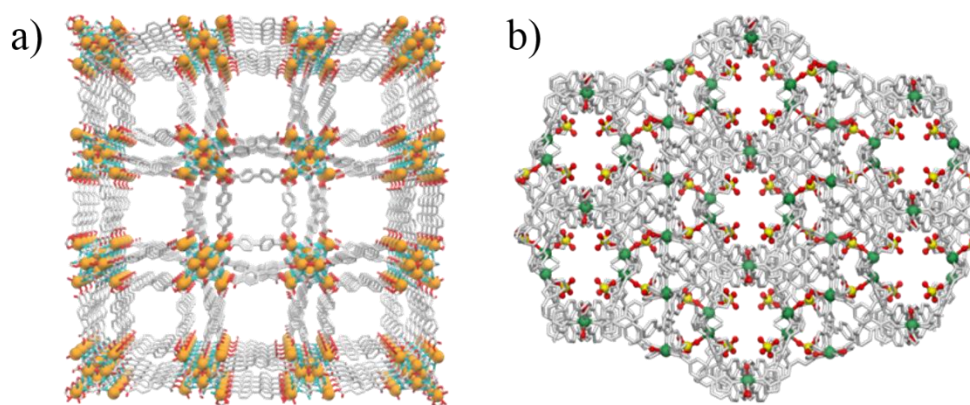


Figure 1.4 3D Packing diagrams revealing type of charge on the backbone of the framework: a) anionic MOF, and b) cationic MOF. The data on crystal structures that relates to reported literature have been reproduced with the permission (colour codes: C, grey; O, red; N, blue; Zr, navy blue; Zn, yellow; Ni, dark green). H-atoms have been left out to retain clarity.

In the case of anionic MOFs, the backbone of the framework carries a remnant anionic charge, which is compensated out by the uncoordinated cations (Figure 1.4b-1.4c). The free counter-ions provide additional ionic functionality, which has been discovered to be exceedingly suitable for a variety of uses. Despite the fact that the partial occupation of uncoordinated ions may result in the obstructing of pores and, as a result, a complete lack of access to the surface area.³²⁻³⁴

1.1.2.2b.1 Strategic Outlook for of iMOFs:

Despite the fact that ionic MOFs offer intrinsically charged networks for the reception of counter-ionic species, the synthetic techniques for target-specific applications are not easy to implement since they lack systematic methodical advancements. In order to successfully introduce ionicity into these MOFs, it is essential to have contributions from both functional organic ligands and metal ions or clusters.²⁶ In addition, because of the charge-induced dipoles that are naturally present in ionic MOFs, certain applications are possible with these materials that are not possible with neutral MOFs. This distinguishes ionic MOFs as a significant and one-of-a-kind class of porous materials. In the following sections, a more in-depth discussion of the role that metal ions and organic ligands play in the synthesis of ionic MOFs as well as the distinctive applications of these materials will be presented.

1.1.2.2b.2 Anionic MOFs:

The primary component of an anionic metal–organic framework (MOF) is a framework backbone bearing negatively charge, while it also contains additional uncoordinated countering cations to balance out the total charge. Anionic metal-organic frameworks are typically constructed using metal cations that have greater coordination numbers. These frameworks produce more ionic character as a result of the increased number of organic ligands that concentrate around the metal nodes. When this transpires, the chemical stability of the molecule improves because the central metal nodes can better shielded by the larger proportion of ligands.³⁵⁻³⁸ constructing anionic metal–organic frameworks (MOFs) is difficult since the majority of the steps involved are unintentional. N, N-dimethylacetamide (DMA), N, N-diethyl formamide (DEF), and N, N-dimethylformamide (DMF), among other organic solvents, can undergo hydrolysis as well as subsequent decarbonylation in hydrothermal or solvothermal method conditions and can produce $[\text{NH}_2\text{Et}_2]^+$ or $[\text{NH}_2\text{Me}_2]^+$ cations, which results in the formation of anionic frameworks. Nowadays, this understanding is deliberately employed to get these cations within the framework intentionally. However, this process is only possible with a small number of organic solvents (Figure 1.5).³⁵⁻³⁸

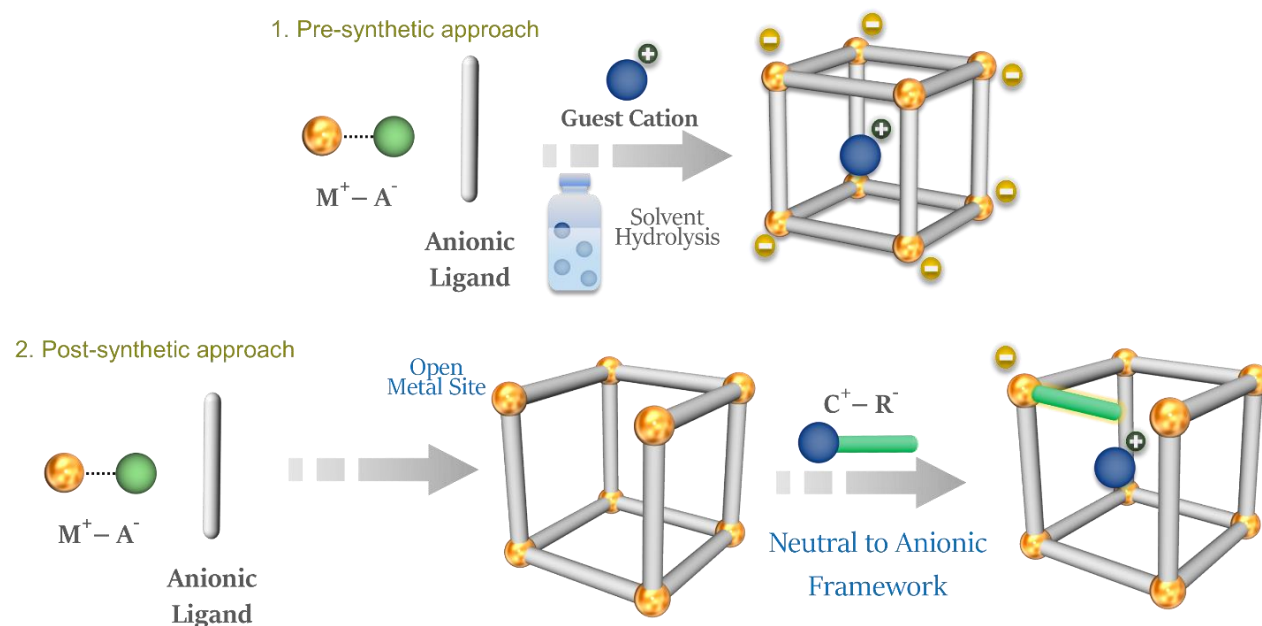


Figure 1.5 Schematic representation of routes to synthesize anionic MOFs via pre-synthetic and post-synthetic methods (reproduced with the permission).

1.1.2.2b.3 Design Strategies and Fabrication of Functional Anionic MOFs:

Considering the fact that the production of anionic frameworks typically occurs by chance, the rational design of anionic metal–organic frameworks (MOFs) has proven to be a difficult problem for researchers. N, N-dimethylacetamide (DMA), N, N-diethylformamide (DEF), and N, N-dimethylformamide (DMF), among other organic solvents, can undergo hydrolysis and subsequent decarbonylation in solvothermal conditions to generate $[NH_2Et_2]^+$ or $[NH_2Me_2]^+$ cations, which result in the generation of anionic frameworks. However, this process is only possible with a limited number of organic solvent. In their ground-breaking research, Rosi and colleagues showed that the well-known anionic MOF bio-MOF-1 ($Zn_8(ad)_4(BPDC)_6 \cdot 0.2Me_2NH_2 \cdot 8DMF \cdot 11H_2O$) included free $[NH_2Me_2]^+$ cations within the pores. These cations are formed in-situ under specific solvent and conditions such as temperature.³⁹ By employing the approach of decomposing organic solvents like DMF, DMA, or DEF, amongst others, in order to generate the counter cations within the MOFs, researchers have been successful in obtaining a number of anionic MOFs.^{40–42} Millange and his colleagues discovered a solid material of the MOF type that had either a standard Fe^{III}/Fe^{II} charge order or a $Fe^{III}0.5Fe^{II}$ charge order.⁴³ Single crystal X-ray diffractions, often known as SC-XRD examinations, provided additional evidence that proved the existence of counter DMA cations. The synthesis and development of a series of microporous anionic MOFs possessing (3,4)-connected C_3N_4 -type framework $[In_3(btc)_4]_n^{3n-}$ was demonstrated in another report that was published in

2009. This report was the result of a collaborative effort between Feng, Bu, and other co-workers.⁴⁴ They have demonstrated that anionic MOF can be prepared under a variety of synthetic conditions, including the following: i) the use of solvothermal decarbonylation of solvents such as triethanolamine (TEOA), DMF, DEF, etc.; ii) the presence of an ionic liquid known as tris(2-hydroxyethyl)methylammonium methylsulfate (TEMA Ms); and iii) a deep eutectic solvent. A further essential pre-synthetic technique for the design and synthesis of anionic metal–organic frameworks (MOFs) is the utilization of charged secondary building units (SBUs). Eddaoudi and colleagues have reported the creation of many anionic MOFs through the utilisation of anionic SBUs in this line of research.^{45,46} A study on an isostructural series of anionic MOFs with *scu* topology was published in 2012 by Zhang and co-workers. The series in question is called $[\text{Me}_2\text{NH}_2]\text{-}[\text{M}_2(\text{bptc})(\mu^3\text{-OH})(\text{H}_2\text{O})_2]$.⁴⁷ An organic linker known as bptc (3,3',4,4'-biphenyltetracarboxylic acid) and a tetranuclear butterfly-like $[\text{M}_4(\text{OH})_2]$ cluster were used to create each and every one of the anionic MOFs. Feng and his colleagues developed a general strategy for achieving varied charges of anionic, cationic, and neutral in In-SBUs by varying the ratio of In^{3+} ions and the organic linker (2,5-furandicarboxylic acid). This was done in order to create the desired charge profile.⁴⁸ In addition, it was discovered that the differentially charged SBUs had a direct influence on the final charges on the overall frameworks, which led to the formation of negatively charged, positively charged, and neutral MOFs.

Post-synthetic modification, often known as PSM methods, are recognized as an effective technique of functionalizing MOFs, in addition to the pre-synthetic approach. In a pioneering work, Long and co-workers presented an approach for implanting LiO^iPr into a neutral MOF, specifically $\text{Mg}_2(\text{DOBDC})$, using PSM in order to transform it to an anionic MOF. This strategy was used to convert $\text{Mg}_2(\text{DOBDC})$.⁴⁹ Because $\text{Mg}_2(\text{DOBDC})$ include Mg^{2+} open metal sites (OMS), the inbound alkoxide anions are able to coordinate to the unsaturated metal centers. This leads to the creation of the anionic framework, which contains the free Li^+ cations as counter ions inside the one-dimensional channels. A chemically stable neutral MOF (UiO-66) was converted into an anionic MOF in 2013 by the same research group using a similar technique. This transformation was accomplished by grafting lithium tert-butoxide (LiOtBu) into the framework. The result was an anionic MOF.⁵⁰ The dehydration of UiO-66 resulted in the formation of unsaturated Zr^{4+} sites. Subsequently, during the PSM, the incoming OtBu^- anions were coordinated to the metal centers, resulting in the formation of an anionic framework with said counter Li^+ cations contained within the pores of framework.

1.1.2.2b.4 Advantages of Anionic MOFs:

The presence of polarizable counter-ions in anionic MOFs confers an added advantage because it makes it possible for ion-exchange activities to take place during the incorporation of a variety of anionic species

into its framework. This freedom of counter ion exchange makes it possible to design and fabricate various functional anionic MOFs with a wide variety of anionic moieties, which would not be possible in neutral MOFs. This is because neutral MOFs cannot accommodate such a wide range of ions. Encapsulating ionic chromophore moieties that already have a high quantum yield by ion exchange, for instance, is all that is required to achieve the improved luminous characteristics and quantum yield of luminescent anionic MOFs. It has been demonstrated that anionic MOFs have a significant potential for the selective sequestration of specific environmental contaminants, whether they be antibiotics, therapeutics or relevant hazardous pollutants. They have been the frontrunners as the next-generation sequester material for the cleanup of harmful ionic environmental pollutants because of their powerful electrostatic contacts and their capacity to exchange ions. Due to their controllable ionic component and their strong charge-induced interactions with the molecules of the incoming guests and the framework, anionic MOFs have demonstrated a significant amount of promise in the fields of toxic pollutant sequestration, gas adsorption, and separation. The major limitations of iMOFs still remain in their processability as standalone powders and their framework stability in harsh chemical conditions, both of which are essential for real-time applications such as wastewater sludge. Despite the enormous potential and promises that iMOFs hold as the ion-exchangers of the next generation, iMOFs still have this major limitation. In order to meet the requirements for commercialization, it is required to solve issues such as cost-effectiveness, large-scale synthesis, and fabrication of more convenient forms. These issues include, but are not limited to, membrane preparation, device fabrication, and other related issues. Ionic metal–organic frameworks (iMOFs) are one of the most important and rapidly developing sub-classes of MOFs, which promise commercial utility as the next generation of ion-exchangers and a viable alternative to ion–exchange resins. Ionic MOFs hold paramount importance as one of the most important and rapidly developing sub-classes of MOFs. The scientific community has identified the next objective for itself as conducting additional research geared toward the bulk synthesis of iMOFs and bringing these compounds from the laboratory bench to commercial platforms.

1.1.2.2b.5 Cationic MOFs:

In a similar fashion, cationic MOFs are generally composed of a framework backbone that is positively charged and additional uncoordinated anions that serve to neutralize the charge of the overall framework. In most cases, the counter anions are allowed to roam freely within the framework's porous channels, where they can also coordinate with the metal center through the medium of weak electrostatic interactions. In recent years, cationic MOFs have demonstrated an amazing potential for a diverse range of applications, including the capture of environmental pollutants, sensing, catalysis, battery application, and other processes. Despite the enormous potential of this field, little has been done in this area. The investigation of cationic MOFs in the fields of industrial extraction/separation and aquatic remediation is still in a very

fledgling phase and evolving continually. The pre-functionalization of the cationic framework backbone and the presence of uncoordinated polar functional anions within the porous voids of cationic MOFs are just two of the many reasons why this type of material is considered to be the next generation of anion exchange material for use in a variety of environmental applications.²⁷

1.1.2b.6 Design and Fabrication of Functional Cationic MOFs:

Synthesis of cationic MOFs can proceed either through a pre-synthetic method or through post-synthetic alterations of a subsidiary (secondary) functionality inside a neutral framework. Both of these methods are possible.⁵¹⁻⁵⁸ Figure 1.6 provides a summary of the logical synthesis procedures that can be used to create cationic MOFs.

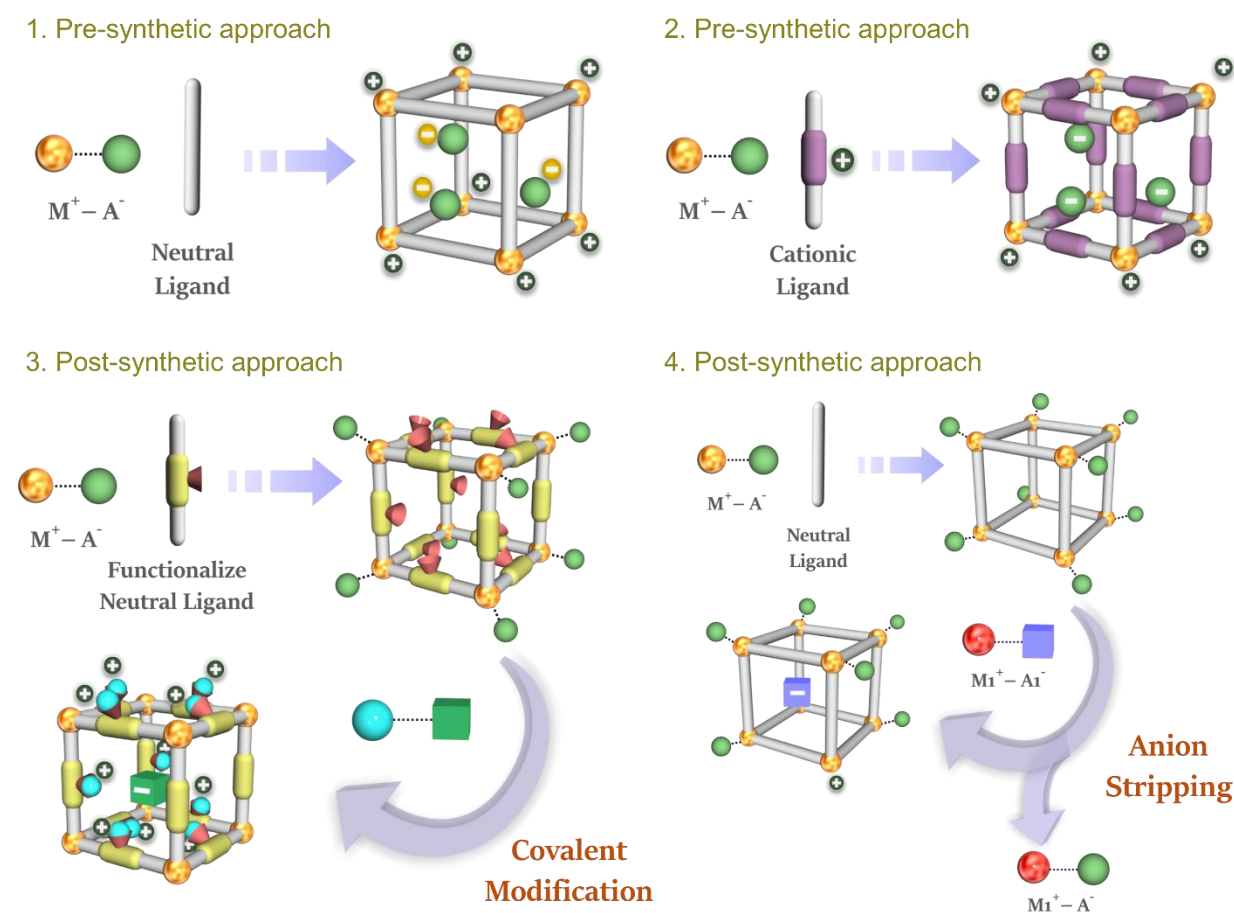


Figure 1.6 A schematic representation of the pre-synthetic and post-synthetic strategies that are deployed in synthesis cationic MOFs (reproduced with the permission).

The pre-synthetic engineering of neutral N-heterocyclic donor moiety linked ligands is where the majority of the work is done when it comes to the primary design strategy for cationic metal–organic frameworks (MOFs). Figure 1.7 illustrates ligands that serve as representative examples of the class. In this context, the five-member terminal donor groups such as triazole, pyrazole, and imidazole, amongst others, are favored over the six-membered heterocycles such as pyrazine and pyridine, due to the former's smaller size and more powerful binding capacity, respectively. These smaller 5-membered N-heterocyclic moieties can lead to a larger density of ligand molecules surrounding the central metal sites, permitting hexa-coordination to the metal nodes and shielding from the action of outside species.

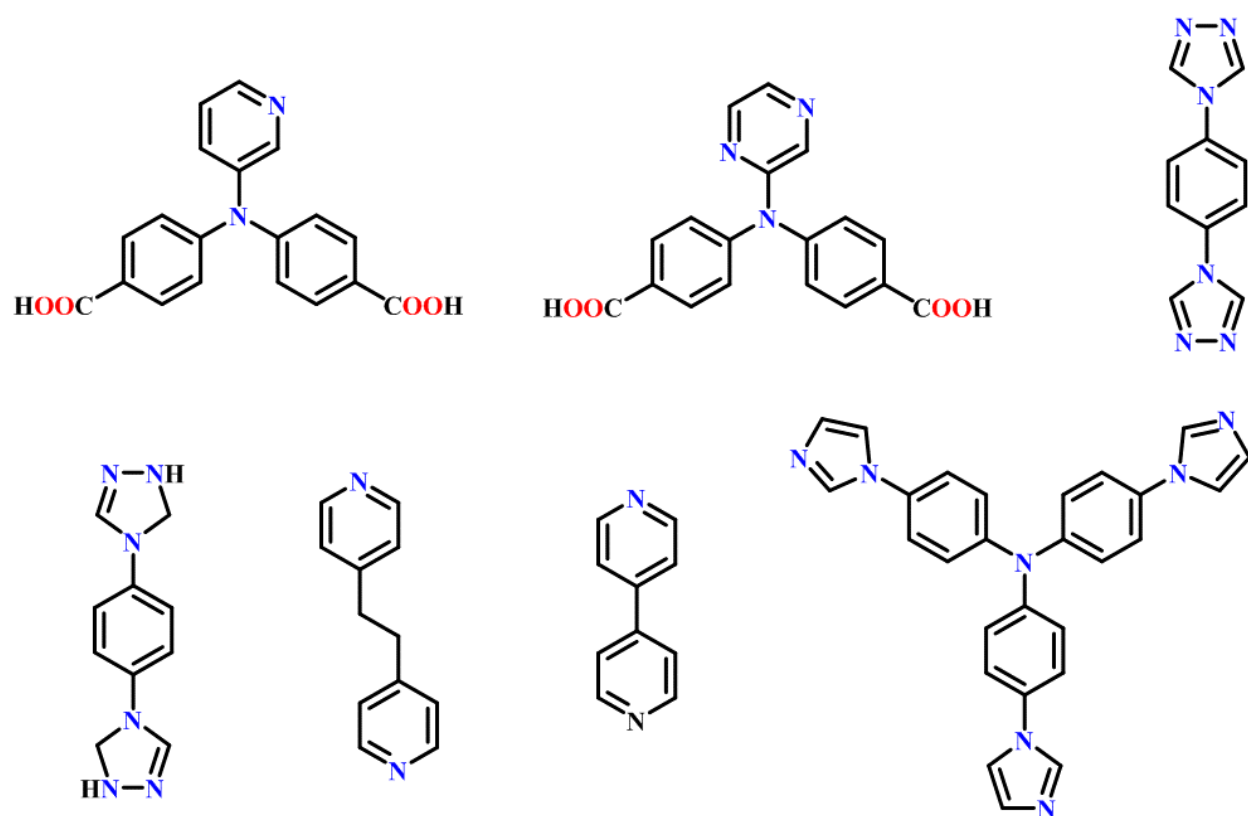


Figure 1.7 A schematic depicting the summary of organic ligands to be used in the synthesis of ionic MOFs.

This will reinforce the area around the coordination sphere of the central metal. In addition, the coordination number of the specific metal ion is satisfied solely by the functional ligands, and the metal center is covered by a high number of 5-membered rings. This high number of 5-membered rings acts as a shield here against

water molecules, which imparts hydrolytic stability in the MOF. Utilizing cationic imidazolium moieties in the ligand backbone is an additional method for synthesizing cationic MOFs via a pre-synthetic strategy. These ligands are made up of positively charged nitrogen atoms, which inherently give the framework a cationic character. Additionally, carboxylic acid-based ligands are utilised in the synthesis of cationic MOF by the deployment of a pre-functionalization strategy. In this approach, the carboxylic acid ligands that have a nitrogen heteroatom (such as a pyridine or pyrazine moiety) appended can be reacted with alkyl halide (R-X) moieties by means of nucleophilic substitution. This reaction results in the formation of an $\text{N-R}^+\text{X}^-$ moiety, with the halide (X^-) anions being uncoordinated within the pores.

The other method, known as post-synthetic modification, is an efficient way to produce cationic MOFs. Neutral MOFs are modified after they have been synthesised. For instance, a PSM-based approach could be used for the oxidation of metal centres, such as Fe^{2+} , which would result in the formation of an oxidised metal centre, Fe^{3+} ; however, this would necessitate the addition of additional negative charge in order to maintain a charge equilibrium throughout the entire framework. Oxidation of these types of MOFs can lead to the production of cationic frameworks that contain extra-framework anions to maintain overall charge balance.

1.1.2.2b.7 Advantages of Cationic MOFs:

Due to their superior features such as tunable architecture, bimodal functionalization in terms of both framework backbone and uncoordinated functional anions, surface functionalization, ease in ion-exchange processes, and so on, cationic metal-organic frameworks (MOFs) have already shown enormous promise to become the leading contenders as the next generation cationic/anion-exchange materials. The tactical functionalization of cationic metal-organic frameworks (MOFs) has resulted in the emergence of critical features such as physicochemical stability and tunable pore size. Both of these features are necessary for the development of sophisticated ionic materials. In addition, cationic MOFs can be tailored in contexts of the framework building units that they use as well as the functionality that is appended to them in order to increase their applicability for selective anion exchange and to improve the overall interactions that guest anions have with the framework. In particular, the tunability of the uncoordinated anions as an extra-framework functionality has evidenced to be a game-changing feature in a variety of applications. These applications include environmental pollutant sensing and capture, catalysis, optoelectronic-based applications, and others. These anions can be varied according to the requirements of the application, and they offer a wide variety of functional anions such as Cl^- , Br^- , SiF_6^- , BF_4^- , SO_4^- , NO_3^- , ClO_4^- , and many others. In addition to these inorganic anions, organic moieties that contain carboxylic acid ($-\text{COOH}$), sulfonic acid ($-\text{SO}_3\text{H}$), or phosphonic acid ($-\text{PO}_3\text{H}$) groups can also serve as the extra framework anion to

ensure that the overall charge of the cationic framework is maintained.

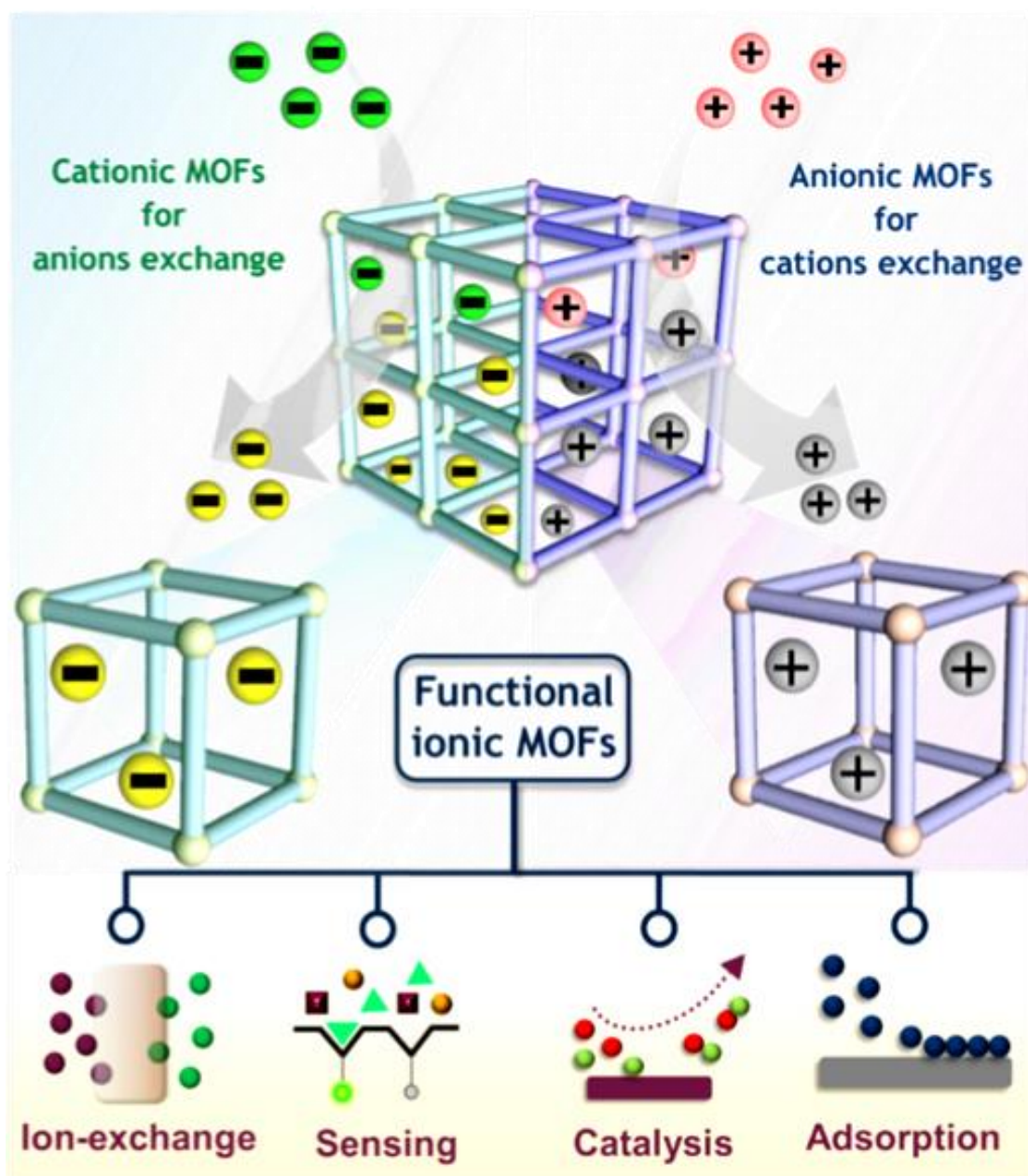


Figure 1.8 A schematic illustration of the wide variety of possible applications for ionic metal–organic frameworks (iMOFs) (reproduced with the permission).

The additional benefit of these uncoordinated anions is that the pore size of the cationic framework can also be tuned by varying these anions. This is an advantage that is not shared by the coordinated anions. As a consequence of this, the nanospace of the cationic framework can be functionalized and tuned by the

functional anions for applications that are target-specific. Furthermore, in the case of applications that are based on ion exchange, cationic MOFs make it possible to exchange the targeted guest anions through an ion-exchange process that also prevents any leaching of the inbound anions. In ion-exchange-based applications, cationic MOFs can therefore convey selectivity while maintaining a high level of efficiency.

1.2 Applications of ionic MOFs:

MOFs have been shown to be suitable for the tackling of a variety of real-world applications (Figure 1.8). These applications include fuel cell applications, the sensing of environmentally hazardous species, gas separation and storage, ion conduction, industrially relevant light hydrocarbon separation, removal of toxic and hazardous waste, magnetism, heterogeneous catalysis, and many more (Figure 1.8).⁵⁹⁻⁶⁷ The realization that structure and properties are inextricably linked has had a significant influence on the lightning-fast progress that MOFs have made toward developing these new applications. In addition to this, the target-specific applications' requirements can be adapted to the functional networks in order to achieve optimal results. MOFs are still in the process of being developed as an important crystalline porous material. They are expected to garner a lot of attention over the course of the next few years for their applications in the real world, this is because MOFs possess such a tremendous amount of potential. The design, synthesis, and functional studies of anionic metal–organic frameworks (MOFs) constructed from ambidentate linkers bearing O- and N-donor atoms that are exclusively selective toward oxo-cations/cations (uranyl ions) and the remediation of toxic aquatic pollutants are the primary focuses of this current thesis. These topics are explored and addressed in the foregoing chapters.

1.2.1 Gas adsorption and separation:

MOFs have drawn unrivalled attention during the past two decades due to their custom molecular topologies and crystal packing patterns, as well as the possibility of using them as functional materials. A wide range of innovative uses for this class of materials, including gas storage, are among their most intriguing developments. Gas and hydrocarbon adsorption-based separation and purification are of utmost significance to industry. The search for sophisticated sorbent materials with specialized architectures is still ongoing due to the growing demand for an energy-efficient and environmentally friendly option for gas separation. Due to their customizable porous structures and substantial surface area, functional MOFs have attracted considerable scientific attention as promising sorbent materials for gas adsorption and separation. The literature is heavily populated with neutral MOFs despite the fact that a lot of research has been done on MOFs for selective gas adsorption and separation. Due to their distinctive structural characteristics and the counter-charged entities housed in nanospace, research on ionic MOFs as gas and vapor sorbent materials has accelerated. In this context, few contemporary examples of anionic MOF-based selective gas

separation and adsorption studies have been highlighted to understand the background of the same. Carbon Capture and Sequestration (CCS) technology, which involves removing CO₂ from industrial exhaust gases, has gotten a lot of attention because it can be done economically and has the potential to cut greenhouse gas emissions by a significant amount. Selective CO₂ capture from flue gases or natural gas refinement, specifically CO₂/H₂ (pre-combustion), CO₂/N₂ (post-combustion), CO₂/O₂ (air separation), and CO₂/CH₄ (natural gas purification), unquestionably provides a difficult task to effectively address this environmental and energy issue. Literature reports on multifunctional MOFs show that in recent years, a design principle-based method has been used to make multifunctional MOFs that successfully use the linker pre-functionalization concept. Navarro and colleagues established in a ground-breaking study a universal approach for modifying porosity as well as sorption characteristics in an anionic MOF via cation-exchange. In this study, they present an anionic MOF called NH₄@1, whose pores contain free NH₄⁺ cations. To create the cation exchange form A@1, NH₄⁺ cations were additionally exchanged with a variety of other cations. Differential uptake in N₂ adsorption experiments on A@1 demonstrated the importance of cation diversity and ion-exchange in adjusting the porosity. The A@1 (A=NH₄⁺, Et₃NH⁺) framework demonstrates substantial interactions with C₂H₂ and CO₂, although it shows low interaction with other gases, according to variable-temperature (273-363K) adsorption studies and gas chromatography investigations. The A@1 framework additionally demonstrated the separation of benzene and cyclohexane as it noted a 5:1 separation ratio for benzene over cyclohexane.⁶⁸ By fine-tuning extra-framework cations in an anionic MOF, (HPP-rho-ZMOF), Eddaoudi and colleagues have achieved the ideal combination of structural functionality needed for the enhancement in hydrogen binding energies (HPP-rho-ZMOF).¹⁰⁹ The investigations indicating influence of diverse cations on adsorptive absorption and energetics toward H₂ has been reported precisely in the literature.⁶⁹ Because of the Li-rho-reduced ZMOF's ionic radius, which creates huge gaps in the MOF for H₂ storage, the authors discovered that it could store a few more H₂ molecules. The results, according to the scientists, demonstrated the electrostatic field within the MOF cavity as being the primary factor in the increased sorption capability of such anionic MOFs.

1.2.2 Sensing:

Luminescent MOFs (LMOFs) are important in applications based on sensing. Among the several approaches, adjusting luminous characteristics by including emissive guest chromophores into the porous structure of MOFs can provide a more straightforward, beneficial, and effective method for creating a viable sensor. By post-synthetically exchanging their unbound cations from the framework with the desired cationic chromophores, such as luminous metals or metal complexes, organic species (dyes), and so forth, anionic MOFs have played a crucial role in fabricating good sensors in this dimension. Here, a few intriguing cases of anionic MOFs using cationic guest chromophores to detect distinct cationic molecules

have been highlighted to gain the background. In 2015, Maji and associates developed a 3D anionic MOF known as AMOF, which contains $[\text{NH}_2\text{Me}_2]^+$ cations inside its pore. The ionic MOF demonstrated selective sensitization of Eu^{3+} cations by exchanging the free framework cations, as well as selective sensitization turn-off detection toward Cu^{2+} ions ($K_{\text{sv}} = 1.986 \times 10^3$).⁷⁰ Researchers have hypothesized that the ligand field splitting of the Cu^{2+} metal ions' d-orbitals was the cause of this turn-off behavior. Additionally, other heavy metal cations, such as Eu^{3+} , Tb^{3+} , Sm^{3+} , and Dy^{3+} , were partially incorporated into the MOF, and it was discovered that this diminished the distinctive emission spectrum of $\text{Eu}^{3+}@\text{MOF}$ at 410 nm following excitation at 317 nm.⁷¹

1.2.3 Catalysis:

Nowadays, catalysis is rendered to be a key method for generating the basic necessities of life, including food, water, and energy. With the world's population rising, the economy expanding at an exponential rate, and raw material costs declining, manufacturing in a sustainable way is crucial, and catalysis plays a big part in this. Due to their highly dense influential metal nodes or secondary building units (SBUs), functionalized organic linkers, highly crystalline nature, controllable active size, high porosity, and large surface area inside the framework, MOFs have been investigated as a potential console in the field of catalysis, especially for heterogeneous catalysis, and have drawn significant attention toward syntheses and material chemistry.⁷² One of the key requirements for developing MOFs-based effective catalytic activity is post-metalation or alteration of the framework.⁷³ The additional free cations inside the framework can readily be replaced with particular catalytically active species, which may result in efficient catalytic activity, making anionic MOFs relevant for heterogeneous catalysis in this regard. Recent investigations have shown that an energy-intensive alternative approach based on MOFs can produce effective heterogeneous catalysts.

1.2.4 Capture and Sequestration of Aquatic Pollutants:

Pure water is the most vital resource for all living things. Industrial growth, rising pollution, water pollutants that are typically composed of highly toxic synthetic organic-inorganic compounds, and other factors have made fresh drinking water increasingly scarce. As a result, new effective and cost-effective environmental remediation techniques have been developed. Due to its high efficiency with rapid kinetics, low operational cost, good selectivity, and, most importantly, better flexibility towards building task-specific promising adsorbents, ion-exchange-based adsorption is thought to be more successful for pollutant removal implementation. Anionic MOFs, one of these effective sorbents, play an important role in the area of remediation of environmental pollutants by separating various types of hazardous cations from water by exploiting crucial features including porosity with large surface area and functional tunability. The ability

to modify anionic MOFs' molecular level functions elevates them to a higher class of sorbent than existing adsorbents.⁷⁴⁻⁷⁶ Among the potentially poisonous pollutants, organic dyes, antibiotics, and pesticides, besides hazardous oxo-anions and oxo-cations, are extremely dangerous industrial and anthropogenic contaminants that severely pollute water. Therefore, it is essential to completely remove these stable species before releasing them into the natural water system. Also, anionic MOFs are a better platform for decontamination than dyes, pharmaceutical waste, and trace and ultra-trace cations, like uranyl cations, when compared to existing traditional materials.

1.2.5 Uranium Capture and Sequestration:

We are living in an age in which the need for energy all across the world keeps skyrocketing, and we are also witnesses to the great turbulence that is shaking our globe. Energy consumption is affected by a wide range of socioeconomic factors, including urbanization, population growth, industrialization, the level of socioeconomic development, and the pace of technological advancement. As a result of the depletion of existing energy sources, the provision of long-term energy that is both sustainable and renewable has emerged as one of the most pressing challenges that humanity must confront.⁷⁷ In light of the numerous environmental problems that are caused by the combustion of fossil fuels, such as pollution, climate change, and the destruction of biodiversity, the development of alternative energy sources is an absolute necessity that carries a great deal of weight in both the scientific and technological communities.⁷⁸ Because it does not contribute significantly to the emission of greenhouse gases, nuclear energy is regarded as one of the most promising low-carbon solutions among established technologies.⁷⁷ Due to the importance of uranium in nuclear reactors, there has been a significant increase in the number of nuclear activities that involve mining, processing, and recovery of uranium. This is essential in order to ensure a steady supply of renewable energy. However, the fact that geological stocks of uranium ores are running low at an alarming rate is a cause for concern. Based on the current rate of use, the world's supply of uranium ores will be exhausted in fewer than a hundred years, or even sooner.⁷⁸ It is estimated that there are around 4.5 billion tons of uranium in the ocean, which makes it a potentially enormous resource that might support the generation of nuclear energy for millennia.⁷⁹⁻⁸⁰ Uranium extraction from seawater calls for cutting-edge research in the field of materials, and it is considered to be one of the seven most sought-after methods of chemical separation, which, if ever perfected, would bring about revolutionary changes on a global scale.⁸¹ Despite the fact that a variety of different adsorbents have been developed in an attempt to extract uranium from saltwater, there has been little success (UES).^{78,82-86} However, their performance in a laboratory setting is typically restricted, and the most of them suffer from extremely low adsorption kinetics, limited uptake capacity, and poor selectivity. This is due to the fact that their uptake capacity is restricted. As a result, the production of brand-new, long-lasting adsorbents that are capable of meeting the strict commercial criteria

that have been established as a result of the economic development of UES is very much required in order to accomplish the urgent demand for a sustainable energy source.⁸⁷ Metal-organic frameworks, often known as MOFs, are a champion material in the field of reticular chemistry. These frameworks are created by the coordination of metal centers (clusters or metal ions) and organic struts.^{88,89}

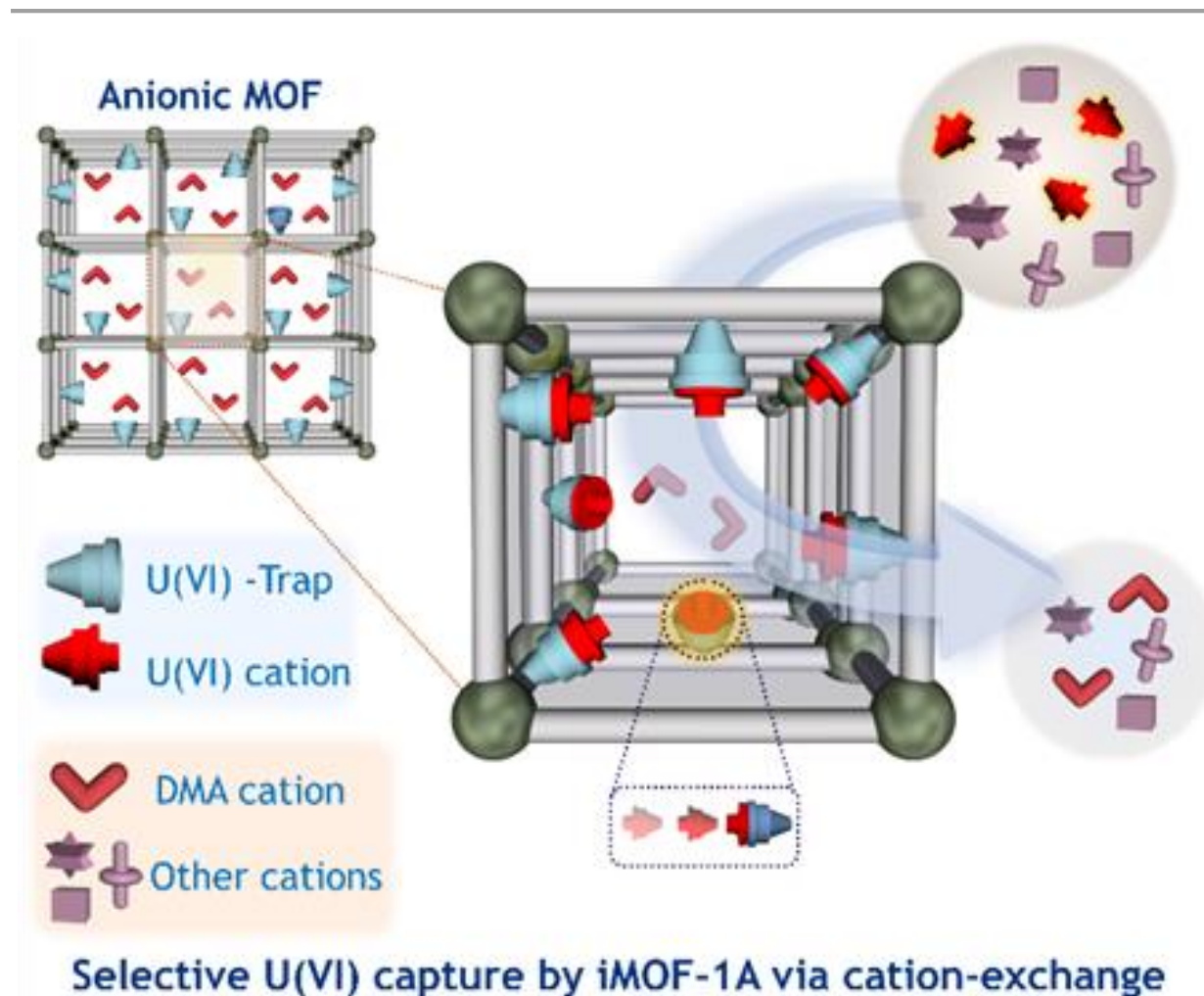


Figure 1.9 A schematic illustration of a trap-grafted anion-exchangeable MOF indicating capture of uranyl ions selectively from a mixture of other interfering cations.

Ionic MOFs, also known as i-MOFs, are potentially the most significant manifestations of MOF-based host matrices. They account for residual charge, which can be either negative or positive, and can be repeatedly exchanged for more appropriate ions. As a result, they are able to impart desirable functional properties. Anionic metal-organic frameworks, also known as iMOF-A, are a subclass of ionic MOFs. Anionic MOFs have been regarded as a class of multifunctional materials due to the numerous propositions they have made in a variety of fields, including selective capture, gas storage, drug delivery, catalysis, photonic applications,

and a great deal more.⁹⁰⁻⁹³ The presence of charged species within the frameworks causes certain interactions, which can be effectively exploited as ion-exchange sorbents for the purpose of sequestering cationic visitors. Because the imprisoned cation serves as a charge-balancing ion and is therefore an essential component of the structure, the possibility of the trapped cationic visitors leaking away is also eliminated. In addition, ionic properties that have Lewis basic sites that aren't difficult to reach can be able to provide further advantages thanks to the selective binding affinity of particular analytes within the frameworks (Figure 1.9).^{94,95} MOF-based adsorption and electrocatalytic extraction techniques have become the leading candidates for the selective capture of a wide variety of pollutants, including radioactive species, due to their unprecedented potential. This is because these techniques have the ability to selectively capture a wide variety of pollutants.^{96,97} The complete thermodynamics of MOF-analyte interactions occurring in aqueous media have been left mostly unexplored, despite the fact that this information is essential for the design of the next-generation of sorbent materials. This is despite the fact that tremendous efforts are currently being devoted to the detailed realization of chemical and structural features that influence the adsorption process.

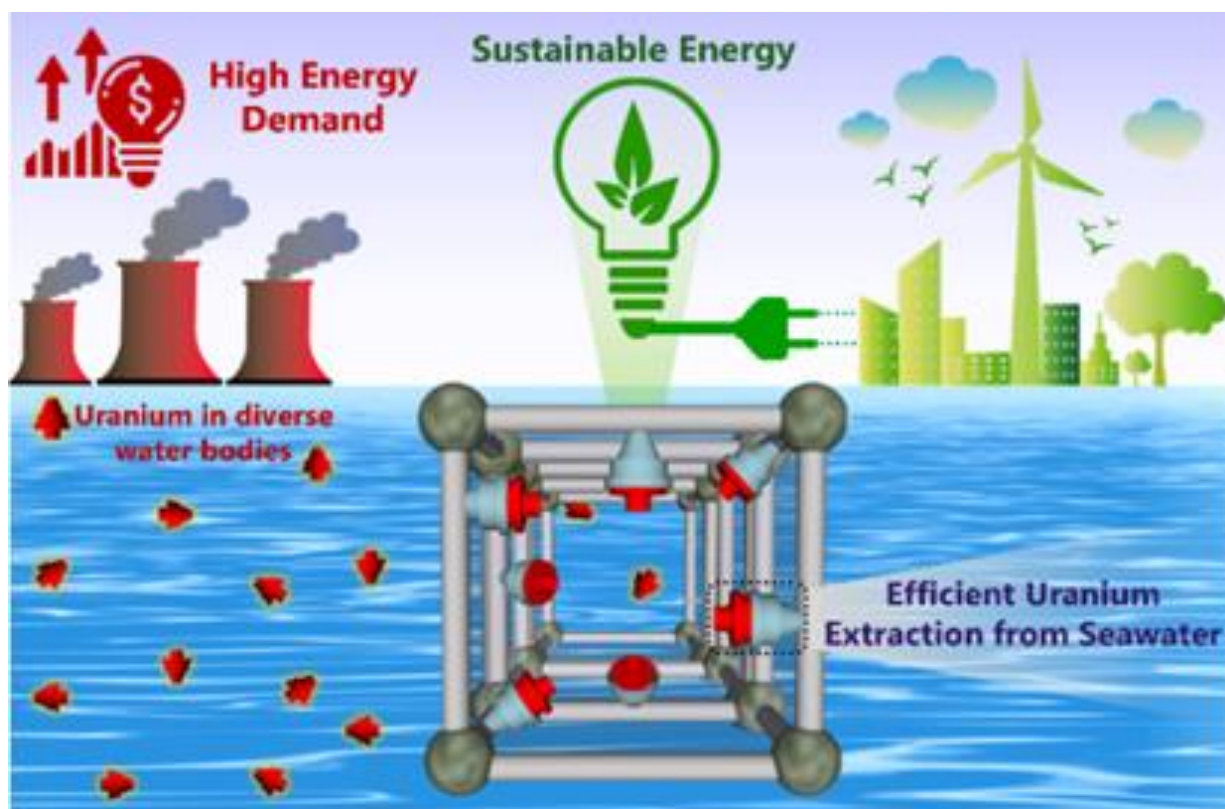


Figure 1.10 Schematic representation illustrating selective uranium separation by ionic sorbents or iMOFs.

Through a combination of ion-exchange and interaction mechanisms, one can aim to make use of an anionic

metal–organic framework (MOF) for the effective recovery of uranium. Owing to aforementioned facts, attempts can be made in direction of selective, fast and effective capture of Uranyl ions and relevant ionic species by attempting synthesis of functionalized or trap grafter ionic adsorbents (Figure 1.9), which should be blended by properties of stability and reusability. Conceiving and developing novel and hydrolytically stable anionic MOFs or comparable materials, as well as deploying critical corroboratory experimental tools for the remediation of priority environmental pollutants, could pave the way for new pathways aimed at efficient uranium extraction, thereby addressing the billion-dollar issue of energy deficit and effective pollutant remediation (Figure 1.10).

1.2.6 Toxic Aquatic Pollutants Remediation:

The misuse or improper application of recently developed antibiotics and pesticides are two examples of anthropogenic wastes that have led to water contamination. The identification of antibiotics and pesticides in wastewater must be conducted expeditiously and judiciously due to the grave ramifications for human health. Considering practical reasons, a suitable sensory material for the sensing and detection of antibiotics and pesticides in aqueous medium is still being explored. Ionic metal-organic frameworks (iMOFs) are a novel type of porous materials that could be used to detect aqueous micropollutants. The neurological system, respiratory system, and reproductive systems of living organisms are all adversely affected by prolonged contact with these dangerous species.⁹⁸ The systematic and routine monitoring of these species has evolved into a key research issue due to the negative effects and high level risk of antibiotics and pesticides in water. Numerous established analytical techniques have been used over the past few decades for the detection of these toxic species, including raman spectroscopy (RS), mass spectroscopy (MS), LC with UV detection (LC-UV), liquid chromatography-tandem mass spectrometry (LC-MS), and ion mobility spectroscopy (IMS).⁹⁹⁻¹⁰² All of these approaches had drawbacks, including lower efficiency, higher costs, longer processing times, and a requirement for specialized employees. Therefore, it has become a current research interest to create easy-to-use, economical, quick-response, highly sensitive methods for the selective detection of dangerous species. According to this perspective, fluorescence-based detection methods have gained popularity due to their high selectivity, sensitivity, rapid sensing response, simplicity of use, and lower cost.¹⁰³⁻¹⁰⁵

Due to its high fluorescent quantum yield, high selectivity and sensitivity, reusability, lower operational and fabrication costs, etc., the luminescent porous materials-based fluorescent technique for detecting target-specific environmental contaminants has recently gotten a lot of attention from researchers.¹⁰⁶⁻¹⁰⁹ Modern porous materials like metal organic frameworks (MOFs), and iMOFs in particular, are showing promise for use in sensing applications in comparison to traditional adsorbents like activated

carbon, zeolites, resin, etc. due to their improved sensitivity, high selectivity, and quick response times.^{107,110}

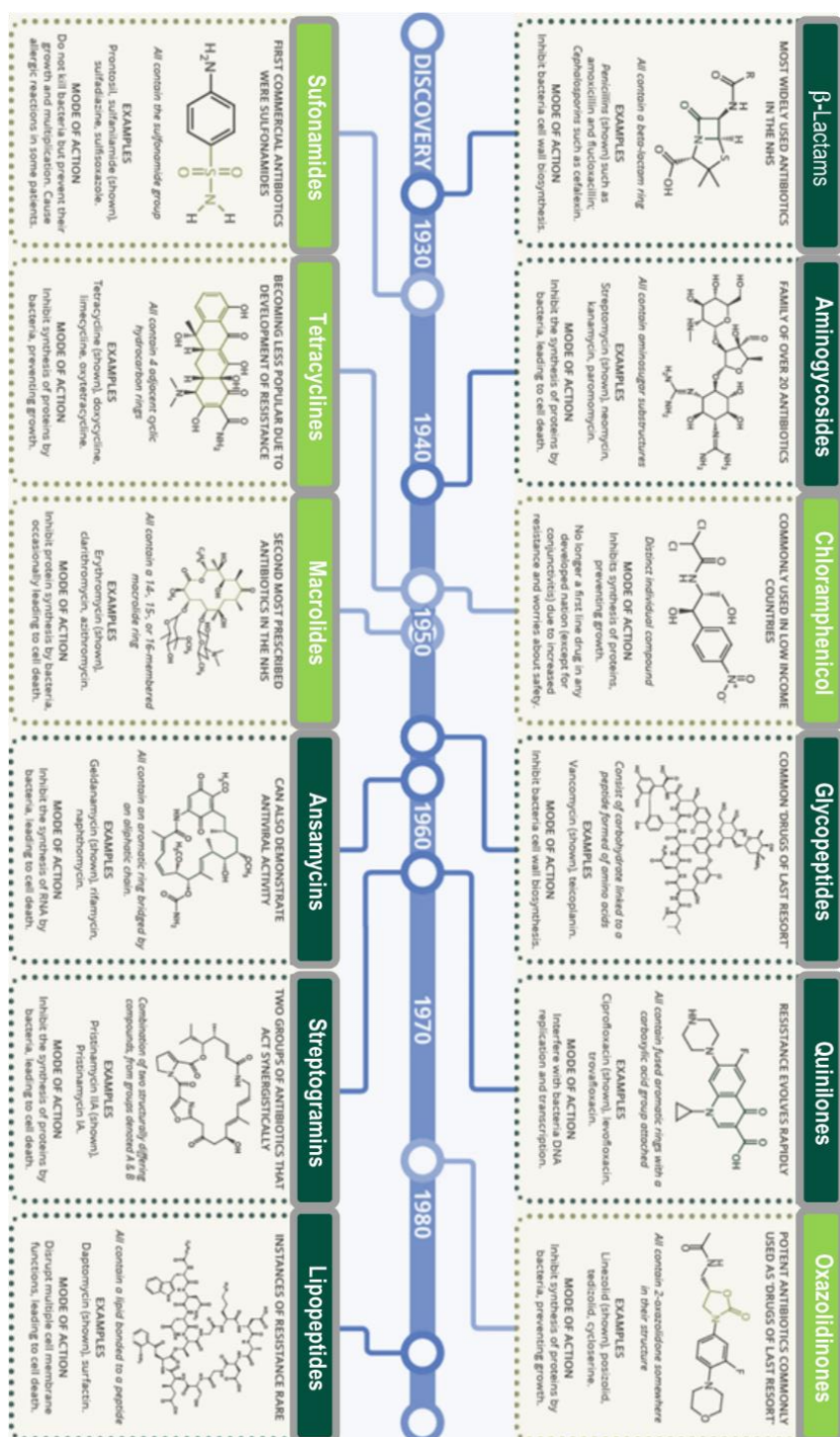


Figure 1.11 Schematic representation illustrating classification of Antibiotics (reproduced with permissions).

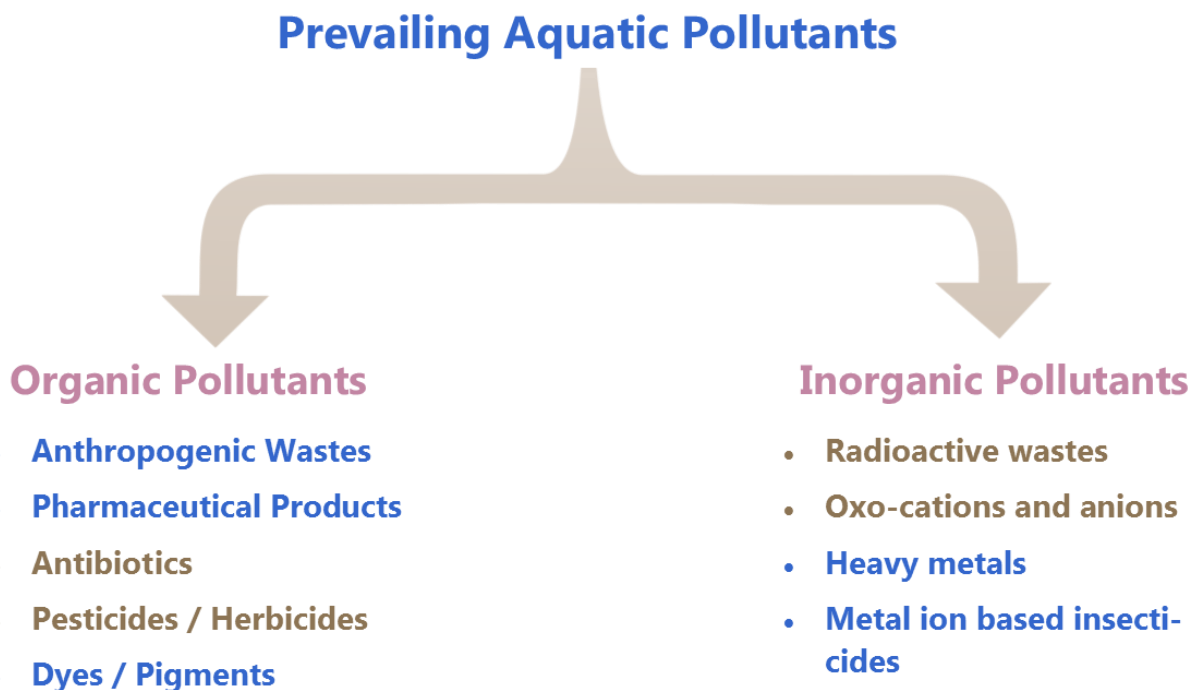


Figure 1.12 Schematic representation illustrating classification of the chemical water pollution.

The detection of these species with affordable, chemically and thermally stable, highly luminous MOFs has rarely been studied, despite the small number of MOF-based antibiotics and pesticide sensing studies that have been published.^{86-91,105,107,111} It is advantageous to build effective sensory materials when such materials with the aforementioned features are successfully developed and fluorophores are intelligently incorporated. These compounds' high porosity and broad surface areas enable quick mass diffusion and robust contact with the analytes, further enhancing their sensitivity and prompt detection response, respectively.¹¹²⁻¹¹⁸ Additionally, these materials' heterogeneous nature and great chemical stability allow for easy and superior regeneration detection abilities as well as "real-time" prospective sensory materials that are beneficial in many environments.¹¹⁹⁻¹²⁰ Hence, the strategic choice of iMOFs as a potential stable sensory material for the specific task of sensitively identifying antibiotics and pesticide residues in steam, taking into account the goal of targeted and sensitive detection as well as the facts of developing a low-cost, simple-to-use, portable, reliable, highly stable, and effective juncture sensory material. However, ionic MOFs, particularly the anionic MOFs are very rarely explored toward the capture of pesticides with competitive capacity. Hence, in order to fast-track the development and explore the huge potential of ionic

MOFs, efforts shall be devoted toward selective sequestration of the toxic anthropogenic and agricultural wastes deploying anionic MOFs.

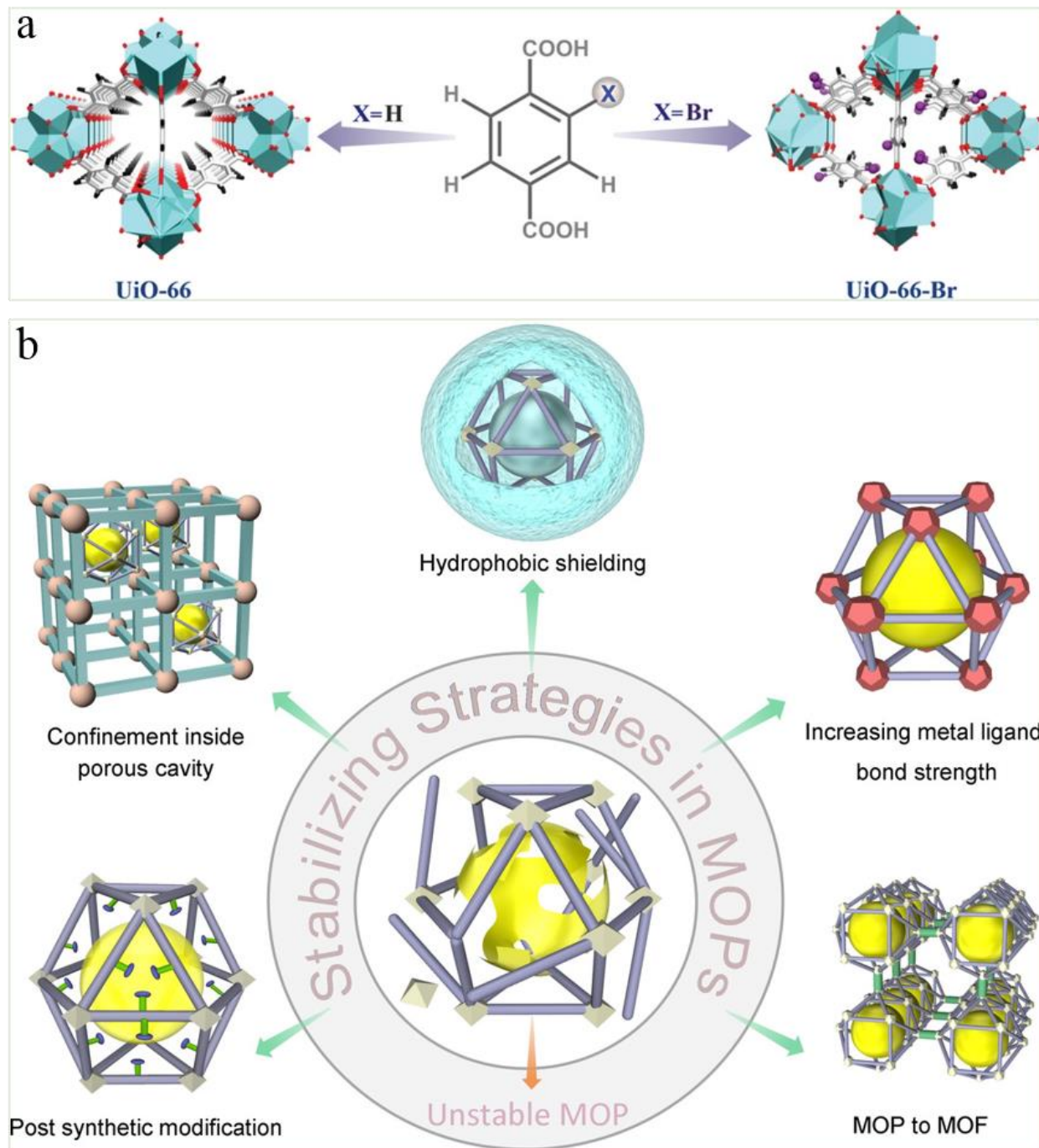


Figure 1.13 Schematic representation illustrating a) End-group tuning in the iso-structural MOFs UiO-66; b) Strategies tuned MOPs intended for potential TENG application (reproduced with the permission).

1.3 Porous Materials for Energy Applications:

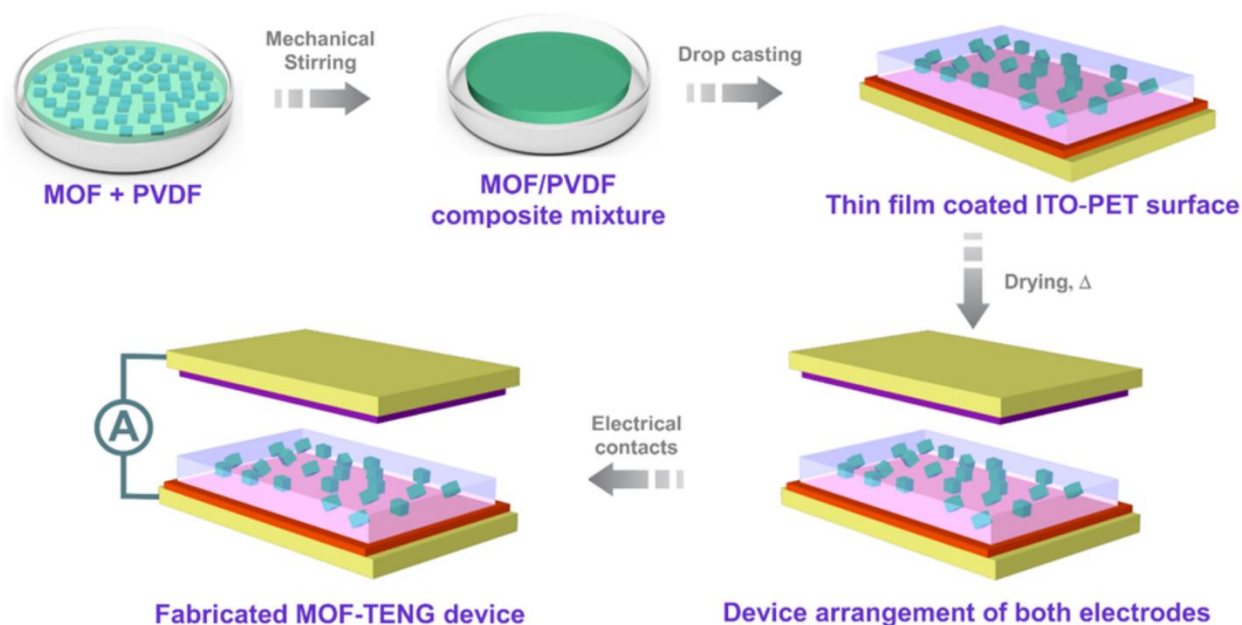


Figure 1.14 Schematic representation general fabrication procedure adopted for MOF and polymer based composite-materials aimed for mechanical energy harvesting device.

Globally, fossil fuels are utilized as a source of energy, which either harms the environment as well as diminishes their source or availability for forthcoming generations. It really has entailed an uptick in the use of renewable energy options. Solar, tidal and wind power may be the most investigated renewable energy sources, but mechanical energy and perhaps other sources of energy have gathered minor attention. The energy from many mechanical movements or motions, including human motion, wind, tidal and so on, has historically been mostly wasted and disregarded. Surprisingly, the scientific community is beginning to recognize alternative energy sources as part of the solution to the intensifying energy-related concerns. In particular, customizable electronics, high-precision sensors, portable high-voltage sources, and distributed micro/nano-power sources have seen great strides in mechanical energy conversion technologies over the past decade. The Triboelectric Nanogenerators (TENGs), which primarily take advantage of the idea of charge separation produced by relative motion between two dissimilar materials in close proximity—the well-known phenomenon of friction being a manifestation of the process—are at the center of this research. The so-called "triboelectric series" depicts the differences between materials based on their ability to transfer or absorb electrons when moving in close proximity, friction is a well-known phenomenon that represents the process. The so-called "triboelectric series" depicts the differences between

materials based on their ability to transfer or absorb electrons when moving in close proximity. To achieve maximum power output, a TENG device combines materials that are further apart in this series. Appropriateness of design facilitating charge transfer is largely determined by the configuration of the device. In the following chapters, this issue has been addressed in detail, which includes a highly stable MOF for reproducible, robust, and tuneable applications in the domain of Triboelectric Nanogenerators (TENG), followed by a brief discussion of results highlighting chemically stable, solution-processable, and hydrophobicity-tuned series of MOPs blended by polymer composites for on-demand self-powered energy devices with efficient rated power (Figure 1.13).

1.3.1 Isostructural MOF Composites for TENG:

Fossil fuels are used as a source of energy on a worldwide scale, which harms the environment and reduces their supply for generations to come. This has made increased usage of renewable energy sources necessary. While solar and wind power are possibly the most researched sources of renewable energy, mechanical energy and other sources have gotten marginal attention. In actuality, the energy from various mechanical motions, including human motion, water-tidal, and wind has historically been largely wasted and disregarded. The existence of such energy sources has fortunately caught the interest of scientists as a potential partial answer.¹²¹ Utilization of MOF derived composites are quite appealing proposition for the development of self-powered unattended electronics and electro-mechanics is the on-demand harvesting of operating power from the dynamic work environment. The triboelectric Nanogenerator, also known as a TENG, is an intriguing piece of equipment that belongs to this category. Its primary objective is to harvest the mechanical energy that is otherwise lost in a variety of working environments. In order to get over the constraints of present energy technology and contribute to the advancement of cleaner energy, Wang and his team devised an efficient technique for TENG manufacture in 2012.¹²²⁻¹²³ The TENG is able to transform a variety of energy forms, including those from mechanical, wind, and water sources, into electricity.¹²⁴⁻¹²⁶ TENG can perform in four distinct operational modes, including single electrode modes, freestanding, , vertical contact-separation, and lateral sliding, using contact electrification and electrostatic induction as operating principles. A tribo-layer and a conducting layer are among two most crucial TENG components since they come into contact with the two different triboelectric materials. They must be attached to a substrate material acting as a support framework in order to make a functional device.^{121,127-129} One of the numerous advantages of TENG is its low cost, straightforward design, high power output, and improved conversion efficiency. Numerous applications, including chemical and biological sensors, large data sensing, therapies, and self-charging, are possible with TENG, hence it is used in numerous self-powered applications due to its simplicity in manufacturing, material choice, high power output, and versatility in producing direct current.¹²⁷⁻¹²⁹ In a typical TENG device, two functional materials that have the advantages

of flexibility and significantly different triboelectric properties (Triboelectric series) are combined to produce charge carrier separation in response to various kinds of mechanical energy stimuli. Despite impressive quality factors such as flyweight-compactness, cost efficiency, high output, and a broad choice of materials for device designs, TENGs continue to fall short on these practical demands continue to fall short on real time demands such as performance tuning, modulatory electronic effects of constituents, and stability features on demand for adverse and ambient working environments.

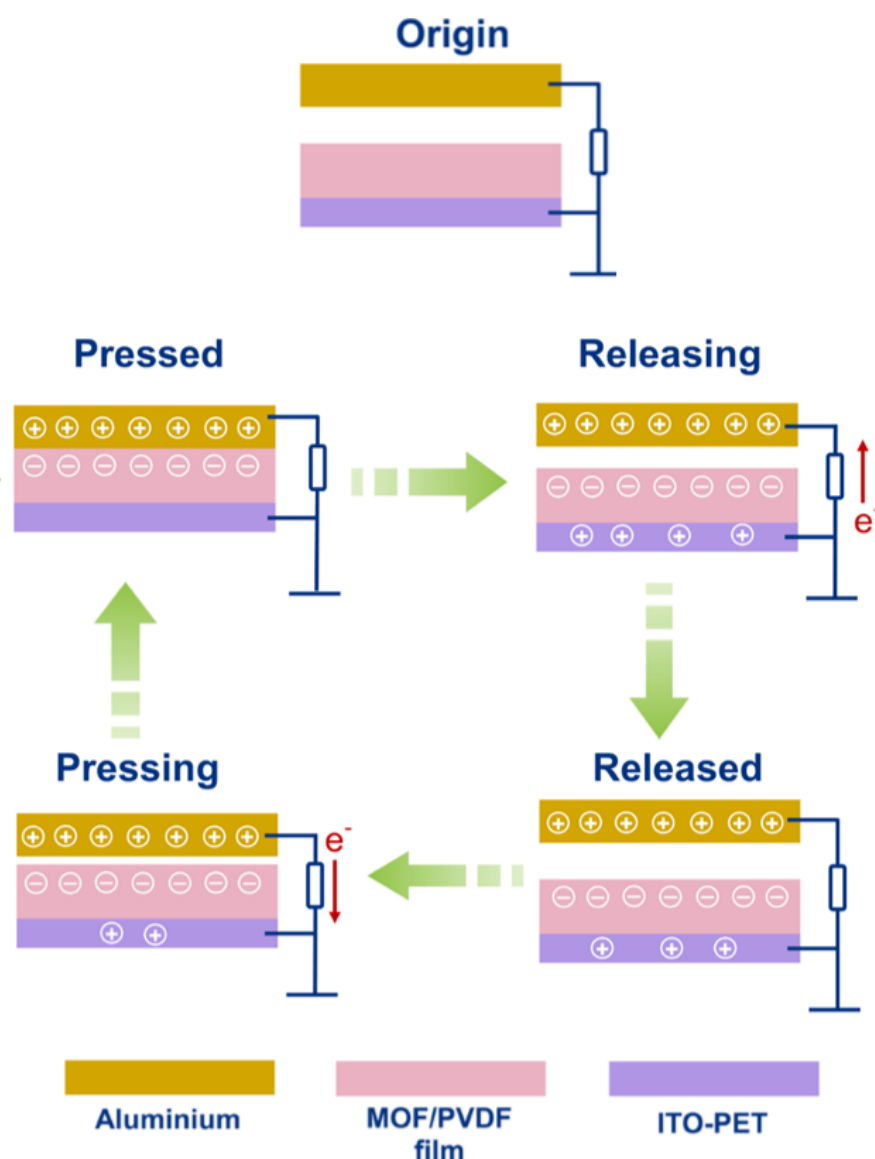


Figure 1.15 Schematic representation illustrating mechanism in contact-separation mode (vertical) with simultaneous stages viz. releasing, released, pressing and pressed (reproduced with the permission).

Considering inherent features for molecular tunability, metal–organic frameworks (MOFs) have the potential to be utilized in ways that are beneficial to the process of optimizing energy conversion. Hydrolytically stable and isostructural series of MOFs can be considered as choice of materials to navigate the systematic tuning MOF functionalities to elucidate the consequent TENG output. Blend of MOF and polymer matrix thus can become the foundation for increased electrification as a direct consequence of the significant increase in charge and TENG output performance owing to functionality tuning in MOFs.

1.3.2 MOP Derived Composites for TENG:

Crystalline porous materials have seen an astounding transformation over the past couple of decades, and researchers from various fields have paid close attention to them.^{130, 131} Metal-organic frameworks (MOFs) and covalent-organic frameworks (COFs) have gotten a significant amount of attention among crystalline porous solids rendering to their large surface area. Further, aforementioned materials (MOFs, COFs, PCPs) have been looked into for a wide range of applications including gas separation and storage, catalysis, sensing, and energy storage or conversion, etc.^{132–137} MOPs, which stand for metal–organic polyhedra, are a subclass of crystalline porous materials that were introduced roughly at the same time as PCPs or MOFs.^{133,134} Several hydrolytically stable (water stable) MOFs and COFs have been produced over the past few years as a result of the understanding of their rational design strategies, which has sped up their advancement toward practical uses.^{135–140} However, the development of carboxylate MOPs for application studies has been severely hampered by the absence of systematic methods to prepare stable MOPs. Despite the fact that there are several general methods has been reported for the synthesis of MOPs bearing voids, still the bulk of carboxylate MOPs reported in the literature have been discovered to be hydrolytically unstable.^{141–144} Because of their instability and loss of crystallinity as a result of the inevitable aggregation-driven blocking of active sites following guest removal, such MOPs' solid-state applications are hampered.^{145,146} There is a lack of a comprehensive design strategy. This is a very useful property for quickly making thin-film based devices, electrolytic solutions and membranes, as well as for a variety of active additives (filler) in polymers and ion channels, as well as for various biochemical applications.¹⁴⁷ But, if stabilized, metal-organic polyhedra (MOP) show great promise for a wide variety of uses and are suitable for solution processing owing to their miscibility in diverse organic solvents.^{148,149}

These MOPs can be chosen considering stability features, such as resistance to a broad pH range, stability under oxidizing and reducing media, and in strongly acidic conditions, which has been mitigated due to tuneable hydrophobic shielding. A prototype approach can be conceptualized towards chemically stable MOPs, whereby the transition from an unstable to a chemically ultra-stable phase can be achieved by performing a quick gram-scale synthesis at ambient temperature (within seconds). Further, these MOPs can

be rationally deployed in the preparation of MOP/PVDF composites at different blending concentrations and fabricated into flexible thin films by means of drop-casting, doctor blading, and electrospinning methods, to give fabricated films that can be moulded into tiny, light-weight, and compact TENG devices. Owing to their gradual increase in hydrophobicity due to shielding by alkyl and aryl groups, such a class of MOPs can be effectively used for tuning of TEMG output and power density as a function of hydrophobic features. If chosen, the right blend of polymer matrix and MOP loading concentration can produce a real-time outcome in terms of tunability, stability, recyclability, and application display in power storage in batteries and capacitors, real-time LED illumination, and mobile and medium-range electronic charging. Considering overall progress and development in the field so far, there is no literature report till now encasing applications of MOP-derived composites in TENG applications. Thus, in view of existing literature and progress in the domain of nanogenerators, MOP-based TENGs can be considered as a potential area of research. MOP–polymer composite materials generally exhibit features of solution processability, which can instill the potential for fabricating thinner and more durable self-powered merchandise (wearable nanogenerator fabrics), as well as flexible self-charging electronics.

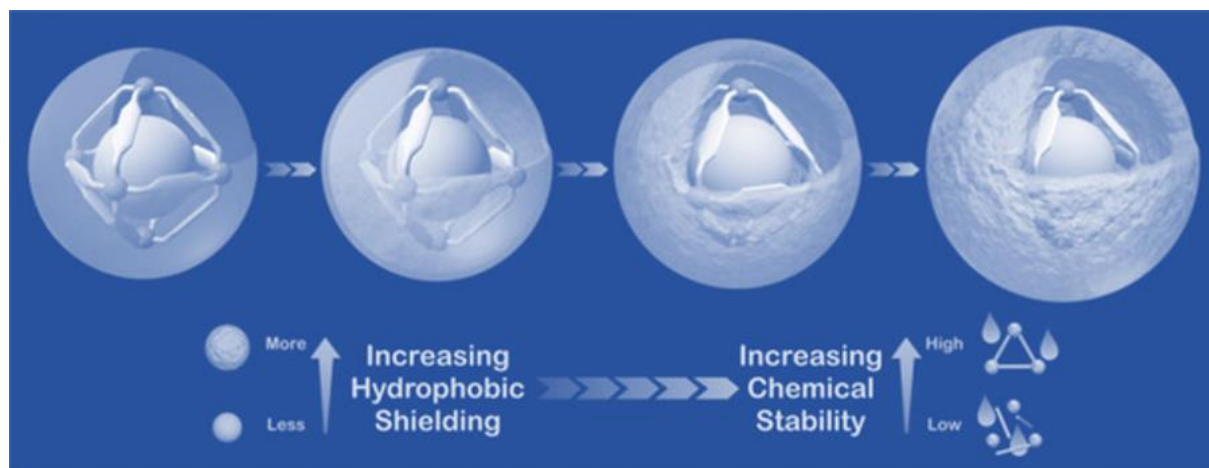


Figure 1.16 Schematic representation illustrating incremental hydrophobic shielding of IPMOP's (reproduced with the permission).

1.4 Thesis Overview at a Glance:

The focus of the current thesis work is primarily on the design and synthesis of novel ambidentate ligands as well as the utilization of a few existing ligand systems to produce application-specific novel anionic MOFs and their thorough application-bound investigation. Additionally, stable and viable functional porous materials are meticulously deployed with an emphasis on energy and environmental applications. Although

anionic MOFs are now the center of extensive research in a number of application areas, still little is understood and explored about their capacity to selectively and efficiently capture uranium for the remediation of harmful aquatic contaminants besides its sequestration aimed for applications in the field of energy, similar is true for their potential rendering to sorting and identification of other toxic aqueous pollutants such as antibiotics or pesticides. Through our understanding of chemistry and expertise in functional porous materials, we set out to address some truly exciting problems in the realms of energy and environment. In line with the theme context, the entirety of the thesis is broken up into two broadened sections, and each of those sections is further broken up into two chapters each. Porous functional anionic MOFs for environmental applications were covered in depth throughout part I with subdivisions into chapters 2 and 3, while advanced porous materials for energy applications were addressed and covered in depth throughout part II with subdivisions including chapters 4 and 5.

We have provided a brief synopsis with necessary insights that have been obtained through the careful application of anionic MOFs and a variety of functional porous materials in aqueous pollutant remediation and applications related to energy, respectively. The systematic design, synthesis, and functional studies of anionic metal–organic frameworks (MOFs) have been primary goals of this work. This is due to the fact that anionic MOFs hold great promise for resolving challenging environmental pollution concerns owing to their inherent ionic nature that minimizes leaching and allows exchange of specific chemical species with greater selectivity, thereby sequestering targeted pollutants and reducing the need for sustainable energy. An insightful review was done on the function that counter cations, which can be either inorganic or organic, play in pore-engineered and trap-grafted functional anionic MOFs to steer the structure-property correlation for a variety of different applications. The results of the research conducted for this thesis into anionic MOFs for the rapid sensing, efficient capture, and consequent sequestration of aqueous and environmental pollutants, as well as novel approaches to device fabrication and structure property correlation for energy application, have been discussed in light of the investigations that are currently considered to be state-of-the-art. It is possible that in the not too distant future, the production of the next generation of ionic materials will allow a compatible path for the resolution of significant industrial and environmental issues. Studies based on functional MOFs and porous materials for sustainable energy-environment applications and cleaning up water pollution might be able to make this a reality.

1.7 References

- [1] A. G. Slater, A. I. Cooper, *Science* **2015**, *348*, aaa8075.
- [2] S. Kitagawa, R. Kitaura, S.-i. Noro, *Angew. Chem. Int. Ed.* **2004**, *43*, 2334-2375.
- [3] H. Li, M. Eddaoudi, M. O'Keeffe, O. M. Yaghi, *Nature* **1999**, *402*, 276-279.

- [4] H. Furukawa, K. E. Cordova, M. O’Keeffe, O. M. Yaghi, *Science* **2013**, *341*, 1230444.
- [5] O. M. Yaghi, M. O’Keeffe, N. W. Ockwig, H. K. Chae, M. Eddaoudi, J. Kim, *Nature* **2003**, *423*, 705-714.
- [6] J.-R. Li, R. J. Kuppler, H.-C. Zhou, *Chem. Soc. Rev.*, **2009**, *38*, 1477-1504.
- [7] J.-R. Li, J. Sculley, H.-C. Zhou, *Chem. Rev.* **2012**, *112*, 869–932.
- [8] N. Stock, S. Biswas, *Chem. Rev.* **2012**, *112*, 933–969.
- [9] X. Liu, Y. Zhou, J. Zhang, L. Tang, L. Luo, G. Zeng, *ACS Appl. Mater. Interfaces* **2017**, *9*, 20255-20275.
- [10] M. D. Allendorf, C. A. Bauer, R. K. Bhakta, R. J. T. Houk, *Chem. Soc. Rev.* **2009**, *38*, 1330-1352.
- [11] W. P. Lustig, S. Mukherjee, N. D. Rudd, A. V. Desai, J. Li, S. K. Ghosh, *Chem. Soc. Rev.* **2017**, *46*, 3242-3285.
- [12] Espallargas, G. M.; Coronado, E., *Chem. Soc. Rev.* **2018**, *47*, 533-557.
- [13] A. Schneemann, V. Bon, I. Schwedler, I. Senkovska, S. Kaskel, R. A. Fischer, *Chem. Soc. Rev.* **2014**, *43*, 6062-6096.
- [14] Z. Chang, D.-H. Yang, J. Xu, T.-L. Hu, X.-H. Bu, *Adv. Mater.* **2015**, *27*, 5432-5441.
- [15] N. C. Burtch, H. Jasuja, K. S. Walton, *Chem. Rev.* **2014**, *114*, 10575-10612.
- [16] S. Yuan, L. Feng, K. Wang, J. Pang, M. Bosch, C. Lollar, Y. Sun, J. Qin, X. Yang, P. Zhang, Q. Wang, L. Zou, Y. Zhang, L. Zhang, Y. Fang, J. Li, H.-C. Zhou, *Adv. Mater.* **2018**, *30*, 1704303.
- [17] J. H. Cavka, S. Jakobsen, U. Olsbye, N. Guillou, C. Lamberti, S. Bordiga, K. P. Lillerud, *J. Am. Chem. Soc.* **2008**, *130*, 13850-13851
- [18] J. An, S. J. Geib, N. L. Rosi, *J. Am. Chem. Soc.* **2009**, *131*, 8376- 8377.
- [19] C. N. R. Rao, S. Natarajan, R. Vaidhyanathan, *Angew. Chem. Int. Ed.* **2004**, *43*, 1466-1496.
- [20] J. Gu, M. Wen, X. Liang, Z. Shi, M. V. Kirillova, A. M. Kirillov, *Crystals* **2018**, *8*, 83.
- [21] A. Schoedel, M. Li, D. Li, M. O’Keeffe, O. M. Yaghi, *Chem. Rev.* **2016**, *116*, 12466-12535.
- [22] G. K. H. Shimizu, R. Vaidhyanathan, J. M. Taylor, *Chem. Soc. Rev.* **2009**, *38*, 1430-1449.

- [23] J. E. Reynolds, S. G. Dunning, C. M. McCulley, S. M. Humphrey, A Survey of Metal-Organic Frameworks Based on Phosphorus and Sulfur-Containing Building Blocks (Elaboration and Applications of Metal-Organic Frameworks; Eds. S. Ma, J. A. Perman), **2018**, 37-141, DOI: 10.1142/9789813226739_0002.
- [24] J.-P. Zhang, Y.-B. Zhang, J.-B. Lin, X.-M. Chen, *Chem. Rev.* **2012**, *112*, 1001-1033.
- [25] B. Manna, A. V. Desai, S. K. Ghosh, *Dalton Trans.* **2016**, *45*, 4060-4072.
- [26] S. Horike, S. Shimomura, S. Kitagawa, *Nat. Chem.* **2009**, *1*, 695-704.
- [27] A. Karmakar, A. V. Desai, S. K. Ghosh, *Coord. Chem. Rev.* **2016**, *307*, 313-341.
- [28] J. A. Johnson, X. Zhang, X. Zhang, J. Zhang, *Current Organic Chemistry*, **2014**, *18*, 1973-2001.
- [29] C. Mao, R. A. Kudla, F. Zuo, X. Zhao, L. J. Mueller, X. Bu, P. Feng, *J. Am. Chem. Soc.* **2014**, *136*, 7579-7582.
- [30] T. Chen, C. Zhang, Y. Qin, H. Yang, P. Zhang, F. Ye, *Materials* **2017**, DOI: 10.3390/ma10080879.
- [31] B. M. Wiers, M.-L. Foo, N. P. Balsara, J. R. Long, *J. Am. Chem. Soc.* **2011**, *133*, 14522-14525.
- [32] S. R. J. Oliver, *Chem. Soc. Rev.* **2009**, *38*, 1868-1881.
- [33] D. Banerjee, D. Kim, M. J. Schweiger, A. A. Kruger, P. K. Thallapally, *Chem. Soc. Rev.* **2016**, *45*, 2724-2739.
- [34] P. Kumar, A. Pournara, K.-H. Kim, V. Bansal, S. Rapti, M. J. Manos, *Prog. Mater. Sci.* **2017**, *86*, 25-74.
- [35] J. An, C. M. Shade, D. A. Chengelis-Czegán, S. Petoud, N. L. Rosi, *J. Am. Chem. Soc.* **2011**, *133*, 1220-1223.
- [36] L. Li, X. Wang, J. Liang, Y. Huang, H. Li, Z. Lin, R. Cao, *ACS Appl. Mater. Interfaces* **2016**, *8*, 9777-9781.
- [37] P. Li, N. A. Vermeulen, X. Gong, C. D. Malliakas, J. F. Stoddart, J. T. Hupp, O. K. Farha, *Angew. Chem. Int. Ed.* **2016**, *55*, 10358-10362.
- [38] H.-F. Ma, Q.-Y. Liu, Y.-L. Wang, S.-G. Yin, *Inorg. Chem.* **2017**, *56*, 2919-2925.
- [39] J. An, S. J. Geib and N. L. Rosi, *J. Am. Chem. Soc.*, **2009**, *131*, 8376-8377.

- [40] E.-Y. Cho, J.-M. Gu, I.-H. Choi, W.-S. Kim, Y.-K. Hwang, S. Huh, S.-J. Kim, Y. Kim, *Cryst. Growth Des.* **2014**, *14*, 5026–5033.
- [41] X.-L. Chen, Y. Pan, X.-Z. Song, *Polyhedron*, **2016**, *117*, 513–517.
- [42] J. Ai, F.Y. Chen, C.Y. Gao, H.R. Tian, Q.J. Pan, Z.M. Sun, *Inorg. Chem.*, **2018**, *57*, 4419–4426.
- [43] M.E. Medina, Y. Dumont, J.-M. Grenechec, F. Millange, *Chem. Commun.*, **2010**, *46*, 7987–989.
- [44] S. Chen, J. Zhang, T. Wu, P. Feng, X. Bu, *J. Am. Chem. Soc.*, **2009**, *131*, 16027–16029.
- [45] F. Nouar, J. Eckert, J.F. Eubank, P. Forster, M. Eddaoudi, *J. Am. Chem. Soc.*, **2009**, *131*, 2864–2870.
- [46] D.F. Sava, V. Kravtsov, F. Nouar, L. Wojtas, J.F. Eubank, M. Eddaoudi, *J. Am. Chem. Soc.*, **2008**, *130*, 3768–3770.
- [47] R.-X. Yao, X. Xu, X.-M. Zhang, *Chem. Mater.* **2012**, *24*, 303–310.
- [48] F. Bu, Q. Lin, Q.G. Zhai, X. Bu, P. Feng, *Dalton Trans.*, **2015**, *44*, 16671–16674.
- [49] B.M. Wiers, M.L. Foo, N.P. Balsara, J.R. Long, *J. Am. Chem. Soc.*, **2011**, *133*, 14522–14525.
- [50] R. Ameloot, M. Aubrey, B.M. Wiers, A.P.G. Figueroa, S.N. Patel, N.P. Balsara, J.R. Long, *Chem. Eur. J.*, **2013**, *19*, 5533–5536.
- [51] S.-i. Noro, R. Kitaura, M. Kondo, S. Kitagawa, T. Ishii, H. Matsuzaka, M. Yamashita, *J. Am. Chem. Soc.* **2002**, *124*, 2568–2583
- [52] H. Fei, L. Paw U, D. L. Rogow, M. R. Bresler, Y. A. Abdollahian, S. R. J. Oliver, *Chem. Mater.* **2010**, *22*, 2027–2032
- [53] I. R. Colinas, K. K. Inglis, F. Blanc, S. R. J. Oliver, *Dalton Trans.* **2017**, *46*, 5320–5325.
- [54] Y.-Q. Chen, G.-R. Li, Z. Chang, Y.-K. Qu, Y.-H. Zhang, X.-H. Bu, *Chem. Sci.* **2013**, *4*, 3678–3682.
- [55] X. Li, H. Xu, F. Kong, R. Wang, *Angew. Chem. Int. Ed.* **2013**, *52*, 13769–13773.
- [56] X. Li, Y. Gong, H. Zhao, R. Wang, *Inorg. Chem.* **2014**, *53*, 12127–12134.
- [57] M. Guo, H. Guo, S. Liu, Y. Sun, X. Guo, *RSC Adv.* **2017**, *7*, 51021–51026.
- [58] Y. Cui, Y. Yue, G. Qian, B. Chen, *Chem. Rev.* **2012**, *112*, 1126–1162.
- [59] E. Coronado, G. M. Espallargas, *Chem. Soc. Rev.* **2013**, *42*, 1526–1539.

- [60] Z. Zhang, Z.-Z. Yao, S. Xiang, B. Chen, *Energy Environ. Sci.* **2014**, *7*, 2868-2899.
- [61] P. Ramaswamy, N. E. Wong, G. K. H. Shimizu, *Chem. Soc. Rev.* **2014**, *43*, 5913-5932.
- [62] E. Barea, C. Montoro, J. A. R. Navarro, *Chem. Soc. Rev.* **2014**, *43*, 5419- 5430.
- [63] C. Wang, X. Liu, N. K. Demir, J. P. Chen, K. Li, *Chem. Soc. Rev.* **2016**, *45*, 5107-5134
- [64] Z. Bao, G. Chang, H. Xing, R. Krishna, Q. Ren, B. Chen, *Energy Environ. Sci.* **2016**, *9*, 3612-3641.
- [65] W. Wang, X. Xu, W. Zhou, Z. Shao, *Adv. Sci.* **2017**, *4*, 1600371.
- [66] Y.-B. Huang, J. Liang, X.-S. Wang, R. Cao, *Chem. Soc. Rev.* **2017**, *46*, 126-157.
- [67] D. Sheng, L. Zhu, C. Xu, C. Xiao, Y. Wang, Y. Wang, L. Chen, J. Diwu, J. Chen, Z. Chai, T. E. Albrecht-Schmitt, S. Wang, *Environ. Sci. Technol.* **2017**, *51*, 3471-3479.
- [68] E. Q. Procopio, F. Linares, C. Montoro, V. Colombo, A. Maspero, E. Barea, J. A. R. Navarro, *Angew. Chem. Int. Ed.* **2010**, *49*, 7308.
- [69] F. Nouar, J. Eckert, J. F. Eubank, P. Forster, M. Eddaoudi, *J. Am. Chem. Soc.* **2009**, *131*, 2864.
- [70] S. Bhattacharyya, A. Chakraborty, K. Jayaramulu, A. Hazra, T. K. Maji, *Chem. Commun.* **2014**, *50*, 13567.
- [71] H. J. Parka, M. P. Suh, *Chem. Sci.* **2013**, *4*, 685.
- [72] Y.-W. Li, J. Xu, D.-C. Li, J.-M. Dou, H. Yan, T.-L. Hu, X.-H. Bu, *Chem. Commun.* **2015**, *51*, 14211.
- [73] J. Li, X. Wang, G. Zhao, C. Chen, Z. Chai, A. Alsaedi, T. Hayatf, X. Wang, *Chem. Soc. Rev.* **2018**, *47*, 2322.
- [74] S. Seth, G. Savitha, J.N. Moorthy, *J. Mater. Chem. A* **2015**, *3*, 22915.
- [75] Y. Zhou, S. Yao, Y. Ma, G. Li, Q. Huo, Y. Liu, *Chem. Commun.* **2018**, *54*, 3006.
- [76] S. Chu, A. Majumdar, *Nature* **2012**, *488*, 294.
- [77] Q. Schiermeier, J. Tollefson, T. Scully, A. Witze, O. Morton, *Nature* **2008**, *454*, 816.
- [78] N. Tang, J. Liang, C. Niu, H. Wang, Y. Luo, W. Xing, S. Ye, C. Liang, H. Guo, J. Guo, Y. Zhang, G. Zeng, *J. Mater. Chem. A* **2020**, *8*, 7588.
- [79] S. Zhang, H. Li, S. Wang, *Chem* **2020**, *6*, 1504.

- [80] C. W. Abney, R. T. Mayes, T. Saito, S. Dai, *Chem. Rev.* **2017**, *117*, 13935.
- [81] D. S. Sholl, R. P. Lively, *Nature* **2016**, *532*, 435.
- [82] M. J. Manos, M. G. Kanatzidis, *Chem. Sci.* **2016**, *7*, 4804.
- [83] T. Zheng, Z. Yang, D. Gui, Z. Liu, X. Wang, X. Dai, S. Liu, L. Zhang, Y. Gao, L. Chen, D. Sheng, Y. Wang, J. Diwu, J. Wang, R. Zhou, Z. Chai, T. E. Albrecht-Schmitt, S. Wang, *Nat Commun* **2017**, *8*, 15369.
- [84] X. Yang, J. Li, J. Liu, Y. Tian, B. Li, K. Cao, S. Liu, M. Hou, S. Li, L. Ma, *J. Mater. Chem. A* **2013**, *2*, 1550.
- [85] J. Li, X. Dai, L. Zhu, C. Xu, D. Zhang, M. A. Silver, P. Li, L. Chen, Y. Li, D. Zuo, H. Zhang, C. Xiao, J. Chen, J. Diwu, O. K. Farha, T. E. Albrecht-Schmitt, Z. Chai, S. Wang, *Nat Commun* **2018**, *9*, 3007.
- [86] D. Wang, J. Song, J. Wen, Y. Yuan, Z. Liu, S. Lin, H. Wang, H. Wang, S. Zhao, X. Zhao, M. Fang, M. Lei, B. Li, N. Wang, X. Wang, H. Wu, *Advanced Energy Materials* **2018**, *8*, 1802607.
- [87] Z. Wang, Q. Meng, R. Ma, Z. Wang, Y. Yang, H. Sha, X. Ma, X. Ruan, X. Zou, Y. Yuan, G. Zhu, *Chem* **2020**, *6*, 1683.
- [88] C. Xiao, M. A. Silver, S. Wang, *Dalton Trans.* **2017**, *46*, 16381.
- [89] Hong-Cai “Joe” Zhou, S. Kitagawa, *Chemical Society Reviews* **2014**, *43*, 5415.
- [90] G. Maurin, C. Serre, A. Cooper, G. Férey, *Chem. Soc. Rev.* **2017**, *46*, 3104.
- [91] D. Banerjee, S. J. Kim, H. Wu, W. Xu, L. A. Borkowski, J. Li, J. B. Parise, *Inorg. Chem.* **2011**, *50*, 208.
- [92] A. B. Spore, N. L. Rosi, *CrystEngComm* **2017**, *19*, 5417.
- [93] P. Li, N. A. Vermeulen, X. Gong, C. D. Malliakas, J. F. Stoddart, J. T. Hupp, O. K. Farha, *Angewandte Chemie International Edition* **2016**, *55*, 10358.
- [94] F. Zarekarizi, S. Beheshti, A. Morsali, *Inorganic Chemistry Communications* **2018**, *97*, 144.
- [95] H. Li, F. Zhai, D. Gui, X. Wang, C. Wu, D. Zhang, X. Dai, H. Deng, X. Su, J. Diwu, Z. Lin, Z. Chai, S. Wang, *Applied Catalysis B: Environmental* **2019**, *254*, 47.
- [96] J. Yu, Y. Cui, H. Xu, Y. Yang, Z. Wang, B. Chen, G. Qian, *Nat Commun* **2013**, *4*, 2719.
- [97] Q. Sun, B. Aguila, J. Perman, A. S. Ivanov, V. S. Bryantsev, L. D. Earl, C. W. Abney, L. Wojtas, S. Ma, *Nat Commun* **2018**, *9*, 1644.

- [98] L. Zhang, N. Pu, B. Yu, G. Ye, J. Chen, S. Xu, S. Ma, *ACS Appl. Mater. Interfaces* **2020**, *12*, 3688.
- [99] A. Mojiri, J. L. Zhou, B. Robinson, A. Ohashi, N. Ozaki, T. Kindaichi, H. Farraji and M. Vakili, *Chemosphere*, 2020, **253**, 126646
- [100] D. Moreno-González, F. J. Lara, N. Jurgovská, L. Gámiz-Gracia and A. M. García-Campaña, *Analytica Chimica Acta*, 2015, **891**, 321–328.
- [101] Hakansson, null Coorey, null Zubarev, null Talrose, null Hakansson, *J Mass Spectrom* **2000**, *35*, 337.
- [102] “Simultaneous Raman Spectroscopy–Laser-Induced Breakdown Spectroscopy for Instant Standoff Analysis of Explosives Using a Mobile Integrated Sensor Platform | Analytical Chemistry,” can be found under <https://pubs.acs.org/doi/full/10.1021/ac902470v>, **n.d.**
- [103] M. Tabrizchi, V. Ilbeigi, *J Hazard Mater* **2010**, *176*, 692.
- [104] M. E. Germain, M. J. Knapp, *Chem. Soc. Rev.* **2009**, *38*, 2543.
- [105] W. P. Lustig, S. Mukherjee, N. D. Rudd, A. V. Desai, J. Li, S. K. Ghosh, *Chem. Soc. Rev.* **2017**, *46*, 3242.
- [106] B. Wang, X.-L. Lv, D. Feng, L.-H. Xie, J. Zhang, M. Li, Y. Xie, J.-R. Li, H.-C. Zhou, *J. Am. Chem. Soc.* **2016**, *138*, 6204.
- [107] S. S. Nagarkar, A. V. Desai, S. K. Ghosh, *Chemical Communications* **2014**, *50*, 8915.
- [108] S. Wang, H. Li, H. Huang, X. Cao, X. Chen, D. Cao, *Chem. Soc. Rev.* **2022**, *51*, 2031.
- [109] E. A. Dolgoplova, A. M. Rice, C. R. Martin, N. B. Shustova, *Chem. Soc. Rev.* **2018**, *47*, 4710.
- [110] L. E. Kreno, K. Leong, O. K. Farha, M. Allendorf, R. P. Van Duyne, J. T. Hupp, *Chem. Rev.* **2012**, *112*, 1105.
- [111] W. Lu, D. Yuan, J. Sculley, D. Zhao, R. Krishna, H.-C. Zhou, *J. Am. Chem. Soc.* **2011**, *133*, 18126.
- [112] X.-Y. Yang, L.-H. Chen, Y. Li, J. C. Rooke, C. Sanchez, B.-L. Su, *Chem. Soc. Rev.* **2017**, *46*, 481.
- [113] P. Kuhn, M. Antonietti, A. Thomas, *Angewandte Chemie International Edition* **2008**, *47*, 3450.
- [114] S. Ren, M. J. Bojdys, R. Dawson, A. Laybourn, Y. Z. Khimiyak, D. J. Adams, A. I. Cooper, *Advanced Materials* **2012**, *24*, 2357.

- [115] W. Mandal, S. Fajal, S. Mollick, M. M. Shirolkar, Y. D. More, S. Saurabh, D. Mahato, S. K. Ghosh, *ACS Appl. Mater. Interfaces* **2022**, *14*, 20042.
- [116] M. G. Mohamed, A. F. M. EL-Mahdy, M. G. Kotp, S.-W. Kuo, *Mater. Adv.* **2022**, *3*, 707.
- [117] J. Wu, F. Xu, S. Li, P. Ma, X. Zhang, Q. Liu, R. Fu, D. Wu, *Advanced Materials* **2019**, *31*, 1802922.
- [118] J. Yu, C. Zhang, *J. Mater. Chem. C* **2020**, *8*, 16463.
- [119] A. Karmakar, A. Kumar, A. K. Chaudhari, P. Samanta, A. V. Desai, R. Krishna, S. K. Ghosh, *Chemistry – A European Journal* **2016**, *22*, 4931.
- [120] A. V. Desai, P. Samanta, B. Manna, S. K. Ghosh, *Chem. Commun.* **2015**, *51*, 6111.
- [121] G. Khandelwal, A. Chandrasekhar, N. P. Maria Joseph Raj, S.-J. Kim, *Advanced Energy Materials* **2019**, *9*, 1803581.
- [122] J.-W. Yoon, J.-H. Kim, C. Kim, H. W. Jang, J.-H. Lee, *Advanced Energy Materials* **2021**, *11*, 2170106.
- [123] Q. Tang, H. Guo, P. Yan, C. Hu, *EcoMat* **2020**, *2*, e12060.
- [124] H. Zou, Y. Zhang, L. Guo, P. Wang, X. He, G. Dai, H. Zheng, C. Chen, A. C. Wang, C. Xu, Z. L. Wang, *Nat Commun* **2019**, *10*, 1427.
- [125] F.-R. Fan, Z.-Q. Tian, Z. Lin Wang, *Nano Energy* **2012**, *1*, 328.
- [126] G. Khandelwal, A. Chandrasekhar, N. R. Alluri, V. Vivekananthan, N. P. Maria Joseph Raj, S.-J. Kim, *Applied Energy* **2018**, *219*, 338.
- [127] B. Dudem, N. D. Huynh, W. Kim, D. H. Kim, H. J. Hwang, D. Choi, J. S. Yu, *Nano Energy* **2017**, *42*, 269.
- [128] Z. L. Wang, T. Jiang, L. Xu, *Nano Energy* **2017**, *39*, 9.
- [129] S. K. Singh, P. Kumar, R. Magdum, U. Khandelwal, S. Deswal, Y. More, S. Muduli, R. Boomishankar, S. Pandit, S. Ogale, *ACS Appl. Bio Mater.* **2019**, *2*, 3164
- [130] I. V. Kolesnichenko, E. V. Anslyn, *Chem. Soc. Rev.* **2017**, *46*, 2385.
- [131] B. Moulton, M. J. Zaworotko, *Chem. Rev.* **2001**, *101*, 1629.
- [132] O. K. Farha, I. Eryazici, N. C. Jeong, B. G. Hauser, C. E. Wilmer, A. A. Sarjeant, R. Q. Snurr, S. B. T. Nguyen, A. O. Yazaydin, J. T. Hupp, *J. Am. Chem. Soc.* **2012**, *134*, 15016.

- [133] R. Matsuda, R. Kitaura, S. Kitagawa, Y. Kubota, R. V. Belosludov, T. C. Kobayashi, H. Sakamoto, T. Chiba, M. Takata, Y. Kawazoe, Y. Mita, *Nature* **2005**, *436*, 238.
- [134] Y. Cui, Y. Yue, G. Qian, B. Chen, *Chem. Rev.* **2012**, *112*, 1126.
- [135] H.-C. Zhou, J. R. Long, O. M. Yaghi, *Chem. Rev.* **2012**, *112*, 673.
- [136] H.-C. Zhou, S. Kitagawa, *Chem. Soc. Rev.* **2014**, *43*, 5415.
- [137] M. C. So, G. P. Wiederrecht, J. E. Mondloch, J. T. Hupp, O. K. Farha, *Chem. Commun.* **2015**, *51*, 3501.
- [138] M. Eddaoudi, J. Kim, J. B. Wachter, H. K. Chae, M. O'Keeffe, O. M. Yaghi, *J. Am. Chem. Soc.* **2001**, *123*, 4368.
- [139] H. Abourahma, A. W. Coleman, B. Moulton, B. Rather, P. Shahgaldian, M. J. Zaworotko, *Chem. Commun.* **2001**, 2380.
- [140] A. J. Howarth, Y. Liu, P. Li, Z. Li, T. C. Wang, J. T. Hupp, O. K. Farha, *Nat. Rev. Mater.* **2016**, *1*, 15018.
- [141] H. Assi, G. Mouchaham, N. Steunou, T. Devic, C. Serre, *Chem. Soc. Rev.* **2017**, *46*, 3431.
- [142] G. Mouchaham, S. Wang, C. Serre, *The Stability of Metal-Organic Frameworks*, Wiley-VCH, Weinheim, **2018**.
- [143] P. G. M. Mileo, T. Kundu, R. Semino, V. Benoit, N. Steunou, P. L. Llewellyn, C. Serre, G. Maurin, S. Devautour-Vinot, *Chem. Mater.* **2017**, *29*, 7263.
- [144] S. Kandambeth, V. Venkatesh, D. B. Shinde, S. Kumari, A. Halder, S. Verma, R. Banerjee, *Nat. Commun.* **2015**, *6*, 6786.
- [145] M. Dan-Hardi, C. Serre, T. Frot, L. Rozes, G. Maurin, C. Sanchez, G. Férey, *J. Am. Chem. Soc.* **2009**, *131*, 10857.
- [146] D. J. Tranchemontagne, Z. Ni, M. O'Keeffe, O. M. Yaghi, *Angew. Chem. Int. Ed.* **2008**, *47*, 5136.
- [147] J. R. Li, H. C. Zhou, *Nat. Chem.* **2010**, *2*, 893.
- [148] H. Furukawa, J. Kim, N. W. Ockwig, M. O'Keeffe, O. M. Yaghi, *J. Am. Chem. Soc.* **2008**, *130*, 11650.

[149] S. Leininger, B. Olenyuk, P. J. Stang, *Chem. Rev.* **2000**, *100*, 853.

Part-I

**Functional Anionic MOFs for Environmental
Applications**

We are living in an age of energy shortage, and keeping the world's energy supply in the face of rising energy consumption while taking into account the risks posed by fossil fuels remains a difficult task. A continuous, dependable, low carbon emission endowed clean energy supply remains a significant obstacle that humanity of the entire world faces.¹ Nuclear power will remain one of the few existing reliable energy sources in the future, as per predictions made by according International Atomic Energy Agency (IAEA). Since nuclear technological advances have the potential to provide energy for future generations, uranium recovery from alternative yet abundant sources including natural seawater has piqued the interest of scientific community.² However, as nuclear technologies advance and clamour for uranium grows, the gap between supply and demand for uranium has grown wider. This is due to the fact that the world's known geological uranium reserves are finite and will be diminished within the next few decades considering approximations made by IAEA.³ In light of the aforementioned perilous situation, scientific interest is growing for the uranium sprawled across the oceans or seawaters.³ The ocean contains 4.5 billion tonnes of uranium, which equates to a nearly limitless supply.^{4,5} As a result, uranium extraction from seawater (UES) is critical to making nuclear energy a long-term energy source. That is why recovery of uranium from seawater has been included in the gamut of seven chemical separations that are expected to have a significant impact and repulse on our society.⁶ Meeting the UES in a timely manner through the development of uranium adsorbents has remained a formidable challenge.^{3,7} We attempted and concentrated our efforts in this section on pore-engineering and consequently trap grafting through selective functionality introduction to obtain stable anionic MOFs by deploying Lewis basic site functionalized ligands and swapping out various uncoordinated cations inside the pore. This section of the thesis is divided into two chapters, chapters 2 and 3. We demonstrated the effectiveness of a novel anionic metal-organic framework (iMOF-1A) adorned with rare Lewis basic pyrazinic sites as a uranyl-specific trap serving as a robust ion exchange material for selective uranium extraction in chapter 2.

The lack of clean drinking water has grown to be a serious issue across many regions of the globe and accounted among major concerns of the twenty-first century.^{8,9} Water contamination poses an increasing risk to the overall ecology and ecosystem as urbanisation and population increase continues.¹⁰ Anthropogenic water pollutants including emergent organic contaminants are a substantial contributor to water pollution. The term "contaminant" is defined as any foreign physical, chemical or biological substance in water by the Safe Drinking Water Act (SDWA). Antibiotics and pesticides are two manmade wastes that are regarded as important pollutants that seriously pollute water.¹³ Penicillin is a well-known antibiotic that has been used as an antimicrobial agent active against bacteria. Due to its capacity to suppress the growth of numerous diseases, it has been widely prescribed and used as a medicine in hospitals for both people and animals.^{14,15} Additionally, since agriculture sector has expanded, it is now

used in fields including fisheries, food production, beekeeping, and other industries.^{13,16,17} However, microbial resistance to antibiotics are brought on by the its overuse. However, antibiotic misuse results in microorganism resistance to them. In line with this, the environment as well as food chain is severely harmed by the abuse or overuse of such substances on animals.¹⁸⁻²⁰ In addition, pesticides, another category of potential organic contaminants, have become "cause for concern." In order to boost productivity, pesticides have been widely utilised in modern agriculture.^{13,21,22} Pesticides are not only highly poisonous to agricultural pests by nature, but also highly water soluble and ultimately reaches to diverse water bodies. The neurological, respiratory, and reproductive systems of living things are adversely affected by prolonged exposure to these dangerous species.²³⁻²⁵ Given the negative effects and high levels of risk posed by the aforementioned organic pollutants in water, thorough and routine monitoring of such species is becoming a critical research area. In chapter 3, in addition to Paraquat capture, the selective and rapid identification of hazardous aquatic pollutants, such as antibiotics and pesticides in aqueous solution, is accomplished by delving into the specific fluorescence quenching mechanism of a recently synthesized highly luminous, electrically rich, porous metal-organic framework (iMOF-4A). In the presence of electron-deficient antibiotics like Nitrofurantoin (NFT) and Nitrofurazone (NFZ), as well as herbicides like Paraquat (PQ) in water, the iMOF-4A demonstrated a specific, significant quenching response, which is discussed in details in the sections to follow by.

References:

- [1] S. Chu, A. Majumdar, *Nature* **2012**, 488, 294.
- [2] Q. Schiermeier, J. Tollefson, T. Scully, A. Witze, O. Morton, *Nature* **2008**, 454, 816.
- [3] N. Tang, J. Liang, C. Niu, H. Wang, Y. Luo, W. Xing, S. Ye, C. Liang, H. Guo, J. Guo, Y. Zhang, G. Zeng, *J. Mater. Chem. A* **2020**, 8, 7588.
- [4] S. Zhang, H. Li, S. Wang, *Chem* **2020**, 6, 1504.
- [5] C. W. Abney, R. T. Mayes, T. Saito, S. Dai, *Chem. Rev.* **2017**, 117, 13935.
- [6] D. S. Sholl, R. P. Lively, *Nature* **2016**, 532, 435.
- [7] M. J. Manos, M. G. Kanatzidis, *Chem. Sci.* **2016**, 7, 4804.
- [8] S. K. Ghosh, *Metal-Organic Frameworks (MOFs) for Environmental Applications*, **2019**.
- [9] I. Ali, *Chem. Rev.* **2012**, 112, 5073.

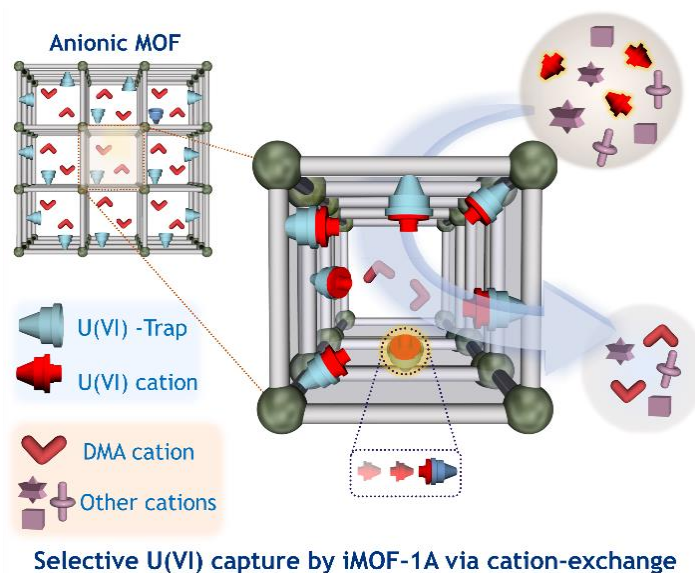
- [10] S. B. Grant, J.-D. Saphores, D. L. Feldman, A. J. Hamilton, T. D. Fletcher, P. L. M. Cook, M. Stewardson, B. F. Sanders, L. A. Levin, R. F. Ambrose, A. Deletic, R. Brown, S. C. Jiang, D. Rosso, W. J. Cooper, I. Marusic, *Science* **2012**, *337*, 681.
- [11] M. Patel, R. Kumar, K. Kishor, T. Mlsna, C. U. Pittman, D. Mohan, *Chemical Reviews* **2019**, *119*, 3510.
- [12] S. Rojas, P. Horcajada, *Chemical Reviews* **2020**, *120*, 8378.
- [13] J. Tang, X. Ma, J. Yang, D.-D. Feng, X.-Q. Wang, *Dalton Trans.* **2020**, *49*, 14361.
- [14] D.-W. Sun, L. Huang, H. Pu, J. Ma, *Chem. Soc. Rev.* **2021**, *50*, 1070.
- [15] W.-B. Zhong, R.-X. Li, J. Lv, T. He, M.-M. Xu, B. Wang, L.-H. Xie, J.-R. Li, *Inorg. Chem. Front.* **2020**, *7*, 1161.
- [16] X. Wang, N. Zhuo, C. Fu, Z. Tian, H. Li, J. Zhang, W. Wu, Z. Yang, W. Yang, *Chemical Engineering Journal* **2017**, *328*, 816.
- [17] N. Xu, Q. Zhang, B. Hou, Q. Cheng, G. Zhang, *Inorg. Chem.* **2018**, *57*, 13330.
- [18] Y.-M. Ying, C.-L. Tao, M. Yu, Y. Xiong, C.-R. Guo, X.-G. Liu, Z. Zhao, *J. Mater. Chem. C* **2019**, *7*, 8383.
- [19] G. Xian, L. Wang, X. Wan, H. Yan, J. Cheng, Y. Chen, J. Lu, Y. Li, D. Li, J. Dou, S. Wang, *Inorganic Chemistry* **2022**, *61*, 7238.
- [20] P. Samanta, S. Let, W. Mandal, S. Dutta, S. K. Ghosh, *Inorg. Chem. Front.* **2020**, *7*, 1801.
- [21] M.-L. Xu, Y. Gao, X. X. Han, B. Zhao, *J. Agric. Food Chem.* **2017**, *65*, 6719.
- [22] P. Samanta, A. V. Desai, S. Let, S. K. Ghosh, *ACS Sustainable Chem. Eng.* **2019**, *7*, 7456.
- [23] D. Tilman, K. G. Cassman, P. A. Matson, R. Naylor, S. Polasky, *Nature* **2002**, *418*, 671.
- [24] S. T. Narendran, S. N. Meyyanathan, B. Babu, *Food Research International* **2020**, *133*, 109141.
- [25] A. Mojiri, J. L. Zhou, B. Robinson, A. Ohashi, N. Ozaki, T. Kindaichi, H. Farraji, M. Vakili, *Chemosphere* **2020**, *253*, 126646.

Chapter 2

Superior Uranium Extraction from Seawater by Trap Grafted Anionic Metal- Organic Frameworks

2.1 Introduction

We live in an era of growing global energy demand and consequent tremendous instability that is affecting our world and society as well! Energy usage changes according to a variety of socio-economic factors, including urbanization, population growth, industrialization, economic development, and technological advancement. Considering the decline of conventional energy sources, long-term sustainable power supply has emerged as one of humanity's most pressing challenges.^[1] Accounting for many ecological difficulties associated with the use of fossil fuels, such as pollution, climate change, and biodiversity crises, the need for alternative forms of energy is critical in both technological and scientific fields.^[2] Nuclear energy has become one of the most preferred low-carbon options among established technologies owing to its negligible commitment to emissions of greenhouse gases.^[1] Because uranium is a vital part of nuclear reactors, the massive increase of nuclear operations related to its mining, processing, and recovery is critical for the dependable supply of sustainable energy. Unfortunately, there is an increasing scarcity of geological deposits of uranium ores that will become depleted in far less than a century or perhaps sooner if world consumption continues at its current rate.^[3]



Scheme 1. A schematic illustration of a trap grafted cation exchangeable MOF that is capable of selectively extracting uranyl ions from a variety of other competing cations.

In this context, the sea possesses around 4.5 million tons of uranium, making it a potentially massive source to support nuclear power production for generations.^[4,5] Uranium recovery from the sea

necessitates cutting-edge materials research and is regarded as one of the seven most important chemical separations that, if perfected, would have revolutionary worldwide impacts.^[6] Despite attempts made to create a variety of novel adsorbent materials for uranium recovery through seawater (UES).^[3,7-11] On a laboratory scale, however, their capabilities are typically restricted, with the majority suffering from incredibly low adsorption kinetics, poor selectivity, and reduced uptake capacity. To meet the crucial demand for continuous power supply, the development of novel long-lasting adsorbent materials that meet the strict commercial requirements imposed by the economic progression of UES is essential.^[13] MOFs constitute flagship materials in reticular chemistry, produced by coordination involving metal centers (clusters or metal ions) and organic scaffolds.^[14,15] Ionic MOFs (i-MOFs) are perhaps the most important MOF-based hosting matrix representations, providing for lingering charges, either negative or positive, that may be recurrently swapped with more suitable ions, hence delivering preferred functional capabilities. Anionic MOFs (iMOF-A), a subtype of ionic MOFs, have indeed been regarded as a family of functional materials due to their numerous uses in preferential capture, gas storage, drug administration, photonic applications, catalysis, and other areas.^[16-19]

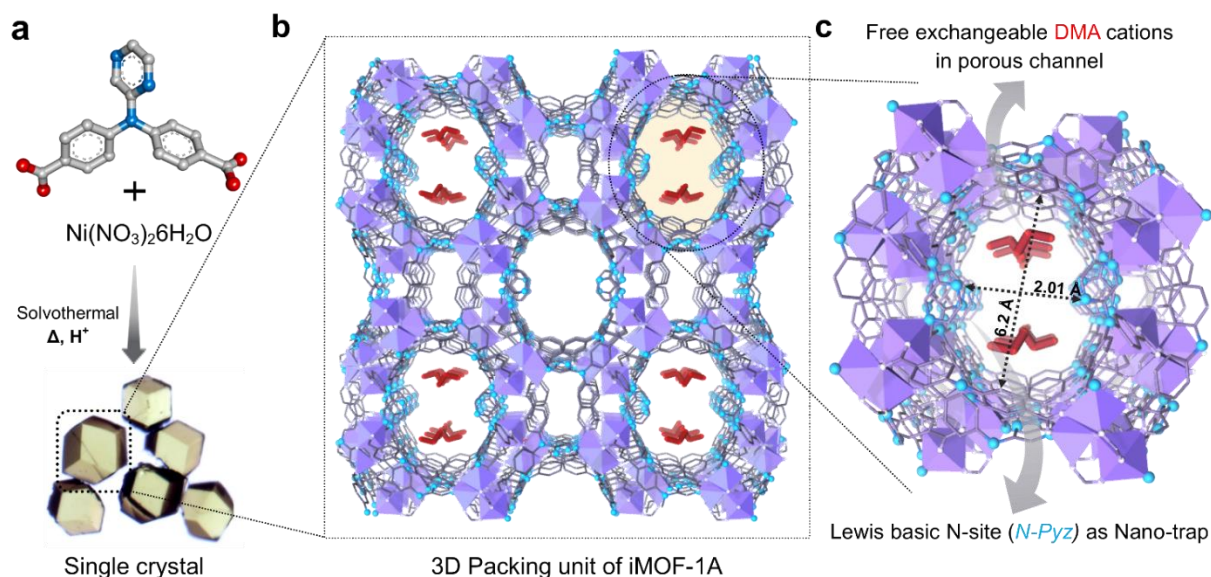


Figure 1. a) Synthetic protocol leading to **iMOF-1A**; b) View (Perspective) of **iMOF-1A** revealing its bi-porous nature containing ultramicroscopic channels sustaining the framework; c) Orderly (repetitive) arrangement of DMA cations inside the pore; (colour codes: purple—Ni, grey—C, white—O, cyan-blue—N, guest—scarlet red (DMA cations), H atoms and solvent molecules are omitted for clarity).

The presence of charged species inside the architectures causes certain interactions that may be effectively used as ion-exchange adsorbents for cationic guest entrapment. Because the captured cation is an intrinsic component of the framework or structure, being a charge-compensating ionic species. Furthermore, given the specific binding affinity of some analytes within the frameworks, ionic characteristics with conveniently accessible Lewis basic sites may provide further advantages (Scheme 1).^[20,21] Because of their remarkable potential, MOF-based adsorption and electrocatalytic extraction approaches have recently emerged as frontrunners for the preferential capture of a wide range of contaminants, including radioactive substances.^[22,23] While immense efforts have been made to fully understand the chemical and structural characteristics that affect the adsorption behavior, the comprehensive thermodynamics of MOF-analyte interaction processes in aqueous solutions has gone largely unexplored, despite the fact that it is critical for designing next-generation sorbents.

We attempted to use an anionic MOF for effective uranium recovery via ion-exchange and interaction mechanisms. Because of the loosely lying dimethyl ammonium (DMA) cations that may be readily replaced, **iMOF-1A**, as a hydrolytically viable anionic framework, has the promise to be a trailblazer throughout this regime. The anionic adsorbent (**iMOF-1A**) recovers 99.8% uranium in only 120 minutes (20000 ppb to 24 ppb) and has an exceptionally high distribution coefficient $K_d^U \geq 0.97 \times 10^6 \text{ mL g}^{-1}$, having a greater affinity towards uranium. When compared to previous documented MOFs, an **iMOF-1A** had a very high uranium adsorption capacity of 1336.8 mg g⁻¹ from water. The material effectively decreased trace quantities of uranium levels in a variety of water sources, including potable water, lake water, river water, and artificial seawater, to less than the Environmental Protection Agency (EPA) drinking water regulations in the United States (U.S.). The anionic adsorbent extracts more than 50% of the uranium from natural seawater (i.e., 7.1 gallons) and recovers 9.38 mg g⁻¹ uranium over 30 days with an excellent enrichment index of 5754. The ITC studies offer a thorough measurement of the thermodynamics of the sorption process in water media, which was previously unknown in the area of uranium capture. Interestingly, the nano-FTIR and TFM experiments revealed that the sequestration mechanism is related to both ion exchange and supramolecular interactions within **iMOF-1A** crystals. Coupled theoretical and experimental analyses also showed that the excellent selectivity and high uranium capacity are due to the development of chelation at the Lewis basic N-sites that are heavily decorated.

2.2 Experimental

2.2.1 Materials and measurements

The procedures described below were used to synthesize **iMOF-1A**. All components, comprising reagents, ligand precursors, and solvents, all commercially available and used without additional processing as received, except as otherwise stated. Removal of solvent in vacuo is the distillation process where the solvent is removed employing a rotating evaporator and an effective vacuum pump. High vacuum was used to dry the products that had been received as solids or syrups. On precoated Merck silica plates of specifications F254, 0.25 mm thickness, analytical thin-layer chromatography was carried out; chemicals were seen by UV light. Using a Perkin-Elmer 1600 FT-IR spectrometer, IR spectra were captured. On a Bruker Avance 400 MHz with CDCl_3 and $\text{DMSO}-d_6$ as the solvent and TMS as the internal standard, NMR spectra were captured. On the Waters Synapt G2, high resolution mass spectroscopy (HRMS) was carried out. The materials were purchased from Sigma-Aldrich, Alfa Aesar, Avra Chemicals and TCI Chemicals depending on their availability.

2.2.2 Syntheses

Synthesis of Intermediate L': For 48 hours, 2-Aminopyrazine (5 g, 52 mmol), and 4-FBN (4 – Fluorobenzonitrile, 13.20 g, 109 mmol), and CsF (cesium fluoride, 16.55 g, 109 mmol) were refluxed in N, N-dimethylformamide (DMF) (250 mL), as shown in Scheme 2. After cooling down reaction mixture to room temperature, it was concentrated in vacuo at 55 °C and extracted into ethyl acetate using a solvent extraction method with a water ethyl acetate 1:1 ratio. The organic phase was collected, dried over sodium sulphate, and vacuum concentrated. On precoated Merck silica plates of specifications F254, 0.25 mm thickness, analytical thin-layer chromatography was carried out to obtain Intermediate L' (13.91 g, 89.9%) as an almond white solid. Yield: ~89.9%. ^1H NMR (400.31 MHz, Chloroform-*d*) (Appendix 1) δ 8.25 - 8.17 (m, 3H), 7.60 (d, $J = 8.7$ Hz, 4H), 7.17 (d, $J = 8.7$ Hz, 4H); ^{13}C NMR (100.67 MHz, CDCl_3) (Appendix 2) δ 151.8, 146.0, 140.7, 137.3, 136.6, 132.0(3C), 123.7(3C), 12 Appendix 3: HRMS Calculated value for $\text{C}_{18}\text{H}_{11}\text{N}_5$ $[\text{M}+\text{H}]^+$: 298.1048; found mass value: 298.1086.

Synthesis of Acid Ligand LH₂: Column purified L' (7.5 g, 17 mmol) and potassium hydroxide (2.30 g, 41 mmol) were refluxed for 24 hours in a 200 mL water/ethanol (1:1) solvent mixture. After allowing the reaction mixture to cool to room temperature, it was acidified with diluted HCl in an ice bath until pH5 was reached. The precipitated product LH₂ (4,4'-(pyrazin-2-ylazanediyl)dibenzoic acid) was easily removed by filtering and thoroughly washing with cold water, same is shown in Scheme 2. Dried LH₂ appeared to be a yellow whitish powder that was purified further using silica gel column chromatography

to remove unwanted imposed spots (MeOH:DCM 15:75). 7.27 g, 86% yield ^1H NMR (DMSO- d_6 , 400.31 MHz) (Appendix 4) δ 9.9, δ 8.30 - 8.20 (m, 3H), 7.94 (d, J = 8.9 Hz, 4H), 7.24 (d, J = 9.0 Hz, 4H); ^{13}C NMR (100.67 MHz, DMSO- d_6) (Appendix 5) 172.0(2C), 159.2, 153.4(2C), 136.3(6C), 130.3 (7C). Appendix 6: HRMS Calculation for $\text{C}_{18}\text{H}_{13}\text{N}_3\text{O}_4$ $[\text{M}+\text{H}]^+$: 336.0940 is exact mass; 336.0978 is found mass value.

Synthesis of iMOF-1A: By combining 290.8 mg (1 mmol) $\text{Ni}(\text{NO}_3)_2 \cdot 6\text{H}_2\text{O}$ and 335.3 mg (1 mmol) 4,4'-(pyrazin-2-ylazanediy) dibenzoic acid (i.e. LH_2) in 30 mL DMF, green single crystals of **iMOF-1A** (compound 1) were obtained, as shown in Scheme 3. The mixture is sonicated again to obtain a homogeneous solution, and 5 mL of 0.08 N HCl is added. The resulting solution is thoroughly mixed and transferred to a teflon-lined, crew-capped glass vial. The vial was heated to 120 °C under autogenous pressure for 48 hours before being slowly cooled to room temperature. Compound 1 single crystals in the shape of a green cube were obtained with an 83% yield (considering metal weight). To improve the yield of crystalline product, the same reaction can be scaled down to 1/10th, i.e. 3 mL DMF and 0.5 mL 0.08N HCl per a single 8 mL glass vial by reducing the scale of total reagent and solvents by order of 10.

2.2.3 Characterizations and physical measurements

Both; Single crystal X-ray measurements and Powder X-ray diffraction (PXRD) patterns were performed to determine and confirm crystal structure of iMOF-1A. With Cu K radiation (λ = 1.5406 Å) at a scan speed of 0.5° (θ) min⁻¹ and a step size of 0.01° in 2θ , powder X-ray diffraction (PXRD) patterns were carried out using a Bruker D8 Advanced X-ray diffractometer at 298 K i.e. at room temperature. On the Perkin-Elmer STA6000, TGA analyser, thermogravimetric analysis profiles were captured with a heating rate of 10 °C min⁻¹ in a N_2 environment. Field-emission scanning electron microscope (FESEM, make: A Zeiss Ultra Plus) with an integrated charge compensator and integrated AsB and EsB detectors (make: Oxford X-max instruments 80 mm²) was used to capture the morphology of the crystalline solids (Carl Zeiss NTS, GmbH). To lessen charge, a 5–10 nm Au coating was sputtered onto the samples. The elemental analysis was performed with a 15 kV voltage and an EDX detector. An accumulation time of 600s was used for data collection. All of the materials were dissolved in isopropanol (0.5 mg/mL) and sonicated for 30 min in preparation for high-resolution TEM examination. The upper portion of the solution was then collected to prepare TEM samples on a lacey carbon-coated copper grid after the samples were left for 2 minutes (Electron Microscopy Science). The HRTEM (JEM-2200FS, JEOL) was used for TEM imaging while it was operating at 200 kV of acceleration voltage. A Bruker 400 MHz NMR spectrometer was used

to record NMR spectra. Parts per million (scale) are used to express carbon chemical changes. Using a KBr pellet and the NICOLET 6700 FT-IR spectrophotometer, the IR spectra were obtained in the 500–4000 cm^{-1} range. BelSorp-Max equipment was used to measure gas adsorption (Bel Japan). The activated samples were heated at 120 °C under vacuum for 12 hours prior to adsorption measurements using BelPrepvacII. Leica DM6B EPI-Fluorescence device was used to record the fluorescence imaging. Simultaneous ICP Spectrometer, ARCOS, was used to perform ICP-AES analysis. Thermo Fisher Scientific's quadrupole inductively coupled plasma mass spectrometry system was used for the ICP-MS operation. Inorganic ventures were used to purchase multi-element standards. Thermo Fischer Scientific's K-Alpha+model and an Al $K\alpha$ source were used for the XPS tests. The supplemental crystallographic data for this work can be found in the CCDC **2208426** file. These data are available from The Cambridge Crystallographic Data Centre at no cost and can be requested through their website at www.ccdc.cam.ac.uk/data request/cif.

2.2.4 Uranium capture study

Adsorption study: Uranyl nitrate hexahydrate ($\text{UO}_2(\text{NO}_3)_2 \cdot 6\text{H}_2\text{O}$) salts were dissolved in deionized water to generate U(VI) solution. A 20 ppm starting concentration of the U solution (comprised of U(VI) ions) was used in kinetics studies. In comparison to the U solution's 45 mL, the adsorbent was 20 mg. Using the data from this time-dependent investigation, we computed the elimination percentage and declining amount of the U with time using the given equations: $D_t = [(C_0 - C_t)/C_0] * 100$, where C_0 and C_t are the initial and final concentrations, respectively, at a given time. The following two equations were used to examine the simplified kinetic models of the pseudo-first-order and pseudo-second-order for the adsorption kinetics:

$$\ln(Q_e - Q_t) = \ln Q_e - k_1 t$$

$$t/Q_t = 1/(k_2 * Q_e) + (t/Q_e)$$

The U solution with an initial concentration of 25–1000 ppm and a pH of 7 was employed in isotherm studies. The U solution was 6 mL, the adsorbent 2 mg, and the contact duration 12 hours. After 12 hours, the filtrate was collected using a syringe filter (0.2 μm), the concentration was determined using ICP-AES, and the following equations were then fitted.

Langmuir Model, $Q_e = (Q_m * C_e)/(K_L + C_e)$; Here C_e (ppm) and Q_e (mg g^{-1}) stand for the equilibrium U concentrations and U adsorbed fraction at equilibrium, respectively. The maximum proportion of U per

mass of adsorbent required to completely form a monolayer is Q_m (mg g^{-1}). The binding strength is related to the constant K_L (mg L^{-1}).

Freundlich Model, $Q_e = K_f \cdot (C_e)^{1/n}$; Here, K_f and $1/n$ (Freundlich model constant) indicates capacity and intensity for adsorption respectively. HNO_3 (1M) and KOH were added to the U solution, which had a pH range of 3 to 9, in the pH-dependent investigation (1 M). The U solution was 4 mL in volume, the adsorbent 2 mg, and the contact duration 12 hours. A binary and well-mixed solution with an initial concentration of 5 ppm and a pH of 7 was employed in the selective adsorption tests. It comprises both U and other metal ions. Adsorbent is administered in doses of 2 mg, 2 mL of solution, and 2 hours of contact time.

The following two equations are used to calculate the K_d value and selectivity (S).

$$K_d = [(C_0 - C_e)/C_e] \cdot (V/m) \cdot 10^3$$

$$S = K_d^U / K_d^M$$

Unit for K_d value is mL/g.

Capture study of U (in presence of other competing ions): Equimolar and mixtures of competing salts (NaCl, KCl, KBr, CaCl_2 , MgCl_2 , $\text{Sr}(\text{NO}_3)_2$, CdCl_2) were added to the U solution in order to conduct capture tests in order to investigate the effects of competing ions. In a 3 mL of U-containing solution, 3 mg of **iMOF-1A** was administered. For two hours, all metal ions were in the same environment (pH 7 and 5 ppm concentration).

Trace amount capture experiments: U capture tests using trace amounts (5000 ppb, 50 ppb, 1000 ppb, 100 ppb, 500 ppb, and 10 ppb) were carried out in a 15 mL drum vial having magnetic stirring bars at room temperature and a constant stirring speed of 400 r.p.m. A solution comprising 5 mL of U and 5 mg of **iMOF-1A** was consumed. The solution was filtered using a syringe equipped with a 0.22 μm nylon membrane filter while being continuously stirred for 2 minutes. Different time intervals were used to measure the kinetic adsorption study.

Kinetics of U removal (from different water samples: potable water, river water, lake water, artificial seawater): The simulated/ model seawater was formed by following an existing literature report. At room temperature, U spiked various water samples (such as 5 ppm, 40 mL) and adsorbents (15 mg) were added to a 50 mL conical with a magnetic stirrer. At the desired time intervals,

aliquots (5 mL) of the mixture were taken and the adsorbents were further filtered through a 0.22 µm nylon membrane filter. ICP-MS was used to determine the U concentrations in the resulting solutions.

U removal kinetics (from the natural seawater): 10 mg of MOF (adsorbents) have been added to 35 mL of seawater (natural) sample and the mixture was mixed at room temperature in order to determine the U removal kinetics from seawater. At required time intervals, aliquots (5 mL) of the mixture were taken and the adsorbents have been filtrated using a syringe fitted with a 0.22 µm (mesh size) membrane filter. The U concentrations in the resulting solutions were determined using ICP-MS.

U extraction from Seawater: We have collected 7.1 gallons of seawater from the Seawater (Arabian sea, Juhu beach, Mumbai) in order to extract uranium from seawater. The experiment was carried out at room temperature with 6 mg of **iMOF-1A** as the adsorbent. ICP-MS was used to analyze the U concentration on a regular basis at suitable intervals.

U uptake via breakthrough experiments: In a mortar pestle, 1.3 g of **iMOF-1A** and 25 g of sand were mixed and filled in a glass tube with an internal aperture of 6 mm and a length of 2.5 ft. To reduce the risk of material leaching, a small amount of cotton was kept at the bottom of the composite and sand mixture. The solution contained U as well as the salts CaCl₂, SrCl₂, Mg(NO₃)₂, CdCl₂, KCl, and NaCl, with an initial concentration of 3 ppm. Excess water treatment were given for column rinsing, even before to the breakthrough experiment, and the flow rate for the outlet solution was set to 0.13 mL/min.

Recyclability test: The U-loaded MOF was regenerated in the presence of 0.001 M K₂CO₃ solution and stirred for 10 hours. **iMOF-1A** is found to be stable and Ni⁺² leaching is not observed (Appendix 11, Appendix 13 and Appendix 20).

2.3 Result and Discussion

As mentioned earlier, **iMOF-1A** was synthesized on a bulk scale (Appendix 1-7) using the solvothermal process, in which a mixture of ligand (LH₂=4,4'-(pyrazin-2-ylazanediyl)dibenzoic acid) and Ni(NO₃)₂·6H₂O was heated at 120 °C in a programmed oven for 48 h (Appendix 1-6 and Scheme 2-3), X-ray diffraction on a single crystal indicated that the substance crystallized in the centrosymmetric cubic (*I*₂₃) space group. The co-ordination microenvironment for **iMOF-1A** was determined to be {[Ni₃L₃(µ-O)][2·DMA]}; where L = 4,4'-(pyrazin-2-ylazanediyl)dibenzoate, which consists of free dimethyl ammonium ((CH₃)₂NH₂⁺ i.e. DMA) cation and free pyrazinic nitrogen sites (Pyz-N) in the (Figure 1). The exchangeable free DMA cations are organized in the channels of the 3D pore, whereas the free Lewis

basic nitrogen sites are densely tethered inside the pore (Appendix 8). Powder X-ray diffraction (PXRD) patterns validated the crystallinity and purity of the bulk phase (Appendix 9). Up to roughly 220 °C, thermogravimetric analysis (TGA) revealed a significant loss of free guest molecules (Appendix 10). Patterns of variable temperature powder X-ray diffraction (VT-PXRD) obtained by heating the compound to elevated temperature proved the complex's structural integrity up to 400 °C. (Appendix 11b). In addition to seawater, the chemical stability of the materials was evaluated by submerging them in various chemical environments (Appendix 11a–11c). Several days of structural stability in water and other solvents was proven by unaltered PXRD signals (Appendix 11a). In addition, the crystal of **iMOF-1A** was immersed in a wide variety of pH solutions, and the identical PXRD patterns indicated the remarkable stability across a wide pH range (Appendix 11a–11c).

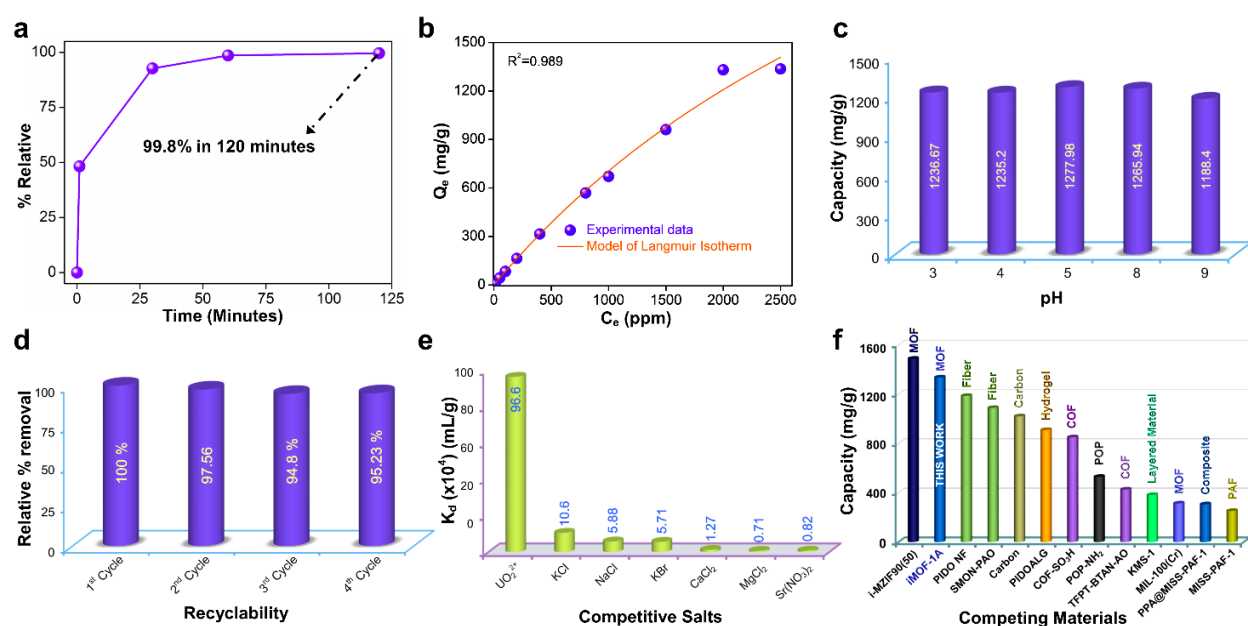


Figure 2. Uranium capture from various uranium-spiked water systems by iMOF-1A. (a) Kinetics of uranium removal efficiency from spiked water samples spiked with 20,000 ppb uranium at $V/m = 2250$ mL g⁻¹. (b) Langmuir isotherms. (c) pH dependent adsorption capacity tests. (d) Recyclability test. (e) Distribution coefficient, K_d value of iMOF-1A for different meddling cations. (f) Comparison of uranium adsorption capacities from uranium-spiked water comprising various reported excellent adsorbents.

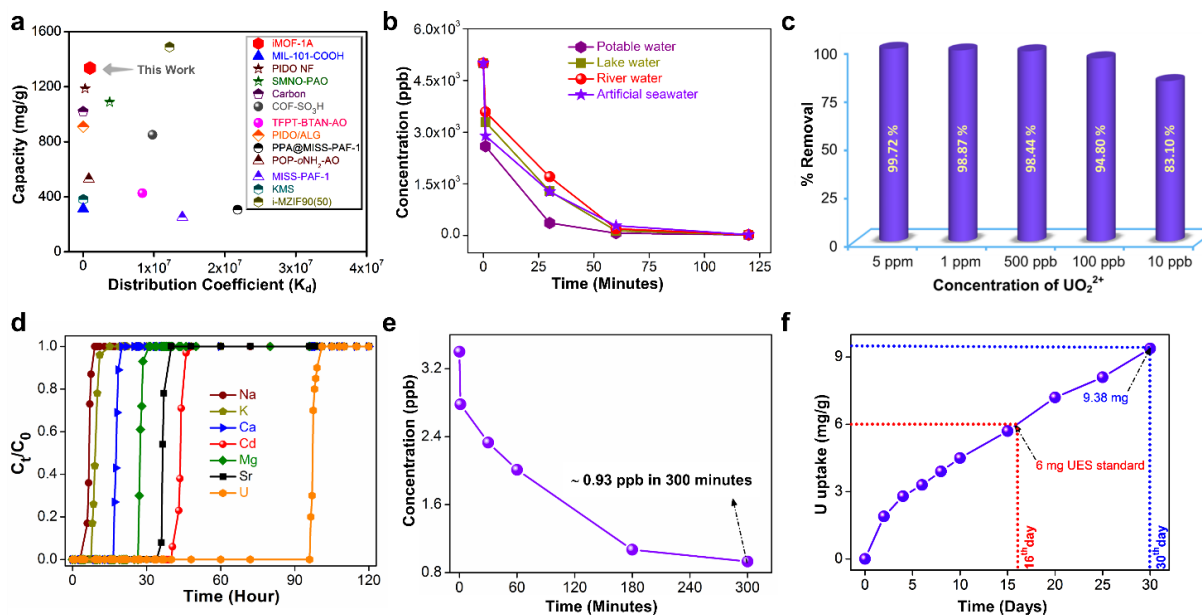


Figure 3. Uranium capture by **iMOF-1A**. (a) Comparison of the distribution coefficient and uranium adsorption capabilities for different good adsorbents from water. (b) At $V/m = 2666.7 \text{ mL g}^{-1}$, the kinetics of uranium extraction efficiency from different water samples spiked with 5000 ppb uranium. (c) The percentage of uranium removed from artificial seawater containing varying concentrations of uranium by **iMOF-1A**, at $V/m = 1000 \text{ mL g}^{-1}$. (d) Breakthrough experiments with an **iMOF-1A** packed bed on a mixed solution containing 3 ppm uranium and 3 ppm other competitive metal cations in water. (e) % of U removed from natural, unadulterated seawater (i.e. natural seawater). (f) During 30 days of immersion in natural seawater (uranyl ion concentration of 3.4 ppb), the adsorption performance for uranyl ions meeting UES criteria.

For uranium capture investigation, we attempted to use the ionic functionality provided by the chemically robust anionic framework containing ordered Pyz-N and tertiary amine sites.^[24,26] As a preliminary screening test, following a few hours of dipping **iMOF-1A** crystals in uranium-laced water, the colour of the solution underwent a slight change and the green crystals turned yellow (Appendix 12-13). Motivated by these results, we conducted systematic uranium sorption studies and tracked them using inductively coupled plasma mass spectrometry (ICP-MS). The saturation capacity in 20 ppm uranium-contaminated water can only be achieved in 120 minutes with low leaching of **iMOF-1A**, in stark contrast to many other adsorbents that require longer adsorption times (Figure 2a, Appendix 14–15, and Appendix Table 1). The experimental results fit well enough with pseudo-second-order kinetics, indicating that

chemisorption is responsible for the sorption of uranyl cation onto **iMOF-1A** (Appendix 16). The experimental isotherm results fit the Langmuir model well, indicating the monolayer chemical adsorption of uranyl ions on ionic adsorbents (Figure 2b and Appendix 16-18). According to the isotherm data, the material absorbed 1336.8 mg g⁻¹ of uranium from the water sample being investigated. Notably, this acquired capacity value is among the best in the MOF domain and unquestionably equivalent to the other good uranium adsorbents previously described (Figure 2f and Appendix Tables 2, 3).^[3,11,25] In addition, the materials adsorbed uranium from a variety of pH solutions, confirming that **iMOF-1A** is a promising candidate for uranium recovery from seawater (Figure 2c, Appendix 19). The recyclability of the ionic adsorbent materials demonstrates their immense potential for recovering uranium from seawater spanning multiple cycles (Figure 2d, Appendix 20 and Appendix Table S4).

High salinity in natural seawater has a significant impact on uranium absorption at trace levels. [27] Capturing trace amounts of uranium selectively from a large variety of competing cations within the same solution is therefore essential for UES.^[11,12,25] The distribution coefficient (K_d) has been determined to evaluate the affinities of uranium towards the framework and its functions (Figure 2e-2f, Figure 3a, and Appendix 21, Appendix Table 5). Materials with a K_d value greater than 10⁴ mL g⁻¹ are identified as suitable for uranium extraction. 28 The estimated K_d value for **iMOF-1A** is significant, 0.97 x 10⁶ mL g⁻¹, which is two orders of magnitude greater and equivalent to the values reported for outstanding adsorbents in the existing literature (Figure 3a and Appendix Tables 3, 5).^[22,29] The unusually high K_d value shows that the framework and uranium ions are able to interact significantly. The materials are also capable of efficiently removing uranium from various water systems, including potable water, river water, lake water, and artificial seawater, to less than 30 ppb, the U.S. Environmental Protection Agency's limit for hazardous waste and drinking water standards (Figure 3b and Appendix 22-26, Appendix Table 6-7).^[30]

A trace amount of uranium was extracted from synthetic seawater (artificial) while pursuing seawater uranium extraction (Appendix 27). It was discovered that the **iMOF-1A** effectively removes trace amounts of uranium from artificial seawater, validating the material's potential for uranium recovery from seawater (Figure 3c). Further, breakthrough tests were conducted using the accurately weighted desolvated phase of **iMOF-1A** to determine the practicality of this material for uranium collection from seawater. The complete passage of all cations through the **iMOF-1A** bed was identified after 21 hours, whereas uranyl cations required 67 hours to do so (Figure 3d, Appendix 28). Strong coordinative interactions found among both uranyl ions and the free Lewis basic nitrogen sites (Pyz-N), delivering a nanopocket-trap in the form of anchoring protruding from the pore surface of the ionic MOF, i.e. **iMOF-**

1A, clarify the phenomenal selectivity towards uranyl cations compared to other cations. All of these impressive experimental results indicate that anionic adsorbents may be used as a new adsorbent for targeted uranium recovery from seawater. **iMOF-1A** was then used to retrieve uranium from natural seawater using samples from the Arabian Sea in Mumbai, India. [31] Within only 30 days, the **iMOF-1A** adsorbed 9.38 mg g⁻¹ of uranium (Figure 3e, 3f and Appendix Table 7) and reduced the uranium concentration by more than half (3.4 ppb to 1.63 ppb) (Figure 3e, 3f and Appendix Table 7). Notably, this quantity is comparable to other amazing adsorbents that have been reported in the literature (Appendix Table 7). The estimated enrichment index for this material is almost 5754, which makes it a great adsorbent for recovering uranium from seawater.

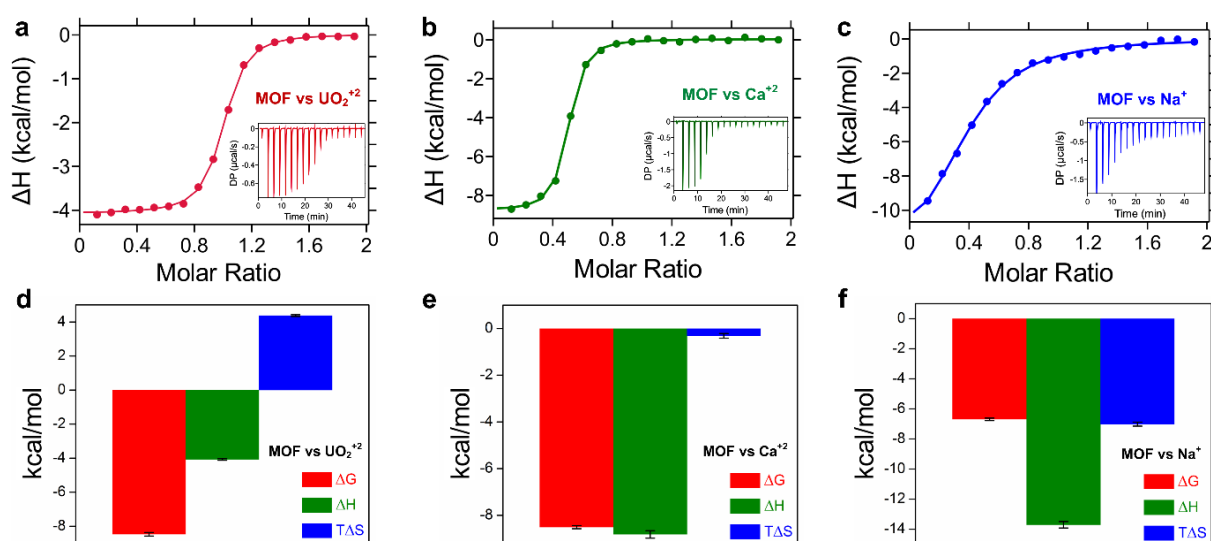


Figure 4. ITC thermograms resulting from injections of (a) UO_2^{2+} salts, (b) Ca^{2+} salts and (c) Na^+ salts. The inset depicts the magnitude of the exothermic peaks. The magnitude of thermodynamic parameters of (d) UO_2^{2+} salts, (e) Ca^{2+} salts and (f) Na^+ salts; demonstrating uranium chemisorption and entropy relevance in comparison to other cations.

To investigate the thermodynamic characteristics underlying the adsorption processes occurring in **iMOF-1A** in aqueous solutions, isothermal titration calorimetry (ITC) studies were conducted on competing cations (Figure 4, Appendix 29–33).^[32,33] ITC measurements provide direct assessment of the entropy, enthalpy, and Gibb's free energy variations underlying adsorption processes and can be measured in a single experiment (Appendix 29–33, Appendix Table 8). In addition to the UO_2^{2+} cations, model divalent and monovalent competing cations, Ca^{2+} and Na^+ , were used for the ITC studies (Figure 4a-c).

The ITC research demonstrates that the adsorption process is thermodynamically favored, as indicated by the negative change in Gibbs free energy, and that the adsorption phenomena depicted in Figure 4a, f operate via exothermic processes. We showed that UO_2^{2+} adsorption is entropically more favorable than the adsorption of other competing model cations (Figure 4d, f). In addition, ITC tests indicated that uranium interacted with Lewis basic nitrogen decorated sites, i.e., Pyz-N, of the scaffolds. This study is the first attempt in the field to look into the thermodynamic properties of uranium adsorption (capture) in water solutions, including the most competitive cations. It has the potential to become a standard integrative tool for future sorption and separation studies in the solution phase.

Extensive experimental and computational experiments (Figures 5–6 and Appendix 34–57 and Appendix Tables 9–10) were conducted to get a comprehensive understanding of the uranium–MOF interaction mechanisms. After the MOF was substituted with uranium, Raman spectra revealed the presence of uranium-specific peaks in the spectrum (Appendix 41). Following adsorption on the surface of **iMOF-1A**, the features of the red vibrational spectra shifted from 932 cm^{-1} to 912 cm^{-1} , as measured by FTIR spectra (Appendix 42). The peak displacement toward a lower vibration frequency confirmed a robust interaction between both the adsorbent surface and cationic uranyl ions. The conclusive proof of framework and uranyl ion interaction was subsequently investigated using XPS (Figure 5a, Appendix 43–47). The XPS survey spectrum displays binding energy peaks for U 4f that have been moved to a lower binding energy area, indicating that uranyl ions interact strongly with **iMOF-1A**. Figure 5a shows that the enhanced features of the N 1s peak showed that uranyl cation interacted a lot with Pyz-N in the frameworks. With a spatial resolution that surpasses the diffraction limit of light, the host-guest interactions at the single-crystal level were investigated using nano-FTIR spectroscopy (Figure 5b, 5c).^[34,35] This method uses a blend of scattering-type scanning near-field optical microscopy (s-SNOM) besides infrared nanospectroscopy to measure the vibrational spectra of separate sub-crystals even when single-crystal X-ray diffraction cannot be used. Due to the local complexity of the framework, its symmetry is broken at a depth of 20 nm along the grain boundary of the **iMOF-1A** crystals, resulting in significantly broadened and extra peak features in the nano-FTIR spectrum in comparison to the far-field ATR-FTIR spectra. Large single crystals are shattered into tiny shards to show their interiors, and then sub-micron crystals that are suited for nano-FTIR local probing are chosen at random. The spectra were then normalized to the silicon substrate spectrum by averaging twelve independent measurements with a 14-second integration time.

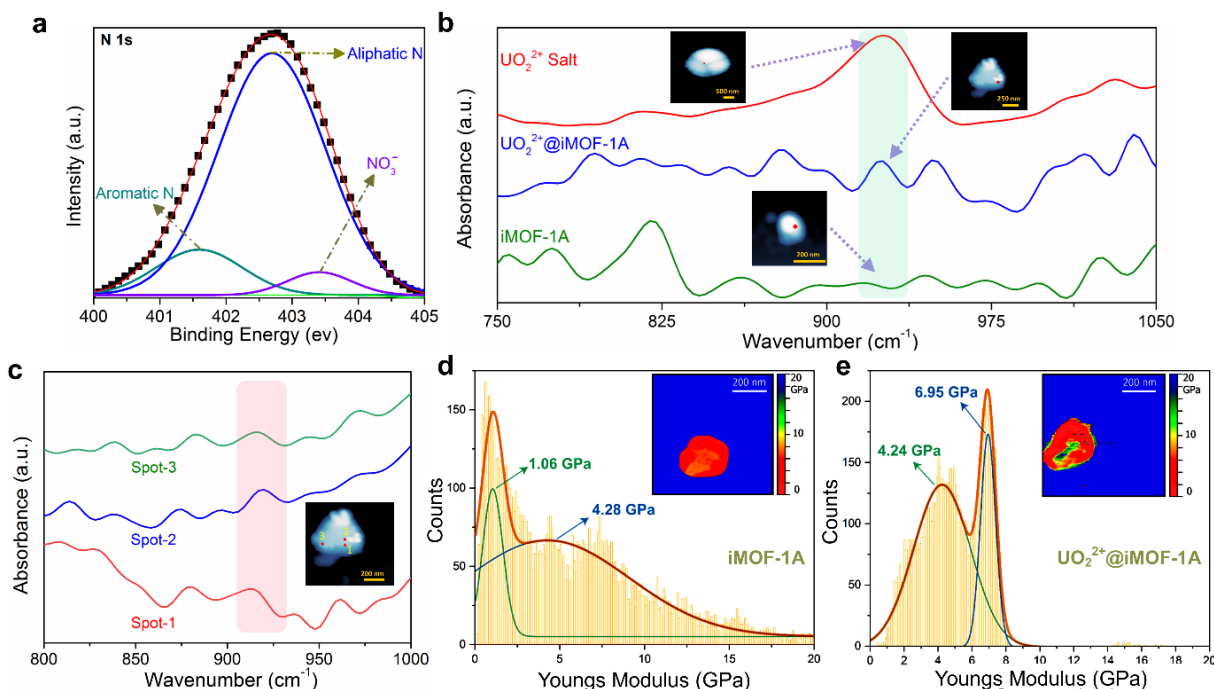


Figure 5. Uranium capture in **iMOF-1A** single crystals; a) Magnified XPS spectra of N 1s for $\text{UO}_2^{2+}@i\text{MOF-1A}$; b) Nano-FTIR spectra of **iMOF-1A**, $\text{UO}_2^{2+}@i\text{MOF-1A}$ and UO_2^{2+} salt, inset: nanoscopic spots corresponding to a probe size of ~ 20 nm; c) Local probing spots of $\text{UO}_2^{2+}@i\text{MOF-1A}$; d) TFM for **iMOF-1A**; e) TFM quantification plots for $\text{UO}_2^{2+}@i\text{MOF-1A}$, TFM reconstructions corresponding to different pressure points showing local stiffnesses of a single crystal.; insets: the Young's modulus map.

By swapping with DMA cations, the development of a distinctive vibrational band of UO_2^{2+} in the $\text{UO}_2^{2+}@i\text{MOF-1A}$ at 926 cm^{-1} establishes the presence of UO_2^{2+} in the MOF host-framework (Figure 5b). The presence of a unique UO_2^{2+} vibrational band in various local regions of randomly chosen MOF single crystal pieces indicates that the exchange process has happened all across the bulk crystals. Within the same crystal fragments, the typical signal for UO_2^{2+} is intermittently redshifted, demonstrating that sequestration is driven by both ion exchange and supramolecular interaction mechanisms (Figure 5c). Using the s-SNOM setup, in contact mode as opposed to tapping mode, a technique known as tip force microscopy can also be used to assess mechanical properties (TFM).^[36,37] The TFM method provides us with the local mechanical characteristics of individual nanocrystals in the form of a map of Young's modulus derived from the surface stiffness measurements of the sample. In the inset pictures, the Young's modulus maps of the crystals are depicted, with the red region representing the TFM probing zone and the

blue region representing the silicon substrate (Figure 5d, 5e). Throughout the pure MOF single crystals, the bimodal gradient of Young's modulus is observed (Figure 5d). Nonetheless, following the uranium exchange procedure, a significantly greater stiffness value of nearly 7 Gigapascal (GPa) appeared in addition to the 4.2 GPa across the crystals (Figure 5e). The appearance of a new modulus all over the crystals shows that uranium capture involves both ion exchange and supramolecular contact.

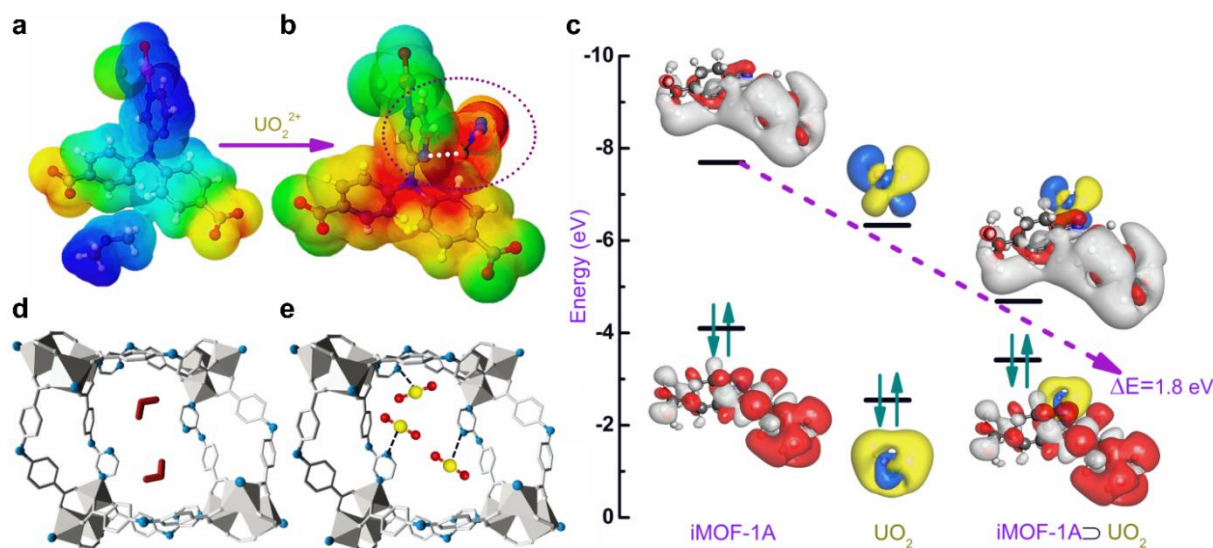


Figure 6. a) ESP of asymmetric unit of **iMOF-1A** and b) ESP of **iMOF-1A** unit after UO₂²⁺ interactions. c) Distribution of HOMO–LUMO in an **iMOF-1A**, UO₂²⁺ and after interaction between **iMOF-1A** and UO₂²⁺. DFT-optimized guest-interaction sites in **iMOF-1A** including; d) exchangeable DMA cations and e) UO₂²⁺, highlights the N...UO₂²⁺ interaction between the framework Pyz-N atoms and UO₂²⁺ molecules.

Simulations based on the density functional theory (DFT) were used to substantiate the experimental results (Figure 6, Appendix 52–55). Figure 6a depicts the ESP of the asymmetric **iMOF-1A** unit, while Figure 6b depicts the ESP of the **iMOF-1A** unit after UO₂²⁺ contacts. It is important to notice that following UO₂²⁺ contacts, the ESP of **iMOF-1A** changes substantially and the coordination of DMA cation to **iMOF-1A** disappears. The work demonstrates that UO₂²⁺ engages preferentially with aromatic nitrogen (Pyz-N) of **iMOF-1A**. In this study, we examined the HOMO-LUMO interactions between **iMOF-1A** and UO₂²⁺ in order to identify changes in energy level. This quantum mechanical data is necessary for evaluating the collective electronic interactions between **iMOF-1A** and UO₂²⁺. The HOMO regulates a molecule's ability to donate electrons, while the LUMO regulates its ability to take electrons.

Consequently, the physicochemical interactions are caused by the active sites between the molecules. Figure 6c depicts the distribution of HOMO–LUMO within **iMOF-1A**, UO_2^{2+} , and **iMOF-1A** following contact with UO_2^{2+} . Initially, prior to UO_2^{2+} interactions, **iMOF-1A** HOMO and LUMO are separated by 4 eV, whereas UO_2^{2+} HOMO–LUMO are separated by 2.4 eV; however, the interaction between **iMOF-1A** and UO_2^{2+} reduced the HOMO–LUMO gap to 1.8 eV. Utilizing frontier molecular orbital theory and Koopman's theorem, theorems were utilized to get the theoretical findings. As observed, the LUMO of UO_2^{2+} sits between the conduction and valence bands of **iMOF-1A**. This permits electron transport from the **iMOF-1A** HOMO to the UO_2^{2+} LUMO, thus decreasing the HOMO–LUMO energy gap of the coupled system.

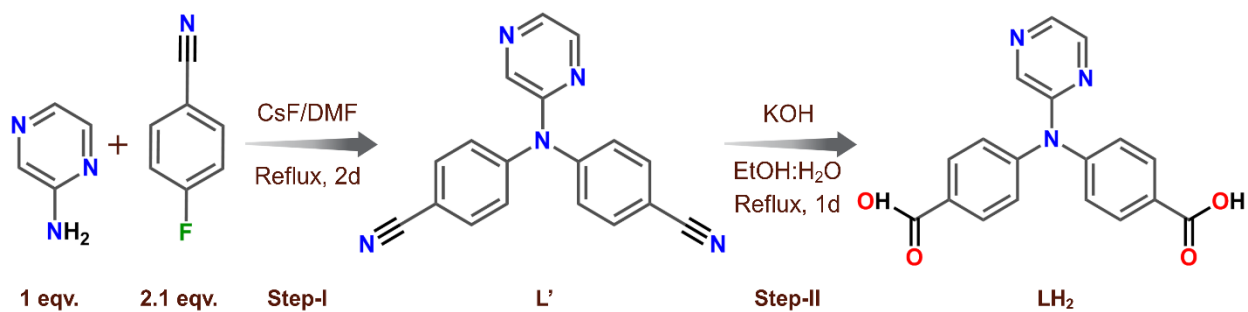
To acquire an additional mechanistic understanding of the current interaction between **iMOF-1A** and UO_2^{2+} , we analyzed the **iMOF-1A** subunit alone (Figure 6d). Since a single subunit of **iMOF-1A** contains two DMA cations, the cation exchange process generates a framework interaction that allows both of the DMA cations to be selectively replaced by a single UO_2^{2+} per subunit; UO_2^{2+} then interacts with the aromatic Lewis basic nitrogen site (Pyz-N) of **iMOF-1A** to stabilize its form within the **iMOF-1A** scaffold. Importantly, the interaction between UO_2^{2+} and **iMOF-1A** is selective and is not affected by the presence of other competing cations like KCl, NaCl, SrCl_2 , CdCl_2 and $\text{Mg}(\text{NO}_3)_2$ (Appendix 52-56).

2.4 Conclusion

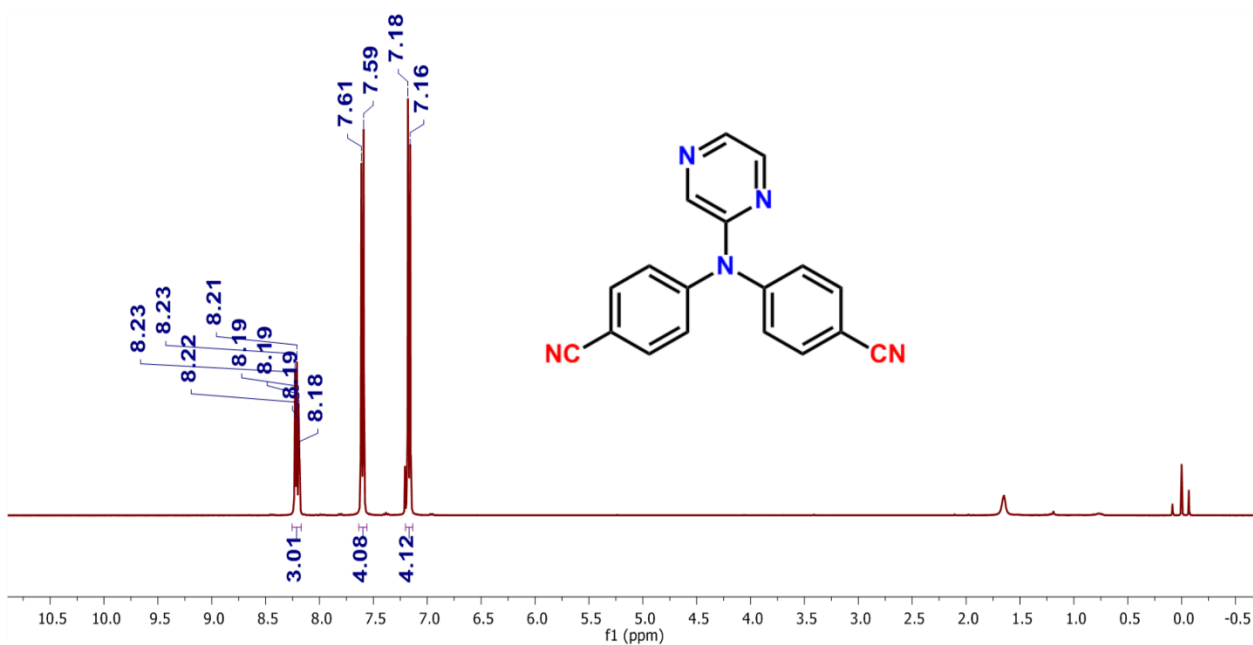
Using the ion exchange and interaction processes, we were capable of successfully accomplishing uranium extraction using a highly stable and new anionic MOF (**iMOF-1A**). The framework has the capability of effective capture of trace levels of uranium in a wide range of water systems, including artificial seawater. This encompasses the framework's ability to capture minute quantities (trace amounts) of uranium. The ionic adsorbent demonstrates ultrafast capture kinetics along with a surprisingly high enrichment index (5754), as well as a high sorption capacity that was deduced dually both from uranium infused (spiked) water and natural seawater. These capacities, which are among the highest values documented in the field of MOFs, were 1336.8 mg g^{-1} and 9.38 mg g^{-1} , respectively. The experiments using nano-FTIR and TFM provided support for the idea that U capture proceeds uniformly throughout the MOF crystals. This finding confirms that ion exchange mechanisms and supramolecular interactions are both involved in the uranium sequestration processes. The findings are further corroborated by computational investigations that are comprehensive and consistent throughout their entirety. The recent findings may lead to new avenues towards efficient uranium extraction coupled with critically important

experimental assessment and molecular level analysis, which will assist in triggering the construction of novel anionic MOFs or similar materials, and the addition of essential corroboratory experimental methods for the remediation of high-risk environmental contaminants.

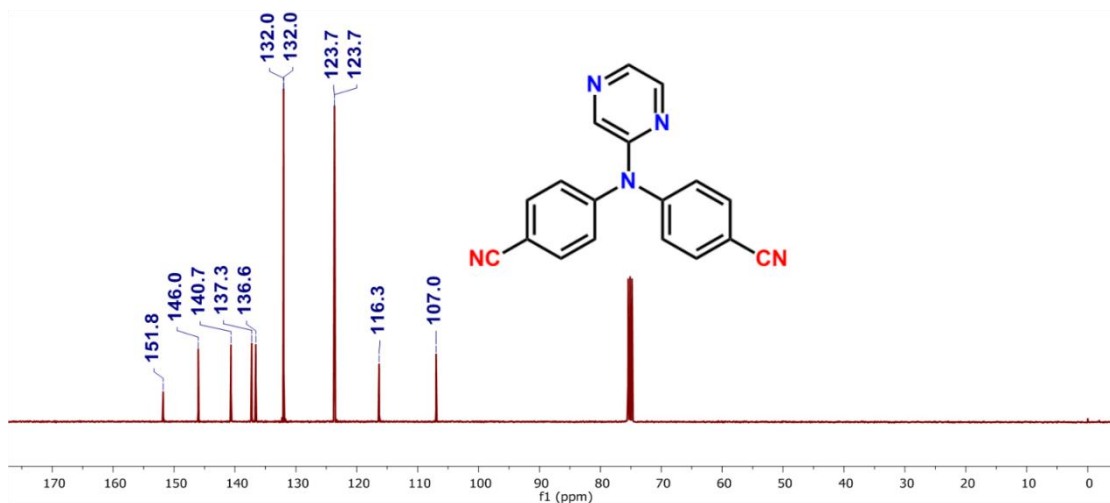
2.5 Appendix Section



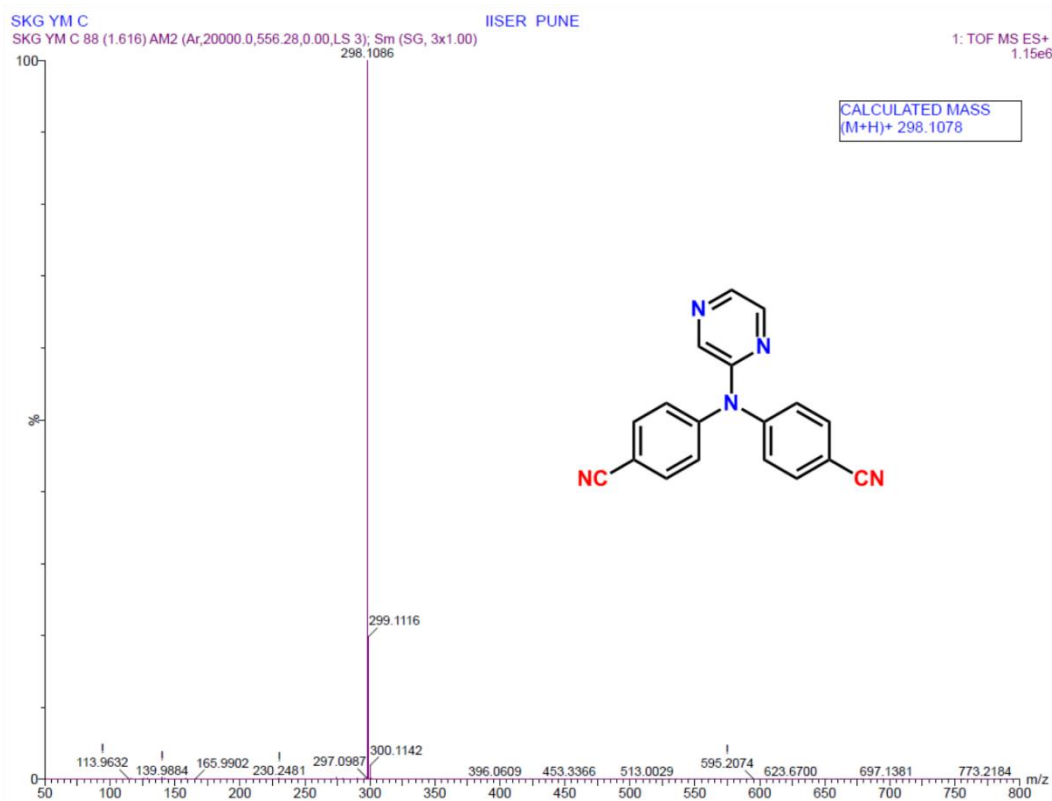
Scheme 2. Synthesis of dicarboxylic acid ligand LH₂.



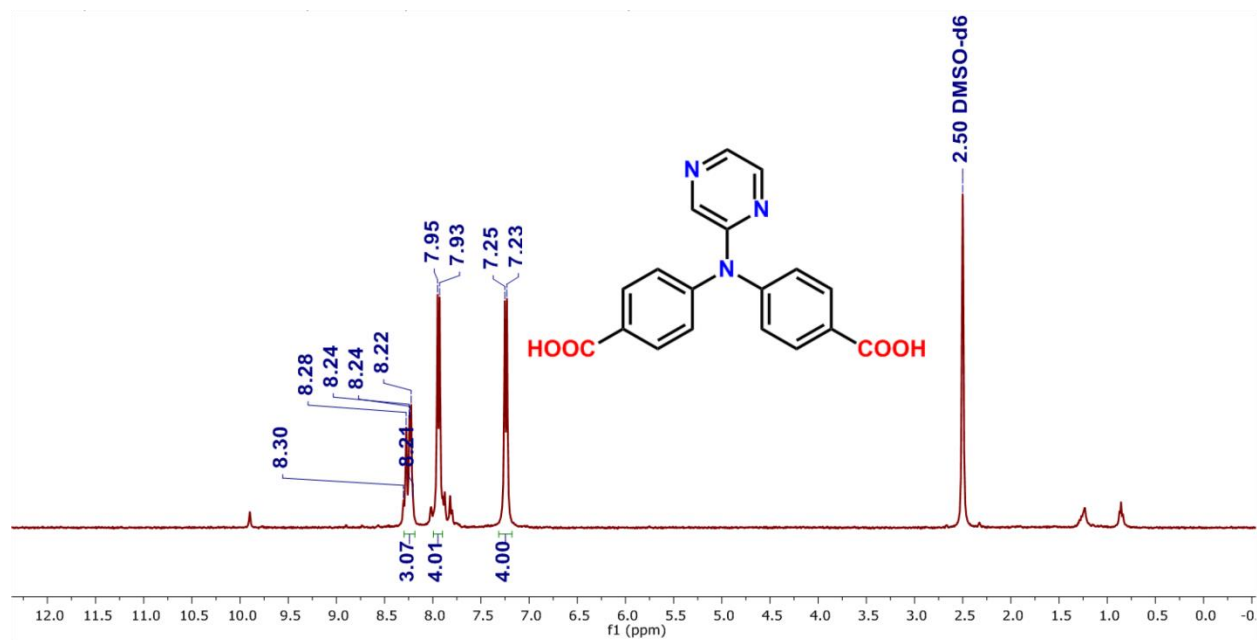
Appendix 1. ¹H NMR spectra for intermediate linker L'.



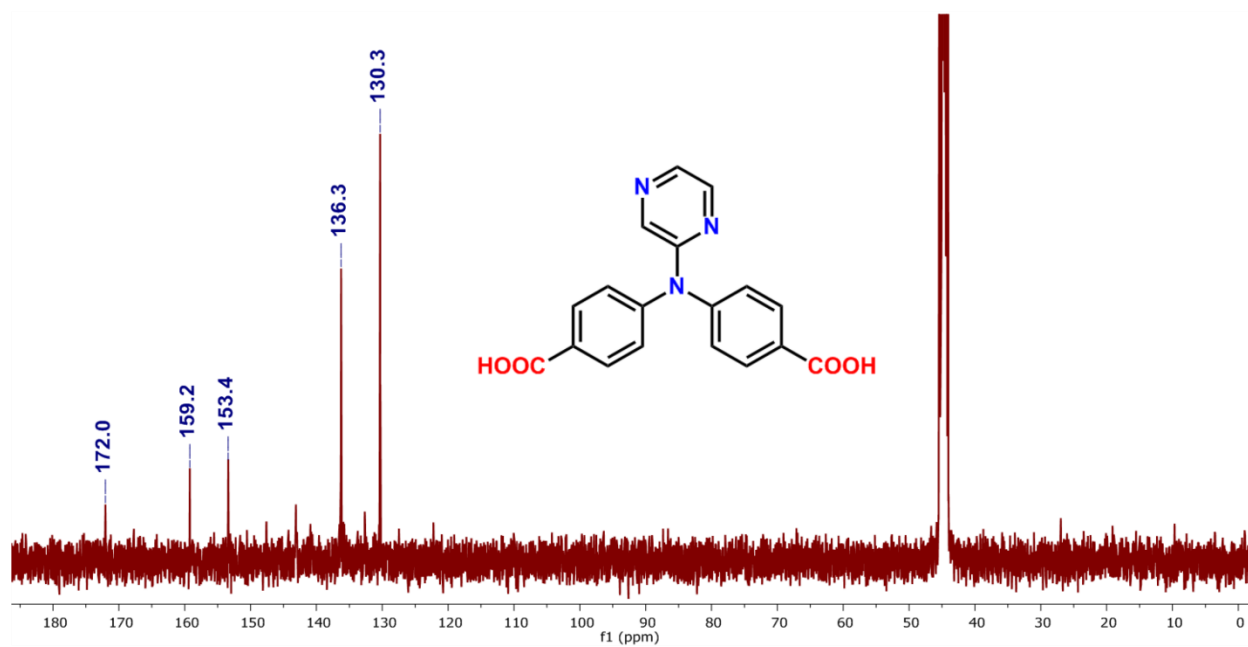
Appendix 2. ¹³C NMR spectra for intermediate linker L'.



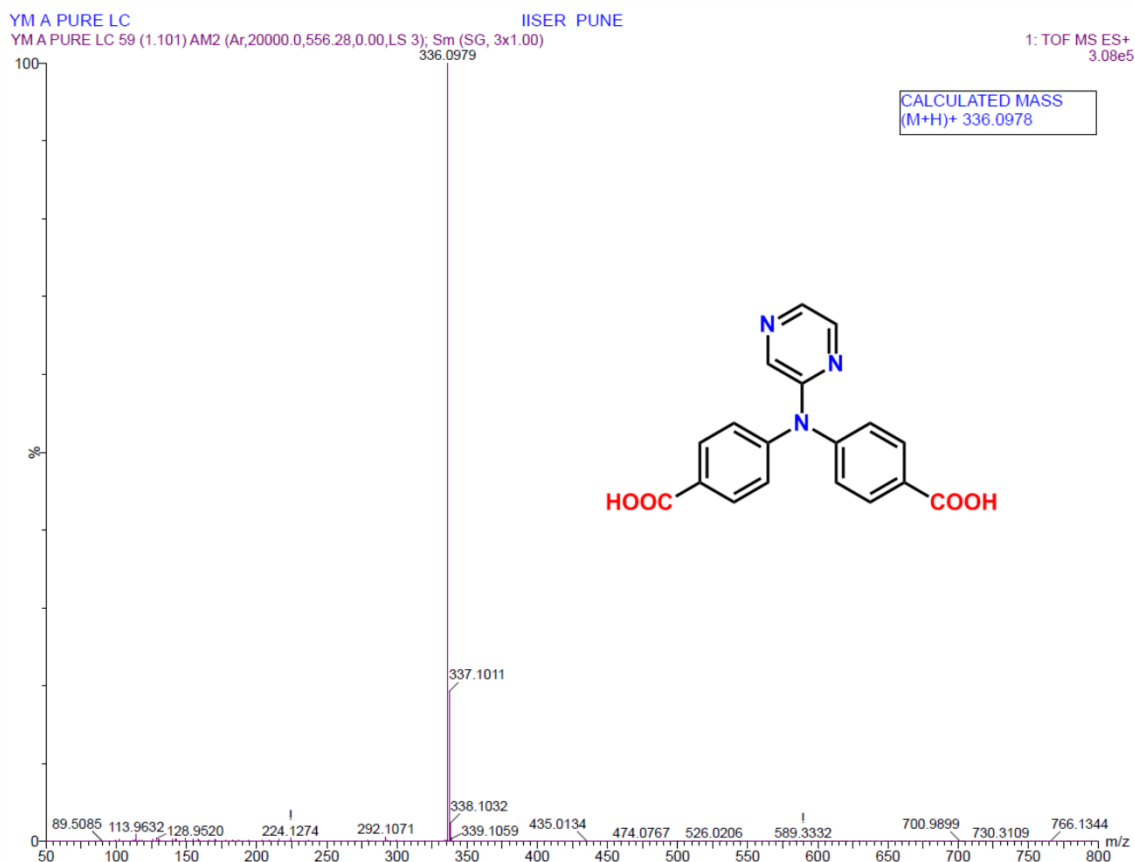
Appendix 3. HRMS spectra for linker L'.



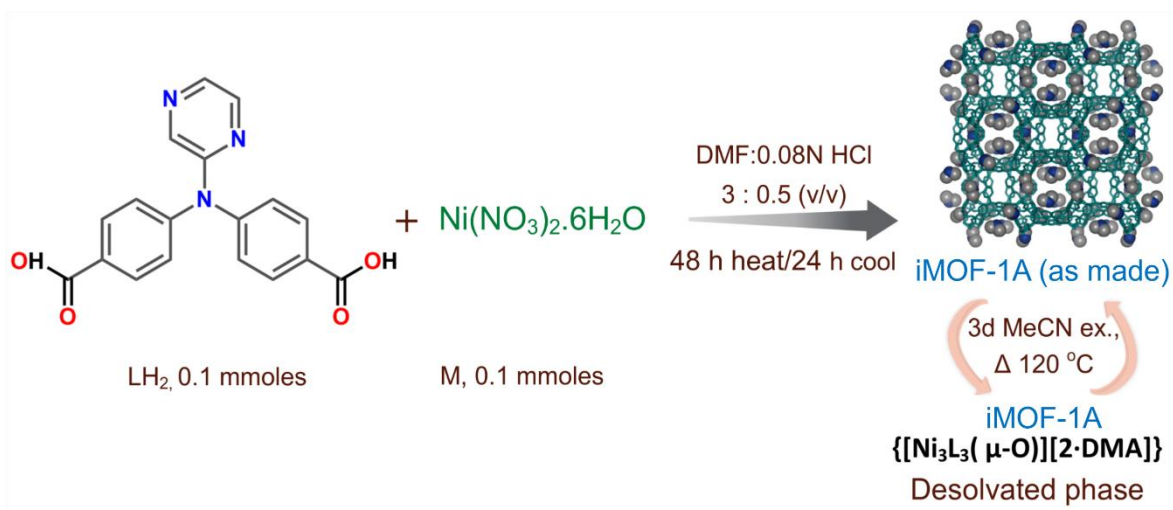
Appendix 4. ¹H NMR spectra for spectra for linker LH₂.



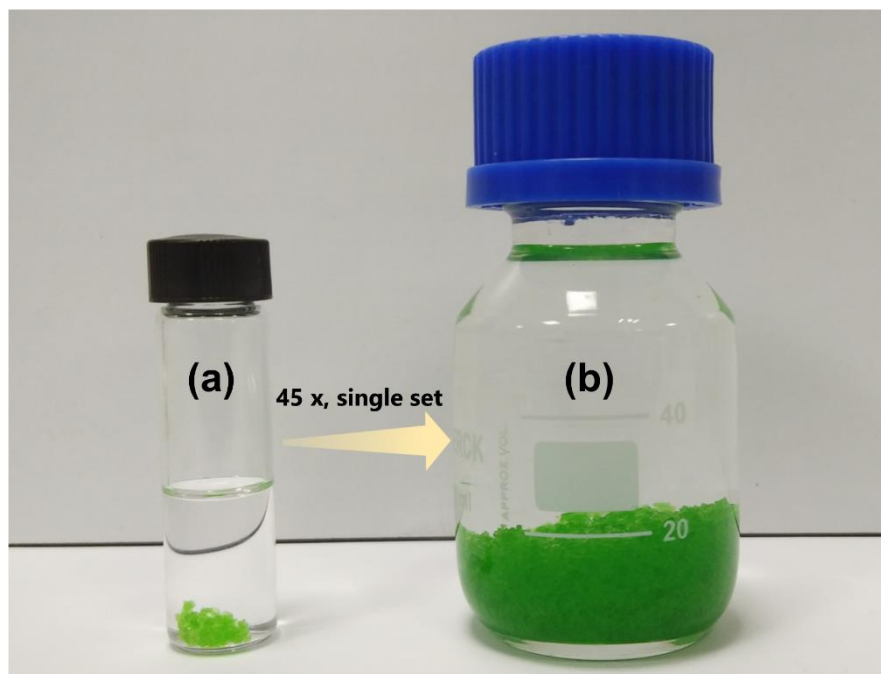
Appendix 5. ¹³C NMR spectra for spectra for linker LH₂.



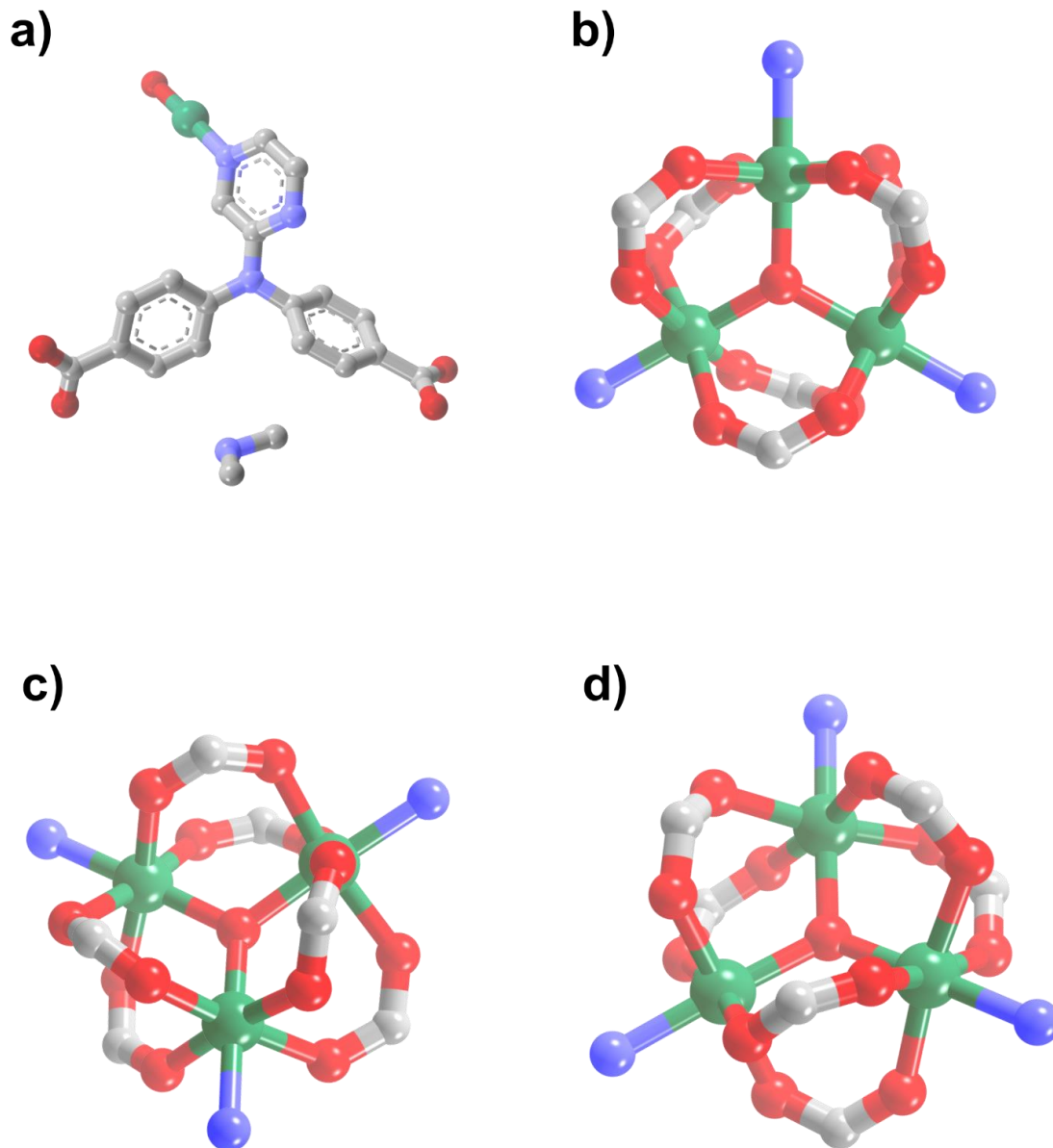
Appendix 6. HRMS spectra for intermediate linker LH₂.



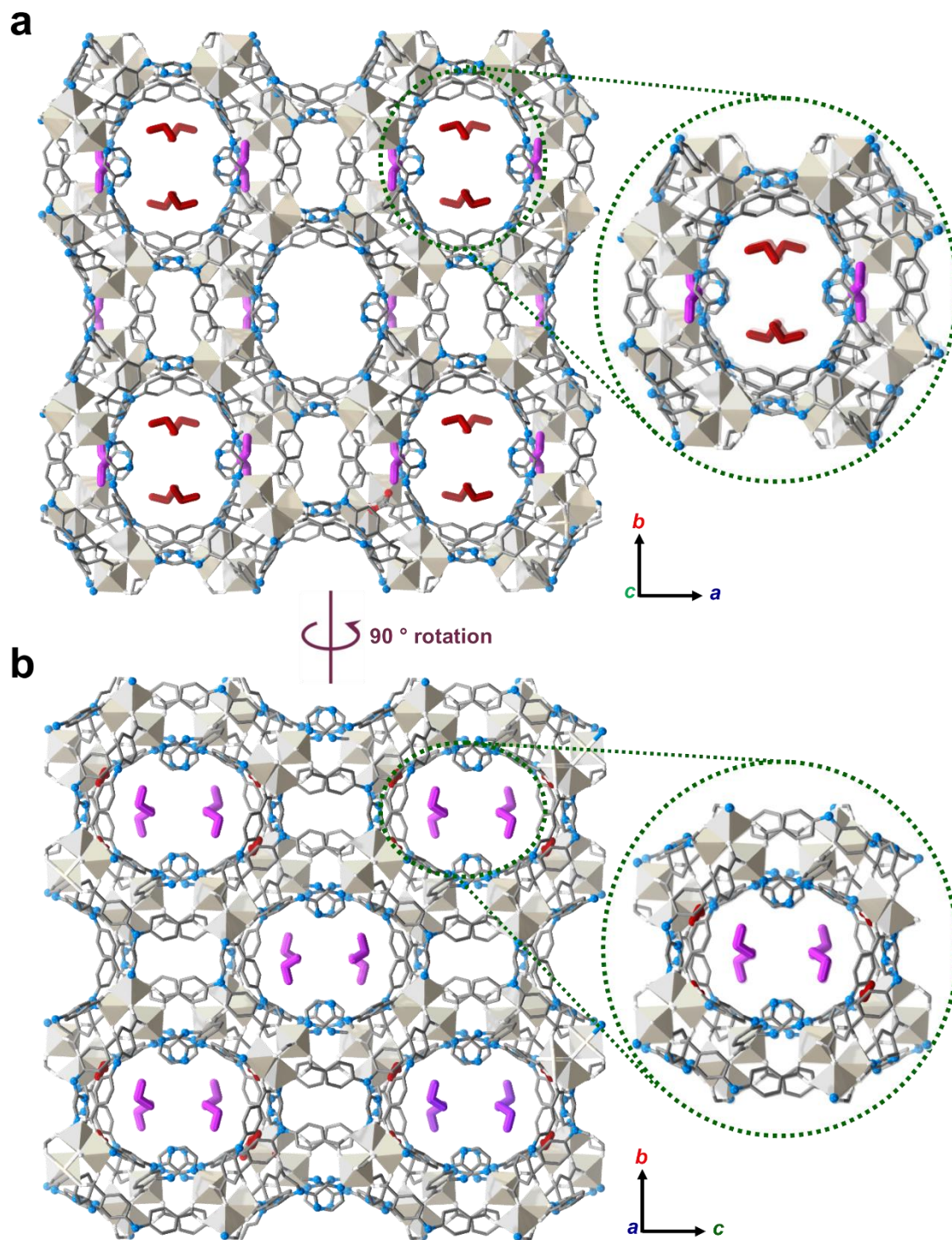
Scheme 3. Synthesis Protocol deployed to obtain studied Ultramicroporous crystalline iMOF-1A.



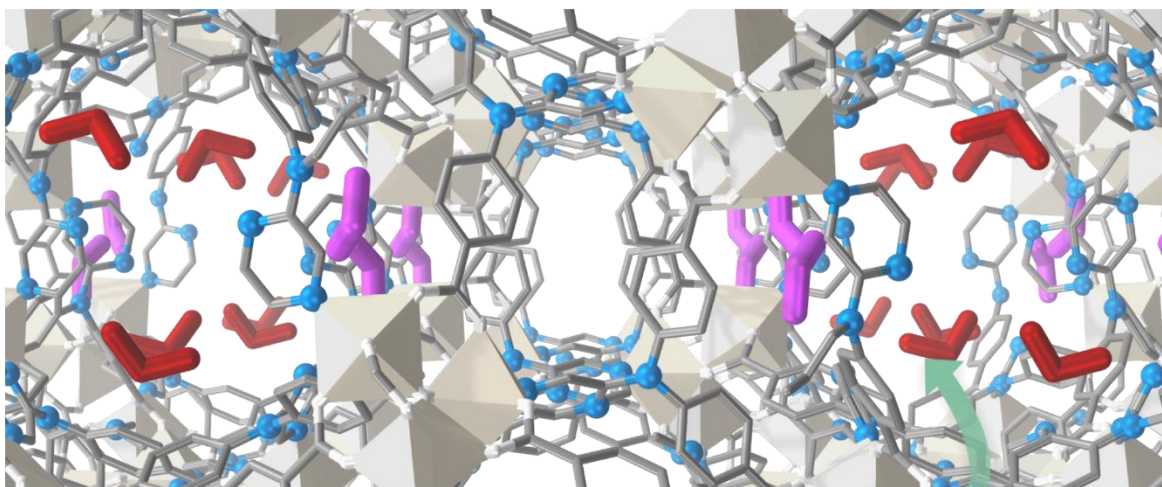
Appendix 7. Scale up; (a) milligram scale ($\sim 490 \pm 20$ mg/batch) to (b) gram scale synthesis (~ 20.9 g/batch) of **iMOF-1A** in unit batch. Scale up ratio; 45x, x: minimum scale up size.



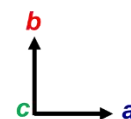
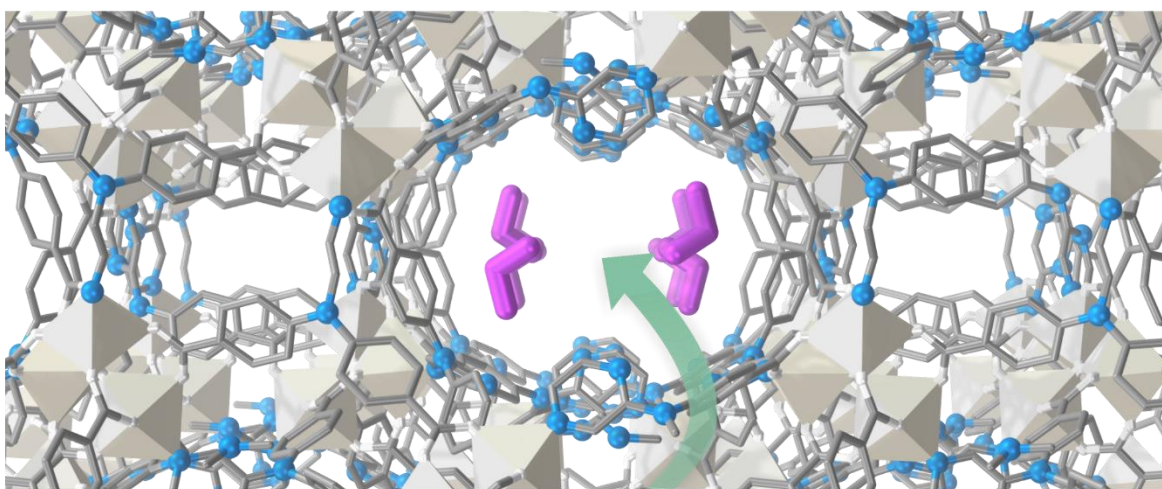
Appendix 8 (A). (a) Asymmetric unit of **iMOF-1A**, and (b-d) Metal node / SBU perspective view at various angles (color codes: grey – C, blue – N, Red – O, green – Ni); H atoms and water molecules are omitted for visual clarity.



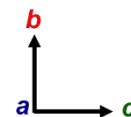
Appendix 8 (B). Orthographic view of **iMOF-1A** showing arrangement of DMA guest cations channelized differently, i.e. in *AB* – type arrangement; along (a) *c*-axis, and along (b) *a*-axis, of an Ultramicroporous channels sustaining the framework.

a

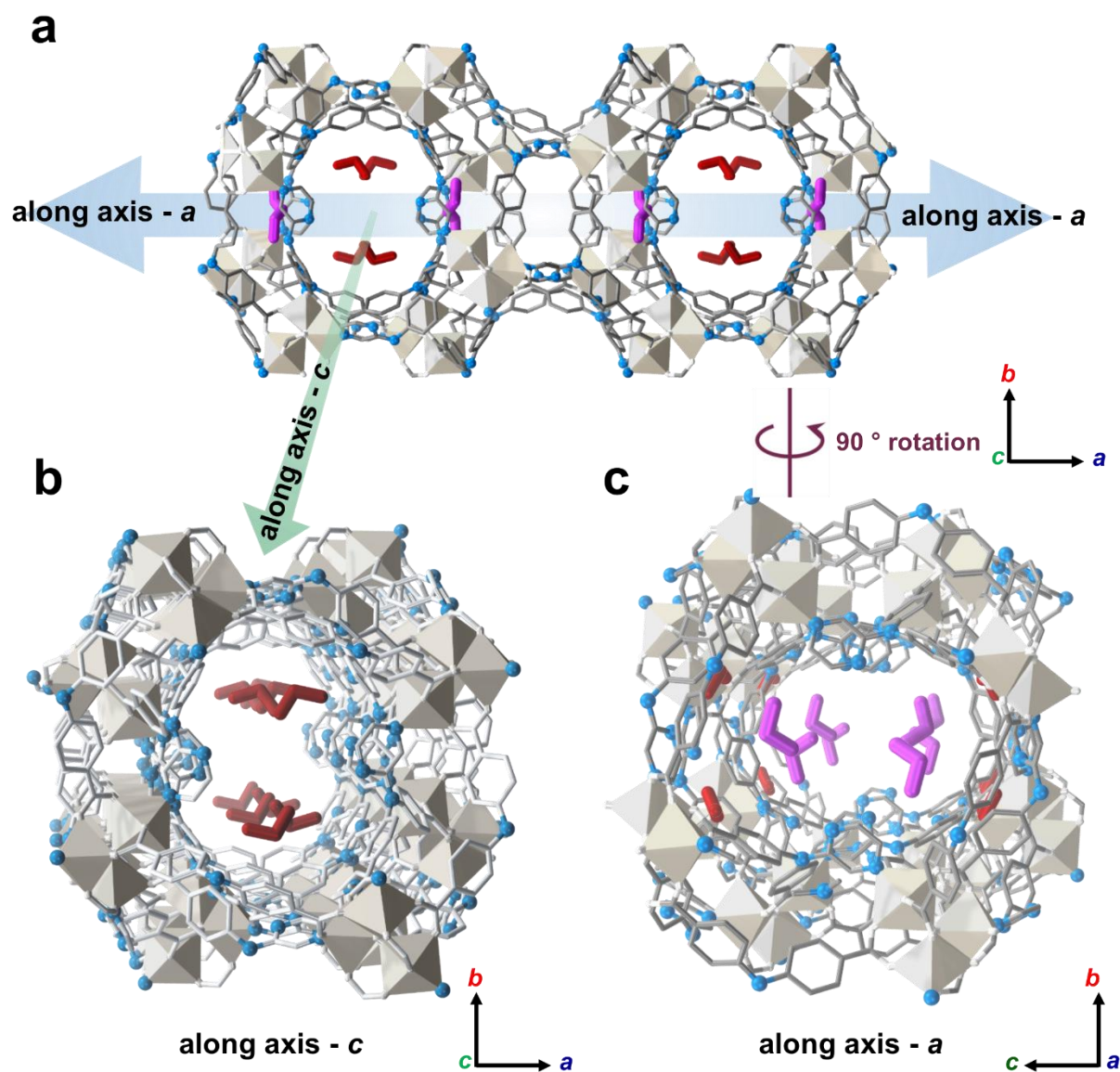
DMA cations along axis - c (A – type arrangement)

**b**

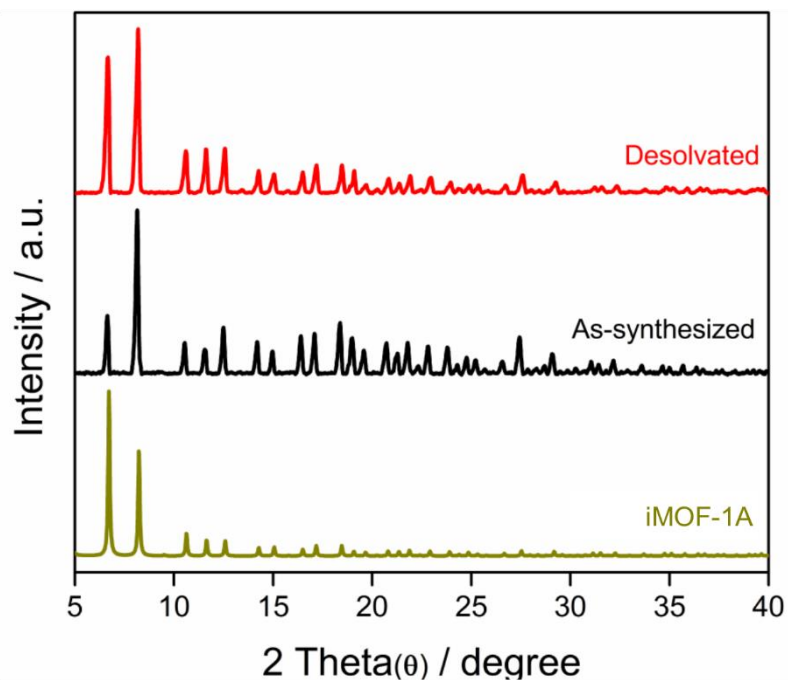
DMA cations along axis - a (B – type arrangement)



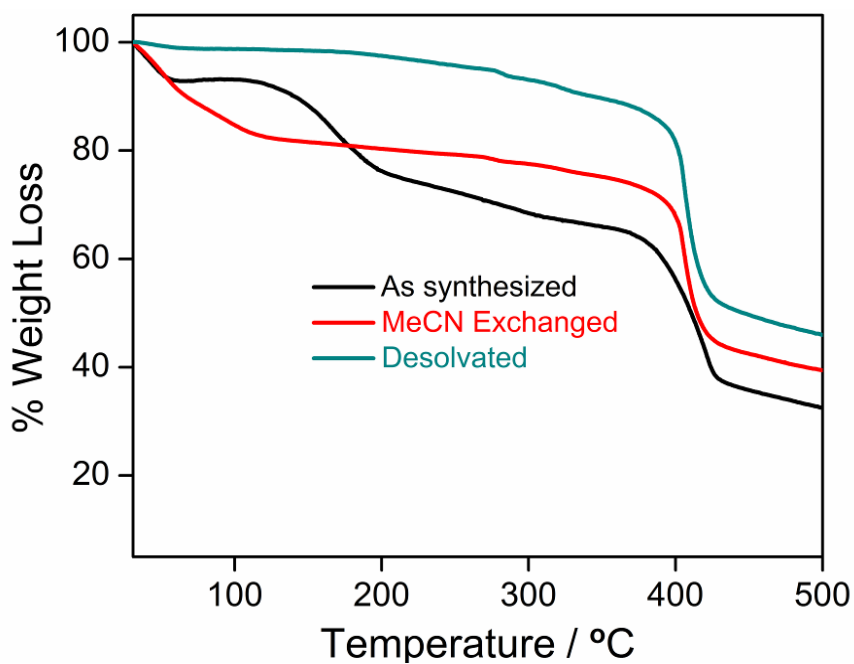
Appendix 8 (C). Perspective packing view of **iMOF-1A**; (a) channelized arrangement (type–A), along– c axis and (b) channelized arrangement (type–B), along– a axis; Similar channelized arrangement is can be viewed along along– b (type–C) (color codes: red/purple – DMA resp., grey – C, blue – N, grey octahedra – Ni). H atoms and solvent molecules are omitted for visual clarity.



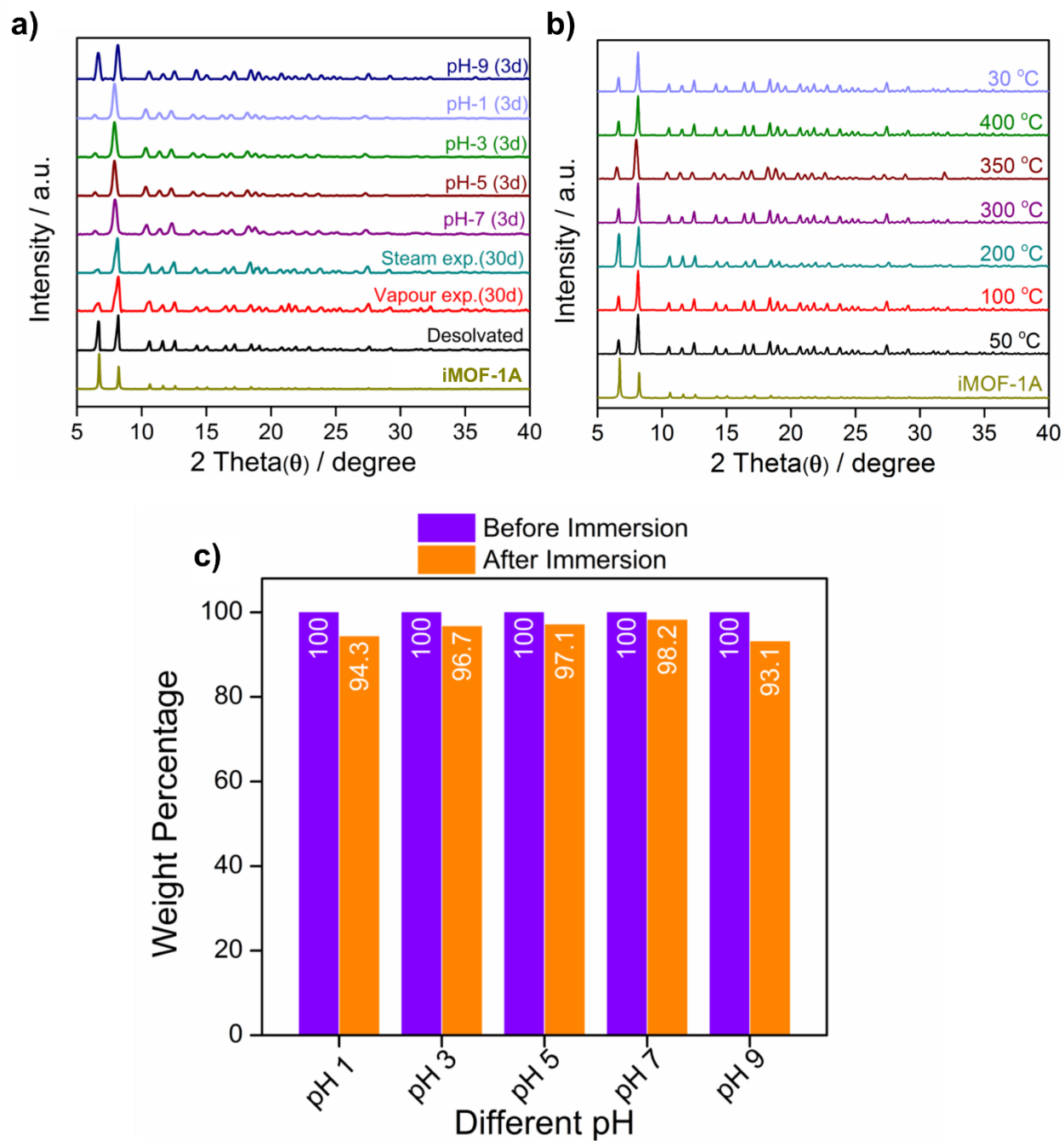
Appendix 8 (D). Packing views of **iMOF-1A** channel; (a) orthographic view along c – axis; (b) perspective packing view of pore along c – axis channel, indicating orderly arranged DMA cations with A – type arrangement, DMA cations in red, and (c) B – type arrangement along a – axis with DMA cations in purple; Same is observed along c – axis channel can be called as C – type arrangement. (colour codes: grey – C, blue – N, grey octahedra – Ni). H atoms and solvent molecules are omitted for visual clarity.



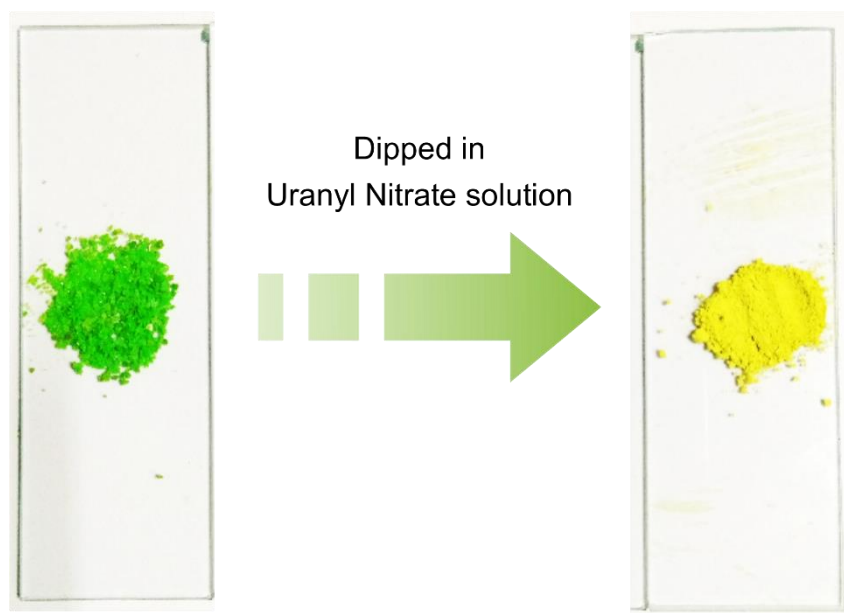
Appendix 9. Characteristics Bragg peaks for both single crystal and bulk phase are confirmed from PXRD patterns of **iMOF-1A** Simulated, As synthesized bulk and desolvated phase.



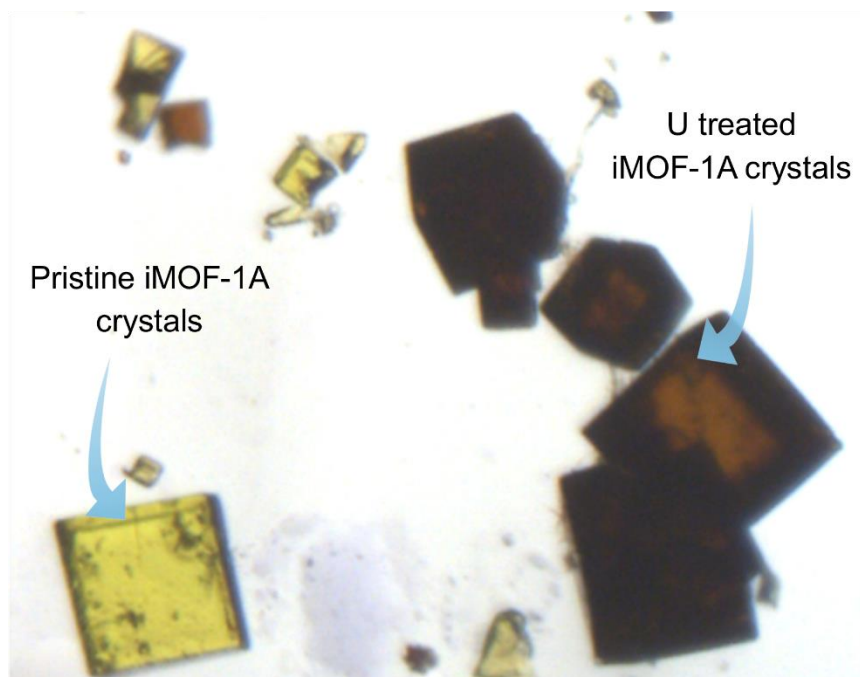
Appendix 10. Thermogravimetric analysis profile for different phases of **iMOF-1A**.



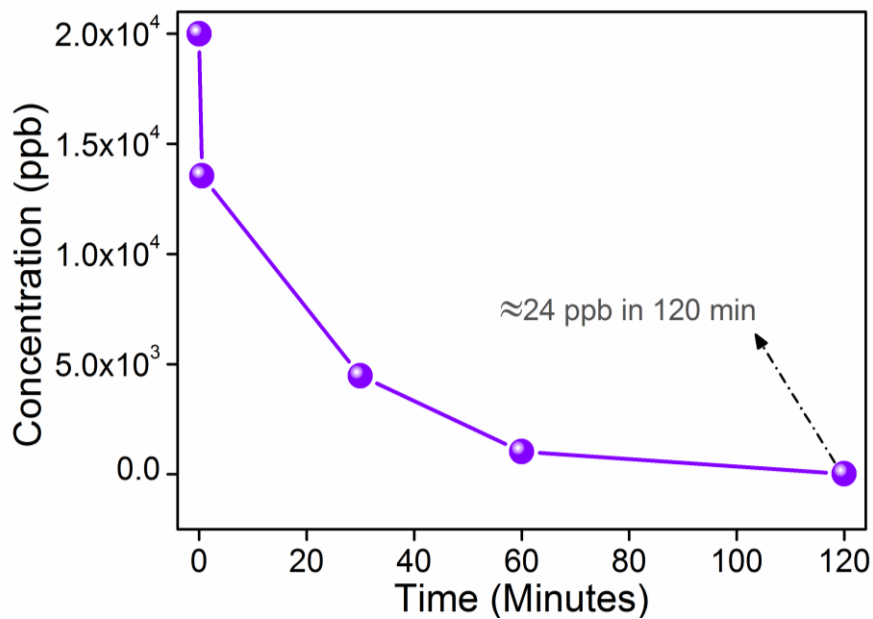
Appendix 11. (a) PXRD patterns in different pH solution (after 3 days); (b) VT-PXRD patterns; (c) Bar diagram represent the acid and base media stability phase of **iMOF-1A**.



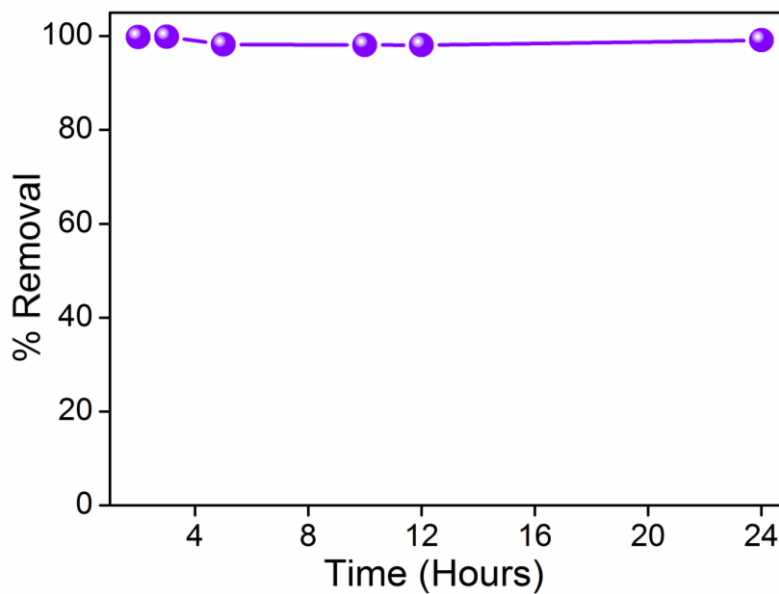
Appendix 12. Visual imaging of **iMOF-1A** before and after U capture studies; dry form.



Appendix 13. Zoomed view visualization of **iMOF-1A** single crystals after several days of saturated U solution treatment; wet form (local contrast in single view).



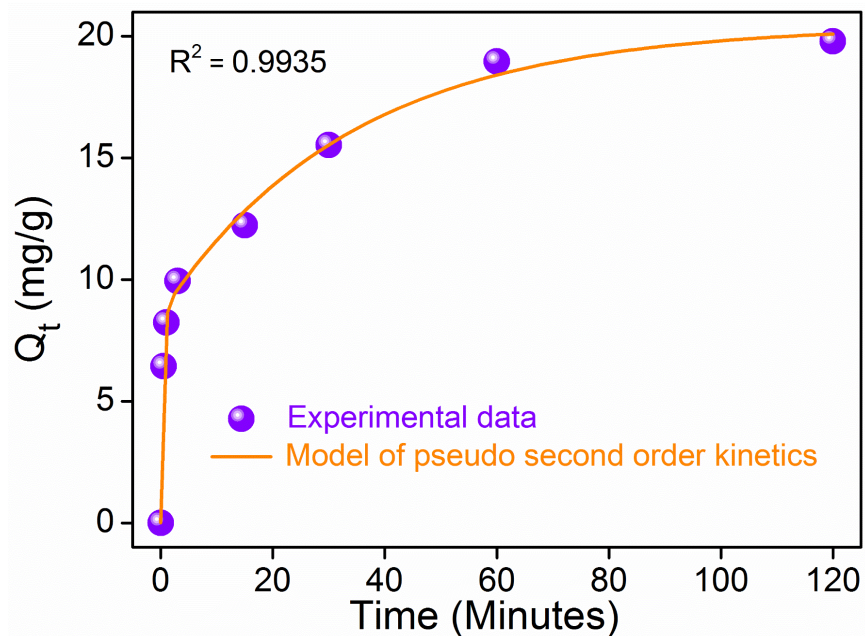
Appendix 14. Kinetics of U removal efficiency by **iMOF-1A** from water spiked with U (20 ppm) at $V/m = 2250 \text{ mL g}^{-1}$.



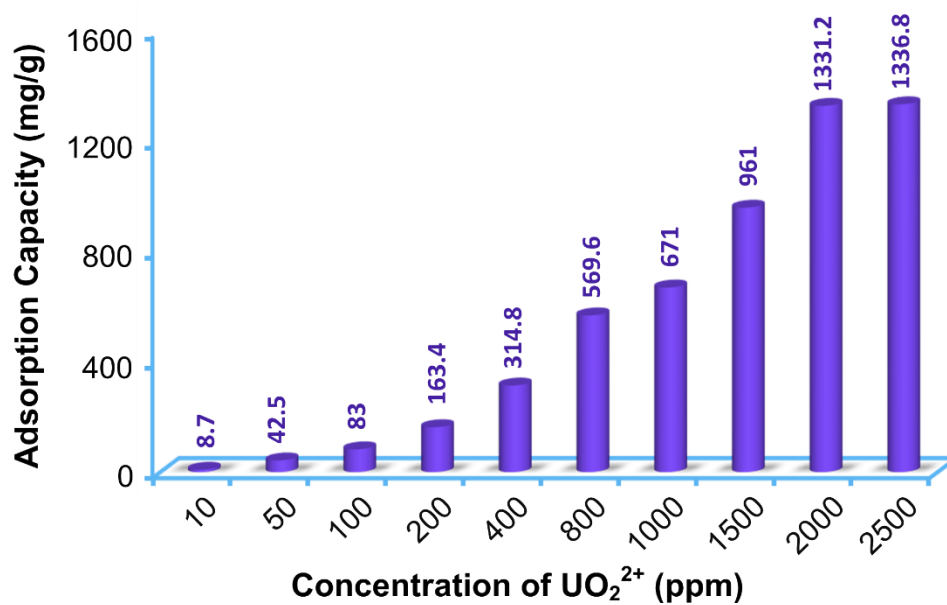
Appendix 15. Leaching test of U from **iMOF-1A** with different time interval.

Appendix Table 1. Comparison of present studies with other related studies / investigations of U extraction for variety of adsorbents conducted on U spiked water.

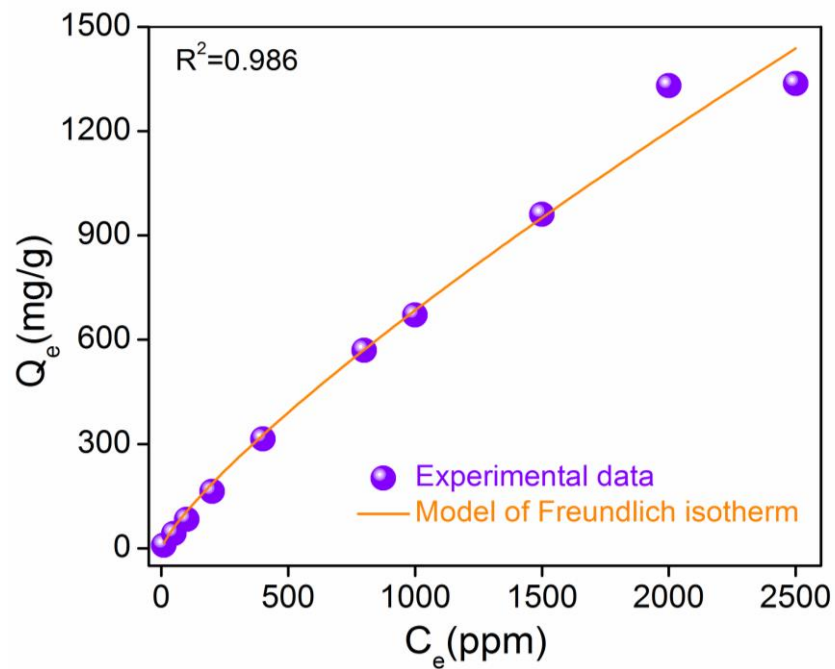
Adsorbents	Type	Contact Time	Reference
i-MZIF90(50)	Ionic macro-MOF	120 min	<i>Energy Environ. Sci.</i> , 2022, 15 , 3462
iMOF-1A	MOF	120 min	This work
COF-TpDb-AO	COF	180 min	<i>Adv. Mater.</i> , 2018, 30 , 1705479
PPA@MISS-PAF-1	Composite	180 min	<i>Chem</i> , 2020, 6 , 1683
MISS-PAF-1	PAF	200 min	<i>ACS Cent. Sci.</i> , 2019, 5 , 1432
FJSM-SnS	Layered Hybrid Thiostannate	1200 min	<i>J. Am. Chem. Soc.</i> , 2016, 138 , 12578
SMON-PAO	Fiber	1600 min	<i>Adv. Funct. Mater.</i> , 2019, 29 , 1805380
BP-PAO	Black Phosphorous	48 h	<i>Angew. Chem. Int. Ed.</i> , 2020, 59 , 1220
Zn ²⁺ -PAO hydrogel	Hydrogel	100 h	<i>Adv. Mater.</i> , 2020, 32 , 1906615



Appendix 16. The uranium sorption kinetics (pseudo second-order kinetics), indicating that the adsorption of uranyl ions onto **iMOF-1A** is attributed to chemical interactions.



Appendix 17. Concentration dependent adsorption capacities for **iMOF-1A** at pH 7.



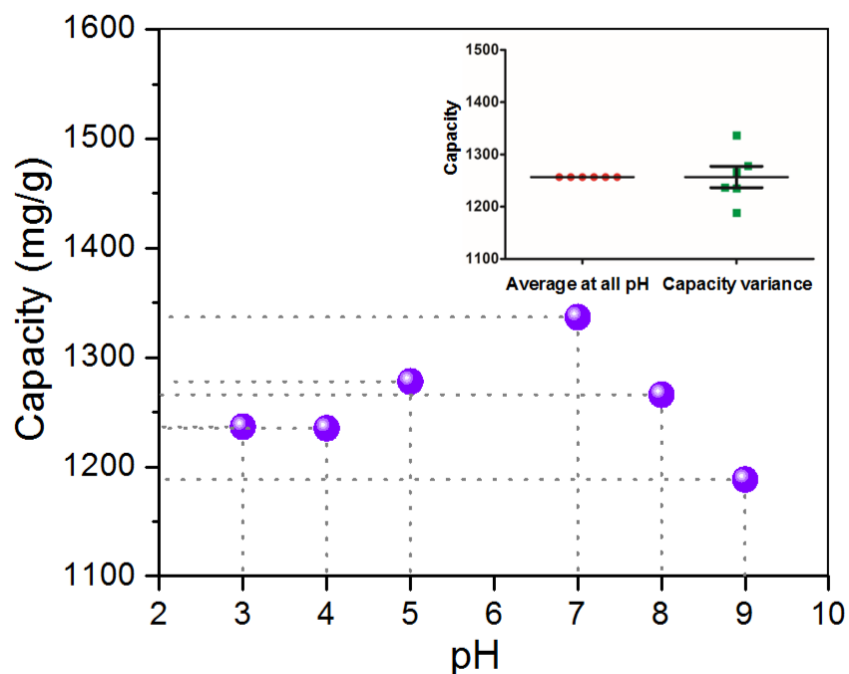
Appendix 18. Freundlich adsorption isotherm for iMOF-1A.

Appendix Table 2. Comparison of present study with other related studies / investigations of U extraction for various MOF derived adsorbents conducted using U spiked water.

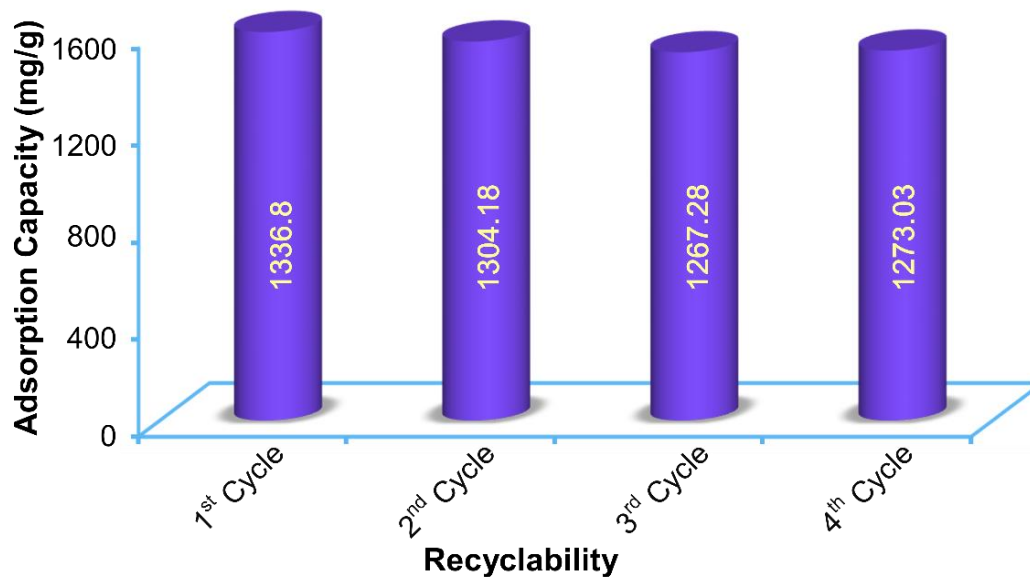
Adsorbents	Type	Capacity (mg/g)	Distribution Coefficient (K_d)	Reference
i-MZIF90(50)	macro-MOF	1489.13	1.22×10^7	<i>Energy Environ. Sci.</i> , 2022, 15 , 3462
iMOF-1A	MOF	1336.8	96.67×10^4	This work
HP-UiO-66	MOF	1217	-	<i>Ind. Eng. Chem. Res.</i> 2019, 58 , 1159
UCY-13	MOF	984	-	<i>J. Mater. Chem. A</i> 2020, 8 , 1849
USC-CP-1	MOF	562	-	<i>Angew. Chem. Int. Ed.</i> 2019, 58 , 18808
RE-MOF	MOF	538	-	<i>ACS Appl. Mater. Interfaces</i> 2020, 12 , 14087
Fe@UiO-66-COOH	Composite	504	-	<i>ACS Appl. Mater. Interfaces</i> 2019, 11 , 21619
AO/MOF	Composite	454.55	-	<i>Environ. Sci.: Nano</i> 2018, 5 , 2000
MIL-101(Cr)-traiziole-COOH	MOF	314	1.8×10^4	<i>ACS Appl. Mater. Interfaces</i> 2016, 8 , 31032
MOF-76	MOF	298	-	<i>Chem. Commun.</i> 2013, 49 , 10415
UiO-66-NH ₂ /Urea-POP	Composite	278	-	<i>Microchimica Acta</i> 2018, 185 , 469
MOF@Cotton	Composites	241.28	-	<i>Sci Rep</i> 2020, 10 , 19271
MOF-2 (UiO-68)	MOF	217	-	<i>Chem. Sci.</i> 2013, 4 , 2396

Appendix Table 3. Comparison of present study with other related studies /investigations of U extraction for variety of adsorbents from U spiked water.

Adsorbents	Type	Capacity (mg/g)	Distribution Coefficient (K_d)	Reference
i-MZIF90(50)	macro-MOF	1489.13	1.22×10^7	<i>Energy Environ. Sci.</i> , 2022, 15 , 3462
iMOF-1A	MOF	1336.8	0.967×10^6	This Work
Zn²⁺-PAO hydrogel	Hydrogel	1188	-	<i>Adv. Mater.</i> , 2020, 32 , 1906615
PIDO NF	Fiber	1187.05 ± 28.45	2.84×10^5	<i>Adv. Energy Mater.</i> , 2018, 8 , 1802607
HTC-AO	Carbon	1021.6	0.5×10^4	<i>J. Mater. Chem. A</i> , 2014, 2 , 1550
BP-PAO	Black Phosphorous	990.60 ± 37.39	-	<i>Angew. Chem. Int. Ed.</i> , 2020, 59 , 1220
UCY-13	MOF	984	-	<i>J. Mater. Chem. A</i> , 2020, 8 , 1849
PIDO/Alg	Hydrogel	910.98	1.72×10^4	<i>Adv. Funct. Mater.</i> , 2019, 29 , 1901009
COF-SO3H	COF	851 mg	9.8×10^6	<i>Adv. Sci.</i> , 2019, 6 , 1900547
POP-<i>o</i>NH₂ -AO	POP	530	8.18×10^5	<i>Nat. Commun.</i> , 2018, 9 , 1644
KMS-1	Layered Metal Sulfide	382	$1.5-4.8 \times 10^4$	<i>J. Am. Chem. Soc.</i> , 2012, 134 , 16441
FJSM-SnS	Layered Hybrid Thiostannate	338.43	2.64×10^4	<i>J. Am. Chem. Soc.</i> , 2016, 138 , 12578
PPA@MISS-PAF-1	Composite	307.3	2.18×10^7	<i>Chem</i> , 2020, 6 , 1683
H-ABP	Fiber	302	-	<i>Energy Environ. Sci.</i> , 2019, 12 , 1979
MISS-PAF-1	PAF	253	1.4×10^7	<i>ACS Cent. Sci.</i> , 2019, 5 , 1432
H₂BHT	Supramolecular Chelator	105	-	<i>Nat. Commun.</i> , 2019, 10 , 819



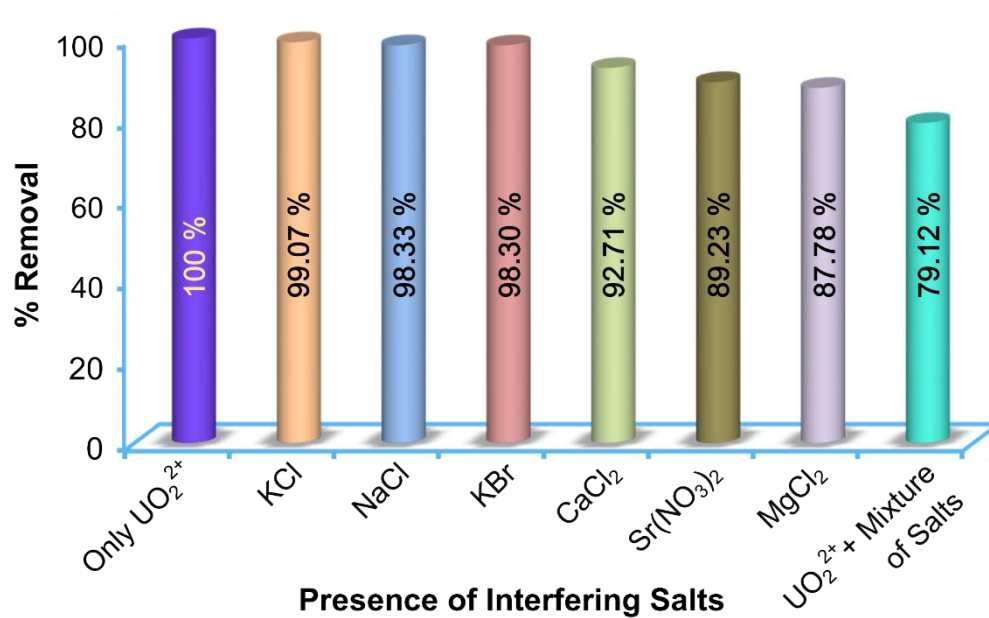
Appendix 19. Adsorption capacity of U from aqueous solution at different pH (inset: two tailed T-test applied, non-significant, indicating less variance in capacity for pH 3-9).



Appendix 20. Recyclability test of iMOF-1A for U recovery from water representing adsorption capacities in different cycles.

Appendix Table 4. Adsorption capacity and elution efficiency (%) of **iMOF-1A** for each experimental cycle conducted during the recyclability test.

Cycle Number	Adsorption Capacity (mg/g)	Elution Efficiency (%)
1	1336.8	100
2	1304.18	97.56
3	1267.28	94.8
4	1273.03	95.23

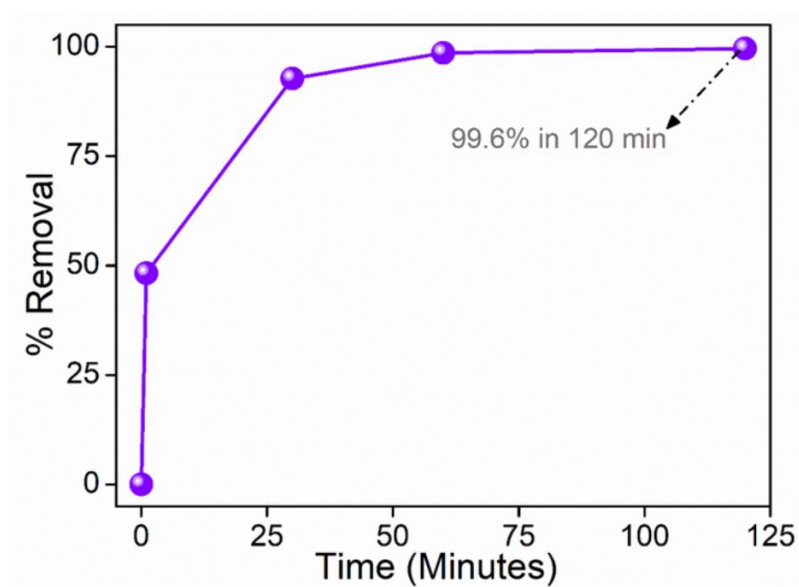


Appendix 21. U removal percentage from a binary and mixture of equal concentration of variety of interfering cations by **iMOF-1A** at $V/m = 1000 \text{ mL g}^{-1}$.

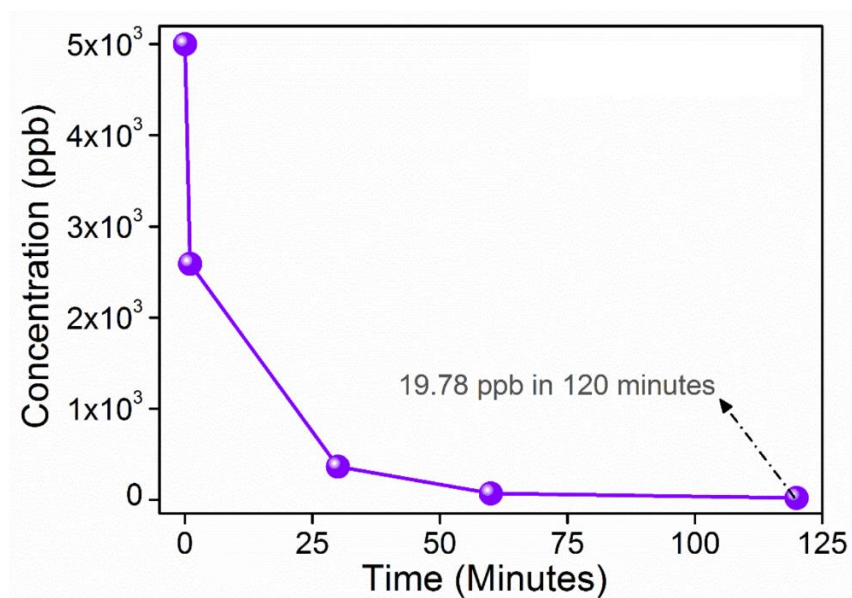
Appendix Table 5. The distribution coefficient (K_d) estimation from a 5 ppm U spiked solution for **iMOF-1A**, at $V/m = 1000 \text{ mL g}^{-1}$.

iMOF-1A	Distribution Constant (K_d^U)	Selectivity (K_d^U/K_d^M)
Only UO_2^{2+}	96.67×10^4	–
KCL	10.65×10^4	9.07
NaCl	5.88×10^4	16.44
Sr(NO₃)₂	0.82×10^4	117.89
KBr	5.78×10^4	16.72
CaCl₂	1.27×10^4	76.11
MgCl₂	0.71×10^4	136.15
Mixture of Salts	0.37×10^4	261.27

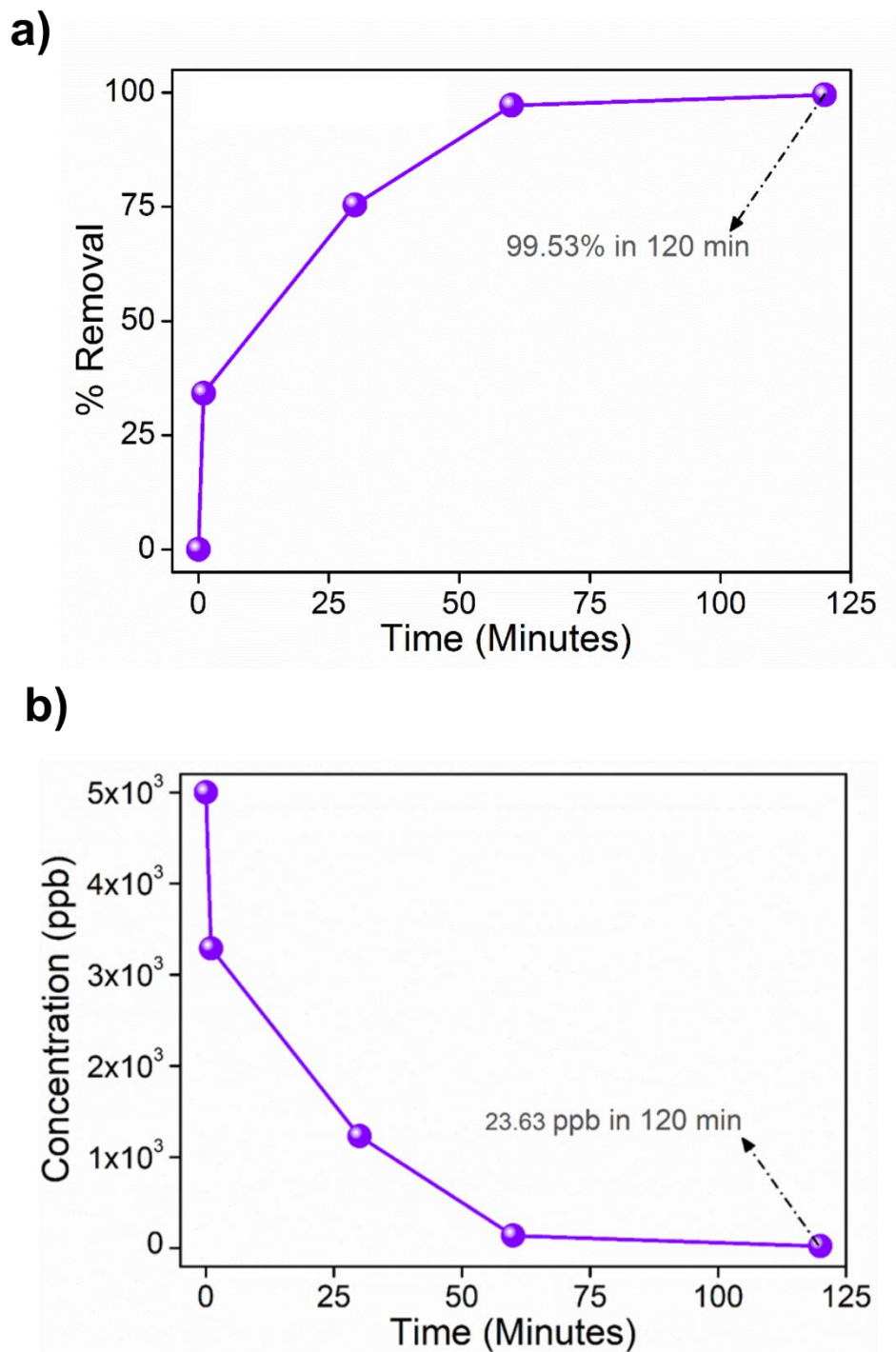
a)



b)

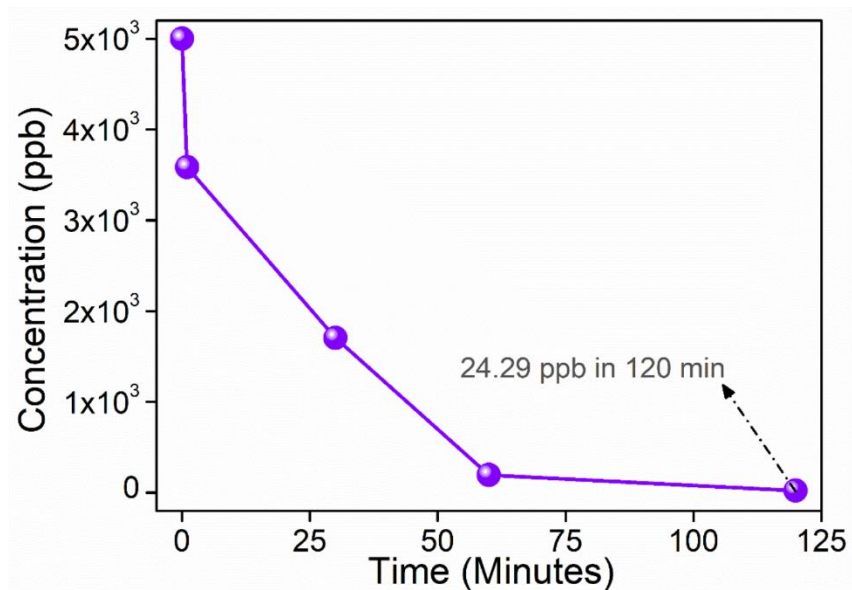


Appendix 22. Removal % at different time interval; (a) recovery of U from 5 ppm U spiked water at a $V/m = 2666.7 \text{ mL g}^{-1}$ by **iMOF-1A**; (b) decrease in the concentration of U from water as a function of time.

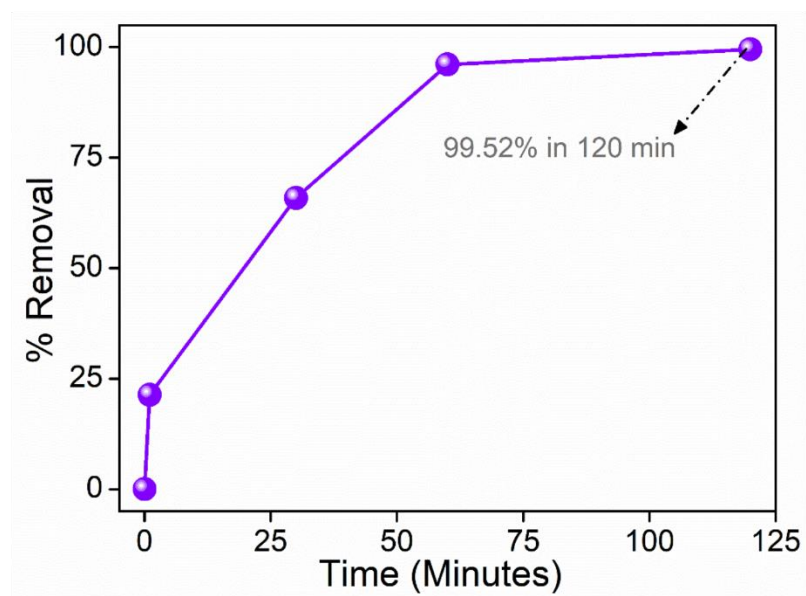


Appendix 23. Removal % at different time interval; (a) recovery of U from 5 ppm U spike lake water at a $V/m = 2666.7 \text{ mL g}^{-1}$ by **iMOF-1A**; (b) decrease seen in the concentration of U from water as a function of time.

a)

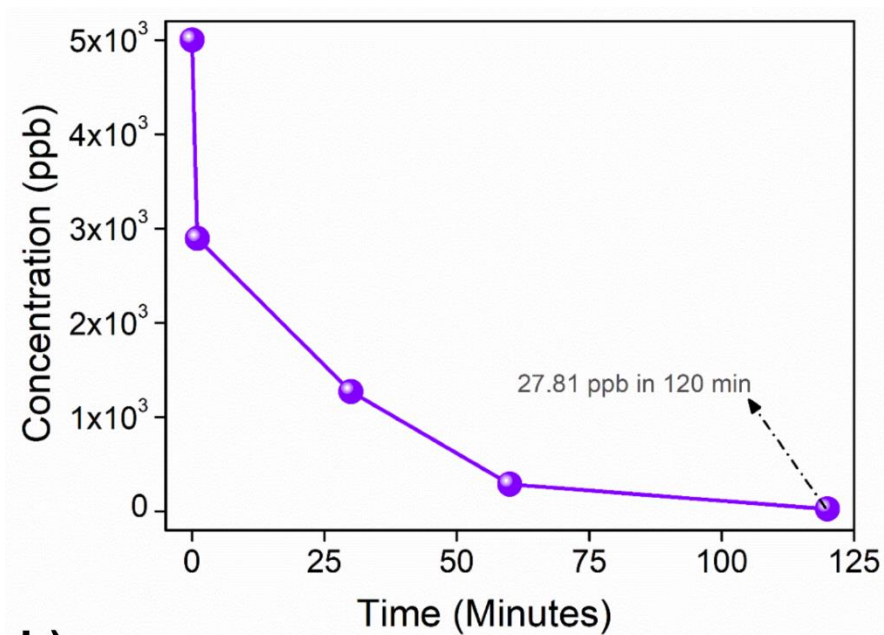


b)

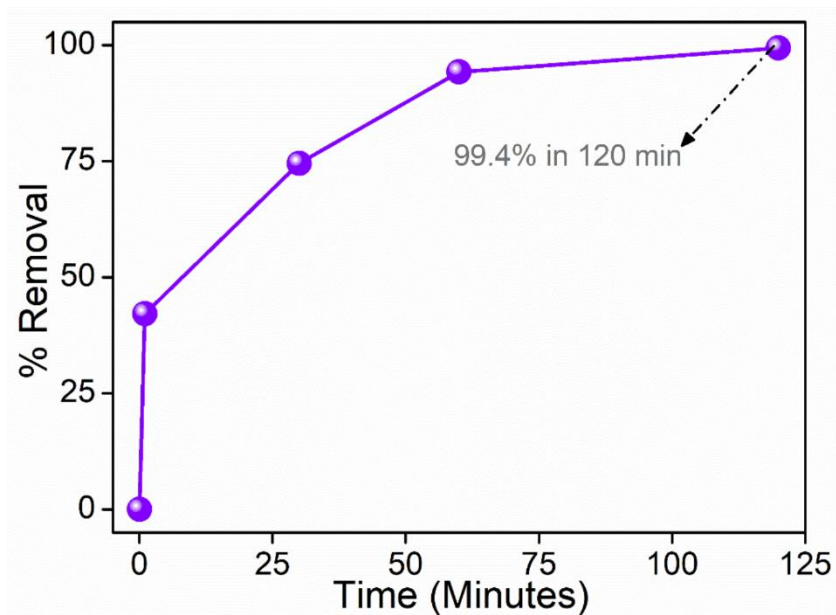


Appendix 24. Removal % at different time interval; (a) decrease seen in the concentration of U from water as a function of time; (b) U recovery from 5 ppm for U spiked river water at a $V/m = 2666.7 \text{ mL g}^{-1}$ by IMOF-1A.

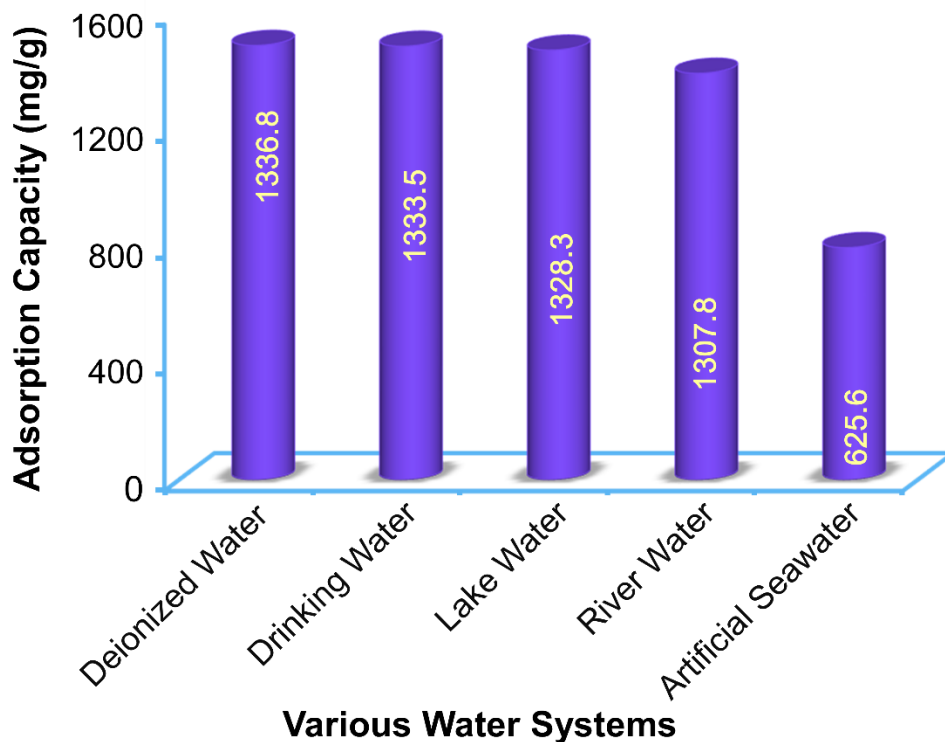
a)



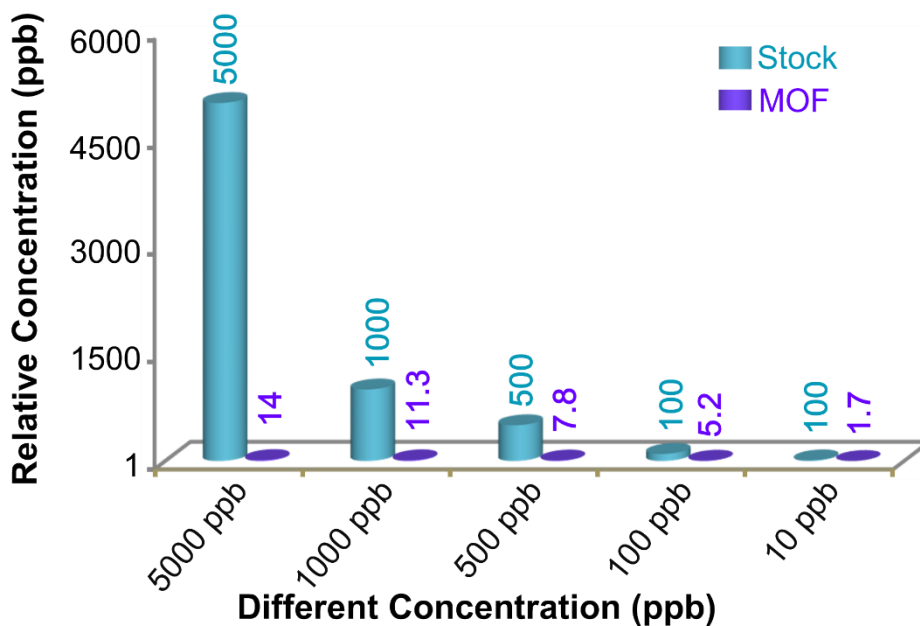
b)



Appendix 25. Removal % at different time interval; (a) Concentration decrease of U from water as a function of time; (b) U recovery from 5 ppm U spiked artificial seawater (ASW) at a $V/m = 2666.7 \text{ mL g}^{-1}$ by iMOF-1A.



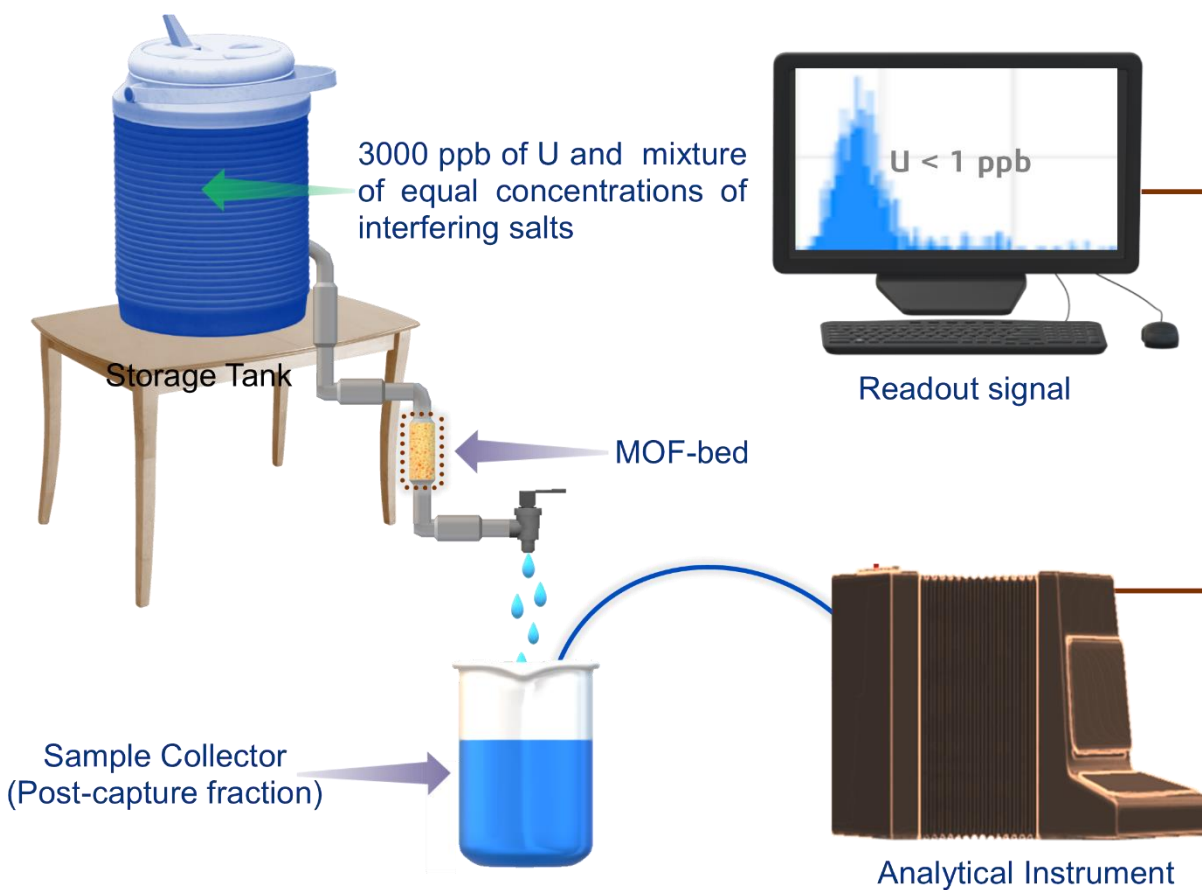
Appendix 26. Comparative of U adsorption capacities of iMOF-1A from variety of U spiked water systems.



Appendix 27. Comparison between Stock and MOF for U recovery from a various trace amount of U spiked Simulated / Artificial Sea Water.

Appendix Table 6. Comparison of present work with other related studies for U adsorption capacity by **iMOF-1A** from deionized water and artificial seawater.

Adsorbents	Deionized Water (mg/g)	Artificial Seawater (mg/g)	Reference
i-MZIF90(50)	1489.13	895.6	<i>Energy Environ. Sci.</i> , 2022, 15 , 3462.
iMOF-1A	1336.80	625.60	This work
V ₂ CT	174	377	<i>ACS Appl. Mater. Interfaces</i> , 2016, 8, 16396
POP-oNH ₂ -AO	530	290	<i>Nat. Commun.</i> , 2018, 9, 1644
AF series of adsorbents	-	200	<i>Ind. Eng. Chem. Res.</i> 2016, 55, 4110
ND-AO	212	121	<i>ACS Appl. Mater. Interfaces</i> , 2016, 8, 28853
MCM; Mesoporous Carbon Materials	97	67	<i>Ind. Eng. Chem. Res.</i> , 2013, 52, 15187



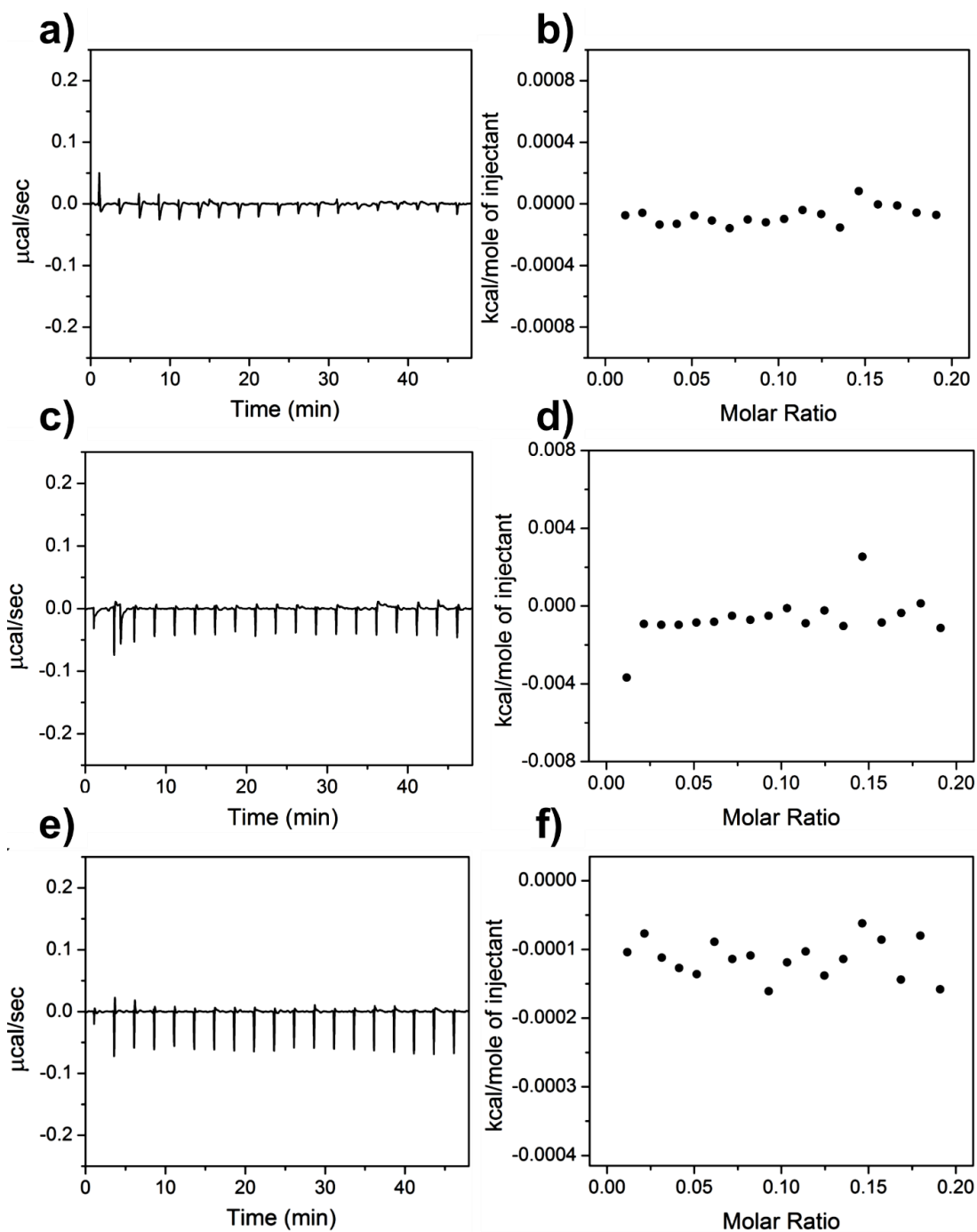
Appendix 28. This schematic depicts the breakthrough experiments performed by **iMOF-1A** packed bed on a solution containing 3 ppm uranium and 3 ppm of other competing metal cations in water.

Appendix Table 7. Comparison of present investigations with other related studies of U extraction from natural-nonspiked seawater for variety of adsorbents.

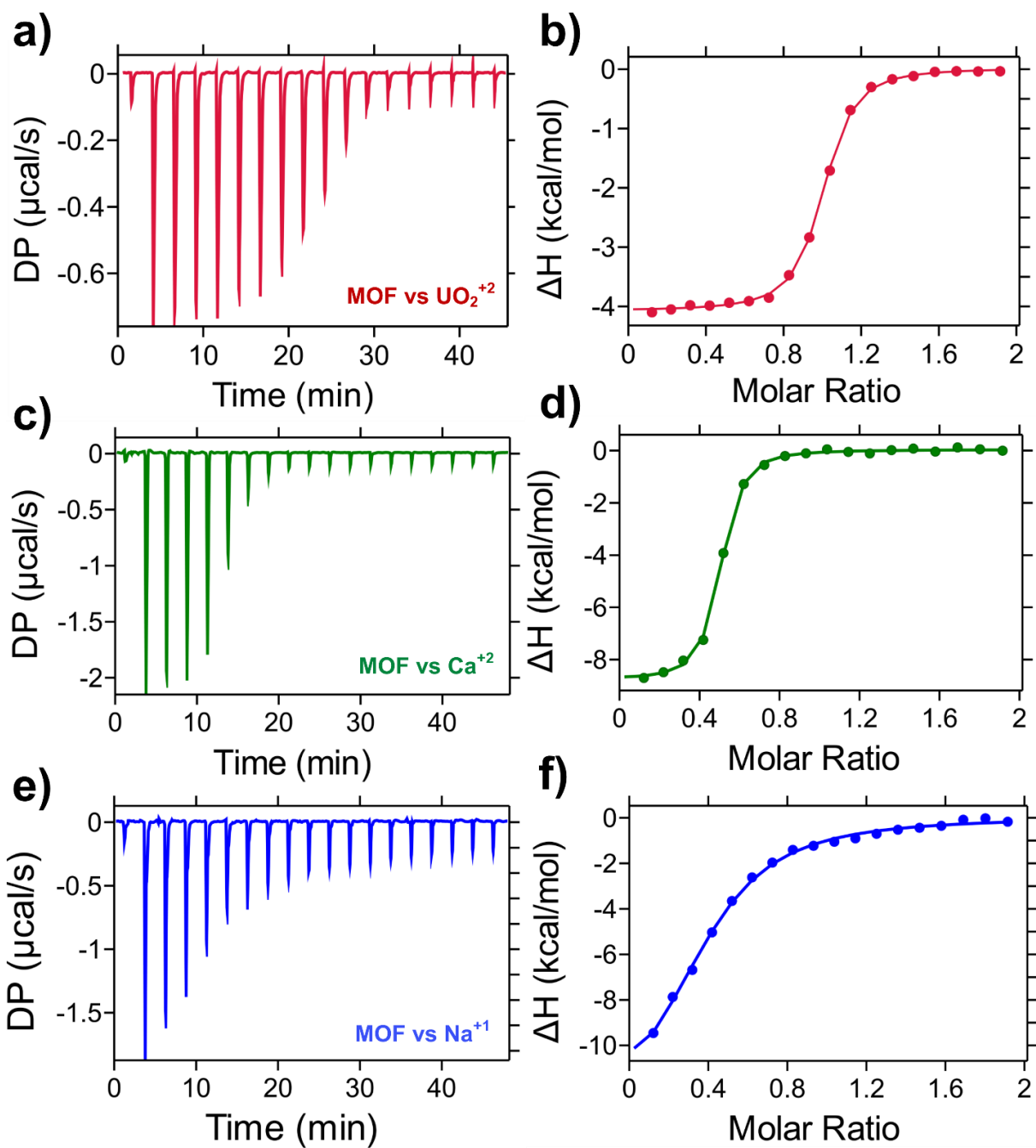
Adsorbents	Type	Capacity (mg/g)	Time (days)	Reference
i-MZIF90(50)	macro-MOF	28.2	25	<i>Energy Environ. Sci.</i> , 2022, 15 , 3462
H-ABP	Fiber	11.5	90	<i>Energy Environ. Sci.</i> , 2019, 12 , 1979
iMOF-1A	MOF	9.38	30	This work
SMON-PAO	Nano Fiber	9.59±0.64	56	<i>Adv. Funct. Mater.</i> , 2019, 29 , 1805380
Zn ²⁺ -PAO	Hydrogel	9.23	28	<i>Adv. Mater.</i> , 2020, 32 , 1906615
PIDO NF	Fiber	8.7	56	<i>Adv. Energy Mater.</i> , 2018, 8 , 1802607
MS@PIDO/Alg	Hybrid Sponge	5.84	56	<i>Adv. Funct. Mater.</i> , 2019, 29 , 1901009
MISS-PAF-1	PAF	5.79	56	<i>ACS Cent. Sci.</i> , 2019, 5 , 1432
PPN-6-PAN	Anti-Biofouling	4.62	30	<i>Adv. Sci.</i> , 2019, 6 , 1900547
POP- <i>o</i> NH ₂ -AO	POP	4.36	56	<i>Nat. Commun.</i> , 2018, 9 , 1644
PAO hydrogel	Hydrogel	4.87	28	<i>Ind. Eng. Chem. Res.</i> , 2015, 55 , 4103-4109

Isothermal Titration Calorimetry

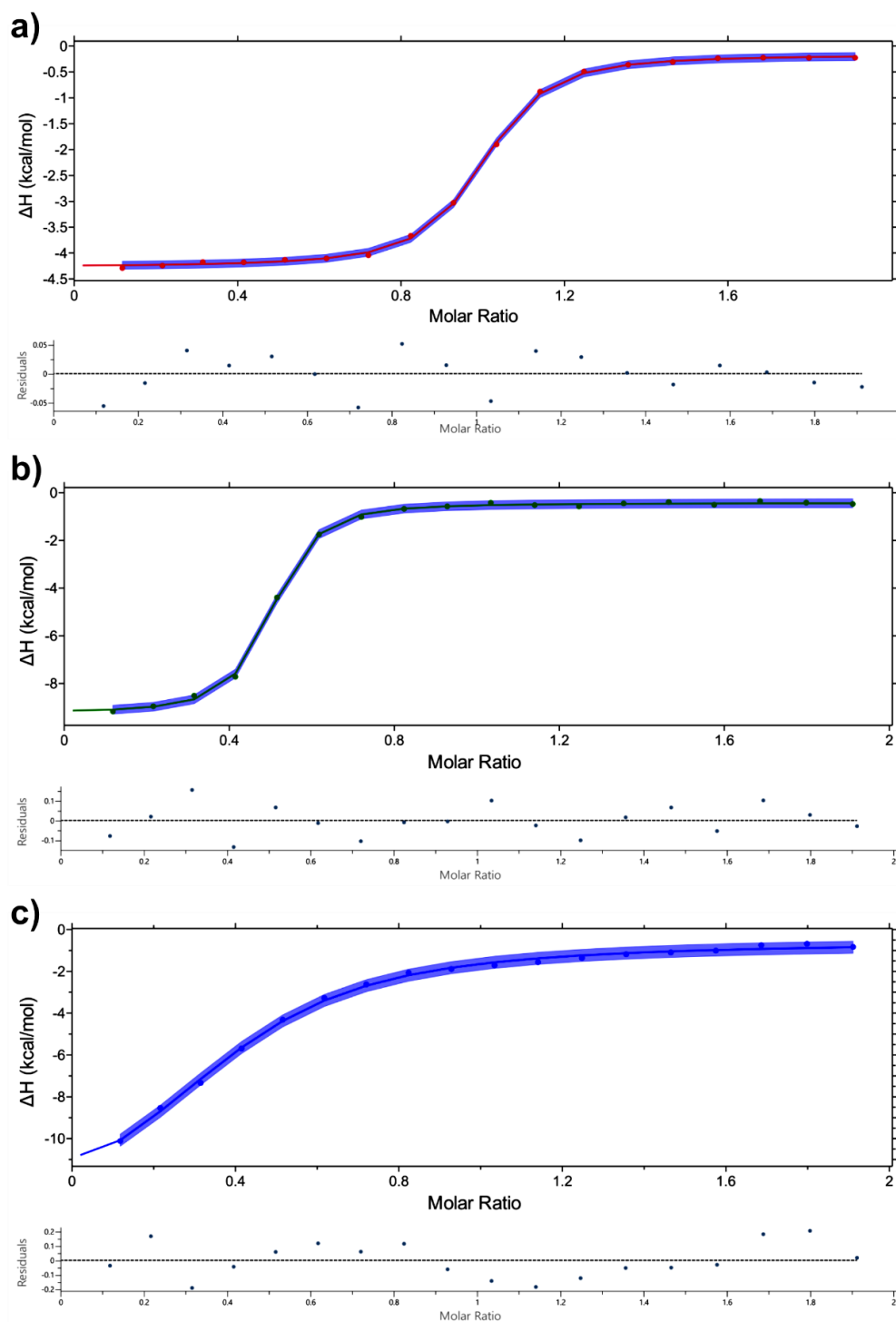
For each set of ITC studies, a Malvern MicroCal PEAQ-ITC microcalorimeter with a 20 (19+1) injections/cycling method capacity, a sample volume of 280 μL with a sample cell size of 200 μL , and an injection syringe volume of 40 μL was used. In a typical ITC experiment, the reference cell is filled with deionized water containing 18.2 megaohms of resistance and 0.055 micro Siemens of conductivity, the sample cell is filled with a MOF suspension, and the syringe contains an analyte solution. For all titrations, MOF suspension was used at a 1 mM concentration for all titrations, while cationic analytes were utilized at 10 mM concentrations. All MOF and analyte solutions were produced or made by using 1 mM Tris-HCl buffer. Their pH levels were corrected to 7.00 using a Tris-HCl buffer at a pH of 7.4. Before collecting thermograms, 15 minutes were spent degassing all solutions. All thermograms were obtained at a constant rate of 750 revolutions per minute. The initial injection volume for each titration was set to 0.4 μL . Using the AGILENT 7800 ICP-MS, all analyte concentrations were measured. At least two titrations were collected for each analyte-MOF pair. The MicroCal PEAQ-ITC analytical software was used for data analysis. The injection temperatures of blank titrations (analyte into blank) were deducted from the injection heats of MOF suspensions. All measurements are taken at 298.15 K temperature.



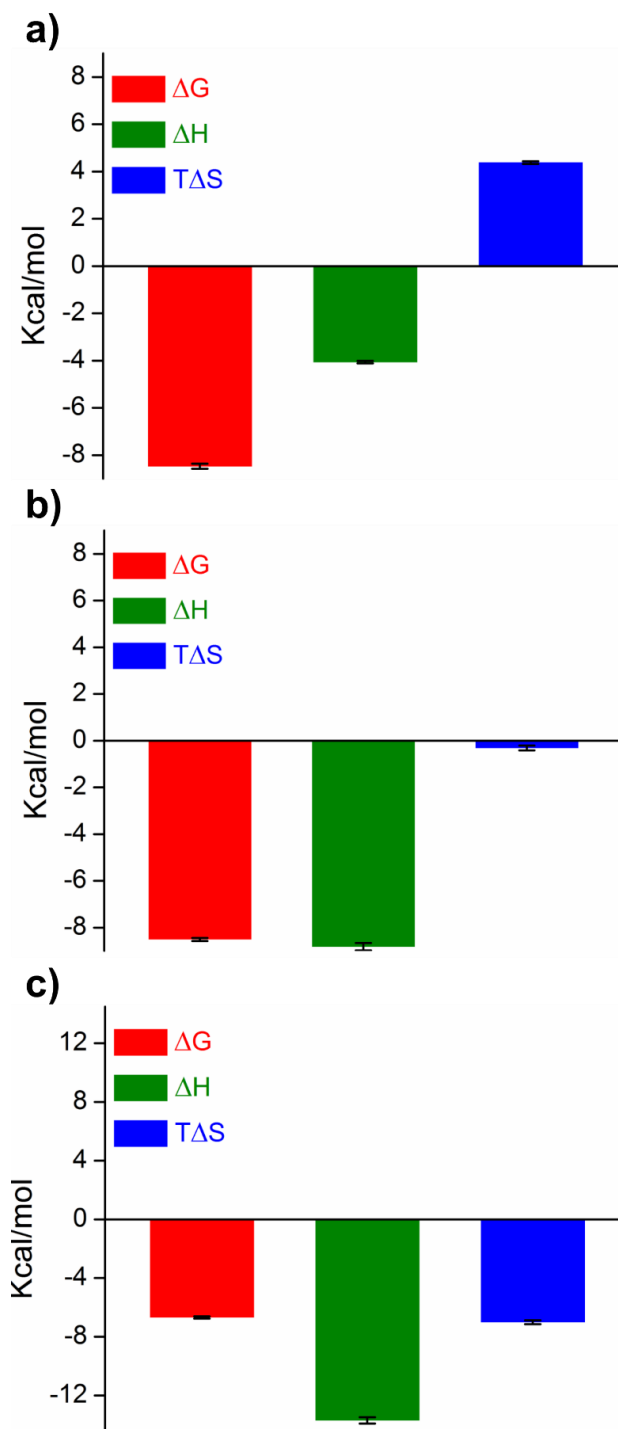
Appendix 29. ITC thermograms and integrated heat plots for injections for (a) & (b) blank titrated against blank (Syringe, Cell, pH=7) (c) & (d) aq. Uranyl nitrate hexahydrate (10 mM, syringe loaded, pH 7) titrated against blank (cell loaded, pH 7) and (e) & (f) Blank (Syringe loaded, pH 7) is titrated against suspension of **iMOF-1A** (10 mM, cell loaded, pH 7).



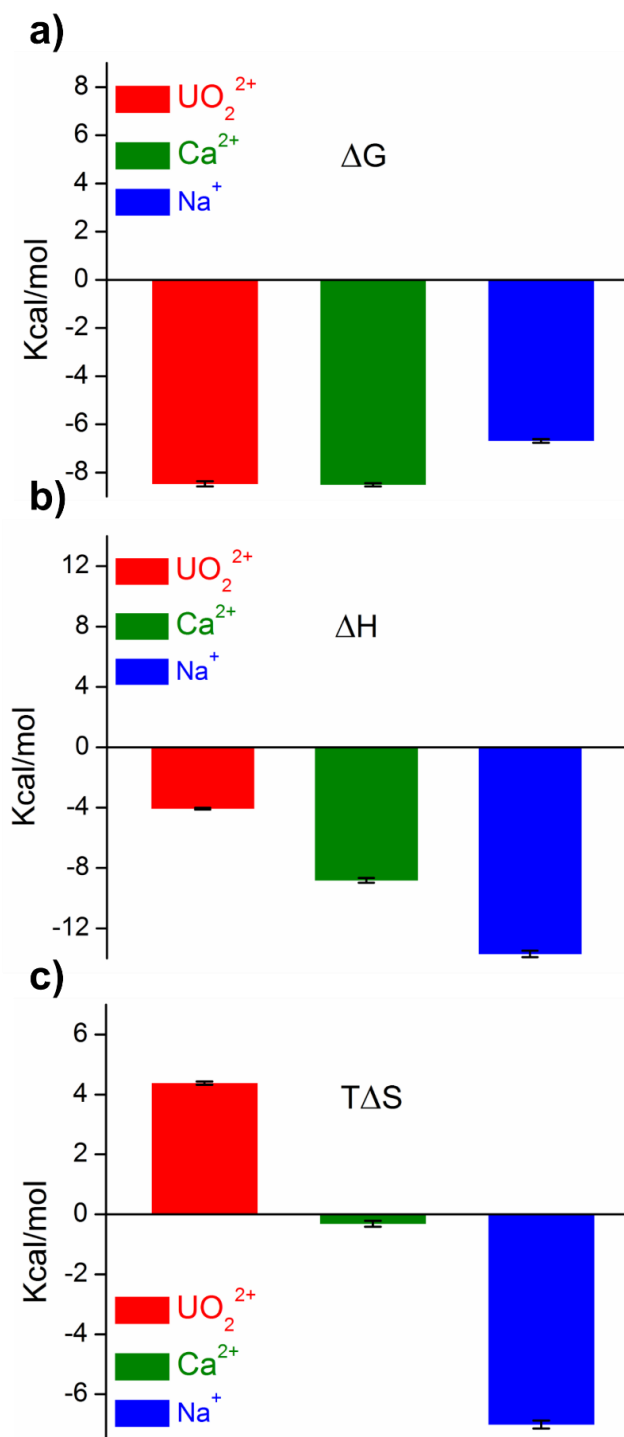
Appendix 30. ITC thermograms and integrated heat plots simultaneously for injections of (a) & (b) UO_2^{2+} titrated against iMOF-1A, (c) & (d) Ca^{2+} titrated against iMOF-1A and (e) & (f) Na^+ titrated against iMOF-1A.



Appendix 31. ITC integrated heat plots indicating minimum error bars and residuals for injections of (a) UO_2^{2+} titrated against **iMOF-1A**, (b) Ca^{2+} titrated against **iMOF-1A** and (c) Na^+ titrated against **iMOF-1A**. All heat plots having χ^2 (χ^2) value within limits.



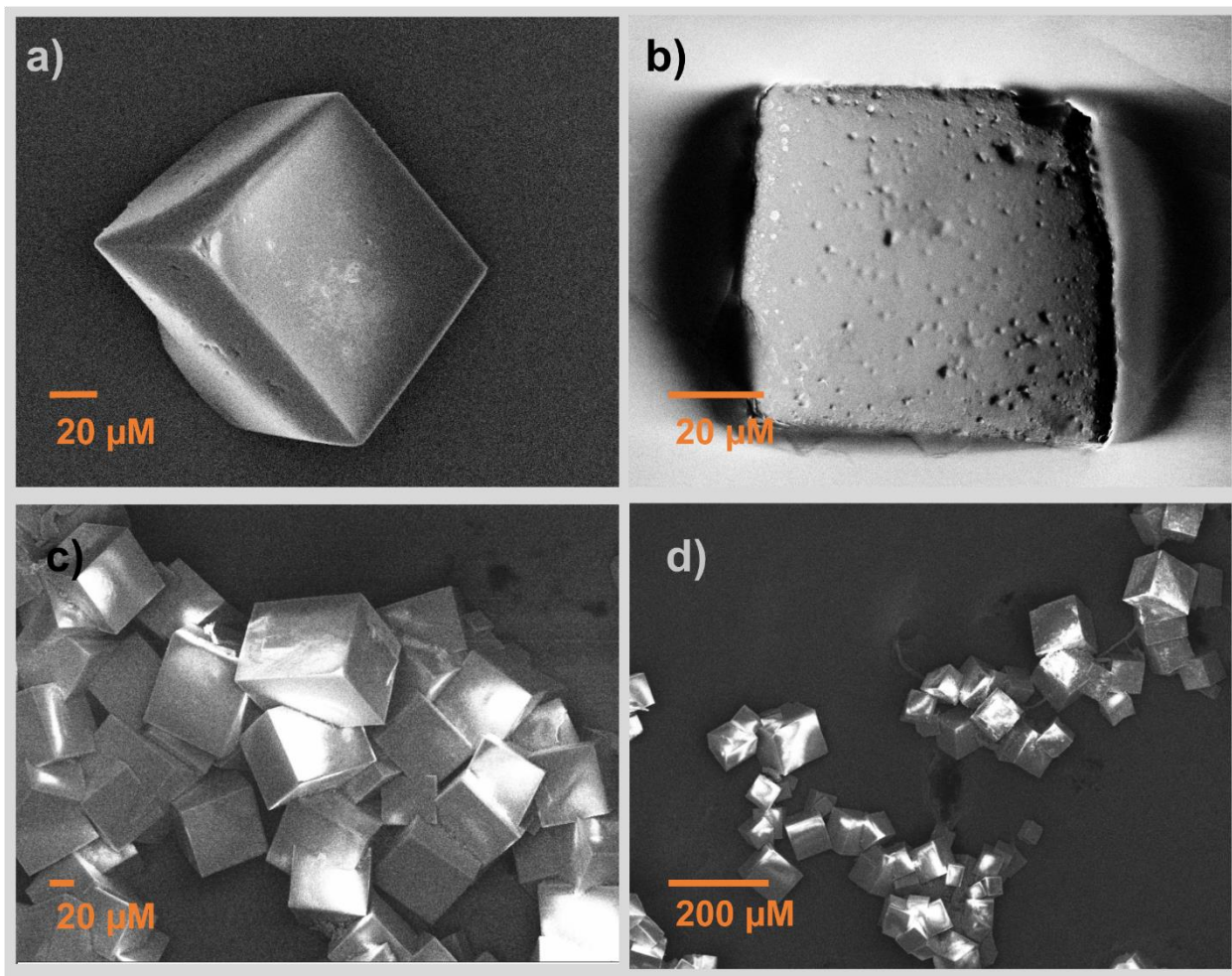
Appendix 32. Thermodynamic parameters for interacting analytes (a) UO_2^{2+} (b) Ca^{2+} and (c) Na^+ indicating changes in Gibbs free energy, enthalpy, entropy for the interactions with **iMOF-1A**. Error bars represent the standard deviation of triplicate measurements.



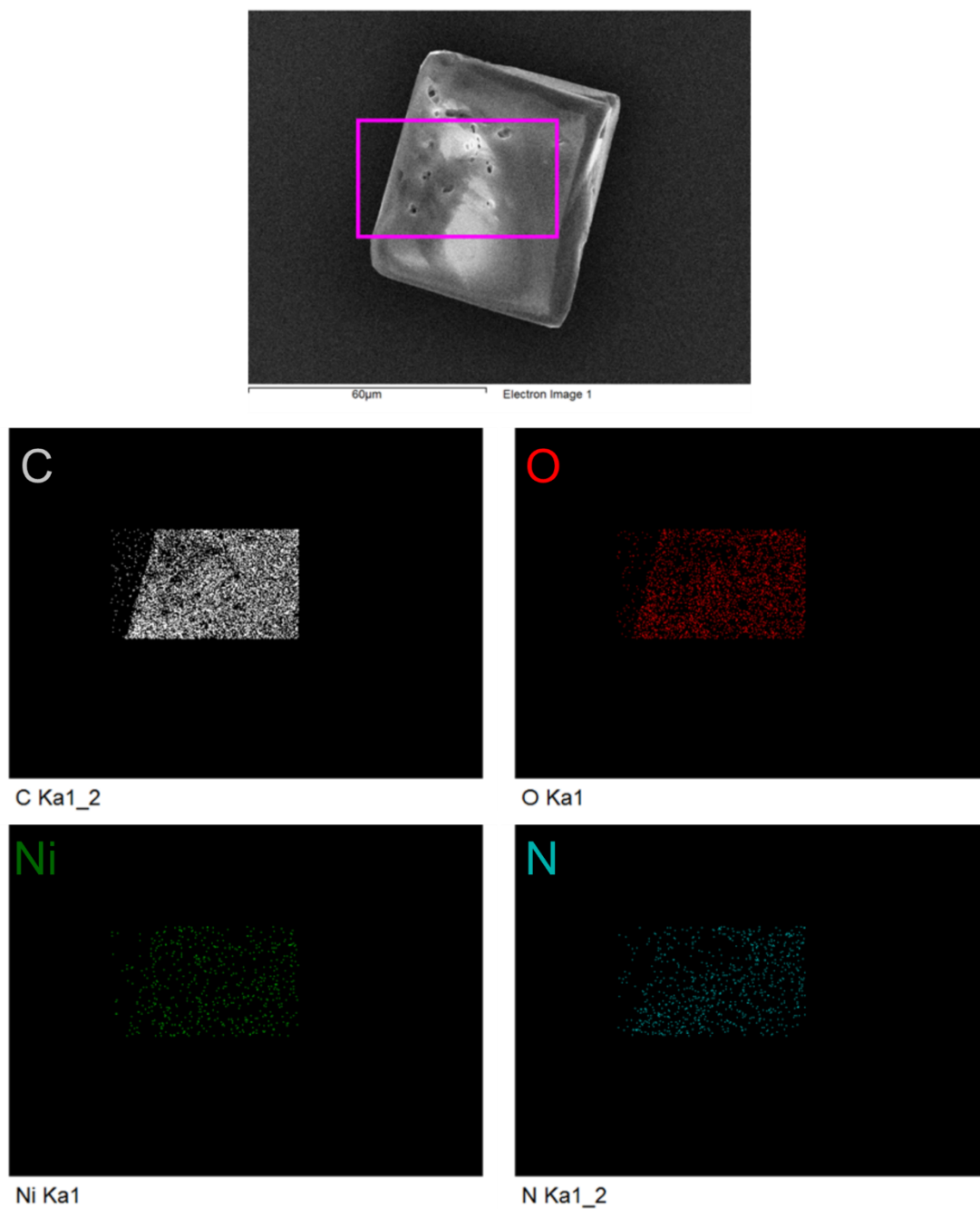
Appendix 33. Trend in each thermodynamic parameter for interacting analytes (a) UO_2^{2+} (b) Ca^{2+} and (c) Na^+ indicating changes in Gibbs free energy, enthalpy, entropy for the interactions with **iMOF-1A**. Error bars represent the standard deviation of triplicate measurements.

Appendix Table 8. The concentration and thermodynamic parameters derived from ITC experiment for prime competing cations captured in **iMOF-1A**.

Parameters	UO ₂ ²⁺	Ca ²⁺	Na ⁺
Temperature (°C)	25.1	25.3	25.2
Bin	Binding	Binding	Binding
[Syr] (M)	1.00E-03	1.00E-03	1.00E-03
[Cell] (M)	1.00E-04	1.00E-04	1.00E-04
Ligand in Cell	MOF	MOF	MOF
N (sites)	0.957	0.460	0.377
KD (M)	6.20E-07	5.90E-07	1.25E-05
ΔH (kcal/mol)	-4.09 ± 0.0512	-8.82 ± 0.1591	-13.70 ± 0.2096
ΔG (kcal/mol)	-8.47 ± 0.1026	-8.51 ± 0.0665	-6.69 ± 0.0799
TΔS (kcal/mol)	4.38 ± 0.0499	-0.313 ± 0.0989	-7.01 ± 0.1351



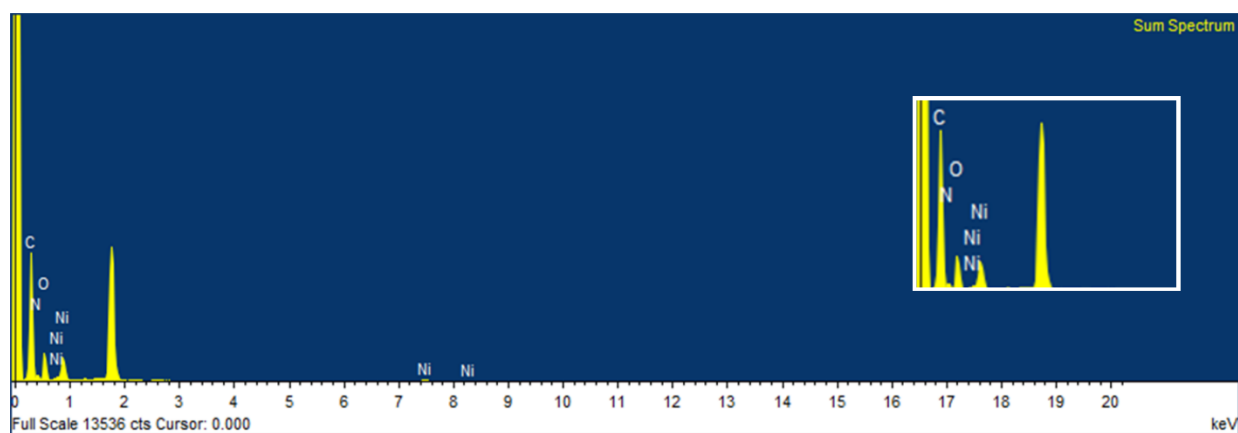
Appendix 34 A). FESEM images of **iMOF-1A**; before capture (**a, c**) and after capture (**b, d**) of uranyl cations indicating retention cubic crystalline morphology of evacuated (desolvated) phase and that of U treated phase, as revealed by FE-SEM analysis.

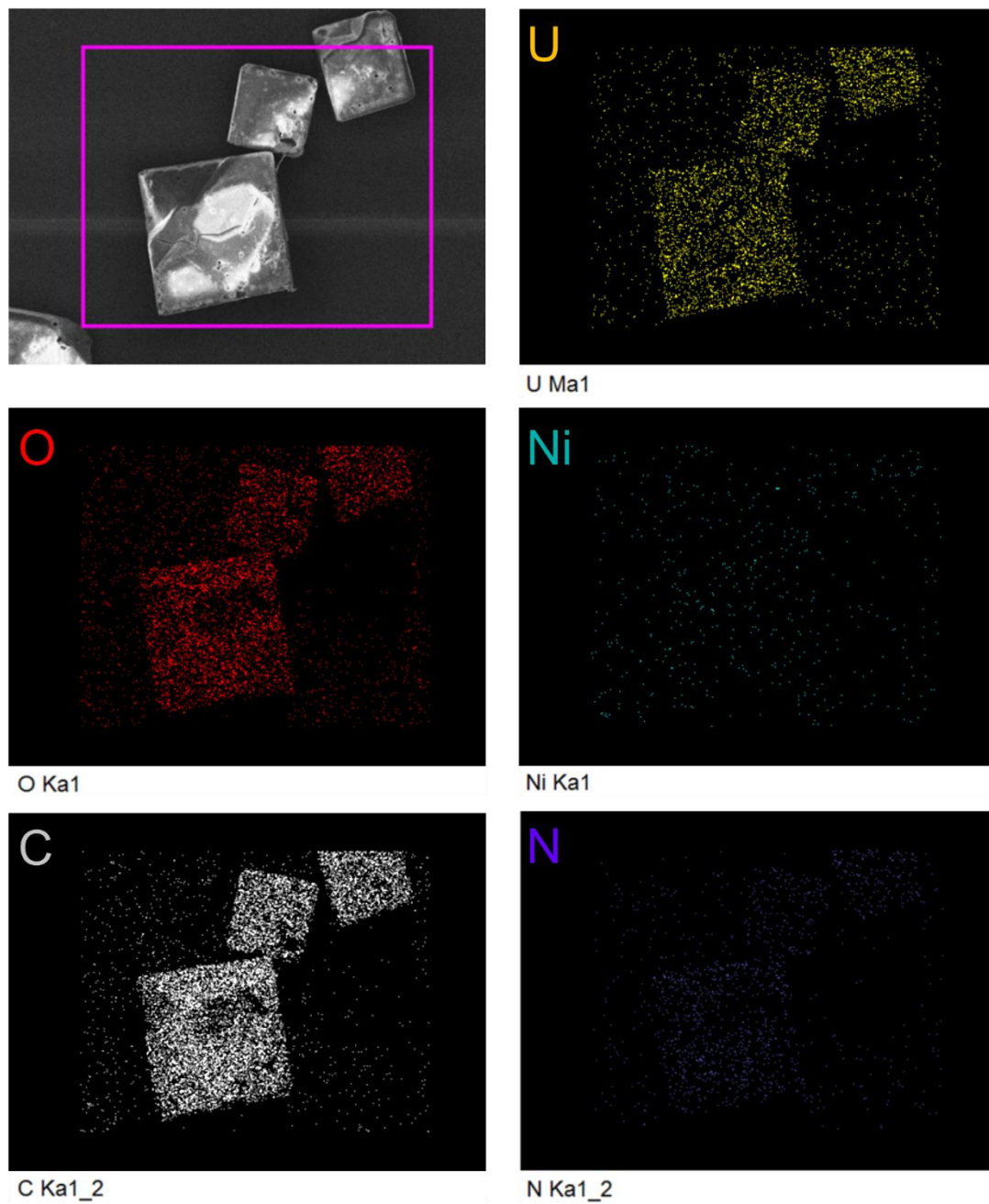


Appendix 34 B). Elemental Mapping profile of desolvated iMOF-1A revealing cubic crystalline morphology of desolvated phase.

Appendix Table 9. EDX analysis of desolvated iMOF-1A.

Element	Weight%	Atomic%
C K	55.12	63.47
N K	12.93	12.76
O K	25.82	22.32
Ni K	6.13	1.44
Totals	100.00	100.00

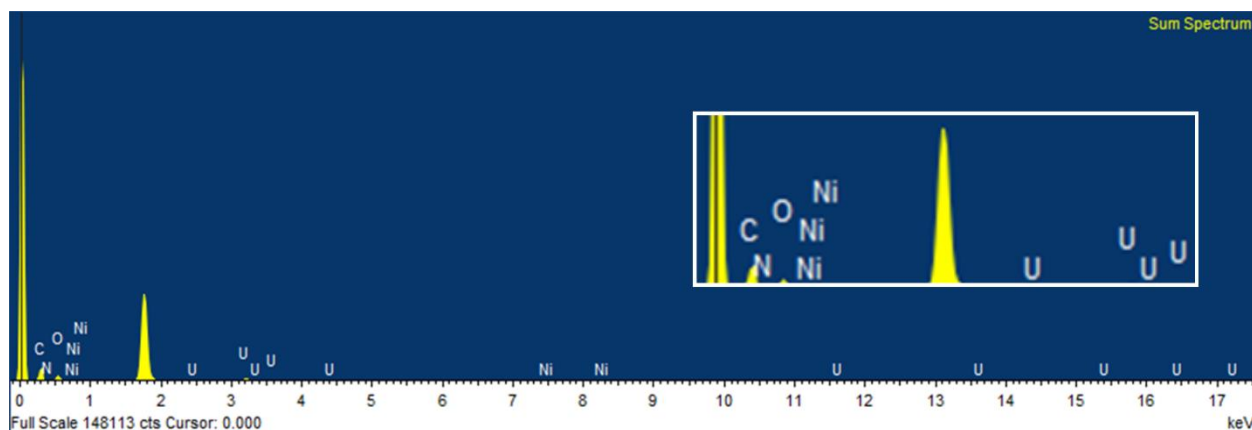
**Appendix 35.** FESEM-EDX spectra of desolvated iMOF-1A.

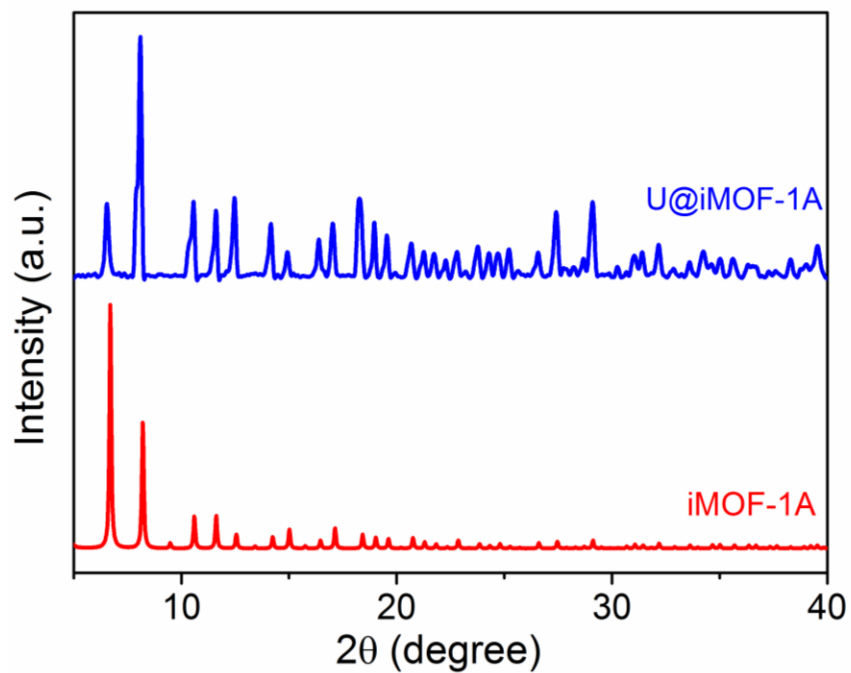


Appendix 36. Elemental Mapping profile of iMOF-1A after 24 hour U capture studies.

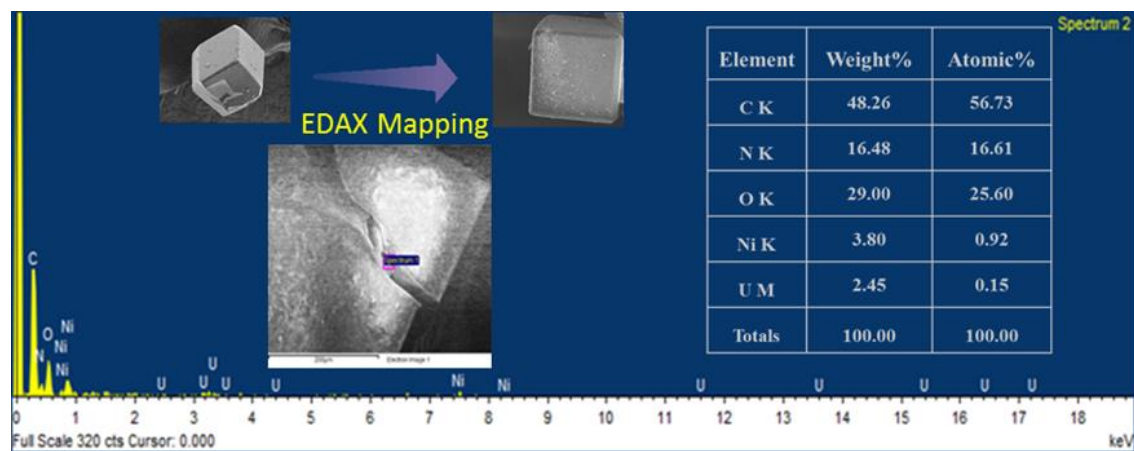
Appendix Table 10. EDX analysis of **iMOF-1A** after 24 hours of U treatment.

Element	Weight%	Atomic%
C K	39.75	56.58
N K	8.38	10.23
O K	29.18	31.18
Ni K	1.69	0.49
U M	20.99	1.51
Totals	100.00	100.00

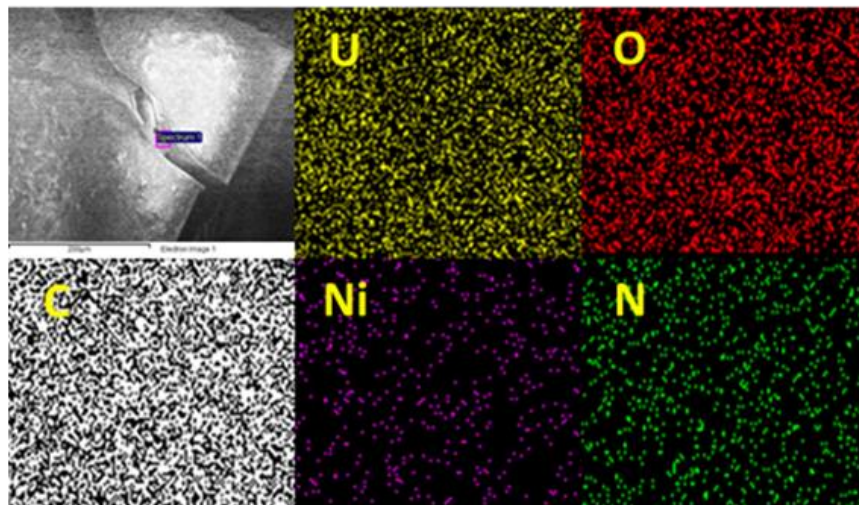
**Appendix 37.** FESEM-EDX spectra of **iMOF-1A** after 24 hours of U treatment.



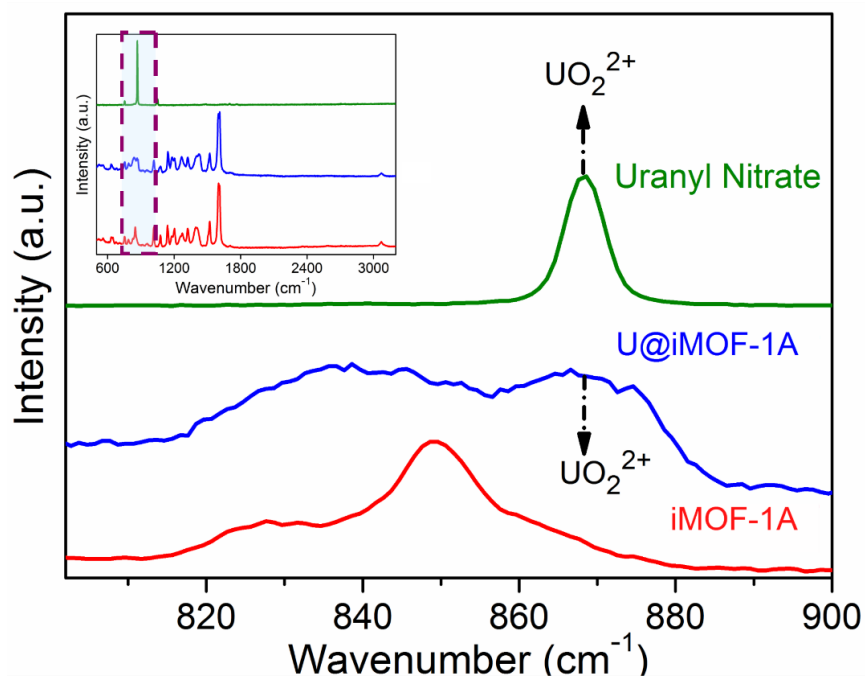
Appendix 38. PXRD patterns of **iMOF-1A** before and after capture study.



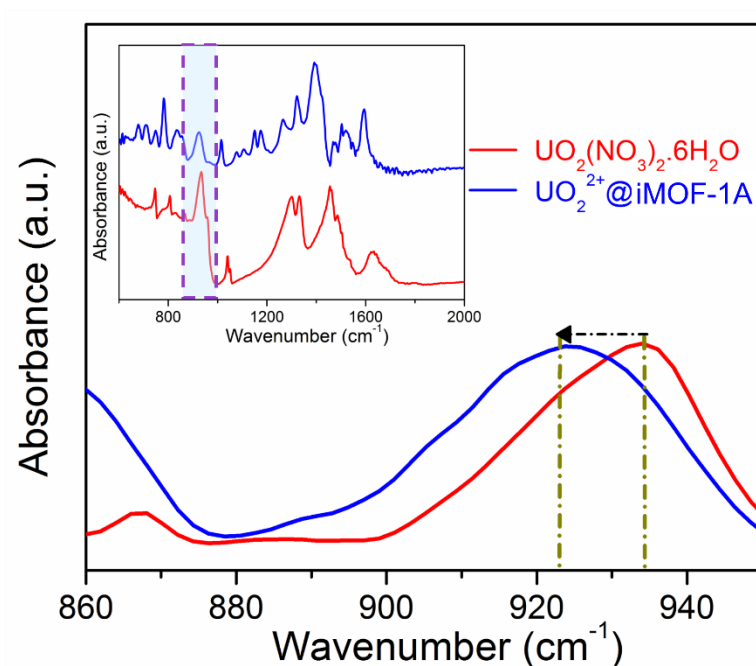
Appendix 39. Elemental mapping from FESEM experiment. In the cracked inside-surface of the MOF (at pink inset) in order to confirm loading of U within the MOF structure.



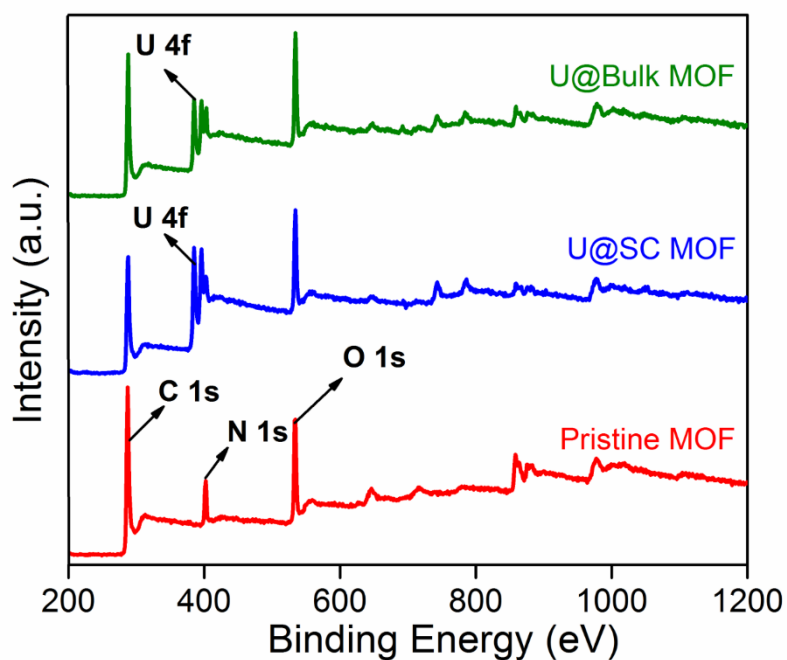
Appendix 40. FESEM-EDX spectra of U loaded **iMOF-1A** revealing inside portion of crystal rendered post-fracking. The mapping shows successful loading of U within the MOF.



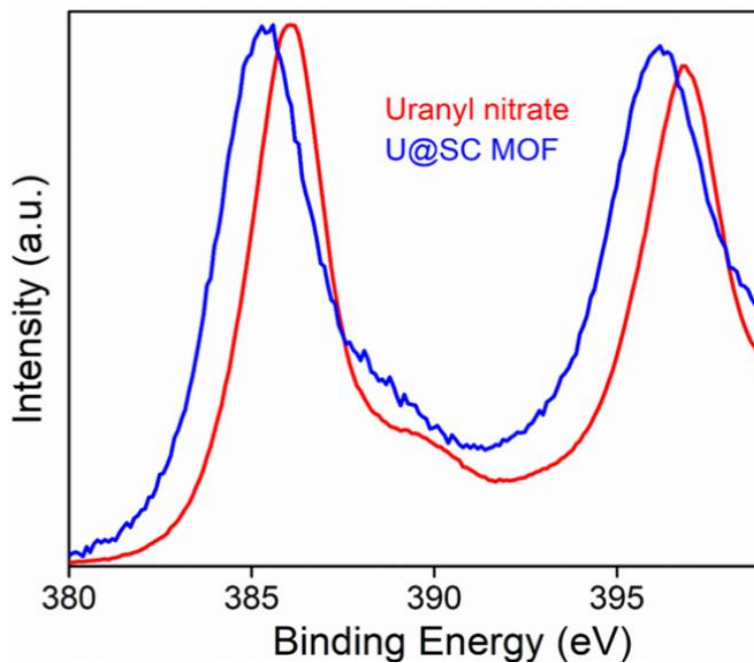
Appendix 41. Raman spectra of individual compounds (Uranyl salt and **iMOF-1A**) and U loaded MOF (**U@iMOF-1A**) rendered for comparison.



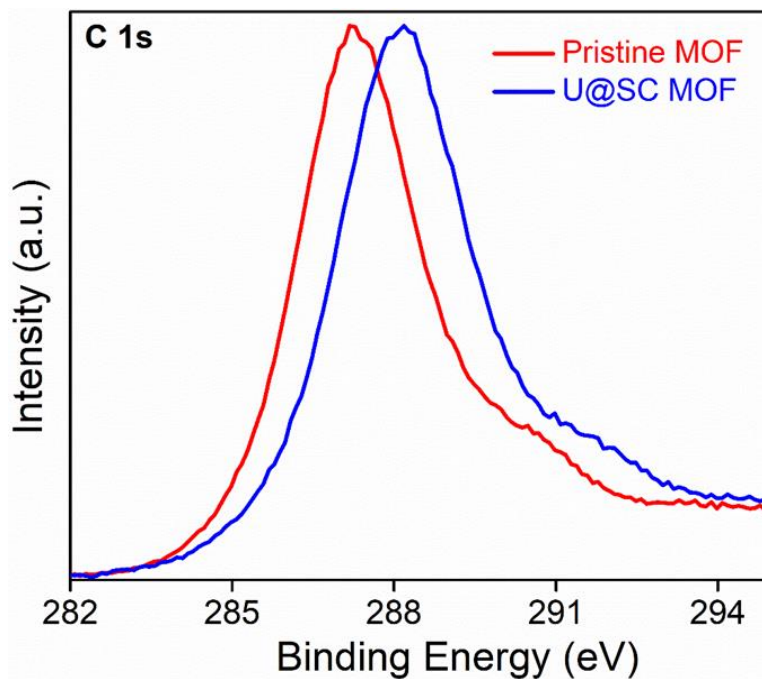
Appendix 42. FTIR spectrum comprising uranyl salts and uranium loaded i-MOF1A, red shifted from 932 cm⁻¹ to 912 cm⁻¹.



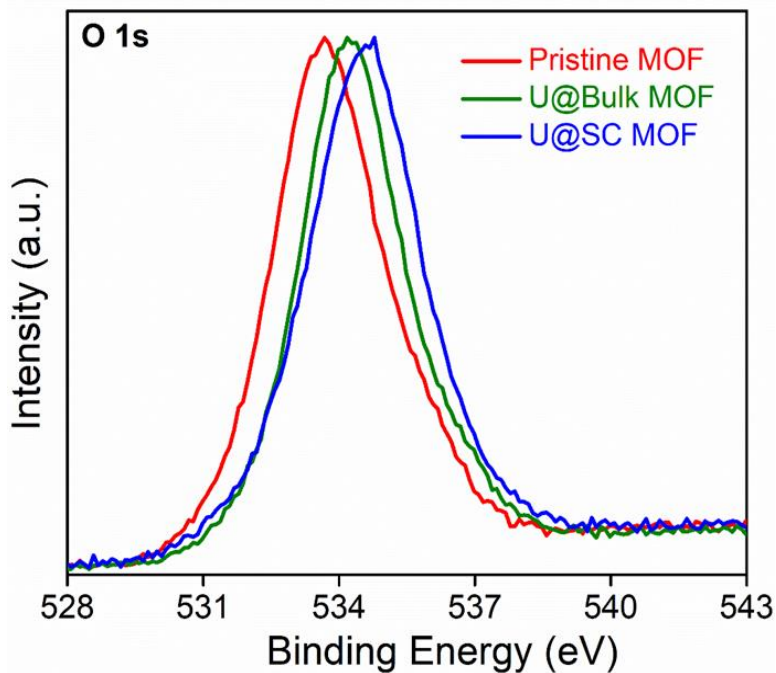
Appendix 43. XPS survey spectrum of iMOF-1A pre and post U capture studies.



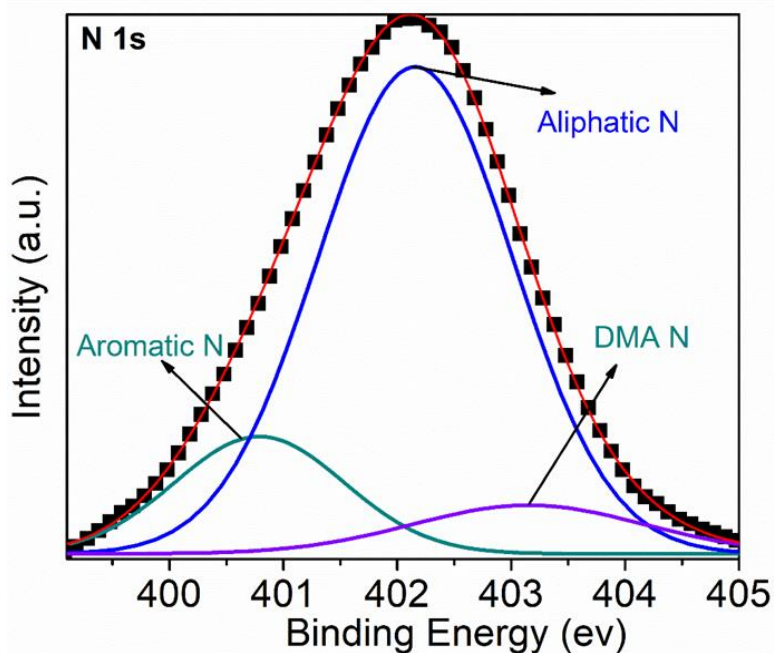
Appendix 44. U@iMOF-1A XPS spectra at high resolution for uranyl nitrate (U 4f). U is more tightly bound with the iMOF-1A, as seen by the shift in the typical peaks for U 4f toward lower binding energy following capture study.



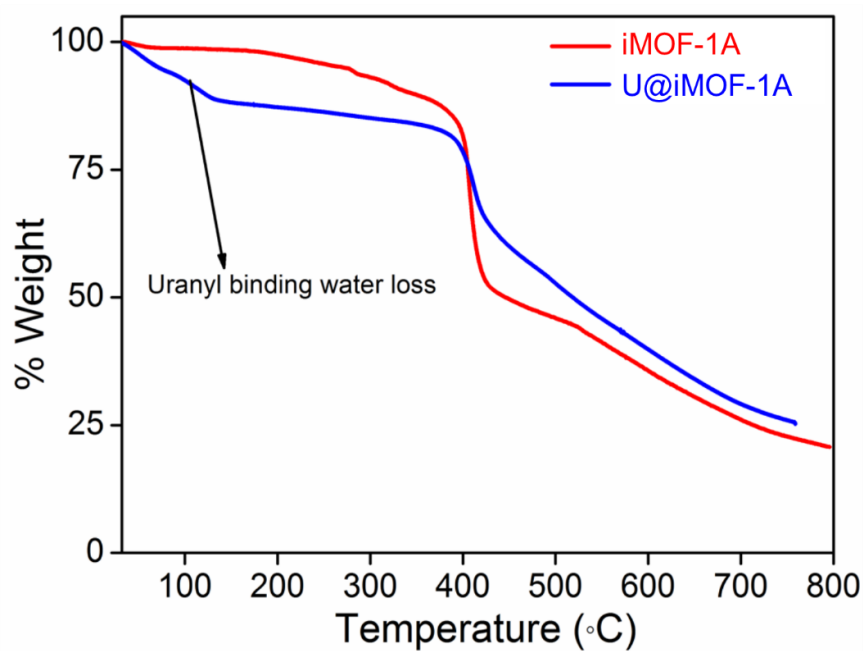
Appendix 45. Comparison the **iMOF-1A**, C 1s XPS spectra with and without the addition of U at high resolution. The loading of U into the framework caused the typical peaks for C to shift towards higher energy, indicating strong interaction between U and the coordinative functional groups of the framework.



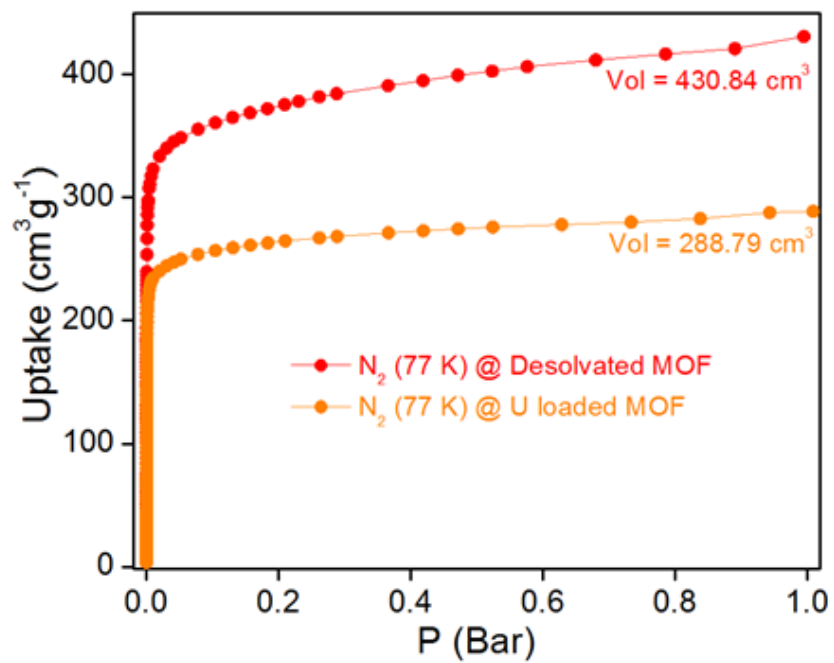
Appendix 46. Spectra of O 1s captured by **iMOF-1A** at high resolution XPS both before and after capturing U. A substantial interaction between U and the framework is indicated by a shift in the typical peaks for O to higher energy after loading of U into the framework.



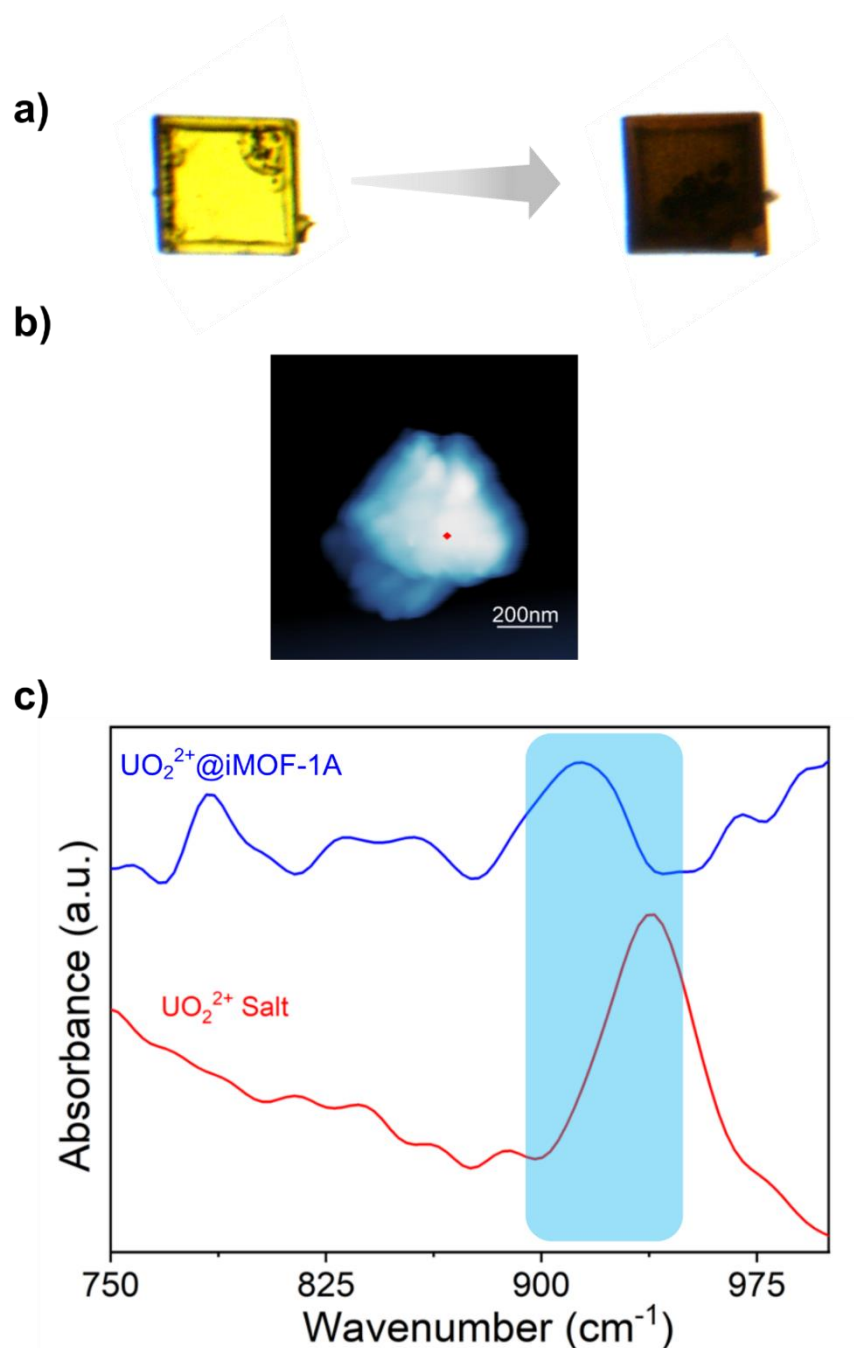
Appendix 47. High resolution XPS spectra of N 1s spectra of pristine **iMOF-1A** (Add N1s Spectra for **iMOF-1A**).



Appendix 48. TGA curves before and after capture studies.

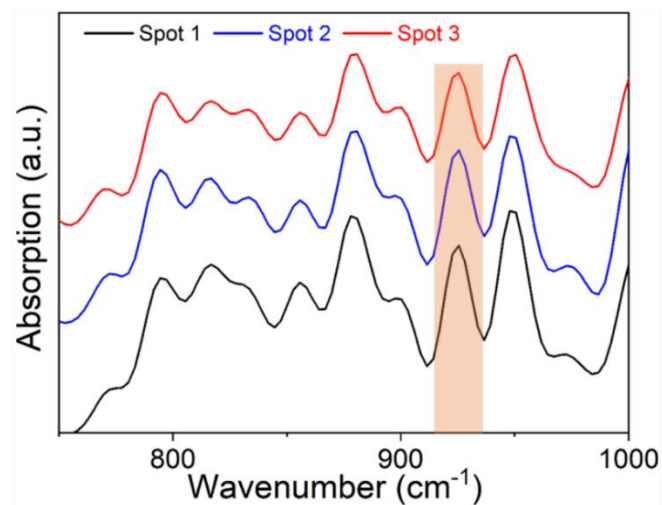
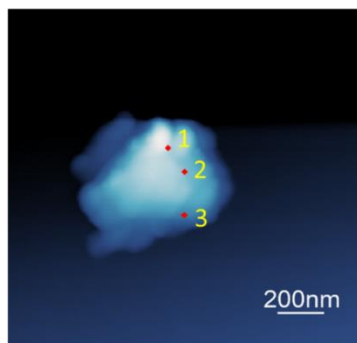


Appendix 49. N₂ sorption isotherms recorded at 77 K before and after U capture studies.

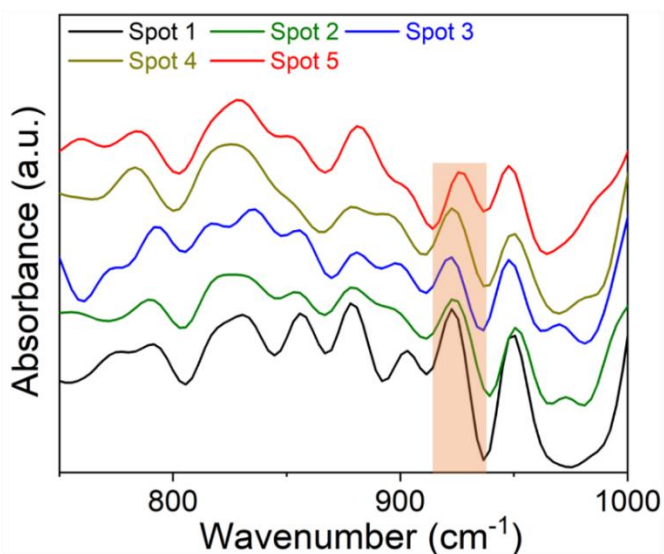
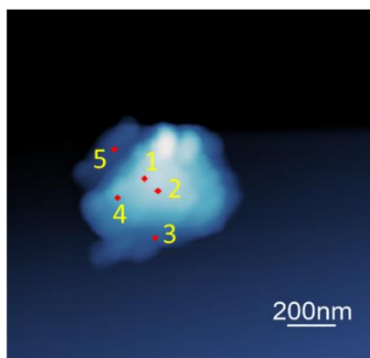


Appendix 50. (a) U capture in single crystal of **iMOF-1A**; (b) Nano-FTIR rendered image UO_2^{2+} @MOF for a spot in a MOF single crystal (red spot on crystal represent the probing region for nano-FTIR); (c) Characteristics vibrational band shifted to lower wavelength after exchanging with U salts indicating strong interaction between frameworks and UO_2^{2+} .

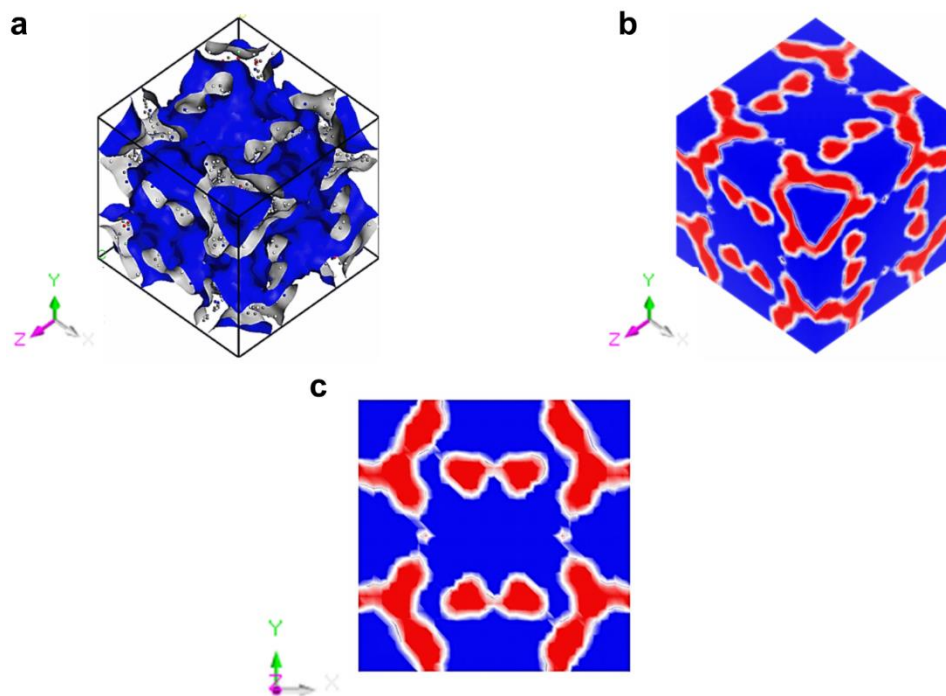
a)



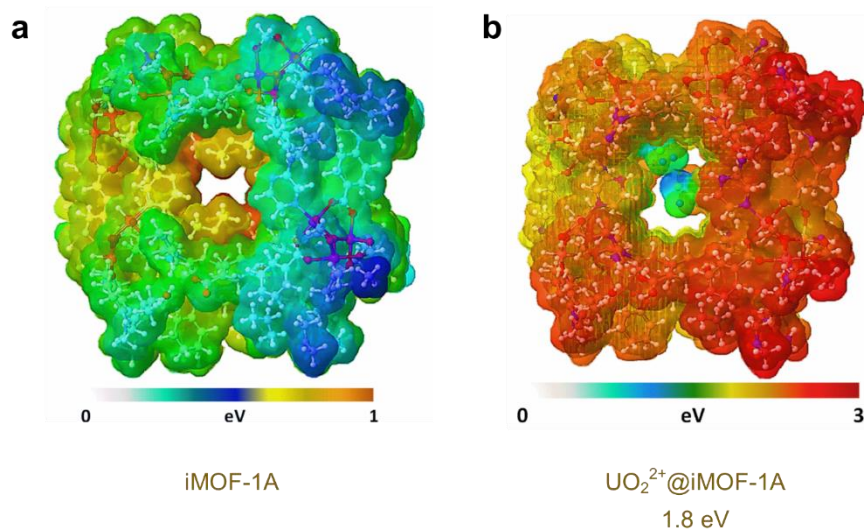
b)



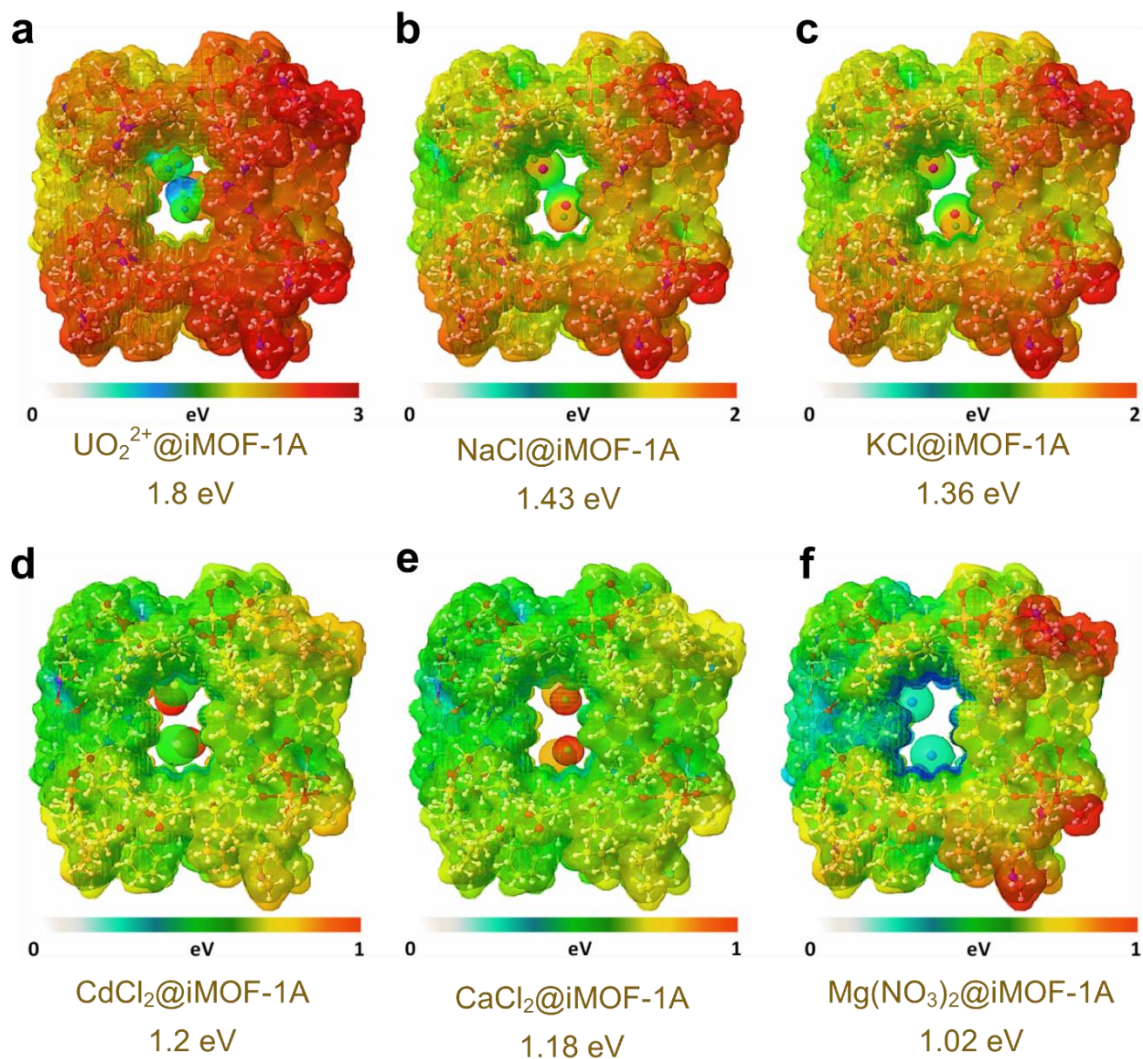
Appendix 51. Nano-FTIR local region for; (a) (probing depth ~ 20 nm) characterization of individual single crystals, vibrational band of UO_2^{2+} in a different regions of a randomly selected MOF single crystal revealing exchange phenomena prevailing throughout in a crystals; b) similar analysis over 5 spots in another U loaded single crystal.



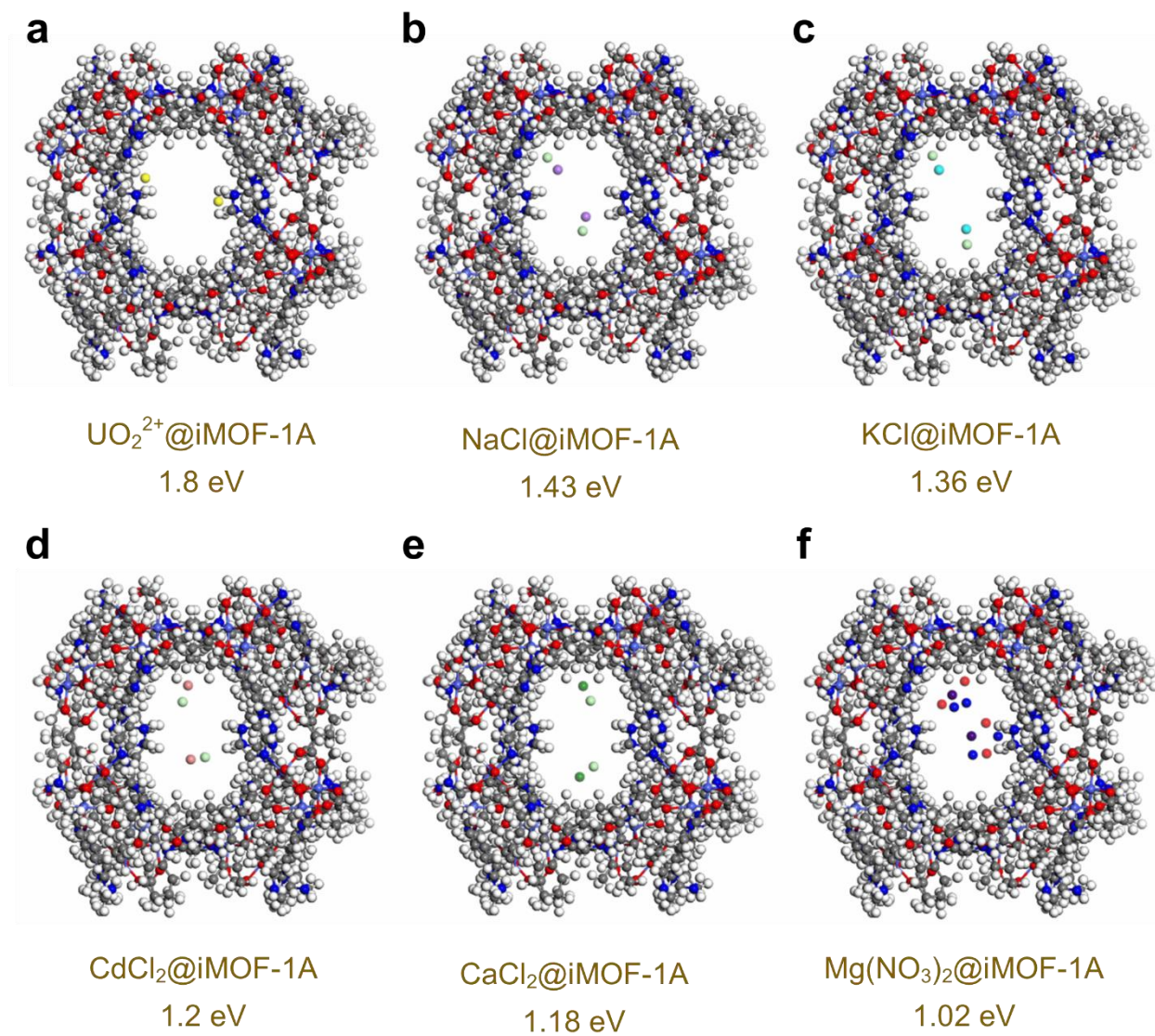
Appendix 52. (a) 3D Cannoli surface of **iMOF-1A**, hows the hollow pore of MOF (in blue colour), (b) 3D cannoli surface with volume; (red color: packed region and blue color: pore volume,), (c) one dimensional cannoli surface along with volume derived from given figure.



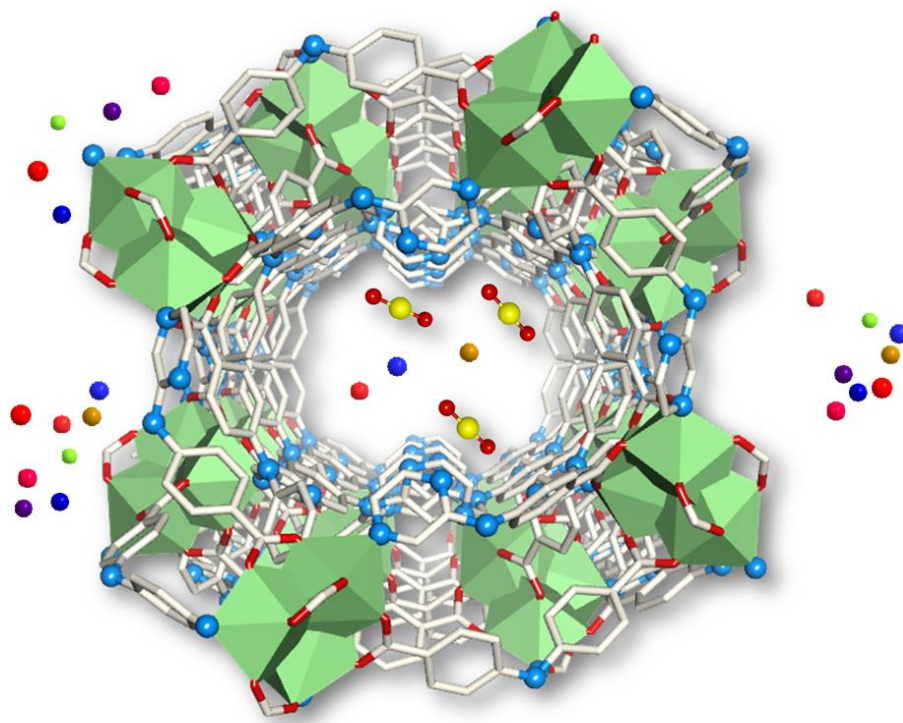
Appendix 53. (a) ESP distribution depiction of **iMOF-1A** (i.e. unit cell) and, (b) ESP distribution seen after UO_2^{2+} interactions. The ESP color scale for both cases represent presence of medium energy (blue), low energy (green), and high energy (red) packets.



Appendix 54. ESP distribution of *iMOF-1A* unit cell post-interaction with variety of cations. (a) UO_2^{2+} , (b) NaCl , (c) KCl , (d) CdCl_2 , (e) CaCl_2 , (f) $\text{Mg}(\text{NO}_3)_2$. The ESP color scale for all above cases represent presence of medium energy (blue), low energy (green), and high energy (red) packets.



Appendix 55. Chemical structure of **iMOF-1A** unit cell after interaction with various cations. **(a)** UO_2^{2+} , **(b)** NaCl , **(c)** KCl , **(d)** CdCl_2 , **(e)** CaCl_2 , **(f)** $\text{Mg}(\text{NO}_3)_2$.



Appendix 56. Simulation studies of **iMOF-1A** pore channel representing selective interaction of UO_2^{2+} in presence of a broad range of interfering/ meddling cations which are commonly present in natural seawater (color codes; U= yellow, O= deep red).

Appendix Table 11. Crystal data and structure refinement for **iMOF-1A**.

Identification code	iMOF-1A (IMF)
Empirical formula	C ₂₅₆ H ₂₆₀ N ₅₂ Ni ₁₂ O ₆₄
Formula weight	5793.66
Temperature	296(2) K
Wavelength	0.71073 Å
Crystal system	Cubic
Space group	I23
Unit cell dimensions	a = 26.252(7) Å, $\alpha=\beta=\gamma=90^\circ$
	b = 26.252(7) Å
	c = 26.252(7) Å
Volume	18092(14) Å ³
Z	2
Density (calculated)	1.064 Mg/m ³
Absorption coefficient	0.675 mm ⁻¹
F(000)	6016
Crystal size	0.100 x 0.100 x 0.100 mm ³
Theta range for data collection	1.900 to 28.243°.
Index ranges	-34<=h<=34, -28<=k<=34, -34<=l<=34
Reflections collected	246223
Independent reflections	7467 [R(int) = 0.0762]

Completeness to theta = 25.242°	99.8 %
Absorption correction	Semi-empirical from equivalents
Max. and min. transmission	0.95 and 0.90
Refinement method	Full-matrix least-squares on F ²
Data / restraints / parameters	7467 / 480 / 410
Goodness-of-fit on F²	1.055
Final R indices [I>2sigma(I)]	R1 = 0.0460, wR2 = 0.1382
R indices (all data)	R1 = 0.0508, wR2 = 0.1434
Absolute structure parameter	0.008(19)
Extinction coefficient	0.00056(13)
Largest diff. peak and hole	0.733 and -0.367 e.Å ⁻³

2.6 References

- [1] S. Chu, A. Majumdar, *Nature* **2012**, 488, 294.
- [2] Q. Schiermeier, J. Tollefson, T. Scully, A. Witze, O. Morton, *Nature* **2008**, 454, 816.
- [3] N. Tang, J. Liang, C. Niu, H. Wang, Y. Luo, W. Xing, S. Ye, C. Liang, H. Guo, J. Guo, Y. Zhang, G. Zeng, *J. Mater. Chem. A* **2020**, 8, 7588.
- [4] S. Zhang, H. Li, S. Wang, *Chem* **2020**, 6, 1504.
- [5] C. W. Abney, R. T. Mayes, T. Saito, S. Dai, *Chem. Rev.* **2017**, 117, 13935.
- [6] D. S. Sholl, R. P. Lively, *Nature* **2016**, 532, 435.
- [7] M. J. Manos, M. G. Kanatzidis, *Chem. Sci.* **2016**, 7, 4804.
- [8] T. Zheng, Z. Yang, D. Gui, Z. Liu, X. Wang, X. Dai, S. Liu, L. Zhang, Y. Gao, L. Chen, D. Sheng, Y. Wang, J. Diwu, J. Wang, R. Zhou, Z. Chai, T. E. Albrecht-Schmitt, S. Wang, *Nat Commun.* **2017**, 8, 15369.
- [9] X. Yang, J. Li, J. Liu, Y. Tian, B. Li, K. Cao, S. Liu, M. Hou, S. Li, L. Ma, *J. Mater. Chem. A* **2013**, 2, 1550.
- [10] J. Li, X. Dai, L. Zhu, C. Xu, D. Zhang, M. A. Silver, P. Li, L. Chen, Y. Li, D. Zuo, H. Zhang, C. Xiao, J. Chen, J. Diwu, O. K. Farha, T. E. Albrecht-Schmitt, Z. Chai, S. Wang, *Nat Commun.* **2018**, 9, 3007.
- [11] S. Mollick, S. Saurabh, Y. D. More, S. Fajal, M. M. Shirolkar, W. Mandal, S. K. Ghosh, *Energy & Environ. Sci.* **2022**, 15, 3462.
- [12] Z. Wang, Q. Meng, R. Ma, Z. Wang, Y. Yang, H. Sha, X. Ma, X. Ruan, X. Zou, Y. Yuan, G. Zhu, *Chem* **2020**, 6, 1683.
- [13] C. Xiao, M. A. Silver, S. Wang, *Dalton Trans.* **2017**, 46, 16381.
- [14] Hong-Cai “Joe” Zhou, S. Kitagawa, *Chem. Soc. Rev.* **2014**, 43, 5415.
- [15] G. Maurin, C. Serre, A. Cooper, G. Férey, *Chem. Soc. Rev.* **2017**, 46, 3104.
- [16] D. Banerjee, S. J. Kim, H. Wu, W. Xu, L. A. Borkowski, J. Li, J. B. Parise, *Inorg. Chem.* **2011**, 50, 208.
- [17] A. B. Spore, N. L. Rosi, *CrystEngComm* **2017**, 19, 5417.
- [18] P. Li, N. A. Vermeulen, X. Gong, C. D. Malliakas, J. F. Stoddart, J. T. Hupp, O. K. Farha, *Angew. Chem., Int. Ed. Engl.* **2016**, 55, 10358.

- [19] F. Zarekarizi, S. Beheshti, A. Morsali, *Inorg. Chem. Commun.* **2018**, *97*, 144.
- [20] H. Li, F. Zhai, D. Gui, X. Wang, C. Wu, D. Zhang, X. Dai, H. Deng, X. Su, J. Diwu, Z. Lin, Z. Chai, S. Wang, *Appl. Catal. B.* **2019**, *254*, 47.
- [21] J. Yu, Y. Cui, H. Xu, Y. Yang, Z. Wang, B. Chen, G. Qian, *Nat Commun.* **2013**, *4*, 2719.
- [22] Q. Sun, B. Aguila, J. Perman, A. S. Ivanov, V. S. Bryantsev, L. D. Earl, C. W. Abney, L. Wojtas, S. Ma, *Nat Commun.* **2018**, *9*, 1644.
- [23] L. Zhang, N. Pu, B. Yu, G. Ye, J. Chen, S. Xu, S. Ma, *ACS Appl. Mater. Interfaces* **2020**, *12*, 3688.
- [24] X. H. Xiong, Z. W. Yu, L. L. Gong, Y. Tao, Z. Gao, L. Wang, W. H. Yin, L. X. Yang, F. Luo, *Adv. Sci.* **2019**, *6*, 1900547.
- [25] D. Wang, J. Song, J. Wen, Y. Yuan, Z. Liu, S. Lin, H. Wang, H. Wang, S. Zhao, X. Zhao, M. Fang, M. Lei, B. Li, N. Wang, X. Wang, H. Wu, *Adv. Energy Mater.* **2018**, *8*, 1802607.
- [26] S. Ma, L. Huang, L. Ma, Y. Shim, S. M. Islam, P. Wang, L.-D. Zhao, S. Wang, G. Sun, X. Yang, M. G. Kanatzidis, *J. Am. Chem. Soc.* **2015**, *137*, 3670.
- [27] Y. Yuan, S. Zhao, J. Wen, D. Wang, X. Guo, L. Xu, X. Wang, N. Wang, *Adv. Funct. Mater.* **2019**, *29*, 1805380.
- [28] W.-R. Cui, C.-R. Zhang, W. Jiang, F.-F. Li, R.-P. Liang, J. Liu, J.-D. Qiu, *Nat Commun.* **2020**, *11*, 436.
- [29] Y. Yuan, Q. Meng, M. Faheem, Y. Yang, Z. Li, Z. Wang, D. Deng, F. Sun, H. He, Y. Huang, H. Sha, G. Zhu, *ACS Cent. Sci.* **2019**, *5*, 1432.
- [30] Q. Sun, B. Aguila, L. D. Earl, C. W. Abney, L. Wojtas, P. K. Thallapally, S. Ma, *Adv. Mater.* **2018**, *30*, 1705479.
- [31] R. Rengarajan, M. M. Sarin, S. Krishnaswami, *Oceanol. Acta* **2003**, *26*, 687.
- [32] S. Kato, R. J. Drout, O. K. Farha, *Cell Reports Physical Science* **2020**, *1*, 100006.
- [33] R. J. Drout, S. Kato, H. Chen, F. A. Son, K. Otake, T. Islamoglu, R. Q. Snurr, O. K. Farha, *J. Am. Chem. Soc.* **2020**, *142*, 12357.
- [34] A. F. Möslein, M. Gutiérrez, B. Cohen, J.-C. Tan, *Nano Lett.* **2020**, *20*, 7446.
- [35] A. F. Möslein, J.-C. Tan, *J. Phys. Chem. Lett.* **2022**, *13*, 2838.
- [36] M. Tricarico, J.-C. Tan, *Mater. Today Nano* **2022**, *17*, 100166.

[37] A. F. Möslein, L. Donà, B. Civaleri, J.-C. Tan, *ACS Appl. Nano Mater.* **2022**, 5, 6398.

Chapter 3

Efficient Recognition and Capture of Specific Toxic Organic Pollutants Using Water-Stable Highly Luminescent Anionic Metal-organic framework

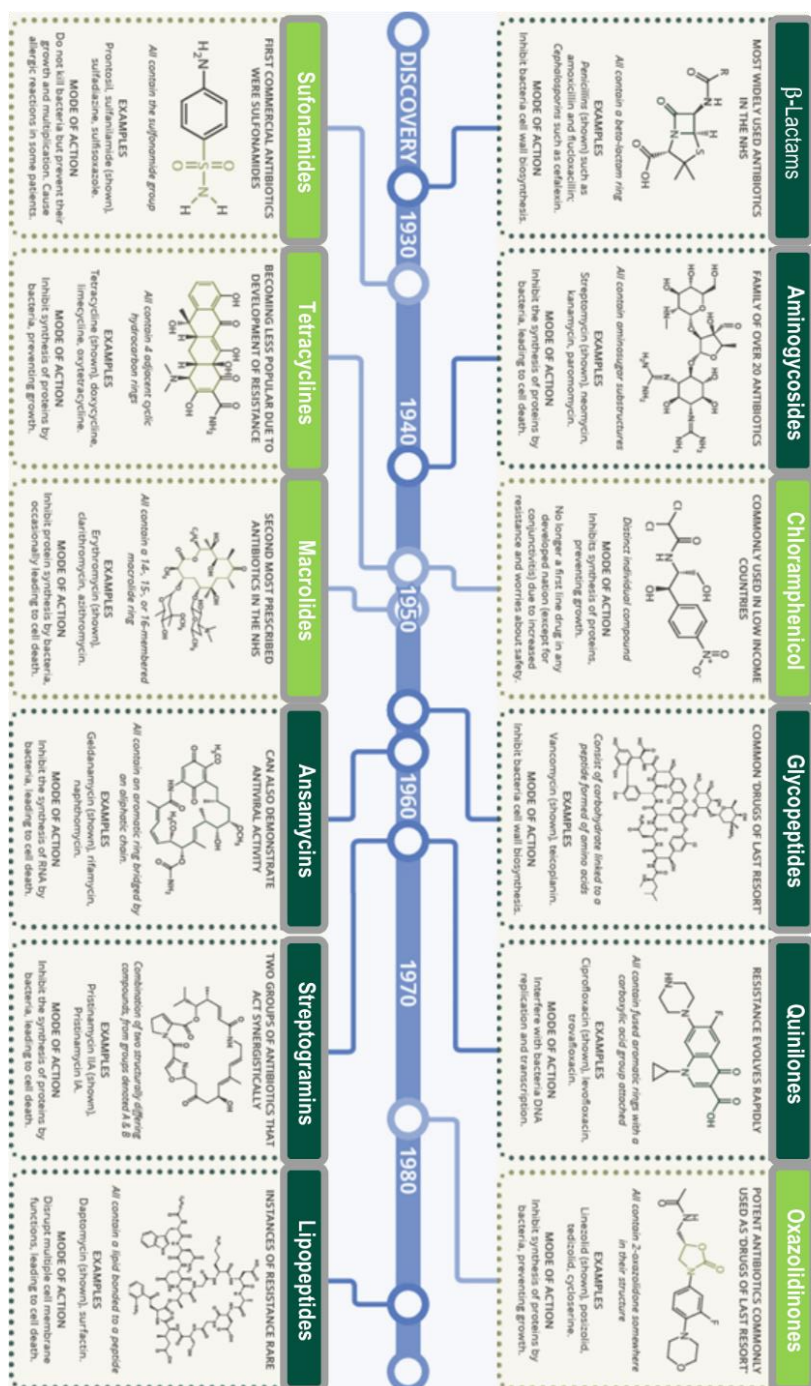
3.1 Introduction

Since the earliest beginnings of uncovering their application-based frontiers, metal-organic frameworks, also known as porous coordination polymers (PCPs), have captivated unrivalled interest over the past twenty years. This is due to the fact that metal-organic polymeric frameworks can have tailor-made molecular topologies and lattice packing motifs in addition to having the potential to be used as functional materials. This family of materials has given rise to a wide variety of applications, some of which include gas adsorption, ion exchange, chemical purification, sensing, ionic conductivity, drug administration, catalysis, and optoelectronics.^[1-9] This category of functionalized crystalline solids has the distinct advantage of being able to have tailorable architectures because of the freedom of adjusting coordination nanospaces that can be achieved as a result of the wide variety of organic linkers that can be used and the multiple oxidation states that can be achieved by the metal nodes.^[10] The search for suited MOF materials is driven primarily by a few unique advantages, including the materials' ordered architectures that include long-range arrangement, coordinately unsaturated metal nodes or open metal sites (OMS), unique microporosity with abundant guest accessibility, and linker modulation-derived pore surface modification.^[11] Even though it is not essential to include all of these previously mentioned aspects in a single MOF in order to derive applicability, it has been shown that even the advent of a single aspect or the tactical amalgamation of different facets is necessary in order to imbue MOFs with specific application areas that are specifically targeted, making them guest-responsive luminescent probes.^[12] The pollution of the world's water supplies has emerged as one of the most urgent challenges facing humanity in the 21st century.^[13] It is generally agreed upon that having access to sanitary and unpolluted waterways is necessary in order to completely comprehend human rights.^[14] The unavoidable increase in the global population, in conjunction with rising rates of urbanization and energy consumption, poses a direct risk to the continuation of life in a sustainable form on planet earth for future generations.^[15] As a consequence of this, the encroachment of natural resources and the production of enormous quantities of hazardous waste are both visible in the ecosystem of the earth and in its bodies of water.^[16] The "Sustainable Development Agenda" of the United Nations continues to focus on making sure that everyone has access to freshwater that is free from contamination, despite the fact that this is already the case.^[17]

Organic micropollutants like antibiotics, pesticides, or herbicides like paraquat are examples of modern type water pollutants. This is due to the fact that organic micropollutants like these can have negative effects on human health, in addition to the fact that organic micropollutants like these can be found in

high concentrations in aquatic systems.^[18] Antibiotics research and use has progressed a lot in past few decades (Scheme 1). Both antibiotics and pesticides see widespread application in the medical treatment of bacterial infections in humans, animals, and plants, as well as in the agricultural production of a wide variety of food products.^[19] On the other hand, the herbicide paraquat (N,N'-dimethyl-4,4'-bipyridinium dichloride), which is also known as methyl viologen, is notorious for the high level of danger it poses to human health when used as a non-selective herbicide.^[20]

The United States Environmental Protection Agency (US-EPA) places a cap on the amount of paraquat that can be present in drinking water at 0.1 $\mu\text{g/L}$, which is equivalent to 0.7 mL/L.^[7] The excessive use, abuse, and even, on occasion, improper use of these potentially harmful species has resulted in severe pollution of the environment. This ubiquitous species has, since the beginning of time, been wreaking havoc on the continuity of life by wreaking havoc on all living organisms.^[21] The ever-increasing human population, in conjunction with the ever-increasing activities that result in the generation of anthropogenic waste, is to blame for the introduction of these hazardous chemical substances into the natural water reserves, which results in the pollution of the essential water resource.^[22] Consequently, taking into consideration the public health concern as well as the significance of water quality, the methodical identification and removal of these waste water contaminants using a technique that is precise and dependable has become an important and topical research interest. In this field, up until this point, there have been a variety of techniques that have been utilized or are currently being researched for the purpose of detecting antibiotics and pesticides. Mass spectrometry (MS), liquid chromatography-mass spectrometry (LC-MS), liquid chromatography with ultraviolet detection (LC-UV), high-performance liquid chromatography (HPLC), gas chromatography-mass spectrometry (GC-MS), Raman spectroscopy, and other similar techniques have all seen significant application in recent years.^[23-25] However, these exclusive instrumental methods are difficult, expensive, time consuming, less efficient, and require expert personnel. Because of these factors, the ability to detect and determine targeted analytes in real time is restricted by these methods.^[25] In addition, the currently utilized strategies for the elimination of paraquat herbicide are neither effective nor sufficiently developed due to the extensive chemical processes that are involved. Therefore, the development of methods that are highly efficient, cost-effective, and simple for the recognition and sequestration of specific pollutants from water media has become highly desirable and a significant concern for the scientific community. This is because water media are a significant source of pollution.



Scheme 1. Decade wise progressive illustration of different classes of antibiotics; depicting bacteriostatic agents used for restricting growth and reproduction (light green) and bactericidal agents employed for bacterial cell death.

According to this point of view, fluorescence-based optical recognition and adsorption followed by ion-exchange-based removal techniques have recently been investigated as potentially useful methods for selectively detecting targeted pollutants in water and specifically separating them from one another, respectively. Both of these techniques are based on optical recognition.^[26,27] It is important to note that fluorescence-based detection techniques have been considered more effective than other conventional sensing technologies. This is due to the benefits of fluorescence-based detection techniques, which include long fluorescent lifetimes, high luminescent quantum yield, large Stokes shifts, strong sensitivity, high selectivity, simplicity, portability, and easy, economical operation. It is important to note that fluorescence-based detection techniques have been considered more effective than other conventional sensing technologies.^[28] Over the course of the last few years, a variety of fluorescent materials have been utilized, along with this straightforward method, in order to facilitate the accurate detection of a wide range of chemicals, pollutants, gases, metal ions, anions, and other types of ions and chemicals.^[29] In addition to this, with that being said, the identification of targeted toxics is not the only solution. After the detection of particular species, effective separation or removal is considered to be more productive towards real-time, effective environmental remediation. In this context, as was mentioned earlier, adsorption, followed by a method that is based on ion exchange, is an excellent strategy for the effective removal of toxic contaminants. Now, even though there has been some encouraging progress made through the utilization of various types of luminescent materials for the selective and sensitive detection of a variety of antibiotics and pesticides as a long-term battle field, more efforts are still required for the point-of-use application. In addition, the selective elimination of paraquat from water media through the utilization of an efficient re-generable material is a highly desirable goal, but it is still a frontier that is infrequently investigated.^[29,32] The majority of the reports that were found in the body of research investigated the potential of materials for either detection or adsorption performance. However, research into the creation of a single material that could simultaneously detect and remove toxic substances from water, such as paraquat, is still evolving and in demand. Additionally, the kinds of materials that can be used for more than one thing would be the best choice for the most effective, efficient, and cost-effective ways to clean up the environment.

In light of the discussion that was just presented, as well as the objective of creating a single material that is capable of efficient identification and sequestration of selective pollutants, we came to the conclusion that the utilization of luminescent functionalized porous materials could be a promising platform for our endeavors. Traditional porous materials, such as zeolites, silicates, activated carbons, and resins, among

others, finding difficulties due to restrictions in pore tunability, having less selectivity, having less sensitivity, and so on. However, there is a new class of porous materials, named as metal-organic frameworks where these issues has been diligently addressed.^[33] In this scenario, outstanding developments in the field of metal-organic frameworks (MOFs) and their potential applications have been the subject of cutting-edge research interest in the recent past.^[34] As an advanced class of porous materials, MOFs, which are crystalline hybrid porous solids constructed from the coordination assembly of metal nodes or metal clusters with organic linkers or ligands, have recently been recognized as one of the most promising candidates for a wide spectrum of applications ranging from energy properties to the environment. MOFs are crystalline hybrid porous solids constructed from the coordination assembly of metal nodes/metal clusters with organic linkers or ligands.^[35] Because of their one-of-a-kind properties, such as the presence of long range ordered structural porosity and a high surface area, as well as the molecular level tuning of functionalities in the organic ligand and secondary building units (SBUs), MOFs can be used as a material for the molecular recognition and selective adsorption of a variety of toxics from water medium. This is due to the fact that MOFs possess molecular-level tuning of functionalities.^[36] In addition, the inherent preconcentration effect in the nanospace of MOFs, along with optimised host-guest interactions, increases the sensitivity towards target-specific analyte detection and adsorption.^[37,38] These findings has been reported extensively in literature. In addition, the heterogeneous nature of MOFs contributed to their excellent reusability, which was another advantage they offered.^[39]

Now, the incorporation of luminescent properties into MOFs is a necessary requirement for the fluorescent-based detection of antibiotics or pesticides using MOFs. The utilization of π -electron rich organic ligands, transition metal cations with d^0 - d^{10} electronic configuration, and incorporation of emissive guest into the nanospaces of MOFs are some of the constructive strategies that help make luminescent MOFs (LMOFs), which are considered to be one of the most promising materials for selective and sensitive detection of various species. In this view, luminescent MOFs (LMOFs) are considered to be one of the most promising. It is important to point out that in the recent past, a large number of LMOFs have been documented as a potential sensory material for the detection of environmentally relevant toxic species. This is something that should be mentioned.^[40,41] On the other hand, research into the sensing ability of LMOFs toward antibiotics or pesticides in water medium has received a relatively smaller amount of attention than it has received in other areas. Once more, one can easily introduce fluorophores with specific interaction sites into the nanopores of MOFs by strategically modifying the organic linkers of MOFs and also by using d^{10} metal cations. This results in high

luminescent nature and selective interaction with targeted analytes, respectively.^[39,40,41] This methodical grafting of functional fluorophores onto LMOFs explored their potential as an excellent medium for the detection of selective antibiotics and pesticides/herbicides. On the other hand, it is possible to achieve adsorption of cationic species such as the toxic paraquat by developing anionic water stable functionalized MOFs. In addition to this, the size of the pores in MOFs is also an important factor in the process of selective adsorption. Therefore, because it was of particular interest to us, we devised a strategic plan for the development of a water-stable anionic functionalized MOF with intense luminescent nature. This material possesses the ability to detect antibiotics and pesticides with high sensitivity and selectivity while simultaneously capturing paraquat-based herbicides from water.

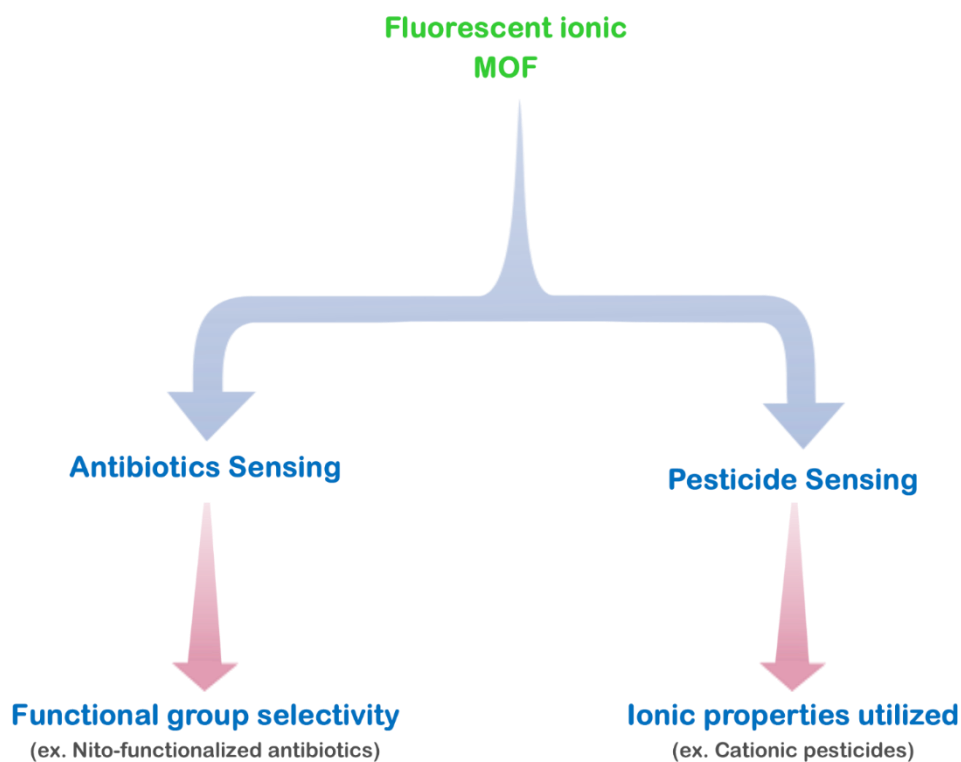


Figure 1. Outlook of the virtues utilized and general approach deployed for sensing and capture studies of anthropogenic waste (antibiotics and pesticides) in the present work.

It is important to point out that although studies based on the detection of antibiotics and pesticides using MOFs have been published in the scientific literature, but only a small number of those studies were carried out using a variety of organic solvents rather than an aqueous medium, and surprisingly least were focused on paraquat capture using MOFs.^[41,42,43] Because of this, the practical real-time sensing

application is severely restricted. It is necessary for the probe to maintain its integrity in water if it is to be used for the detection of aqueous phase pollutants and for the application of MOFs in their removal. In addition, the scope of the majority of these studies is typically restricted to the detection of only such species. It has not yet been demonstrated that water-stable luminescent MOFs are capable of performing selective adsorption, which is then followed by the detection of herbicides like paraquat (Figure 1). In addition, there are a minuscule number of studies that investigated the process of either recognizing or removing paraquat from water medium.^[21,44]

3.2 Experimental

3.2.1 Materials

All of the chemicals and reagents, starting materials, and solvents were acquired commercially and utilized without additional purification. Paraquat (PQ) was acquired from Sigma-Aldrich with desired purity. Since all medicines and pesticides have a hazardous nature, wearing the appropriate safety equipment (masks, gloves) is always recommended.

3.2.2 Synthesis

Synthesis of iMOF-4A: By combining 0.03 mmol of $\text{Cd}(\text{NO}_3)_2 \cdot 4\text{H}_2\text{O}$, 0.03 mmol of 5-aminoisophthalic acid (AIA: $\text{H}_2\text{NC}_6\text{H}_3\text{-1,3}-(\text{CO}_2\text{H})_2$) and 0.03 mmol of Benzene-1,4-dicarboxylic acid (BDC: $\text{C}_6\text{H}_4\text{-1,4}-(\text{CO}_2\text{H})_2$) DMF: o-xylene in the ration of 2:1 mL and 0.3 mL 0.05 N HCL at 105 °C for 48 hours (before being slowly cooled to room temperature), single crystals of **iMOF-4A**. Crystals in the shape of a sheet and rectangular blocks were obtained with an 86% yield (considering metal weight). A light-transparent to yellowish crystals were formed after the reaction. Initially formed product was washed with DMF to remove any soluble pre-cursor then further subjected to solvent exchange by means MeCN exchange for 72 hours (dipping **iMOF-4A** in MeCN) and swapping out the aliquots of solvent daily prior subjecting it to activation. The synthesis of MOF material has been shown to render itself insoluble in those solvents. It was filtered off after three days and then activated at 100 °C for 24 hours.

3.2.3 Physical measurements and Characterizations

Both; Single crystal X-ray measurements and powder X-ray diffraction (PXRD) patterns were performed to determine and confirm crystal structure of iMOF-4A. Single-crystal X-ray data of **iMOF-4A** were collected at temperature close to or retained to 150 K using a Bruker D8 Venture Duo X-ray

diffractometer (it is equipped with Microfocus X-ray source, that is being operated at 50 W; 50 kV/1 mA), graded multilayer optics for monochromatic Mo K α radiation ($\lambda = 0.71073 \text{ \AA}$) focused X-ray beam and Photon 100 CMOS chip based detector system. Crystal was placed on CryoLoops (nylon, Hampton Research) with Paraton-N (oil, Hampton Research) and PXRD were performed using Bruker D8 Advanced X-ray diffractometer at room temperature having Cu K α radiation ($\lambda = 1.5406 \text{ \AA}$). Thermogravimetric analysis patterns were evaluated using Perkin-Elmer STA6000, TGA analyzer in N₂ atmosphere with 10 °C min⁻¹ of heating rate. The morphological features of iMOF-4A's crystalline phase was recorded using instrument model identified Zeiss Ultra Plus field-emission scanning electron microscope (FESEM) having an integral charge compensator and embedded AsB and EsB detectors (Carl Zeiss NTS, GmbH). Sputter-coating was deployed on ample surface with a Au film (5-10 nm) to minimize charging, only on requirement or whenever necessary otherwise avoided. The elemental analysis was performed at a fixed voltage which is equipped with an EDX detector. Acquisition of data done over 600 seconds. BelSorp-Max gas adsorption instrument was used (Bel Japan). The activated samples were heated in a vacuum at 120 °C for or over 12 hours with BelPrepVacII before undertaking adsorption measurements. The Jobin Yvon Fluoromax-4 spectrofluorometer (HORIBA Scientific) with stirring attachment was used for the fluorescence measurements. Analyses of UV-vis absorption in an optical quartz cuvette (10 mm path length) were conducted using a Shimadzu UV 3600 UV /Vis /NIR spectrophotometer over the full spectrum of 200-800 nm. On a Fluorolog-3 spectrofluorometer, the steady-state photoluminescence studies were captured (HORIBA Scientific). Clear, high-detail, background-free images of the required compounds were obtained using a confocal laser scanning microscope (Zeiss, Oberkochen, Germany; Model LSM 10). The fluorescence imaging was done using model identified as DM6B EPI-Fluorescence instrument of Leica make. Crystallographic information file report generation is in progress with crystallographer along with R factor of 5.4, however these data will be made available at earliest from The Cambridge Crystallographic Data Centre at no cost and can be requested through their website at www.ccdc.cam.ac.uk/data_request/cif.

In order to gain further mechanistic perspective into the molecular level pathway for selective and dynamic photoluminescence quenching mediated by antibiotics and pesticides, we carried out First-principle calculations based on density functional theory (DFT) and obtained HOMO - LUMO energy gaps for subunit of MOF and subunit for various antibiotics and pesticides. DFT calculations were performed in the application Discovery Studio 2017 (Accelrys). All of the MOF calculations were carried out with a high standard of accuracy. The DMol3 code was taken into account for the single-point energy

calculations with the three-parameter B3LYP function. Starting with geometry optimization with the same parameters (Auto mode Multiplicity factor, Double Numeric Plus Polarizing (DNP+) basis set, and water as solvent), MOF, antibiotic, and pesticide molecule structures were completely relaxed. The geometry of the MOF was then relaxed, and a structural simulation was run using the simulated annealing method to identify potential sites of antibiotic and pesticide interactions.

3.2.4 Recyclability Test

Following the initial NFT or NFZ detection cycle, the MOF was then separated by centrifugation from the suspension in a 2 ml Eppendorf. The compound was then rinsed with water and MeCN and left to dry at room temperature for few hours. After two hours in a 75 °C oven, the MOF powder was once again contained in a water-acetonitrile (3:2) combination and utilised in a sensing titration experiment to detect antibiotics (NFT and NFZ) and pesticides (paraquat). We then carried out the same steps for the remaining sensing cycles. For paraquat dependant recycling, process is described in details in the paraquat sorption studies. **iMOF-4A** is stable to aforementioned antibiotics solution and stability of the **iMOF-4A** can be correlated appropriately from Figure 3 and Appendix 3-4.

3.2.5 Paraquat Capture Studies

Paraquat adsorption experiments

By dissolving a required quantity of Paraquat in deionized water ($R=18.2 \text{ M}\Omega\cdot\text{cm}$), desirable concentrations of Paraquat solutions were achieved. During the sorption studies, the concentration of the solutions was monitored using UV-Vis spectroscopy. The tests described below were carried out for MOF. Wherever possible, PES membrane filters with 25mm diameter and 0.45 micron pore size were employed.

Paraquat adsorption kinetics

In a Paraquat solution (20 mL, 0.05 mM), the adsorbent / MOF (20 mg) was added. Before being mixed at room temperature, the resulting mixture was sonicated for the first 10 seconds. 2 mL of the solution were extracted and filtered using a 0.45 m PES membrane filter at various time intervals. UV-Vis spectroscopy analysis at 257 nm was used to determine the remaining amount of Paraquat.

The amount of Paraquat at given time interval t , q_t , was estimated by:

$$q_t = \frac{(C_i - C_t) \cdot V \cdot M_w}{m},$$

Where C_i and C_t are the initial/ beginning and timed (t) Paraquat concentrations, q_t (mg g^{-1}) is the quantity of Paraquat adsorbed at time t (min), M_w is molecular weight for Paraquat and m (g) is the amount of **iMOF-4A** used for adsorption.

The data thus obtained was fitted with a pseudo-second-order kinetic model:

$$\frac{t}{q_t} = \frac{1}{k_{obs} q_e^2} + \frac{t}{q_e},$$

Where k_{obs} is denoted pseudo-second-order rate constant ($\text{mg g}^{-1} \text{min}^{-1}$) while q_t and q_e represents the adsorbate uptake per g of adsorbent at time interval t and at equilibrium, respectively, (mg/g).

Paraquat sorption

iMOF-4A (2.5 mg) was then added to 5 mL paraquat solutions of different initial (beginning) concentrations (0.5, 0.6, 0.7, 0.8, 0.9, 1.0, 1.5, 2.0 mM). The sonicated suspension was mixed/ rotated at room temperature overnight until equilibrium is reached. After filtering the solutions through a 0.45 μm membrane, they were further subjected to UV-Vis spectroscopic evaluation (absorbance at 257 nm) of the new paraquat concentrations.

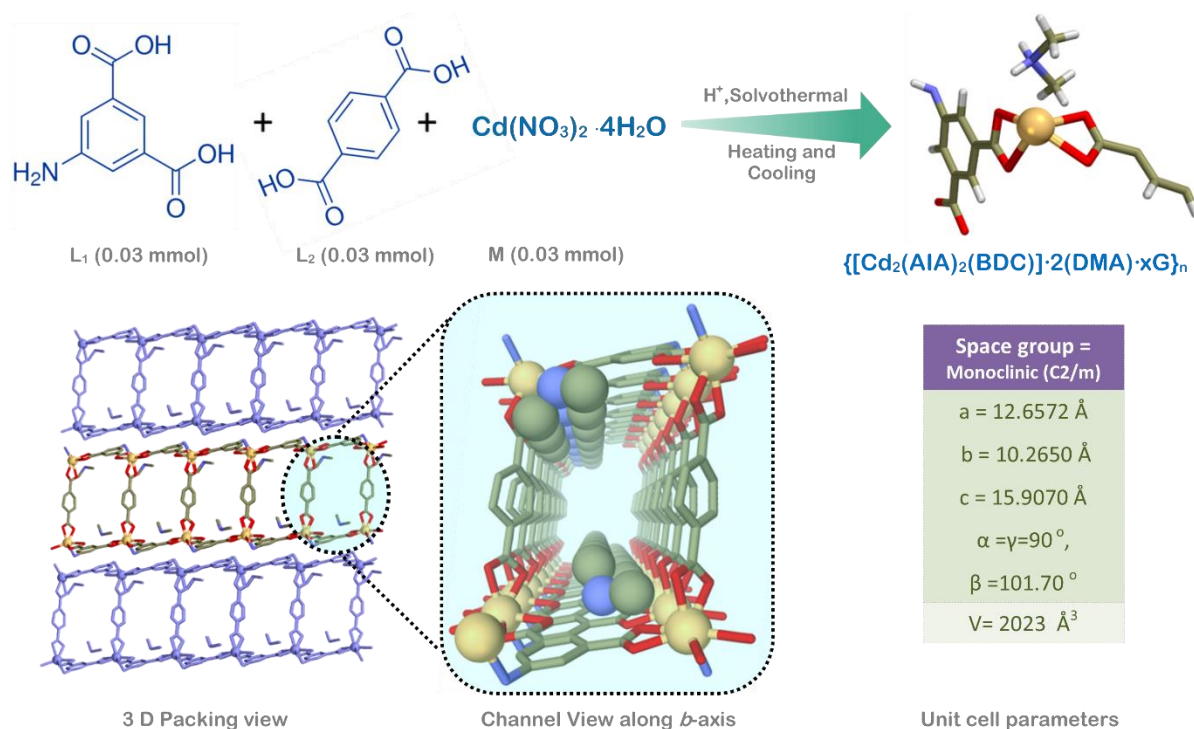
MOF regeneration for Paraquat studies

To the 15 mL Paraquat solution (0.05 mM), 20 mg MOF was poured and stirred for 10-15 minutes. The mixture was subjected to centrifugation for 10 minutes at 10000 rpm, and the supernatant is removed. Methanol (15 mL) was then added to the residual MOF in the pellet, which was again stirred for 15 minutes before being centrifuged again. The MOF was washed four times with methanol, dried, and utilized in the following adsorption cycle for Paraquat adsorption.

3.3 Result and Discussion

iMOF-4A compound was produced through the reaction of a synthetic organic ligands (L_1 and L_2) with $\text{Cd}(\text{NO}_3)_2$ metal salts in a solvent mixture consisting of 2:1 DMF: *o*-xylene (Scheme 2). For more

information regarding the ligand synthesis and characterizations, structural features, see the Appendix section for further details. Large crystals of an off-white colour and a block shape were produced as a result of the solvothermal process (Scheme 2). **iMOF-4A** formed in a monoclinic crystal structure, as determined by single-crystal X-ray diffraction (SCXRD), which has a monoclinic, $C2/m$ space group (Scheme 2, Appendix 1) with coordination environment comprising $\{[Cd_2(AIA)_2(BDC)] \cdot 2(DMA) \cdot xG\}_n$ with lattice parameters as $a = 12.6572 \text{ \AA}$, $b = 10.2650 \text{ \AA}$, $c = 15.9070 \text{ \AA}$ and angles as $\alpha = \gamma = 90^\circ$, $\beta = 101.70^\circ$. As seen, the asymmetric unit of **iMOF-4A** is composed of one Cd (II) metal ion, one AIA unit, half of one BDC unit (which are forming by in-situ hydrolysis of the ligand during MOF synthesis), and one unit of free DMA cation, where AIA stands for 5-amino isophthalic acid, and BDC stands for 1,4-benzene dicarboxylic acid also G stands for the guest molecule (Scheme 2, Figure 2). It was also found from the SCXRD data of **iMOF-4A** that the coordination environment of the metal center (Cd (II)) is octahedral with six coordination bonds.



Scheme 2. Illustration of synthetic scheme, asymmetric unit, cell parameter and structural feature of **iMOF-4A** (sequentially left to right). (C: grey, N: blue, Cd^{+2} : yellow, O: red, H atoms omitted for clarity)

This information was obtained from the compound. Among them, four coordination bonds were assembled to the metal center with two individual oxygen atoms of both hydrolyzed AIA and BDC linker, and the remaining two coordination bonds were connected with oxygen and nitrogen atoms of one water and amine group of AIA linker, respectively. In total, six coordination bonds were seen (Scheme 2). Reticular extension of two individual ligands (AIA and BDC) containing carboxylic O-donor based ditopic ligand along with one water molecule and one amino group surrounding a Cd(II) metal ion fabricated a 2D sheet like network, which further constructed in an overall porous framework. Cd(II) metal ion (Scheme 1-2, Figure 2, Appendix 2).

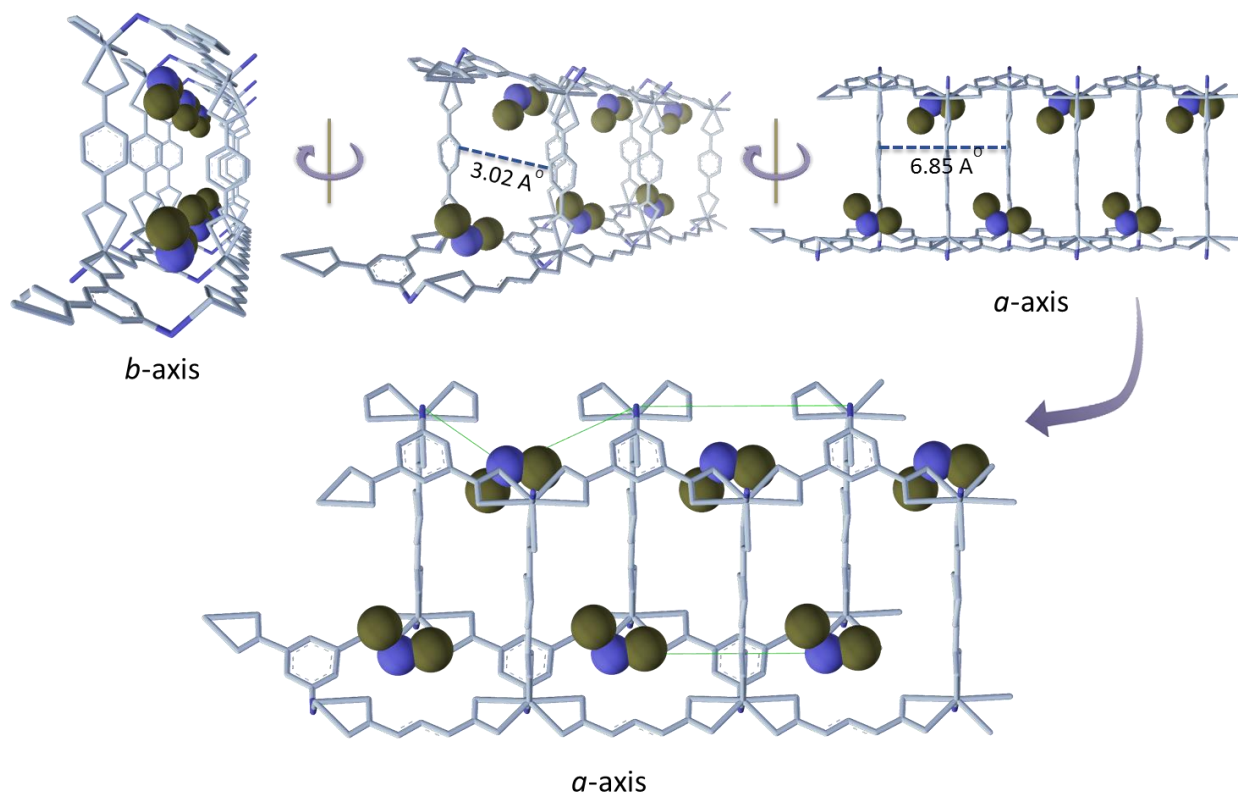


Figure 2. Insights on structural features, guest arrangements (DMA) and pore (channel) apertures viewed along *a* & *b* crystallographic axes for **iMOF-4A**.

The previously described one-dimensional porous channel of the MOF is made up of free-exchangeable DMA cations. These cations helped to keep the framework's overall charge in equilibrium, turning it into an anionic structure (Figure 2). In addition, the data from the single-crystal X-ray crystallographic measurements (SCXRD) revealed the presence of electron-rich aromatic benzene rings of the linkers,

which were systematically aligned through the porosity channel of the MOF. These rings had the potential to operate as accessible sites for the guest analytes that were being targeted (Figure 2, figure 5). In addition to this, such a configuration results in a significant distance between the cadmium metal nodes that are close to one another (Figure 2, Appendix 2). The packing diagram of **iMOF-4A** showed a one-dimensional channel pore with a rectangular effective pore aperture of 3.02 Å along the crystallographic axis b-axis, and the accessible void volume for unit cell of the **iMOF-4A** was predicted to be 2023 Å. **iMOF-4A** also had a crystallographic axis that ran parallel to the b-axis and a-axis (Figure 2, Appendix 1,2). Following the single crystal examination, a powder X-ray diffraction (PXRD) investigation was carried out in order to assess the bulk phase purity of the MOF sample that had been manufactured. The bulk-phase purity of the MOF was demonstrated by the good collaboration between the simulated and as-synthesized phase PXRD patterns (Figure 3a). The PXRD profile also reveals that the as-made phase of the MOF has a highly crystalline structure. After that, a thermogravimetric study, also known as TGA, was performed in order to investigate the thermal behavior of **iMOF-4A**. The thermogravimetric analysis (TGA) profile of the as-synthesized phase of MOF showed an initial loss of weight at two different temperatures (first at > 50 °C and second at > 130 °C), which corresponds to the loss of occluded solvent molecules, o-xylene and DMF, respectively, trapped in the pores of the MOF while it was being synthesized (Figure 3b). In addition, the TGA profile indicated that the MOF exhibited a high level of thermal stability (i.e., > 250 °C). Analysis using field emission scanning electron microscopy (FESEM) was utilized so that researchers could investigate the surface morphology of the MOF. The FESEM images of the as-synthesized MOF samples displayed microcrystalline crystals with a robust character that were **iMOF-4A**. (Figure 3b, Appendix 4-6). After that, the as-synthesized MOF sample was desolvated, and then it underwent a solvent exchange with acetonitrile. This was done so that the porosity nature of the MOF could be investigated afterwards (MeCN). The as-made crystals were submerged in the MeCN solvent for a period of seven days as part of the activation process for the MOF (during which the solvent was replaced twice a day by a fresh one). After a week had passed, the crystals were allowed to air-dry at ambient temperature before being subjected to a vacuum treatment and heated at 120 °C (see the Appendix section for details). PXRD analysis of the MeCN exchange and desolvated phase of the MOF revealed high crystallinity as well as structural integrity that was comparable to that of the simulated structure (Figure 3a). These observations provided further support for the hypothesis that the MOF possesses a highly resilient nature upon activation and solvent exchange. In addition, the total replacement of pristine solvents with MeCN and the additional removal of MeCN solvent from the pores

of the MOF were observed from the TGA profiles of the solvent exchanged and desolvated phases, respectively. These phases were distinguished from one another by the fact that they were in opposite phases (Figure 2b). The TGA profile likewise demonstrated that the MOF exhibited a high degree of heat stability when in the desolvated state. In addition, it was discovered that the robust microcrystalline surface morphological nature of the MOF was maintained both in the phase in which the solvent was exchanged and the phase in which it was desolvated. This finding was supported by the FESEM pictures (Appendix 4-6). In addition, a FESEM-EDX study and an elemental mapping analysis were carried out in order to acquire an idea about the elemental composition of the MOF. Both sets of results indicated that there was a uniform distribution of all of the important components across the crystal surfaces of the desolvated MOF samples (Appendix 5-6). As a result, when the desolvated phase of the MOF had been prepared, the samples were put through an examination to determine their permanent porosity. In order to accomplish this, an adsorption-desorption measurement of nitrogen gas at a low temperature (77 K) was carried out. The N₂ sorption data confirmed the usual microporous character of the MOF due to its sharp uptake of gas at low pressure with a type-I uptake profile (Figure 3c).

Activated phase of **iMOF-4A** shows the maximum N₂ uptake around 300 mL/g. The NLDFT pore size distribution was computed using this gas absorption profile, which confirmed the presence of micropores throughout the porous framework of the **iMOF-4A**. After that, the crystals were submerged in water at room temperature for seven days while an investigation of the water stability of the MOF was carried out. After taking the crystals out of the water, they were allowed to dry on a piece of paper before being transferred to another container for analysis. The PXRD profile of the water-treated phase showed a high level of crystallinity in addition to the absence of any structural deformation (Figure 3a). In addition to this, the similar TGA profile displayed a high degree of thermal stability even after the water was treated (Figure 3b). In addition, the microcrystalline structure of the MOF was found to be the same throughout, which led to the discovery of aqueous phase stability (Figure 3b, Appendix 3a, 3b). All of these results show that the MOF is very resistant to being broken down or hydrolyzed by water, which is a must-have for the applications that involve detecting aqueous phases. After the successful execution of these structural characterizations, an investigation into the optical properties of **iMOF-4A** was carried out, making use of a variety of the following characterization tools: Under UV light, the powder had a colour that was very intensely blue, despite its white appearance during the day (Figure 1). Images of the same very dark blue hue were seen when fluorescence microscopy was performed. As soon as we noticed that the powder had a highly luminescent colour, we hollered to collect the absorbance maxima of **iMOF-4A**.

Based on the results of the diffuse reflectance spectroscopy (DRS) profile, it was determined that the MOF absorbs the most light at a wavelength of (λ_{\max}) ~ 320 nm. Again, the solid-state photoluminescence (PL) emission spectra were recorded in the wavelength range of ~ 350 to 600 nm after exciting the MOF powder at a wavelength of approximately ~ 320 nm. The intensity of the emission profile was at its highest point at a maximum value of ~ 425 nm. A similar finding was made in the case of the MOF sample in water (solution-state PL profile) (Figure 4, Appendix 8-9).

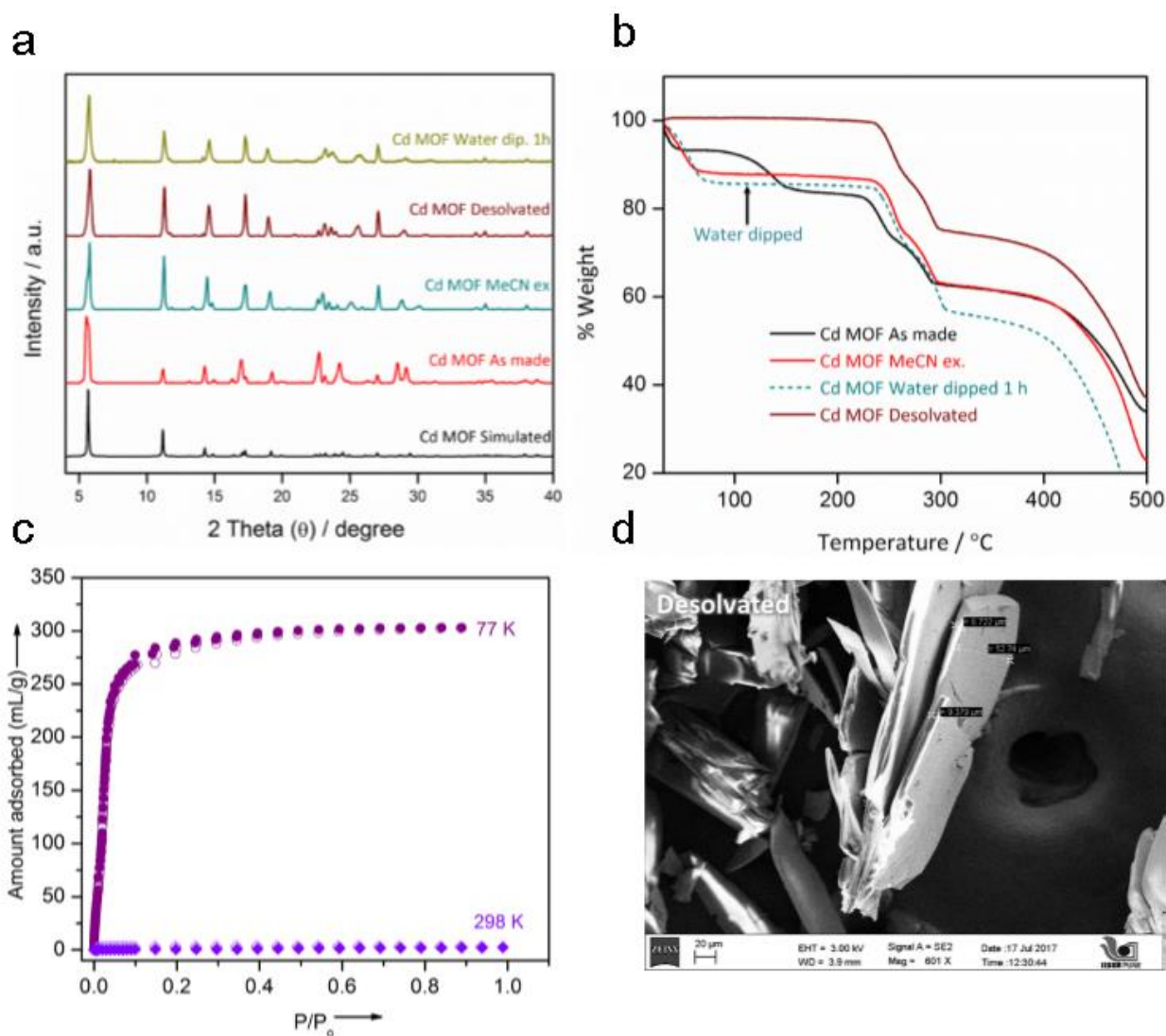


Figure 3. (a) Comprehensive analysis of PXRD spectra of the Cd MOF (i.e. **iMOF-4A**). (b) TGA profile of **iMOF-4A** (Cd MOF) under different scenarios. (c) N₂ adsorption isotherm for **iMOF-4A** (d) FESEM image of desolvated phase of **iMOF-4A**.

3.3.1 Sensing Studies:

Encouraged by these unique properties, such as their high luminescent nature, their porosity with a large surface area, and their water stability, the PL response of the **iMOF-4A** was tested for the sensing of various antibiotics and pesticides in water. Considering the facts, one is the essential requirement of potential sensory materials for aqueous phase real-time sensing applications, and another is the high hydrolytic stability of the probe, **iMOF-4A**, which was examined for a sensing experiment in an aqueous medium. For these studies, a wide variety of antibiotics, such as nitrofurazone (NFZ), nitrofurantoin (NFT), sulphapyridine (SPD), sulphaguanidine (SGD), sulphathiazole (STZ), ciprofloxacin (CPF), ampicillin (APC), norfloxacin (NFC), kanamycin (KMC), neomycin (NMC), spectinomycin (STC), amoxicillin (AMC), and a diverse class of pesticides, such as paraquat (PQ), 2,4-dichloro-1-(4-nitrophenoxy)benzene (Nitrofen), 2,6-Dichloro-4-nitroaniline (DCNA), cypermethrin (CPM), chlorpyrifos (CHPS), carbetamide (CBM), (Appendix 7, Appendix 12), were selected as model toxic water pollutants to demonstrate the sensitive detection ability of **iMOF-4A** towards selective antibiotics and pesticides in water (Figure 4, Appendix 8-9). At first, to test the fluorescence response of the MOF towards the aforementioned antibiotics a through sensing titration experiment was conducted (see supporting information for details).

After recording the fluorescence emission intensity of the pristine MOF, more spectra were recorded with the addition of each aqueous solution of antibiotic, individually, with an incremental addition of 20 μL and a total volume of 300 μL (Figure 4a,4d, Appendix 8-9). Among the various antibiotics, upon gradual addition, only nitrofurazone and nitrofurantoin were found to quench the emission intensity of **iMOF-4A** (Figure 4a,4d and Appendix 8,9). Whereas, the emission intensity was observed to be unchanged or slightly decreased upon the incremental addition of other antibiotics (Appendix 8,9). This result primarily illustrated the potent of **iMOF-4A** for the selective detection of NFT and NFZ compared to other antibiotics in water. Further, this result has been reorganized in a bar diagram profile to explore the relative percentage quenching of all the antibiotics (Figures 4a-4e). In addition to this, for a potential real-time chemical sensor, high selectivity, or the sharp response towards target analytes in the presence of other interference, is an important parameter for practical application. Therefore, the binary selectivity test for antibiotics sensing with **iMOF-4A** was performed, following the similar sensing experiment (Appendix 12-28). Interestingly, it was found that the MOF exhibited a significant fluorescence quenching response towards only NFT and NFZ, even in the presence of an equal amount of other

antibiotics individually (Figure 4, Appendix 8,9). This data validated the highly selective nature or anti-interference ability of the MOF towards selective antibiotic detection in aqueous medium.

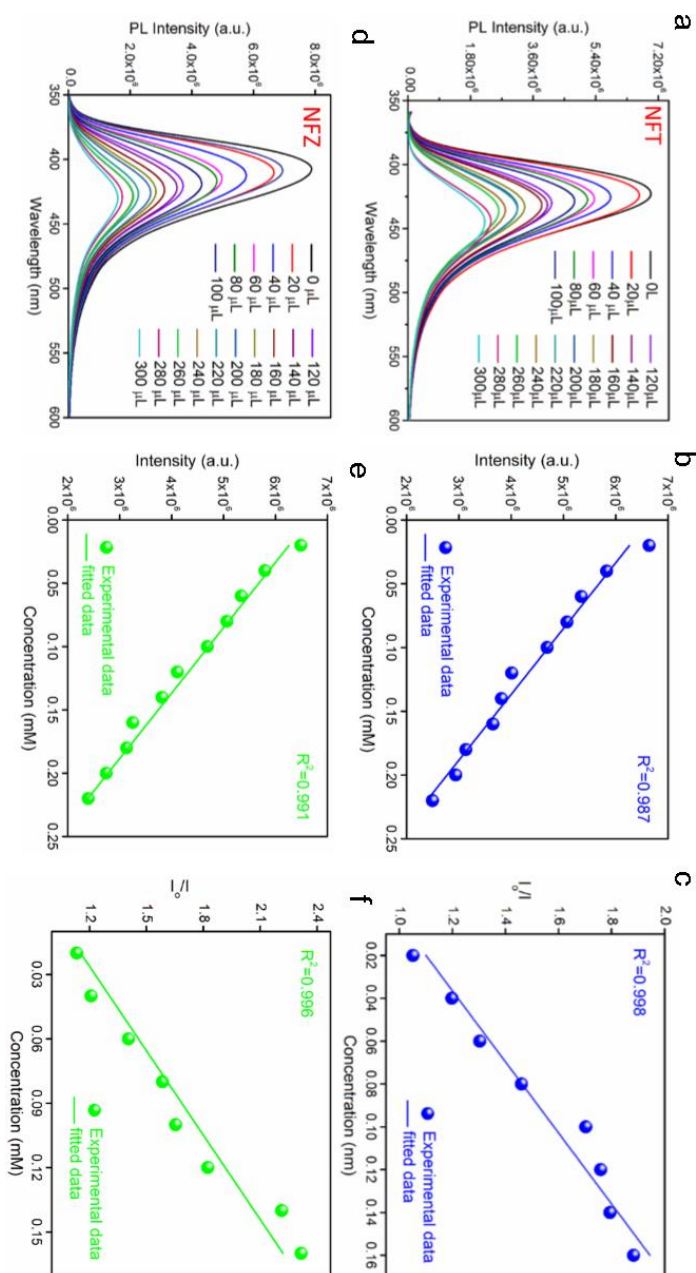


Figure 4. Sensing experiments derived studies of antibiotics: (a, d) Fluorescence emission spectra for iMOF-4A in diverse concentrations of NFT and NFZ their aqueous solutions. (b, e) Respective

Stern–Volmer plots for **iMOF-4A** in different concentrations of NFT and NFZ their aqueous solutions. (c, f) LOD estimation plots showing quenching response of **iMOF-4A** for NFT and NFZ, respectively.

Henceforth, motivated by the strong fluorescence quenching response by NFT and NFZ antibiotics, further detail sensing studies were carried out with **iMOF-4A**. For this, again, a typical titration experiment has been conducted (see supporting information for detail). The emission intensity of the MOF was found to be quenched gradually upon the incremental addition of 1 mmol of aqueous solutions of NFT and NFZ individually (Figure 4, Appendix 9). Moreover, from these PL profiles, the quenching efficiencies for both NFT and NFZ were quantitatively determined using the Stern-Volmer (S-V) equation, $I_0/I = K_{S-V} [M]$, (where I_0 and I are the PL intensities in the absence and presence of the analytes, respectively, K_{S-V} is the quenching constant, and M is the concentration of the analyte). [N1] From the K_{S-V} plot, it was observed that a linear relationship was formed for both the cases of concentration of NFT and NFZ with their respective intensities (Figure 4a-4d). Furthermore, the quenching constant (K_{S-V}) values were calculated as 6.02×10^4 and $7.62 \times 10^4 \text{ M}^{-1}$ for NFT and NFZ (Figure 4), respectively. It should be pointed out that the S-V plots were found to deviate from their linearity at higher concentrations, indicating the coexistence of both static and dynamic quenching properties behind the fluorescence quenching mechanisms of both NFT and NFZ, which is further explained. Now, apart from the selectivity, the high sensitivity of a sensory probe is an essential criterion in order to make it suitable for the promising sensing application. For this, the limit of detection (LOD) values of **iMOF-4A** towards NFT and NFZ were calculated by plotting the decrease in the PL intensity upon progressive addition of concentrations of analytes (see appendix section for further details). From the linear fitting plot between these two parameters, the LOD values for NFT and NFZ were calculated as 6.68 and 7.18 ppm, respectively, with the correlation coefficient values (R^2) of 0.987 and 0.991 (Figure 4c, 4f). In addition to this, the kinetics or the time-dependent response of the quenching phenomenon of **iMOF-4A** was explored for NFT and NFZ antibiotics. For this experiment, a certain amount of analyte was added to the aqueous suspension of MOF and further kept for treatment with rotation at different time intervals. The emission intensity of **iMOF-4A** was found to be quenched rapidly and completely within 1 min of treatment, whereas upon further increasing the time with the same amount of analyte, only a slight change in the emission was observed (Figure 4, Appendix 8, 9). This observation explored the rapid detection response of **iMOF-4A** towards selective antibiotics in water. All these results of high quenching efficiency and LOD values, along with rapid detection ability, promote **iMOF-4A** as one of the best performing sensing materials compared to other reported materials in the realm of antibiotic sensing.

Following this, the aqueous phase fluorescence detection of a variety of the aforementioned pesticides by **iMOF-4A** was investigated in greater detail. At first, these most commonly used pesticides, including paraquat, a non-selective herbicide (Appendix 12), were chosen for the sensing titration experiments following a similar previous protocol. Upon incremental addition of a total of 300 μL of a 1 mmol concentration of each pesticide individually into the aqueous suspension of **iMOF-4A**, the PL emission intensity was found to be quenched only in the case of paraquat, among the others (Figure 6a). Compared to paraquat, the emission profiles of other pesticides were found to be unchanged or slightly changed with the progressive addition of those analytes. This data was further plotted which represented the relative percentage quenching of all the selected pesticides. This study explored the selective turn-off response of **iMOF-4A** to paraquat only. The quenching efficiencies of **iMOF-4A** for these pesticides follow the order of **Paraquat** > **2,6-DC-4-NA** > **Carbetamide** > **Chloropyrifos** > **Cypermethrin** > **2,4-DC-1,4-NPB**. In addition to this, we further tested the anti-interference ability or binary selectivity of the MOF towards paraquat in the presence of other pesticides (Appendix 29a-29d). For this, a similar experiment was performed as in the case of antibiotics (see the Appendix section for details). As a result, it was found that upon addition of other pesticides (1 mmol), the emission intensity was slightly changed, whereas when we induced an equal amount of paraquat (1 mmol), the intensity became rapidly reduced. This analysis revealed that **iMOF-4A** exhibited a highly selective quenching nature toward the detection of paraquat in water, even in the presence of other pesticides. This was the case even when other pesticides were present as competing species. These data can also be visualized in a different way by using the bar diagram profile that is shown in figure 7b. Now, this selective detection ability of **iMOF-4A** towards paraquat in water, further inspired us to perform in-depth sensing studies.

For which, again, a through titration experiment was conducted against paraquat with a similar procedure. Upon gradual addition of an aqueous paraquat solution, the emission intensity was observed to be quenched progressively (Figure 6a). From this PL profile, the fluorescent quenching efficiency of PQ was quantitatively determined by the S-V equation, as done in the case of antibiotics. The S-V plot for PQ was found to be linear at low concentration ranges; however, upon increasing the concentration of the PQ, the plot deviated from linearity and moved upward (Figure 6c). This type of nonlinear S-V profile phenomenon in a sensing study indicated the adsorption or energy transfer process between the analytes and the probe. Moreover, a high quenching constant (K_{S-V}) value ($4.93 \times 10^4 \text{ M}^{-1}$) of **iMOF-4A** towards PQ was calculated, which is among the best performing materials reported to date. Again, the sensitivity of PQ detection in water systems is highly desirable, for which we determine the LOD value of PQ based

on the standard deviation of five repeated emission data sets of pristine MOF and the K_{S-V} value of PQ (see supporting information for details) (Figure 6a, 6b).

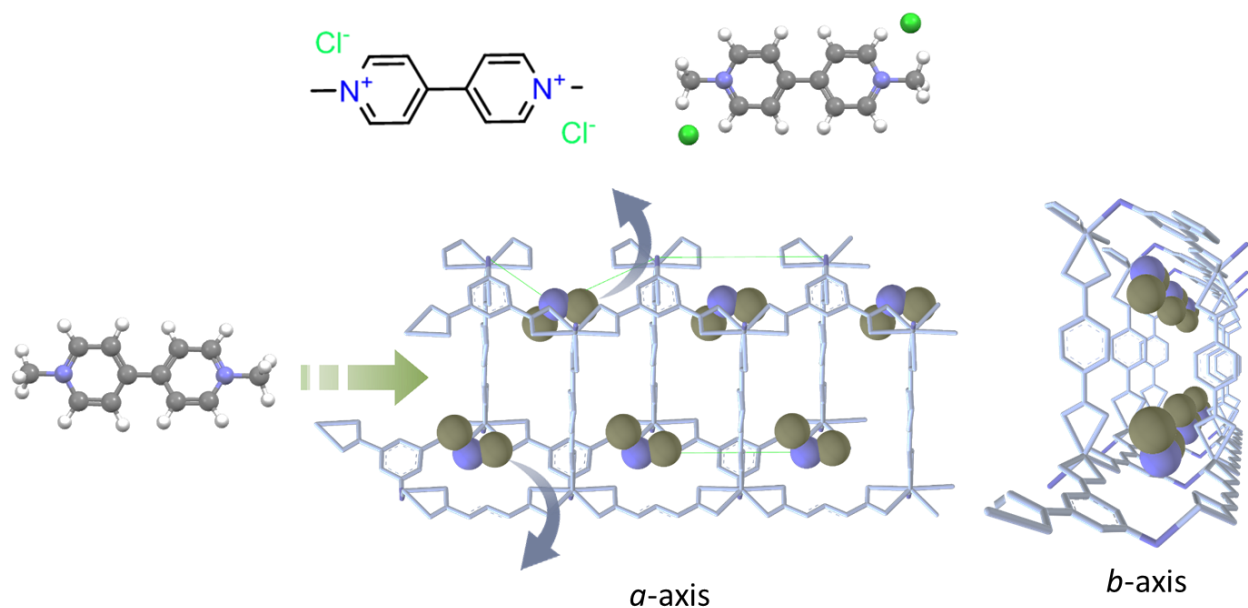


Figure 5. Depiction illustrative exchange process desired in **iMOF-4A** swapping DMA for paraquat (PQ).

A very low detection limit was revealed for PQ capture, which corresponds to 1.79 ppm, which is the highest among all the reported materials used for paraquat detection. This makes **iMOF-4A** a promising and reliable sensing material for the selective and sensitive detection of paraquat in real water samples too.

3.3.2 Sensing Mechanism

In light of the successful sensing results described above, we have proposed the following mechanism as a possible explanation for how **iMOF-4A** can selectively detect antibiotics (NFT and NFZ) and pesticides (PQ) in water. According to the reports that can be found in the scientific literature, the primary factor that contributes to the reduction in the luminescence intensity of MOFs is either the framework deformation or the electron/energy transfer process that occurs between the fluorophores and the analytes. PXRD data of antibiotics and paraquat treated MOF samples were collected by us so that we could test the first possible mechanism. Even after the sensing studies, the PXRD patterns of the treated samples were found to be an exact match with the PXRD patterns of the pristine phase MOF. This unequivocally

demonstrated that the crystallinity of the material had been preserved along with its robust structural integrity (Figure 3a). In addition, the surface morphological characterization was performed with the assistance of FESEM after the sensing studies were completed. This validation of the retention of the morphology after the addition of antibiotics and pesticides was accomplished (Figure 3b,3c and Appendix 3,4-6). Moreover, according to the EDX data, the homogeneous distribution of all the relevant elements throughout the crystals of the analytes treated **iMOF-4A** samples revealed that the chemical composition of the MOF had not been altered in any way (Appendix 5, 6b, 6c). Following the sensing study, it was discovered that the MOF exhibited similar behavior in terms of its thermal stability. All of these data suggested that the decrease in emission intensity of **iMOF-4A** was not caused due to structural deformation, which further ruled out the first possible quenching mechanism. This was because structural deformation was not the cause of the decrease. After that, we move on to investigate the other mechanisms that are responsible for the turn-off of the antibiotic and the sensing of the paraquat in the water. In the process of fluorescence quenching, the presence of energy transfer is strongly suggested by the deviation of the linear line in the S-V plot for NFT, NFZ, and PQ. This deviation was previously discussed. As a result, in order to investigate the role that fluorescence resonance energy transfer (FRET) plays in the origin of intensity quenching phenomena, the UV-vis spectra of all of the analytes (including all pesticides and antibiotics) were recorded. In addition, these spectra were plotted against the emission profile of **iMOF-4A**, which revealed the following result when it was done. FRET is one of the predominant mechanisms behind fluorescence quenching of **iMOF-4A**, both by selective antibiotics (NFT and NDZ) and pesticides (PQ) in water. This is because FRET involves the exchange of electrons between two molecules with different chemical structures. Hereafter, in order to get insight into another possible mechanism i.e., photoinduced electron transfer (PET), the density functional theory (DFT) studies were performed. With the help of DFT calculation, the highest occupied molecular orbital (HOMO) and lowest unoccupied molecular orbital (LUMO) of both the unit of MOF and analytes (all the antibiotics) were calculated and further compared (Figure 8). Among all the antibiotics, the LUMO of NFT and NFZ were found to lower in energy position with compare to LUMO of unit of MOF, which subsequently exist closest to the HOMO of MOF (Figure 8). However, in case of all other antibiotics the LUMOs are positioned far from the HOMO of the unit of the MOF. This observation revealed that upon exciting the system with UV-light, the electron of the MOF become excited, and further transferred from the LUMO of MOF to the LUMO of NFT and NFZ (antibiotics) via a photoinduced electron transfer (PET) process, which consequently decreased the luminescent intensity of the overall MOF-system. Now,

apart from the antibiotics, in case of pesticides or paraquat, similar observation was observed. For this upon photo irradiation, electron transfer from the MOF to paraquat become dominant, which caused selective turn-off response. However, other pesticides do not exhibit such phenomena owing to their high energy level of LUMOs. Again, this result indicated that the PET is another mechanism for the fluorescence quenching of **iMOF-4A** by selective antibiotics and paraquat.

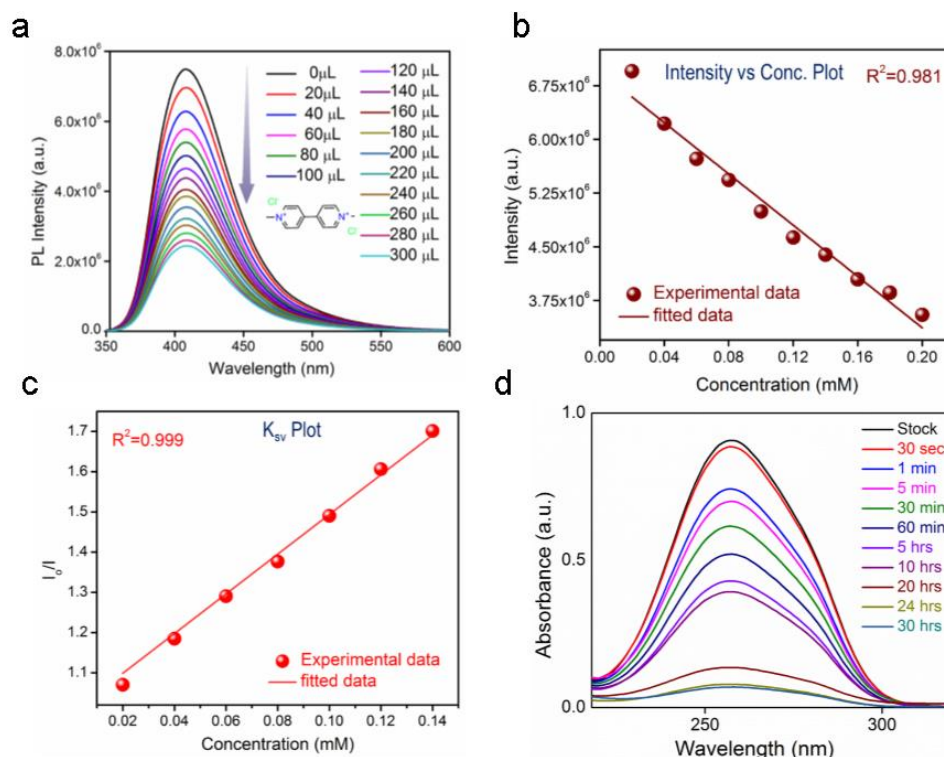


Figure 6. Sensing and capture studies of pesticides: (a) Fluorescence emission spectra (quenching) of **iMOF-4A** in gradient concentration paraquat aqueous solutions. (b) Thereby obtained LOD estimation plots for **iMOF-4A** at aforementioned concentrations of aqueous paraquat solutions. (c) K_{sv} plots obtained from quenching response towards paraquat. (d) UV-Vis spectra of Paraquat at different time interval of incubation with **iMOF-4A** indicating incremental capture.

Moreover, **iMOF-4A** is constructed with electron-rich benzene moiety-based organic linkers and free DMA cations, which play a crucial role in the various supramolecular interactions (such as hydrogen bonding interactions, van der Waals interactions, etc.) as well as electrostatic interactions with the NFT, NFZ antibiotics, and paraquat pesticide. To explore these molecular interactions, DFT calculations were carried out using the linkers of the MOF with the aforementioned analytes. The geometry optimized

structure of the ligand of MOF and NFT, NFZ, and paraquat forms complexes as depicted by binding energy changes revealed post DFT calculations. The formation of these complexes between the respective analytes and unit of MOF plays a significant role in the specific binding for sensing. In order to gain further insight into the molecular interactions, the electrostatic surface potential (ESP) was calculated, which demonstrated the strong interaction with binding energies of between the ligands of the MOF and NFT, NFZ, and paraquat, respectively. Therefore, the fluorescence intensity of **iMOF-4A** was selectively and strongly quenched by NFT, NFZ, and paraquat. Furthermore, to understand the nature of the quenching process, lifetime measurement was conducted. The life expectancy of the MOF before and after treatment with antibiotics (NFT and NFZ) and pesticides (PQ) were measured and further compared. The average lifetimes of pristine and analytes treated MOF exhibited no significant changes. This demonstrated the presence of static quenching behind this turn-off response by NFT, NFZ, and paraquat in a water medium. At this point, considering all the factors, it can be concluded that the selective quenching behavior of **iMOF-4A** towards NFT, NFZ, and paraquat was mainly caused by the combined effect of FRET, PET, and different suitable interactions between the probe and analytes. As a result of the high selectivity, sensitivity, fast response, low detection limits, and ability to detect in water medium that **iMOF-4A** possesses, we are attempting to further investigate its regeneration recognition ability towards NFT and paraquat sensing.

This ability is extremely significant for a real-time sensory material because it enables the material to detect the substance in question. The recyclability of the system was evaluated after the first cycle sensing experiment was carried out in accordance with a protocol very similar to the one described above. This was then followed by multiple iterations of washing/centrifugation/washing procedures. Following the completion of the compound's final cleansing with water, it was dried in an oven before being put to use in the subsequent round of sensing experiments. This process as a whole was repeated for a total of five cycles in order to obtain the conclusive quenching efficiencies, which were then plotted in the form of a bar diagram profile. The data on the recyclability of the NFT showed a superior sensing ability to that of the **iMOF-4A**, as there was not a significant reduction in the efficiencies that were observed. In the same vein, the results of the recyclability test for paraquat demonstrated high quenching efficiency even after several cycles. The purpose of these studies was to investigate the viability of **iMOF-4A** as a candidate for use in long-term, real-world, environmentally relevant organic micro-pollutant detection applications.

3.3.3 Paraquat Capture Study

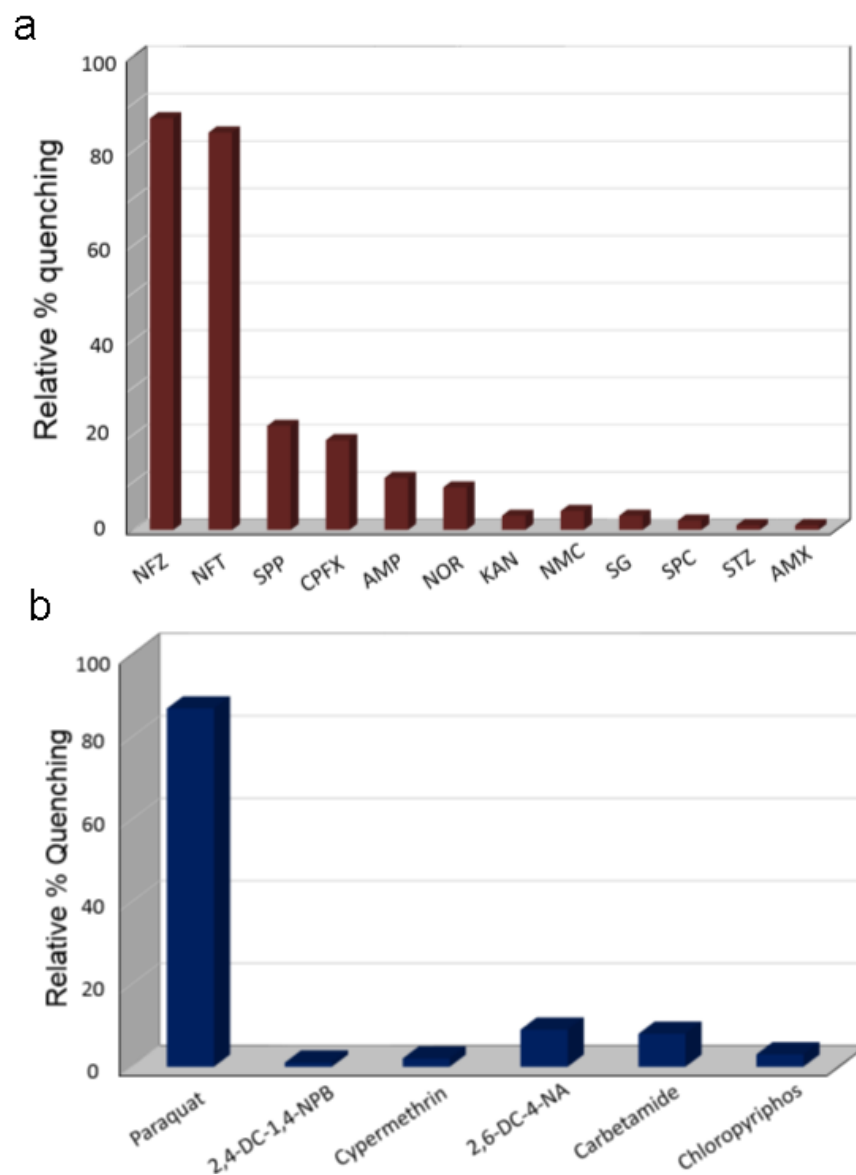


Figure 7. (a) Plots highlighting selective fluorescence quenching response of **iMOF-4A** for range of antibiotics indicating effective quenching response by NFZ and NFT, respectively. (b) Plots highlighting selective fluorescence quenching response of **iMOF-4A** for range of pesticides (grouped herbicides) indicating standalone quenching response by Paraquat.

As mentioned earlier, only a few porous materials have been utilized so far in the literature, either as detection mediums or as adsorbent platforms, for the effective removal of toxic paraquat from water. However, materials that possess both the ability to selectively detect paraquat in water as well as the

ability to efficiently sorb paraquat from water present a clear advantage for the effective remediation of the environment. Inspired by the above successful sensing results and considering the unique properties of **iMOF-4A** (Figure 4a, Figure 7b and Appendix 11), e.g., its anionic nature with free exchangeable DMA cations inside the 1D channel pores of the porous MOF (Figure 5), we were further motivated to explore the paraquat sorption ability of **iMOF-4A** in water. A typical capture experiment (batch method) was conducted for the removal of paraquat from water. At first, for the kinetic experiment, a 0.05 mmol concentration solution of paraquat was chosen, and treated with **iMOF-4A** at different times (see the experimental section in the supporting information for details).

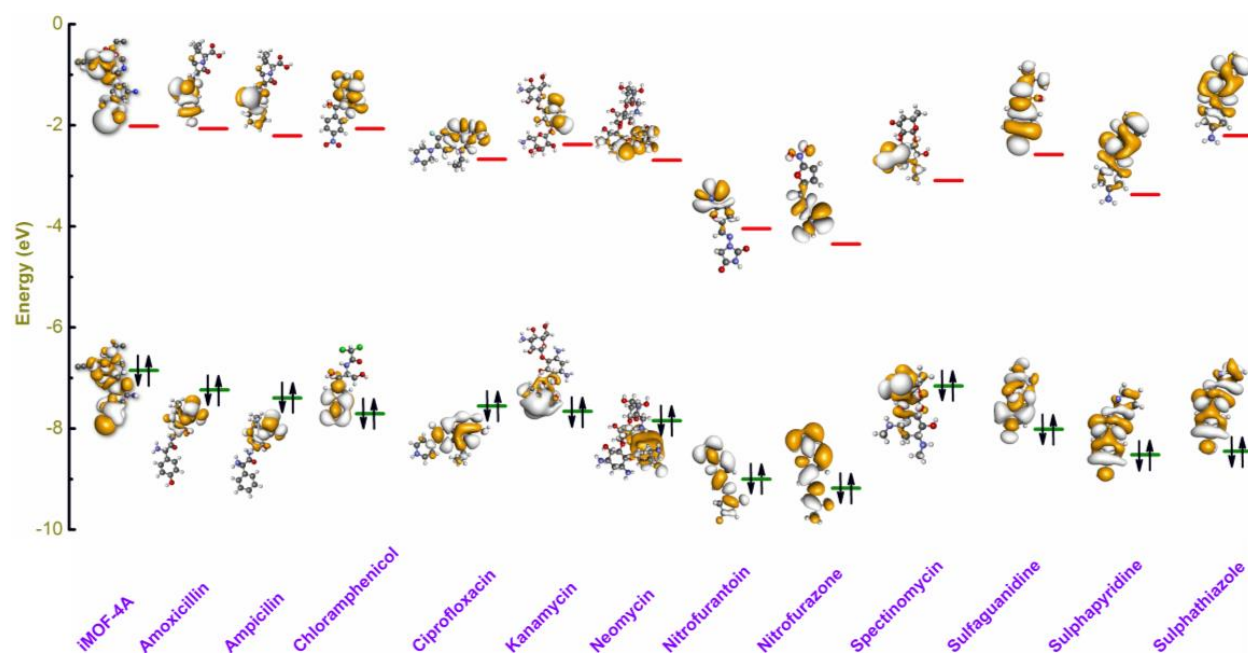


Figure 8. HOMO-LUMO energy levels of unit of **iMOF-4A** and different antibiotics.

After certain time intervals, the compound was separated from the paraquat solution with a filter, and the filtrate was examined by UV-vis spectroscopy to obtain the final concentration of the PQ. The UV-vis profile of the MOF treated solution exhibited a continuous decrease in the concentration of paraquat (Figure 6d). From this UV-vis profile, we further calculated the captured amount for paraquat and it was estimated invariable around $\sim 22 \text{ mg g}^{-1}$. Percentage removal of paraquat with different contact times (Figure 6d). **iMOF-4A** removed $\sim 58\%$ of paraquat from water within 10 hours of treatment and almost $\sim 93\%$ removal within 30 hours (Figure 6d). This data indicated rapid removal of PQ from a water medium by **iMOF-4A**. Furthermore, these kinetics data were found to be well fitted with the pseudo-

second-order model fitting, with a high adsorption rate constant. Thereafter, exchange capacity is an important factor in order to explore the full potential of an ideal adsorbent. Therefore, next we evaluated the saturation capacity of paraquat in a high concentration solution and further treated it with **iMOF-4A**.

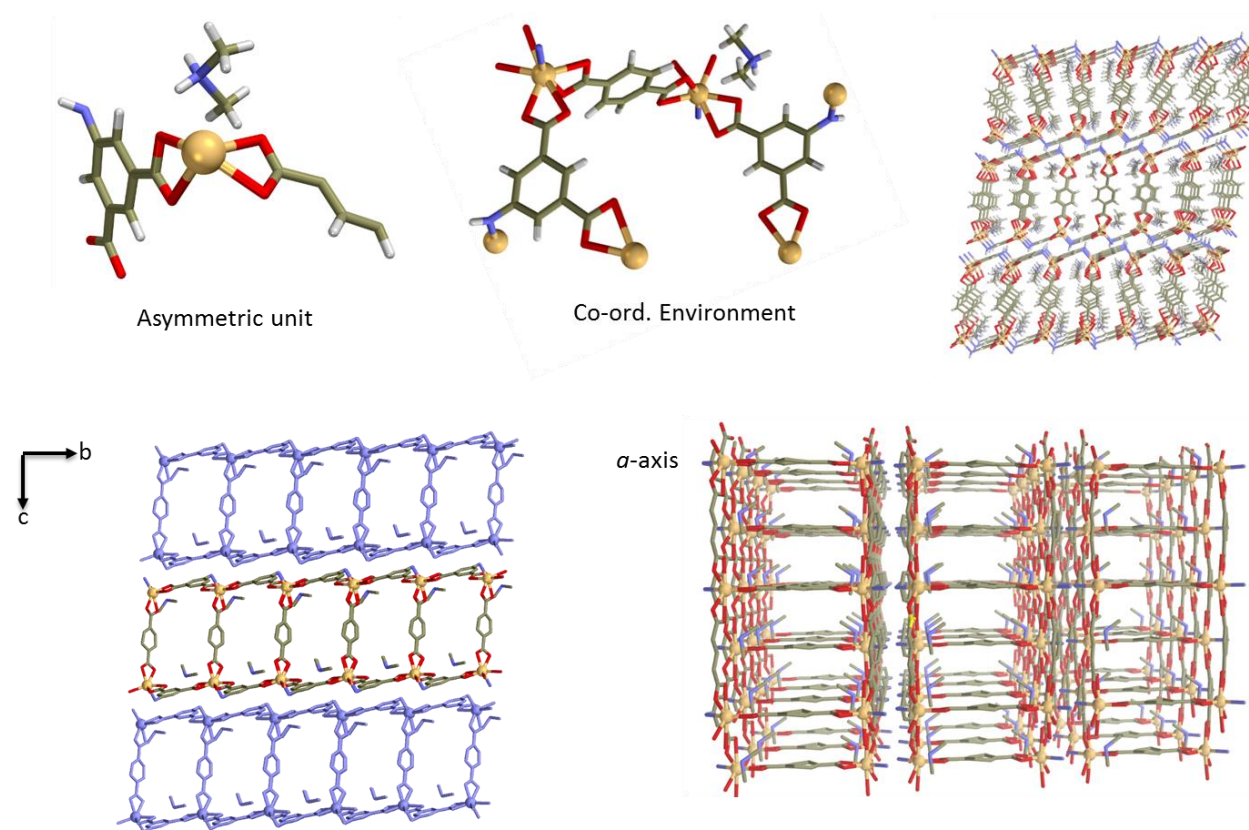
3.4 Conclusion

In summary, steered by the elucidated appropriate interactions among electron-rich and electron-deficient moieties, structured sensing experiments of electronically unsaturated hazardous micropollutants were carried out by developing easy to produce (a cost-effective), highly luminescent, and water stable ionic Metal-organic Framework. The **iMOF-4A** was produced through a straightforward reaction consisting of a single step synthesis, and it was discovered to be extremely luminescent in addition to being hydrolytically robust in nature. Proposed work includes a promising sensory material for the detection of antibiotics and pesticides in water. Ionic metal-organic frameworks (iMOFs) are an innovative class of porous materials that may be useful for the detection of aqueous micropollutants.

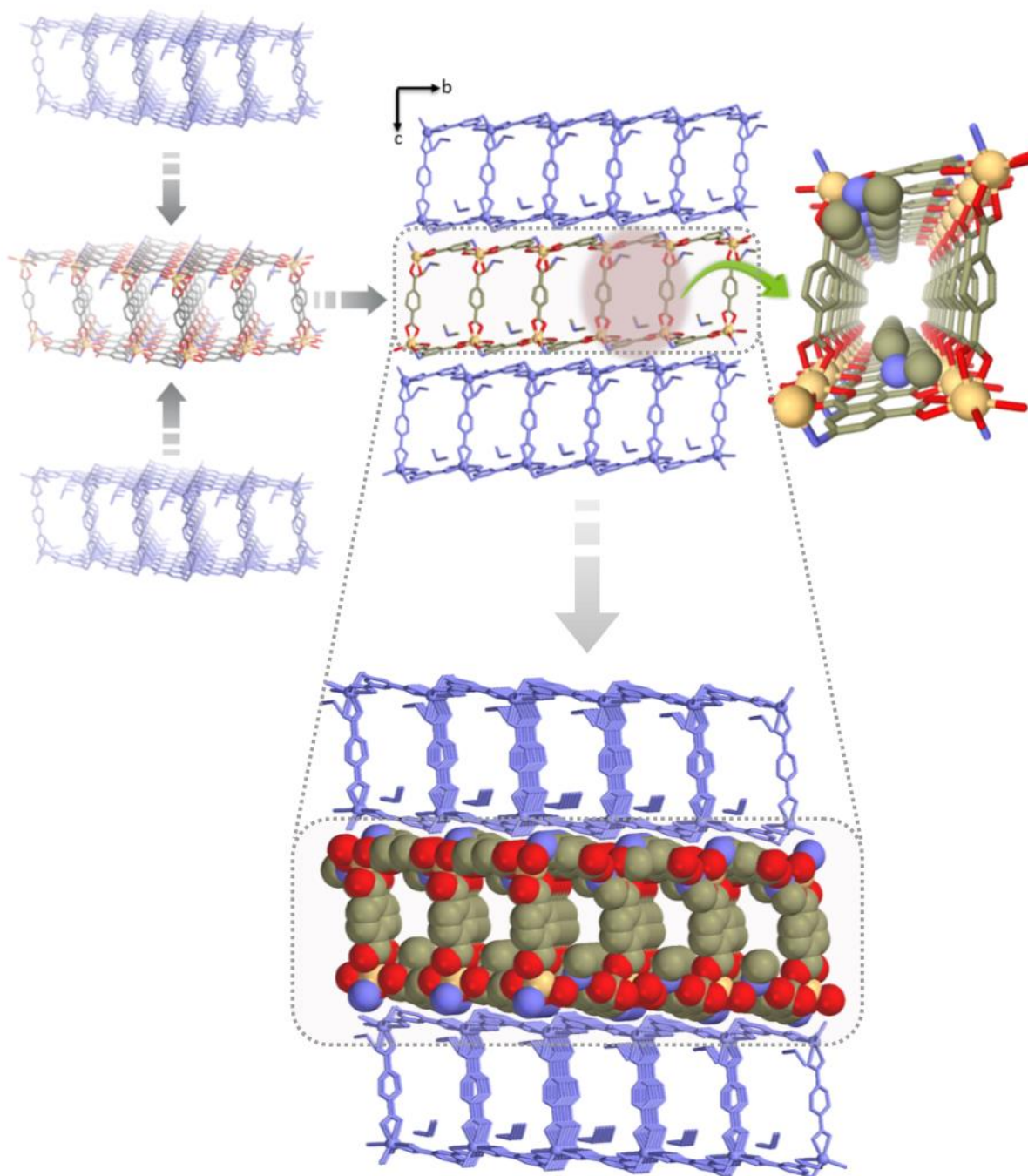
We examined the fluorescence quenching process of a newly developed very bright, electrically rich, porous metal-organic framework in order to detect antibiotics and pesticides in aqueous solution (**iMOF-4A**). In the presence of electron-deficient antibiotics like Nitrofurantoin (NFT) and Nitrofurazone (NFZ) and herbicides like Paraquat (PQ) in water, the **iMOF-4A** showed a particular, considerable quenching response. Both NFT and NFZ were detected at detection limits of 6.68 ppm and 7.18 ppm, respectively, demonstrating the **iMOF-4A**'s exceptional sensitivity. However, they were among the best-performing bright MOF-based sensing materials, with PQ detection limits of 1.79 ppm. The selectivity analysis study showed that **iMOF-4A** was exceptionally selective since its fluorescence detection performance was not significantly affected by the presence of the many different antibiotics and pesticides that were present at the time of the study. Furthermore, it may be regenerated for ongoing usage without appreciable loss of functionality following a detection test. In addition, time-resolved photoluminescence lifespan decay analyses and density functional theory were used to shed light on the in-depth mechanistic investigation of **iMOF-4A**'s detecting skills (DFT). These studies point to two mechanisms, photo-induced electron transfer (PET) and fluorescence resonance energy transfer (FRET), as the causes of selective quenching of emission. Additionally, an isothermal titration calorimetry (ITC) experiment was conducted to show that **iMOF-4A** can pick up low concentrations of electron-deficient antibiotics from a model of hospital wastewater. Finally, an **iMOF-4A**-based mixed-matrix membrane has been designed and implemented to reproduce real-time antibiotic detection in water. Therefore, current concerns that have developed as a

result of excessive use, abuse, or misuse of anthropogenic wastes (newly developed antibiotics and pesticides) can be effectively addressed by means of the strategies described above that are deployed through porous functional materials in order to effectively restrict or limit the direct negative effects of the hazardous pollutants mentioned.

3.5 Appendix Section



Appendix 1. Structural features of iMOF-4A viewed along crystallographic axes.



Appendix 2. Stacking of two dimensional layers to give three dimensional crystal lattice, zoomed view of pore channel showing ordered arrangement of DMA cations.

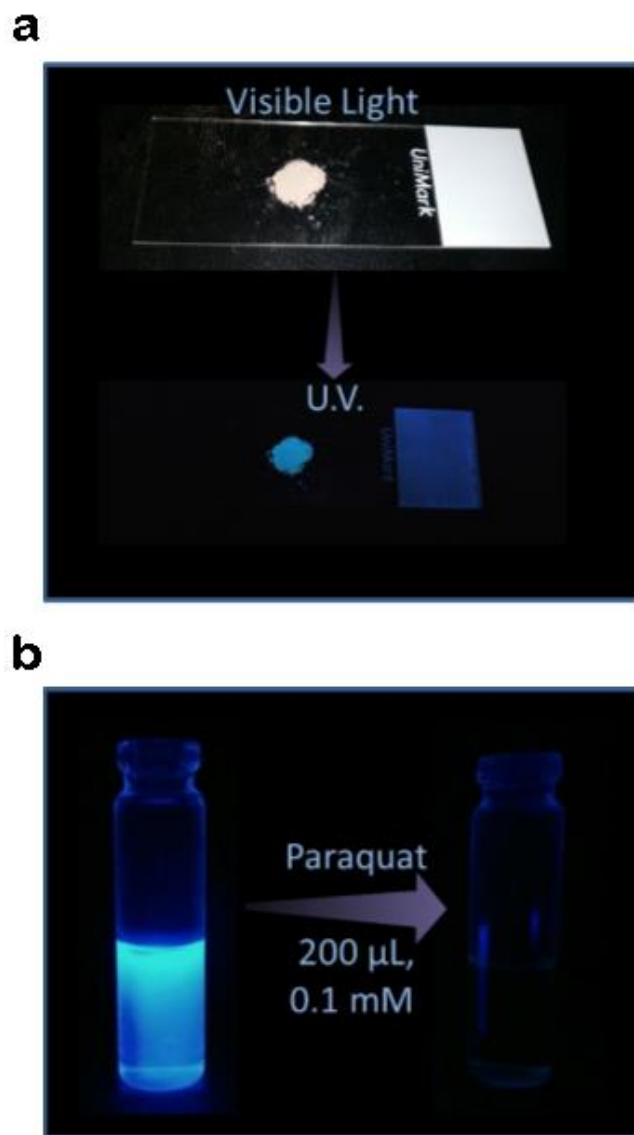
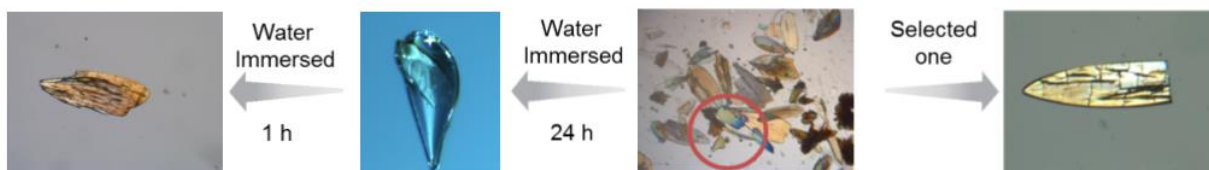
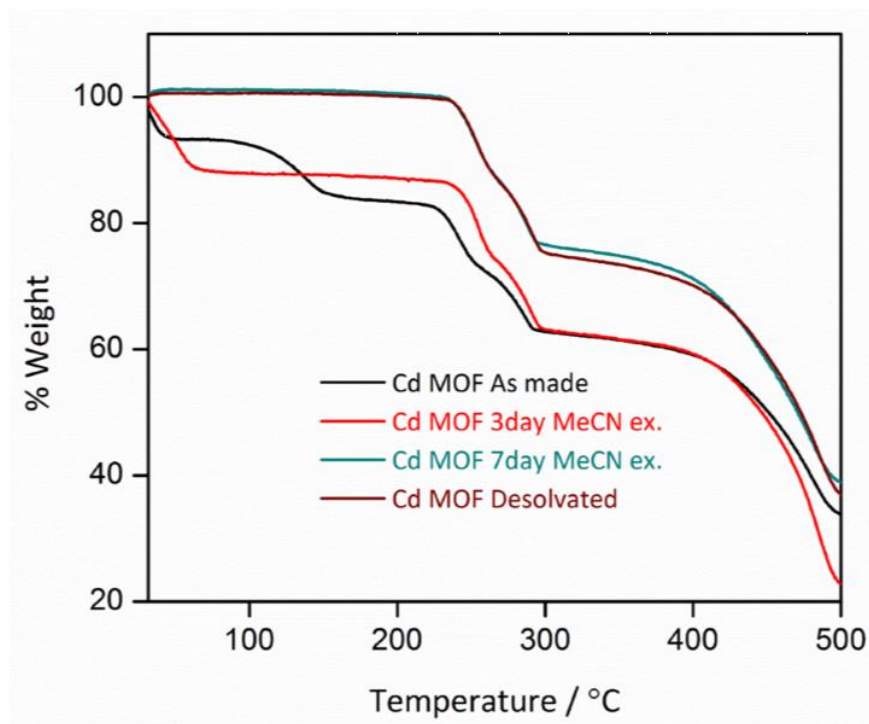


Illustration 1. (a) UV exposed activated solid phase of iMOF-4A. (b) Aqueous paraquat treatment of iMOF-4A powdered crystals revealing observable fluorescence quenching.

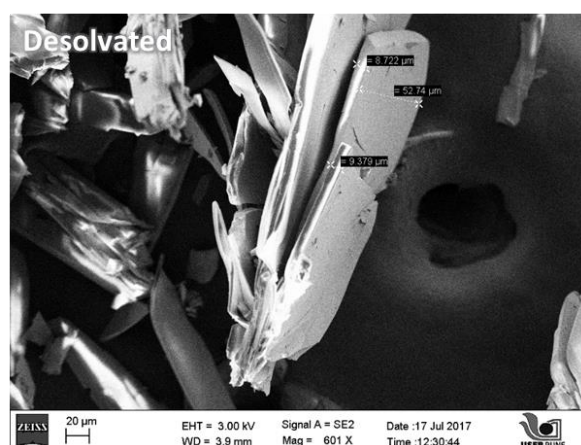
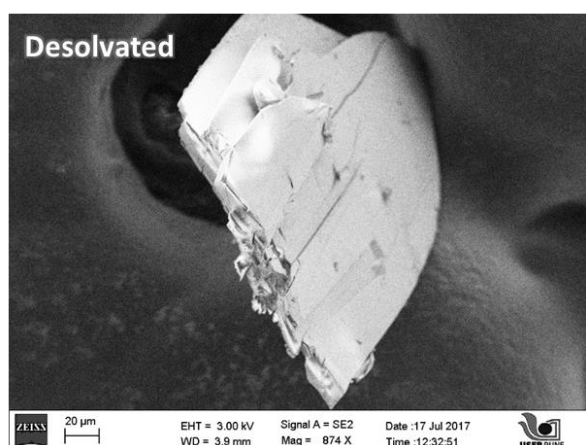
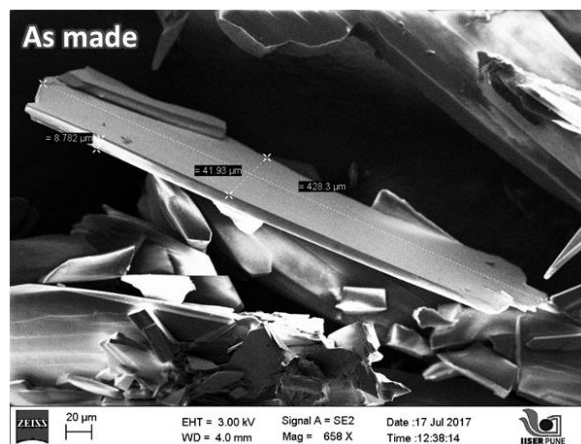
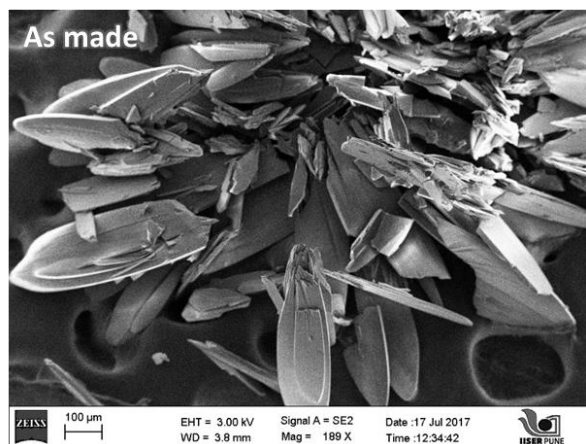
a



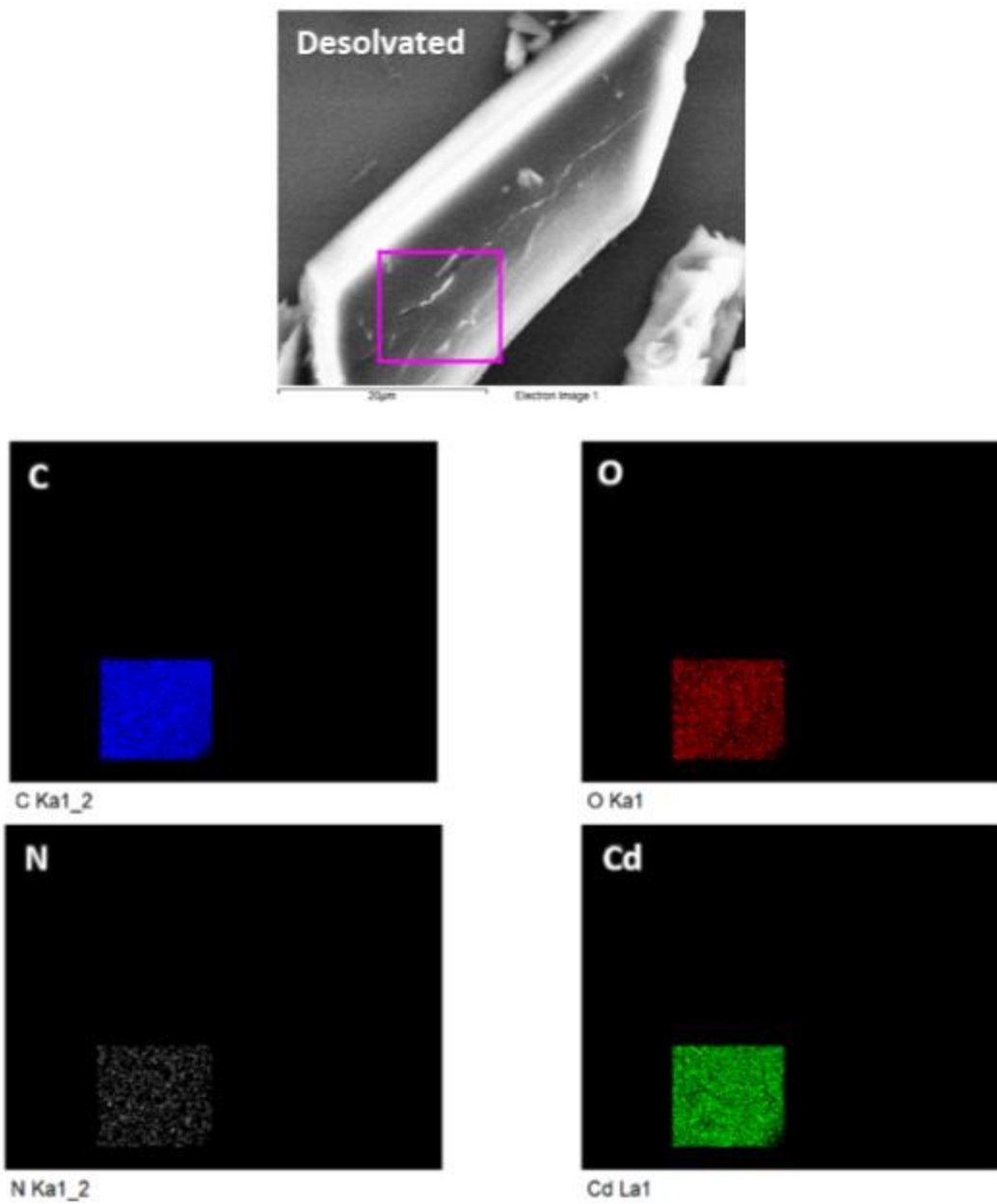
b



Appendix 3. (a) Differential water treatment and selected crystal for crystallographic and Thermogravimetric analysis. (b) Thermogravimetric analysis is **iMOF-4A** crystal revealing stability and desolvated phase until ~250 °C.

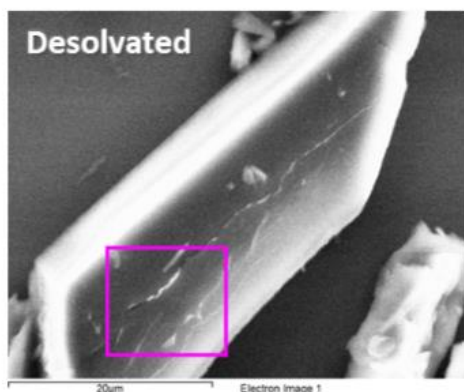


Appendix 4. FESEM analysis of iMOF-4A crystal, top row indicated as made crystals while bottom row indicates desolvated crystal revealing morphological retention post-desolvation.



Appendix 5. FESEM analysis revealing elemental mapping for elements (C, N, O, Cd) for **iMOF-4A** desolvated crystal; inset: region selected for analysis.

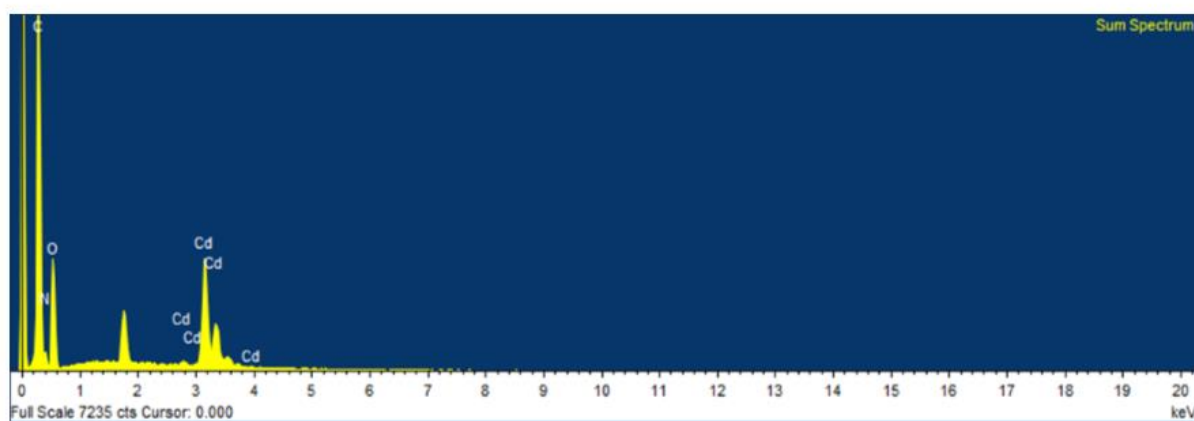
a



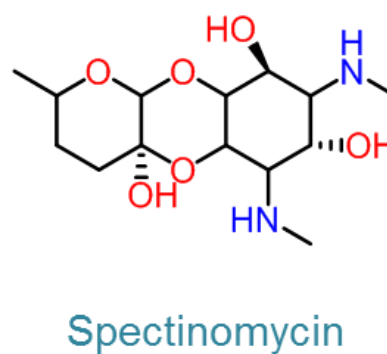
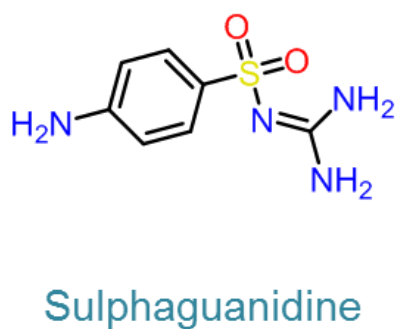
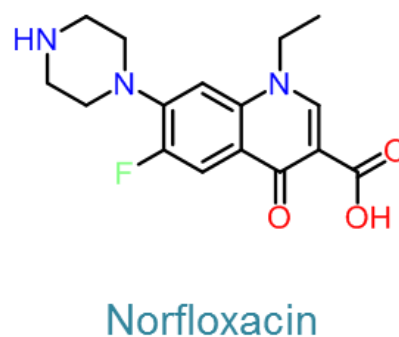
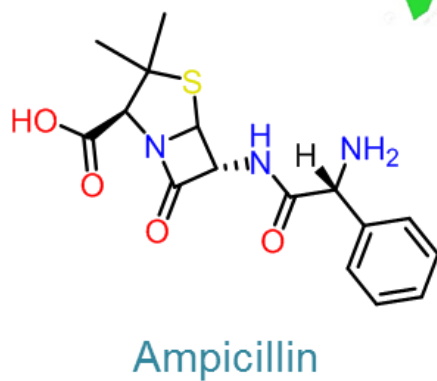
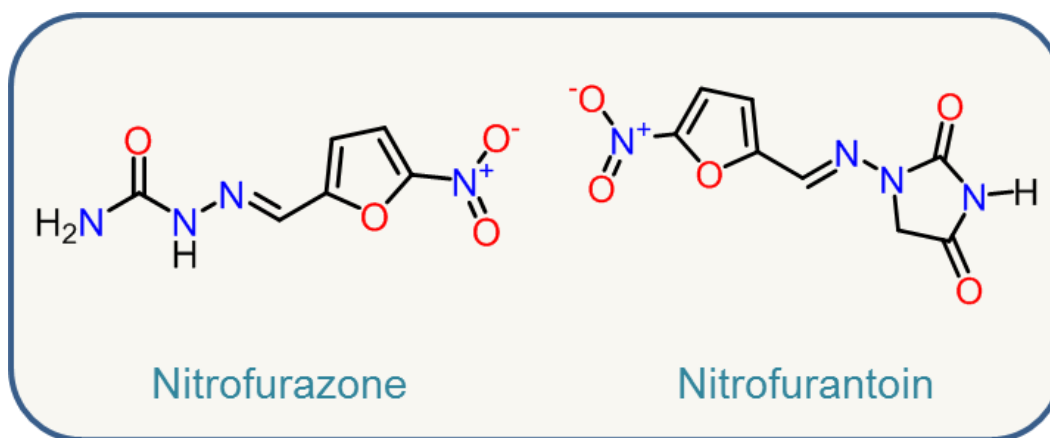
b

Element	Weight%	Atomic%
C K	43.96	63.13
N K	0.16	0.20
O K	30.39	32.76
Cd L	25.48	3.91
Totals	100	100

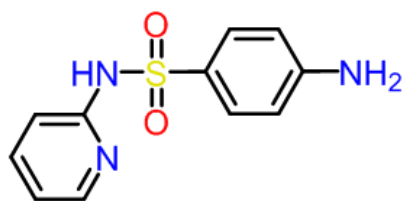
c



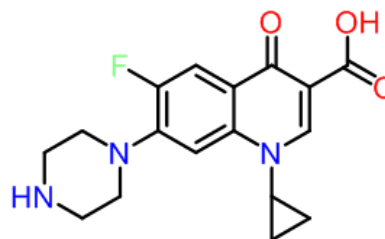
Appendix 6. (a) Area under analysis for FESEM and EDAX. (b) Atomic % of elements found post EDAX analysis. (c) Full scale EDAX spectrum showing presence of above listed elements that constitutes iMOF-4 crystals.



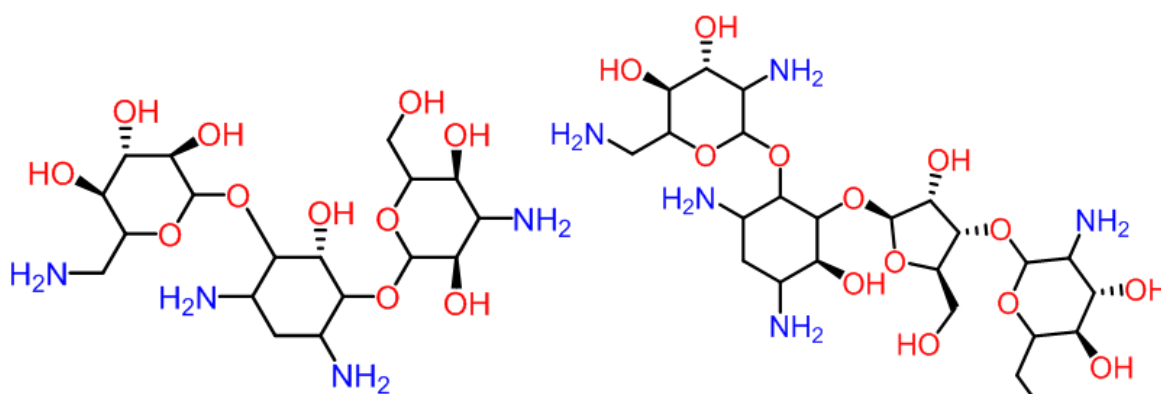
Appendix 7 A). Group of Antibiotics comprising different classes that are selected for sensing experiments; inset: antibiotics that resulted into fluorescence quenching response for **iMOF-4A**



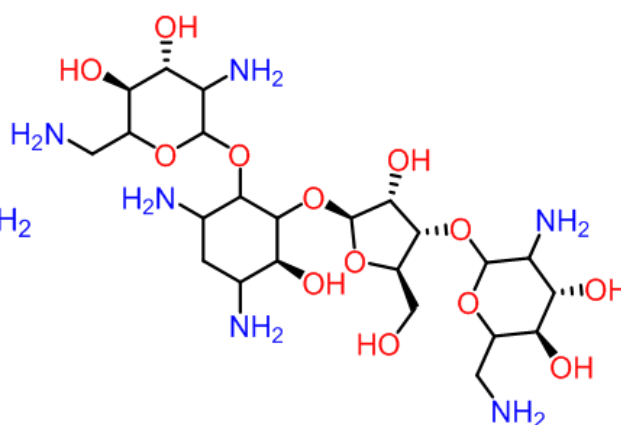
Sulphapyridine



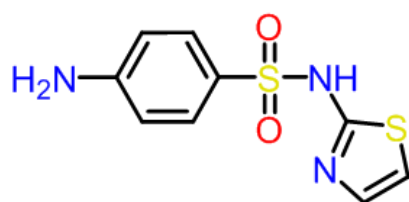
Ciprofloxacin



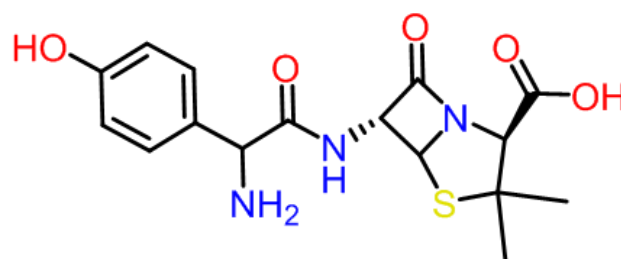
Kanamycin



Neomycin

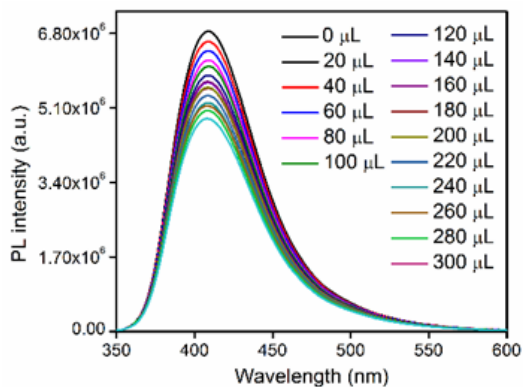


Sulphathiazole

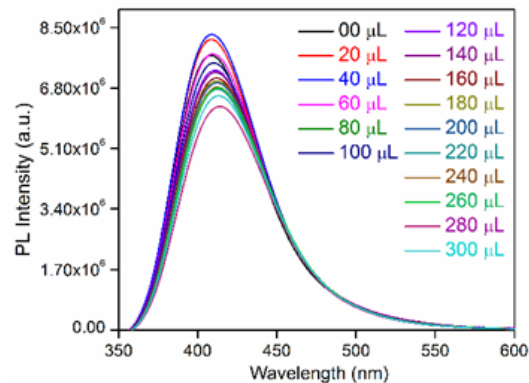


Amoxicillin

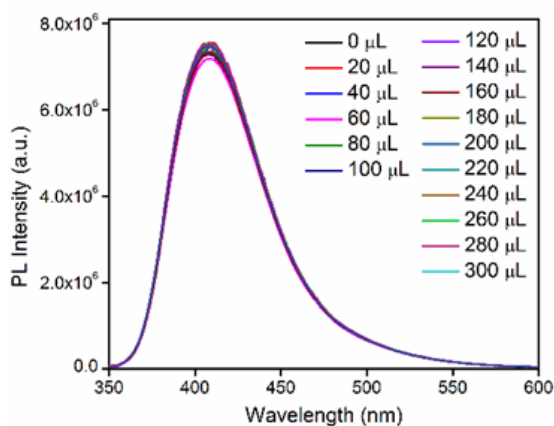
Appendix 7. A). Group of Antibiotics selected for sensing experiments, all of above listed *do not* produced observable fluorescence quenching response.



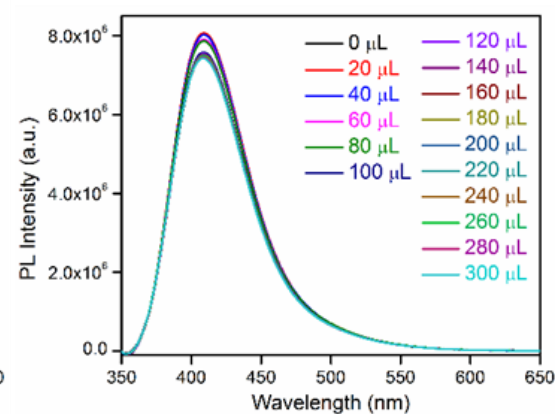
Sulphapyridine



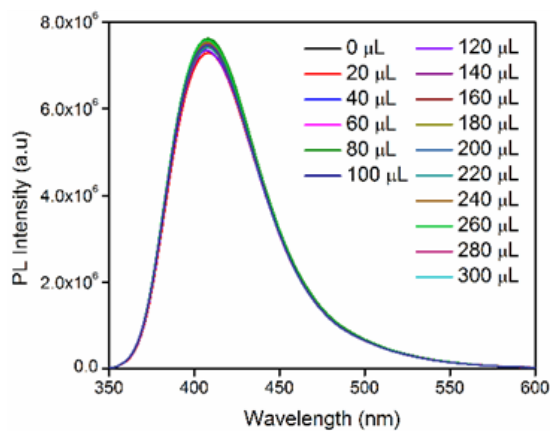
Ciprofloxacin



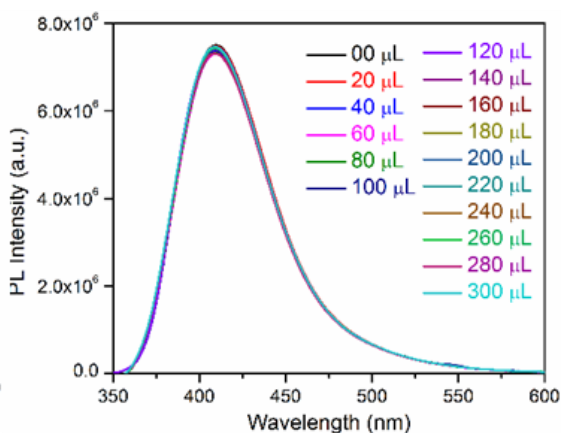
Kanamycin



Neomycin

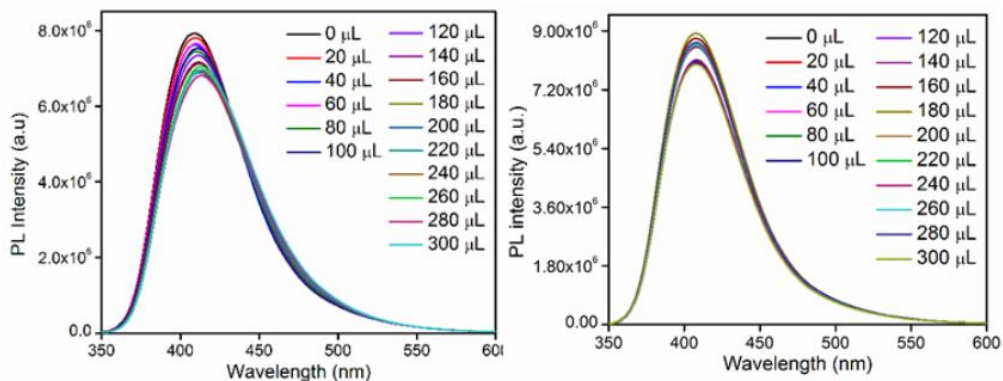


Sulphathiazole



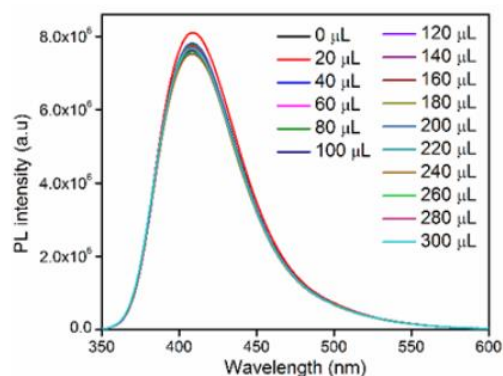
Amoxicillin

Appendix 8. Selective fluorescence quenching response of different antibiotics (Sulphapyridine, ciprofloxacin, kanamycin, neomycin, sulphathiazole, amoxicillin, respectively)



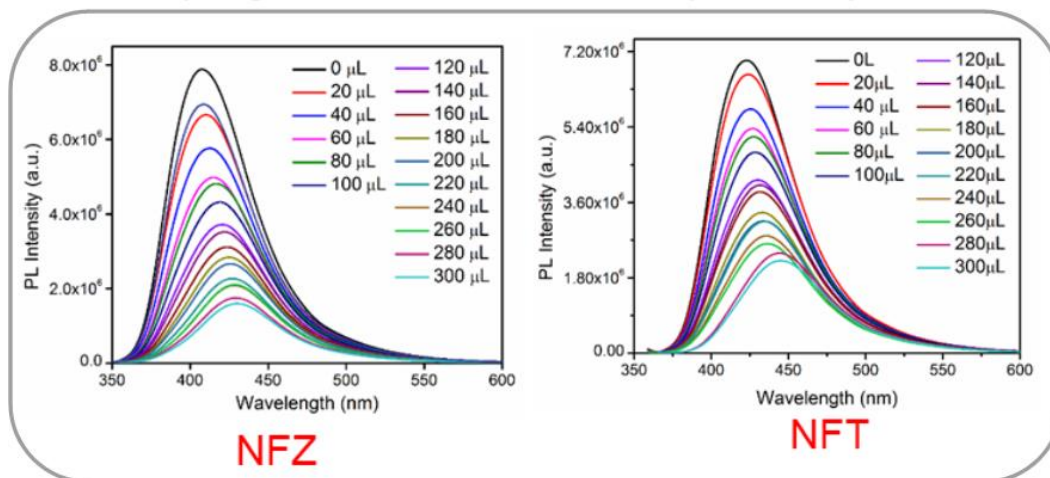
Ampicilline

Norfloxacin



Sulphaguanidine

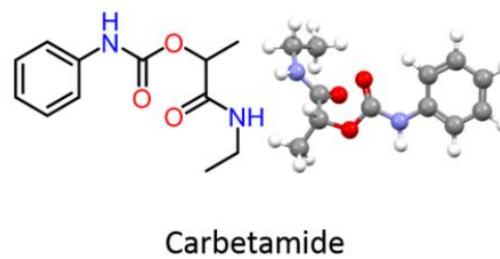
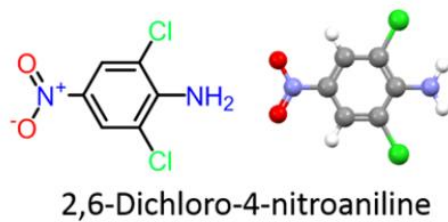
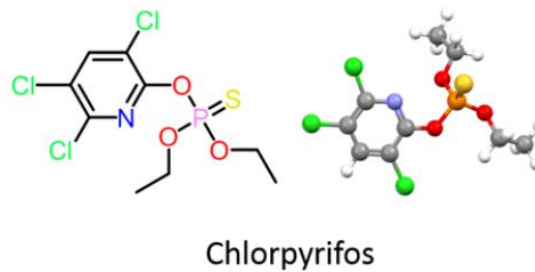
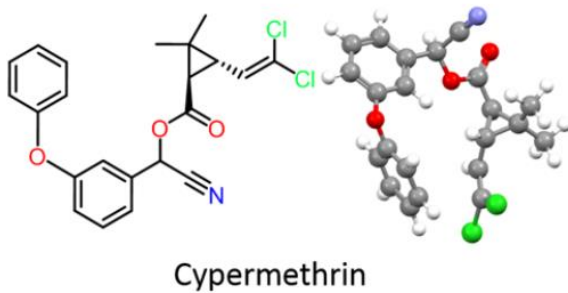
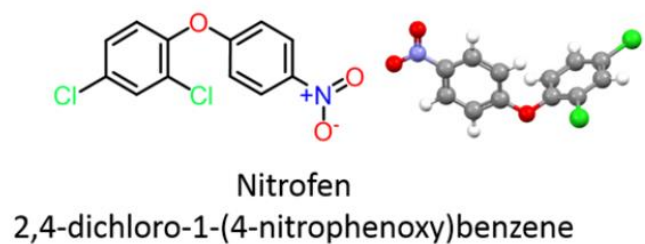
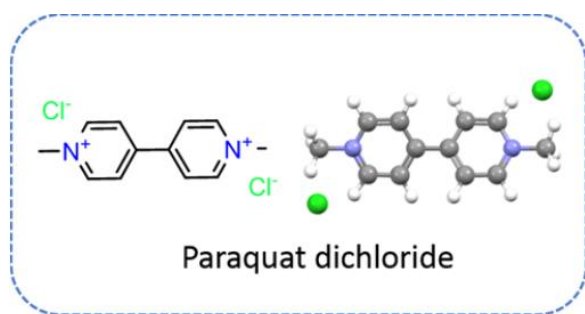
Spectinomycin



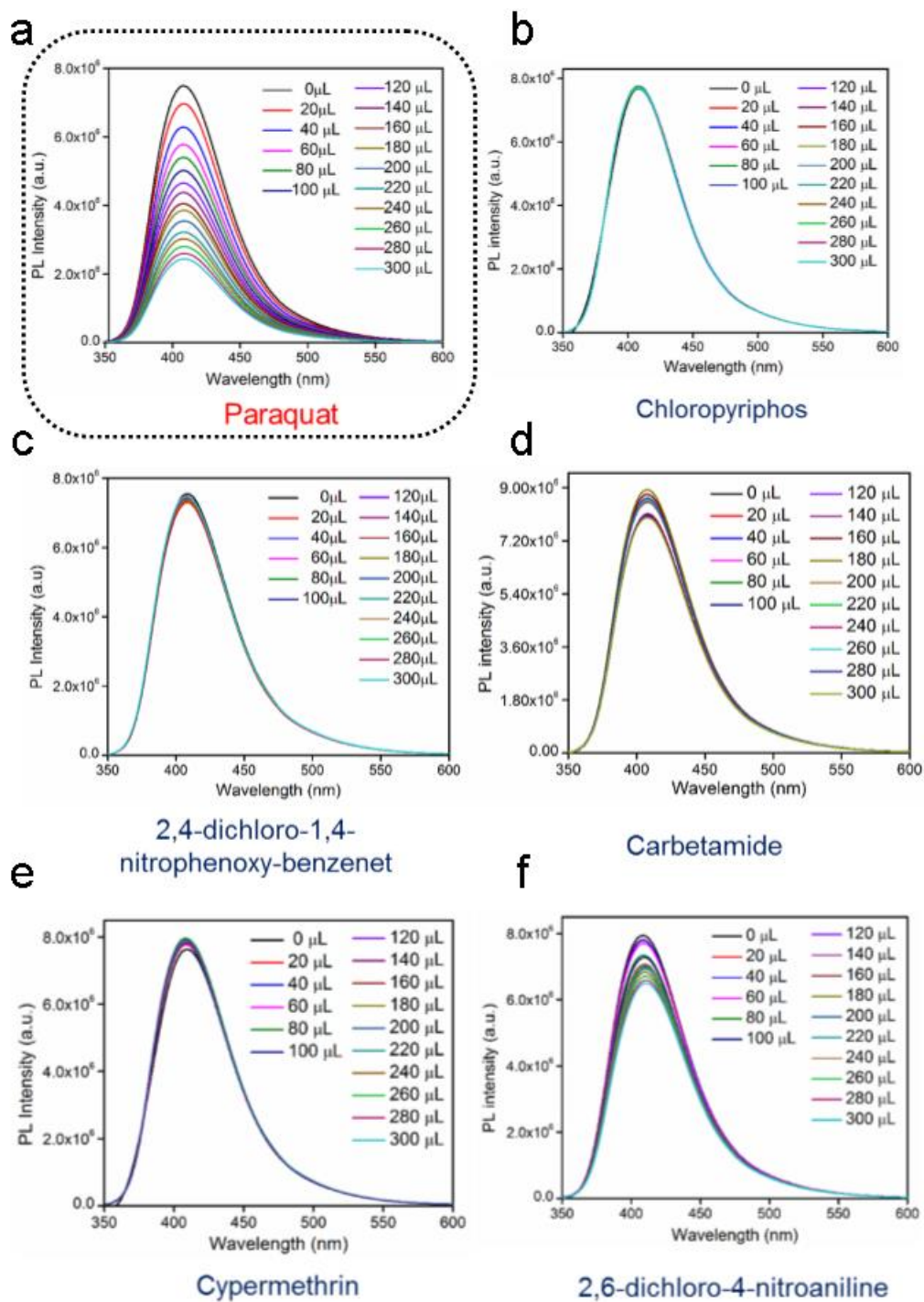
NFZ

NFT

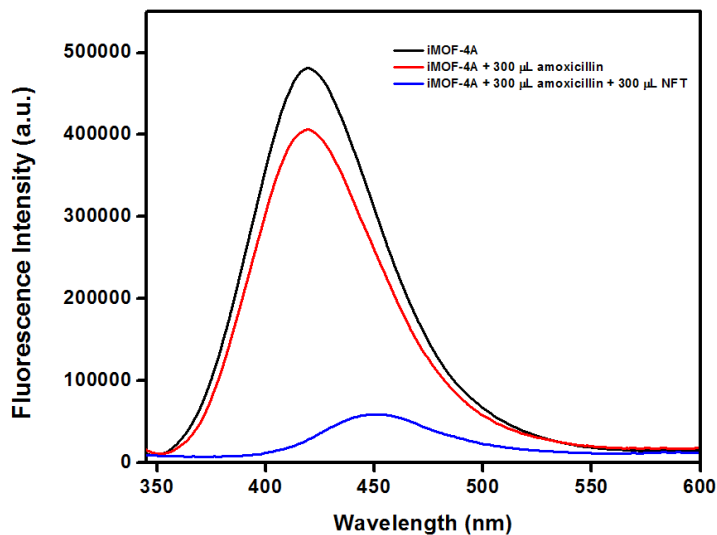
Appendix 9. Selective fluorescence quenching response of different antibiotics; ampicillin, norfloxacin, sulphaguanidine, spectinomycin, nitrofurazone (NFZ) and nitrofurantoin (NFT) respectively. NFZ and NFT showing notable fluorescence quenching response for **iMOF-4A**.



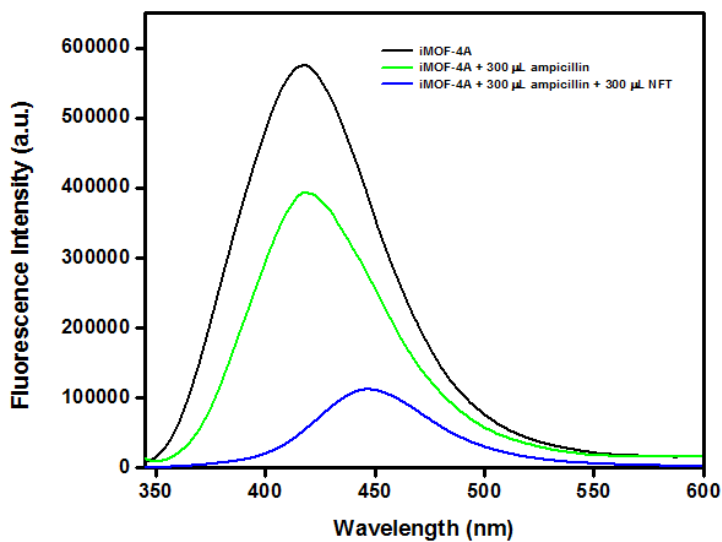
Appendix 10. Chemical structures of the group of different pesticides selected for sensing and capture studies; inset: pesticide (paraquat) of choice for sensing studies.



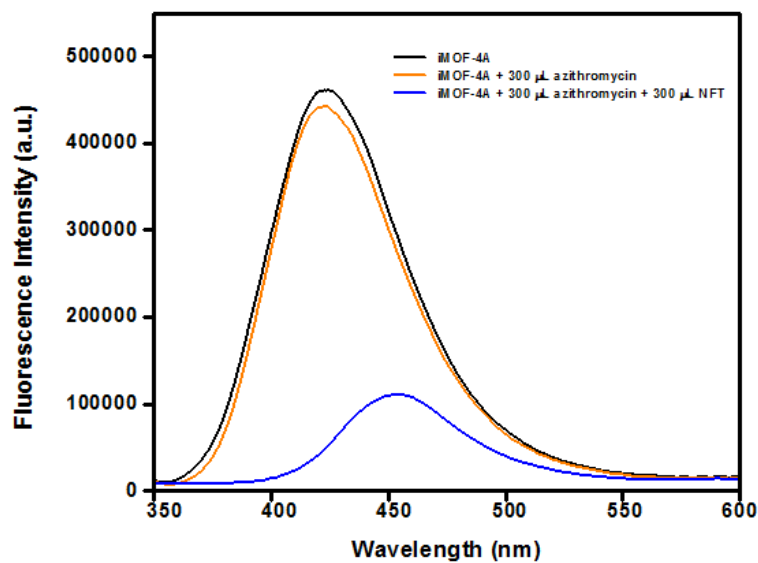
Appendix 11. Fluorescence quenching response of **iMOF-4A** for variety of pesticides including (a) paraquat, (b) chloropyrifos, (c) 2,4-dichloro-1-(4-nitrophenoxy)benzene, (d) carbetamide, (e) Cypermethrin, (f) 2,6-dichloro-4-nitroaniline.



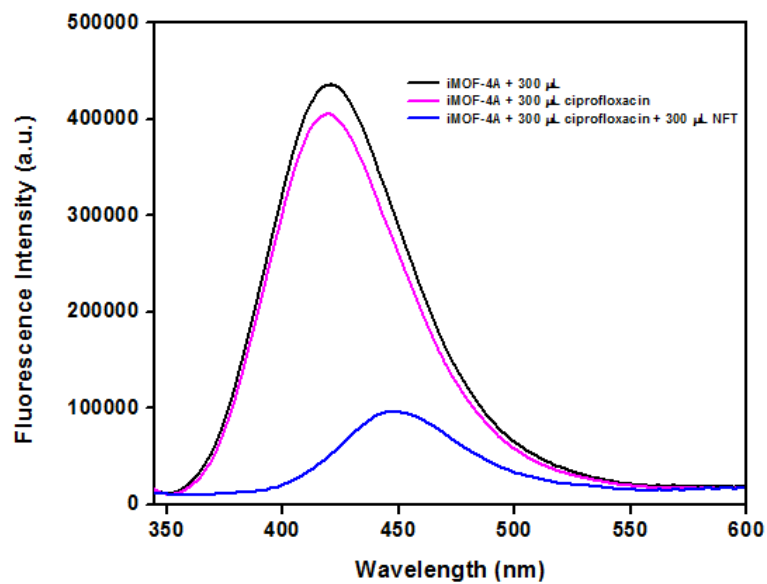
Appendix 12. Fluorescence quenching response of **iMOF-4A** for amoxicillin titrated against NFT in aliquots of 300 μ L each.



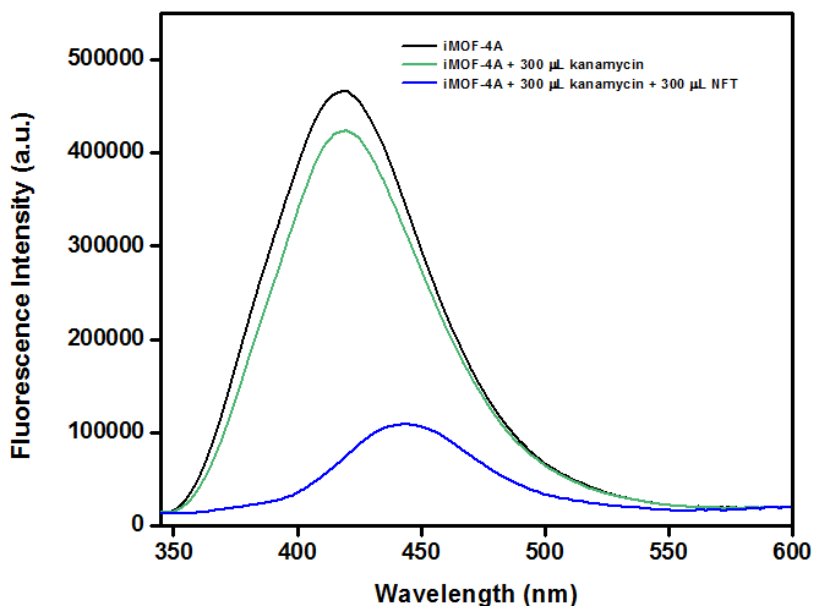
Appendix 13. Fluorescence quenching response of **iMOF-4A** for ampicillin titrated against NFT in aliquots of 300 μ L each.



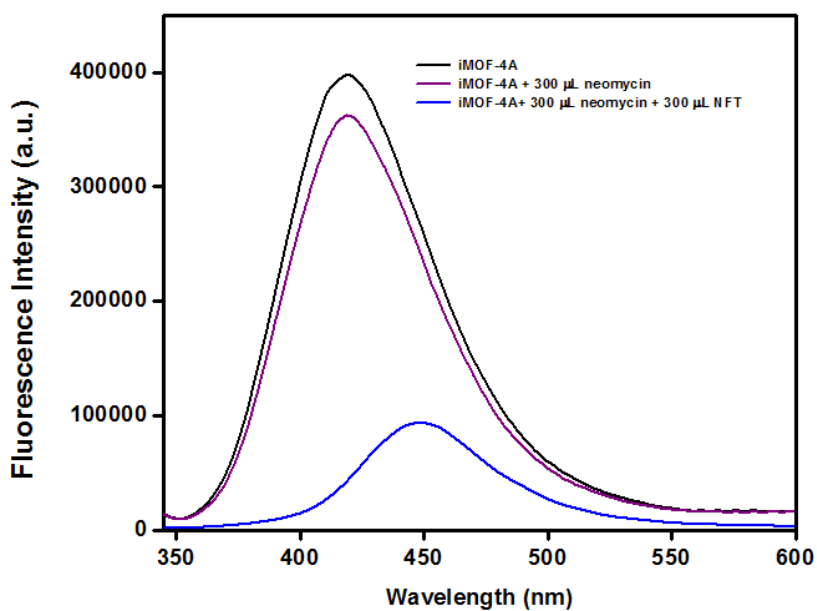
Appendix 14. Fluorescence quenching response of **iMOF-4A** for azithromycin titrated against NFT in aliquots of 300 μL each.



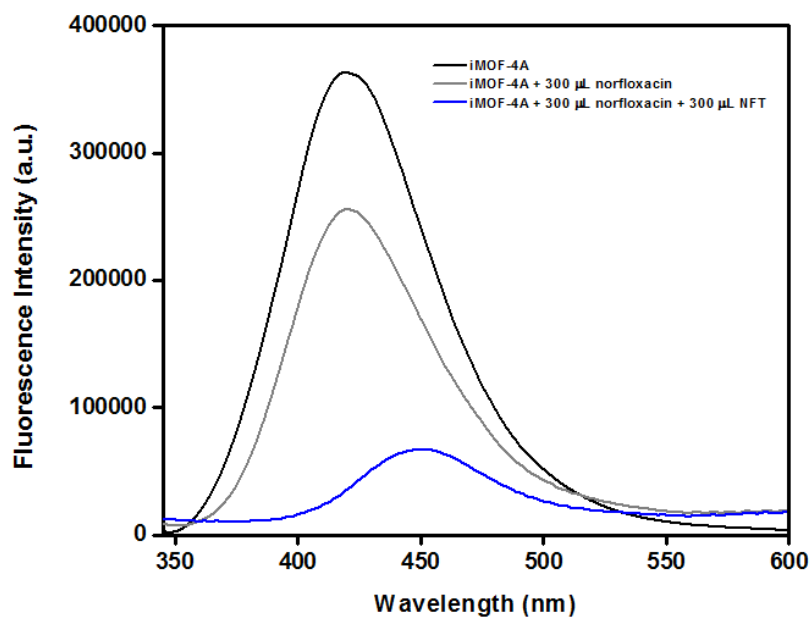
Appendix 15. Fluorescence quenching response of **iMOF-4A** for ciprofloxacin titrated against NFT in aliquots of 300 μL each.



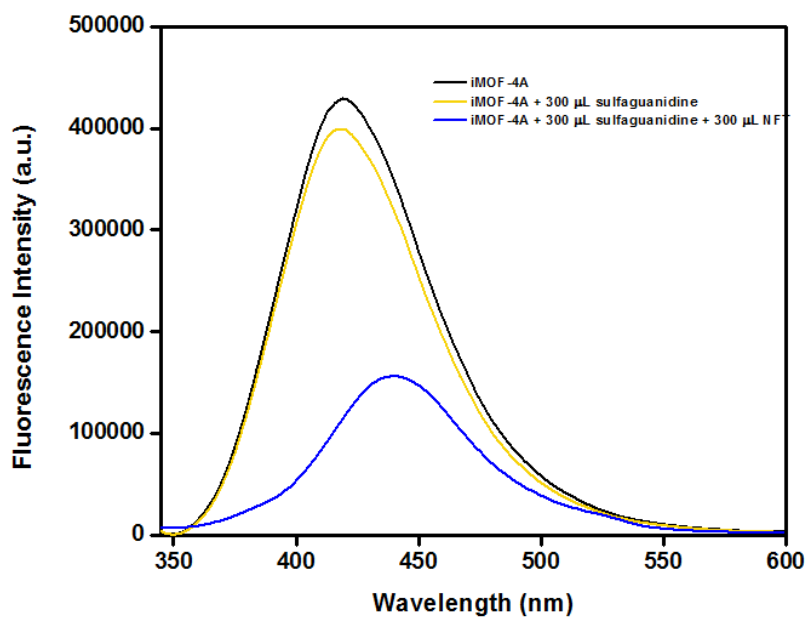
Appendix 16. Fluorescence quenching response of **iMOF-4A** for kanamycin titrated against NFT in aliquots of 300 μL each.



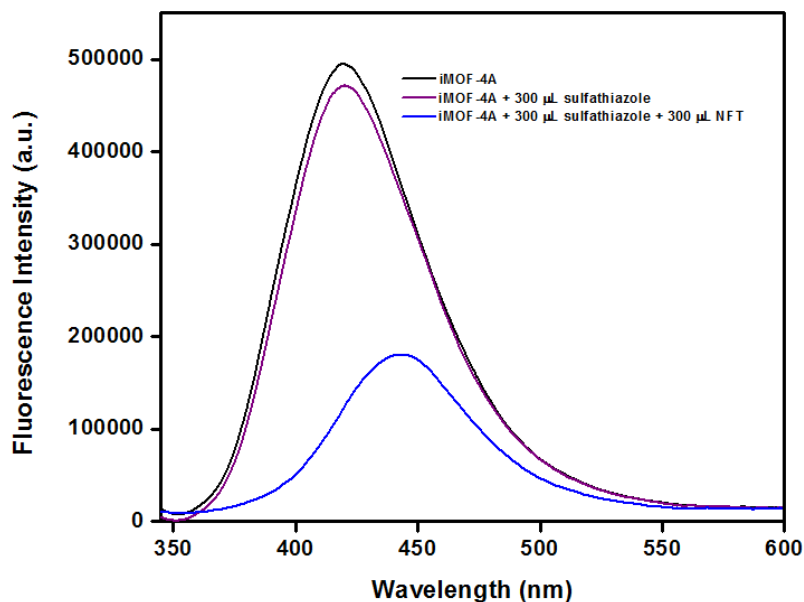
Appendix 17. Fluorescence quenching response of **iMOF-4A** for neomycin titrated against NFT in aliquots of 300 μL each.



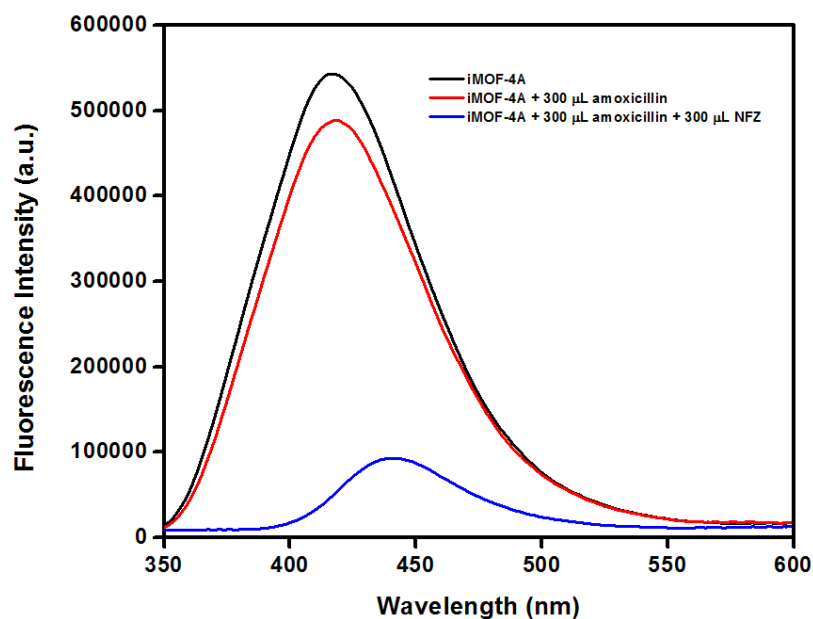
Appendix 18. Fluorescence quenching response of **iMOF-4A** for norfloxacin titrated against NFT in aliquots of 300 μ L each.



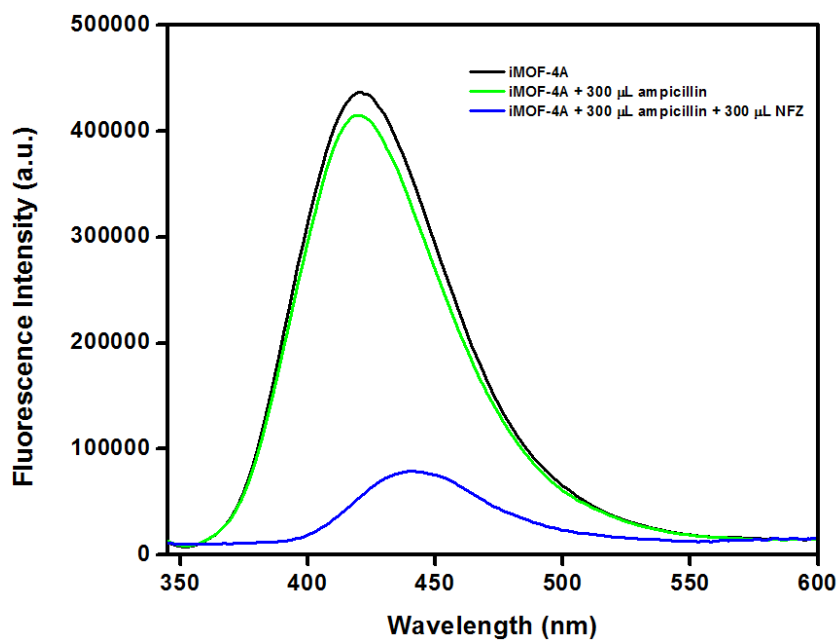
Appendix 19. Fluorescence quenching response of **iMOF-4A** for sulphaguanidine titrated against NFT in aliquots of 300 μ L each.



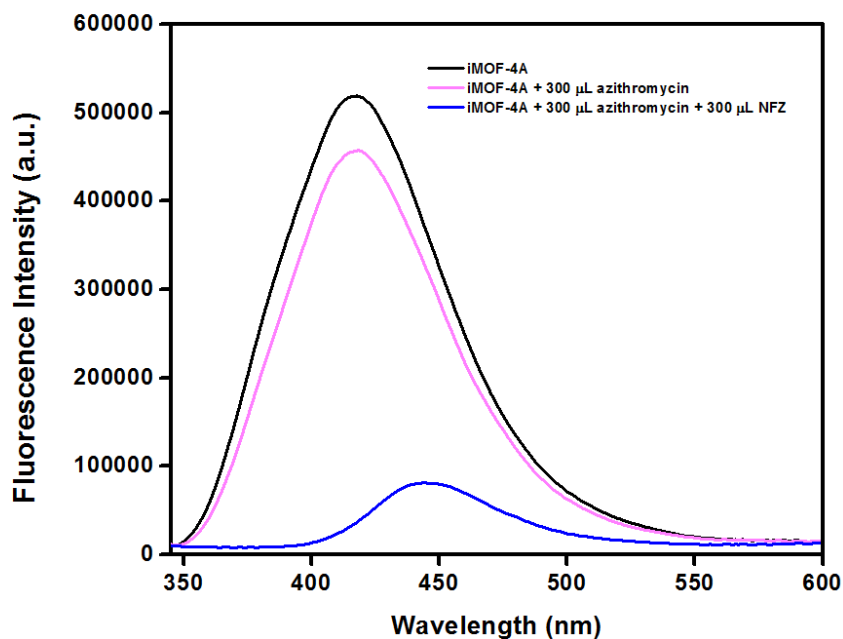
Appendix 20. Fluorescence quenching response of **iMOF-4A** for sulfathiazole titrated against NFT in aliquots of 300 μ L each.



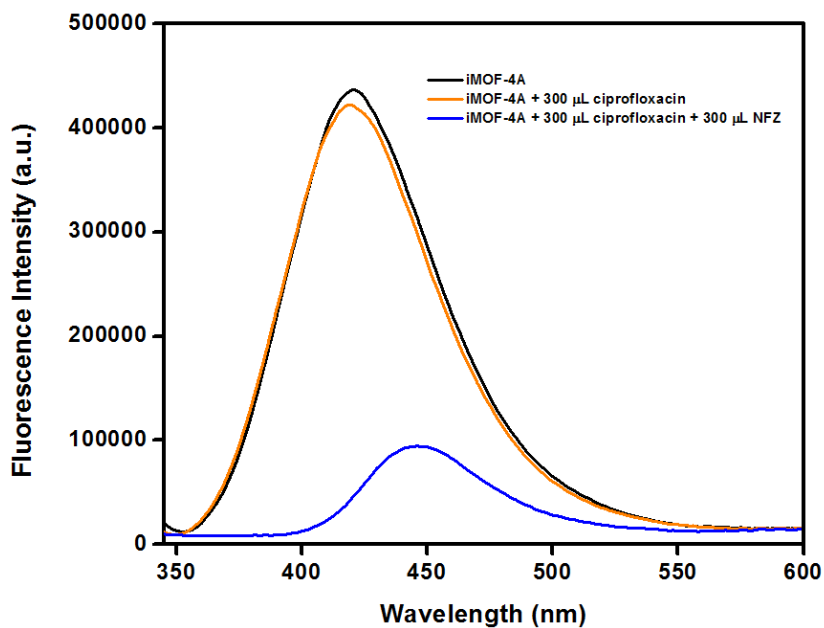
Appendix 21. Fluorescence quenching response of **iMOF-4A** for amoxicillin titrated against NFZ in aliquots of 300 μ L each.



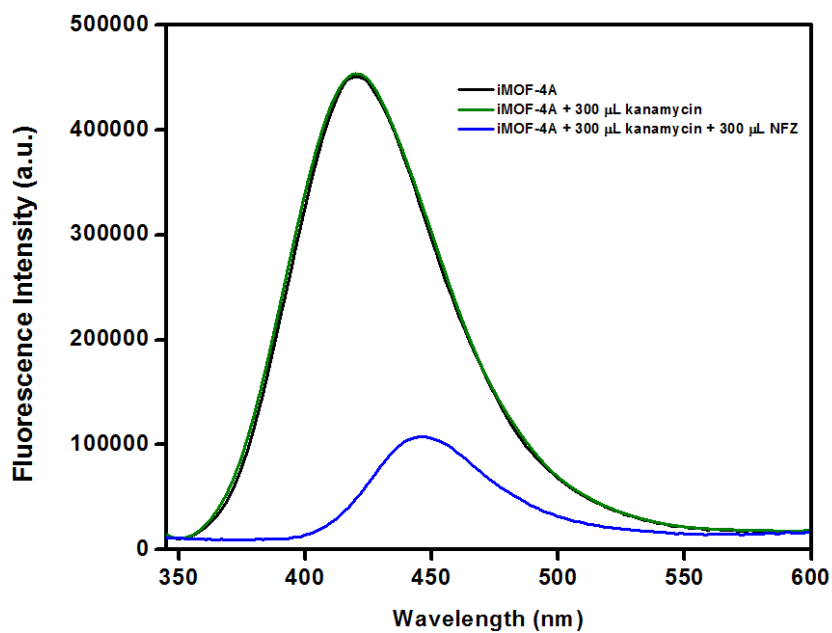
Appendix 22. Fluorescence quenching response of **iMOF-4A** for ampicillin titrated against NFZ in aliquots of 300 μ L each.



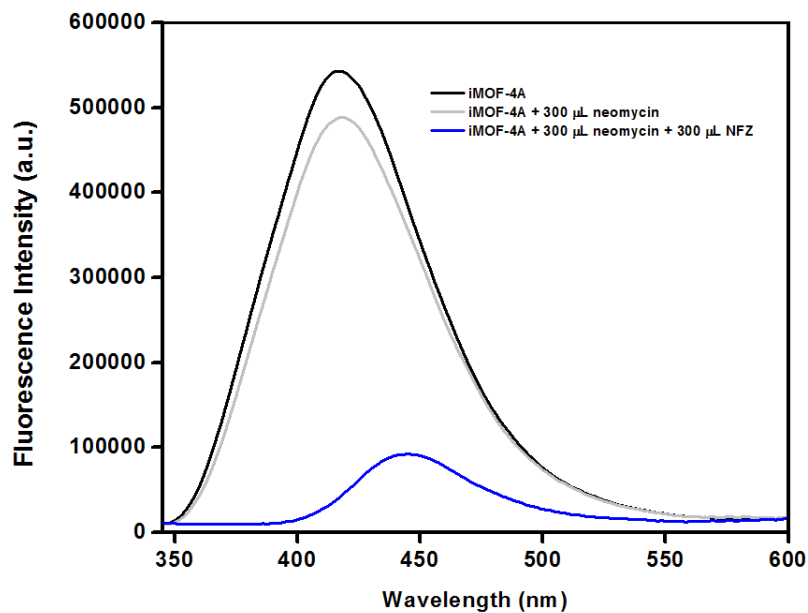
Appendix 23. Fluorescence quenching response of **iMOF-4A** for azithromycin titrated against NFZ in aliquots of 300 μ L each.



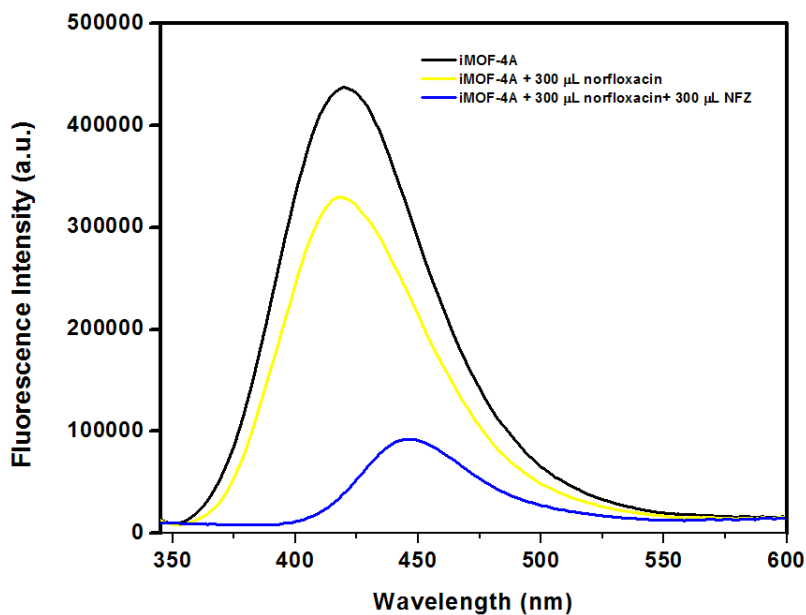
Appendix 24. Fluorescence quenching response of **iMOF-4A** for ciprofloxacin titrated against NFZ in aliquots of 300 μ L each.



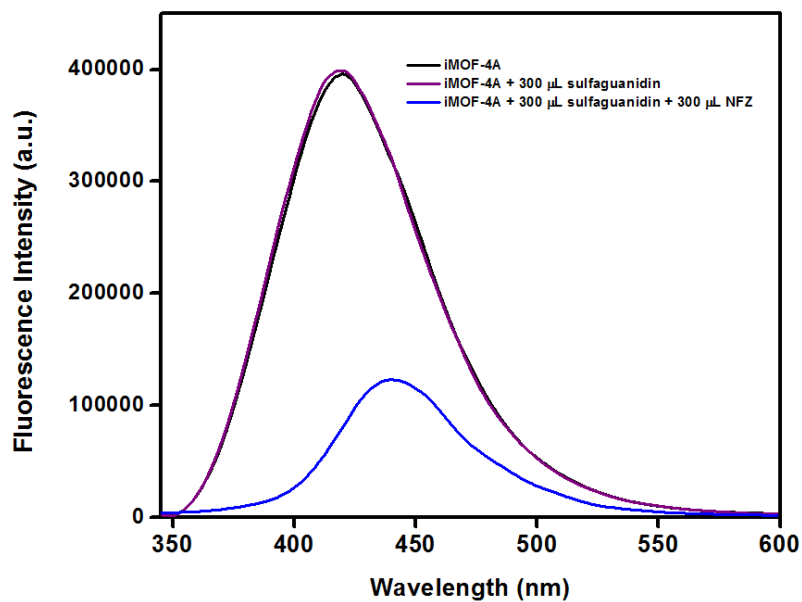
Appendix 25. Fluorescence quenching response of **iMOF-4A** for kanamycin titrated against NFZ in aliquots of 300 μ L each.



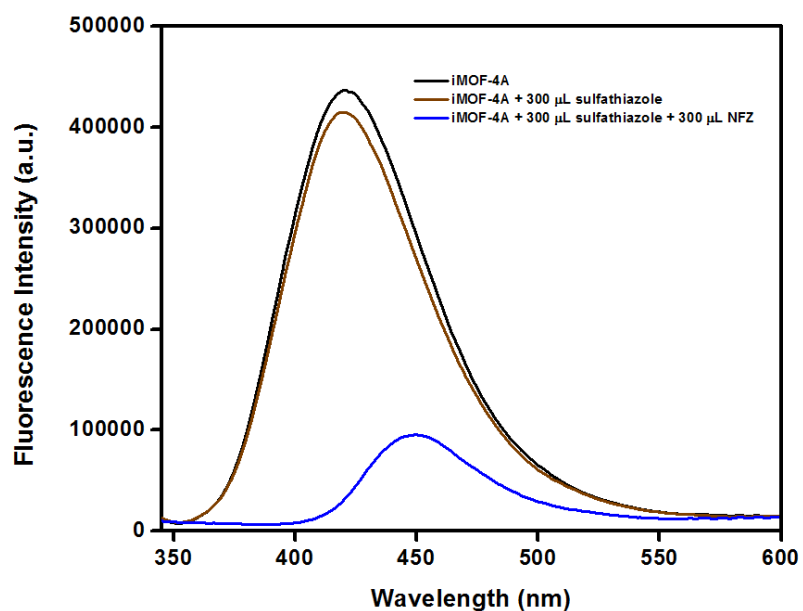
Appendix 26. Fluorescence quenching response of **iMOF-4A** for neomycin titrated against NFZ in aliquots of 300 μ L each.



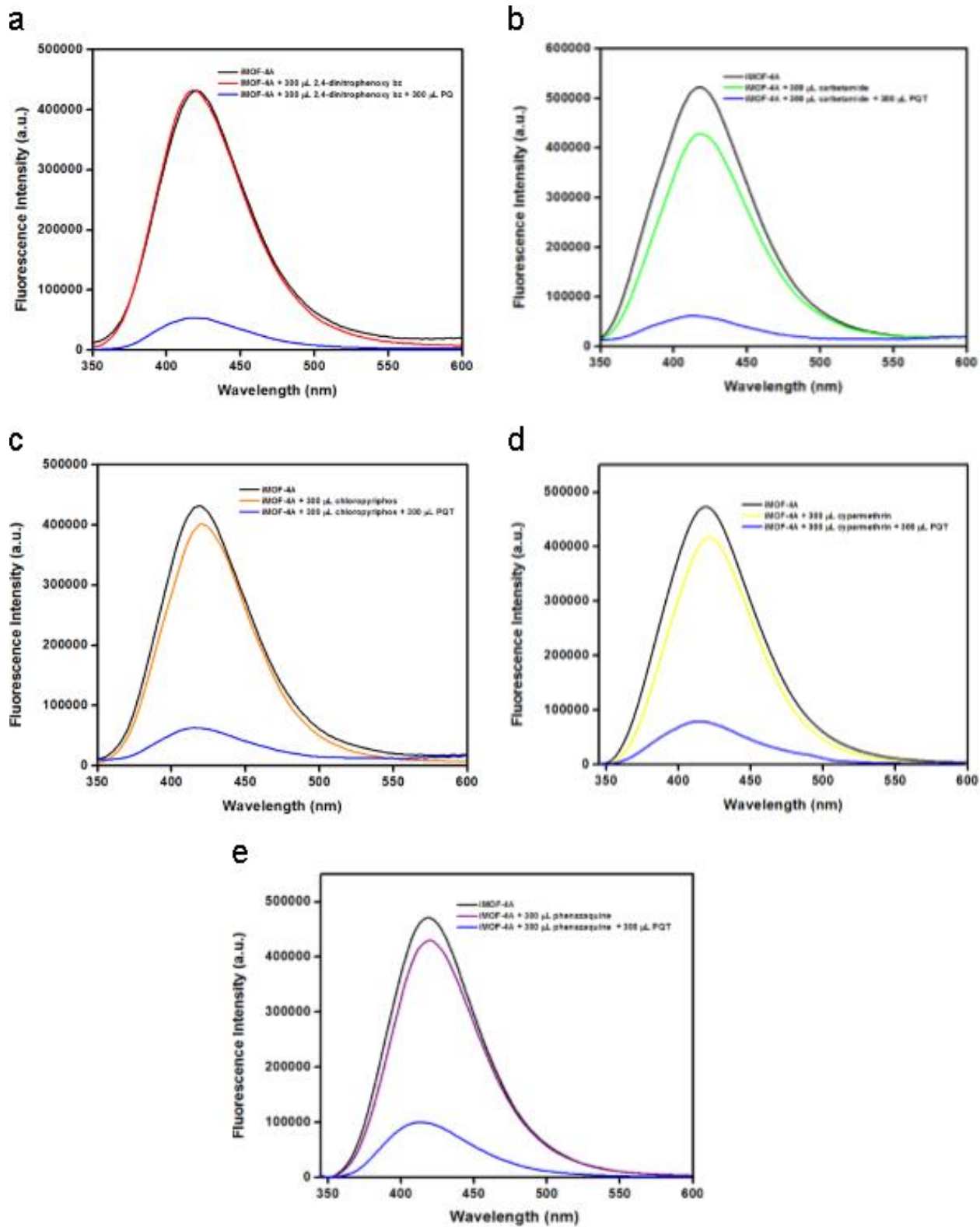
Appendix 27. Fluorescence quenching response of **iMOF-4A** for norfloxacin titrated against NFZ in aliquots of 300 μ L each.



Appendix 27. Fluorescence quenching response of **iMOF-4A** for sulphaguanidine titrated against NFZ in aliquots of 300 μ L each.



Appendix 28. Fluorescence quenching response of **iMOF-4A** for sulfathiazole titrated against NFZ in aliquots of 300 μ L each.



Appendix 29. Selective fluorescence quenching response given by **iMOF-4A** upon treatment of 300 μL of (a) 2,4-dichloro-1-(4-nitrophenoxy)benzene, (b) Carbetamide, (c) Chloropyriphos, (d) Cypermethrin, (e) Phenazaquin followed by the addition of 300 μL of PQ in each.

3.5 References:

- [1] S. L. James, *Chem. Soc. Rev.* **2003**, 32, 276.
- [2] J. A. Mason, M. Veenstra, J. R. Long, *Chem. Sci.* **2013**, 5, 32.
- [3] P. Nugent, Y. Belmabkhout, S. D. Burd, A. J. Cairns, R. Luebke, K. Forrest, T. Pham, S. Ma, B. Space, L. Wojtas, M. Eddaoudi, M. J. Zaworotko, *Nature* **2013**, 495, 80.
- [4] Z. Hu, K. Tan, W. P. Lustig, H. Wang, Y. Zhao, C. Zheng, D. Banerjee, T. J. Emge, Y. J. Chabal, J. Li, *Chem. Sci.* **2014**, 5, 4873.
- [5] C. Orellana-Tavra, E. F. Baxter, T. Tian, T. D. Bennett, N. K. H. Slater, A. K. Cheetham, D. Fairen-Jimenez, *Chem. Commun.* **2015**, 51, 13878.
- [6] M. Kim, J. F. Cahill, H. Fei, K. A. Prather, S. M. Cohen, *J. Am. Chem. Soc.* **2012**, 134, 18082.
- [7] S. S. Nagarkar, S. M. Unni, A. Sharma, S. Kurungot, S. K. Ghosh, *Angew Chem Int Ed Engl* **2014**, 53, 2638.
- [8] C. He, D. Liu, W. Lin, *Chem. Rev.* **2015**, 115, 11079.
- [9] V. Stavila, A. A. Talin, M. D. Allendorf, *Chem. Soc. Rev.* **2014**, 43, 5994.
- [10] A. Karmakar, P. Samanta, A. V. Desai, S. K. Ghosh, *Acc. Chem. Res.* **2017**, 50, 2457.
- [11] B. Chen, N. W. Ockwig, A. R. Millward, D. S. Contreras, O. M. Yaghi, *Angewandte Chemie International Edition* **2005**, 44, 4745.
- [12] L. Keith, W. Telliard, *Environ. Sci. Technol.* **1979**, 13, 416.
- [13] S. Mukherjee, A. V. Desai, Y. D. More, A. I. Inamdar, S. K. Ghosh, *ChemPlusChem* **2016**, 81, DOI 10.1002/cplu.201680861.
- [14] M. Palmer, E. Bernhardt, E. Chornesky, S. Collins, A. Dobson, C. Duke, B. Gold, R. Jacobson, S. Kingsland, R. Kranz, M. Mappin, M. L. Martinez, F. Micheli, J. Morse, M. Pace, M. Pascual, S. Palumbi, O. J. Reichman, A. Simons, A. Townsend, M. Turner, *Science* **2004**, 304, 1251.
- [15] D. R. Godschalk, *Natural Hazards Review* **2003**, 4, 136.
- [16] “Resolution adopted by the General Assembly on 25 September 2015. Transforming our world: the 2030 Agenda for Sustainable Development — European Environment Agency,” can be found under <https://www.eea.europa.eu/policy-documents/resolution-adopted-by-the-general>, **n.d.**

- [17] M. B. Luo, Y. Y. Xiong, H. Q. Wu, X. F. Feng, J. Q. Li, F. Luo, *Angewandte Chemie International Edition* **2017**, *56*, 16376.
- [18] D. Tilman, K. G. Cassman, P. A. Matson, R. Naylor, S. Polasky, *Nature* **2002**, *418*, 671.
- [19] S. T. Narendran, S. N. Meyyanathan, B. Babu, *Food Research International* **2020**, *133*, 109141.
- [20] A. Mojiri, J. L. Zhou, B. Robinson, A. Ohashi, N. Ozaki, T. Kindaichi, H. Farraji, M. Vakili, *Chemosphere* **2020**, *253*, 126646.
- [21] J. Tang, X. Ma, J. Yang, D.-D. Feng, X.-Q. Wang, *Dalton Trans.* **2020**, *49*, 14361.
- [22] S. B. Grant, J.-D. Saphores, D. L. Feldman, A. J. Hamilton, T. D. Fletcher, P. L. M. Cook, M. Stewardson, B. F. Sanders, L. A. Levin, R. F. Ambrose, A. Deletic, R. Brown, S. C. Jiang, D. Rosso, W. J. Cooper, I. Marusic, *Science* **2012**, *337*, 681.
- [23] D. Moreno-González, F. J. Lara, N. Jurgovská, L. Gámiz-Gracia, A. M. García-Campaña, *Analytica Chimica Acta* **2015**, *891*, 321.
- [24] null Hakansson, null Coorey, null Zubarev, null Talrose, null Hakansson, *J Mass Spectrom* **2000**, *35*, 337.
- [25] M. Tabrizchi, V. Ilbeigi, *J Hazard Mater* **2010**, *176*, 692.
- [26] M. E. Germain, M. J. Knapp, *Chem. Soc. Rev.* **2009**, *38*, 2543.
- [27] W. P. Lustig, S. Mukherjee, N. D. Rudd, A. V. Desai, J. Li, S. K. Ghosh, *Chem. Soc. Rev.* **2017**, *46*, 3242.
- [28] B. Wang, X.-L. Lv, D. Feng, L.-H. Xie, J. Zhang, M. Li, Y. Xie, J.-R. Li, H.-C. Zhou, *J. Am. Chem. Soc.* **2016**, *138*, 6204.
- [29] S. Mandal, A. Dey Bhowmik, A. Mukhuty, S. Kundu, K.-N. Truong, K. Rissanen, A. Chattopadhyay, P. Sahoo, *Sci Rep* **2022**, *12*, 9307.
- [30] D.-W. Sun, L. Huang, H. Pu, J. Ma, *Chem. Soc. Rev.* **2021**, *50*, 1070.
- [31] M.-L. Xu, Y. Gao, X. X. Han, B. Zhao, *J. Agric. Food Chem.* **2017**, *65*, 6719.
- [32] D. Shetty, S. Boutros, T. Skorjanc, B. Garai, Z. Asfari, J. Raya, A. Trabolsi, *J. Mater. Chem. A* **2020**, *8*, 13942.
- [33] J. Zhang, S. Xiang, P. Wu, D. Wang, S. Lu, S. Wang, F. Gong, X. Wei, X. Ye, P. Ding, *Science of The Total Environment* **2022**, *811*, 152351.
- [34] C. Du, Z. Zhang, G. Yu, H. Wu, H. Chen, L. Zhou, Y. Zhang, Y. Su, S. Tan, L. Yang, J. Song, S. Wang, *Chemosphere* **2021**, *272*, 129501.
- [35] B. S. Pilgrim, N. R. Champness, *ChemPlusChem* **2020**, *85*, 1842.

- [36] Y. D. More, S. Saurabh, S. Mollick, S. K. Singh, S. Dutta, S. Fajal, A. Prathamshetti, M. M. Shirolkar, S. Panchal, M. Wable, S. Ogale, S. K. Ghosh, *Advanced Materials Interfaces* **n.d.**, *n/a*, 2201713.
- [37] S. S. Nagarkar, A. V. Desai, S. K. Ghosh, *CrystEngComm* **2016**, *18*, 2994.
- [38] S. S. Nagarkar, B. Joarder, A. K. Chaudhari, S. Mukherjee, S. K. Ghosh, *Angewandte Chemie* **2013**, *125*, 2953.
- [39] A. Bavykina, N. Kolobov, I. S. Khan, J. A. Bau, A. Ramirez, J. Gascon, *Chem. Rev.* **2020**, *120*, 8468.
- [40] L. E. Kreno, K. Leong, O. K. Farha, M. Allendorf, R. P. Van Duyne, J. T. Hupp, *Chem. Rev.* **2012**, *112*, 1105.
- [41] H.-Y. Li, S.-N. Zhao, S.-Q. Zang, J. Li, *Chem. Soc. Rev.* **2020**, *49*, 6364.
- [42] X. Fang, B. Zong, S. Mao, *Nano-Micro Lett.* **2018**, *10*, 64.
- [43] H. Chen, P. Fan, X. Tu, H. Min, X. Yu, X. Li, J.-L. Zeng, S. Zhang, P. Cheng, *Chemistry – An Asian Journal* **2019**, *14*, 3611.
- [44] Q. Xie, Y. Li, Z. Lv, H. Zhou, X. Yang, J. Chen, H. Guo, *Sci Rep* **2017**, *7*, 3316.

Part-II

**Advanced Porous Materials for Energy
Applications**

Worldwide reliance on fossil fuels for energy production is detrimental to ecosystems and threatens future supplies. Therefore, there has been a shift toward using renewable energy. Mechanical energy and other sources have likely received less attention than wind and solar power. Human motion, wind, and tidal energy are all examples of mechanical motions that have historically been underutilised. Fortunately, researchers are beginning to see alternative energy as a viable option for addressing the world's mounting energy crises. Wearable electronics, high-precision sensors, portable high-voltage sources, and distributed micro/nano-power sources are just some of the areas where mechanical energy conversion technologies have made great strides in the last decade. Triboelectric nanogenerators (TENGs) are central to this development because they rely on the principle of charge separation brought about by relative motion between two dissimilar materials in close proximity; the familiar phenomenon of friction is an expression of this process. Thereby, over the past few years, Triboelectric nanogenerators have received a great deal of attention in the renewable energy space.^[1,3] The triboelectric effect and electrostatic induction were first successfully coupled by Wang and his team in 2012, allowing TENGs to generate tiny amounts of electricity.^[1-5] Since then, TENGs have advanced greatly, and interest in studying them has exploded around the world. This alternative energy source emerges as the world undergoes an energy revolution and takes giant leaps away from burning fossil fuels.^[4] It's also happening at the same time that a lot of sophisticated sensors and gadgets are being invented. Prioritization has shifted from device optimization to the 'energy bottleneck,' or the question of how to provide sustainable power for all these devices, for example, consider all the smartphones, tablets, and wearable sensors that people rely on regularly. In order to produce a research that broadens the scope of understanding and application of TENGs throughout results, we have made an effort to condense and comprehend the most recent developments in the field of TENGs for energy generation. We have done this by using our thorough understanding of these developments in a thematic manner. With a focus on developing nanogenerator devices that can be deployed for wearables, waves, winds, and transportation, the same has been lucidly summarised in the following chapters with emphasis on noteworthy results in a concise manner and highlighting particularly necessary results. We also look ahead to the opportunities and challenges that lie ahead for TENGs.

We attempted and concentrated our efforts in this section on developing unique composites initially and then devices for real time applications by using advanced porous materials and their features tuned properties that are blended by polymer based composites. The triboelectric series illustrates the variation in electron transfer and absorption between materials at close proximity. Materials that are further apart in this series are used as partners in a TENG device to achieve maximum power output. How the device is set up has a significant impact on how well the design facilitates charge transfer. Chapters 4 and 5 make up this section. In chapter four, we used a highly stable MOF for a repeatable, robust, and tuneable

application in the domain of Triboelectric Nanogenerators, and in chapter five, we used a chemically stable, solution processable, and hydrophobicity tuned series of MOPs blended by Polymer composites as a first-of-its-kind example for on-demand self-powered energy devices that are correlated to hydrophobicity features of chemically functionalised metal-organic polyhedra (MOP), highlighting a first-of-its-kind example in the domain of MOP.^[6]

References:

- [1] F. Fan, Z. Tian, Z. L. Wang, **2012**, DOI 10.1016/J.NANOEN.2012.01.004.
- [2] K. R. S. D. Gunawardhana, N. D. Wanasekara, R. D. I. G. Dharmasena, *iScience* **2020**, *23*, 101360.
- [3] C. Wu, A. C. Wang, W. Ding, H. Guo, Z. L. Wang, *Advanced Energy Materials* **2019**, *9*, 1802906.
- [4] H. Askari, Z. Saadatnia, A. Khajepour, M. B. Khamesee, J. Zu, *Advanced Engineering Materials* **2017**, *19*, 1700318.
- [5] J. Wang, H. Wang, N. V. Thakor, C. Lee, *ACS Nano* **2019**, *13*, 3589.
- [6] Y. D. More, S. Saurabh, S. Mollick, S. K. Singh, S. Dutta, S. Fajal, A. Prathamshetti, M. M. Shirolkar, S. Panchal, M. Wable, S. Ogale, S. K. Ghosh, *Advanced Materials Interfaces* n.d., *n/a*, 2201713.

Chapter 4

Highly Stable and End-group Tuneable Metal–organic Framework / Polymer Composite for Superior Triboelectric Nanogenerator Application

4.1 Introduction

The worldwide reliance on fossil fuels has a negative impact on the environment and threatens future generations' access to these resources. As a result, it's become more important than ever to rely on sustainable energy sources. Although solar and wind power have garnered the greatest attention, other forms of renewable energy, such as mechanical power, have been less well investigated. In reality, until recently, much of the energy available from various mechanical motions, such as human motion, wind, and water tidal energy, was wasted and disregarded. Fortunately, scientists have started to take note of these alternative energy sources, which can help alleviate some of the pressures on the energy sector.^[1,2] Indeed, the last ten years have seen significant development in mechanical energy conversion technologies, particularly in the areas of distributed micro/nano-power sources, portable high-voltage sources, wearable electronics, and high-precision sensors. Triboelectric nanogenerators (TENG) are at the center of this development; these devices essentially utilize the idea of charge separation achieved by relative motion between two dissimilar materials in close proximity, with the familiar phenomenon of friction being a representation of this process. As seen in the so-called triboelectric series, the differences between materials arise from their different capacities to donate or take electrons in the context of the relative movement mode.^[3] The TENG device's maximum power output is achieved by pairing dissimilar materials located further apart in this series. The way the devices are set up has a lot to do with how well a certain design lets charge flow between them.

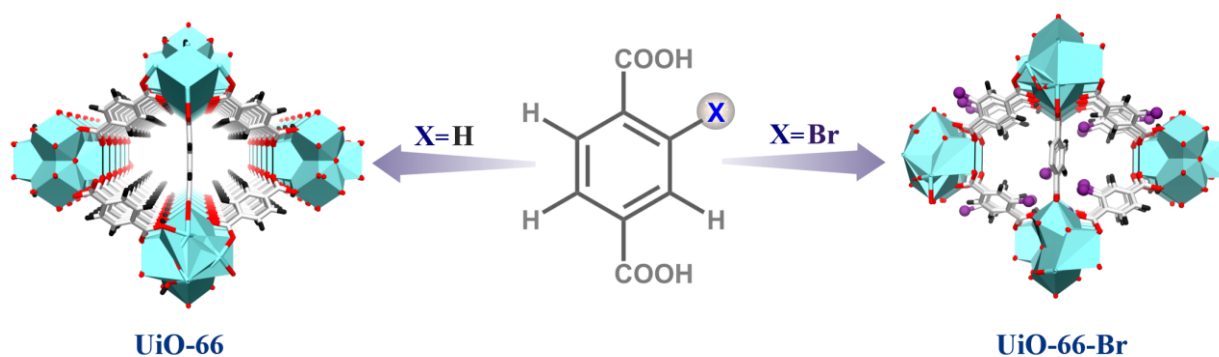
In 2012, Wang and co-workers developed an efficient method for TENG fabrication to overcome the limitations of current energy technology and thereby aiding the development of sustainable energy sources.^[5] The TENG is capable of converting a wide range of energy forms into electricity, such as those derived from mechanical, wind, biomechanical, wave, and water flows.^[7-9] Using contact electrification and electrostatic induction, the TENG can operate in four different modes such as single electrode modes, freestanding, vertical contact-separation, and lateral sliding. Considering that the two distinct triboelectric materials which come into contact with one another, a tribo-layer and a conductive layer are the two of the most important TENG components, and they must be bonded to a substrate material acting as a support framework in order to create a working device.^[1,10-12] The cost-effectiveness, simplicity of design, large power output, and better conversion efficiency of TENG are only a few of the many benefits of this device.^[10] Several strategies have been deployed in performance enhancements of TENG, such as low-energy ion irradiation that can directly modify the chemical bonds and thereby functional groups of

triboelectric polymers at molecular levels. This method modifies the target polymer's electrification capabilities with negligible modification in its mechanical flexibility and surface roughness.^[11] Variable rheological forging release times can be utilized to regulate crystallinity, molecular orientation and dielectric constant of materials. These variations in molecular structure and crystallinity result in unique electrification performance prior and after corona polarization, proposing several strategies for increasing the triboelectric outcome of electret and non-electret polymers.^[12]

Further, precise modulation of currents that are induced on skin can be brought to a sensitive virtual tactile sensation by means of electro-tactile (ET) devices.^[13] TENGs may be used for a multitude of applications such as big data sensing, biological and chemical sensors, therapeutics and self-charging.^[1,16-18] Indeed, a rising number of self-powered applications are expected to be based on TENGs, because of its ease of manufacture, material selection, high power output, and ability to produce direct current using a variety of approaches.^[10,14,15] Polymers prevail over metals in the triboelectric series, acting as the basic building blocks for TENG manufacture.^[19,20] However, selective and orderly functionalization of polymeric materials is difficult, which instigates a strong need for the development and deployment of alternate multifunctional materials for TENG application. Metal Organic Frameworks in view of their molecular tuneability, appears to be the promising candidates in this respect.^[1,14,16] MOFs have recently been used to harvest energy via a triboelectric nanogenerator (TENG), which combines the triboelectric effect with electrostatic induction.^[21,22] Literature reports reveal TENGs fabricated from zeolitic imidazole framework members, HKUST-1, and a few other MOFs, including UiO series.^[21,23] Due to their excellent performance and versatility, MOFs are employed as multi-functional materials in the triboelectric series.^[21-23] MOFs can serve as positive or negative triboelectric materials depending on the functional group. Due to improved charge holding capability, the bromine-functionalized porous materials produce higher output with PVDF as the opposite layer than their non-bromine-containing counterparts do.^[24] Fluorinated MOFs can also be highly tribonegative materials.^[25] Long-term development requires nontoxic MOFs with no negative effects on the environment or biological systems.^[21] In the future, non-toxic and biocompatible MOFs could be used to make new TENG-based stents and biodegradable sensors.^[21,25]

Besides, MOFs are well-known for their rich architectures and diverse functions, which are governed by ligands or metal ions, and have emerged as a new class of porous materials that promises to be the next generation functional porous materials, with added advantage of pre and post-synthetic functionalization's. Unlike the majority of MOFs, zirconium-based MOFs are recognized for their

excellent stability due to strong coordination interaction between the zirconium metal ions and the organic ligands, which molds them into suitable platform for the development of composite materials.^[26-28] UiO-66 (UiO: University of Oslo), MOF with a $Zr_6O_4(OH)_4$ cluster joined by a terephthalic linker, which is also prone to pre-synthetic functionalization by modifying length and functionality of the ligand which offers desired features of interest to the aforementioned TENG application.^[1,29] UiO-66 has exceptional chemical and thermal stability, easy to synthesize, and has a relatively large surface area in conjunction with adjustable functionalities.^[29] The influence of organic ligands on the characteristics of Zr-based metal-organic framework (Zr-MOF) for applications such as sensing, separation, and catalysis is extensively documented in the literature, but it still awaits rational and efficient utilization in the nanogenerator arena.^[30] The family of UiO-66 MOFs inherits the great potential to be utilized to extend the triboelectric series as well as to find applications in the fields of mechanical energy harvesting.^[31] Herein, we have introduced a functional group driven tuning of organic moiety (and thus MOF) that directly influence the TENG output performance. To achieve this, isorecticular frameworks of UiO-66 (compound 1) and UiO-66-Br (compound 2) are strategically used, which have identical dimensional and operating conditions of composite-fabricated devices (1/PVDF and 2/PVDF), thus providing rational platform to elucidate, deploy and exploit functional groups electronic effects to govern TENG output performance. It allowed us to understand and utilize the virtue of tunable properties at nanoscale and to exploit its concurrent effect at bulk scale for MOF-TENG derived self-powered system and subsequent sensor applications. The guest free phases of compound 1 and compound 2 are probed as a potential triboelectric layer by means of MOF/PVDF composite in the TENG device.

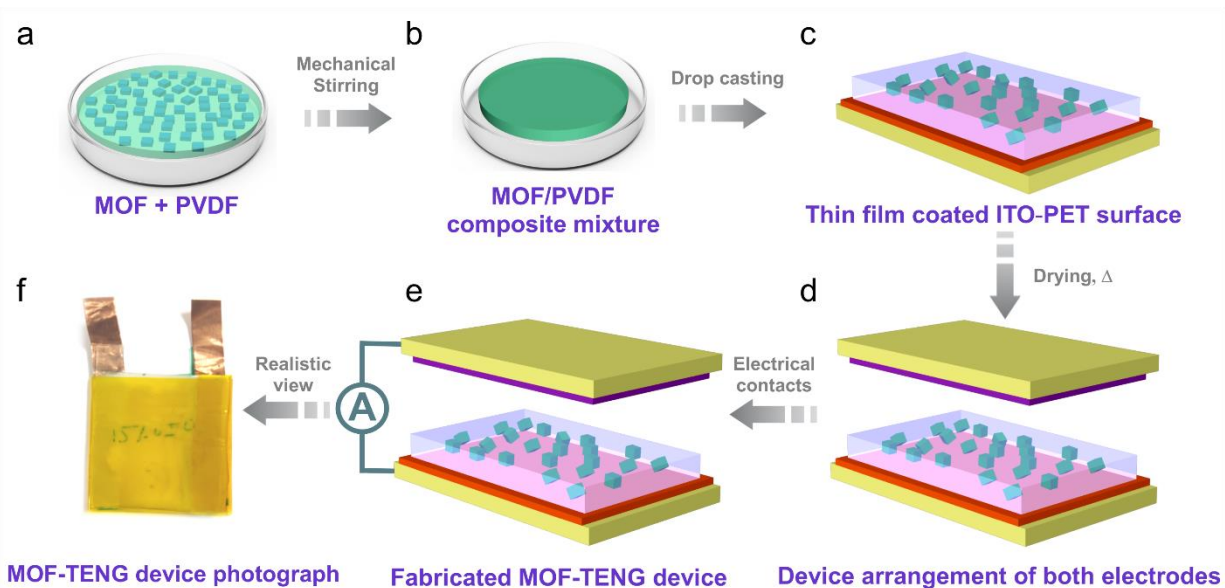


Scheme 1: Schematic illustration of the synthesis of compound 1 (UiO-66) and 2 (UiO-66-Br) by ligand functionalization.

Compound 1 made up of $Zr_6O_4(OH)_4$ secondary building units (SBUs) linked together by 1,4-benzene-

dicarboxylate (BDC) ligands to form porous frameworks with *Fm-3m* face-centered cubic structure (Scheme 1).^[32] The framework is made up of octahedral pores that are linked to smaller tetrahedral cavities by relatively thin windows of around 5 Å. UiO-66's (1 and 2) marked stability is due to their robust SBUs and high coordination number.^[32,34] It is well reported that by inserting functionalized BDC ligands with diverse chemical groups (e.g., -COOH, -NH₂, -NO₂, -OH, -Br and -F), alters the gas adsorption, fluorescence, detection capacity for explosive stimuli, improved mechanical stability, considerable enhancement in CO₂/CH₄ separation performance, and other physical and chemical characteristics as compared to pristine UiO-66 MOF.^[30,37,38] Thereby compound 2 is synthesized by functionalization of the BDC linker by -Br group in place of H, i.e., tuning ligand chemistry that has resulted in a multifold (2.92 times) increase in open circuit voltage that improved for 2/PVDF when compared to 1/PVDF, thereby dramatically altering the features, while maintaining the framework's stability. The synthesis of the compounds 1 and 2 was verified by structural elucidation methods and Fourier transform infrared spectroscopy (FTIR) besides morphological examinations. The average surface roughness (R_a) value was investigated which is crucial for TENG devices. The flexible aluminium electrode layered over PVDF was selected as the opposite layer to UiO/PVDF in the TENG device owing to their positive and negative positions within the triboelectric series. The surface potential assessment (KPFM) and the precise electrical characterization confirmed the negative behavior of the UiO-66 family members when confined into PVDF.^[9] The UiO-66/PVDF exhibits the highest output in the sequential trend as $PVDF < TENG-1 < TENG-2$. The fabricated device was extensively characterized for its stability and durability with steady long term voltage output load-matching analysis, resistance to ambient conditions, and diverse capacitor charging. The device was ultimately used to power a variety of low rating electronics like light-emitting diodes (LEDs).

To the best of our knowledge, this is the maiden report on the advancement and tuning of MOF-based composites for TENG applications through systematic changes in organic ligand chemistry while deliberately maintaining identical conditions in terms of framework isoreticularity, composite dimensions, and procedure adopted for component and device fabrication. The present study thus attempts to pin down rational and mechanistic understanding to electronic effects attributed to ligand substituted functionalities (halogen substitution) and significantly enhance the triboelectric properties of MOF composites in a systematic way.



Scheme 2: Stepwise fabrication procedure (a-e) adopted for 1/PVDF and 2/PVDF composite based mechanical energy harvesting device; f) as made device.

4.2 Experimental

4.1.1 Materials

UiO-66 and UiO-66-Br (compound 1 & 2 respectively) were synthesized by methods reported below. Unless otherwise noted, all materials including reagents, ligand precursors and solvents were commercially available and used as received and without further purification. Sigma Aldrich Co., Ltd. provided the zirconium tetrachloride ($ZrCl_4$), PVDF, H_2BDC , and $H_2BDC-Br$. Rankem supplied N, N-dimethylformamide (DMF), and hydrochloric acid (HCl, 37%), while Avra Chemicals supplied benzoic acid (BA). All chemicals were used exactly as they were received. Products obtained as solids or syrups were dried using routine lab ovens. Spacer is purchased from 3M Tape. Aluminium sheet is purchased from physics equipments.

DMF refers to N,N-Dimethylformamide

PVDF refers to polyvinylidene difluoride ($-(C_2H_2F_2)_n-$)

ITO refers to Indium Tin Oxide ($In_{2-x}Sn_xO_3$)

PET refers to Polyethylene terephthalate ($(C_{10}H_8O_4)_n$)

These chemicals were used without further purification.

4.2.2 Materials Synthesis

4.2.2.a) Synthesis of UiO-66 (1) and UiO-66-Br (2) : Zr-BDC MOF i.e. UiO-66 (1) was synthesized by dissolving ZrCl_4 (0.053 g, 0.227 mmol) and Terephthalic acid (H_2BDC) (0.034 g, 0.227 mmol) at room temperature in N, N' -dimethylformamide (DMF) (24.9 g, 340 mmol). The resulting mixture was sealed in teflon lined stainless steel vessel and heated for 24 hours at 120°C in a programmed oven. The crystallization process was carried out in the oven under static circumstances. The resultant solid was filtered, repeatedly washed with DMF, and dried at room temperature after cooling in air to room temperature. Obtained MOF was dipped in MeOH for 4 days to exchange occluded solvent molecules with MeOH and solvent was replaced at interval of every 12 hours. The MeOH exchanged MOF was filtered and heated at 100°C under vacuum for 12 hours to get guest free compound 1. Thus obtained MOF was used for all measurements. Compound 2 was synthesized and activated in a similar manner, except using 2-Bromoterephthalic acid as the ligand. ^[56,57,62]

4.2.2.b) Composite film preparation: MOF/PVDF composites were prepared by loading various wt. % of compound 1 & 2 in the viscous PVDF solution. 1 gram of PVDF pellets were stirred for 4 hours in 10 ml of DMF at 60°C . compound 1 & 2 were finely grinded to yield powdered material which is further activated at 100°C under vacuum, weighed and mixed with PVDF solution in the weight percent ratio (MOF 1 & 2 : 5%, 10%, 15%, 20%). This viscous mixture then further drop-casted on ITO-coated PET surface (substrate) and dried at 80°C for 6 hours in hot air oven to obtain finely dried thin composite films and ensuring curing of the PVDF polymer (Scheme 3). Similar films can be prepared by air drying for 24 hour and well as by doctor blading methods with retention of similar dimensions of thickness. MOF/PVDF composite films thus obtained are in the range of ~ 266 to $289\ \mu\text{M}$ (refer Appendix 13, S14) and further deployed for device fabrication. ^[58-61]

4.2.2.c) Fabrication of TENG device: ITO-coated PET is deployed as one electrode and Al-coated PET as another. Both electrodes are coupled together retaining space among them by means of spacer with thickness of ~ 1.5 mm. Electrical contacts were established at the ends of the electrodes with the help of copper tape/wires. Finally, the fabricated device was laminated on outer surface with the Kapton tape to attain electrical isolation. The thickness and the effective size of the as-fabricated device were found to be ~ 2.5 mm and $2.5 \times 2.5\ \text{cm}^2$, respectively.

4.2.3 Physical Measurements

4.2.3.a) Characterization: Bruker D8 Advanced X-Ray diffractometer used for powder X-ray diffraction patterns which are seen in the 5° to 40° 2θ range using Cu $K\alpha$ radiation ($\lambda = 1.5406 \text{ \AA}$). The FTIR Spectra were obtained using a Bruker ALPHA-II FTIR-eco ATR in the region of $500\text{-}4000 \text{ cm}^{-1}$ with total reflection (ATR) mode attenuation. Bel Japan's BelSorp-max device was used to study gas adsorption experiment. FEI Quanta 3D dual beam FESEM at 30KV was used to create the SEM images. Voltage and current were also measured on Keithley multimeter (DMM 7510 & 2450) with variable resistance. Asylum Research MFP-3D used for KPFM analysis of composite films. For the impact force and frequency source, we used mechanically modified sewing machine setup coupled with calibrated DC motor and precision impact striker. We measured force using PASPORT Force Sensor.^[59,60,63]

4.2.3.b) Nanogenerator performance measurements: Keithley multimeter (DMM 7510) was used to measure open circuit voltage of $10 \text{ M}\Omega$ to $1 \text{ G}\Omega$ input impedance at variable impact force with 5, 10 and 15 Hz frequency. For the impact force and frequency source, we used mechanically modified and fabricated sewing machine setup. Force measurement done using PASPORT Force Sensor. Voltage and current were also measured on Keithley multimeter (DMM 7510 & 2450) with variable load resistance. *Voltages are rendered as Open Circuit Voltage until external load is deployed.*

4.2.3.c) Molecular simulation studies: Discovery Studio 2017 (Accelrys) used to simulate the molecular level interactions in 1/PVDF and 2/PVDF. The DFT calculations were performed at fine quality calculation level. Initially, using DMOL3 and B3LYP hybrid function the asymmetric of the 1/PVDF and 2/PVDF units were fully geometry relaxed. For the calculations, the Multiplicity factor was kept in Auto mode, double numeric plus polarizing (DNP+) basis set with water as solvent. The ground state electron density was used to derive the electrostatic potential (ESP) on the van der Waals (VDW) surfaces (isodensity = 0.001 a.u.) of 1/PVDF and 2/PVDF units. XRD patterns were refined using Rietveld refinement method. For the refinement Fullprof (Ver. April 2022) was used.^{9,10} The line broadening of diffraction pattern was corrected using LaB6 and refinement was carried out to determine structural parameters. Using Maximum Entropy Method (MEM) we determine electron density of both the samples. The MEM analysis was carried out using Dysnomia software.^[63,66]

4.2.4 Equations:

V_p : The maximum instantaneous value of a function as measured from the zero-volt level. For the waveform shown above, the peak amplitude and peak value are the same, since the average value of the function is zero volts.

V_{pp} : The full voltage between positive and negative peaks of the waveform; that is, the sum of the magnitude of the positive and negative peaks.

V_{rms} : The root-mean-square or effective value of a waveform.

V_{avg} : The level of a waveform defined by the condition that the area enclosed by the curve above this level is exactly equal to the area enclosed by the curve below this level.

$$V_{pp} = V_{rms} \times \frac{2}{\sqrt{2}} = V_p \times 2 = V_{avg} \times \pi$$

$$V_{avg} = \frac{1}{\pi} \times \int_0^{\pi} V_p \sin \theta \, d\theta = \frac{2V_p}{\pi} = 0.637 \times V_p$$

$$V_{rms} = V_{pp} \times \frac{1}{2\sqrt{2}} = 0.353 \times V_{pp} = V_p \times 0.707$$

$$V_p = \frac{V_{pp}}{2} = \frac{V_{avg}}{0.637}$$

4.2.5 Statistical Analysis:

4.2.5.a) Sample Size (n), Standard deviation, t-test type and correction applied for Figures S36, S37, S38, S39, S41, S42, S43: The separate dataset of mean from the test data is created to compare the data points (n). The data is represented with respective mean and SD. Each data point (n) represents a peak of voltage either on positive side as $V_{oc}(+)$ or negative side as $V_{oc}(-)$. Non-significant comparisons are not shown in the graph suggesting the data is consistent and does not change significantly. Two tailed Student's t-test with Welch's correction is performed to analyze the data. **ns** = non-significant, * $p < 0.05$, ** $p < 0.01$, *** $p < 0.001$.

4.2.5.b) Sample Size (n), Standard deviation, t-test type and correction applied for Appendix 40 and Appendix 44: The data is represented with respective mean and SD. Each data point (n) represents a peak of voltage either on positive side or negative side. Non-significant comparisons are not shown in the graph suggesting the data is consistent and does not change significantly. Two tailed one way ANOVA

with Tukey's multiple comparisons is performed to analyze the data. **ns** = non-significant, * $p < 0.05$, ** $p < 0.01$, *** $p < 0.001$.

To perform the above tests, we used a software "Graphpad Prism".

Statistical data analysis for aforementioned figures are plotted below in appendix section.

4.3 Result and Discussion

Nanocrystalline Compound 1 and 2 were synthesized by using reported protocol, wherein its Br substituted derivative (compound 2) was synthesized via pre-synthetic functionalization (Scheme 1).^[39-41] Both the abovementioned compounds were washed extensively with DMF and dried subsequently. Thus obtained solid compounds were subjected to MeOH exchange over four days to remove occluded high boiling solvent molecules and further neatly activated at 100 °C for 12 h under vacuum to get guest free phase. Phase purity was confirmed by matching the PXRD patterns of pristine and activated compounds 1 and 2 with simulated XRD patterns (Appendix 1 and 2). Thus obtained solids were then deployed to form composite film by drop-casting method (Scheme 2) in addition to doctor blading method, both exhibited same morphological features in FESEM (Appendix 13, 14).^[42] Mixing of finely grinded and activated phases of with viscous PVDF solution, 1/PVDF and 2/PVDF composites were prepared by the method shown in scheme-2.^[42] Powder X-ray diffraction (PXRD), fourier transform infrared (FTIR) spectroscopy, thermogravimetric analysis (TGA), gas adsorption, and field emission scanning electron microscopy (FESEM) were used to evaluate the structural integrity of compound 1 and 2 before and after the composite preparation. Atomic force microscopy (AFM), Dielectric measurements, kelvin probe force microscopy (KPFM), electrical output analysis, capacitor charging and molecular simulation studies were performed on the MOF/PVDF composites in order to corroborate observed results with the perceived mechanism. **Figure 1a** shows PXRD patterns obtained on compound 1, 2, 1/PVDF, 2/PVDF, 2/PVDF treated with water, 2/PVDF used for TENG purpose for 45 days and pristine PVDF film. From the PXRD patterns, it is evident that compound 1 and 2 retained the structural integrity and matched well with respective simulated patterns. We note that despite of bromine functionalization, XRD pattern of 2 is well matched with compound 1. Both XRD pattern shows characteristics diffraction peaks present at $2\theta = 7.4^\circ$, 8.5° , and 25.7° corresponds to plane (111), (002) and (006) respectively.^[39,40,43] These characteristics peaks are consistent with previously reported diffraction peaks reported for 1 and 2 (Figure 1a).

Further, Peaks corresponding to pure compounds are well reflected in the PXRD of composite films 1/PVDF and 2/PVDF assuring composite formation along with retention of crystallinity.^[39-40] Incorporation of 1 and 2 in PVDF also evaluated using Rietveld refinement method.^[44] We note that XRD pattern of pristine PVDF film evidently shows presence of alpha (α) phase, which is paraelectric in nature.^[45] From the refinement it is evident that electron density in 2/PVDF is relatively high compared to that of 1. It could be due to presence of two electronegative functionalities, fluorine and bromine. In case of both compounds, the diffraction features of alpha phase of PVDF observed to be suppressed, this could be due to highly crystalline nature of 1 and 2. We further performed stability of 2/PVDF film under different conditions, i.e. after water treatment and keeping 2/PVDF film for TENG operation over intermittent interval spanning up to 45 days, discussed in brief under output and stability section.

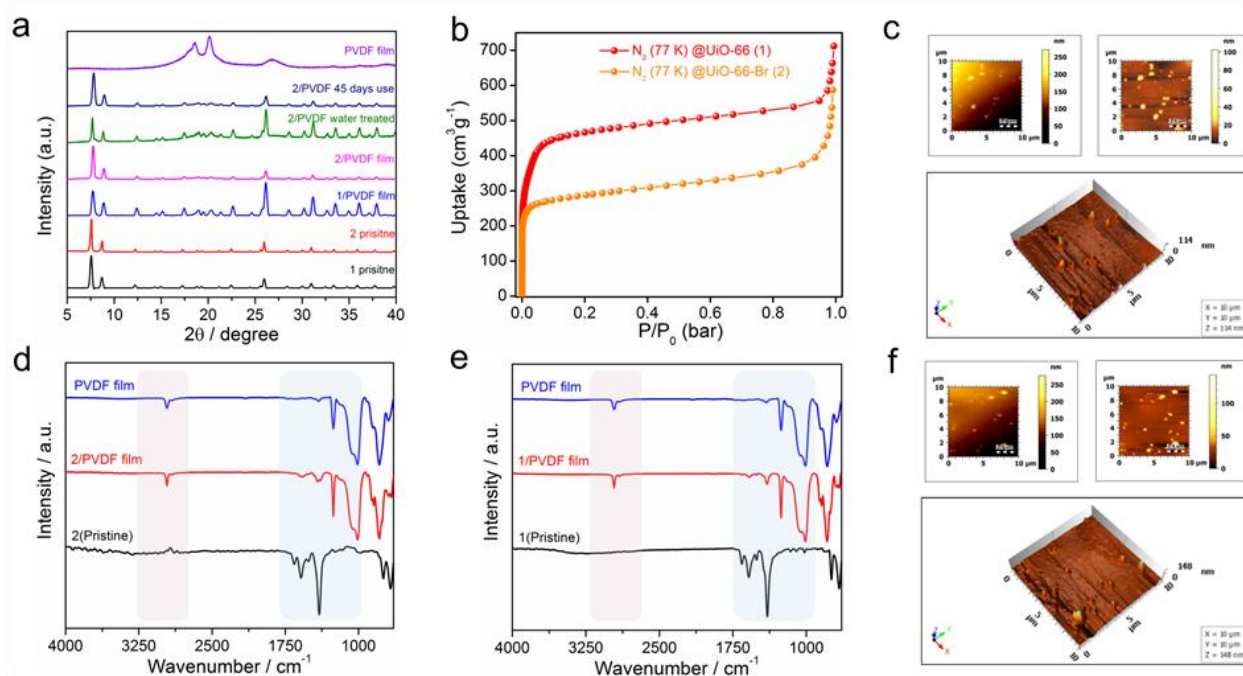


Figure 1: a) PXRD data of pristine compound 1 and 2 and their composites. b) N_2 adsorption isotherm of compound 1 (red) and compound 2 (orange) at 77K, c) AFM images indicating trace, retrace and surface topography (3D profile) of 10 wt % of 1/PVDF. d) IR spectra of pristine compounds (black) composites (red) and PVDF films (blue). e) IR spectra of pristine compounds (black) composites (red) and PVDF films (blue). f) AFM images indicating trace, retrace and surface topography (3D profile) of 10 wt % of 2/PVDF.

The FTIR spectrum of compound 1 and 2, and that of PVDF is depicted in Figure 1d and 1e and well matched with reports in the literature.^[39,40,43] It's well reported in literature that FTIR bands of 1 and 2 exhibits significant resemblance with each other.^[47] Composites 1/PVDF and 2/PVDF exhibits combined features of isolated spectrum of pure compounds (1, 2 and PVDF) indicating composite formation (Figure 1d, 1e). The spectral band appeared at 1660 cm^{-1} corresponds to C=O stretching vibrations of H₂BDC and H₂BDC-Br. Aside from that, the H₂BDC ligand's O–C–O symmetric (at 1400 cm^{-1}) and asymmetric (at 1600 cm^{-1}) stretching IR bands were also discernible. IR bands at 1507 cm^{-1} are attributed to the vibration of aromatic ring C=C bonds, whereas IR peaks at $667, 752$ and 807 cm^{-1} have been linked to –OH and C–H vibrations in the H₂BDC ligands. CH₂ stretching vibrations at 2854 and 2923 cm^{-1} are found in the pristine PVDF film. Further characteristics stretching vibration of –CF₂ groups can be seen at $1120\text{--}1280\text{ cm}^{-1}$.^[48] Composite 1/PVDF and 2/PVDF also confirms the presence of IR peaks corresponding to pure constituents, notably CH₂ stretching vibrations around ~ 2854 and 2923 cm^{-1} are seen in composite are renders to pure PVDF film. Also, both composites shows peaks at $667, 752$ and 807 cm^{-1} are attributed to –OH and C–H bond vibrations in the H₂BDC ligands.^[43,48]

Figure 1b reveals the findings of N₂ adsorption-desorption isotherms at 77K, which were performed to examine the porosity of the framework. Both compounds exhibited type-I N₂ adsorption-desorption isotherms, confirming the microporous nature of the MOFs.^[49] The specific surface area values for compound 1 and 2 are $1285.6\text{ m}^2\text{ g}^{-1}$ and $1049.20\text{ m}^2\text{ g}^{-1}$ respectively. As anticipated, Compound 1 exhibited higher specific surface area when compared to compound 2. Brunauer, Emmett and Teller (BET) surface area was lowered in compound 2 due to bromo-functionalized ligands. As previously reported, the pore volume for compound 1 and 2 is nearly same and retained their porosity despite ligand alteration.^[48-50] Thus study reveals the influence of the bulkiness of the additional bromine functionalities on the overall quantity of adsorbed N₂ (at 77 K). Field emission scanning electron microscopy (FESEM) was deployed to probe surface morphologies of the composite films 1/PVDF, 2/PVDF and PVDF alone. The SEM images rendering composite films reveals the random and incremental distribution of MOF particles on and within the polymer matrix (Appendix 11-13). Rise in the particle distribution was seen in accordance with their % weight loading of 1 and 2 in the polymer matrix retaining order $5\% < 10\% < 15\% < 20\%$. **Cross-section of single electrode energy harvester** having bilayer is shown in SEM image that confirms a **comparable thickness of $\sim 395.4\text{ }\mu\text{m}$ and $\sim 425.1\text{ }\mu\text{m}$** for the embedded film of compound 1 and 2 respectively, as shown in Appendix 14. Film thickness was meticulously retained closely identical in view of judicious comparison of TENG output performance. Upon EDAX mapping over the selective

area of composite films by avoiding coalescence of other layers, qualitative confirmation was derived for presence of Br in 2/PVDF along with other common elements (C, O, Zr, F) of 1/PVDF (Appendix 15, 16). Similar feature is observed for pure compounds 1 and 2 (Appendix 10 B) confirming presence of Br in 2.

Thermal stability compound 1, 2 and their respective composite films at various wt% loading and that of PVDF powder along with the pristine film is verified by means of TGA. The thermal stability of the pristine PVDF film, which has a partially fluorinated structure, is upto ~ 400 °C, followed by a single step degradation pattern. All Zr-MOF particles exhibited significant thermal stability in the air until ~ 350 °C, beyond which a consistent degradation pattern is observed.^[40] Whereas, composite films of 1/PVDF and 2/PVDF revealed significantly improved thermal stability by blending stability features of both film and MOF, as depicted in **Appendix 8, 9**. Thus 10 wt% composites of 1/PVDF and 2/PVDF exhibited peak stability nearly upto 500 °C revealing desired enhancement in thermal stability feature and then gradual weight loss.

Atomic force microscopy (AFM) was employed to probe surface feature of the composite films (**Figure 1c, 1f** and Appendix 17, 18). The TENG's performance is heavily influenced by surface roughness. The TENG's output is known to be affected by the average surface roughness (R_a).^[50-52] TENG's output ascents when the R_a value rises to a certain level because it creates greater surface area for optimum interaction between the materials through plausible friction, leading to a considerably higher amount of charge formation. Surface topography (3D profile) of 10 wt % of 1/PVDF and 2/PVDF were particularly scanned commonly over the area of $100 \mu\text{m}^2$ in trace-retrace movement in X and Y-direction (two dimensional) which further revealed that the surface roughness feature of 2/PVDF is enhanced thereby enrooting higher surface dependent properties such as availed area for friction surface and charge accumulation. Above scanned area represent maximum peak height profile of 114 nm for 1/PVDF while 148 nm for 2/PVDF directly indicating high variation of roughness feature and peak profiles for later (**Figure 1c, 1f**). The R_a parameter of 2/PVDF is evidently superior when compared to 1/PVDF. AFM measurements at random areas spanning same length ($1.2 \mu\text{m}$) also in line with above observation denoting elevated peak height parameters for 2/PVDF.

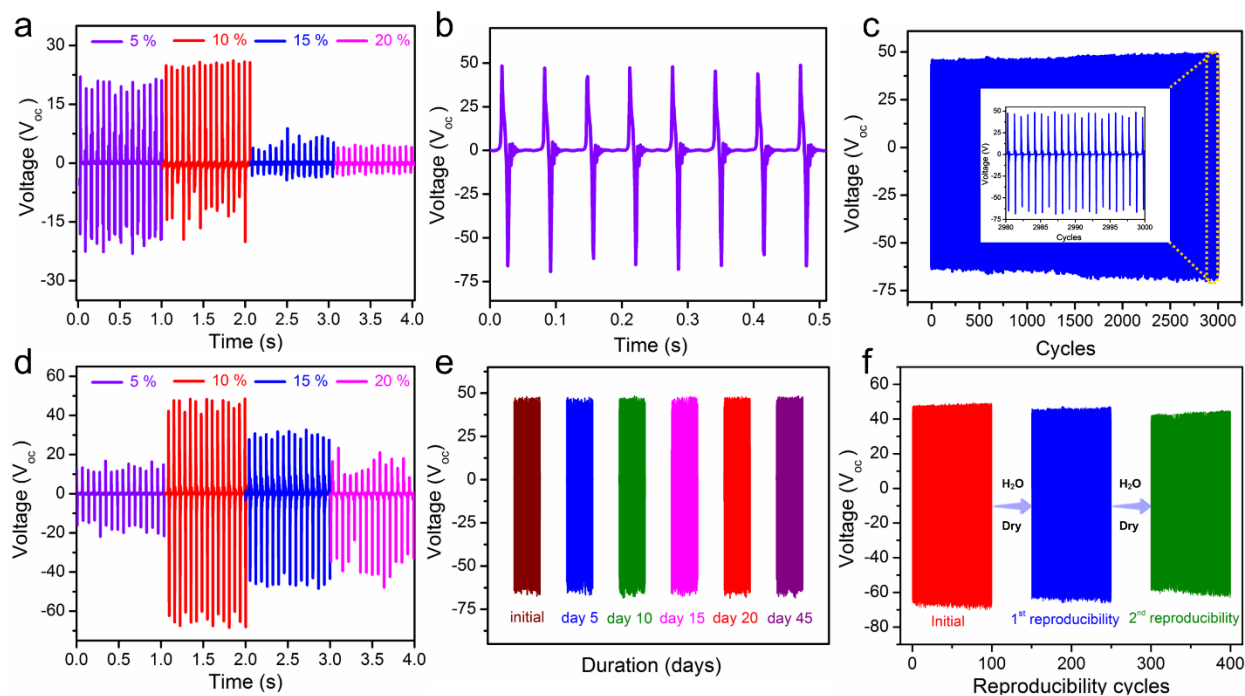


Figure 2: a) The open circuit voltage versus time graph for different wt % of 1/PVDF. b) Resolved view of V_{oc} over half second run time. c) V_{oc} reproducibility for TENG-2 over 3000 cycles, i.e. mechanical durability test performed on 10 wt % 2/PVDF (TENG-2) device with an applied force of 24 N and frequency of 15 Hz. d) The open circuit voltage versus time graph for different wt % of 2/PVDF. e) Reproducibility of TENG-2 device after several days of use. f) Performance reproducibility of TENG-2 device after 2 consecutive water dip-dry operations. For Figure 2a, 2b, 2d, 2e; Sample size (n) = 15, Probability (P) = * $p < 0.05$, ** $p < 0.01$, *** $p < 0.001$ and for Figure 2c; (n) = 20, (P) = * $p < 0.05$, ** $p < 0.01$, *** $p < 0.001$.

Mechanical energy harvester has been fabricated as illustrated in scheme 2, having one electrode made up by putting thin film of MOF/PVDF on ITO coated PET, while other electrode is made up of Al-layered PET, both electrodes are connected with Cu contacts for electrical connection. The device is further laminated externally to provide encapsulation and insulation. The devices made up of variable wt.% (5, 10, 15, 20) for 1/PVDF and those of variable wt.% for 2/PVDF were subjected to triboelectric output performance measurement with force values of 10, 18 and 26 N at 5, 10, 15 Hz frequency, respectively (Appendix 22–24). 10 wt.% of 1/PVDF and 2/PVDF embodied devices dispensed maximum output, hence were chosen for further detailed investigation of nanogenerator performance and stability tests, and

labelled as *TENG-1* and *TENG-2*, respectively. The triboelectric output performances from all produced devices were assessed by applying a continuous force of 26 N normal to the surface of as-fabricated device. For device measurements, a custom-built force set-up connected to an oscilloscope was used. PVDF film alone delivered average open circuit voltage (V_{oc}) of 7.82 V. The *TENG-2* device (10 wt. % 2/PVDF) achieved a consistently optimal recordable triboelectric output voltage (V_{oc}) of 55.21 V and a peak-to-peak voltage (V_{p-p}) of 110.41 V, whereas the *TENG-1* (10 wt. % 1/PVDF) achieved a V_{oc} of 18.92 V and a V_{p-p} of 37.85 V. (Figure 2a, 2d and Appendix Table 1).

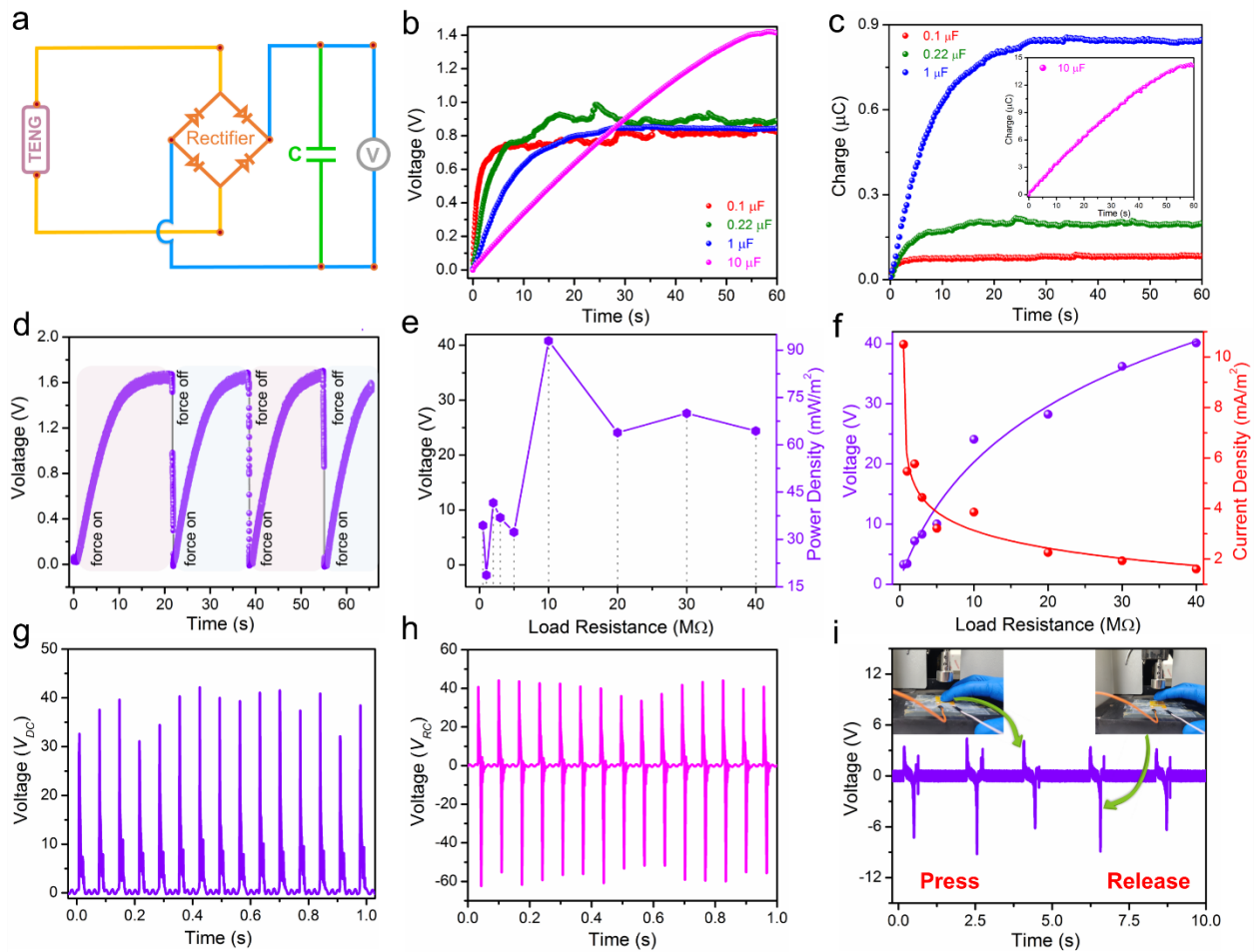


Figure 3: a) The Schematic illustration of a full-wave bridge rectifier circuit diagram. b) Capacitor charging curves for 0.1, 0.22, 1 and 10 μF capacitors employing the 10 wt % 2/PVDF (*TENG-2*). c) Charge stored in various capacitors. d) 1 μF capacitor charging-discharging profile by the output of *TENG-2*. Voltage, e) Power density and f) Current density plots as a function of load resistance

corresponding to the *TENG-2* device, g) DC rectified voltage output (~ 45 V) after bridge rectifier derived from *TENG-2* for 10 μ F capacitor charging, h) Resistance capacitor circuit voltage output (V_{RC}) at 150 ohm load and 10 μ F capacitor, i) Output voltages under diverse biomechanical scenarios i.e. gentle press and release. Figure g to i); (n) = 15, (P) = * $p < 0.05$, ** $p < 0.01$, *** $p < 0.001$.

Considering the fact that applicability of device is rendered by its stability and endurance, *TENG-2* was subjected to endurance test for 3000 cycles (Figure 3c and Video S2) to verify its stability and output steadiness, and the same device was further tested nearly for over 1.5 month with intermittent intervals (Figure 2e). The performance variance throughout the aforementioned period was negligible. Whereas previously reported devices shows significant drop in performance over the incremental period of time and thus devices reported literature, lack such reproducibility and V_{oc} steadiness, proving to be one of its kind standout-feature among all MOF-*TENG* devices reported until now. Structural integrity was retained as revealed by post performance PXRD as shown in the Appendix 26, 27. Further humidity resistance of device was tested by subjecting it to conditions of 30 °C at 98% relative humidity (RH) over 24 h, re-drying neatly and then examining, the device was found to deliver unaltered performance (Appendix 28). We also dipped the device in water for 5 min (harsh condition), then soaked, dried in air and under sunlight, and re-examined further, repeating the operation over 2 cycles. It retained its performance with negligible drop in V_{oc} , thus proving it to be most promising candidate for the real applications and electronics (Figure 2f). The device was also evaluated under a variety of load resistances to assess MOF-*TENG*'s practical applicability and subsequent outcome in terms of power density enhancement with respect to load resistance were noted.

To assess the application potential of the UiO/PVDF-based *TENG*; the voltage, current, and power were examined by subjecting the chosen device i.e. *TENG-2* with various external loads (Figure 3e, 3f). Performance retention and consistency were examined by testing five different *TENG-2* devices for V_{oc} output and it revealed outstanding consistency, with V_{p-p} **110.41 V** and steady output of V_{rms} **39.04 V** (Appendix 29, 30). Notably, *TENG-2* delivered DC rectified voltage (V_{DC}) output of ~ 45 V after bridge rectifier derived for 10 μ F capacitor charging (Figure 3g) and resistance-capacitor circuit voltage output (V_{RC}) was found to be equal to pre-mentioned V_{p-p} at 150 ohm load resistance (R_L) (Figure 3h) and 10 μ F capacitor.

Kelvin probe force microscopy (KPFM) and dielectric measurements were used to determine surface potential (ϕ_s) features and comparative negative behavior of composite films. A finely powdered

nanocrystalline sample of compounds 1 and 2 compressed into the shape of a disc / pellet was further utilized for dielectric measurements. Aluminium adhesive foils were used as the top and bottom electrodes of the compressed disc. Dielectric constant trend was measured as a function of frequency. Figure 4c reveals enhanced dielectric constant for 2/PVDF due to linker functionalization by bromine, thus effect of substituents on dielectric property is evocatively observed, however, sample preparation and pellet thickness also affects trend in dielectric constant, hence conditions of analysis and sample preparation are crucial and were retained precisely identical.^[53] **Figure 4a, 4b** denotes mapped value of ϕ_s for 1/PVDF and 2/PVDF spanning the similar dimensions of area. It is evidently seen that MOF/PVDF films exhibits negative surface potential when compared with positive Al-electrode of energy harvester device (Appendix Table 3), as developed surface potential of 1/PVDF and 2/PVDF is negative, -0.13 V and -2.69 V are being mean ϕ_s respectively. For 1/PVDF film KPFM surface potential confirmed the presence of large positive surface potential region representing the highest positive contact potential difference of the order of 0.095 V (95 mV) and negative potential maximum up to -0.355 V (-355 mV) over the fixed area. The positive surface potential might be coming from UiO-66 and negative surface potential region composed of PVDF due to presence of highly electronegative fluorine group. On the other hand, KPFM studies on 2/PVDF shows drastic change in surface potential over the area. The surface potential was observed to be negative having voltage distribution in the range -2.38 to -3.00 V. This could be attributed to presence of two highly electronegative groups' fluorine and bromine in PVDF and compound 2 respectively. Thus based on the KPFM studies, we can conclude that 1/PVDF and 2/PVDF can act as negative triboelectric materials in TENG. Scheme 2e demonstrates the 3D architecture of UiO-TENG device, designed in vertical contact-separation mode with aluminium and UiO-66(Zr) family members as the positive and negative material, respectively. Energy harvester device employs aluminium and polyethylene terephthalate polymer (PET) as an electrode and substrate simultaneously. The TENG's underlying working mechanism is attributed to the coupling effect of electrostatic induction and contact electrification.^[10,14,15] Figure 4d represents the operating mechanism of UiO-TENG with aluminium and UiO-66-X/PVDF (X=H/ Br) as interacting layers.

Figure 4d reveals the underlying working mechanism of TENG. Initially, in absence of applied force, charge cannot be generated on the device's constituent layers, resulting in a zero potential difference. The Device, when fully pressed, the two layers make full contact and generate equal and opposite charges. The positive triboelectric behavior of aluminium is attributed to electron transfers to the UiO/PVDF composite layer, having left negative charge UiO/composite layer and positive charge on the aluminium.

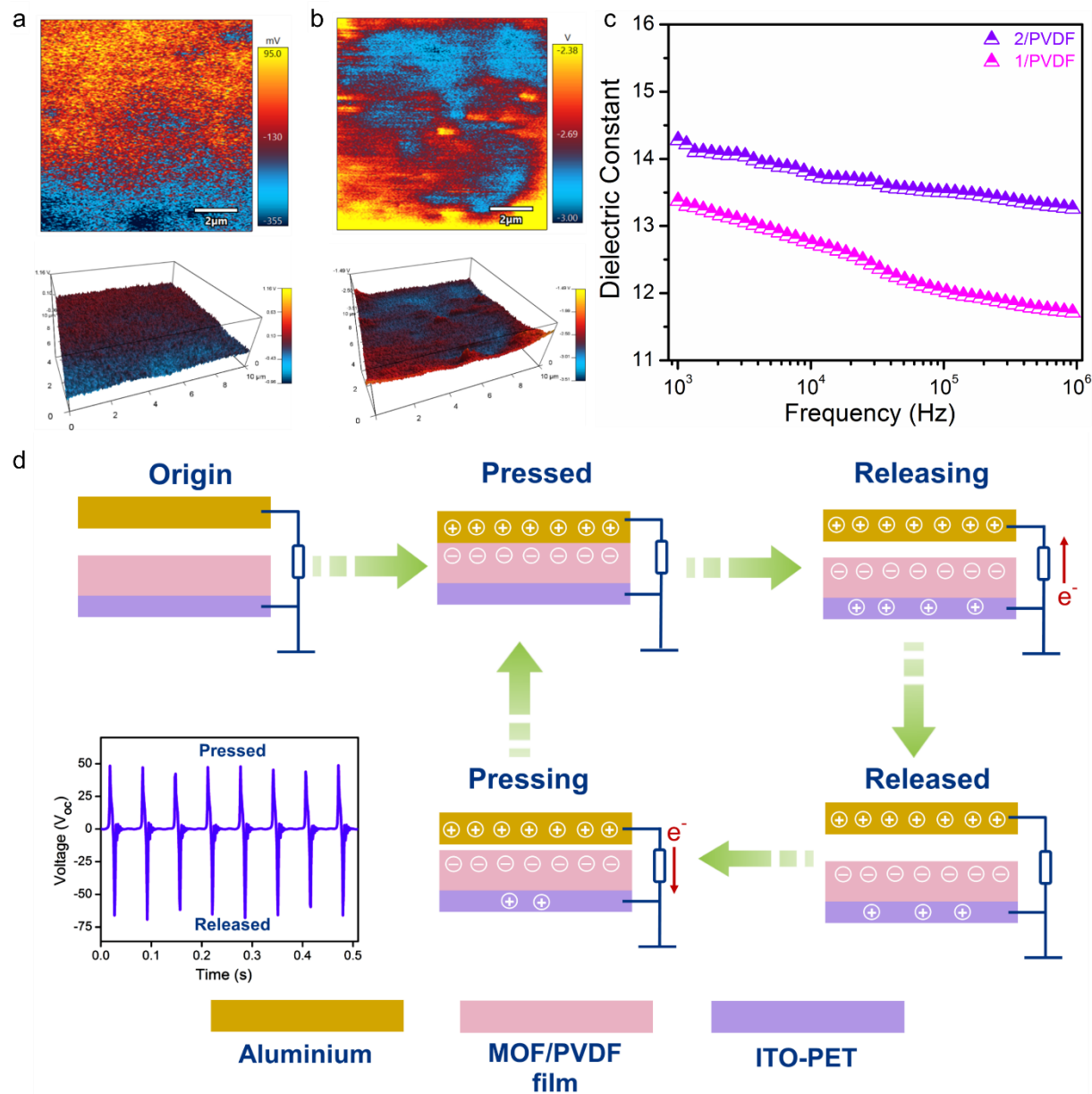


Figure 4: KPFM profiles of 10 wt% each for; a) 1/PVDF and b) 2/PVDF confirming the negative V_{CPD} . c) Frequency dependence of the real part of the complex dielectric constant for 1/PVDF and 2/PVDF, both at 10 wt %. d) Mechanism in vertical contact-separation mode with different stages viz. releasing, released, pressing and pressed and signal pulse.

The UiO-TENG tends to revert to its original form once the external force is removed, resulting in the emergence of an electrical potential difference. The potential difference drives electrons from the bottom

electrode of the UiO/PVDF composite side to the top aluminium electrode, resulting in the half cycle of the output. The UiO-TENG attains its complete released state, thereby the condition of highest potential difference. Upon force application, the UiO-TENG is pressing, consequently creating a reverse flow of electrons, which generates the other half cycle of the output. When the two layers come into full contact, i.e., are in pressed state, the charges are being neutralized thus attaining an equilibrium condition (Figure 4d sequentially). The procedure is then repeated in the presence or absence of the force-generating the UiO-TENG output.

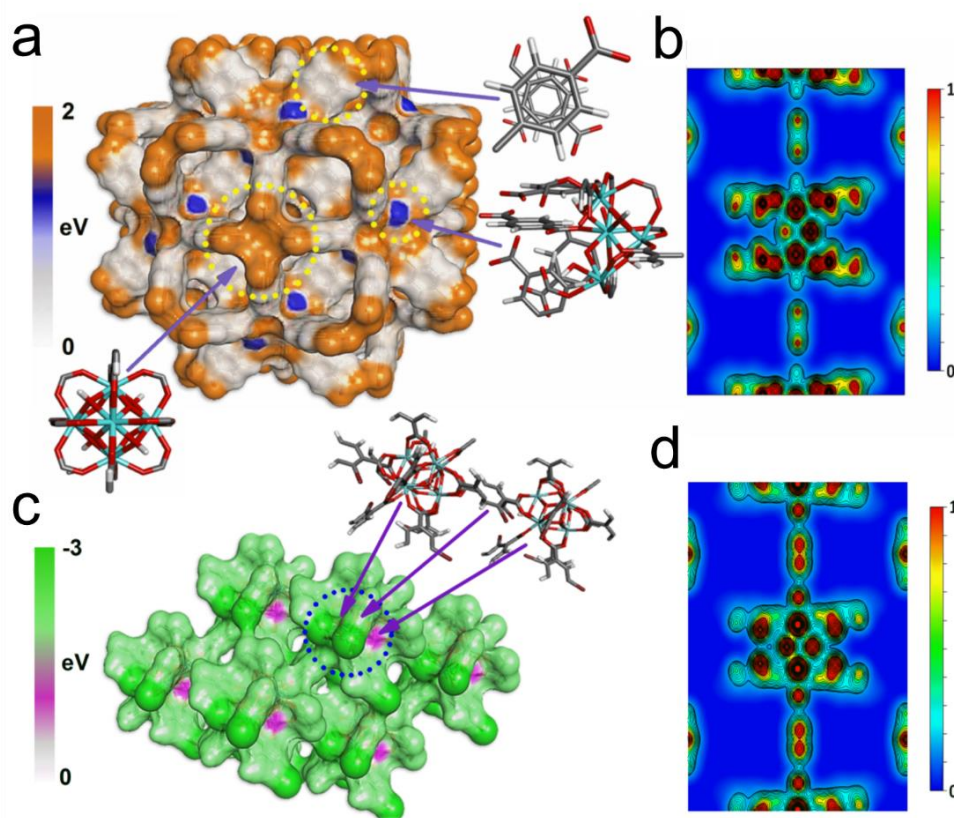


Figure 5: a) ESP distribution for 1/PVDF, b) electron density of 1 obtained through MEM analysis in the (111) plane, c) ESP distribution for 2/PVDF and d) electron density of 2 obtained through MEM analysis in the (111) plane. The MEM study shows that Br incorporation drastically changes the electron density of UiO-66 lattice.

Gain in output performance with increasing loading of 1 and 2 is ascribed to interfacial polarization between MOF and polymer matrices resulting in higher dielectric feature for MOF/PVDF composite.

Interfaces in heterogeneous materials induce Maxwell-Wagner-Sillars-type polarization, resulting in a considerable shift in the overall dielectric constant due to charge carrier buildup at heterogeneous system interfaces because of variations in filler and matrix conductivity. Once optimal loading (10 wt. %) for 2 is reached, the spacing between constituent dipoles is optimum, producing maximum output voltage. Further rise in concentration over 10 wt. % causes poor composite insulation, thus electrical breakdown, and a drop in the output voltage is seen.^[9,54]

Computational investigations corroborates experimental observations. In order to confirm the above observations, we performed density functional theory (DFT) studies on the 1 and 2. Base polymer utilized for composite preparations is PVDF-alpha phase. It is being paraelectric in nature, hence its contribution is neglected in the DFT studies. **Figure 5a, 5c** shows ESP distribution for 1/PVDF and 2/PVDF which has been consistent with experimental KPFM results. **ESP description** in compound 1, the electronic surface potential (ESP) surface shows the existence of intermolecular C-Zr-O contacts, which are highlighted with bright blue spots, C-Zr-H contacts are highlighted with bright brown surfaces and van der Waals contacts are attributed with white surface. In compound 2, the ESP surface shows the bright green and purple surfaces adjacent to each other having contribution from C-Br-H and C-Zr-O respectively. While pale green whitish surfaces show contribution from van der Waals contacts. Moreover, we obtained electron density of 1/PVDF and 2/PVDF in (111) direction using maximum-entropy method (MEM) (Figure 5b, 5d and Appendix 5, 6).^[46] In 1/PVDF, we observed presence of electron density from 1 subunit (central electron density) and distinct electron density lobes on either side of subunit. On the other hand, in compound 2, the electron density of subunit is coordinated with bromine induced excess electron density lobes. Thus, bromine functionalization enhances overall electron density when compared to compound 1 and makes coherent formation of potential packets adjacent to each other (Figure 5, MEM analysis). The XRD analysis indicate that Br incorporation drastically alters electron density of UiO-66 lattice, thereby developing electron density lobes within UiO-66 lattice (Figure 5b, 5d). The potential utility of the best-performing 10 wt. % 2/PVDF device, i.e. *TENG-2*, was demonstrated by storing the harvested energy in various capacitors. As discerned from the charging curves, the output voltage rapidly increases, the capacitor saturates and reaches values of 0.89, 1.00, 0.86, and 1.48 V in 60 s across the respective 0.1, 0.22, 1 and 10 μF capacitors (Figure 3b). Notably, 0.1, 0.22, and 1 μF capacitors charged quite rapidly and saturated within 6.1, 16.3 and 20.1 seconds, respectively. Charging-discharging cycles of *TENG-2* (Figure 3d) performed on 1 μF capacitor are notably frequent and highly precision-reproducible, evidencing promising feature of *TENG-2* for on-demand application. The measured charges

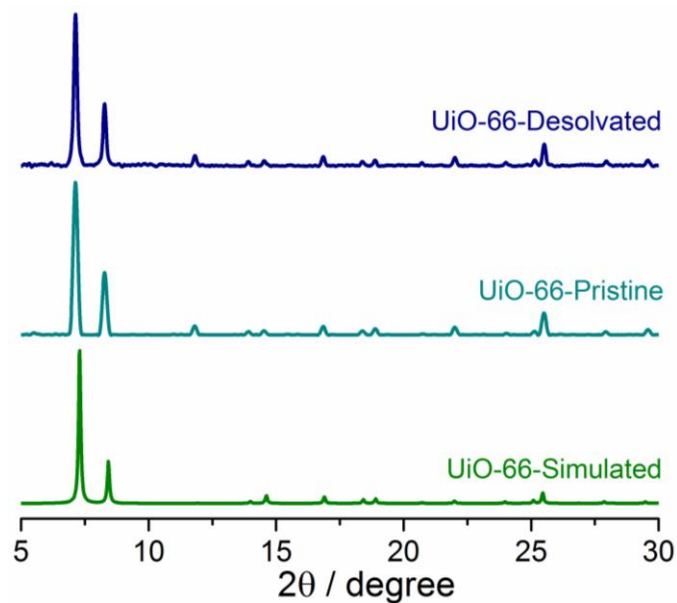
corresponding to 0.1, 0.22, 1 and 10 μF capacitors were summed upto to be 0.088, 0.22, 0.86 and 14.8 μC (Figure 3c) along with 0.040, 0.11, 0.37 and 11.1 μJ energy stored in respective capacitors (Appendix 31). *TENG-1* and *TENG-2* delivers short circuit current (I_{sc}) averaging **66 nA** and **472 nA** respectively.

In addition, the charging of the 10 μF capacitor to 1.45 V under a minute time and at a constant impact force of 26 N with a frequency of 15 Hz (Supplementary Video S1) made a green LED flash (Supplementary Movie S3, Appendix 35). Notably, *TENG-2* devices are **flyweight** and weighs around **~680 mg** (± 10 mg) hence paves way for utilization in wearable electronics. Statistical analyses were performed on significant sample sizes, confirming reproducibility and consistency in the resultant TENG output data (Appendix 36-44). These findings show that the designed MOF-based mechanical energy harvester can be readily envisioned as a potential power source for low-consumption micropower circuits.

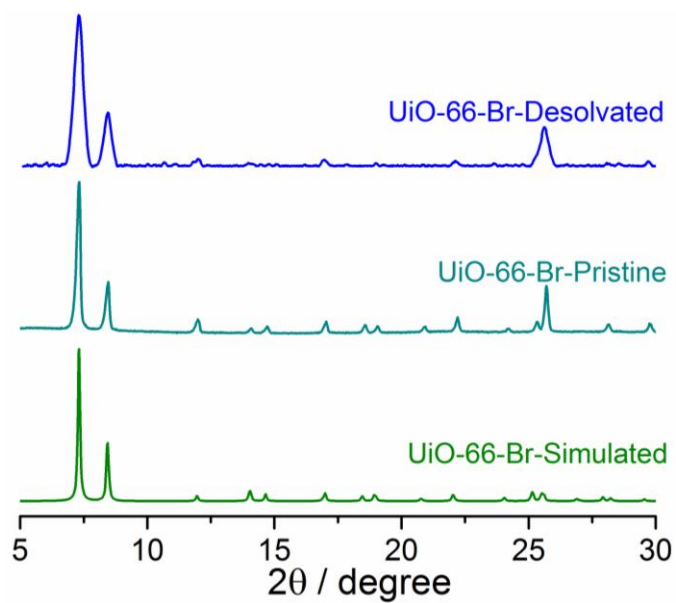
4.4 Conclusion

This study introduces a rational strategy of linker functionality tailoring in a stable isorecticular material (UiO-66 family) for superior TENG-based application performance. Pre-synthetic design and fabrication approaches have been successfully demonstrated by taking advantage of the strong and controllable EW capabilities of constituents that are exploited by linker functionalization, proving to be a realistic option for improving TENG output. The flexibility of PVDF and the controllability of MOF doping level enabled the design of a flexible, robust, and light-weight TENG that can work in a vertical contact-separation mechanism, rendering an impressive and steady output. The TENG devices are subsequently implemented for mechanical energy harvesting applications, yielding a maximum $V_{\text{p-p}}$ averaging at 110.41 V and V_{rms} of 39.04 V with a maximum power density value of 92.93 mW/m^2 for the optimal loading of a 10 wt.% 2/PVDF device (*TENG-2*). *TENG-2* displayed enhanced performance, 2.91 times higher than *TENG-1* and 14.12 times higher than PVDF film, besides a steady I_{sc} of 472 nA owing to the linker tunability feature. The fabricated devices' energy storage capabilities have been demonstrated by storing the harvested energy in a variety of electrolytic capacitors. Thus, MOFs and their tuned features can be rationally exploited to achieve sustained mechanical energy harvester performance of interest to a wide range of low-to-moderate energy-based TENG applications.

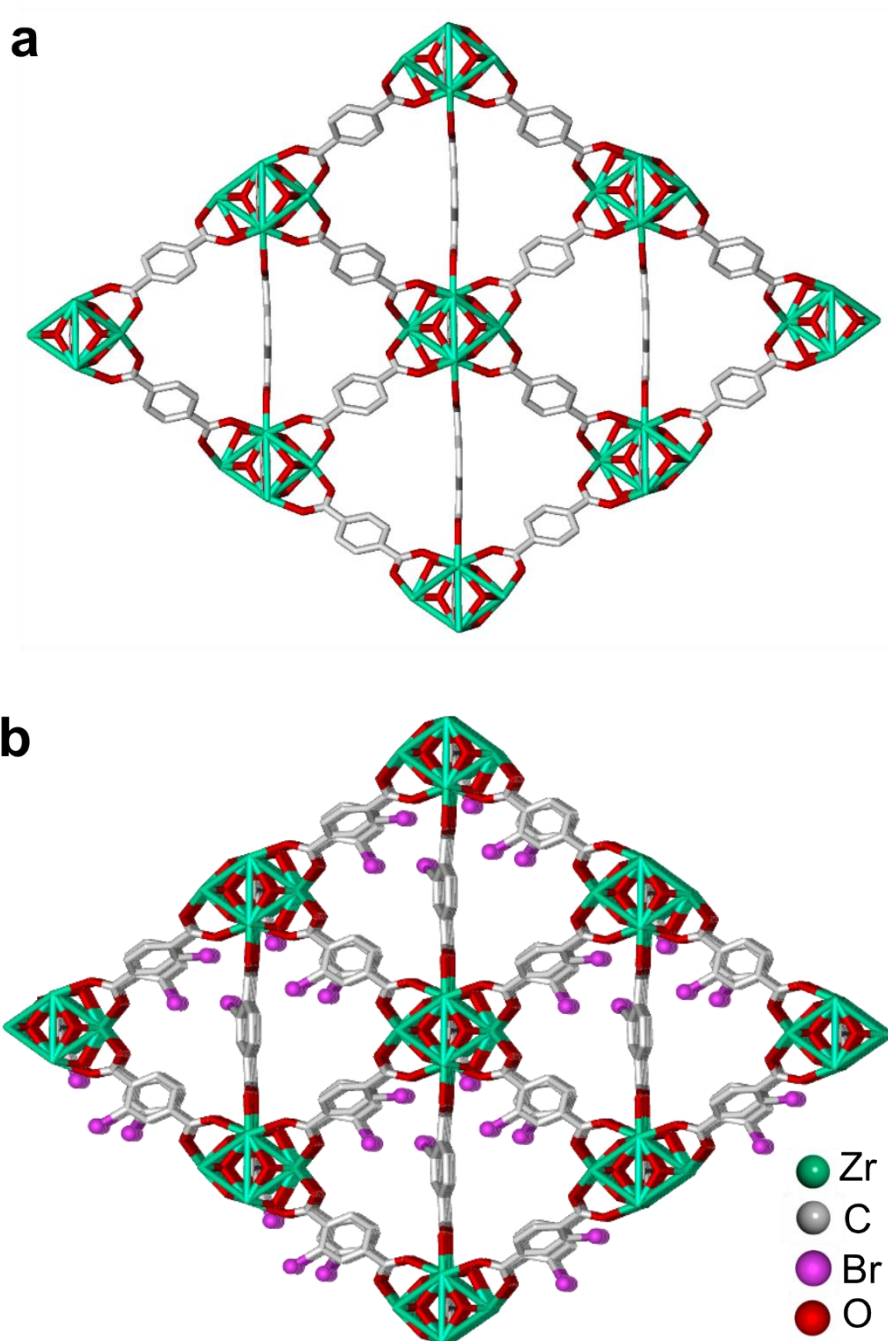
4.5 Appendix Section



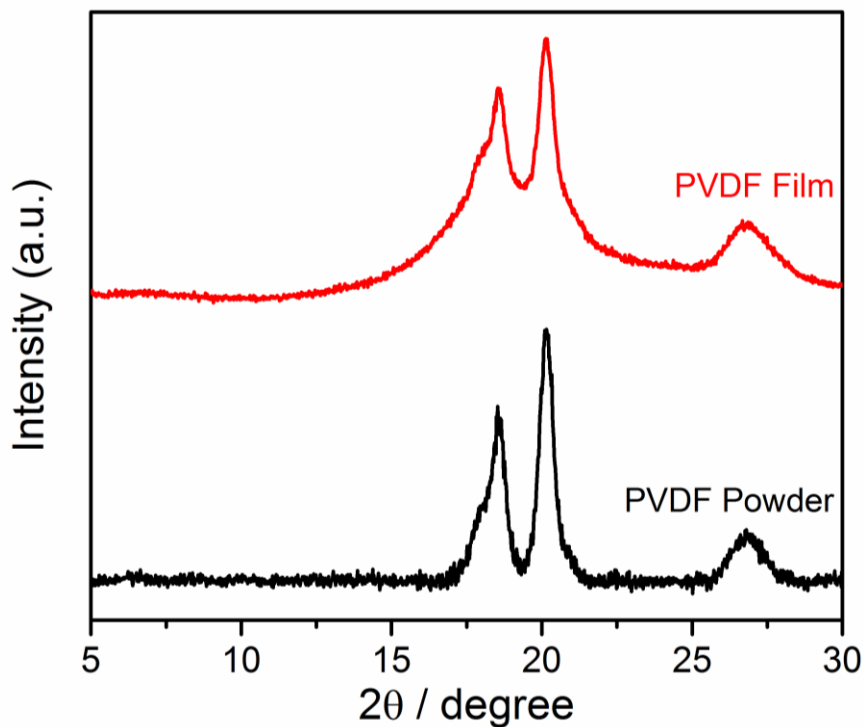
Appendix 1. Comparison of the experimental PXRD data of UiO-66 (compound-1) and the simulated pattern from the unit cell.



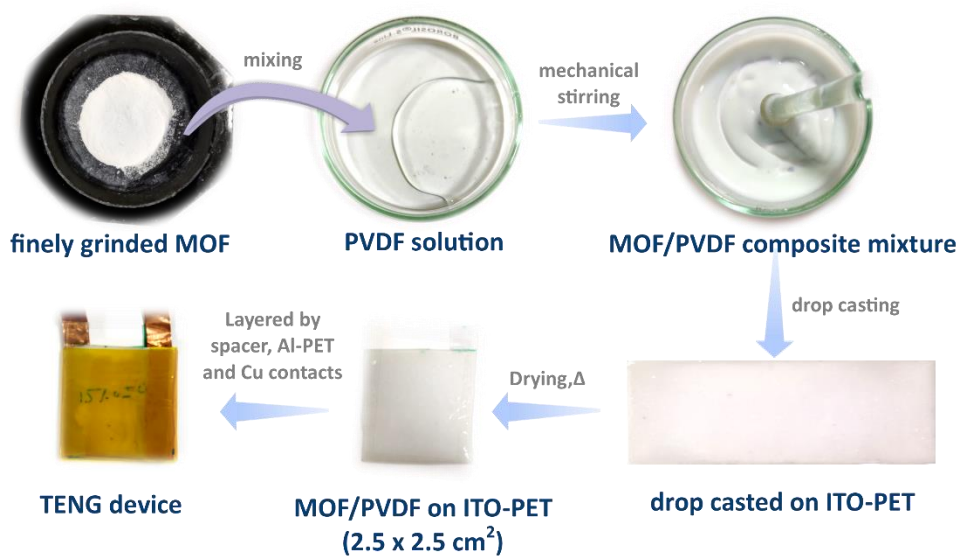
Appendix 2. Comparison of the experimental PXRD data of UiO-66-Br (compound-2) and the simulated pattern from the unit cell.



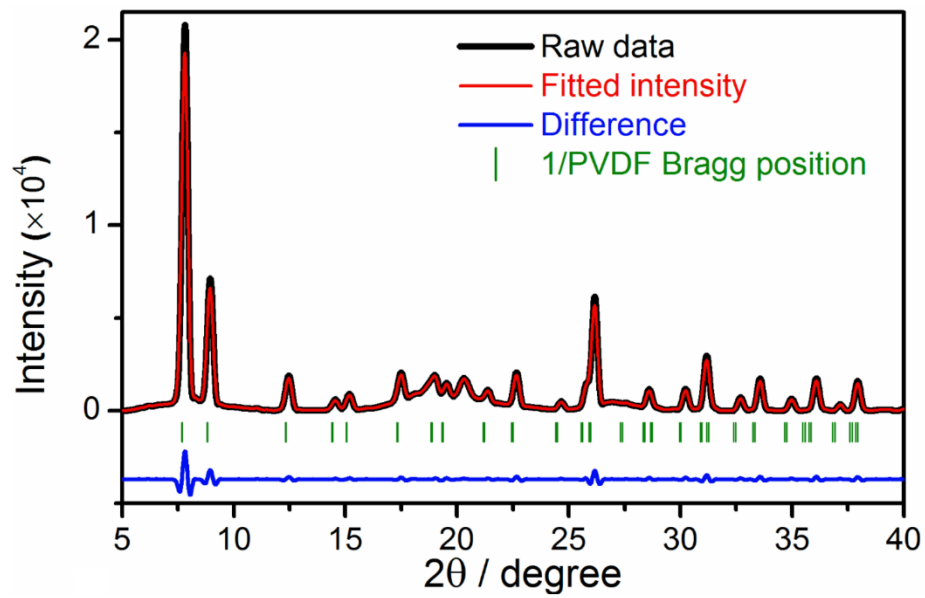
Appendix 3. Packing diagram of the three dimensional network in compound 1 and 2 viewed between a and c-axis for 1 and along a-axis for 2 (solvents and hydrogen atoms are omitted for clarity).



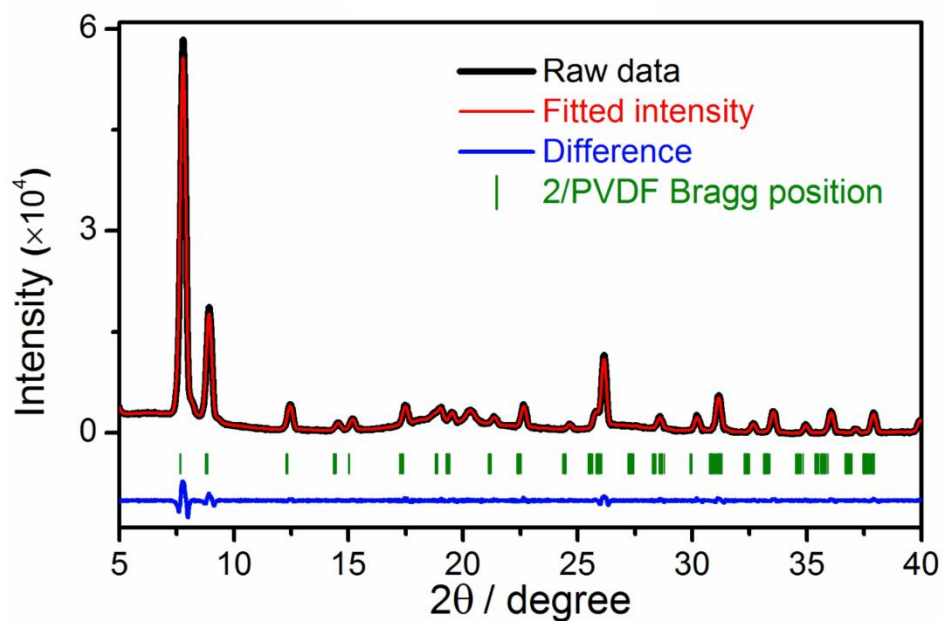
Appendix 4. Comparison of the experimental PXRD pattern of PVDF powder and PVDF film.



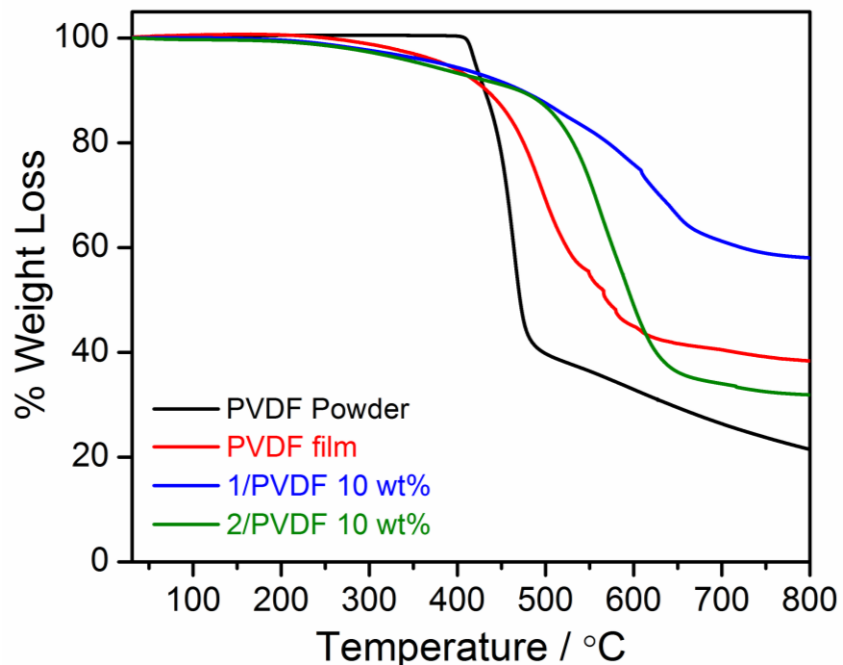
Scheme 3. The photographic illustration for the MOF/PVDF composite film preparation on ITO-coated PET.



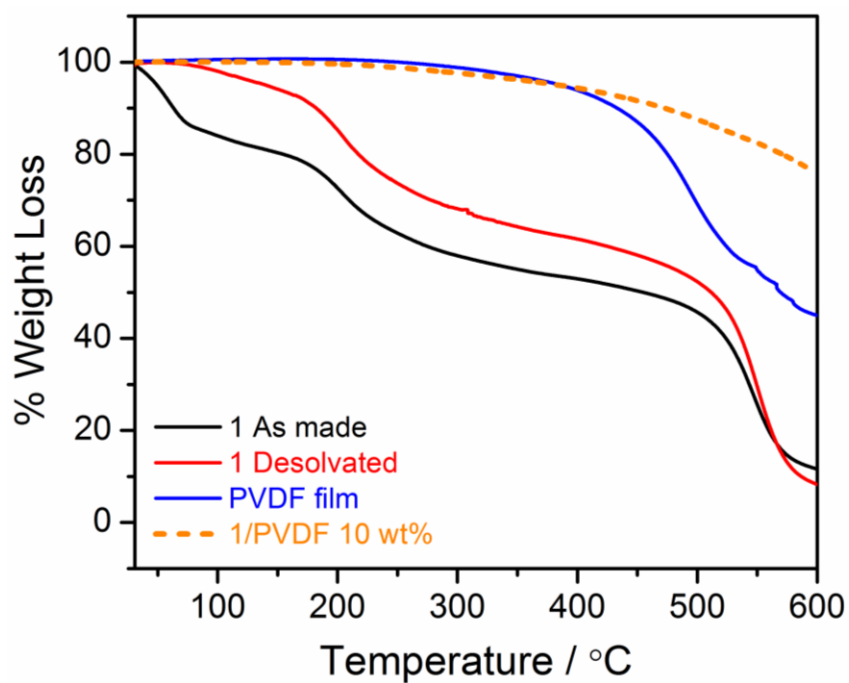
Appendix 5. Rietveld refined XRD pattern of 1/PVDF.



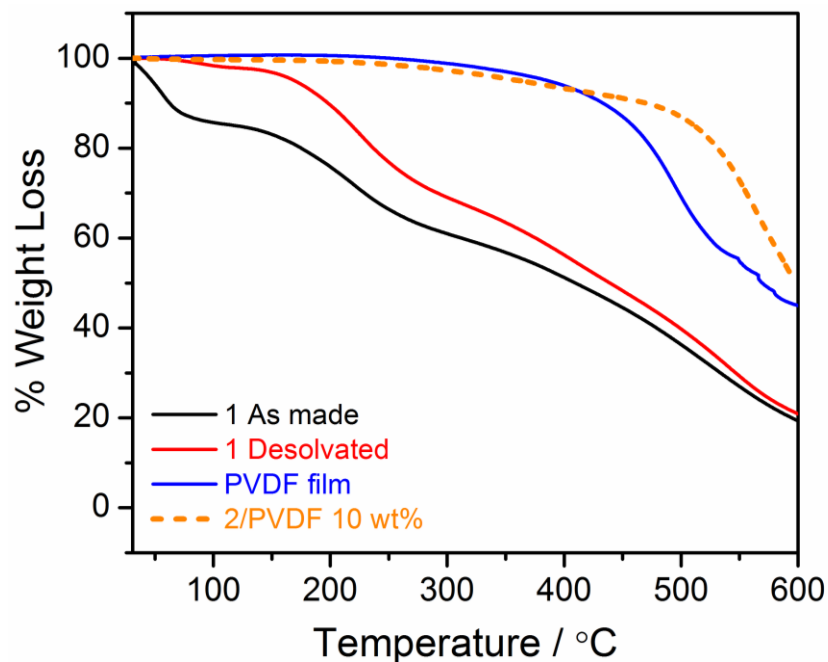
Appendix 6. Rietveld refined XRD pattern of 2/PVDF.



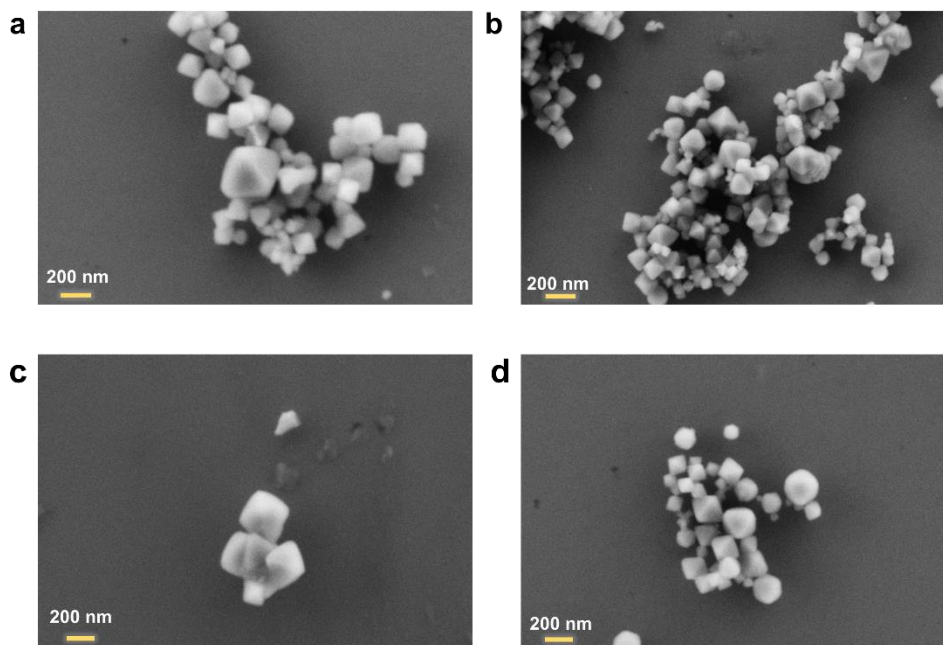
Appendix 7. Thermogravimetric analysis of pristine PVDF, PVDF film, 1/PVDF and 2/PVDF at 10 wt % loading each composite at various wt %.



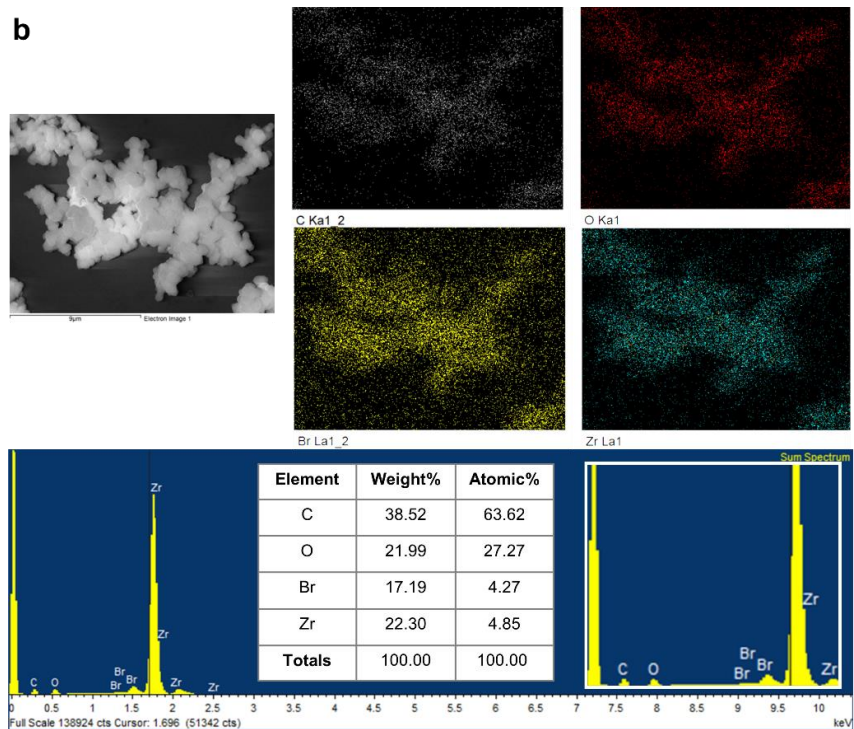
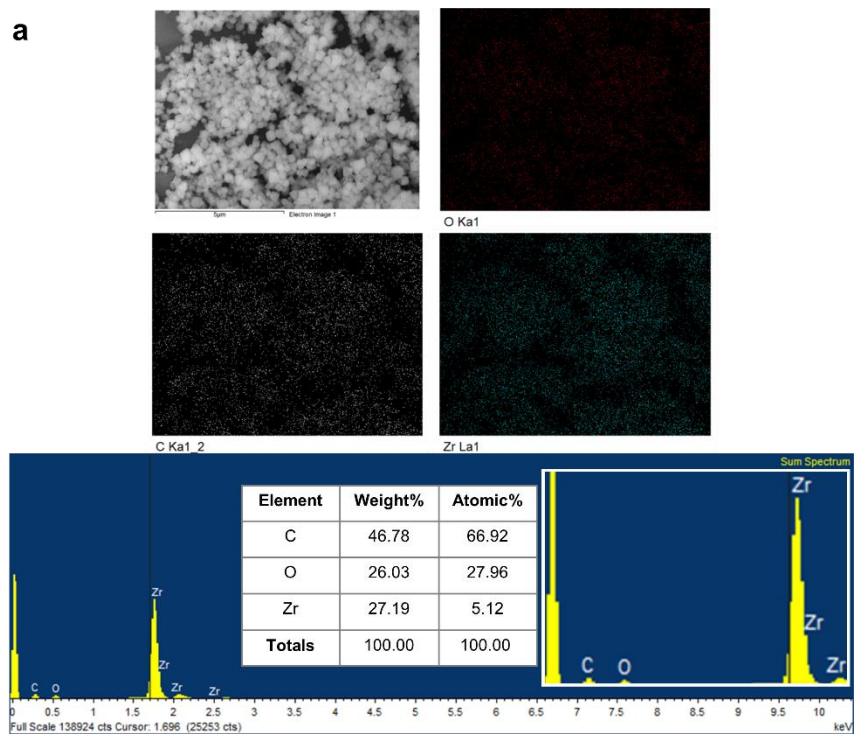
Appendix 8 . Thermogravimetric analysis of 1, 1/PVDF composite at 10 wt % loading.



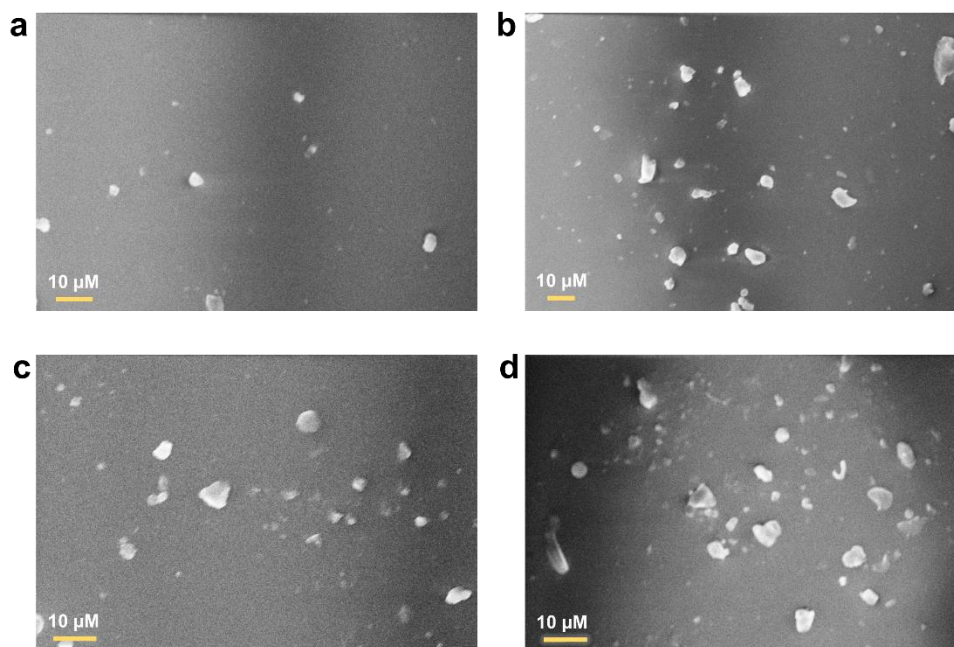
Appendix 9. Thermogravimetric analysis of 2, 2/PVDF composite at 10 wt % loading.



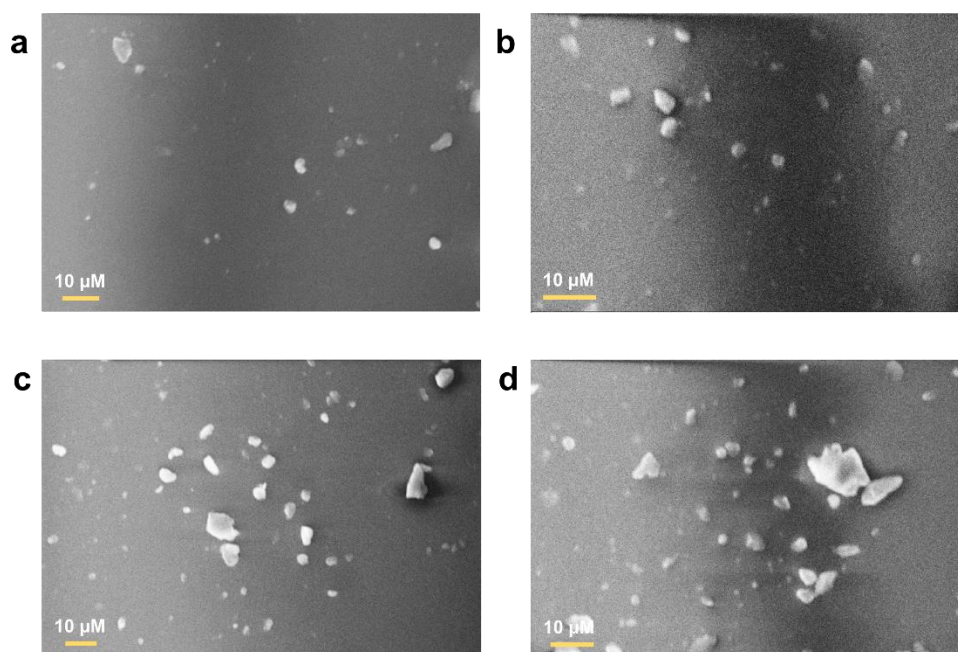
Appendix 10 A). FESEM images for the compound 1 (a, c) and 2 (b, d) at 200 nm resolution scale.



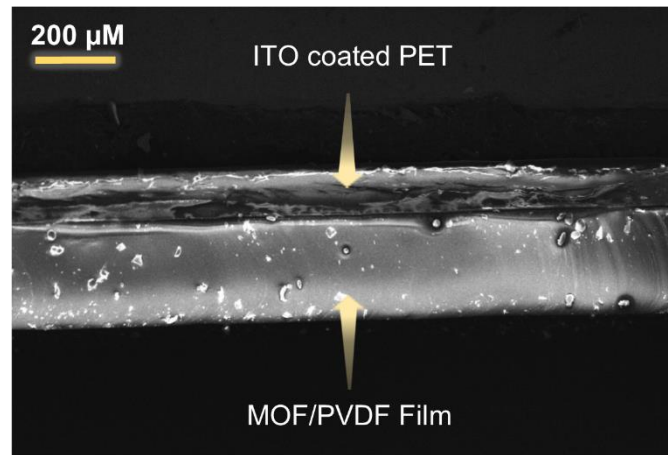
Appendix 10 B). EDX mapping profile and spectra for the compound 1 (a) and compound 2 (b) at bulk.



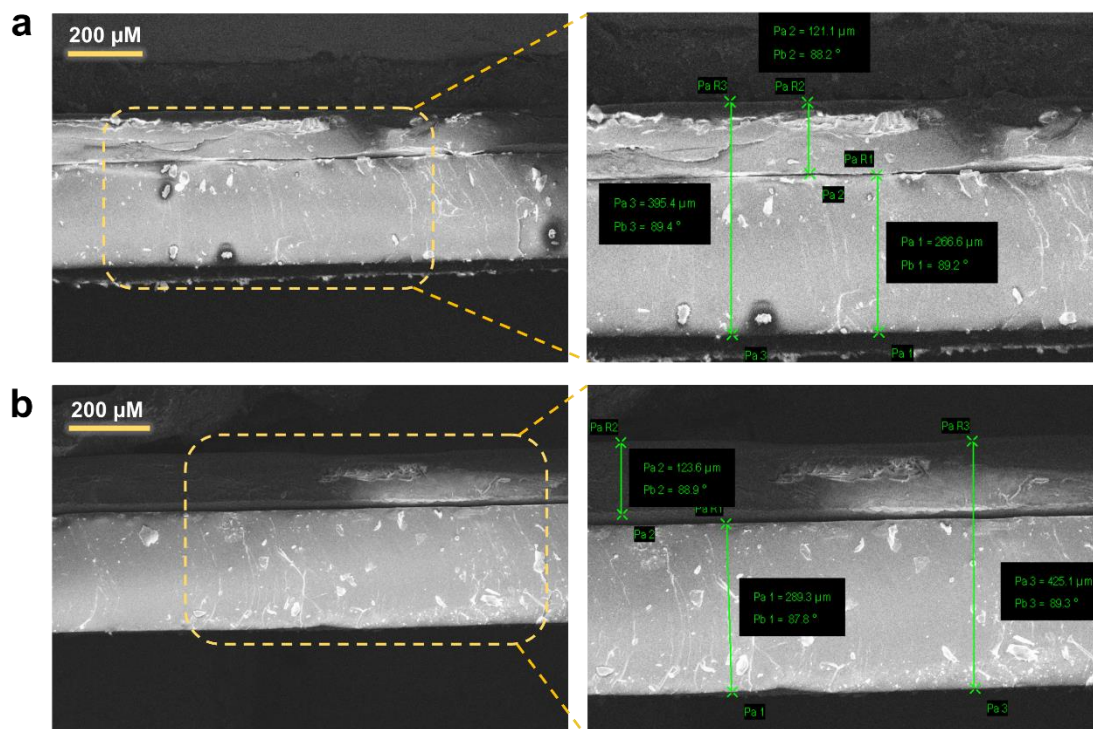
Appendix 11. FESEM images of the (a) 5 (b) 10 (c) 15 and (d) 20 wt % **1**/PVDF composite films.



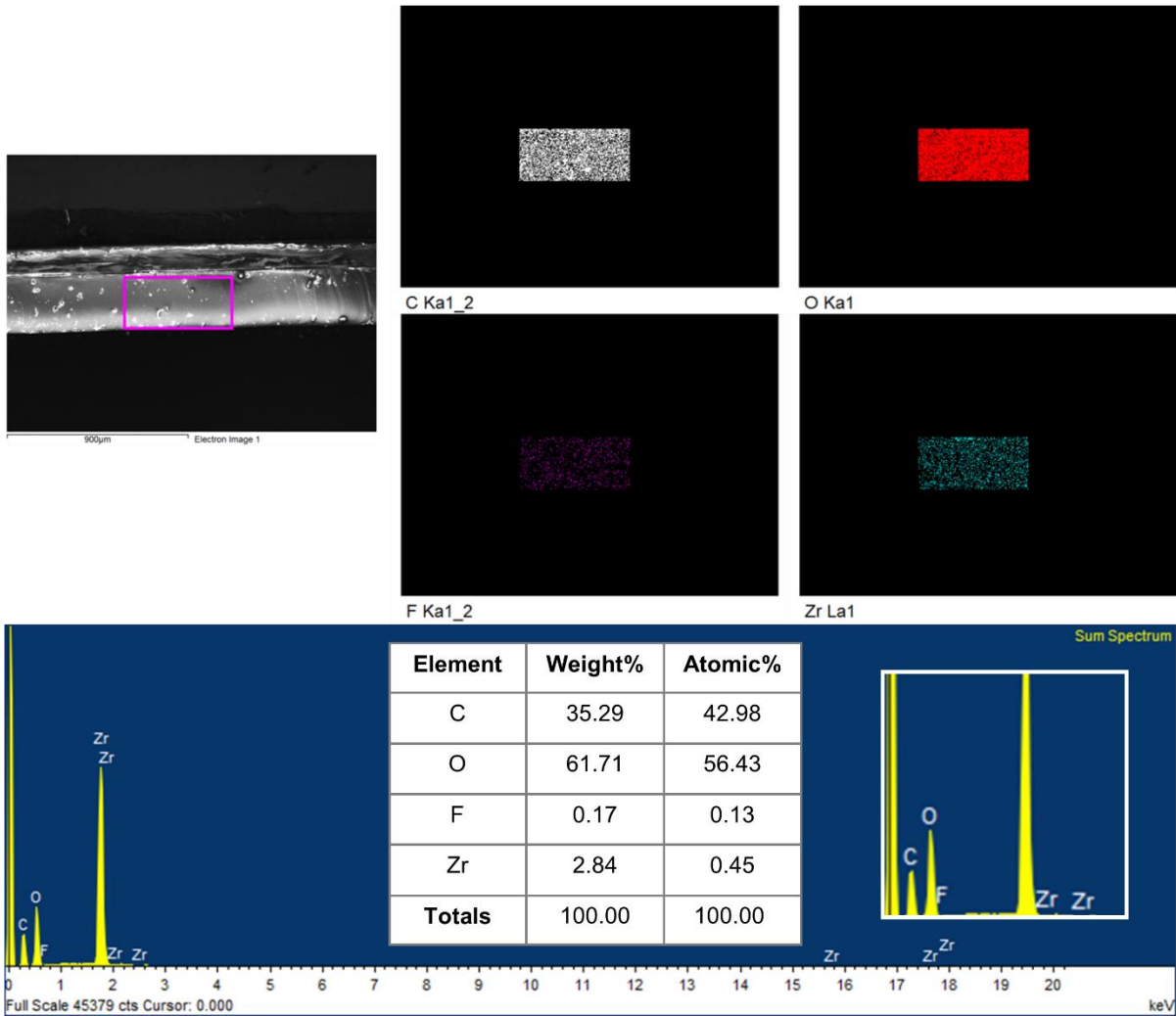
Appendix 12. FESEM images of the (a) 5 (b) 10 (c) 15 and (d) 20 wt % **2**/PVDF composite films.



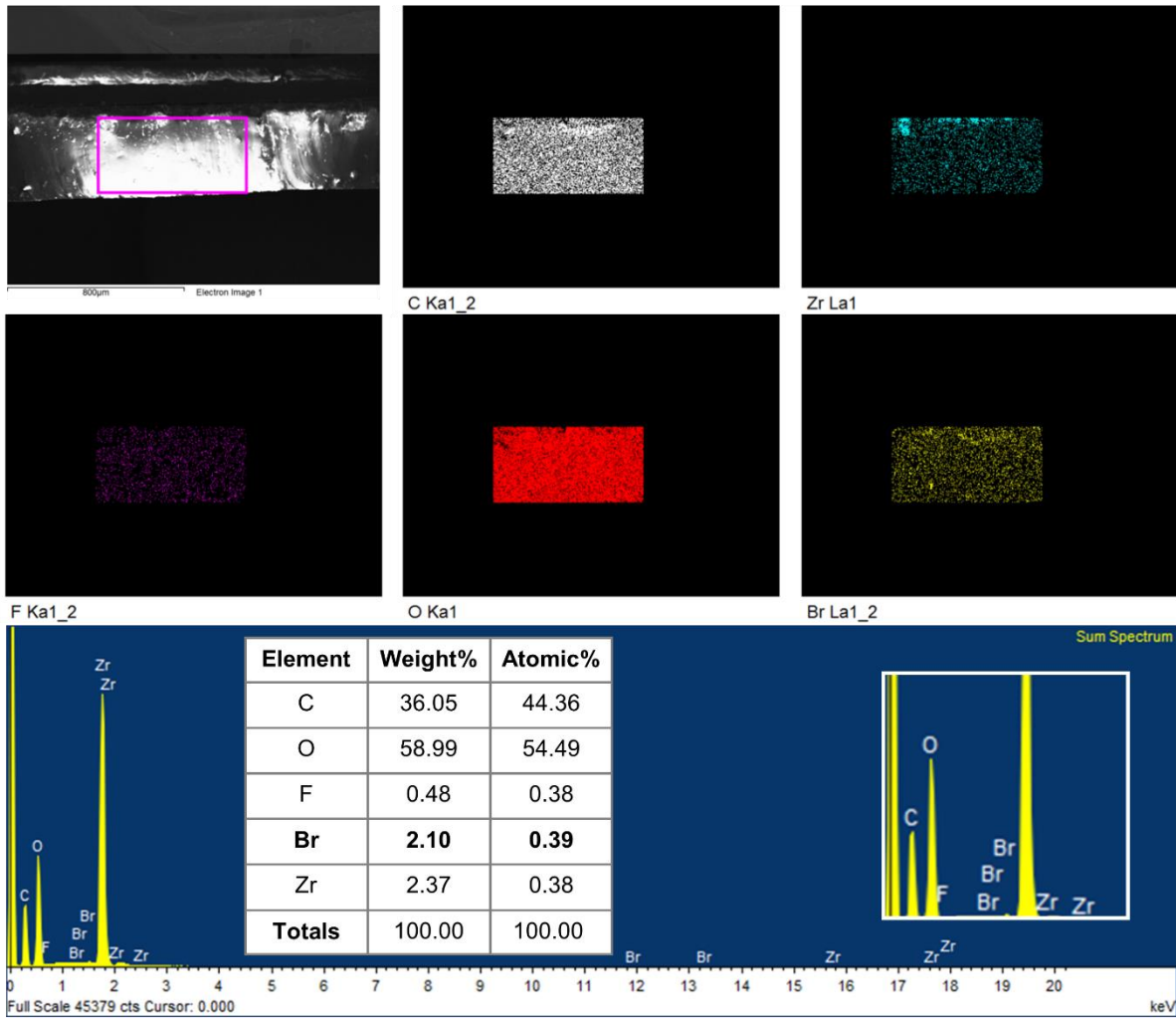
Appendix 13. FESEM image general representation of the cross section imaging composed of PET surface-coated with ITO and layered by MOF/PVDF composite film, seen simultaneously from top to bottom, prepared by doctor-blading method.



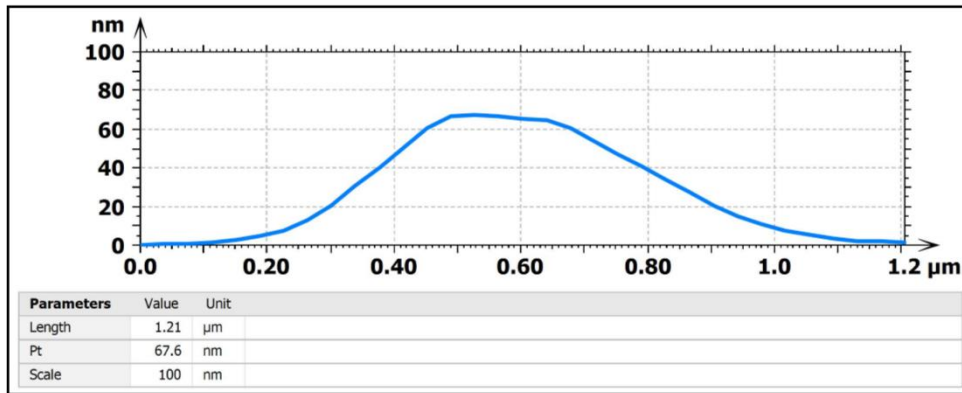
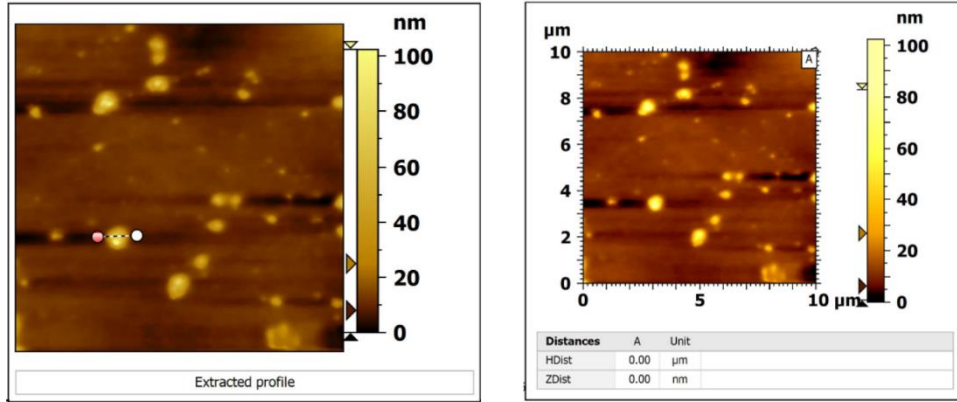
Appendix 14. FESEM images of the cross section of 1/PVDF (a) and 2/PVDF (b). Cross-section for single electrode of the harvester showing a comparable thickness of $\sim 395.4 \mu\text{m}$ for the embedded film of 1 and $\sim 425.1 \mu\text{m}$ for the embedded film of 2.



Appendix 15. EDX mapping profile and spectra for film specific area of 10 wt% of 1/PVDF composite film.

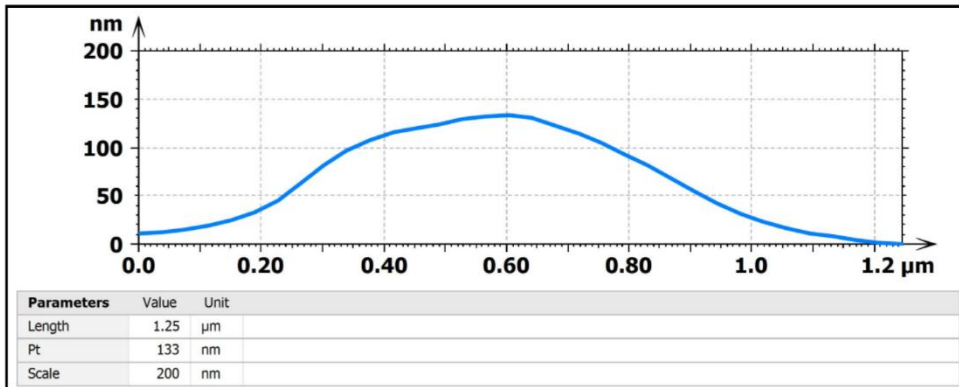
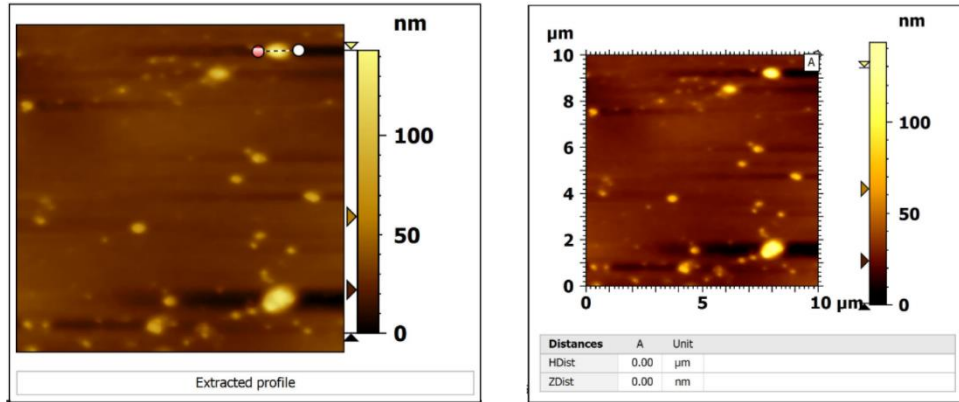


Appendix 16. EDX mapping profile and spectra for film specific area of 10 wt% of 2/PVDF composite film, confirming presence of Br in the composite.



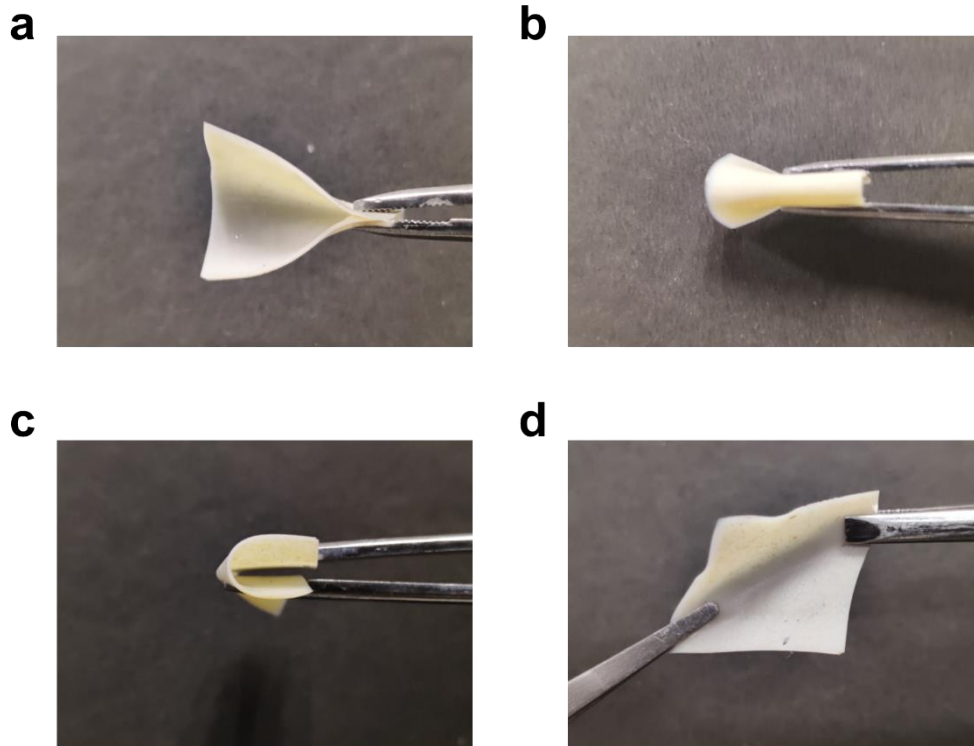
ISO 25178		
Height Parameters		
Sq	6.24	nm
Ssk	5.63	
Sku	51.4	
Sp	103	nm
Sv	11.6	nm
Sz	114	nm
Sa	3.02	nm
EUR 15178N		
Amplitude Parameters		
Sa	3.02	nm
Other 3D Parameters		
Miscellaneous		
Smean	-0.0457	nm
Sdar	100	μm ²
Spar	100	μm ²

Appendix 17. AFM images of 1/PVDF composite film, trace and retrace in the X-direction, and Y-direction, line roughness profile with height parameters simultaneously.

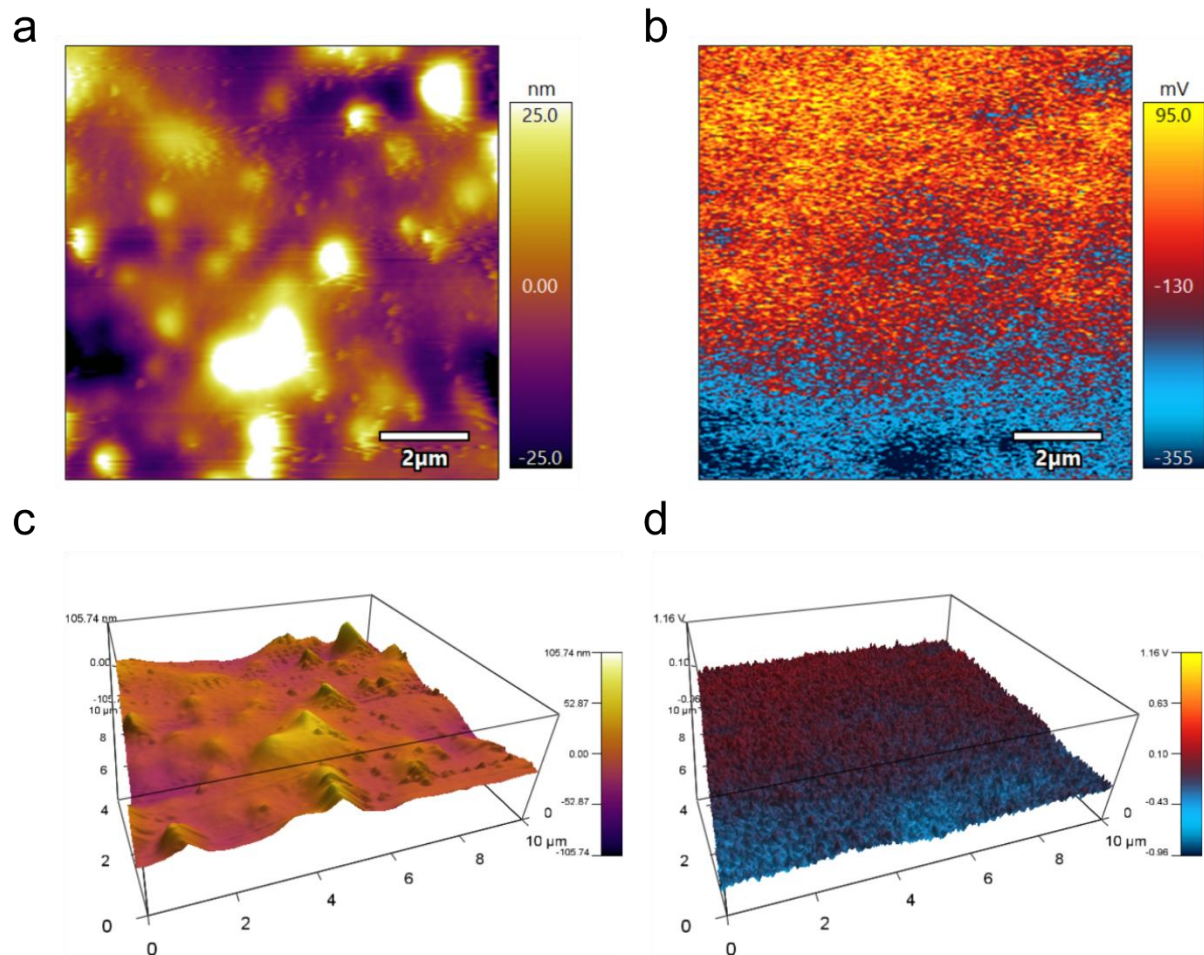


ISO 25178			
Height Parameters			
Sq		9.52	nm
Ssk		5.28	
Sku		48.1	
Sp		119	nm
Sv		28.5	nm
Sz		148	nm
Sa		4.44	nm
EUR 15178N			
Amplitude Parameters			
Sa		4.44	nm
Other 3D Parameters			
Miscellaneous			
Smean		-0.0359	nm
Sdar		100	μm ²
Spar		100	μm ²

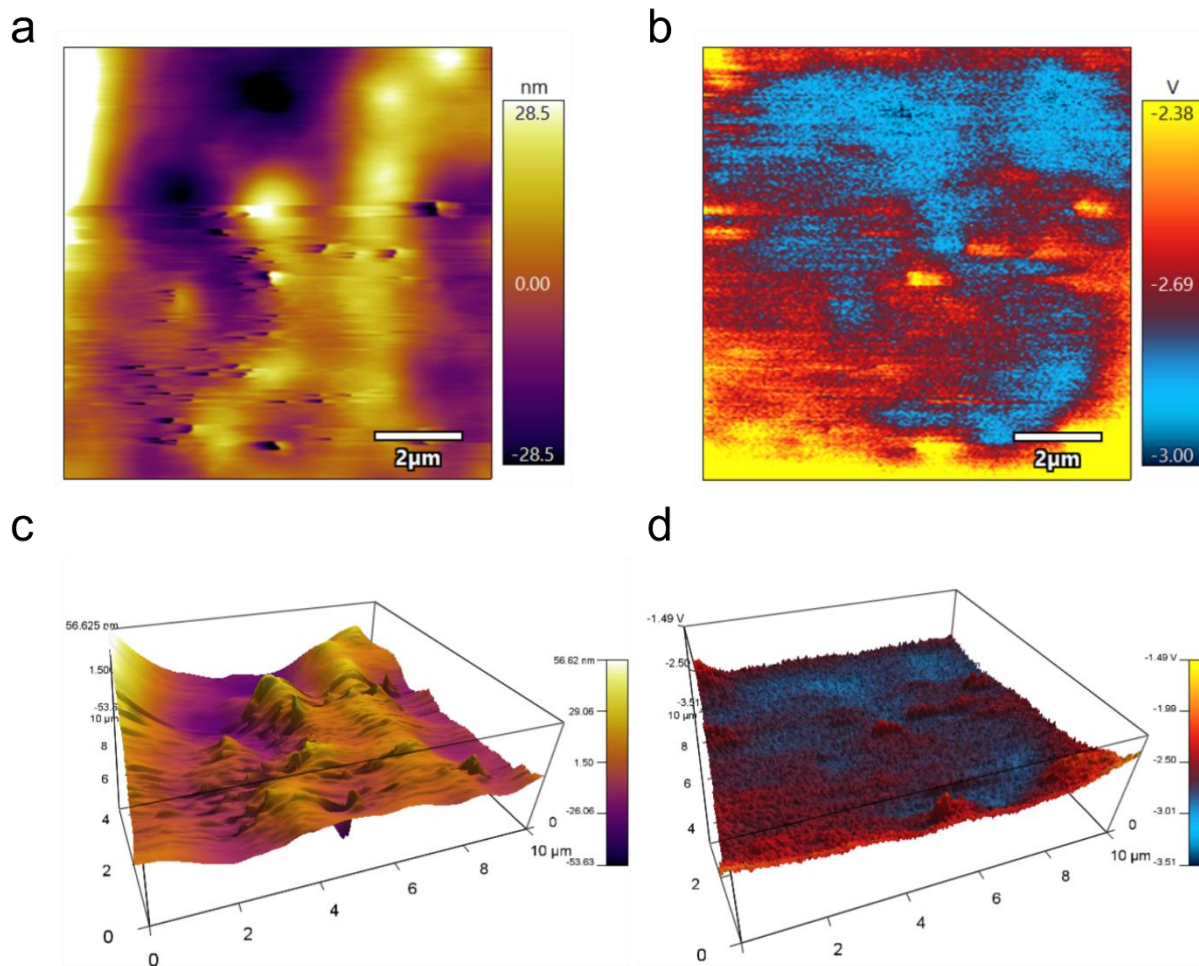
Appendix 18. AFM images of 2/PVDF composite film, trace and retrace in the X-direction, and Y-direction, line roughness profile with height parameters simultaneously.



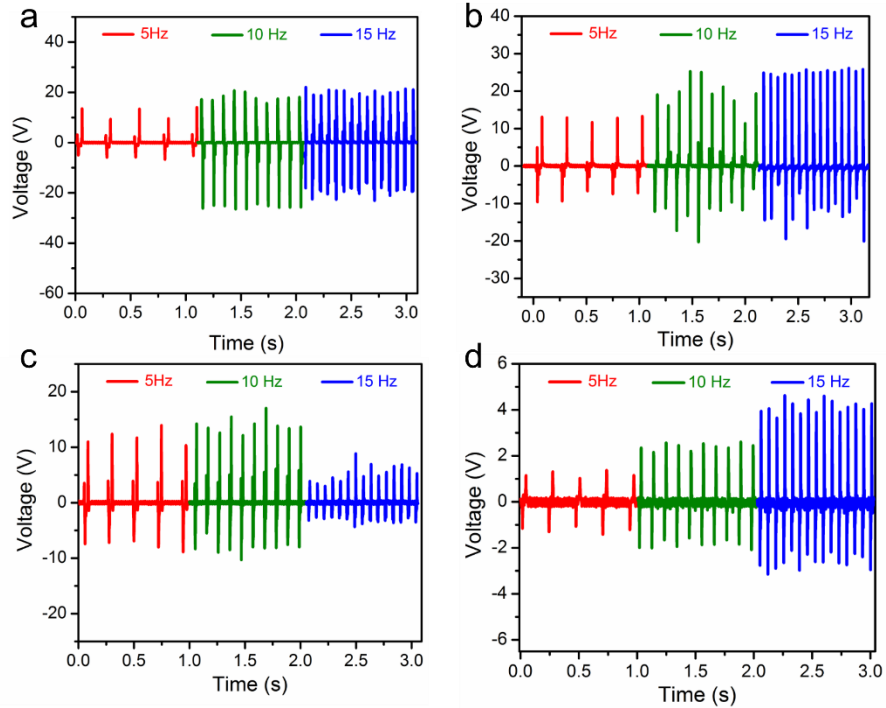
Appendix 19. Flexible composites exhibiting (a) bending (b) axial rolling and (c) cross rolling (d) stretching operations.



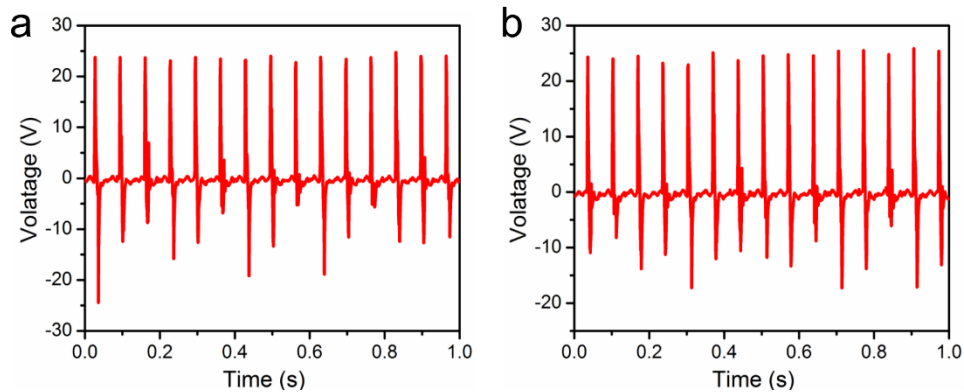
Appendix 20. The surface potential mapping using KPFM for 1/PVDF at 10 wt %.



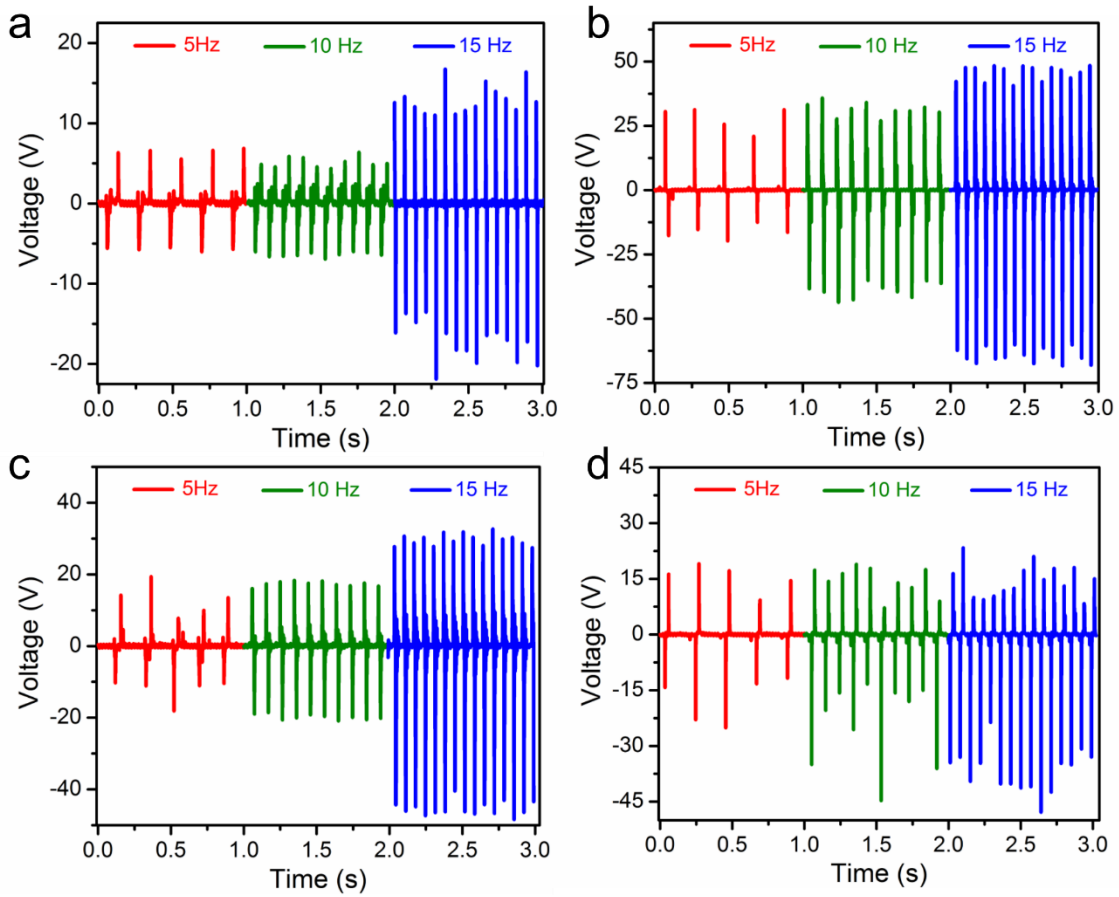
Appendix 21. The surface potential mapping using KPFM for 2/PVDF at 10 wt %.



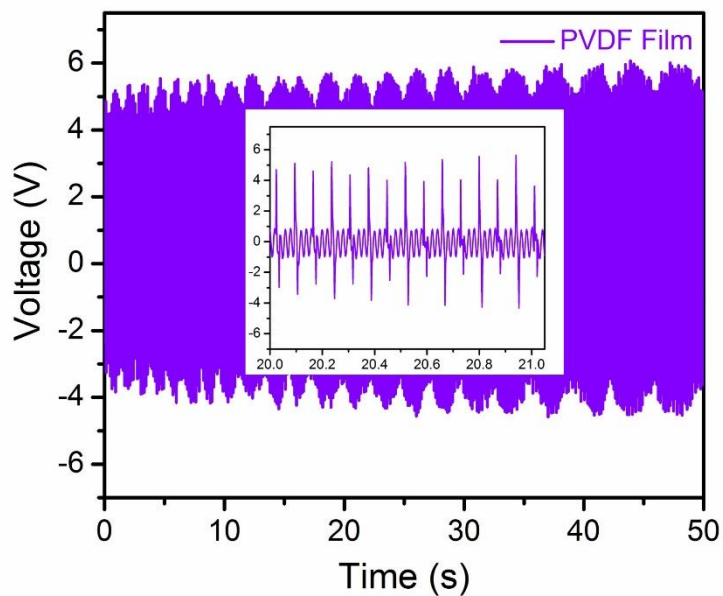
Appendix 22. Effect of frequency of impact on open circuit voltage of $2.5 \times 2.5 \text{ cm}^2$ area for 1/PVDF TENG devices using (a) 5%, (b) 10%, (c) 15% and (d) 20% weight loading respectively. Force realized at 5Hz, 10Hz, 15 Hz was 10N, 18N, 26N respectively. For (b) @15Hz; (n) = 15, (P) = * $p < 0.05$, ** $p < 0.01$, *** $p < 0.001$, refer Appendix 36 for statistical distribution.



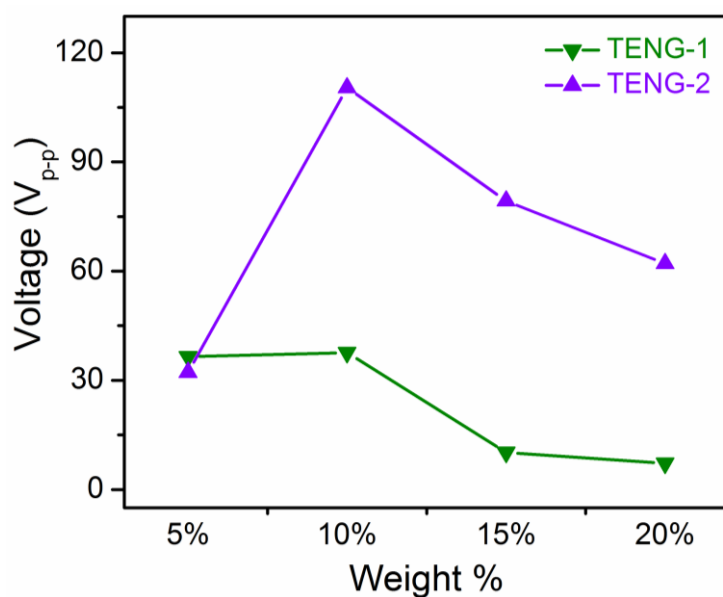
Appendix 23. Open circuit voltage measurements performed on two independent 10 wt % 1/PVDF (TENG-1) composite devices.



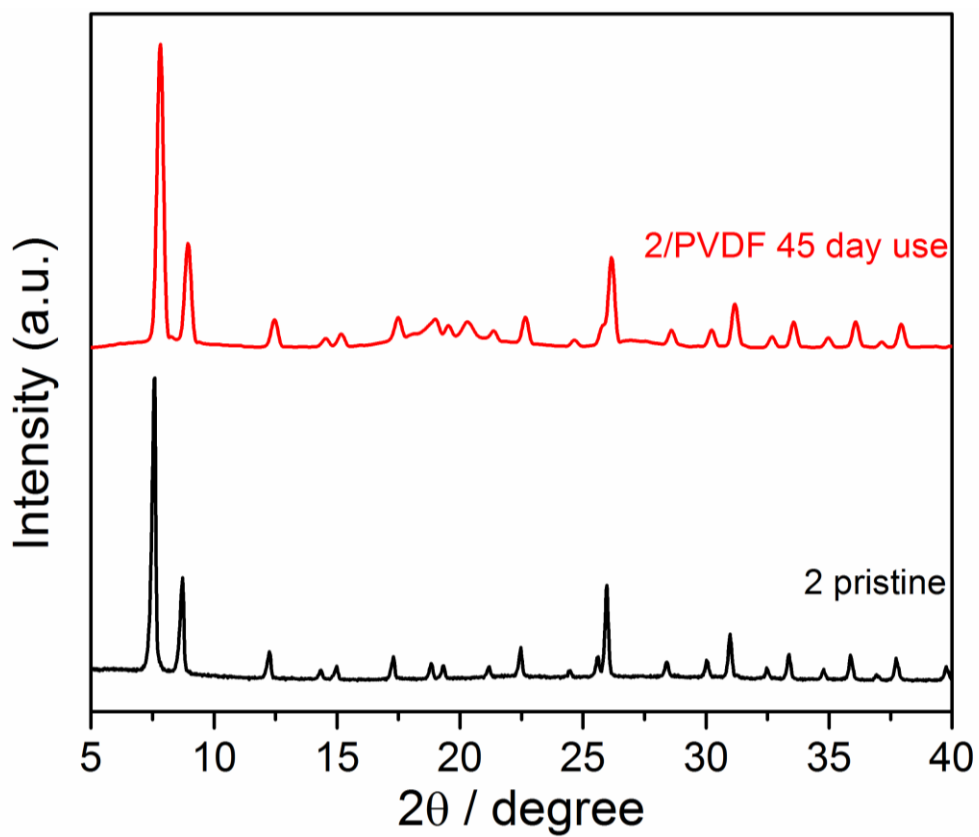
Appendix 24 a). Effect of frequency of impact on open circuit voltage of 2.5 x 2.5 cm² area for 2/PVDF TENG devices using (a) 5%, (b) 10%, (C) 15% and (d) 20% weight loading respectively. The force realized at 5Hz was 10N, at 10Hz it was 18N and at 15Hz was 26N. For (b) @15 Hz; (n) = 15, (P) =* p<0.05, ** p<0.01, *** p<0.001.



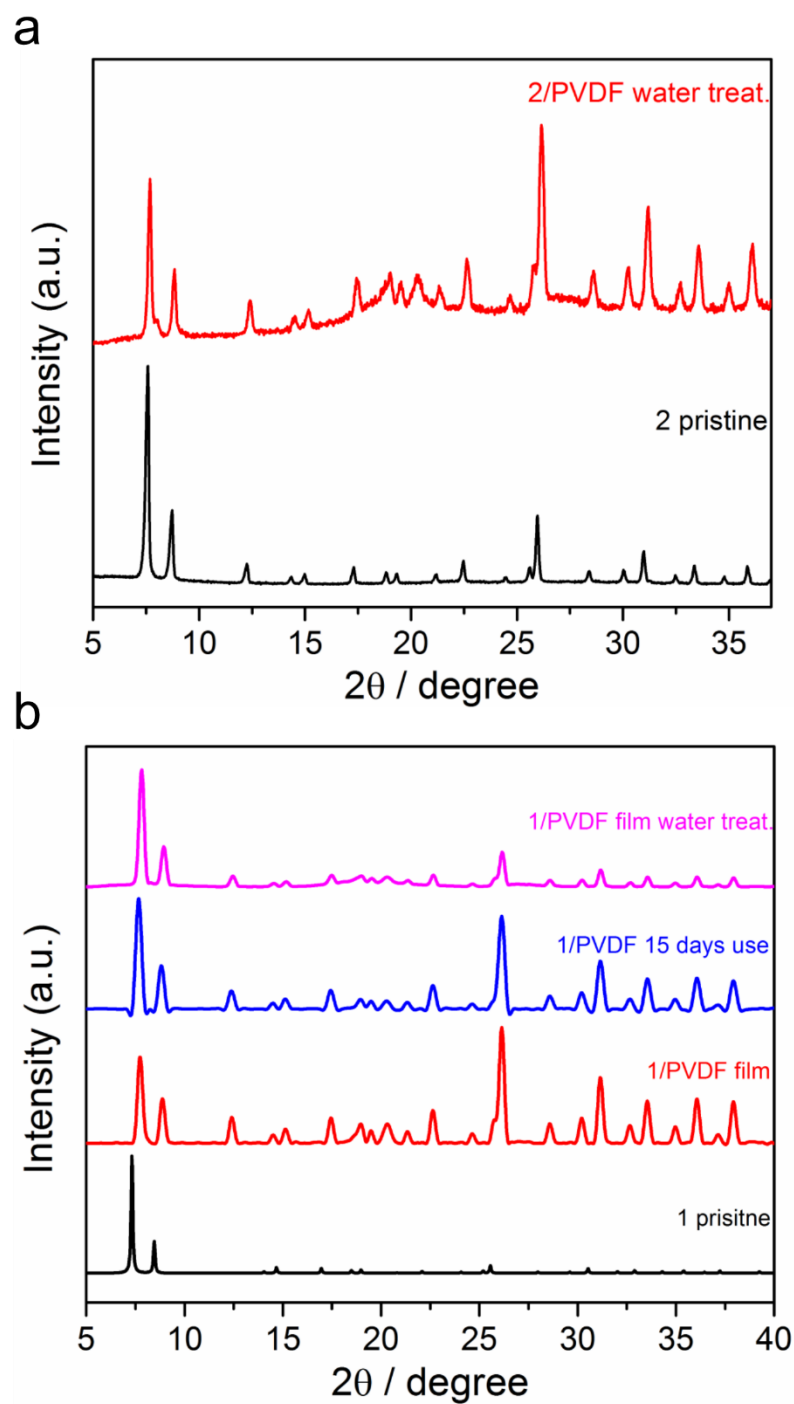
Appendix 24 b). Effect of frequency of impact on open circuit voltage of $2.5 \times 2.5 \text{ cm}^2$ area for PVDF-only TENG devices using 0% weight loading of MOF sample. The force realized at 15Hz was 26N.



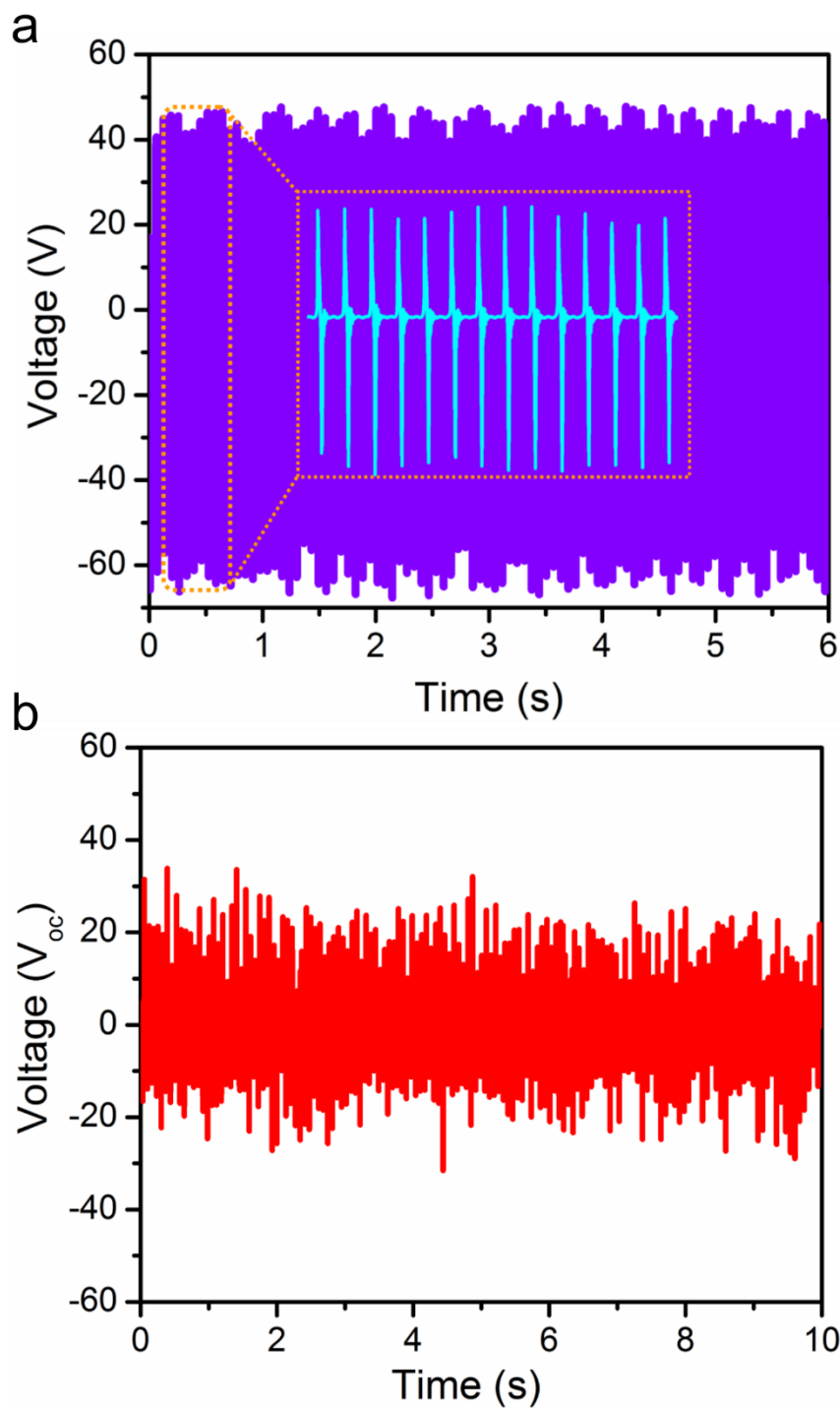
Appendix 25. Comparison of the experimental voltage output for TENG-1 and TENG-2 energy harvester at different wt % loading.



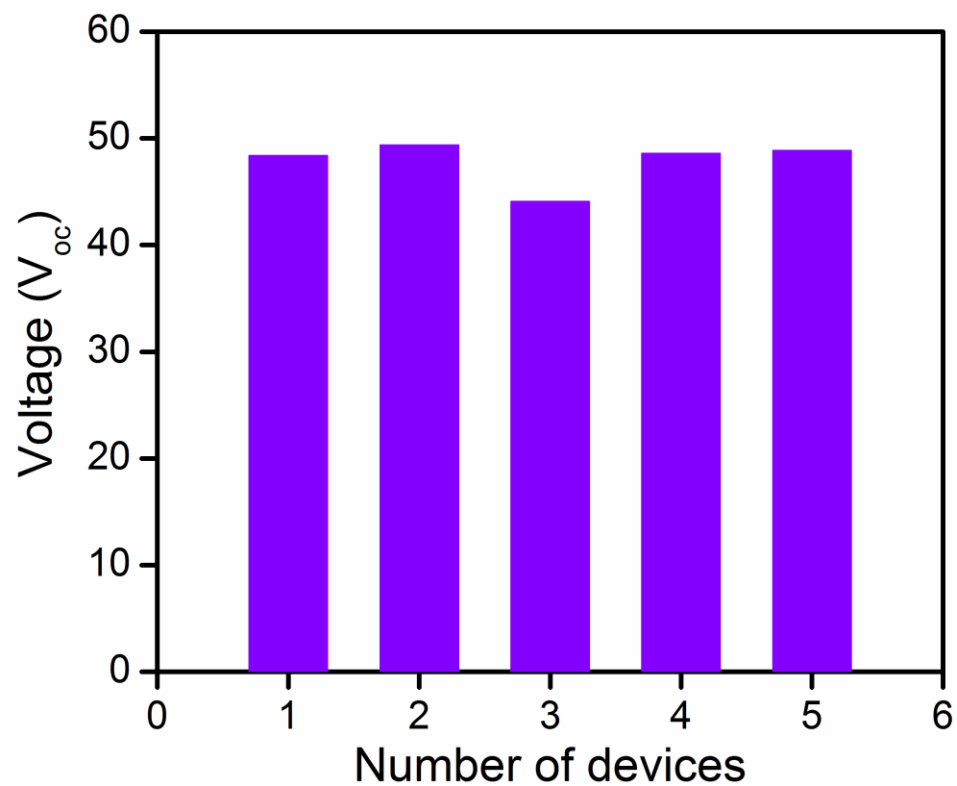
Appendix 26. Comparison of the experimental PXRD data of 2 and 2/PVDF after 45 days of use.



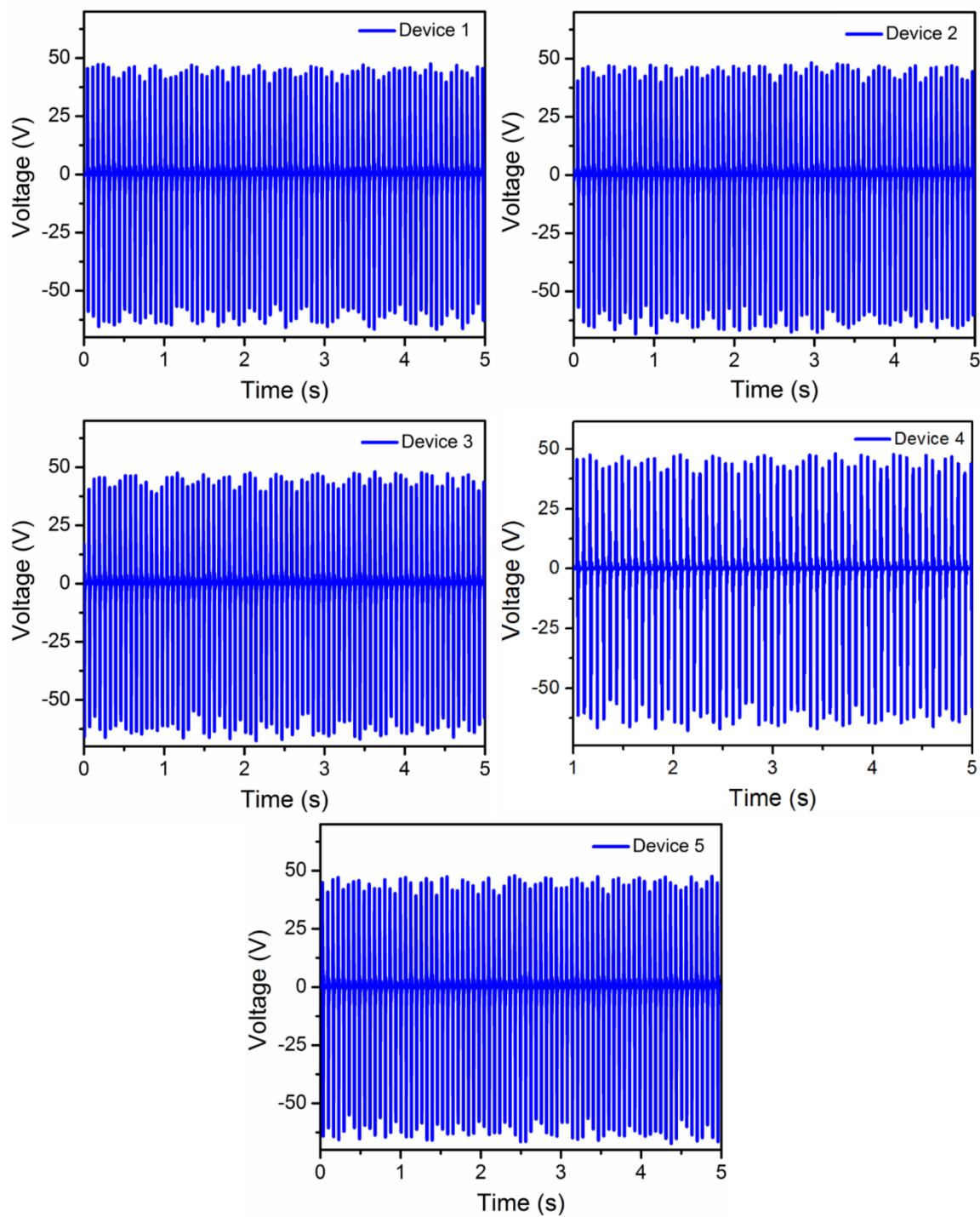
Appendix 27. Comparison of the experimental PXRD data of **a**). **2** and **2/PVDF** (i.e. TENG-2) after two consecutive water treatment cycles; **b**). **1** and **1/PVDF** (i.e. TENG-1) after post 15 day's measurement and after a water treatment cycle.



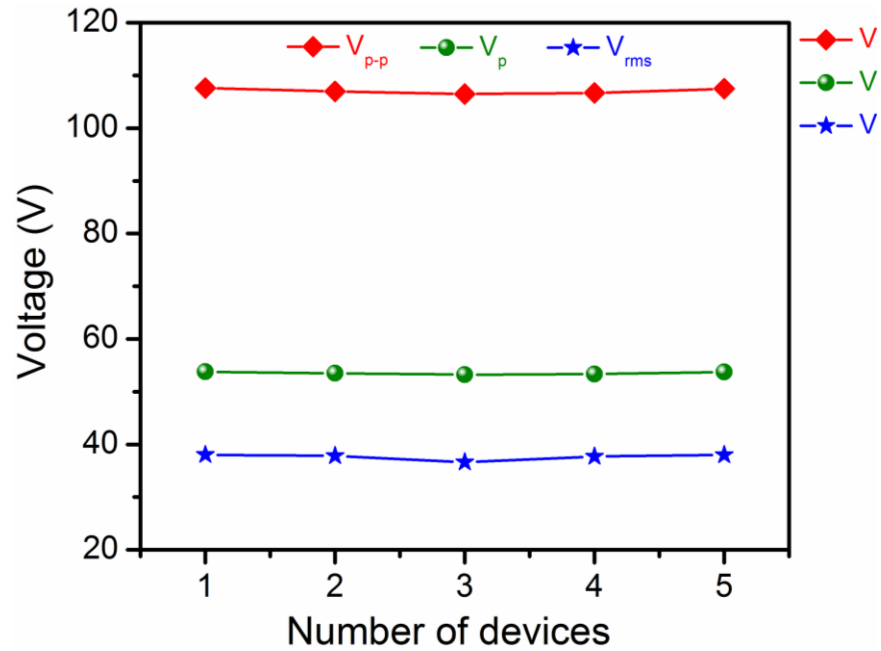
Appendix 28. Open circuit voltage measurements conducted on dried 10 wt % **a).** 2/PVDF composite device (TENG-2) after exposing it to 98% RH over 24 h; **b).** 1/PVDF composite device (TENG-1) after exposing it to 98% RH over 24 h. For (a); (n) = 20, (P) = * $p < 0.05$, ** $p < 0.01$, *** $p < 0.001$.



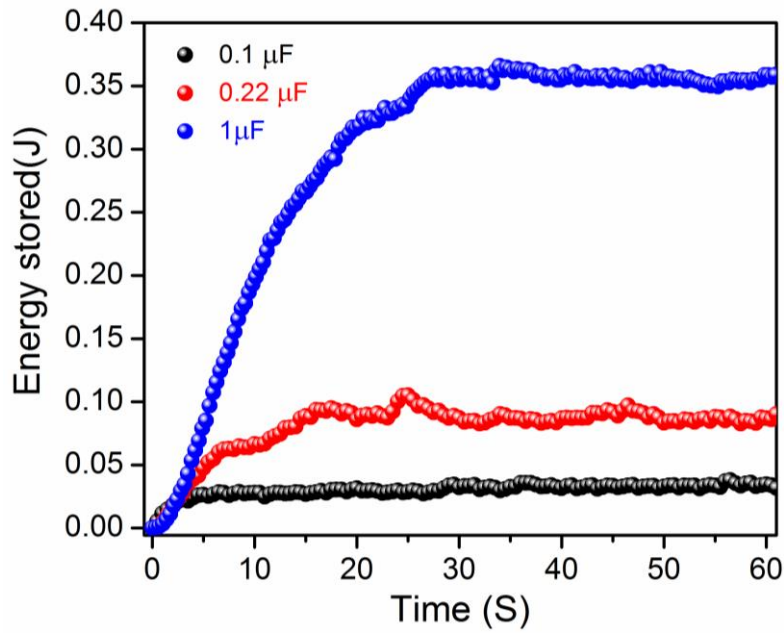
Appendix 29 a). Bar plot for the open circuit voltage measurements conducted on five separate 10 wt % 2/PVDF composite devices (TENG-2 series).



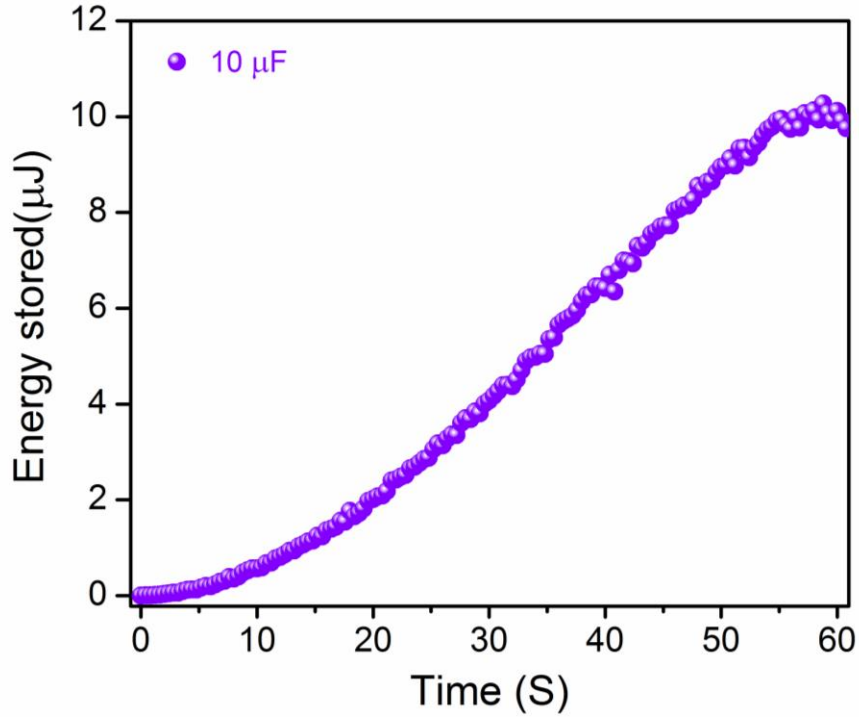
Appendix 29 b). Open circuit voltage measurements conducted on five separate 10 wt % 2/PVDF composite devices (TENG-2 series).



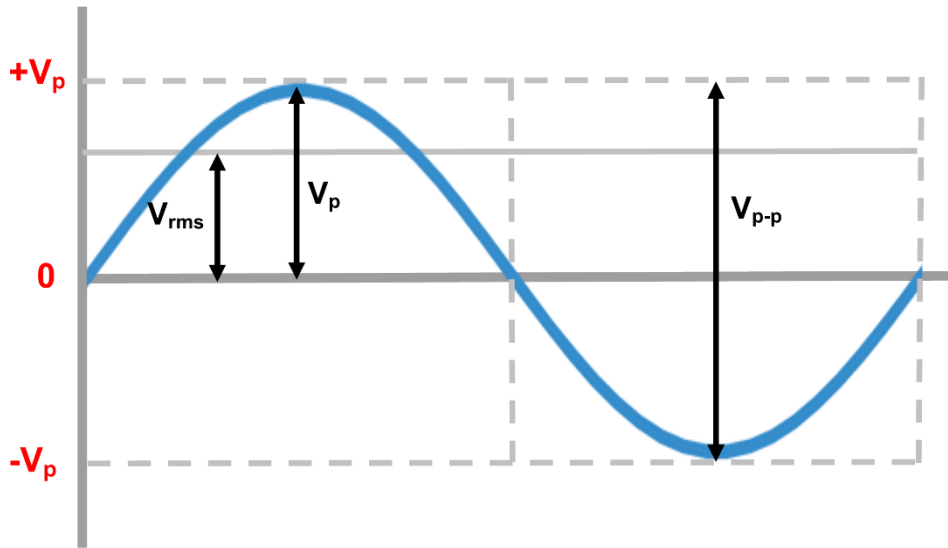
Appendix 30. V_{p-p} , V_p and V_{rms} output of five fabricated 10 wt% 2/PVDF TENG devices. (n) = 15, (P) = * p<0.05, ** p<0.01, *** p<0.001.



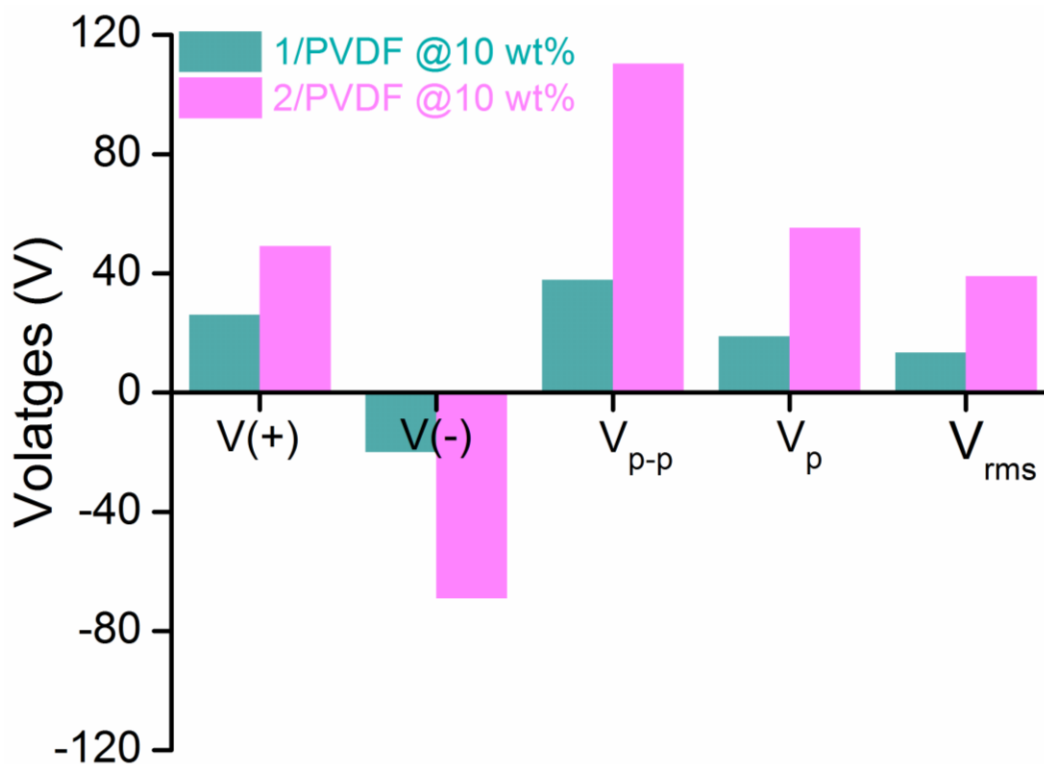
Appendix 31. The TENG-2 device generated plot of energy stored by 0.1, 0.22 and 1 μF capacitors throughout a minute operational time.



Appendix 32. The TENG-2 device generated plot of energy stored by 10 μF capacitor throughout a minute operational time.



Appendix 33. General illustration of signal waveform and attributed voltage measurement parameters as V_p , V_{p-p} , V_{rms} .



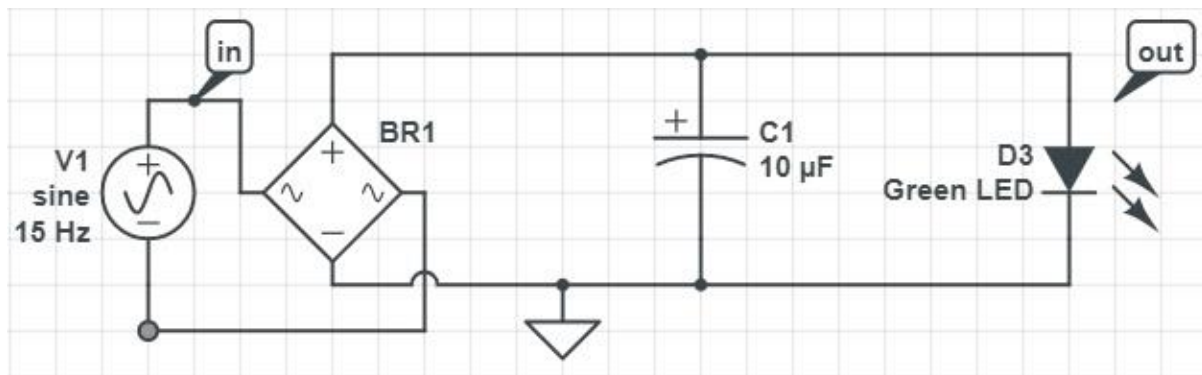
Appendix 34. Open circuit voltage parameters measured for 10 wt % of selected devices for 1/PVDF and 2/PVDF.

Voltage (V_{oc})	1/PVDF TENG	2/PVDF TENG
V_{p-p}	37.85 V	110.41 V
V_p	18.92 V	55.21 V
V_{rms}	13.38 V	39.04 V
$V_{p(+)}, V_{p(-)}$	26.14 V, -20.07V	49.12 V, -68.95 V

Appendix Table 1. Comparative table of open circuit voltages V_p , V_{p-p} , V_{rms} measured for 1/PVDF and 2/PVDF.

Capacitor	Voltage (V)	Charge stored (μC)	Energy derived (μJ)
0.1 μF	0.89 V	0.088 μC	0.04 μJ
0.22 μF	1.00 V	0.22 μC	0.11 μJ
1 μF	0.86 V	0.86 μC	0.37 μJ
10 μF	1.48 V	14.8 μC	11.1 μJ

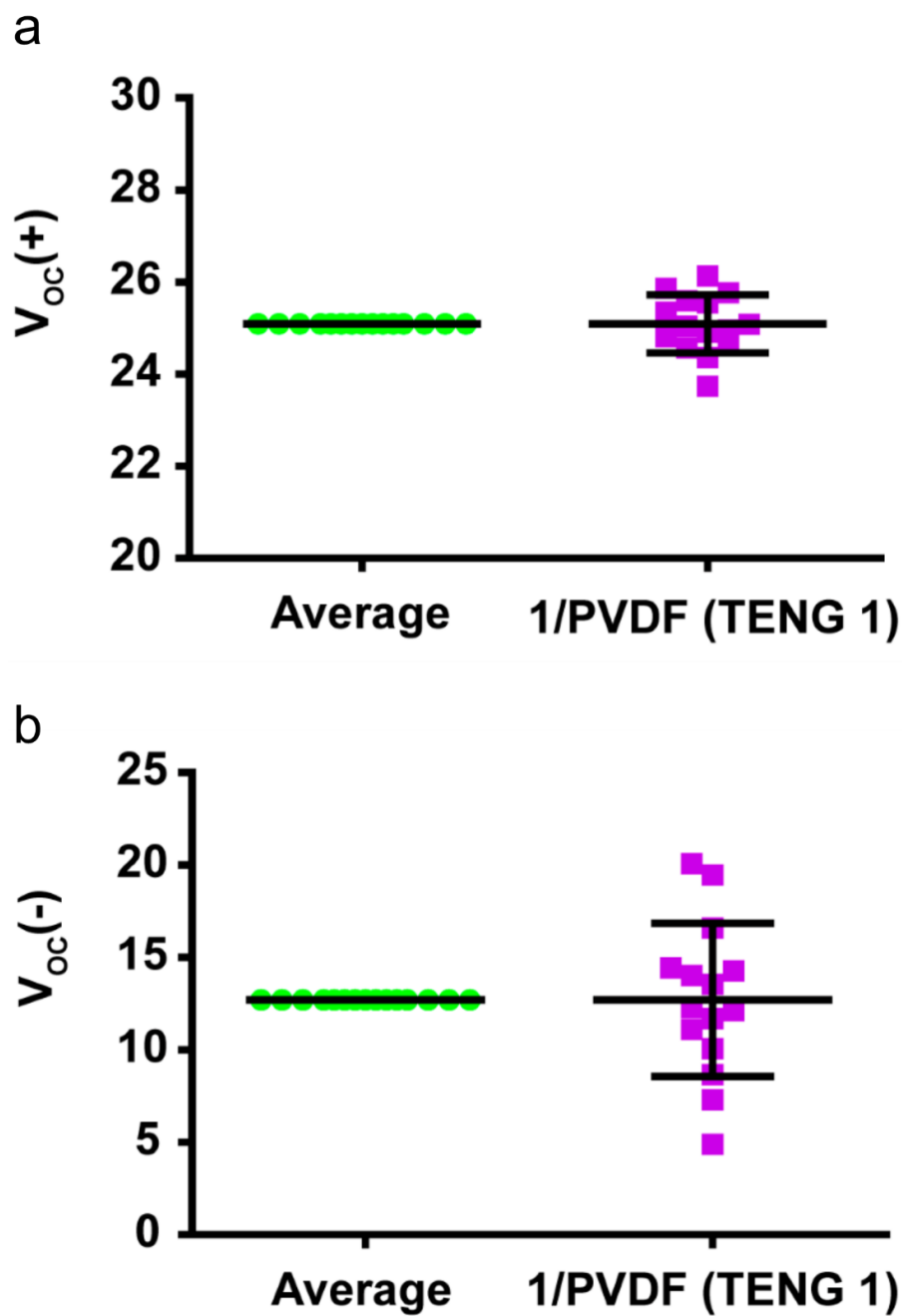
Appendix Table 2. Comparative table of voltage derived, charge and energy thus obtained from TENG-2 device after 60 sec operation.



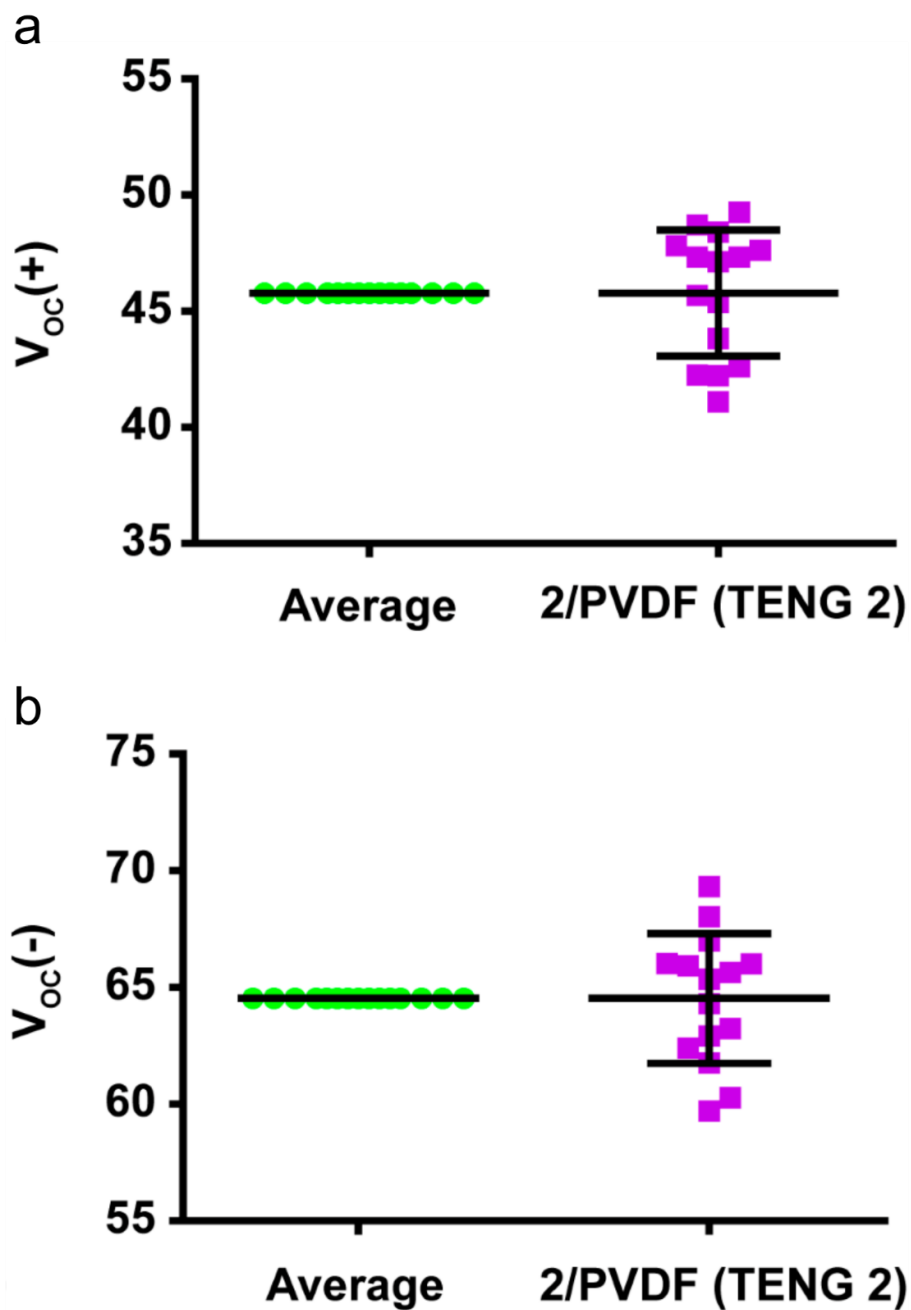
Appendix 35. Circuit diagram illustrative of circuit deployed for single green LED illumination by using 10 μF capacitor.

Acceptor (-)	e^-	Donor (+)
PTFE		Al
PDMS		Cu
FEP		Skin
Kapton		Nylon
PET		PET
Silicone		Ag
PS		Au
Cellulose		Cellulose
PVDF		PU
Polyolefine		PVA
Acrylic		Steel
Rubber		Chi-Gly
Graphene		Kapton
Alginate		Textile
PVA		Latex
		ITO
		CB/CNT
		Acrylic
		Silk
		Graphene

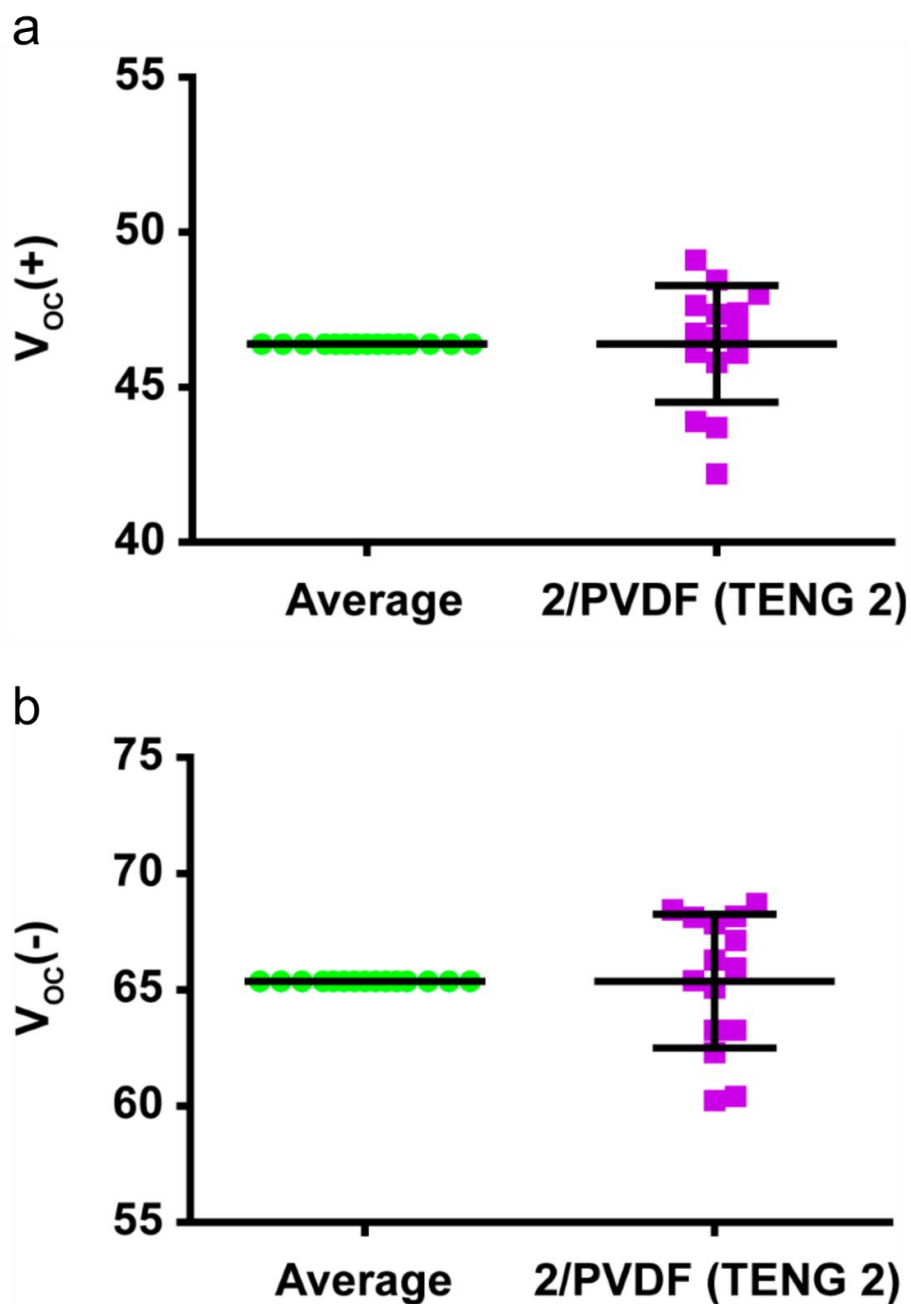
Appendix Table 3. Network of electron acceptors and donors are paired in the selected literature reports.^[67] Blue arrow indicates combination utilized in present study.



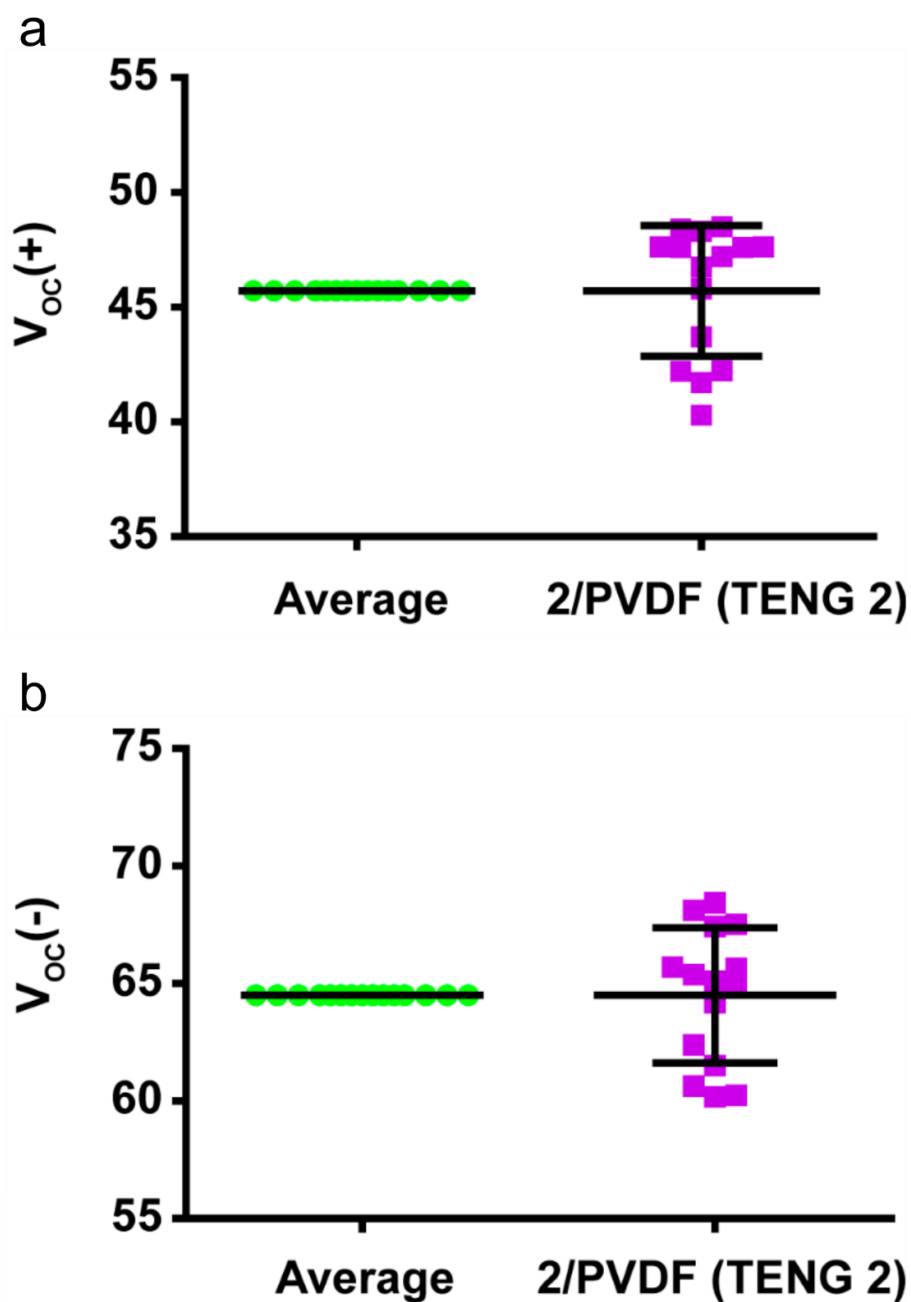
Appendix 36. Data represents the corresponding Figure 2a in the main manuscript. Statistical analysis of 1/PVDF 10% composite film (TENG-1). Each data point ($n=15$) represents a peak of voltage either on positive side as $V_{oc}(+)$ or negative side as $V_{oc}(-)$. The ns comparisons are not shown; data is consistent and does not change significantly. Student's t-test applied with Welch's correction. * $p<0.05$, ** $p<0.01$, *** $p<0.001$.



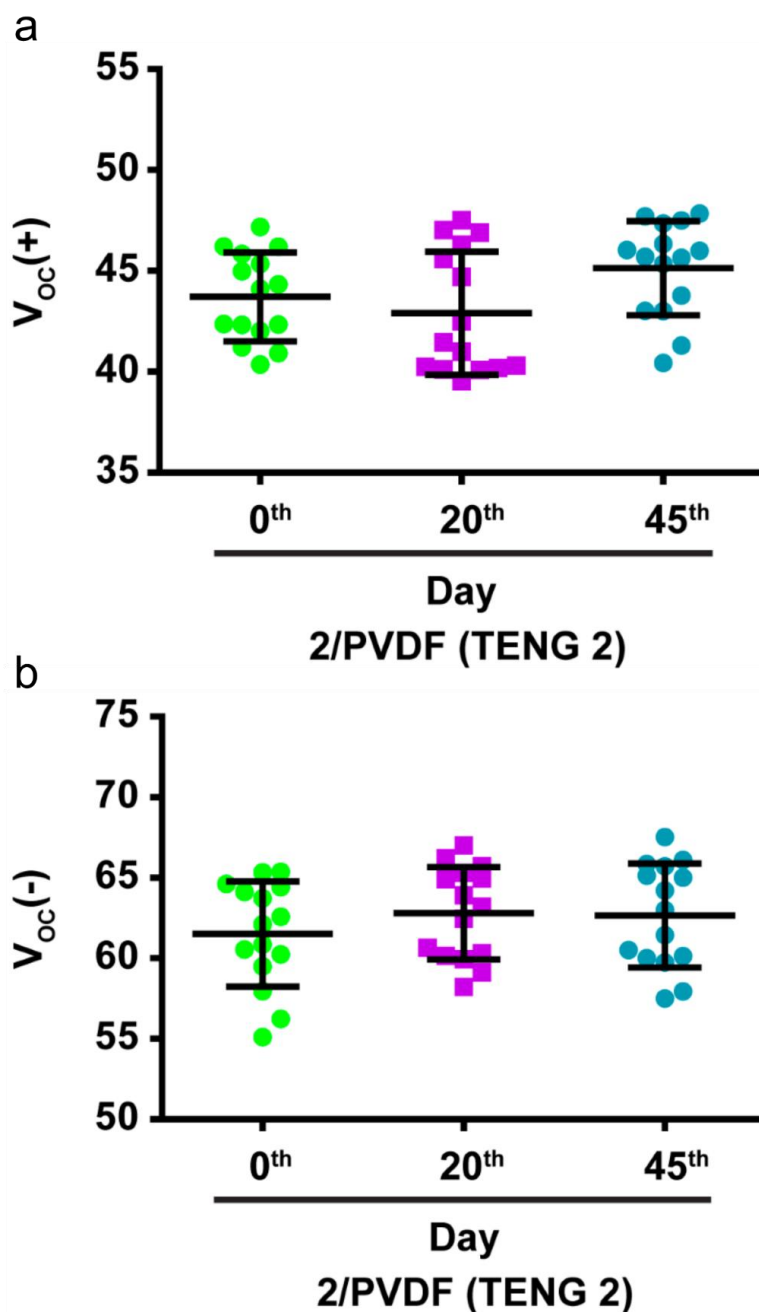
Appendix 37. Data represents the corresponding Figure 2b in the main manuscript. Statistical analysis of 2/PVDF 10% composite film (TENG-2). Each data point ($n=15$) represents a peak of voltage either on positive side as $V_{oc}(+)$ or negative side as $V_{oc}(-)$. The ns comparisons are not shown; data is consistent and does not change significantly. Student's t-test applied with Welch's correction. * $p<0.05$, ** $p<0.01$, *** $p<0.001$.



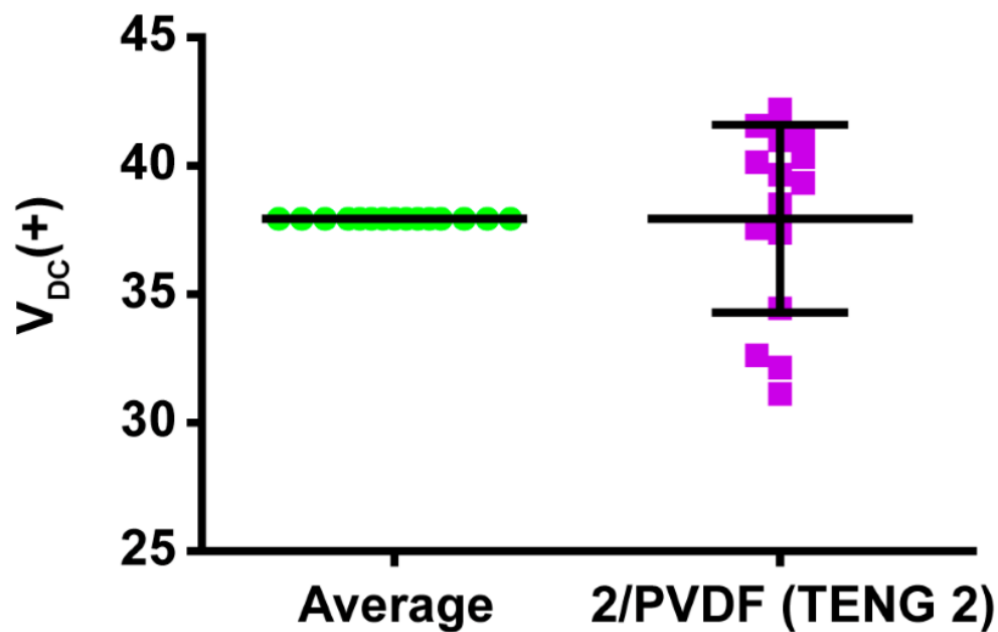
Appendix 38. Data represents the corresponding Figure 2c in the main manuscript. Statistical analysis of 2/PVDF 10% composite film (TENG-2). Each data point (n=20) represents a peak of voltage either on positive side as $V_{oc}(+)$ or negative side as $V_{oc}(-)$. Total data points considered for experiment were n=3000 on each side respectively. The ns comparisons are not shown; data is consistent and does not change significantly. Student's t-test applied with Welch's correction. * $p < 0.05$, ** $p < 0.01$, *** $p < 0.001$.



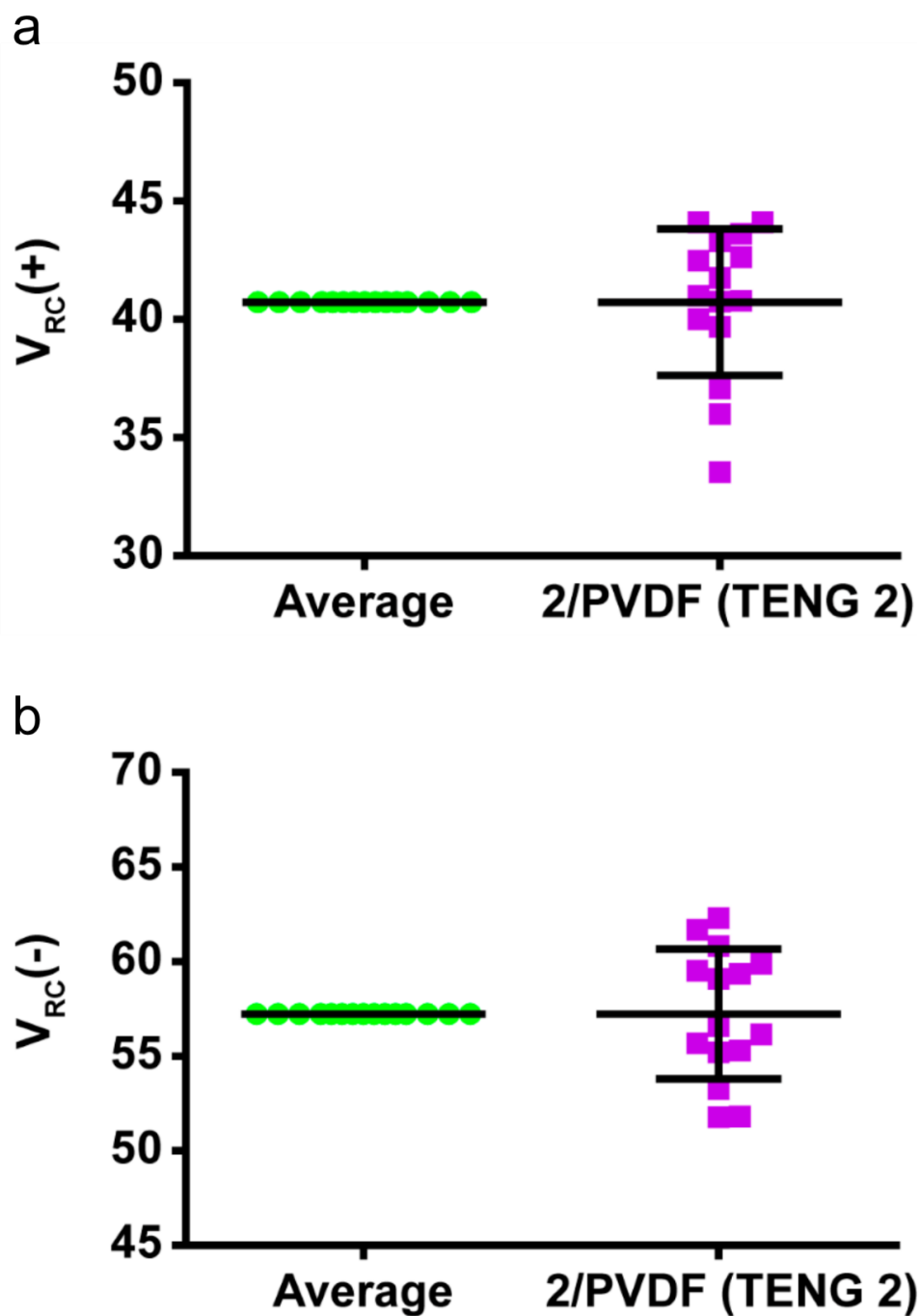
Appendix 39. Data represents the corresponding Figure 2d in the main manuscript. Statistical analysis of 10% of 2/PVDF composite film (TENG-2). Each data point ($n = 15$) represents a peak of voltage either on positive side as $V_{oc}(+)$ or negative side as $V_{oc}(-)$. The ns comparisons are not shown; data is consistent and does not change significantly. Student's t-test applied with Welch's correction. * $p < 0.05$, ** $p < 0.01$, *** $p < 0.001$.



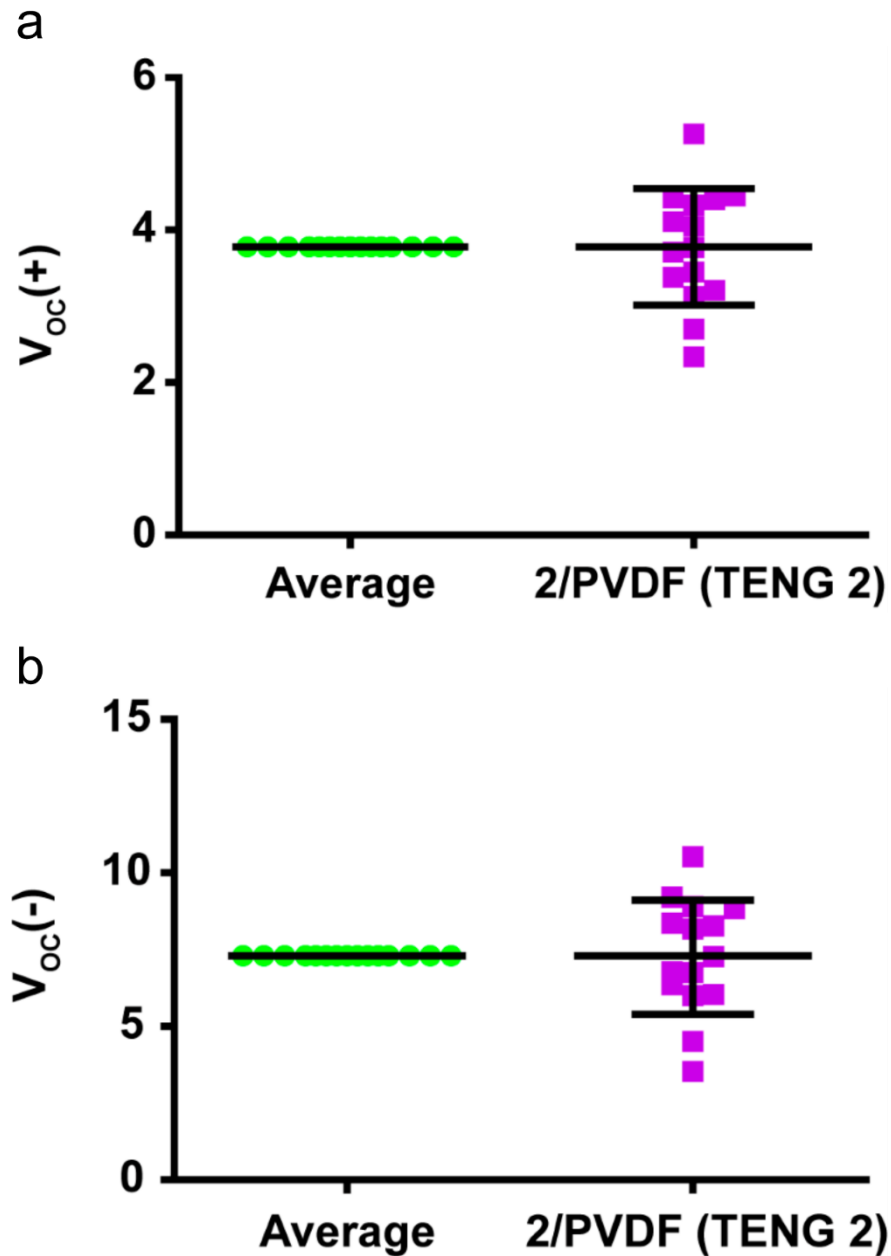
Appendix 40. Data represents the corresponding Figure 2e in the main manuscript and represented with respective mean and SD. In 3 data sets (measured at day 1, after 20 days and after 45 days), each data point ($n=15$) represents a peak of voltage either on positive side or negative side. The ns comparisons are not shown, data is consistent. One way ANOVA with Tukey's multiple comparisons is performed to analyze the data. * $p<0.05$, ** $p<0.01$, *** $p<0.001$.



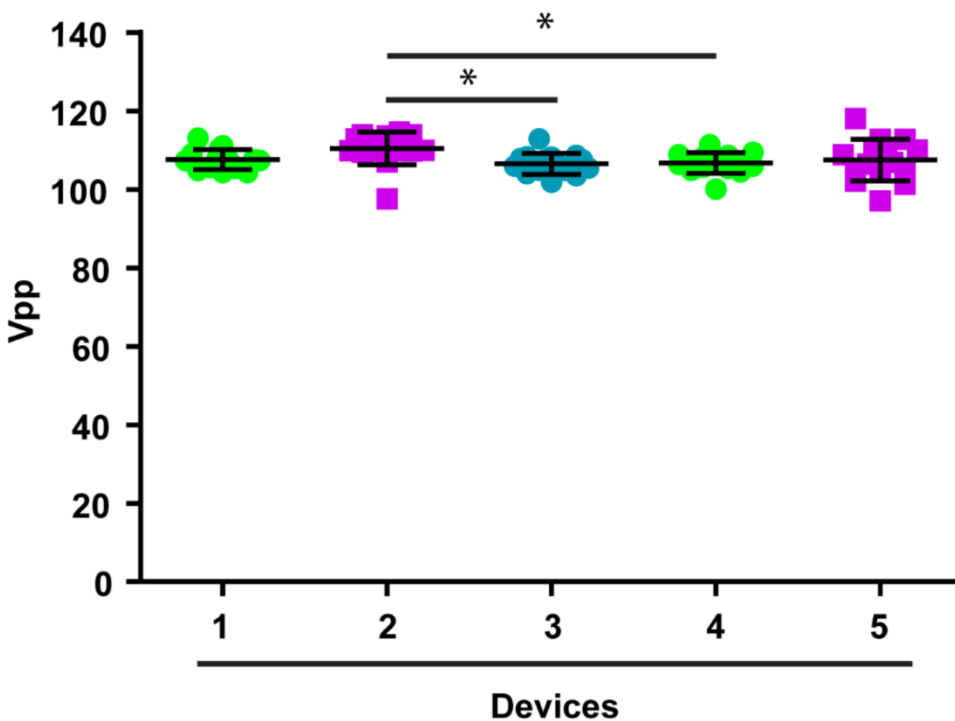
Appendix 41. Data represents the corresponding Figure 3g in the main manuscript. Statistical analysis of 2/PVDF 10% composite film (TENG-2). Each data point ($n=15$) represents a peak of voltage (V_{DC}). The ns comparisons are not shown; data is consistent and does not change significantly. Student's t-test applied with Welch's correction. * $p<0.05$, ** $p<0.01$, *** $p<0.001$.



Appendix 42. Data represents the corresponding Figure 3h in the main manuscript. Statistical analysis of 2/PVDF 10% composite film (TENG-2). Each data point ($n=15$) represents a peak of voltage (V_{RC}), either on positive side or negative side. The ns comparisons are not shown; data is consistent and does not change significantly. Student's t-test applied with Welch's correction. * $p<0.05$, ** $p<0.01$, *** $p<0.001$.



Appendix 43. Data represents the corresponding Figure 3i in the main manuscript, i.e. voltages under biomechanical scenario. Statistical analysis of 2/PVDF 10% composite film (TENG-2). Each data point ($n=15$ accounted, $n=5$ depicted in manuscript) represents a peak of voltage (V_{oc}), either on positive side or negative side. The ns comparisons are not shown; data is consistent and does not change significantly. Student's t-test applied with Welch's correction. * $p<0.05$, ** $p<0.01$, *** $p<0.001$.



Appendix 44. Data represents the corresponding Appendix 30 and represented with respective mean and SD. Device's reproducibility data is depicted. In 5 data sets (measure for 5 devices), each data point (n=15 presented here for calculation purpose, actual dataset has n=75 for each set) represents a peak of voltage (V_{oc}) either on positive side or negative side. The ns comparisons are not shown, data is consistent. One way ANOVA with Tukey's multiple comparisons is performed to analyze the data. * $p < 0.05$, ** $p < 0.01$, *** $p < 0.001$.

Supplementary Movies: Can be found online by using given link

<https://onlinelibrary.wiley.com/doi/full/10.1002/admi.202201713>

Video S1: Demonstrative movie showing fast charging of 10 μF capacitor by 10 wt % 2/PVDF composite based device (TENG-2).

Video S2: Movie revealing voltage steadiness and longtime performance of 10 wt % 2/PVDF composite based device (TENG-2).

Video S3: Movie demonstrating LED illumination of using 10 μF capacitor by continuous tapping mode on 10 wt % 2/PVDF composite based device (TENG-2).

Video S4: Movie demonstrating bio-mechanical energy harvesting in simple gentle tapping mode using human finger on 10 wt % 2/PVDF composite based device (TENG-2).

4.6 References

- [1] G. Khandelwal, A. Chandrasekhar, N. P. Maria Joseph Raj, S.-J. Kim, *Advanced Energy Materials* **2019**, *9*, 1803581.
- [2] J.-W. Yoon, J.-H. Kim, C. Kim, H. W. Jang, J.-H. Lee, *Advanced Energy Materials* **2021**, *11*, 2170106.
- [3] Q. Tang, H. Guo, P. Yan, C. Hu, *EcoMat* **2020**, *2*, e12060.
- [4] H. Zou, Y. Zhang, L. Guo, P. Wang, X. He, G. Dai, H. Zheng, C. Chen, A. C. Wang, C. Xu, Z. L. Wang, *Nat Commun* **2019**, *10*, 1427.
- [5] F.-R. Fan, Z.-Q. Tian, Z. Lin Wang, *Nano Energy* **2012**, *1*, 328.
- [6] G. Khandelwal, A. Chandrasekhar, N. R. Alluri, V. Vivekananthan, N. P. Maria Joseph Raj, S.-J. Kim, *Applied Energy* **2018**, *219*, 338.
- [7] B. Dudem, N. D. Huynh, W. Kim, D. H. Kim, H. J. Hwang, D. Choi, J. S. Yu, *Nano Energy* **2017**, *42*, 269.
- [8] Z. L. Wang, T. Jiang, L. Xu, *Nano Energy* **2017**, *39*, 9.
- [9] S. K. Singh, P. Kumar, R. Magdum, U. Khandelwal, S. Deswal, Y. More, S. Muduli, R. Boomishankar, S. Pandit, S. Ogale, *ACS Appl. Bio Mater.* **2019**, *2*, 3164.
- [10] Z. Lin Wang, *Faraday Discussions* **2014**, *176*, 447.
- [11] S. Li, Y. Fan, H. Chen, J. Nie, Y. Liang, X. Tao, J. Zhang, X. Chen, E. Fu, Z. L. Wang, *Energy Environ. Sci.* **2020**, *13*, 896.
- [12] Z. Liu, Y. Huang, Y. Shi, X. Tao, H. He, F. Chen, Z.-X. Huang, Z. L. Wang, X. Chen, J.-P. Qu, *Nat Commun* **2022**, *13*, 4083.
- [13] Y. Shi, F. Wang, J. Tian, S. Li, E. Fu, J. Nie, R. Lei, Y. Ding, X. Chen, Z. L. Wang, *Science Advances* **2021**, *7*, eabe2943.
- [14] Z. L. Wang, *ACS Nano* **2013**, *7*, 9533.
- [15] J. Luo, L. Xu, W. Tang, T. Jiang, F. R. Fan, Y. Pang, L. Chen, Y. Zhang, Z. L. Wang, *Advanced Energy Materials* **2018**, *8*, 1800889.
- [16] G. Khandelwal, A. Chandrasekhar, R. Pandey, N. P. Maria Joseph Raj, S.-J. Kim, *Sensors and Actuators B: Chemical* **2019**, *282*, 590.
- [17] Z. Lin, B. Zhang, H. Guo, Z. Wu, H. Zou, J. Yang, Z. L. Wang, *Nano Energy* **2019**, *64*, 103908.
- [18] J. Luo, Z. Wang, L. Xu, A. C. Wang, K. Han, T. Jiang, Q. Lai, Y. Bai, W. Tang, F. R. Fan, Z. L. Wang, *Nat Commun* **2019**, *10*, 5147.

- [19] H. Zou, Y. Zhang, L. Guo, P. Wang, X. He, G. Dai, H. Zheng, C. Chen, A. C. Wang, C. Xu, Z. L. Wang, *Nat Commun* **2019**, *10*, 1427.
- [20] R. Zhang, H. Olin, *EcoMat* **2020**, *2*, e12062.
- [21] G. Khandelwal, N. P. Maria Joseph Raj, V. Vivekananthan, S.-J. Kim, *iScience* **2021**, *24*, 102064.
- [22] Z. Chen, Y. Cao, W. Yang, L. An, H. Fan, Y. Guo, *J. Mater. Chem. A* **2022**, *10*, 799.
- [23] R. Wen, R. Feng, B. Zhao, J. Song, L. Fan, J. Zhai, *Nano Res.* **2022**, DOI 10.1007/s12274-022-4731-6.
- [24] L. Zhai, S. Cui, B. Tong, W. Chen, Z. Wu, C. Soutis, D. Jiang, G. Zhu, L. Mi, *Chemistry – A European Journal* **2020**, *26*, 5784.
- [25] Y.-M. Wang, X. Zhang, D. Yang, L. Wu, J. Zhang, T. Lei, R. Yang, *Nanotechnology* **2022**, *33*, 065402.
- [26] M. Kandiah, M. H. Nilsen, S. Usseglio, S. Jakobsen, U. Olsbye, M. Tilset, C. Larabi, E. A. Quadrelli, F. Bonino, K. P. Lillerud, *Chem. Mater.* **2010**, *22*, 6632.
- [27] Y. Gu, S. Ted Oyama, *Journal of Membrane Science* **2007**, *306*, 216.
- [28] X. Liu, N. K. Demir, Z. Wu, K. Li, *J. Am. Chem. Soc.* **2015**, *137*, 6999.
- [29] K. Huang, B. Wang, S. Guo, K. Li, *Angewandte Chemie* **2018**, *130*, 14088.
- [30] S. S. Nagarkar, A. V. Desai, S. K. Ghosh, *Chemical Communications* **2014**, *50*, 8915.
- [31] G. Khandelwal, N. P. Maria Joseph Raj, S.-J. Kim, *Advanced Functional Materials* **2020**, *30*, 1910162.
- [32] S. Balčiūnas, D. Pavlovaitė, M. Kinka, J.-Y. Yeh, P.-C. Han, F.-K. Shieh, K. C.-W. Wu, M. Šimėnas, R. Grigalaitis, J. Banys, *Molecules* **2020**, *25*, 1962.
- [33] L. Valenzano, B. Civalleri, S. Chavan, S. Bordiga, M. H. Nilsen, S. Jakobsen, K. P. Lillerud, C. Lamberti, *Chem. Mater.* **2011**, *23*, 1700.
- [34] J. K. Bristow, K. L. Svane, D. Tiana, J. M. Skelton, J. D. Gale, A. Walsh, *J. Phys. Chem. C* **2016**, *120*, 9276.
- [35] G. W. Peterson, M. McEntee, C. R. Harris, A. D. Klevitch, A. W. Fountain, J. R. Soliz, A. Balboa, A. J. Hauser, *Dalton Transactions* **2016**, *45*, 17113.
- [36] P. G. Yot, K. Yang, F. Ragon, V. Dmitriev, T. Devic, P. Horcajada, C. Serre, G. Maurin, *Dalton Transactions* **2016**, *45*, 4283.
- [37] Q. Yang, A. D. Wiersum, P. L. Llewellyn, V. Guillerm, C. Serre, G. Maurin, *Chemical Communications* **2011**, *47*, 9603.

- [38] H. Jasuja, J. Zang, D. S. Sholl, K. S. Walton, *J. Phys. Chem. C* **2012**, *116*, 23526.
- [39] C. Y. Chuah, J. Lee, J. Song, T.-H. Bae, *Membranes* **2020**, *10*, 154.
- [40] B. Ghalei, K. Wakimoto, C. Y. Wu, A. P. Isfahani, T. Yamamoto, K. Sakurai, M. Higuchi, B. K. Chang, S. Kitagawa, E. Sivaniah, *Angewandte Chemie International Edition* **2019**, *58*, 19034.
- [41] J. H. Cavka, S. Jakobsen, U. Olsbye, N. Guillou, C. Lamberti, S. Bordiga, K. P. Lillerud, *J. Am. Chem. Soc.* **2008**, *130*, 13850.
- [42] X. Ma, Y. Chai, P. Li, B. Wang, *Acc. Chem. Res.* **2019**, *52*, 1461.
- [43] X. Cai, T. Lei, D. Sun, L. Lin, *RSC Adv.* **2017**, *7*, 15382.
- [44] X. Ma, Y. Chai, P. Li, B. Wang, *Acc. Chem. Res.* **2019**, *52*, 1461.
- [45] M. M. Shirolkar, C. Hao, X. Dong, T. Guo, L. Zhang, M. Li, H. Wang, *Nanoscale* **2014**, *6*, 4735.
- [46] K. Momma, T. Ikeda, A. A. Belik, F. Izumi, *Powder Diffraction* **2013**, *28*, 184.
- [47] X. Liao, X. Wang, F. Wang, Y. Yao, S. Lu, *J Inorg Organomet Polym* **2021**, *31*, 756.
- [48] E. Shamsaei, M. M. Nasef, H. Saidi, A. H. Yahaya, *Radiochimica Acta* **2014**, *102*, 351.
- [49] X. Mu, J. Jiang, F. Chao, Y. Lou, J. Chen, *Dalton Trans.* **2018**, *47*, 1895.
- [50] M. N. Timofeeva, V. N. Panchenko, J. W. Jun, Z. Hasan, M. M. Matrosova, S. H. Jung, *Applied Catalysis A: General* **2014**, *471*, 91.
- [51] S. Lee, Y. Lee, D. Kim, Y. Yang, L. Lin, Z.-H. Lin, W. Hwang, Z. L. Wang, *Nano Energy* **2013**, *2*, 1113.
- [52] W. Tang, C. Zhang, C. B. Han, Z. L. Wang, *Advanced Functional Materials* **2014**, *24*, 6684.
- [53] C. Huang, G. Lu, N. Qin, Z. Shao, D. Zhang, C. Soutis, Y.-Y. Zhang, L. Mi, H. Hou, *ACS Appl. Mater. Interfaces* **2022**, *14*, 16424.
- [54] Z. L. Wang, *Materials Today* **2017**, *20*, 74.
- [55] J. H. Cavka, S. Jakobsen, U. Olsbye, N. Guillou, C. Lamberti, S. Bordiga, K. P. Lillerud, *J. Am. Chem. Soc.*, **2008**, *130*, 42, 13850.
- [56] B. Ghalei, K. Wakimoto, C. Y. Wu, A. P. Isfahani, T. Yamamoto, K. Sakurai, M. Higuchi, B. K. Chang, S. Kitagawa, E. Sivaniah, *Angew. Chem.*, **2019**, *131*, 19210.
- [57] X. Cai, T. Lei, D. Sund, L. Linde, *RSC Adv.*, **2017**, *7*, 15382.
- [58] E. Shamsaei, M.M. Nasef, H. Saidi, and A. H. Yahaya, *Radiochim. Acta.*, **2014**, *102*, 351.
- [59] G. Khandelwal, A. Chandrasekhar, N.I P. M. Joseph Raj, S.-J. Kim, *Adv. Energy Mater.* **2019**, *9*, 1803581.

-
- [60] S. Singh, P. Kumar, R. Magdum, U. Khandelwal, S. Deswal, Y. More, S. Muduli, R. Boomishankar, S. Pandit, S. Ogale, *ACS Appl. Bio Mater.*, **2019**, 2, 3164.
- [61] C. Y. Chuah, J. Lee, J. Song, T.-H. Bae, *Membranes*, **2020**, 10, 154.
- [62] B. Ni, W. Sun, J. Kang, Y. Zhang, *J. Phys. Chem. C.*, **2020**, 124, 11595.
- [63] Recent Developments of the Program FULLPROF, in Commission on Powder Diffraction (IUCr). *Newsletter*, **2001**, 26, 12.
- [64] M. M. Shirolkar, C. Hao, X. Dong, T. Guo, L. Zhang, M. Li, H. Wang, *Nanoscale* **2014**, 6, 4735.
- [65] K. Momma, T. Ikeda, A. A. Belik, F. Izumi, *Powder Diffraction*, **2013**, 28, 184.
- [66] R. Zhang, H. Olin, *EcoMat.*, **2020**, 2, e12062.

Chapter 5

Surface Feature Tuned Metal-organic Polyhedra for Triboelectric Nanogenerator: Self-Powered Sensors for Wearable Electronics

5.1 Introduction

Throughout the previous fifty years, miniaturization per Moore's law has been at the forefront of the electronics industry's road map. The doubling of the number of devices on a chip, for instance, is more of an economic imperative than a physical law of nature.^[1] Thanks to advances in solid-state electronics, a variety of functions can now coexist on a single silicon chip. The development of integrated circuits laid the groundwork for subsequent advancements in areas such as increased dependability, decreased size, faster computation, decreased power consumption, and others. Second, the evolution of wireless and mobile communication technologies is the next major innovation. The advent of the internet, together with advances in computer technology and the capacity to transmit data via optical fiber, has had a profound impact on every part of the globe. Third, in recent decades, the advancement of medical science and medical treatment for all has been inextricably intertwined with the expansion of mobile device capability, allowing for the full use of contemporary sensor technology to create a safer and healthier environment for everyone. If one can make the mobile electronics self-powered, however, the systems can run adequately and continuously without interruption, which will have a profound effect on all of these developments. This is essential for the Internet of Things (IoT), because we are primarily concerned with transient items in motion. No matter what kind of technology you employ, there is one universal truth: electronics require electricity to function. Therefore, the final major effort is directed toward making gadgets self-powered. All of this talk about miniaturization, wireless portability, usefulness, and self-powering systems may be summarized into these four categories in Figure. 1. The other three areas build upon the foundation of self-powering.^[1] Respective frontiers can be foreseen being broken into in the near future.

Wang and co-workers introduced the concept of self-powering in response to the invention of piezoelectric nanogenerators (PENGs), which utilize the piezoelectric effect of nanostructures to convert extremely small mechanical energy into electricity.^[2] The domain of nanoenergy has much to learn from this study.^[2,3,4] It wasn't until 2012 that the triboelectric Nanogenerator (TENG) was developed.^[5,6,7] When two distinct materials come into physical friction or contact, electrostatic charges are formed on their surfaces. This creates a potential fall when the given surfaces are separated by a physical means or applied mechanical force, which thereby drives electrons to move between the two electrodes built on the top and bottom surfaces of the two different materials. Global interest in nanogenerators research has been sparked by the technology's utility in a wide variety of contexts. This includes its use as a power

source and in self-powered sensors for a wide variety of purposes, including those in the Internet of Things (IoT), surveillance systems, healthcare, medical technology, infrastructure tracking or monitoring, and environmental monitoring.

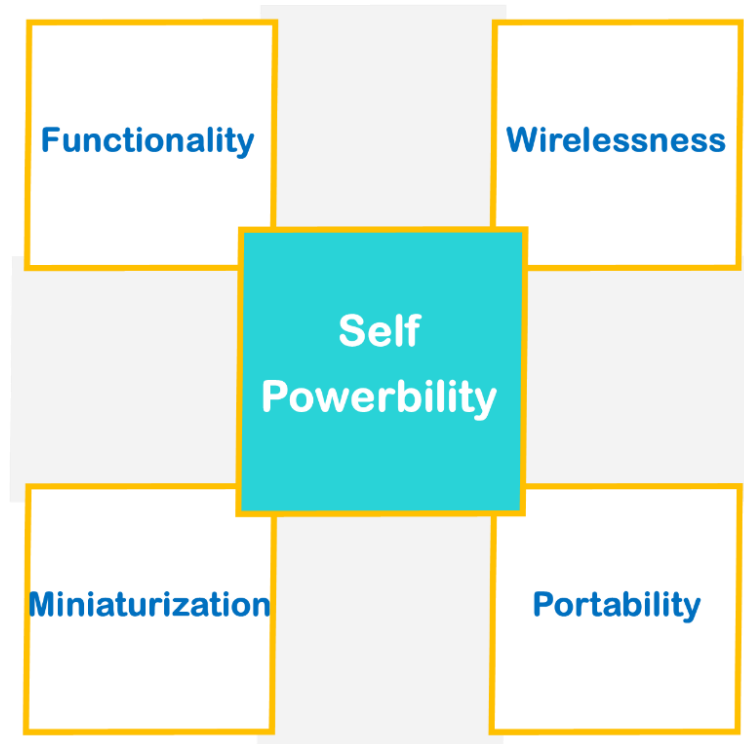


Figure 1. Depiction of a summary of the major stages of development of microelectronics and communication technologies, as well as newly emerging fields.

Self-powered systems can benefit greatly from harnessing the sun's, water's, wind's, and earth's kinetic and potential energies, as well as mechanical and biochemical processes. A summary of the advantages and disadvantages of these various energy sources is provided in Figure 2. So-called hybrid energy technology refers to devices that can concurrently harvest various forms of energy.^[8,9] The effects of electromagnetic induction, electrostatic attraction, piezoelectricity, and triboelectricity are nowadays considered prime mechanisms that can be navigated for mechanical energy harvesting. In Figure 3, we can see a comparison and summary of these effects, along with an analysis of their respective strengths and uses. Their underlying physics of energy harvesting via piezoelectric and triboelectric effects needs to be well understood prior to realizing them in real time applications.

Energy source	Mechanical	Solar	Thermal	Biochemical
Form	Any motion, movement or vibration	Sunlight	Heat	Organic and Living matter
Harvesting Principle	Electromagnetic, Electrostatic, Piezoelectric, Triboelectric	Photovoltaic	Thermoelectric	Biochemical reactions
Approximate power	10-100 mW/cm ²	5-30 mW/cm ²	0.01-0.1 mW/cm ²	0.1-1 mW/cm ²
Pros	Ubiquitous and abundant in broad power output and frequency ranges, freely available	Microfabrication compatible mature technology, long lifetime, DC & high power output	No moving parts required, long lifetime and time reliability, high DC output	Biocompatible/degradable clean energy, environmentally friendly, abundant in biological entities
Cons	AC output, non continuous nature	Limited by poor environmental conditions, not available at night	Low efficiency, large size, a large and sustained thermal gradients required	Low power output, less reliability, limited lifetime
Potential Applications	Remote sensing and monitoring, wearable systems, blue energy, internet of things	Remote sensing and environmental monitoring	Structural-health monitoring for engines-machines, wearables, biomedical devices	In vivo applications, biocompatible, biomedical devices application

Figure 2. A comparison of energy production from several sources.

Polymers come out on top in the triboelectric series, surpassing metals, and they serve as the fundamental building blocks for the production of TENG.^[10,11] However, because it is challenging to functionalize polymeric materials in a selected and orderly fashion, there is an urgent requirement for the research, development, and implementation of alternative multifunctional materials that may be used in TENG applications. In this regard, it seems that metal organic frameworks are going to be the most viable alternatives because of the fundamental tunability they possess.^[6,12,13] In recent years, MOFs have been put into practice in the process of energy harvesting by means of a triboelectric nanogenerators. TENGs are being manufactured from zeolitic imidazole framework members, HKUST-1, as well as just a few additional MOFs, along with the UiO series, according to findings reported in the literature.^[14,15] MOFs are used as multi-functional materials in the triboelectric category because of the better performance and adaptability that they offer.^[14,15] MOFs, relying mostly on the functional group that they carry, can act as either positive or negative triboelectric materials. Bromine-functionalized porous materials yield greater performance with PVDF as the opposing layer than their counterparts that do not contain bromine. This is because of the better charge holding capabilities of the bromine-functionalized substances.^[16] Fluorinated metal–organic frameworks (MOFs) have the potential to be very tribonegative compounds.^[17]

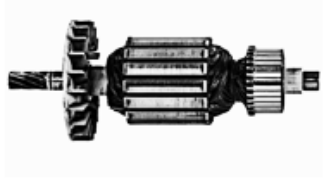

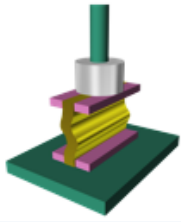

Mechanical Energy Harvesting	Electrostatic	Electromagnetic	Piezoelectric	Triboelectric
Illustration				
Harvesting Principle	Electromagnetic induction	Electrostatic induction	Piezoelectric effect and electrostatic induction	Contact electrification and electrostatic induction
Impedance Type	Resistive	Capacitive	Capacitive	Capacitive
Pros	High efficiency, easy to scale up	Light weight	Easy nanoscale fabrication	Flyweight, high power output, high efficiency, cost effective, simple fabrication
Cons	Heavy magnet requirements, low output for miniaturized devices	Pre-charge require, low output, high matched impedance	Low output and low efficiency, pulsed output, high matched impedance	pulsed output, high matched impedance

Figure 3. A comparison and summary of diverse effects, along with an analysis of their respective strengths and uses.

Considering outstanding features of polymers comprising piezoelectric capabilities, ideal flexibility, and low acoustic impedance, ferroelectric polymers for instance poly(vinylidene fluoride) (PVDF) as well as its copolymers are commonly employed in nanogenerators.^[18] The β -phase of PVDF and its copolymers was shown to be the most beneficial of the several crystalline phases of PVDF and thus its copolymers in terms of enhancing the electric performances of nanogenerators.^[19-21] In order to further increase the output performance of PVDF-based TENGs, several efforts have been made to boost the β -phase content of PVDF, also known as the surface charge density. For instance, several inorganic nanomaterials, such as BaTiO₃ nanoparticles (NPs), graphene nanosheets (NSs), and silver nanowires (NWs) were incorporated into the polymer matrix in order to increase the polar β -phase content or the dielectric characteristic.^[22-24]

However, the composite film comprising organic and inorganic constituents has inherent flaws, and these imperfections will cause damage to the compatibility and flexibility of the nanogenerators, making them too heavy to be worn and rendering them unusable. In addition, the surface modification approaches are also essential strategies to hasten the development of TENG research.^[25–29] Examples of techniques that have been used to increase the surface area of friction materials include surface micro pattern, electrospinning and the template technique besides doctor blading.^[30–32] It has been demonstrated that using this structural design as a means to enhance the surface area is an effective technique. Thus utilization structural design turns out to be an efficient method for elevating the surface charge density of frictional materials.^[25–29] However, the aforementioned procedures necessarily result in more complicated production processes and more simpler methods with least resource and time utilization gains importance in order to construct practically relevant Nanogenerator devices.

The utilization of the ferroelectric polymer P(VDF-TrFE) as a positive friction material has been widely described in the scientific literature.^[33,34] The aforementioned materials are mostly composed of the β -phase and carry an outstanding dielectric response as well as high crystallization. In such situations, inserting controlled PS microspheres led to an effective demonstration of the unique surface of the lotus-leaf microstructure.^[35] This not only results in an expanded contact area of the friction material but also demonstrates excellent permittivity. Such dielectric feature augmentation might be ascribed to the Maxwell-Wagner-Sillars polarization, which is caused by the buildup of electric charge carriers at the interface of a heterogeneous system as a result of the difference in conductivity across the fillers (active material) and the polymer matrix. In addition, the use of CTAB to graft the positively charged amino groups onto the PS microspheres has been shown in an earlier report. This results in the consequent surface potential of the positive friction material being substantially enhanced. Constructed TENGs are likely to have superior output performance and have the potential to attain an optimum output power density that would be greater than that of undoctored and pristine P (VDF-TrFE)-based TENGs, correspondingly. In contrast to an inorganic particle addition, the suitability as well as flexibility of the all-organic polymer composite can be reliably ensured, which also provides the basis for utilizing such an idea to prepare composites that are durably elastic, stable, and reusable over long periods of time, thereby achieving prolonged service lives for the fabricated devices.^[34,35]

Similarly, prior moving ahead with our idea of PVDF based Metal-organic Polyhedra (MOP) doped TENGs, the extensive utilization and exploration of PVDF based TENG devices has been done by Ghosh and co-workers which also find basis for our take on deployment of PVDF for the MOP based composite

utilizations.^[36] In the aforementioned research, a new foundation has been laid by means of functional group guided tuning of organic moiety (and hence MOP), which directly impacts the TENG performance level, this also serves as a basis for our speculation of ligand governed effect on the thereby formed MOP-TENG. The isorecticular frameworks of UiO-66 (derivative 1) and UiO-66-Br (derivative 2) were deliberately utilized so that direct influence of specific constituent attributes can be speculated or exploited. These architectures have comparable spatial and operating conditions for composite-fabricated devices (1/PVDF and 2/PVDF), which also provides a logical platform to expound, deploy, and leverage functional group electronic influence to regulate TENG conversion efficiency.^[36] It made it possible for us to comprehend and utilize the benefit of adjustable characteristics at the nanoscale, as well as leverage its contemporaneous influence at the bulk scale, for the purpose of MOF-TENG derived self-powered systems and future sensor applications. Thus, considering the aforementioned factors, if MOPs are blended with appropriate polymeric matrices like PVDF, they can also serve as comparative tribonegative materials. MOPs that are stable, easy to synthesize, and not harmful to the environment or biological systems gain desirability and are thereby needed for long-term development. In the not too distant future, non-toxic and biocompatible MOPs may be utilized in the production of novel TENG-based implants, stents as well as disposable sensors.^[34,35,38]

The family of crystalline porous materials known as "Metal–organic Polyhedra" (MOP) is an intriguing major development with a wide range of possible uses. Their capacity to be dispersed in solution and, as a result, to be processed, which enables a diverse range of fabrication techniques, makes them the material of choice for the nanogenerator arena. However, MOPs have not yet been tamed and, as a result, have not been investigated in the field of micro-nanoenergy applications; to put it more plainly, the benefits of their characteristics have not yet been utilized for nanogenerator applications, in particular for TENG. Although metal–organic frameworks and metal–organic porous solids have comparable potential because of their intrinsic porosities as well as physicochemical characteristics, the profitability of carboxylate MOPs is currently in its infancy due to a lack of systematic development addressing their stabilities. This is one of the reasons why MOPs were considered to be rudimentary. In consideration of the aforementioned hurdles, we have utilized the virtue of our own pre-reported series of MOPs as comprising an a priori strategy to stabilize MOP systems in which the metal–ligand linkages are generally weak and are now being protected and thus stabilized by the synthesis of chemically resistant carboxylate MOPs by outer-surface functionalization, a de-novo approach. Chemical inertness is thus achieved while maintaining the structural integrity of the framework throughout a wide range of pH values, in strongly

acidic circumstances as well as in oxidizing and reducing media, the most important step is to fine-tune the hydrophobic shielding.^[38] All those factors make this material a good choice for TENG applications. These features were also correlated by molecular modeling, providing evidence that supports these findings. A prototype method for making MOPs that are chemically stable retains value for further TENG fabrication. It is essential to note that the domain of nanogenerators demands real time applications and thus scalability for desired applications, and hence the aforesaid MOPs (i.e., IPMOP) make it possible by shifting from an unstable domain to a chemically ultra-stable regime blended with the desired feature of gram-scale scalability and shorter time (in seconds) that avoid energy intensiveness, i.e., at room temperature.^[38] Thus considering virtues of MOPs for TENG application and its absence in TENG arena, herein, rendering its incremental hydrophobicity and its subsequent impact on triboelectric output in this chapter, we deployed our previously published series of MOPs, namely IPMOP-n (n = I, II, III, IV, i.e., IPMOP-A, IPMOP-PA, IPMOP-IL, and IPMOP-V), for strategic application in Triboelectric Nanogenerators (TENG) through composite based flyweight device fabrication.^[37] The charge building mechanism at the interface of polymer/MOP composites was discovered in a unique way. Crystalline porous materials, such as MOP, have a substantial potential for a variety of applications and are well suited for solution processing due to their miscibility in different organic solvents. Despite the fact that inherent porosities and physicochemical characteristics of MOPs and metal-organic frameworks (MOFs) are comparable, the use of carboxylate MOPs is constrained by a lack of chemical stability. A series of cages known for their a priori methodology for fabricating chemically resistant carboxylate MOPs through outer-surface functionalization were used in conjunction with a combination of suitable compositing polymers to stabilize MOP systems with weak metal-ligand bonds in order to benefit from their combined properties. These MOPs were carefully chosen for their high stability, which includes resistance to a wide pH range, stability in highly acidic environments, and stability in oxidizing and reducing media, which has been reduced by tuneable hydrophobic shielding. These results are supported by research on molecular modelling. A quick gram-scale synthesis at ambient temperature was used in a prototype technique for chemically stable MOPs to transition from an unstable to a chemically ultra-stable phase (within seconds). Using drop-casting, doctor blading, and electrospinning techniques, these MOPs were formed into flexible thin films and strategically employed in the production of MOP/PVDF composites at different blending concentrations. These films were all formed into tiny, portable, and small TENG devices. The devices showed triboelectric output at extremely low optimum concentrations in the order of IPMOPs, as IPMOP-A, IPMOP-V, IPMOP-PA, and IPMOP-IL, due to the continuous rise in

hydrophobicity produced by shielding by alkyl and aryl groups. The power density increased simultaneously at 201.66 mW/m², 552.8 mW/m², 1095.5 mW/m², and 513 mW/m². After being put through real-time tests, the selected devices, namely **IPMOP-IL/PVDF@5%**, shown remarkable application display in power storage in batteries and capacitors, real-time LED, and mobile and medium-range electronic charging. The materials' solution processability makes it possible to create foldable self-charging devices as well as lighter and more durable self-powered products, making this the first report in the cage-based TENG arena with such remarkable electric output qualities.

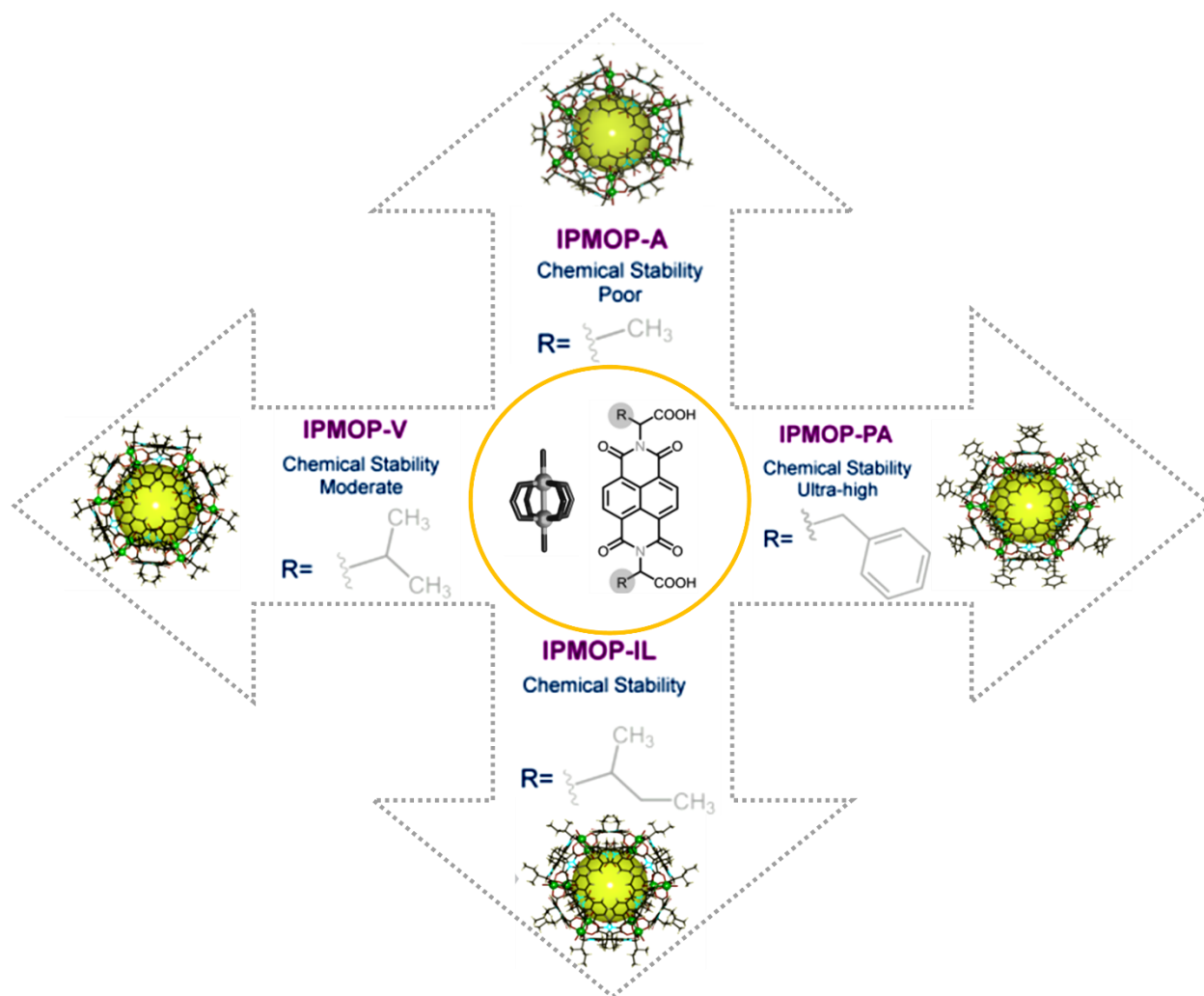


Figure 4. Strategy for the synthesis of MOPs and their respective crystal forms. The progression of their chemical stabilities is depicted.

5.2 Experimental

5.1.1 Materials

All four amino acids, 1,4,5,8 naphthalenetetracarboxylic dianhydride, and 2,6-Lutidine were bought from Sigma-Aldrich. We bought $\text{Cu}(\text{NO}_3)_2 \cdot 3\text{H}_2\text{O}$ from Merck. The reagents and solvents were commercially available and were not further refined before being used. All solvents, including standardized buffer solutions, were acquired from Spectrochem. Products obtained as solids or syrups were dried using routine lab ovens. Spacer and aluminium sheets are obtained from 3M Tape and physics equipments respectively.

DMF refers to N,N-Dimethylformamide

PVDF refers to polyvinylidene difluoride ($-(\text{C}_2\text{H}_2\text{F}_2)_n-$)

ITO refers to Indium Tin Oxide ($\text{In}_{2-x}\text{Sn}_x\text{O}_3$)

PET refers to Polyethylene terephthalate ($(\text{C}_{10}\text{H}_8\text{O}_4)_n$)

These chemicals were used as received / without further purification.

5.2.2 Materials Synthesis

All four ligands, H_2LA , H_2LPA , H_2LIL and H_2LV are synthesized by our previously reported protocol.^[37]

5.2.2.a) Synthesis of IPMOPs : All of the synthesis was completed using our already-proven methodologies, which are described in more detail below. Due to the need for immediate synthesis and the nature of the application, room temperature synthesis with the shortest synthesis time was chosen, as shown below.^[37]

Room temperature Synthesis of IPMOP-A: A mixture of H_2LA (2.050 gm, 5 mmol) and $\text{Cu}(\text{NO}_3)_2 \cdot 3\text{H}_2\text{O}$ (1.208 gm, 5 mmol) were dissolved in 100 mL DMF and added 100 mL p-xylene as co-solvent. After that 1 mL 2,6 Lutidine added as a base for cage formation. During addition of base solution cage precipitate is formed within seconds and after few hours green cubic shaped crystal were appeared from precipitate. Yield ~ 0.797 gm.^[37] Onwards called as IPMOP-1.

Room Temperature Synthesis of IPMOP-PA: A mixture of H_2LPA (2.8 gm, 5 mmol) and $\text{Cu}(\text{NO}_3)_2 \cdot 3\text{H}_2\text{O}$ (1.208 gm, 5 mmol) were dissolved in 100 mL DMF and added 100 mL IPA as co-

solvent. After that 1 mL 2,6 Lutidine added as a base for cage formation. During addition of base solution cage precipitate is formed within seconds and after few hours green cubic shaped crystals were appeared from precipitate.^[37] Yield ~ 0.86 gm. Onwards called as IPMOP-2.

Room Temperature Synthesis of IPMOP-IL: A mixture of H₂LIL(2.3 gm, 5 mmol) and Cu(NO₃)₂.3H₂O (1.208 gm, 5 mmol) were dissolved in 100 mL DMF and added 100 mL 1,4 Dioxane as co-solvent. After that 1 mL 2,6 Lutidine added as a base for cage formation. During addition of base solution cage precipitate is formed within seconds and after few hours green cubic shaped crystal were appeared from precipitate.^[37] Yield ~ 0.73 gm. Onwards called as IPMOP-3.

Room temperature Synthesis of IPMOP-V: A mixture of H₂LV (2.470gm, 5 mmol) and Cu(NO₃)₂.3H₂O (1.208 gm, 5 mmol) were dissolved in 100 mL DMF and added 100 mL MeOH as co-solvent. After that 1 mL 2,6 Lutidine added as a base for cage formation. During addition of base solution cage precipitate is formed within seconds and after few hours green cubic shaped crystal were appeared from precipitate.^[37] Yield ~ 0.81 gm. Onwards called as IPMOP-4.

5.2.2.b) Composite film preparation: MOP/PVDF composites were prepared by loading various wt. % of IPMOP-1, IPMOP-2, IPMOP-3 and IPMOP-4 compounds in the viscous PVDF solution. 1 gram of PVDF pellets were stirred for 4 hours in 10 ml of DMF at 60 °C. IPMOP compounds (1 & 4) were finely grinded to yield powdered material which is further activated at 100 °C under vacuum, weighed and dissolved in THF and then further mixed with PVDF solution in the weight percent ratio (IPMOP 1 to 4 : 1%, 3%, 5%, 8% and 10%). This viscous mixture then further drop-casted on ITO-coated PET surface (substrate) and dried at 80 °C for 6 hours in hot air oven to obtain finely dried thin composite films and ensuring curing of the PVDF polymer. Similar films were prepared by electrospinning method additionally, besides air drying for few hours and well as by doctor blading methods with retention of similar dimensions of thickness. MOP/PVDF composite films thus obtained are in the range of ~200 to 1200 μM and further deployed for device fabrication.

5.2.2.c) Fabrication of TENG device: One of the electrodes is made out of ITO-coated PET, and the other is made out of Al-coated PET. The two electrodes are linked together using a spacer that has a thickness of less than 1.5 mm to maintain the gap between them. Copper tape and wires were utilized in order to successfully create electrical connections at the electrodes' point of termination. In order to provide electrical isolation, the gadget that had been constructed was finished by having the exterior

surface laminated with Kapton tape. It was determined that the as-fabricated device had a thickness of around 2.5 mm and an optimum size of approximately 2.5 cm².

5.2.3 Physical Measurements

5.2.3.a) Characterization: Powder X-ray diffraction patterns can indeed be recognized in the range of 5° to 40° 2θ whilst employing Cu Kα radiation ($\lambda = 1.5406 \text{ \AA}$), which is measured by the advanced X-ray diffractometer known as the Bruker D8. The FTIR Spectra were acquired by employing a Bruker ALPHA-II FTIR-eco ATR in the range of 500-4000 cm⁻¹ while operating in total reflection (ATR) mode attenuation. In this experiment on gas adsorption, the BelSorp-max equipment manufactured by Bel Japan was utilized. In order to produce the SEM pictures, an FEI Quanta 3D dual beam FESEM operating at 30KV was utilized. On a Keithley multimeter (DMM 7510 & 2450) with variable resistance, we also measured the voltage and the current. The KPFM analysis of composite films was performed with an Asylum Research MFP-3D. We employed a mechanically customized sewing machine configuration that was paired with a calibrated DC motor and a precision impact striker as the source of the impact force and frequency. We used a PASPORT Force Sensor to take the readings on the force.

5.2.3.b) Nanogenerator performance measurements: The open circuit voltage of a variable impact force (5 to 34 N) with 5Hz, 10Hz, 15 Hz, 20 Hz and 28 Hz frequency was measured with a Keithley multimeter (DMM 7510). The range of input impedance measured was MΩ to GΩ. We made use of a sewing machine configuration that had been mechanically changed and constructed in order to generate the impact force and frequency. The PASPORT Force Sensor was used to carry out the force measurement. On a Keithley multimeter (DMM 7510 & 2450) with variable load resistance, we also measured the voltage and the current. Until an external load is introduced, the voltages are considered to be Open Circuit Voltage.

5.2.4 Equations:

V_p : The highest possible value that can be achieved instantaneously by a function when measured from the level of zero volts. Because the function has an average value of zero volts, the waveform that was just presented has the same peak amplitude and peak value. This is because the average value of the function is zero.

V_{pp} : The voltage that exists between the waveform's positive and negative peaks in its entirety; that is, the magnitude that is equal to the sum of the positive and negative peaks.

V_{rms} : The root-mean-square value of a waveform, also known as its effective value.

V_{avg} : The level of a waveform that is determined by the requirement that the area encompassed by the curve above this level is precisely equal to the area enclosed by the curve below this level. This level is also referred to as the symmetry level.

$$V_p = \frac{V_{pp}}{2} = \frac{V_{avg}}{0.637}$$

$$V_{pp} = V_{rms} \times \frac{2}{\sqrt{2}} = V_p \times 2 = V_{avg} \times \pi$$

$$V_{avg} = \frac{1}{\pi} \times \int_0^{\pi} V_p \sin \theta \, d\theta = \frac{2V_p}{\pi} = 0.637 \times V_p$$

$$V_{rms} = V_{pp} \times \frac{1}{2\sqrt{2}} = 0.353 \times V_{pp} = V_p \times 0.707$$

5.3 Result and Discussion

A family of crystalline compounds called IPMOP-A, IPMOP-PA, IPMOP-IL, and IPMOP-V were synthesized using our own published procedure at room temperature in the shortest amount of time (a few seconds of reaction time), which is also explained in the experimental section.^[37] Both the synthesis methods and the structures of the crystalline solid are reported and precisely mimicked to reproduce the bulk phase of IPMOP compounds.^[37] IPMOP-A, IPMOP-PA, IPMOP-IL, and IPMOP-V are the names given to the derived MOPs when the amino acids in discussion are alanine (A), valine (V), isoleucine (IL), and phenylalanine (PA), respectively. In the presence of 2,6-lutidine as a base, we were able to obtain IPMOP at room temperature (on a gram scale) in a few seconds (Figure 4 and Appendix 1–5, Appendix 7). Each MOP has twelve ligand molecules and twelve water molecules that combine to form neutral cages (Figure 4, Appendix 7). The neutral cages have the following general formula: $[\text{Cu}_{12}(\text{L}_x)_{12}(\text{H}_2\text{O})_{12}]$. The corresponding ligand systems L_A , L_{PA} , L_{IL} , and L_V are referred to as L_x . Each cage molecule has twenty-four alkyl groups that, when arranged in an exohedral fashion, decorate the entirety of the globular cage's exterior surface (Appendix 7). Each of the cages has eight triangular windows that have a mean aperture of about 2 Å, and the average diameter of the inner cavity is about 15 Å. Each bimetallic paddle-wheel Cu^{II} unit is coordinated with two terminal water molecules. One of these

water molecules points into the inner cavity of the polyhedron; the other water molecule points away from the exterior of the polyhedron. The aforementioned compounds were subjected to a thorough washing with DMF and were then dried after the treatment. To remove any occluded, high-boiling solvent molecules, the solid compounds that were obtained in this manner were first put through an activation procedure by heating them in a vacuum chamber in order to obtain a guest-free phase. It was determined that the phase was pure by comparing the PXRD patterns of the unaltered and activated compounds with the patterns of the simulated XRD (Appendix 2–5).



Scheme 1. A depiction of the sequential fabrication approach deployed for the IPMOP-n/PVDF composite-based mechanical energy harvesting device.

The produced compounds were employed to construct the composite film using drop-casting (Scheme 1) and doctor blading methods; however, both methods are comparable as FESEM analysis revealed that the two methods produced identical morphological features. The process shown in Scheme 1, which involved combining finely powdered and activated fractions of IPMOP compounds with a viscous PVDF solution, was used to create composites of IPMOP-n/PVDF.^[36] Composite films thus formed were examined using powder X-ray diffraction (PXRD), field emission scanning electron microscopy (FESEM), RAMAN

spectroscopy, thermogravimetric analysis (TGA), fourier transform infrared (FTIR) spectroscopy, and gas adsorption; both before and after composite fabrication. Refer to the Appendix section for further details. The IPMOP/PVDF composites were put through a number of tests, including kelvin probe force microscopy (KPFM), atomic force microscopy (AFM), electrical output analysis, and capacitor charging, in an effort to reconcile experimental results with the presumed mechanisms reported in literature.^[36]

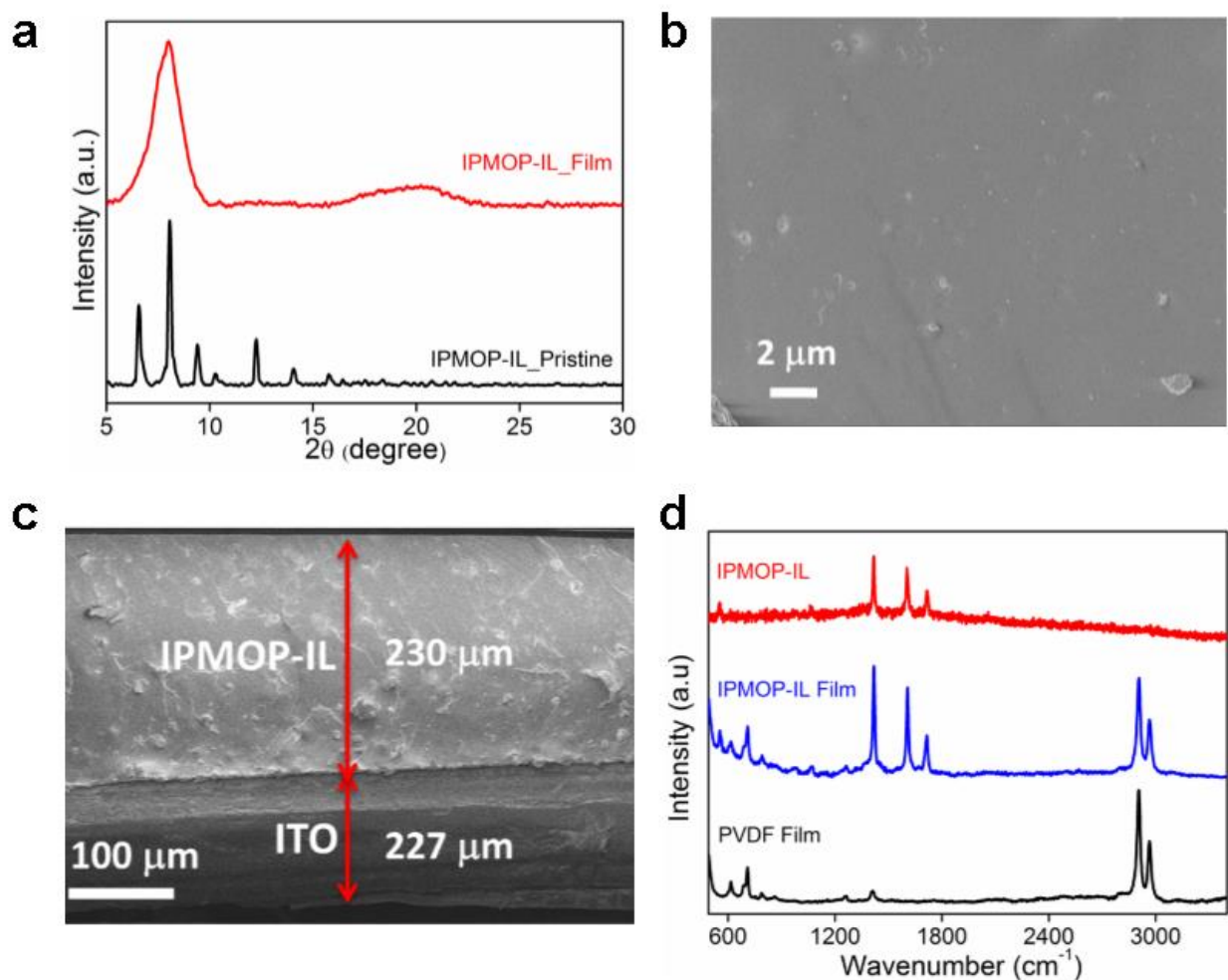


Figure 5. a) XRD data of pristine IPMOP-IL and its composite film. b) FESEM images of the (5 wt % IPMOP-IL/PVDF composite films. c) FESEM image revealing cross section of a composite film made of PET surface-coated by ITO and overlaid by IPMOP-IL/PVDF composite film. d) Raman spectra of pristine PVDF film compounds (black), composites (red) and PVDF films (blue). e) IR spectra of PVDF film (black), activated IPMOP-IL (red) and composite films (blue).

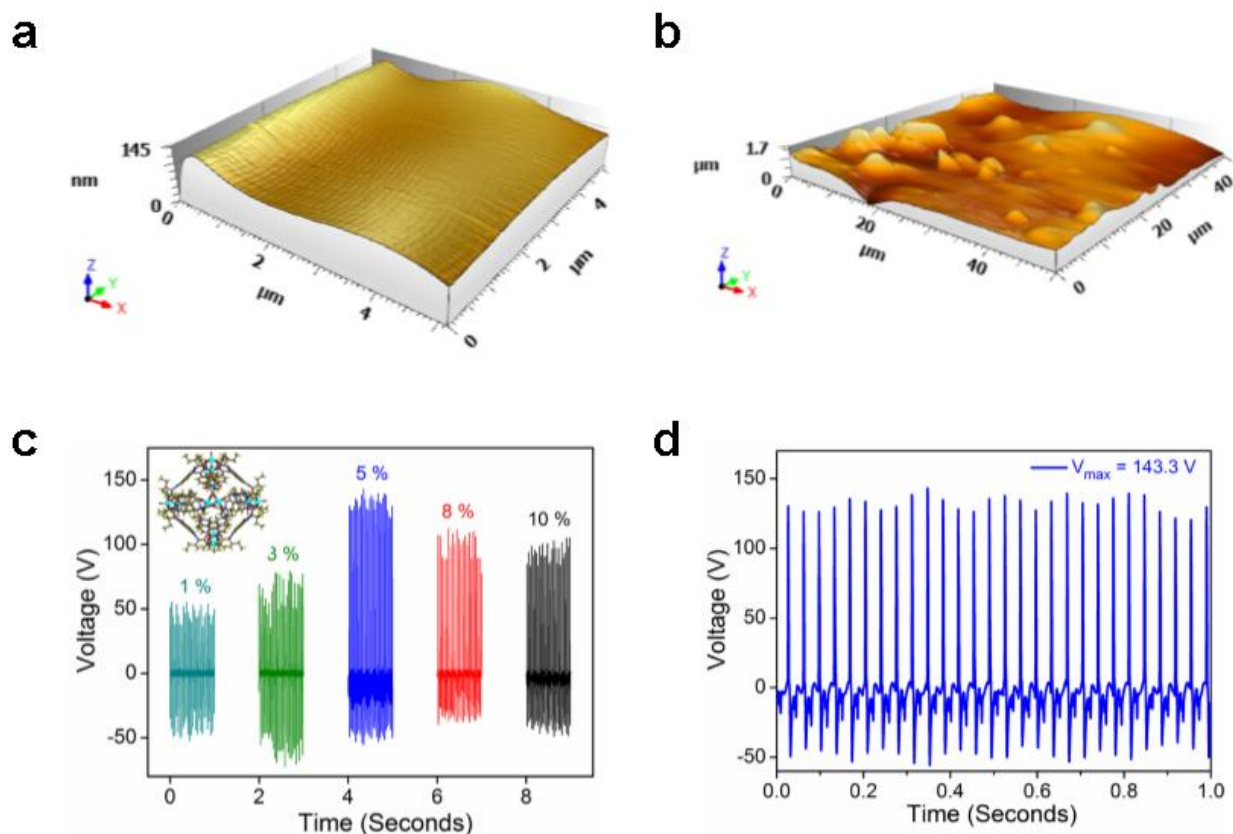


Figure 6. a) AFM images revealing surface topography (3D profile) of PVDF. b) AFM images indicating surface topography (3D profile) of 5 wt % of **IPMOP-IL/PVDF** i.e. (**IPTENG-3**). c) Open circuit voltage (V_{oc}) output variation of IPMOP-IL at incremental wt% loading into PVDF. d) Maximum V_{oc} obtained for **IPTENG-3** (i.e. 5 wt % of **IPMOP-IL/PVDF**).

Figure 5 highlights corroboratory characterization of individual IPMOP-IL and its composite film abbreviated as **IPMOP-IL/PVDF** or **IPTENG-3**. Figure 5a confirms phase retention of MOP in the composite film while Figure 5b and Figure 5c reveals surface features of 5 wt % loaded **IPMOP-IL/PVDF** composites and selected film thickness for device fabrication and performance measurement simultaneously. For **IPTENG-3** device fabrication, composite film with average thickness size $230 \mu\text{m}$ was used. Raman spectra revealed the existence of characteristic peaks for IPMOP-IL when it is loaded into PVDF, thus formed composite **IPMOP-IL/PVDF** comprises spectral features of PVDF film and IPMOP-IL showing notable presence of peaks (figure 5d). IPTENG-n ($n = 1, 2, 3, 4$) devices were prepared by following stepwise mechanism shown in Scheme 1. By varying the weight percentages of IPMOP-1,

IPMOP-2, IPMOP-3, and IPMOP-4 compounds in the viscous PVDF solution, MOP/PVDF composites were created. 10 ml of DMF and 1 gram of PVDF pellets were agitated at 60 °C for 4 hours. IPMOP compounds (1 and 4) were finely ground to produce powdered material, which was then activated at 100 °C under vacuum, weighed, and dissolved in THF before being combined with PVDF solution in the following weight-to-percentage ratio (IPMOP 1 to 4: 1%, 3%, 5%, 8%, and 10%). After being drop-cast on an ITO-coated PET surface (substrate), this viscous mixture was then baked in a hot air oven at 80 °C for six hours to produce thin, finely dried composite films and ensure the PVDF polymer's curing. In addition to air drying for a few hours, comparable films were also made using the doctor blading process and electrospinning, all while maintaining the same thickness dimensions. The resulting MOP/PVDF composite films, which range in thickness from 200 to 1200 μM (Appendix 25), are then used to fabricate devices (Scheme 1). The surface properties of the composite films were examined using atomic force microscopy (AFM) (Figures 6a, 6b and Appendix 26, 27). The effectiveness of the TENG is significantly affected by the surface's roughness. It is well established that the mean surface roughness impacts the TENG's output (R_a).^[37] When the R_a value is high enough, it provides a larger area for materials to interact optimally through believable friction, resulting in a vastly increased amount of charge generation and hence a boost in TENG production. Two-dimensional (2D) scanning of the surface topography (3D profile) of PVDF film alone and 5 wt% **IPMOP-IL/PVDF** across an area of identical dimensions demonstrated that the surface roughness characteristic of **IPMOP-IL/PVDF** is enhanced, enrooting greater surface-dependent qualities including available area for friction surface and charge buildup. High fluctuation in roughness feature and peak profiles is directly indicated by the scan results shown above, which show a tuned peak height pattern on PVDF film and **IPMOP-IL/PVDF** film, where S_q value is increased several fold in the latter case, respectively (Appendix 26 and 27). It's clear that **IPMOP-IL/PVDF** has a better R_a value than PVDF film alone. Consistent with the aforementioned finding, AFM measurements were taken at randomly selected regions covering the same length. Open circuit voltage (V_{oc}) profiles for selected best performing device (**IPTEENG-3**) is shown (Figure 6c, 6d) besides V_{oc} for other TENG devices (Appendix 28, Appendix table 21). Figure 6d indicates peak maxima for output voltage reaching upto 143.3 V for 5 wt % **IPTEENG-3** device, the best performing device.

Figure 7a reveals the variation in the performance displayed by IPTENG-n devices, and the **IPTEENG-3** device clearly supersedes other devices made other than IPMOP-IL composite films. For the **IPTEENG-3** device, its voltage reproducibility (average voltage, V_{av}) was analyzed over seven days; however, devices were exposed to humidity and ambient conditions of temperature and environment (30 °C at 98% relative

humidity (RH), exposed over 24 h) as the device is aimed for real-time applications, thereby confirming astounding reproducibility and durability entailing its potential for targeted applications. Further the effect of impact force on open circuit voltage on $2.0 \times 2.0 \text{ cm}^2$ area for **IPTENG-3** device with respect to incremental frequency was elucidated and incremental V_{oc} was noted and device withstands flawlessly even at 36 N force also giving reproducible output (figure 7c). The Effect that the frequency of impact has on the open circuit voltage region using the **IPTENG-3** device having aforementioned dimensions revealed a high frequency output rising consistently up to 28 Hz simultaneously observed as function of incremental impact force (figure 7d).

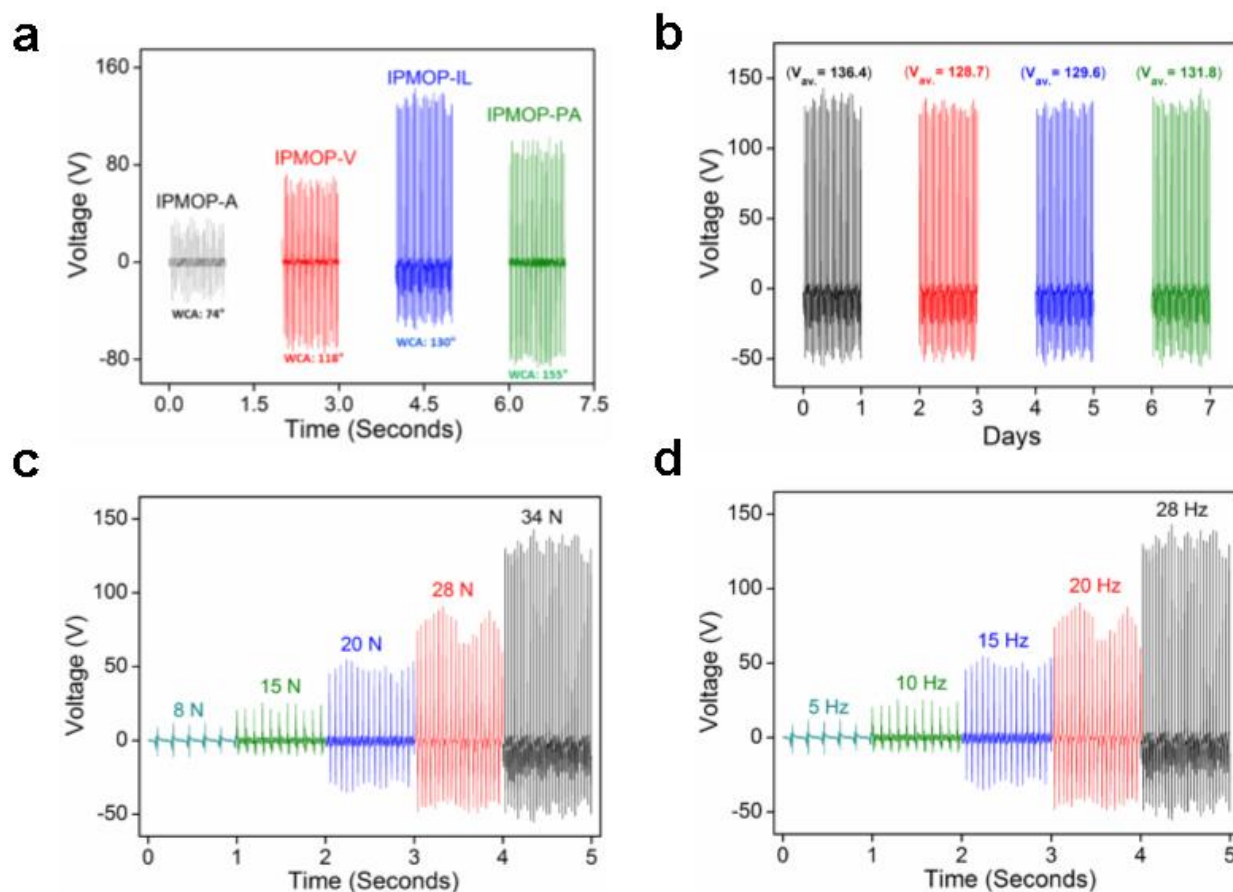


Figure 7. a) V_{oc} output for 5 wt % loaded IPMOP-A/PVDF, IPMOP-PA/PVDF, IPMOP-IL/PVDF, and IPMOP-V/PVDF composite films derived TENG devices. b) Average V_{oc} of 5 wt % of IPMOP-IL/PVDF i.e. (IPTENG-3). c) Effect of impact force on open circuit voltage on $2.0 \times 2.0 \text{ cm}^2$ area for

IPTENG-3 device with respect to incremental frequency. d) Effect of frequency of impact on open circuit voltage of $2.0 \times 2.0 \text{ cm}^2$ area for **IPTENG-3** device.

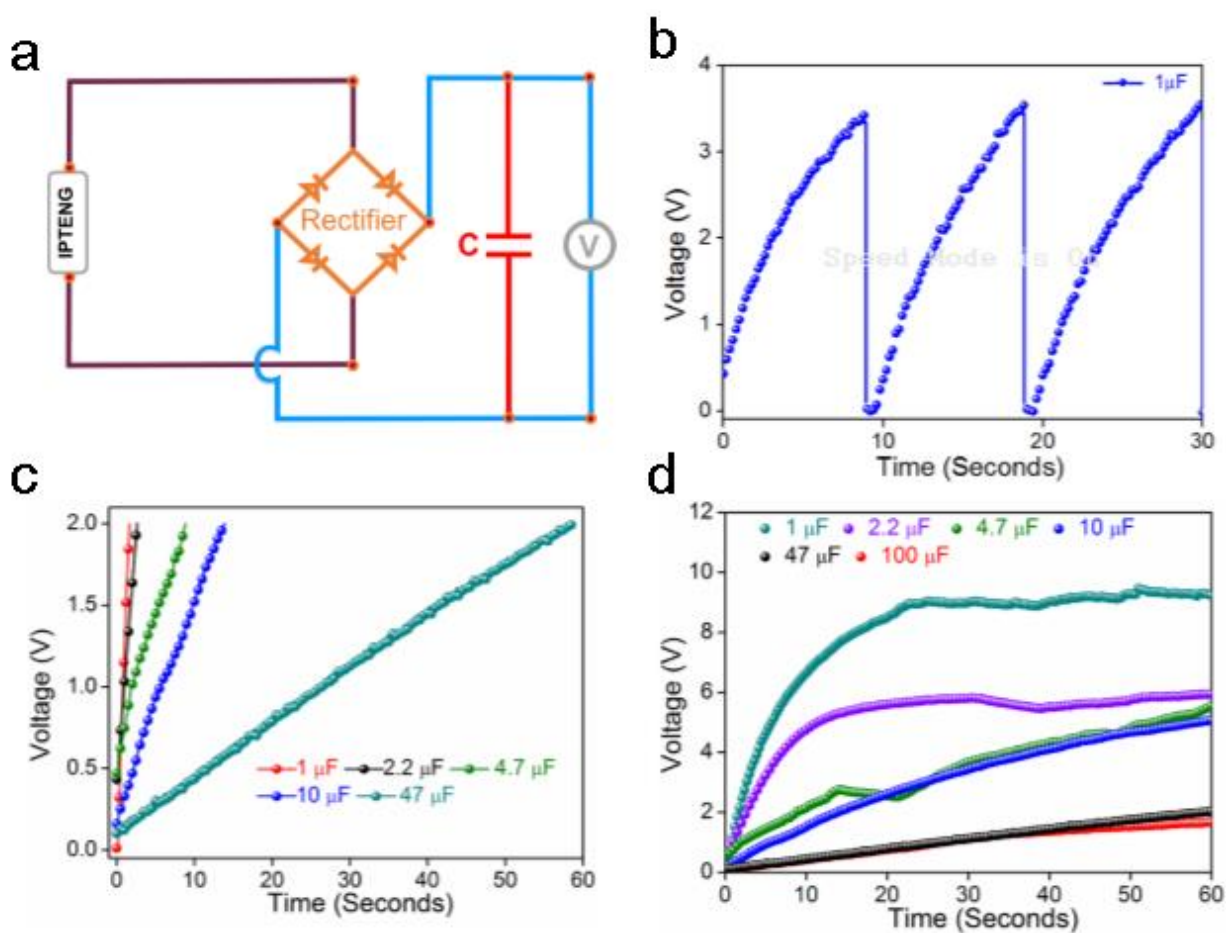


Figure 8. a) The schematic representation of a full-wave bridge rectifier circuit diagram. b) $1 \mu\text{F}$ capacitor charging-discharge pattern as indicated by the output of **IPTENG-3** device. c) Capacitor charging curves for 1 , 2.2 , 4.7 , 47 , and $100 \mu\text{F}$ capacitors depicting fast charging in shorter span by the $5 \text{ wt } \% \text{ IPMOP-IL/PVDF}$ (**IPTENG-3**). d) Capacitor charging curves depicting saturation attenuation for 1 , 2.2 , 4.7 , 47 , and $100 \mu\text{F}$ capacitors employing the **IPTENG-3** device.

Figure 8a shows the combination of circuit deployed for capacitor charging and electrical application rendering performance analysis. In order to determine the extent to which the $5 \text{ wt } \% \text{ IPMOP-IL/PVDF}$ -based TENG could be utilized in a variety of contexts, the voltage, current, and power were measured by

loading the same device, denoted as **IPTENG-3**, with an assortment of different kinds of external load resistance (Figure 8b-8d and Figure 9, Appendix 31–34).

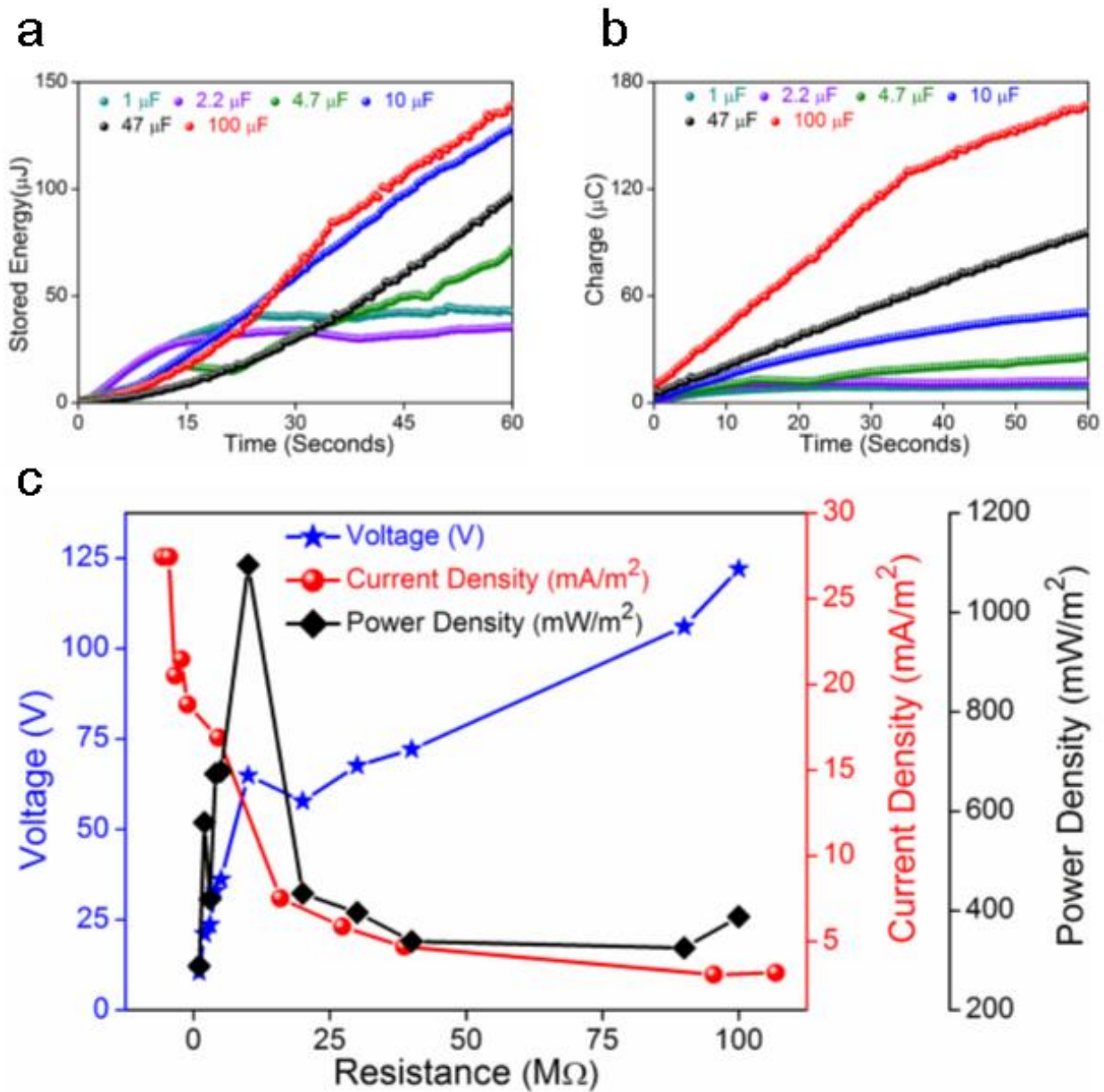


Figure 9. a) Energy stored in various capacitors by the output of **IPTENG-3** device. b) Charge stored in various capacitors by the output of **IPTENG-3** device. c) Summarized voltage, power density current density plots as a function of load resistance corresponding to the **IPTENG-3** device.

In order to evaluate the performance retention and consistency of ten different **IPTENG-3** devices, the Voc output of each one was evaluated. The findings demonstrated exceptionally high consistency, with a peak voltage of 110.41 volts and a stable output (Appendix 29). Additionally, the average open circuit output voltage was 131.7 volts (Appendix 29, 30 and Appendix table 3). As can be seen from the charging profiles, the output voltage shoots up quickly, the capacitor saturates, and it reaches values of 2 V in less than 60 seconds throughout the respective 1, 2.2, 4.7, 10 and 47 μF capacitors. This can be deduced from the fact that the output voltage fastly enhances as the capacitor fills up (Figure 8c). When considering the actual time utilization for the requirements of fast charging, it is noteworthy that the capacitors stated above charged quite quickly and became saturated within the shortest time intervals. **IPTENG-3's** ability to perform charging and discharging cycles (shown in Figure 3d) on a capacitor with a capacity of 1 μF at a high frequency and with a high degree of precision reproducibility demonstrates that this technology may be useful for on-demand implementations. Figures 9a and 9b reveal the energy stored and charge accumulated in 60 sec by the capacitors having capacitances of 1, 2.2, 4.7, 10, 47, and 100 μF respectively. The overall output performance for **IPTENG-n** ($n=1-4$) was comprehensively analyzed by keeping simultaneously increasing external load resistances upto 100 $\text{M}\Omega$ which enabled precise measurement of current and power densities for each of the **IPTENG** device (appendix 33). The best suited **IPTENG-3** device revealed outstanding performance, steady output and epitome power density value upto 1095.5 mW/m^2 (at load resistance of 10 $\text{M}\Omega$). Thereby **IPTENG-3** retains its desirability and were examined further for real time applications including li-ion battery charging and hence cellphone power support, trimmer battery and operations as well as LED illuminations proving its potential for real time applications.

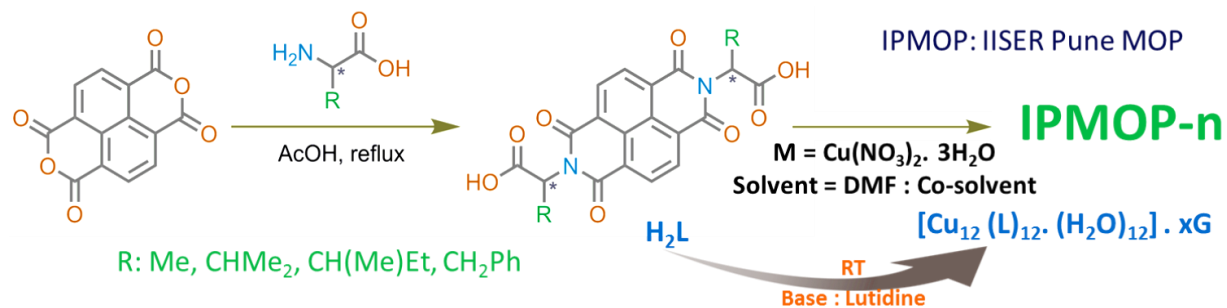
5.4 Conclusion

The proposed work includes a maiden report that entails a corroboratory strategy of linker-driven hydrophobicity tuning in a series of cages (**IPMOP** family) for rationally regulating the output of Nanogenerators in response to real-time TENG applications. A broad range of ultra-stable materials are blended with PVDF to produce potentially deployable TENG devices by adopting hydrophobic shielding as the cornerstone strategy. The propensity of MOP compounds to attain chemical stability even when the metal-ligand interaction is weak by nature led to their inherent properties that are meticulously utilized. Observations support the judicious application of various alkyl groups (generated from the ligands) to the cages' outer surfaces, which not only increases the hydrophobicity around the metal core but also

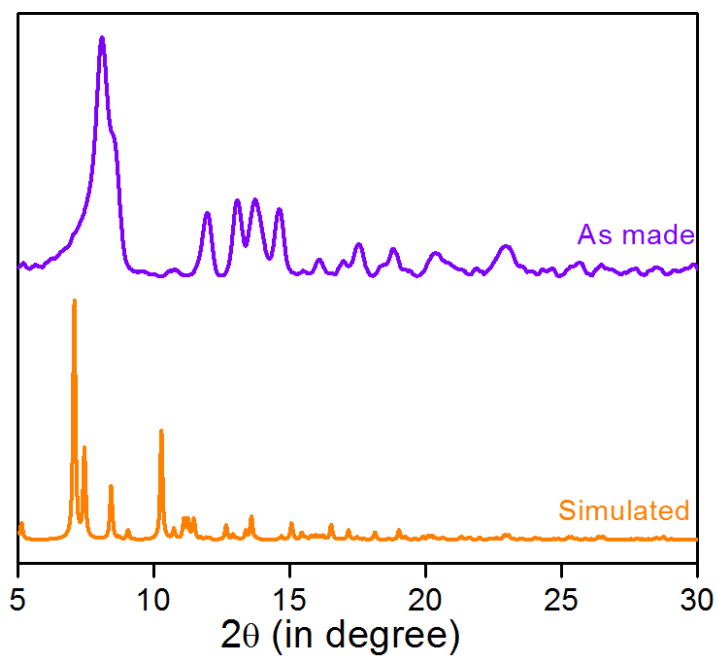
contributes to the overall stability of the framework. Current findings for the generalization of chemically addressable MOPs and their successful fabrication into flyweight devices will offer instant, simple ways to build different stable cage-based composites for targeted applications, in addition to those in the Nanogenerator arena. Pre-synthetic design and fabrication techniques have thus been successfully demonstrated and have shown to be a practical solution for improving TENG output by making use of the strong and controllable surface features produced by gradient hydrophobicity of constituents that are tapped by linker functionalization.

The flexibility of PVDF and the precise controllability of MOP doping level, in addition to utilizing its property of being a solution processable material, made it possible to construct a flexible, strong, and lightweight TENG that can operate in a vertical contact-separation mechanism and produce a remarkable and consistent output. Following their implementation, the TENG devices are used for mechanical energy harvesting applications, producing a maximum power density of 1095.5 mW/m² for the ideal loading of a 5 wt % 3/PVDF device (**IPTEG-3**) at a load resistance of 10 M Ω . When compared to the unblended PVDF film and the other IPTENG composite devices, **IPTEG-3** exhibited the highest performance. By putting the collected energy in various electrolytic capacitors, the constructed devices' capacity for energy storage has been demonstrated. As a result, in the first place, MOPs and their adjusted properties can be rationally utilized to produce unremitting mechanical energy harvester performance that is desirable to a variety of low-to-moderate energy-derived TENG applications.

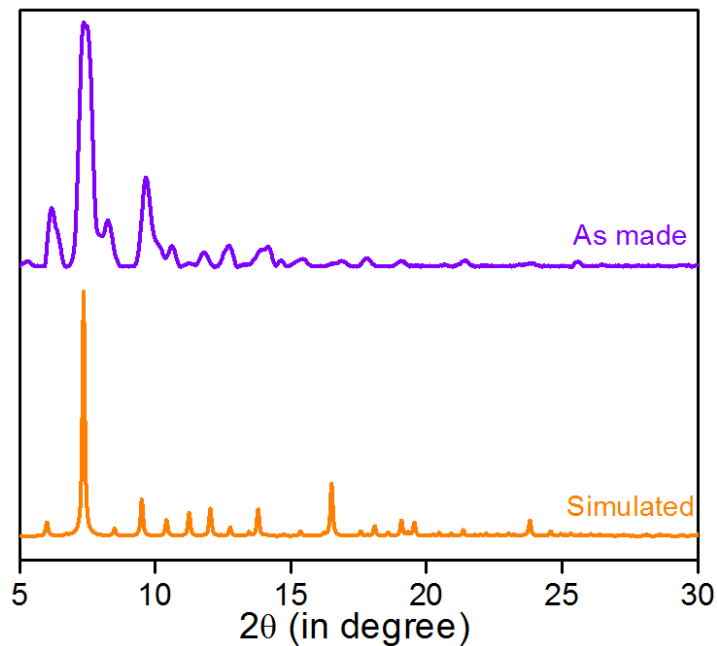
5.5 Appendix Section



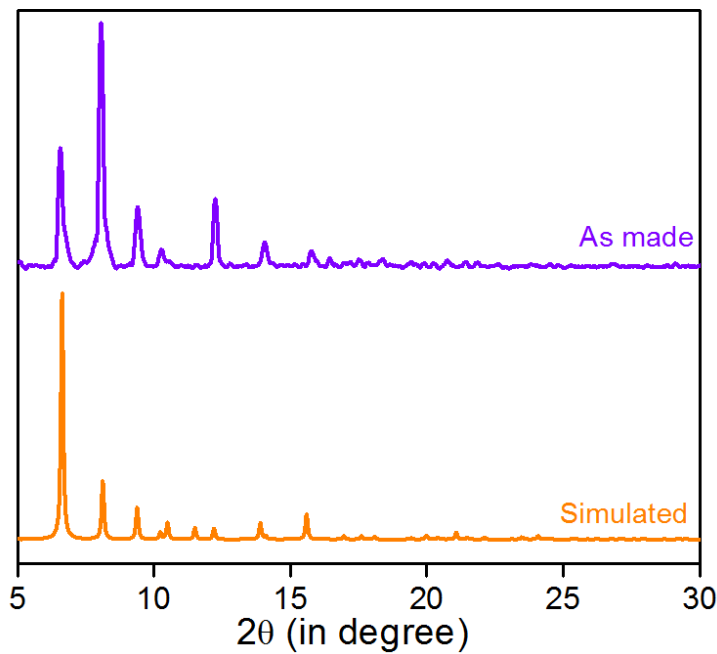
Appendix 1. General synthesis scheme deployed for room temperature synthesis of all four MOPs.



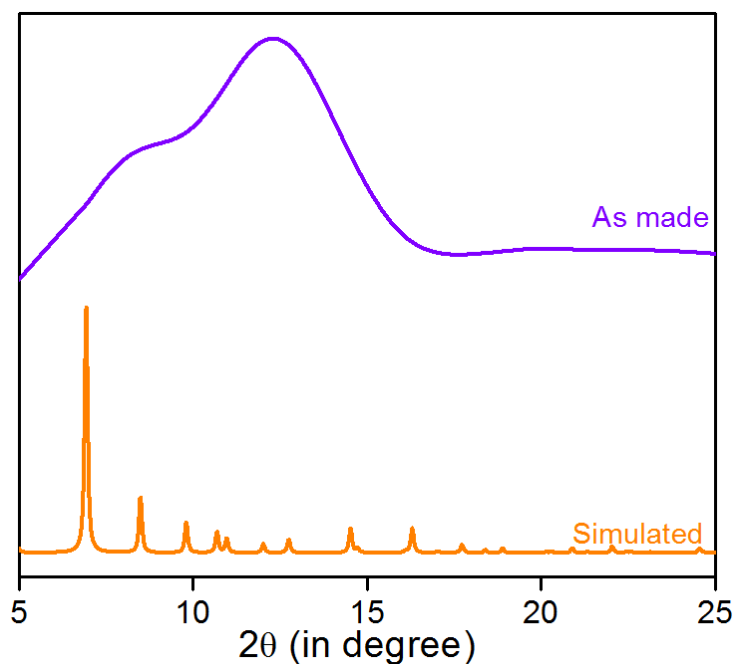
Appendix 2. Comparison of the experimental PXRD data of IPMOP-A, and the simulated pattern from the unit cell.



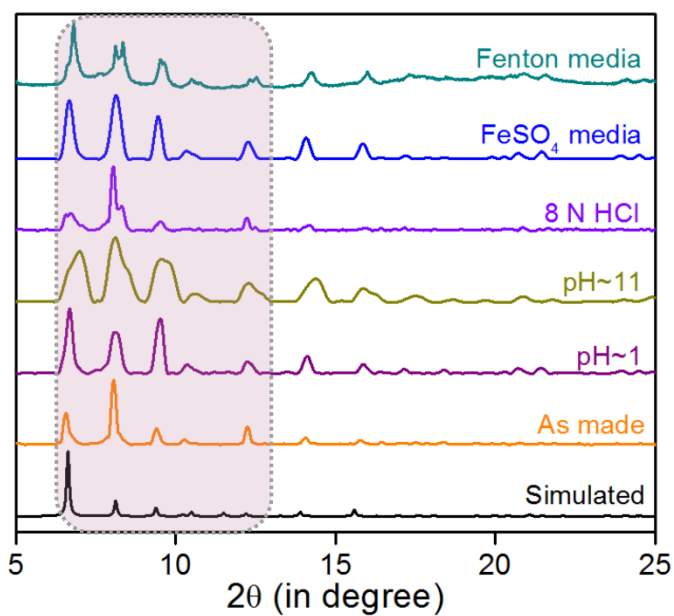
Appendix 3. Comparison of the experimental PXRD data of IPMOP-PA and the simulated pattern from the unit cell.



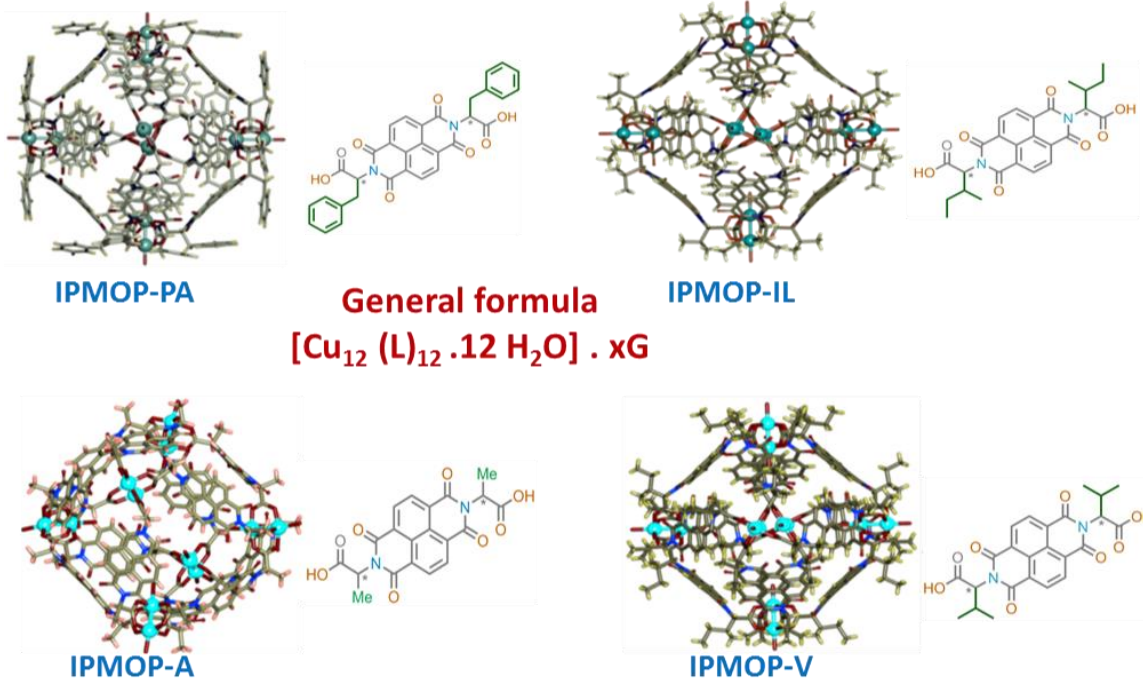
Appendix 4. Comparison of the experimental PXRD data of IPMOP-IL and the simulated pattern from the unit cell.



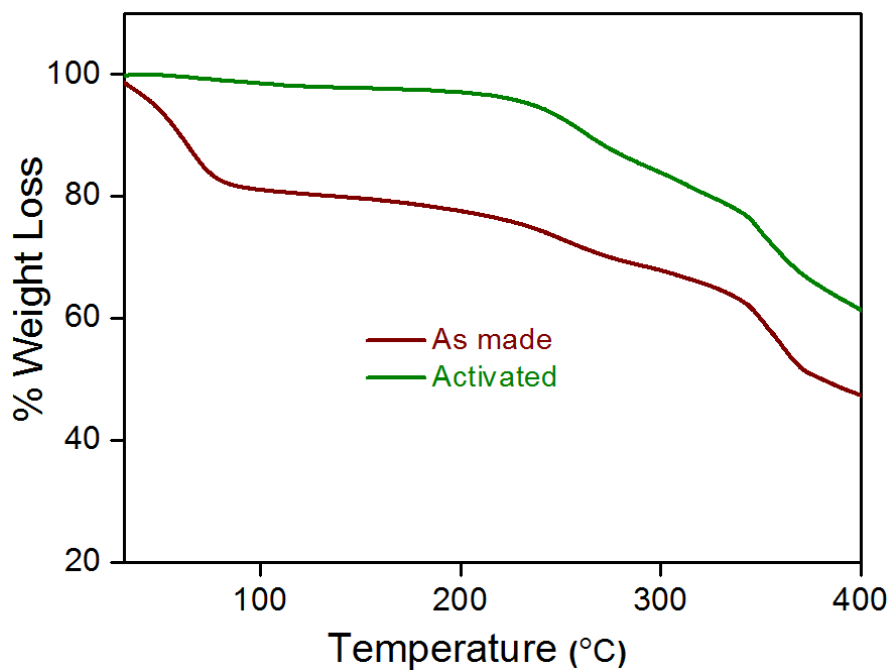
Appendix 5. Comparison of the experimental PXRD data of IPMOP-V and the simulated pattern from the unit cell.



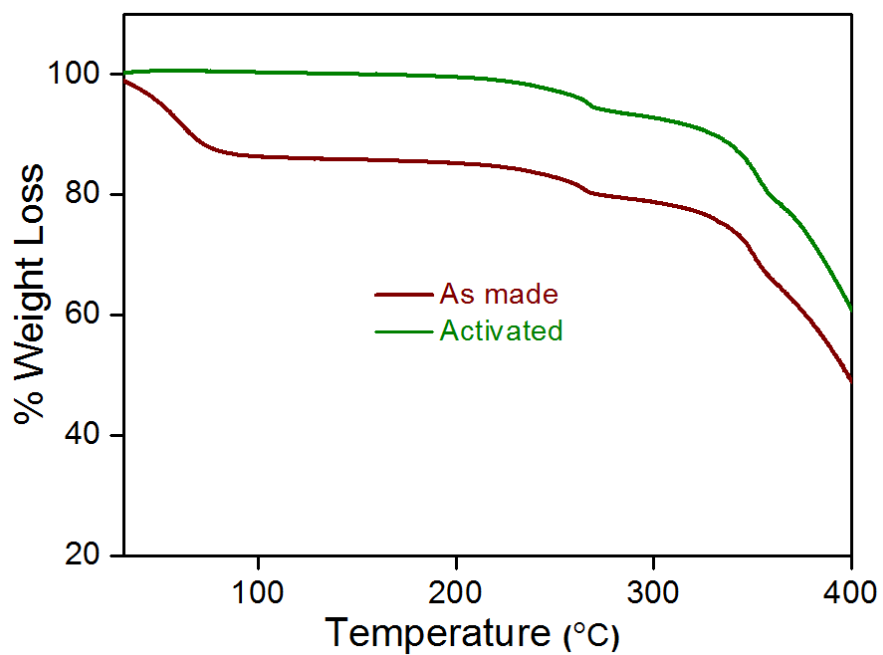
Appendix 6. Comparison of the PXRD data of IPMOP-IL under diverse chemical conditions and the simulated pattern from the unit cell.



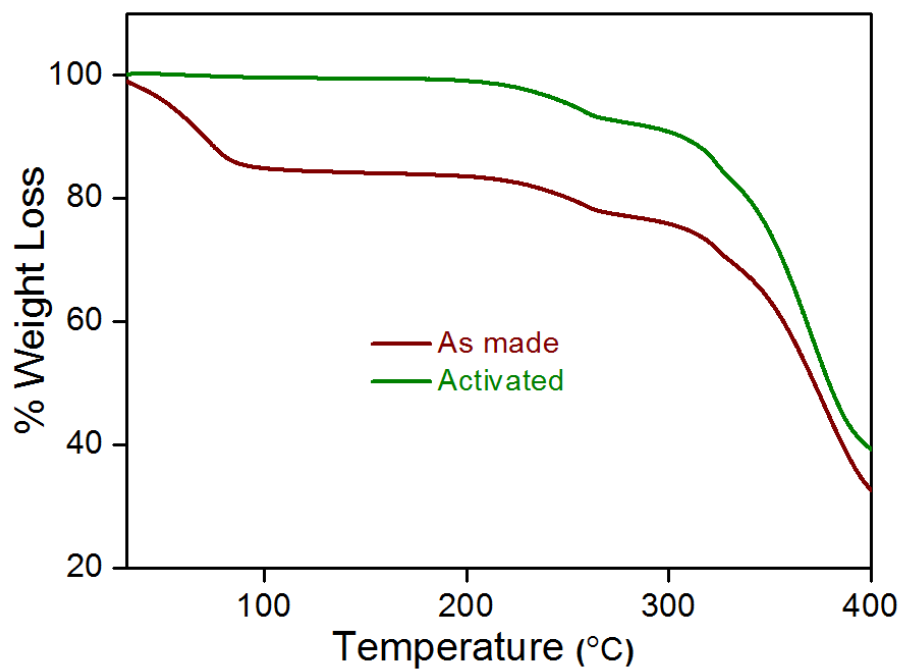
Appendix 7. Individual MOPs with their respective linkers showing difference in hydrophobic shielding of Metal node.



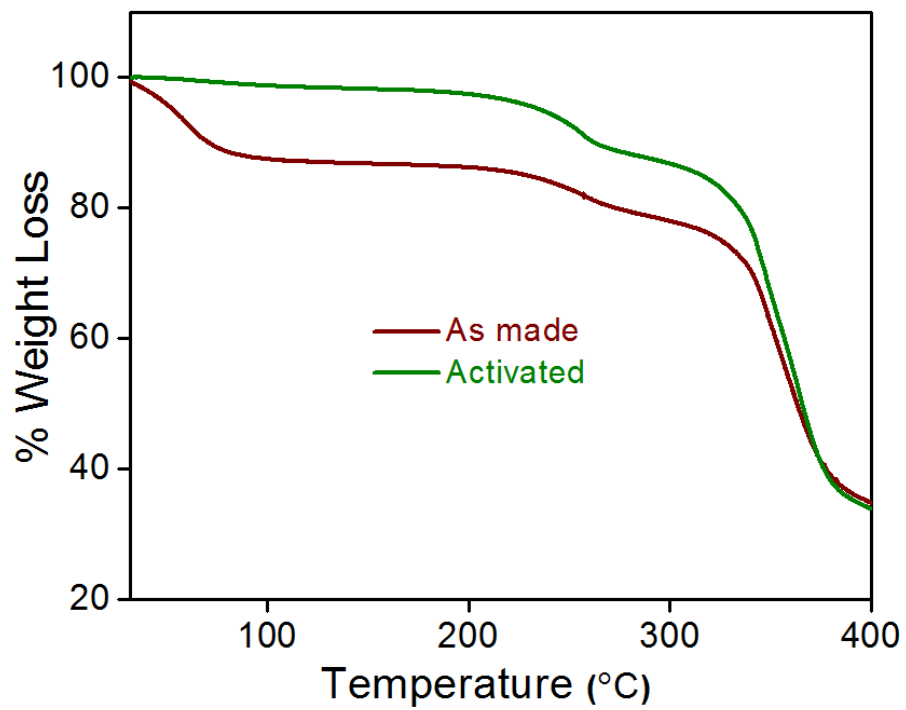
Appendix 8. Thermogravimetric analysis of pristine IPMOP-A.



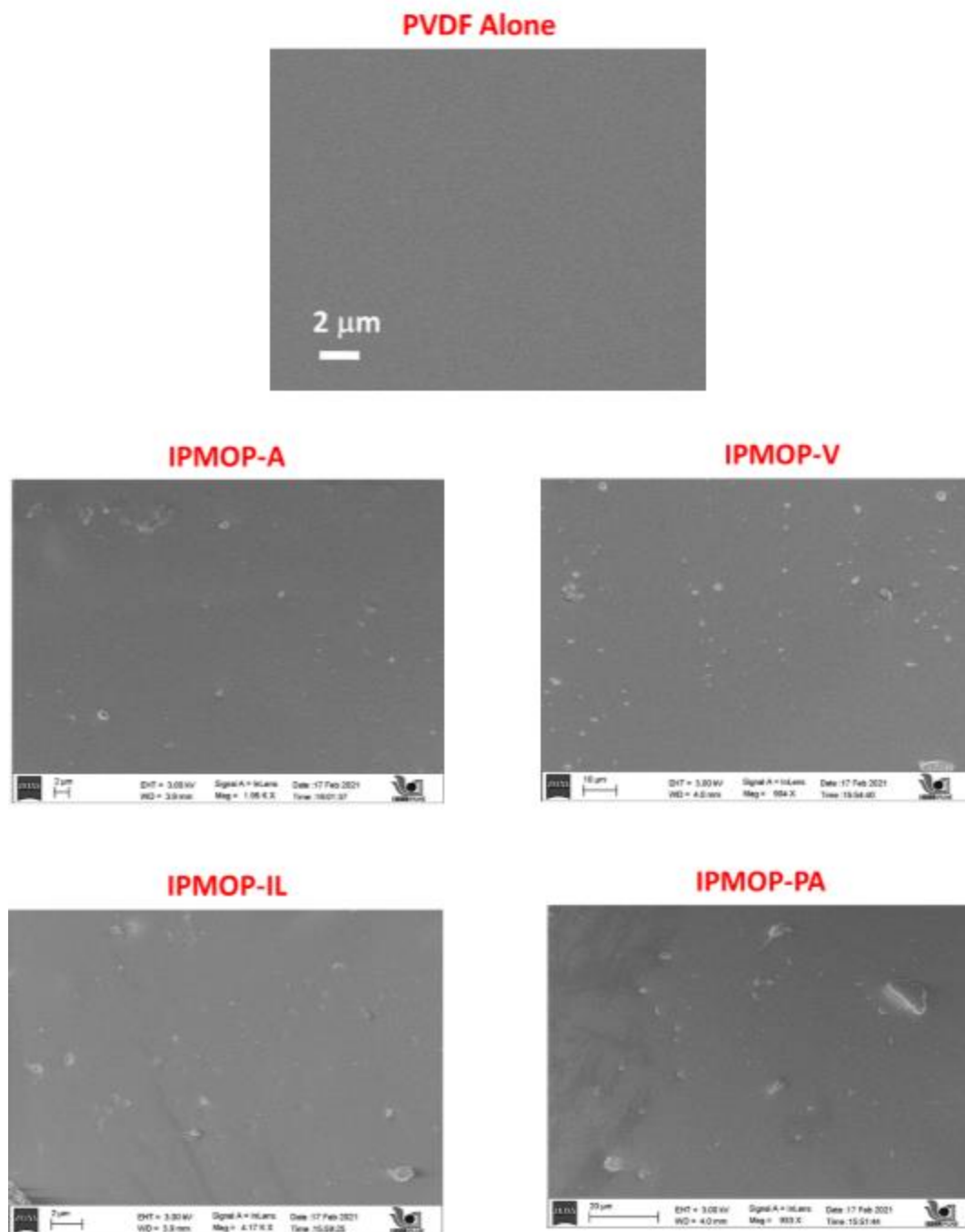
Appendix 9. Thermogravimetric analysis of pristine IPMOP-PA.



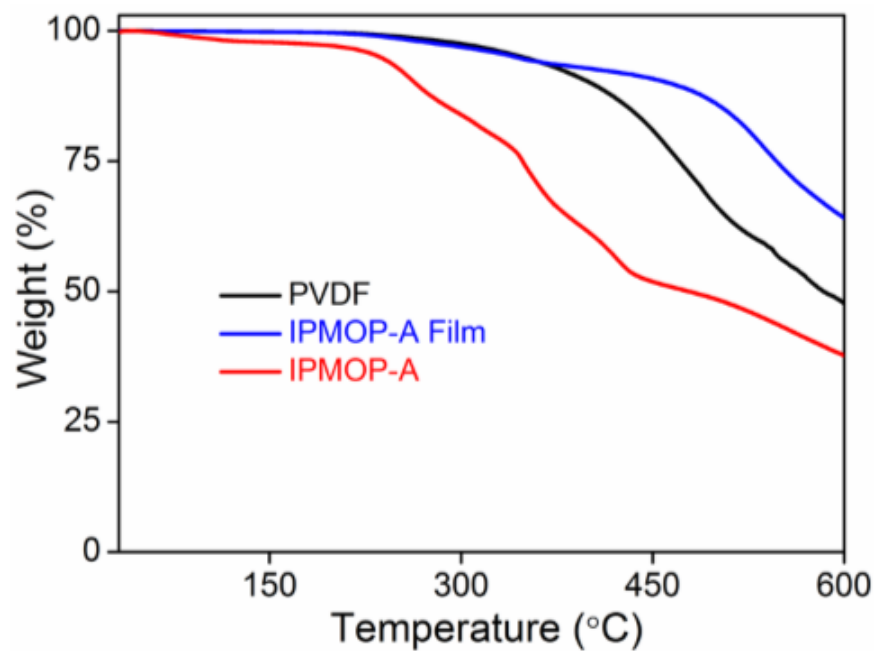
Appendix 10. Thermogravimetric analysis of pristine IPMOP-IL.



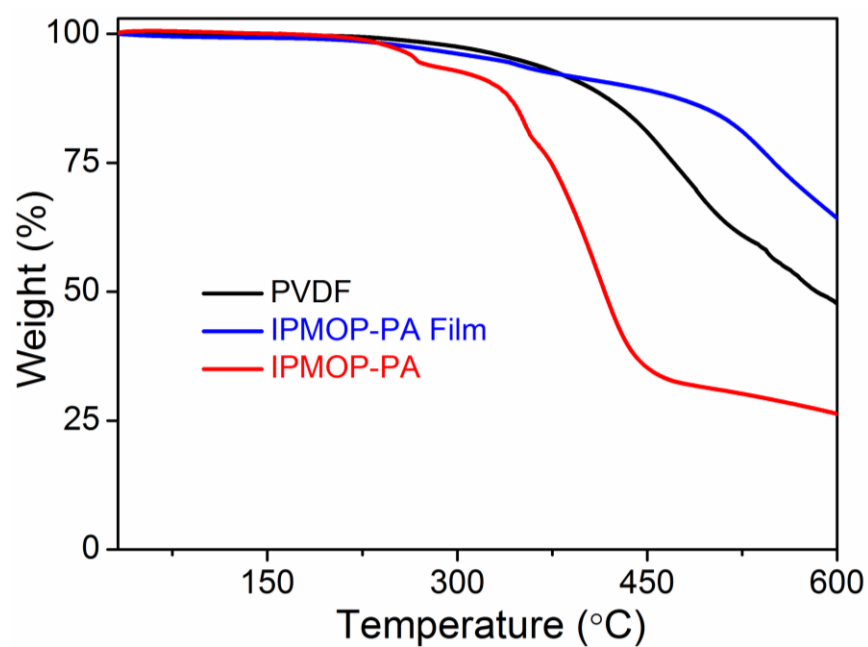
Appendix 11. Thermogravimetric analysis of pristine IPMOP-V.



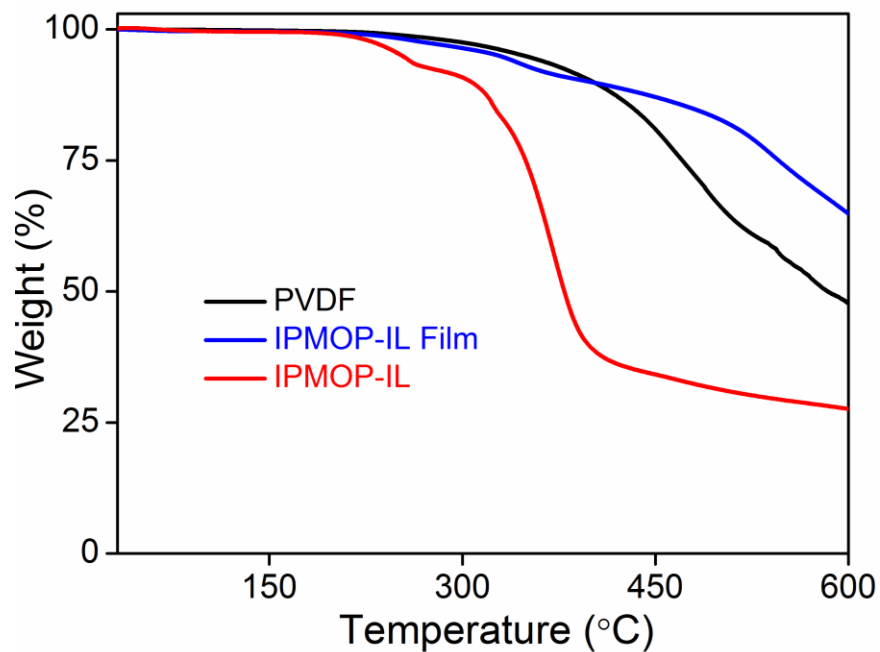
Appendix 12. FESEM images of the respective IPMOPs at 5 wt % in PVDF composite films.



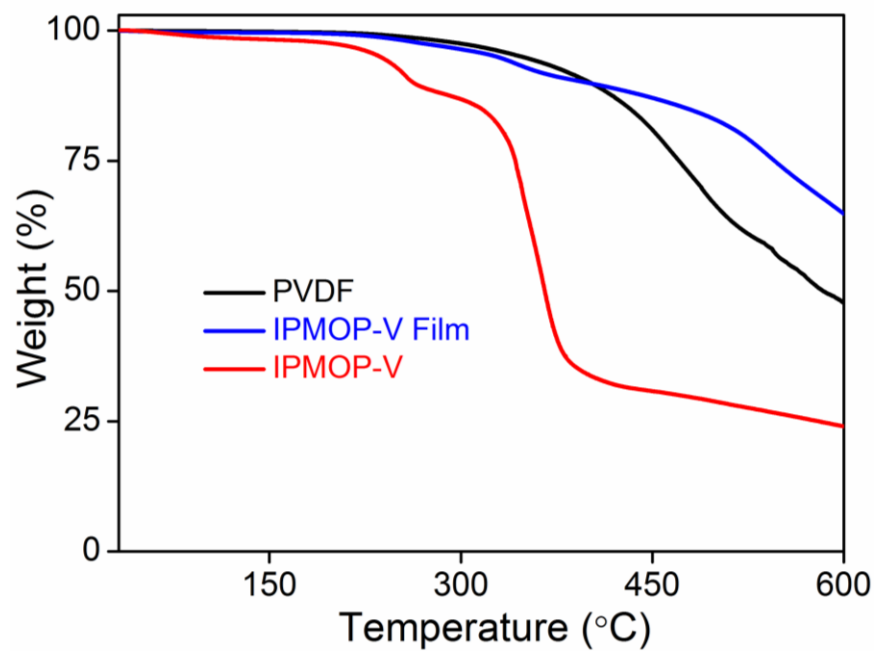
Appendix 13. Thermogravimetric analysis 5 wt % loaded composite film of IPMOP-A.



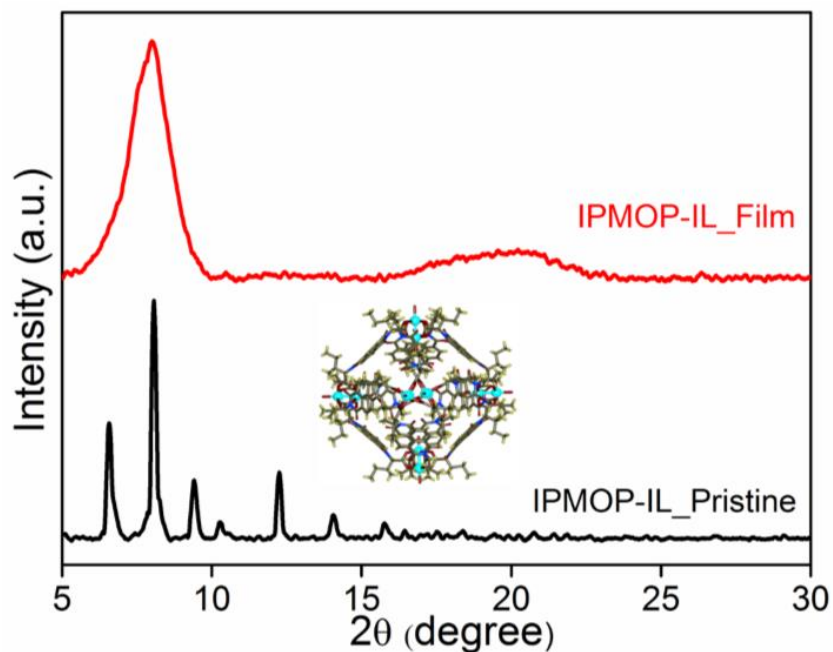
Appendix 14. Thermogravimetric analysis 5 wt % loaded composite film of IPMOP-PA.



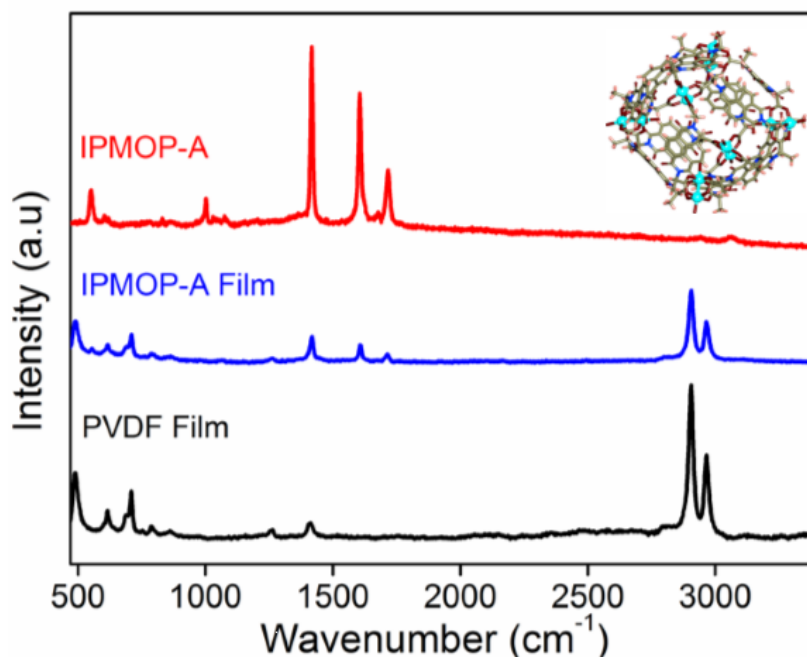
Appendix 15. Thermogravimetric analysis 5 wt % loaded composite film of IPMOP-IL.



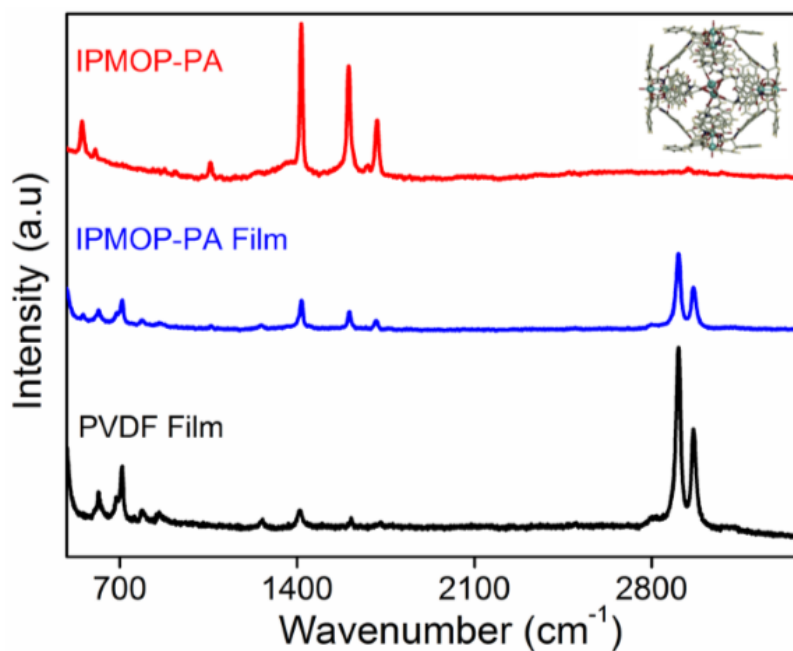
Appendix 16. Thermogravimetric analysis 5 wt % loaded composite film of IPMOP-IL.



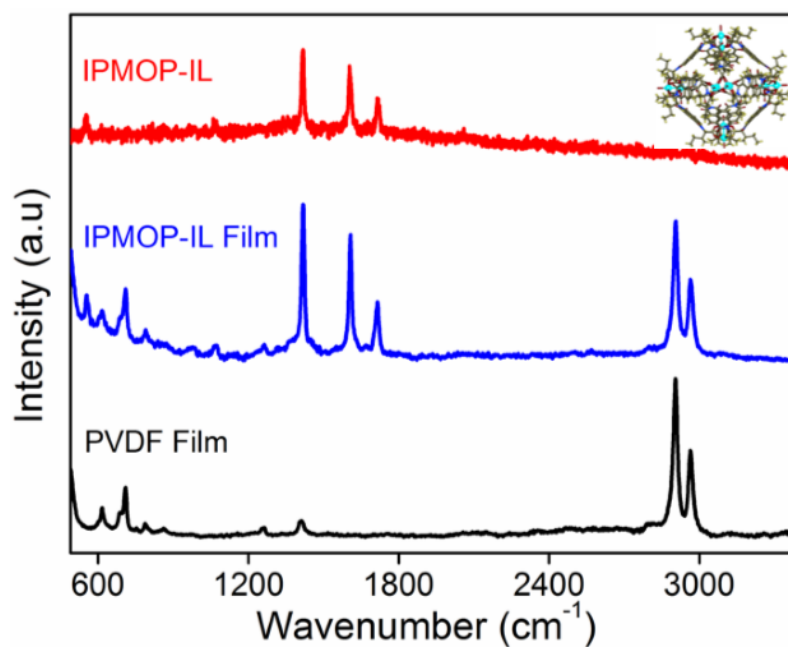
Appendix 17. Comparison of the experimental PXRD data of IPMOP-IL composite film with 5% loading (IPTENG-3) and the simulated pattern from the unit cell.



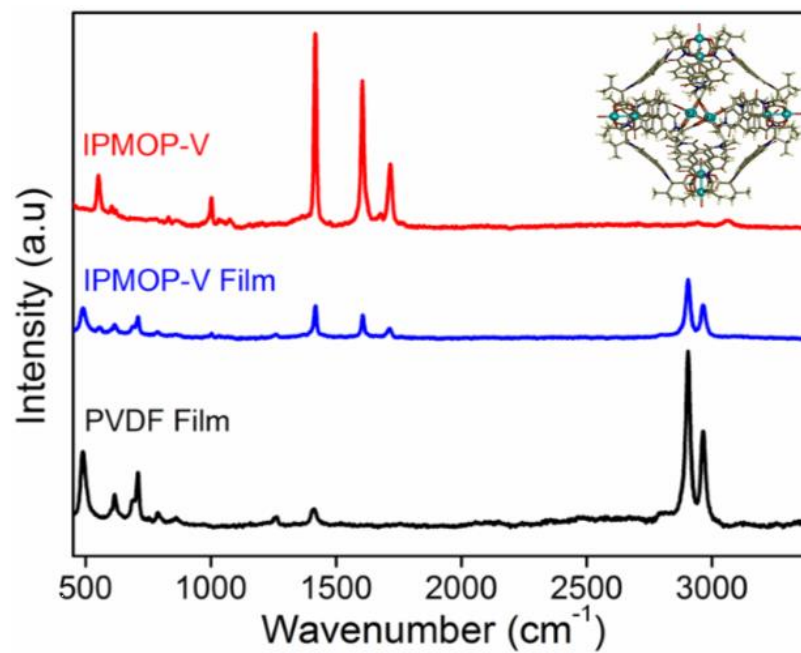
Appendix 18. Raman spectra of pristine MOP compounds, PVDF films and MOP/PVDF composite films at 5% loading for IPMOP-A.



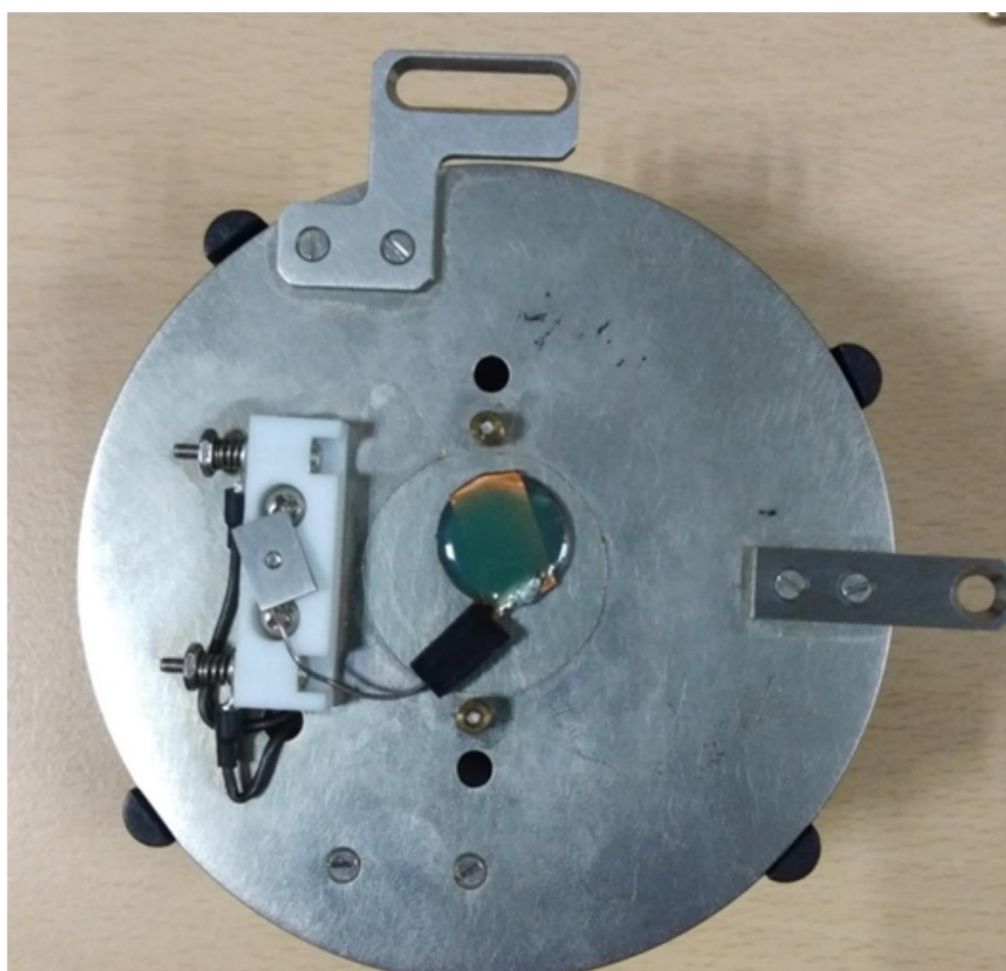
Appendix 19. Raman spectra of pristine MOP compounds, PVDF films and MOP/PVDF composite films at 5% loading for IPMOP-PA.



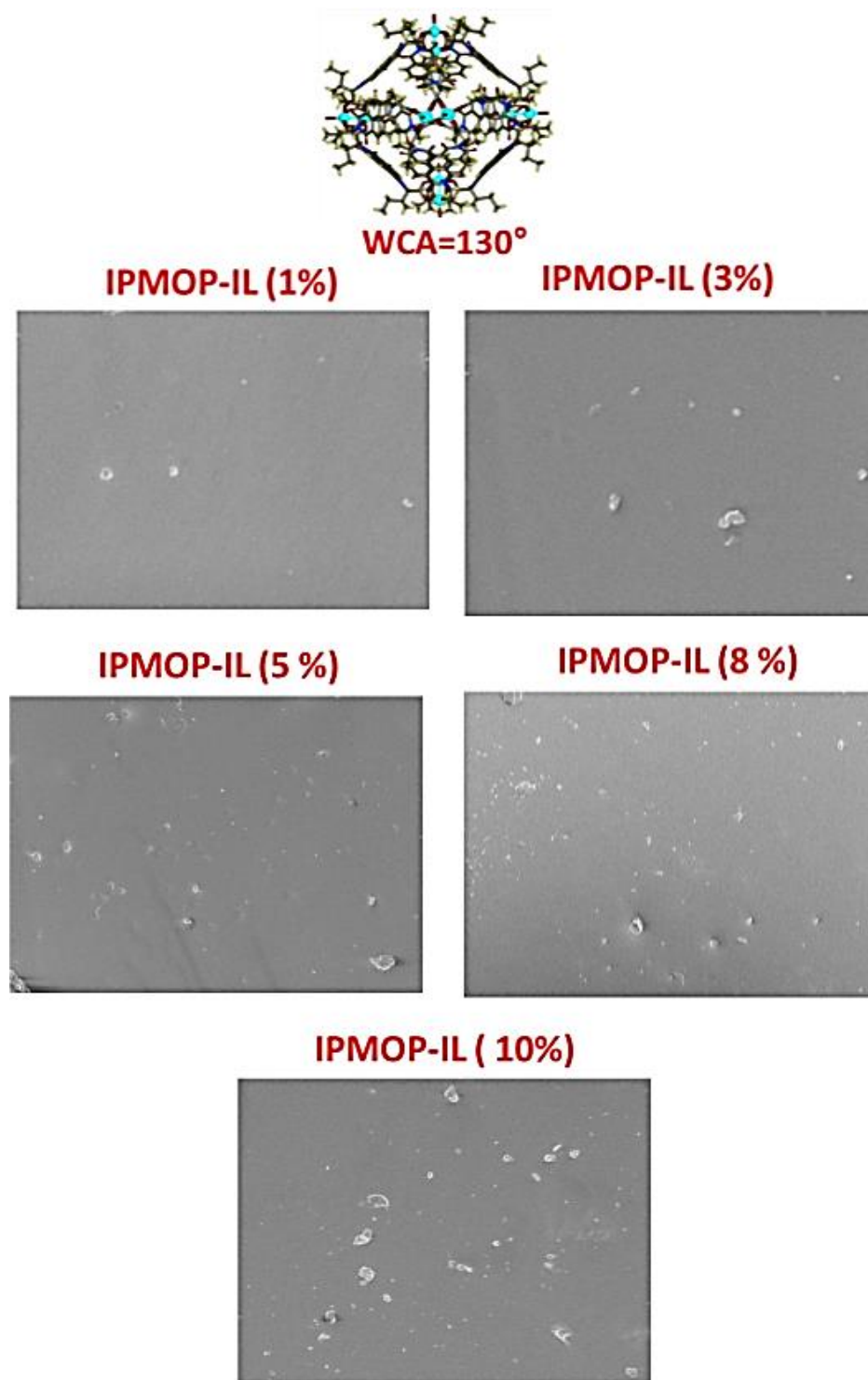
Appendix 20. Raman spectra of pristine MOP compounds, PVDF films and MOP/PVDF composite films at 5% loading for IPMOP-IL.



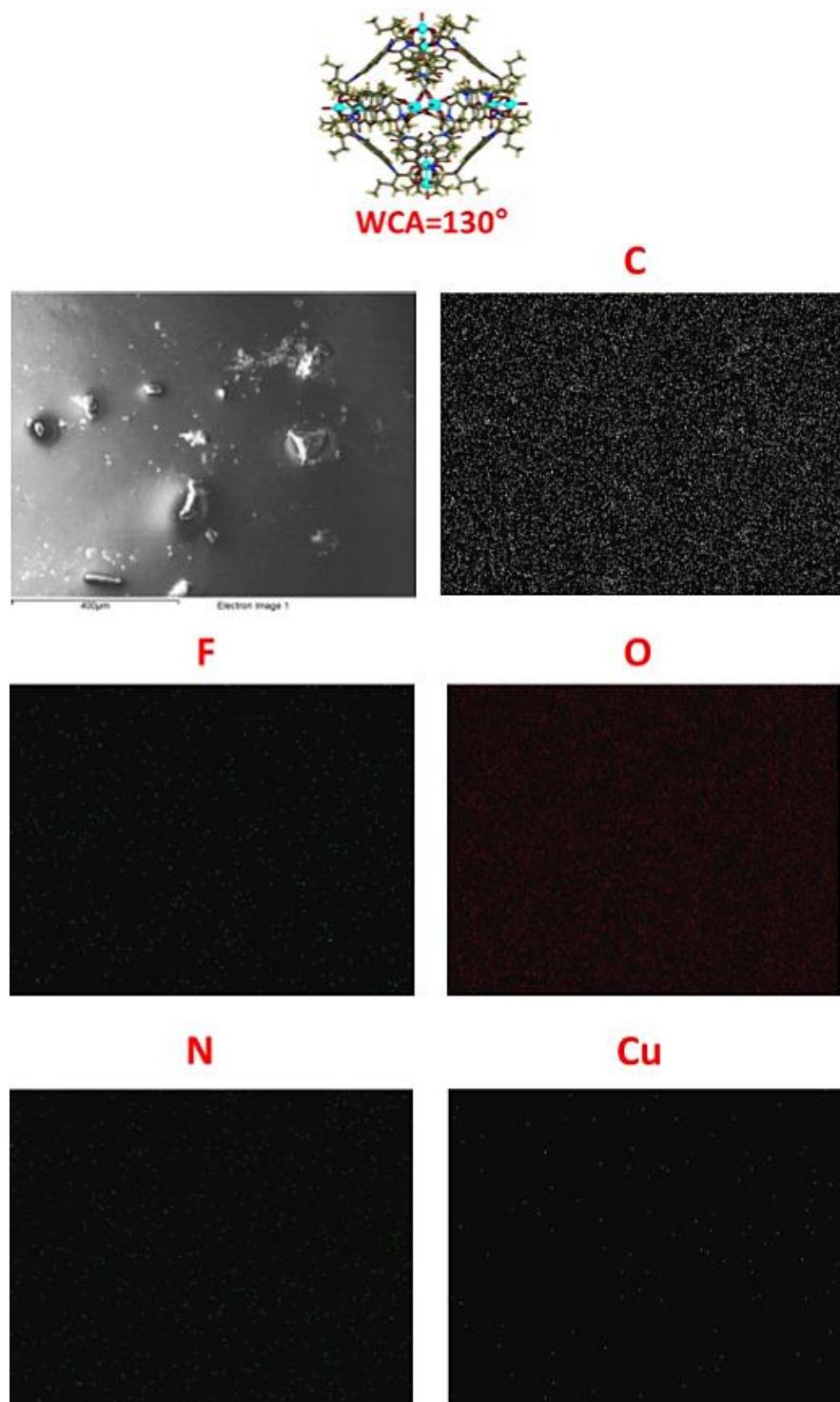
Appendix 21. Raman spectra of pristine MOP compounds, PVDF films and MOP/PVDF composite films at 5% loading for IPMOP-V.



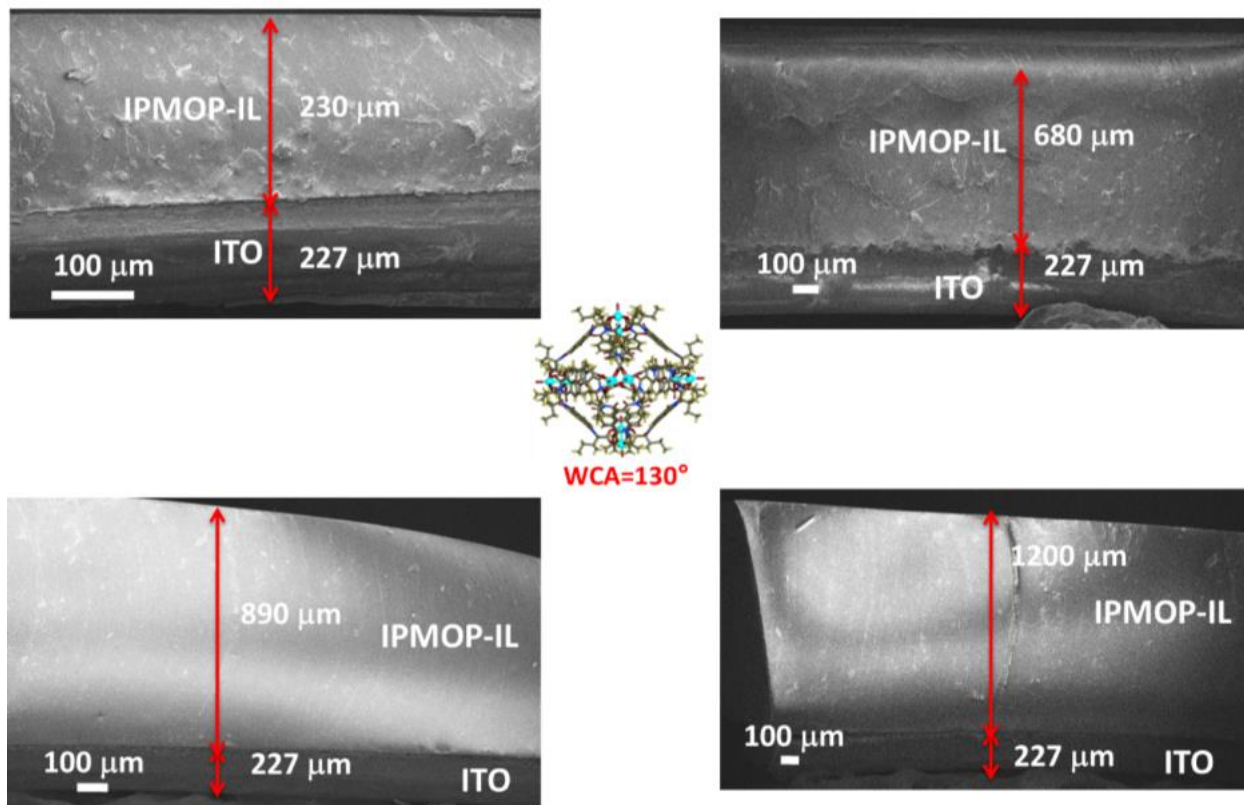
Appendix 22. Incremental loading of IPMOP in PVDF prepared on metal conducting substrate for AFM. Tailor-made setup deployed for AFM analysis.



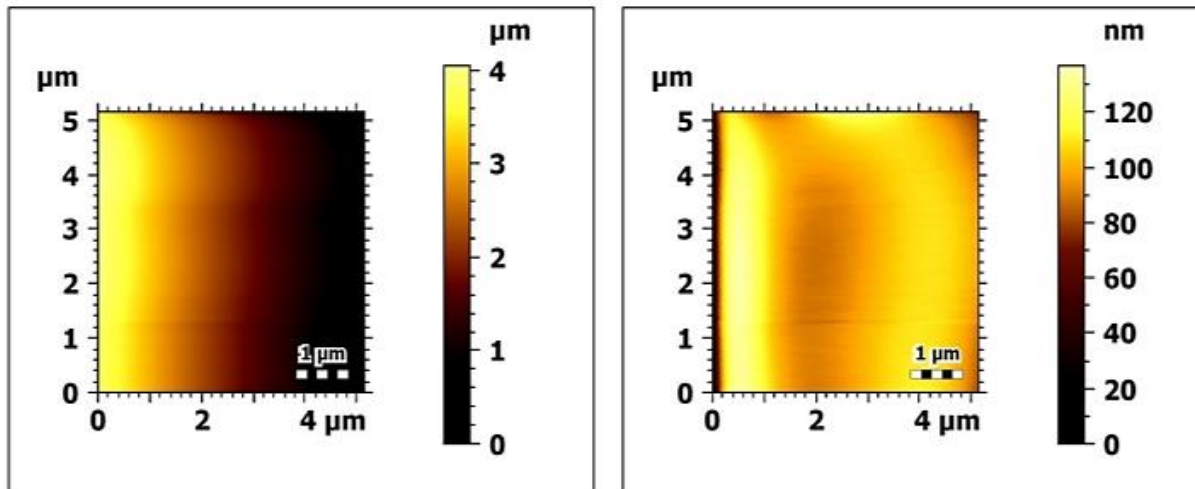
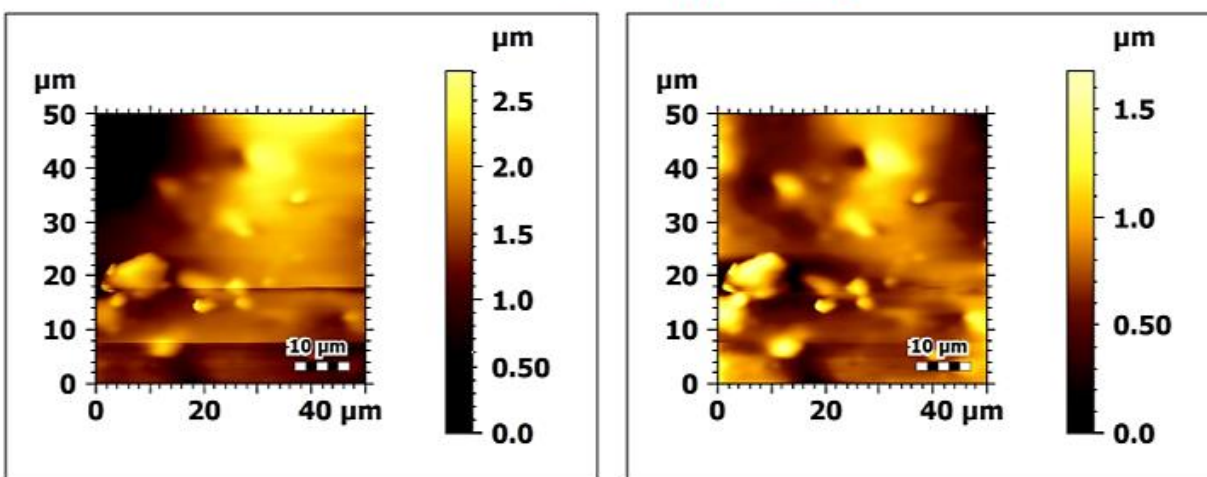
Appendix 23. FESEM images of the 1, 3, 5, 8, 10 wt % **IPMOP-IL/PVDF** composite films.



Appendix 24. FESEM imaging and EDX mapping profile PMOP-IL@ 5 wt% composite.



Appendix 25. FESEM images of the cross section of IPMOP-IL/PVDF (5 wt % loading) prepared at variable thickness range revealing controllability of composite thickness fabrication.

PVDF**IPMOP-IL (5 wt%)**

Appendix 26. AFM images of PVDF and IPMOP-IL (5 wt %) / PVDF composite film, trace and retrace in the X-direction, and Y-direction, line roughness profile with height parameters simultaneously.

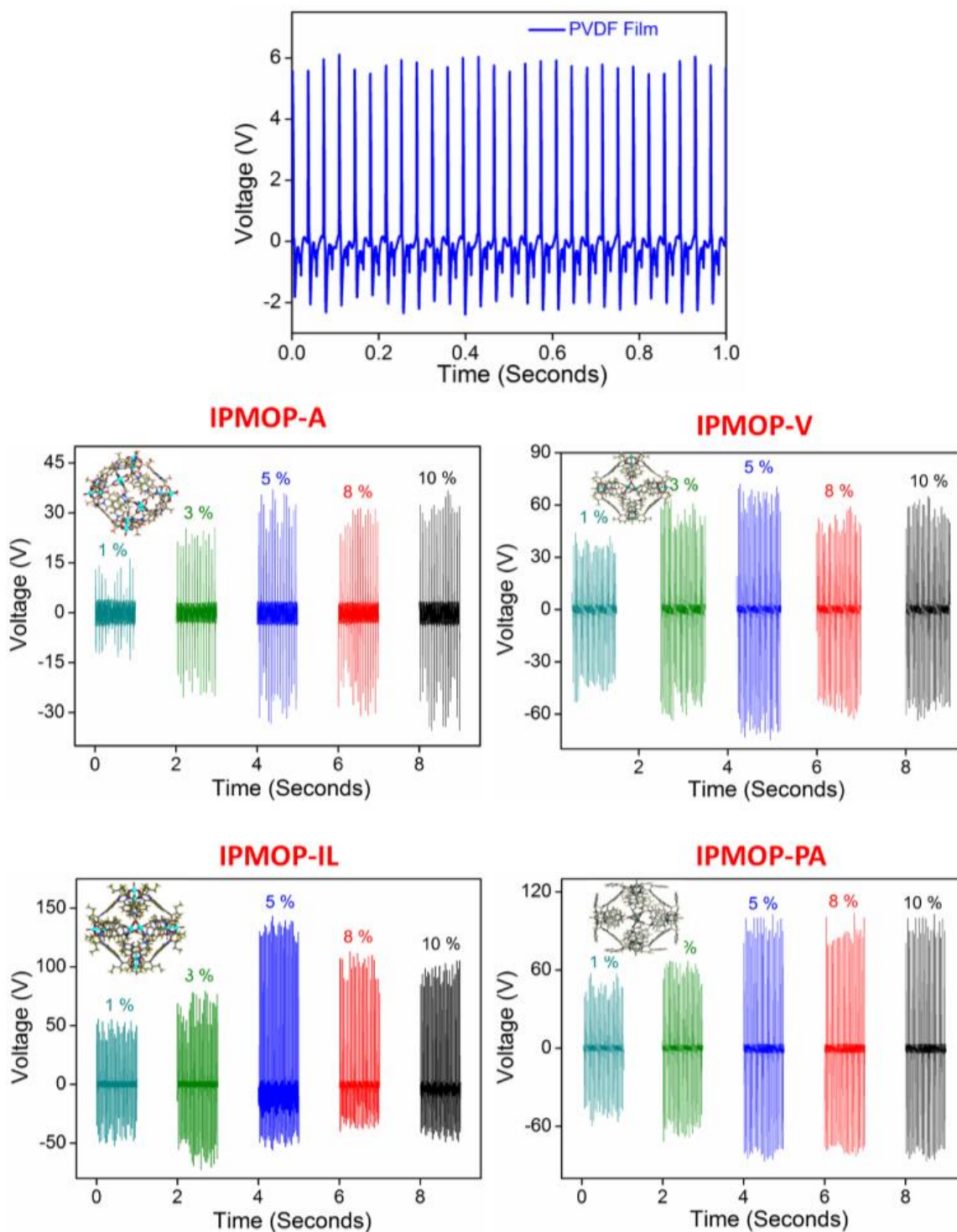
PVDF

ISO 25178			
Height Parameters			
Sq		15.0	nm
Ssk		-1.83	
Sku		13.0	
Sp		36.1	nm
Sv		109	nm
Sz		145	nm
Sa		9.85	nm
EUR 15178N			
Amplitude Parameters			
Sa		9.85	nm
Other 3D Parameters			
Miscellaneous			
Smean		0.0186	nm
Sdar		26.6	μm^2
Spar		26.5	μm^2

IPMOP-IL (5 wt%)

ISO 25178			
Height Parameters			
Sq		0.232	μm
Ssk		0.530	
Sku		3.83	
Sp		0.916	μm
Sv		0.780	μm
Sz		1.70	μm
Sa		0.177	μm
EUR 15178N			
Amplitude Parameters			
Sa		0.177	μm
Other 3D Parameters			
Miscellaneous			
Smean		-7.99e-005	μm
Sdar		2530	μm^2
Spar		2500	μm^2

Appendix 27. Line roughness profile with height parameters obtained from AFM measurements of PVDF and IPMOP-IL (5 wt %) / PVDF composite films.



Appendix 28. Effect of gradient wt % loading on frequency and output over open circuit voltage of 2 x 2 cm² area for PVDF film and respective IPMOP-n/PVDF composite films moulded TENG devices.

IPMOP-A

Composites (wt %)	Output Voltage (V)
1	6.52
3	15.58
5	22.50
8	19.82
10	22.70

IPMOP-V

Composites (wt %)	Output Voltage (V)
1	31.64
3	46.33
5	53.08
8	41.40
10	47.37

IPMOP-IL

Composites (wt %)	Output Voltage (V)
1	37.74
3	50.48
5	132.84
8	77.31
10	80.90

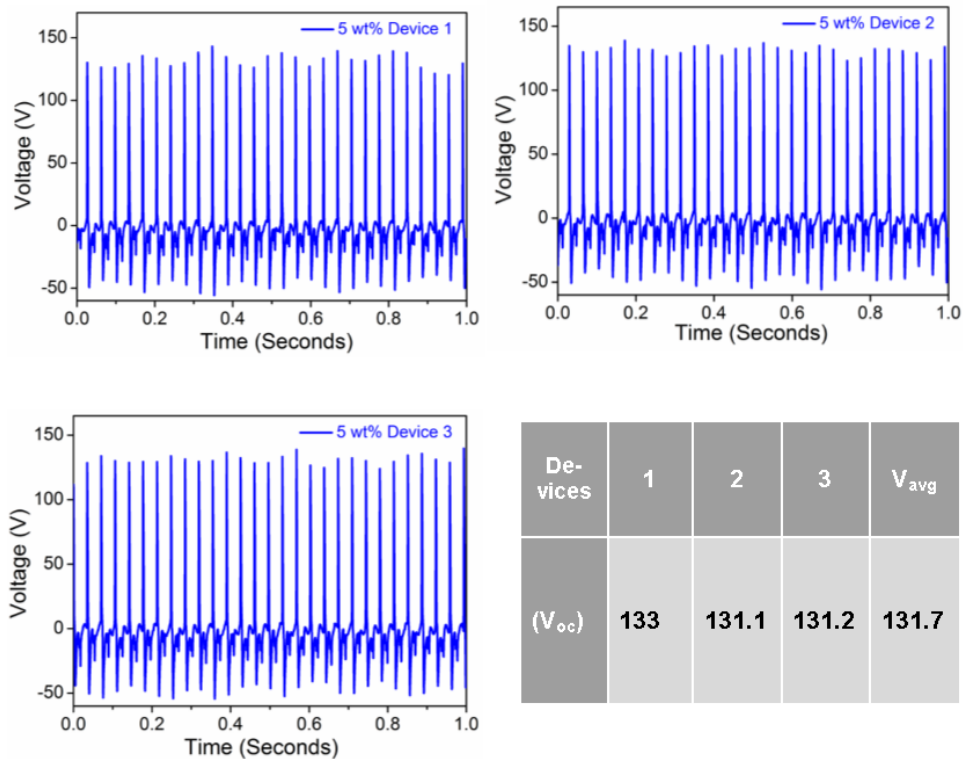
IPMOP-PA

Composites (wt %)	Output Voltage (V)
1	39.68
3	50.66
5	75.59
8	73.87
10	72.41

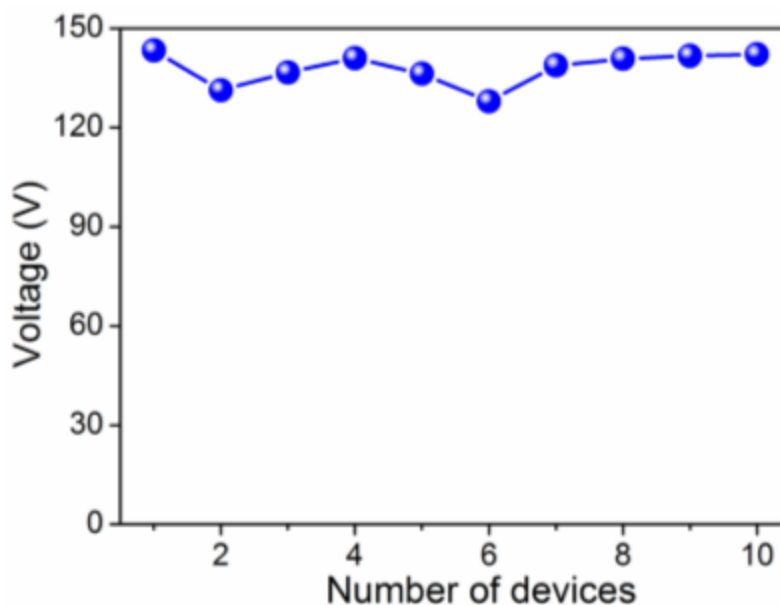
Appendix Table 1. Comparison tables representing Open circuit voltage measurements conducted separate IPMOP-n/PVDF composite based TENG devices with respect to their incremental wt % loading, i.e. 1, 3, 5, 8, 10 wt% respectively.

Composites (5 wt %)	Average Output Voltage (V)
IPMOP-A	22.49
IPMOP-V	53.09
IPMOP-IL	132.84
IPMOP-PA	75.59

Appendix Table 2. Open circuit voltage measurements conducted on five separate 5 wt % IPMOP-n/PVDF composite derived devices (IPTENG-n series).



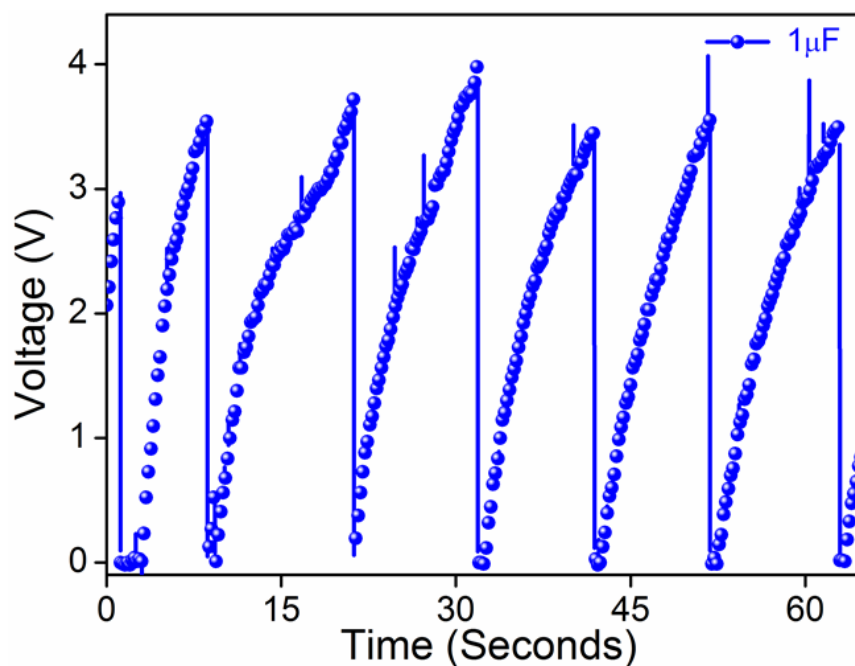
Appendix 29. Open circuit voltage measurements performed on three independent 5 wt % IPMOP-IL/PVDF (IPTENG-3) composite devices.



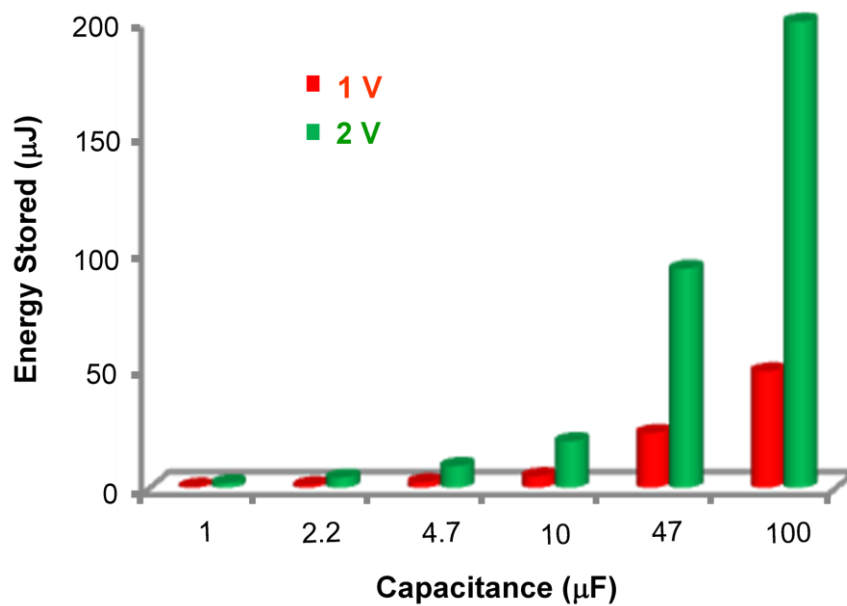
Appendix 30. Open circuit voltage (V_{oc} max) measurements performed on 10 independent 5 wt % IPMOP-IL/PVDF (IPTENG-3) composite devices.

Time (days)	Open Circuit Voltage (V_{oc})
1	136.4
2	128.7
4	129.6
6	131.8

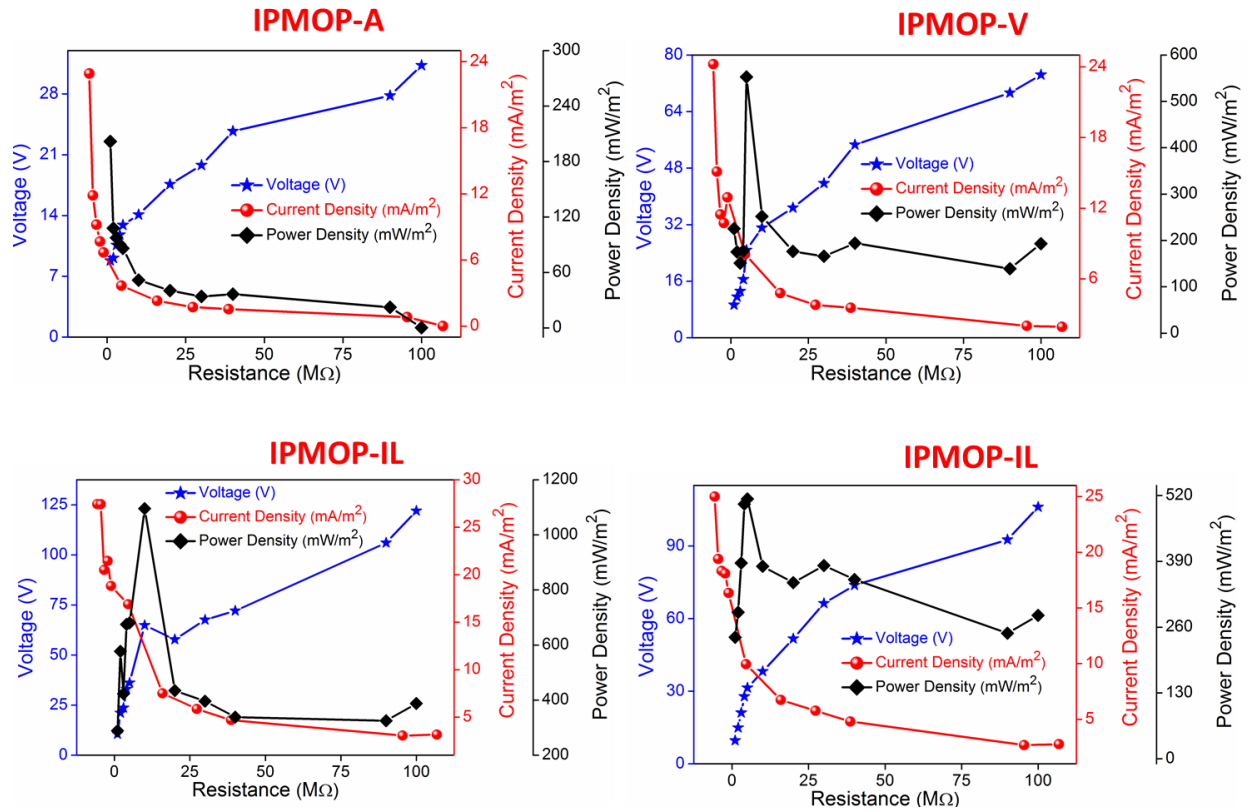
Appendix Table 3. Open circuit voltage (V_{oc} max) measurements performed on 5 wt % IPMOP-IL/PVDF (IPTENG-3) composite device after water treatment.



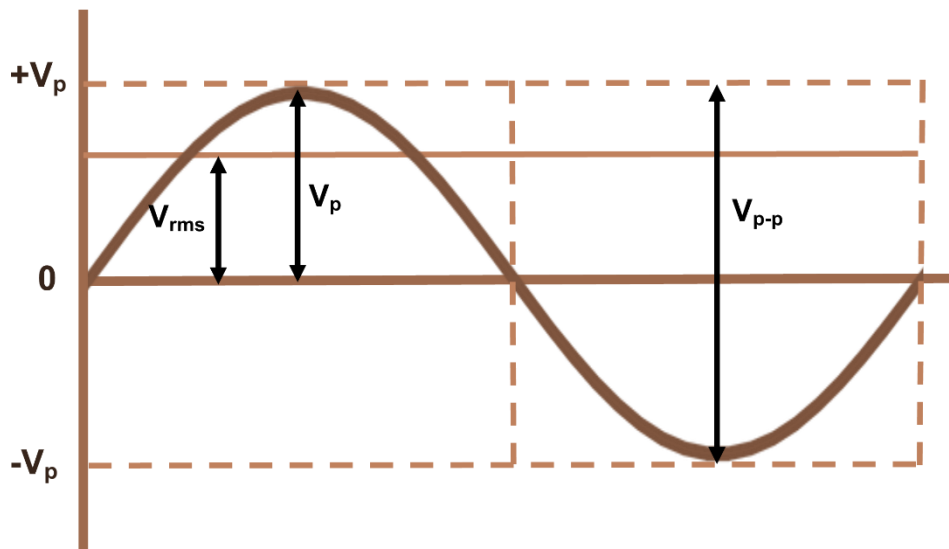
Appendix 31. 1 μF capacitor fast charging-discharging profile over a minute by the output of **IPTEG-3** (5 wt% IPMOF-IL/PVDF) voltage.



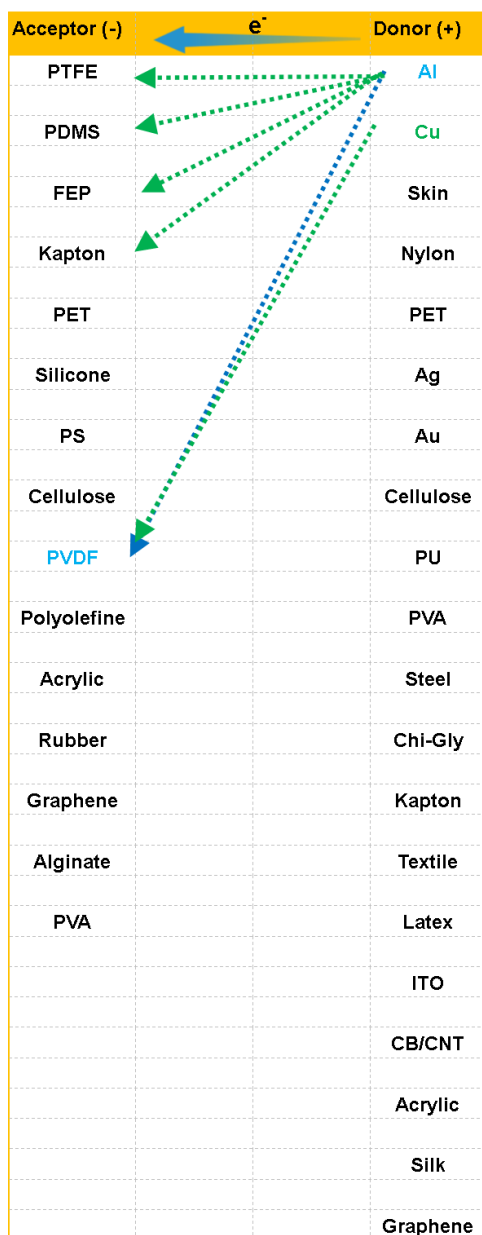
Appendix 32. Maximum energy stored with respect to capacitors deployed for 1 V and 2 V values.



Appendix 33. Performance summary representing voltage, power density and current density plots as a function of load resistance corresponding to the IPTENG Series of devices.



Appendix 34. General illustration of signal waveform and attributed voltage measurement parameters as V_p , V_{p-p} , V_{rms} .



Appendix Table 4. Network of electron acceptors and donors are paired in the selected literature reports.^[36] Blue arrow indicates combination utilized in present study.

5.6 References

- [1] Z. L. Wang, *Materials Today* **2017**, *20*, 74.
- [2] Z. L. Wang, J. Song, *Science* **2006**, *312*, 242.
- [3] R. Yang, Y. Qin, L. Dai, Z. L. Wang, *Nature Nanotech* **2009**, *4*, 34.
- [4] Z. L. (Zhong L. Wang, *Nanogenerators for Self-Powered Devices and Systems*, Georgia Institute Of Technology, **2011**.
- [5] F.-R. Fan, Z.-Q. Tian, Z. Lin Wang, *Nano Energy* **2012**, *1*, 328.
- [6] Z. L. Wang, *ACS Nano* **2013**, *7*, 9533.
- [7] Z. L. Wang, J. Chen, L. Lin, *Energy Environ. Sci.* **2015**, *8*, 2250.
- [8] C. Xu, X. Wang, Z. L. Wang, *J. Am. Chem. Soc.* **2009**, *131*, 5866.
- [9] C. Xu, Z. L. Wang, *Advanced Materials* **2011**, *23*, 873.
- [10] H. Zou, Y. Zhang, L. Guo, P. Wang, X. He, G. Dai, H. Zheng, C. Chen, A. C. Wang, C. Xu, Z. L. Wang, *Nat Commun* **2019**, *10*, 1427.
- [11] R. Zhang, H. Olin, *EcoMat* **2020**, *2*, e12062.
- [12] G. Khandelwal, A. Chandrasekhar, N. P. Maria Joseph Raj, S.-J. Kim, *Advanced Energy Materials* **2019**, *9*, 1803581.
- [13] G. Khandelwal, A. Chandrasekhar, R. Pandey, N. P. Maria Joseph Raj, S.-J. Kim, *Sensors and Actuators B: Chemical* **2019**, *282*, 590.
- [14] G. Khandelwal, N. P. Maria Joseph Raj, V. Vivekananthan, S.-J. Kim, *iScience* **2021**, *24*, 102064.
- [15] R. Wen, R. Feng, B. Zhao, J. Song, L. Fan, J. Zhai, *Nano Res.* **2022**, DOI 10.1007/s12274-022-4731-6.
- [16] L. Zhai, S. Cui, B. Tong, W. Chen, Z. Wu, C. Soutis, D. Jiang, G. Zhu, L. Mi, *Chemistry – A European Journal* **2020**, *26*, 5784.
- [17] Y.-M. Wang, X. Zhang, D. Yang, L. Wu, J. Zhang, T. Lei, R. Yang, *Nanotechnology* **2021**, *33*, 065402.
- [18] A. Chen, C. Zhang, G. Zhu, Z. L. Wang, *Advanced Science* **2020**, *7*, 2000186.

- [19] S. Cheon, H. Kang, H. Kim, Y. Son, J. Y. Lee, H.-J. Shin, S.-W. Kim, J. H. Cho, *Advanced Functional Materials* **2018**, *28*, 1703778.
- [20] J. W. Lee, H. J. Cho, J. Chun, K. N. Kim, S. Kim, C. W. Ahn, I. W. Kim, J.-Y. Kim, S.-W. Kim, C. Yang, J. M. Baik, *Science Advances* **2017**, *3*, e1602902.
- [21] P. Martins, A. C. Lopes, S. Lanceros-Mendez, *Progress in Polymer Science* **2014**, *39*, 683.
- [22] K. Shi, B. Sun, X. Huang, P. Jiang, *Nano Energy* **2018**, *52*, 153.
- [23] S.-R. Kim, J.-H. Yoo, J.-W. Park, *ACS Appl. Mater. Interfaces* **2019**, *11*, 15088.
- [24] S.-H. Bae, O. Kahya, B. K. Sharma, J. Kwon, H. J. Cho, B. Özyilmaz, J.-H. Ahn, *ACS Nano* **2013**, *7*, 3130.
- [25] S. Wang, Y. Zi, Y. S. Zhou, S. Li, F. Fan, L. Lin, Z. L. Wang, *J. Mater. Chem. A* **2016**, *4*, 3728.
- [26] S.-H. Shin, Y. H. Kwon, Y.-H. Kim, J.-Y. Jung, M. H. Lee, J. Nah, *ACS Nano* **2015**, *9*, 4621.
- [27] S.-H. Shin, Y. E. Bae, H. K. Moon, J. Kim, S.-H. Choi, Y. Kim, H. J. Yoon, M. H. Lee, J. Nah, *ACS Nano* **2017**, *11*, 6131.
- [28] Y. Jie, Q. Jiang, Y. Zhang, N. Wang, X. Cao, *Nano Energy* **2016**, *27*, 554.
- [29] X.-S. Zhang, M.-D. Han, R.-X. Wang, F.-Y. Zhu, Z.-H. Li, W. Wang, H.-X. Zhang, *Nano Lett.* **2013**, *13*, 1168.
- [30] P. Zhao, N. Soin, K. Prashanthi, J. Chen, S. Dong, E. Zhou, Z. Zhu, A. A. Narasimulu, C. D. Montemagno, L. Yu, J. Luo, *ACS Appl. Mater. Interfaces* **2018**, *10*, 5880.
- [31] F.-R. Fan, L. Lin, G. Zhu, W. Wu, R. Zhang, Z. L. Wang, *Nano Lett.* **2012**, *12*, 3109.
- [32] Y. J. Fan, X. S. Meng, H. Y. Li, S. Y. Kuang, L. Zhang, Y. Wu, Z. L. Wang, G. Zhu, *Advanced Materials* **2017**, *29*, 1603115.
- [33] L. Yao, Z. Zhang, Q. Zhang, Z. Zhou, H. Yang, L. Chen, *Nano Energy* **2021**, *86*, 106128.
- [34] Z. Zhou, Z. Zhang, Q. Zhang, H. Yang, Y. Zhu, Y. Wang, L. Chen, *ACS Appl. Mater. Interfaces* **2020**, *12*, 1567.
- [35] Q. Zhang, Z. Zhu, D. Shen, H. Yang, *Colloids and Surfaces A: Physicochemical and Engineering Aspects* **2019**, *569*, 171.
- [36] Y. D. More, S. Saurabh, S. Mollick, S. K. Singh, S. Dutta, S. Fajal, A. Prathamshetti, M. M. Shirolkar, S. Panchal, M. Wable, S. Ogale, S. K. Ghosh, *Advanced Materials Interfaces* **n.d.**, *n/a*, 2201713.

[37] S. Mollick, S. Mukherjee, D. Kim, Z. Qiao, A. V. Desai, R. Saha, Y. D. More, J. Jiang, M. S. Lah, S. K. Ghosh, *Angewandte Chemie* **2019**, *131*, 1053.

[38] S. K. Singh, P. Kumar, R. Magdum, U. Khandelwal, S. Deswal, Y. More, S. Muduli, R. Boomishankar, S. Pandit, S. Ogale, *ACS Appl. Bio Mater.* **2019**, *2*, 3164.

Chapter 6

Summary and Perspectives

6.1 Summary and Perspectives

In summary, target-specific anionic MOFs were designed and synthesized during the course of this thesis for in-depth studies and subsequent rational understanding towards energy and environmental applications. Additionally, functional porous materials (neutral, property tuneable, and hydrolytically robust porous materials, i.e., MOPs and MOFs) that are stable, compatible, and viable are carefully applied with an emphasis aimed at energy solutions, besides exploring their diversified thorough fabrication techniques and application-bound investigation.

Although a significant amount of research is currently being carried out and centered on anionic MOFs in a variety of application areas, little is known and explored in the previously reported literature about their potential to selectively and effectively capture uranium for the remediation of harmful aquatic contaminants beyond its sequestration aimed at applications in the field of energy (besides environmental concerns). The same is true of their potential application to the sorting and identification of other toxic aqueous pollutants such as antibiotics or pesticides. We set out to address some of the most intriguing and notably highlighted issues in the fields of energy and the environment using our knowledge of chemistry and practice-driven expertise in functional porous materials. Considering the flow of evolution of our approach, the whole thesis is therefore halved into two larger sections, emphasizing sequential applications representing respective spectrum of application-bound porous materials. In view of the above, structure-property correlation-driven development of anionic MOFs has been further emphasized and utilized for specific targeted applications. Previously, the lack of stability of anionic frameworks in diverse chemical and aquatic conditions severely limited their applicability and thereby remained unexplored in the majority of practical aspects or uses. Issues of stability and recyclability are discussed along with the rational approaches to tuning the counter functional cations for target-specific applications in anionic frameworks, which is implied to be a key takeaway from this thesis work. This approach is crucial for the development of anionic MOFs to be the next generation of ionic functional porous materials towards practical implementation. Nanogenerators (NG), utilizing the virtues of MOFs and MOPs, is a multifunctional, tuneable platform, thus extending the applications of a TENG. In order to successfully harvest irregular mechanical energy, we constructed a straightforward, distinctive, reusable, and fly wight-flexible NG comprised of a series of MOFs and MOPs highlighting tuning in a particular property. This was done in an effort to better understand the intricate design concepts affecting NG, structure-property relations are well exploited under a specified set of conditions. The TENG's mechanisms were carefully examined and shown. Advanced tuning and stabilization techniques made it possible for results to demonstrate the benefits of APMs in a wide variety of applications.

The constraints on transforming these materials into usable or readily workable forms still persist, notwithstanding the importance of fundamental understanding and scientific investigation of such materials at the molecular level. MOFs are often obtained as crystalline powders, sometimes as nanocrystals, making it challenging to deploy them directly as solid-state sorbent materials in real-time applications. Besides that, another critical component is the conservation of material performance and drawing efficiency from the molecular level to the practical workable scale, which must be addressed carefully prior to real-time application of these materials. Scalability, reusability, and cost-energy footprint are other prime challenges that researchers are diligently investigating at the moment. As a result, during the coming years, researchers may focus on simultaneously developing functional ionic MOFs and composite materials or well-fabricated devices for industrial, energy, and environmental applications as well as improving their aspects of stability and efficiency in a configuration or form that can be used under operating conditions or for desired real-time applications.

Attachments

Rights, Permissions and License Agreements



This is a License Agreement between Yogeshwar Dnyaneshwar More ("User") and Copyright Clearance Center, Inc. ("CCC") on behalf of the Rightsholder identified in the order details below. The license consists of the order details, the Marketplace Permissions General Terms and Conditions below, and any Rightsholder Terms and Conditions which are included below.

All payments must be made in full to CCC in accordance with the Marketplace Permissions General Terms and Conditions below.

Order Date	25-Apr-2023	Type of Use	Republish in a thesis/dissertation
Order License ID	1348246-1	Publisher	ROYAL SOCIETY OF CHEMISTRY
ISSN	1364-548X	Portion	Image/photo/illustration

LICENSED CONTENT

Publication Title	Chemical communications	Rightsholder	Royal Society of Chemistry
Article Title	Ionic Metal-Organic Frameworks (iMOFs): Progress and Prospects as Ionic Functional Materials	Publication Type	e-Journal
Author/Editor	Royal Society of Chemistry (Great Britain)	Start Page	13676
Date	01/01/1996	End Page	13698
Language	English	Issue	99
Country	United Kingdom of Great Britain and Northern Ireland	Volume	58

REQUEST DETAILS

Portion Type	Image/photo/illustration	Distribution	Worldwide
Number of Images / Photos / Illustrations	3	Translation	Original language of publication
Format (select all that apply)	Electronic	Copies for the Disabled?	Yes
Who Will Republish the Content?	Academic institution	Minor Editing Privileges?	No
Duration of Use	Life of current edition	Incidental Promotional Use?	No
Lifetime Unit Quantity	Up to 499	Currency	EUR
Rights Requested	Main product		

NEW WORK DETAILS

Title	Ionic metal-organic frameworks (iMOFs): progress and prospects as ionic functional materials	Institution Name	Indian Institute of Science Education and Research , Pune
Instructor Name	Prof. Sujit K Ghosh	Expected Presentation Date	2023-04-30

ADDITIONAL DETAILS

Order Reference Number	N/A	The Requesting Person/Organization to Appear on the License	Yogeshwar Dnyaneshwar More
-------------------------------	-----	--	----------------------------

REQUESTED CONTENT DETAILS

Title, Description or Numeric Reference of the Portion(s)	Ionic metal-organic frameworks (iMOFs): progress and prospects as ionic functional materials	Title of the Article/Chapter the Portion Is From	Ionic Metal-Organic Frameworks (iMOFs): Progress and Prospects as Ionic Functional Materials
Editor of Portion(s)	Dutta, Subhajit; More, Yogeshwar D.; Fajal, Sahel; Mandal, Writakshi; Dam, Gourab K.; Ghosh, Sujit K.	Author of Portion(s)	Dutta, Subhajit; More, Yogeshwar D.; Fajal, Sahel; Mandal, Writakshi; Dam, Gourab K.; Ghosh, Sujit K.
Volume of Serial or Monograph	58	Issue, if Republishing an Article From a Serial	99
Page or Page Range of Portion	13676-13698	Publication Date of Portion	2022-12-13

Marketplace Permissions General Terms and Conditions

The following terms and conditions (“General Terms”), together with any applicable Publisher Terms and Conditions, govern User’s use of Works pursuant to the Licenses granted by Copyright Clearance Center, Inc. (“CCC”) on behalf of the applicable Rightsholders of such Works through CCC’s applicable Marketplace transactional licensing services (each, a “Service”).

1) **Definitions.** For purposes of these General Terms, the following definitions apply:

“License” is the licensed use the User obtains via the Marketplace platform in a particular licensing transaction, as set forth in the Order Confirmation.

“Order Confirmation” is the confirmation CCC provides to the User at the conclusion of each Marketplace transaction. “Order Confirmation Terms” are additional terms set forth on specific Order Confirmations not set forth in the General Terms that can include terms applicable to a particular CCC transactional licensing service and/or any Rightsholder-specific terms.

“Rightsholder(s)” are the holders of copyright rights in the Works for which a User obtains licenses via the Marketplace platform, which are displayed on specific Order Confirmations.

“Terms” means the terms and conditions set forth in these General Terms and any additional Order Confirmation Terms collectively.

“User” or “you” is the person or entity making the use granted under the relevant License. Where the person accepting the Terms on behalf of a User is a freelancer or other third party who the User authorized to accept the General Terms on the User’s behalf, such person shall be deemed jointly a User for purposes of such Terms.

“Work(s)” are the copyright protected works described in relevant Order Confirmations.

2) **Description of Service.** CCC’s Marketplace enables Users to obtain Licenses to use one or more Works in accordance with all relevant Terms. CCC grants Licenses as an agent on behalf of the copyright rightsholder identified in the relevant Order Confirmation.

3) **Applicability of Terms.** The Terms govern User’s use of Works in connection with the relevant License. In the event of any conflict between General Terms and Order Confirmation Terms, the latter shall govern. User acknowledges that Rightsholders have complete discretion whether to grant any permission, and whether to place any limitations on any grant, and that CCC has no right to supersede or to modify any such discretionary act by a Rightsholder.

4) **Representations; Acceptance.** By using the Service, User represents and warrants that User has been duly authorized by the User to accept, and hereby does accept, all Terms.

5) **Scope of License; Limitations and Obligations.** All Works and all rights therein, including copyright rights, remain the sole and exclusive property of the Rightsholder. The License provides only those rights expressly set forth in the terms and conveys no other rights in any Works

6) **General Payment Terms.** User may pay at time of checkout by credit card or choose to be invoiced. If the User chooses to be invoiced, the User shall: (i) remit payments in the manner identified on specific invoices, (ii) unless otherwise specifically stated in an Order Confirmation or separate written agreement, Users shall remit payments upon receipt of the relevant invoice from CCC, either by delivery or notification of availability of the invoice via the Marketplace platform, and (iii) if the User does not pay the invoice within 30 days of receipt, the User may incur a service charge of 1.5% per month or the maximum rate allowed by applicable law, whichever is less. While User may exercise the rights in the License immediately upon receiving the Order Confirmation, the License is automatically revoked and is null and void, as if it had never been issued, if CCC does not receive complete payment on a timely basis.

7) **General Limits on Use.** Unless otherwise provided in the Order Confirmation, any grant of rights to User (i) involves only the rights set forth in the Terms and does not include subsequent or additional uses, (ii) is non-exclusive and non-transferable, and (iii) is subject to any and all limitations and restrictions (such as, but not limited to, limitations on duration of use or circulation) included in the Terms. Upon completion of the licensed use as set forth in the Order Confirmation, User shall either secure a new permission for further use of the Work(s) or immediately cease any new use of the Work(s) and shall render inaccessible (such as by deleting or by removing or severing links or other locators) any further copies of the Work. User may only make alterations to the Work if and as expressly set forth in the Order Confirmation. No Work may be used in any way that is unlawful, including without limitation if such use would violate applicable sanctions laws or regulations, would be defamatory, violate the rights of third parties (including such third parties' rights of copyright, privacy, publicity, or other tangible or intangible property), or is otherwise illegal, sexually explicit, or obscene. In addition, User may not conjoin a Work with any other material that may result in damage to the reputation of the Rightsholder. Any unlawful use will render any licenses hereunder null and void. User agrees to inform CCC if it becomes aware of any infringement of any rights in a Work and to cooperate with any reasonable request of CCC or the Rightsholder in connection therewith.

8) **Third Party Materials.** In the event that the material for which a License is sought includes third party materials (such as photographs, illustrations, graphs, inserts and similar materials) that are identified in such material as having been used by permission (or a similar indicator), User is responsible for identifying, and seeking separate licenses (under this Service, if available, or otherwise) for any of such third party materials; without a separate license, User may not use such third party materials via the License.

9) **Copyright Notice.** Use of proper copyright notice for a Work is required as a condition of any License granted under the Service. Unless otherwise provided in the Order Confirmation, a proper copyright notice will read substantially as follows: "Used with permission of [Rightsholder's name], from [Work's title, author, volume, edition number and year of copyright]; permission conveyed through Copyright Clearance Center, Inc." Such notice must be provided in a reasonably legible font size and must be placed either on a cover page or in another location that any person, upon gaining access to the material which is the subject of a permission, shall see, or in the case of republication Licenses, immediately adjacent to the Work as used (for example, as part of a by-line or footnote) or in the place where substantially all other credits or notices for the new work containing the republished Work are located. Failure to include the required notice results in loss to the Rightsholder and CCC, and the User shall be liable to pay liquidated damages for each such failure equal to twice the use fee specified in the Order Confirmation, in addition to the use fee itself and any other fees and charges specified.

10) **Indemnity.** User hereby indemnifies and agrees to defend the Rightsholder and CCC, and their respective employees and directors, against all claims, liability, damages, costs, and expenses, including legal fees and expenses, arising out of any use of a Work beyond the scope of the rights granted herein and in the Order Confirmation, or any use of a Work which has been altered in any unauthorized way by User, including claims of defamation or infringement of rights of copyright, publicity, privacy, or other tangible or intangible property.

11) **Limitation of Liability.** UNDER NO CIRCUMSTANCES WILL CCC OR THE RIGHTSHOLDER BE LIABLE FOR ANY DIRECT, INDIRECT, CONSEQUENTIAL, OR INCIDENTAL DAMAGES (INCLUDING WITHOUT LIMITATION DAMAGES FOR LOSS OF BUSINESS PROFITS OR INFORMATION, OR FOR BUSINESS INTERRUPTION) ARISING OUT OF THE USE OR INABILITY TO USE A WORK, EVEN IF ONE OR BOTH OF THEM HAS BEEN ADVISED OF THE POSSIBILITY OF SUCH DAMAGES. In any event, the total liability of the Rightsholder and CCC (including their respective employees and directors) shall not exceed the total

amount actually paid by User for the relevant License. User assumes full liability for the actions and omissions of its principals, employees, agents, affiliates, successors, and assigns.

12) **Limited Warranties.** THE WORK(S) AND RIGHT(S) ARE PROVIDED "AS IS." CCC HAS THE RIGHT TO GRANT TO USER THE RIGHTS GRANTED IN THE ORDER CONFIRMATION DOCUMENT. CCC AND THE RIGHTSHOLDER DISCLAIM ALL OTHER WARRANTIES RELATING TO THE WORK(S) AND RIGHT(S), EITHER EXPRESS OR IMPLIED, INCLUDING WITHOUT LIMITATION IMPLIED WARRANTIES OF MERCHANTABILITY OR FITNESS FOR A PARTICULAR PURPOSE. ADDITIONAL RIGHTS MAY BE REQUIRED TO USE ILLUSTRATIONS, GRAPHS, PHOTOGRAPHS, ABSTRACTS, INSERTS, OR OTHER PORTIONS OF THE WORK (AS OPPOSED TO THE ENTIRE WORK) IN A MANNER CONTEMPLATED BY USER; USER UNDERSTANDS AND AGREES THAT NEITHER CCC NOR THE RIGHTSHOLDER MAY HAVE SUCH ADDITIONAL RIGHTS TO GRANT.

13) **Effect of Breach.** Any failure by User to pay any amount when due, or any use by User of a Work beyond the scope of the License set forth in the Order Confirmation and/or the Terms, shall be a material breach of such License. Any breach not cured within 10 days of written notice thereof shall result in immediate termination of such License without further notice. Any unauthorized (but licensable) use of a Work that is terminated immediately upon notice thereof may be liquidated by payment of the Rightsholder's ordinary license price therefor; any unauthorized (and unlicensable) use that is not terminated immediately for any reason (including, for example, because materials containing the Work cannot reasonably be recalled) will be subject to all remedies available at law or in equity, but in no event to a payment of less than three times the Rightsholder's ordinary license price for the most closely analogous licensable use plus Rightsholder's and/or CCC's costs and expenses incurred in collecting such payment.

14) **Additional Terms for Specific Products and Services.** If a User is making one of the uses described in this Section 14, the additional terms and conditions apply:

a) ***Print Uses of Academic Course Content and Materials (photocopies for academic coursepacks or classroom handouts).*** For photocopies for academic coursepacks or classroom handouts the following additional terms apply:

i) The copies and anthologies created under this License may be made and assembled by faculty members individually or at their request by on-campus bookstores or copy centers, or by off-campus copy shops and other similar entities.

ii) No License granted shall in any way: (i) include any right by User to create a substantively non-identical copy of the Work or to edit or in any other way modify the Work (except by means of deleting material immediately preceding or following the entire portion of the Work copied) (ii) permit "publishing ventures" where any particular anthology would be systematically marketed at multiple institutions.

iii) Subject to any Publisher Terms (and notwithstanding any apparent contradiction in the Order Confirmation arising from data provided by User), any use authorized under the academic pay-per-use service is limited as follows:

A) any License granted shall apply to only one class (bearing a unique identifier as assigned by the institution, and thereby including all sections or other subparts of the class) at one institution;

B) use is limited to not more than 25% of the text of a book or of the items in a published collection of essays, poems or articles;

C) use is limited to no more than the greater of (a) 25% of the text of an issue of a journal or other periodical or (b) two articles from such an issue;

D) no User may sell or distribute any particular anthology, whether photocopied or electronic, at more than one institution of learning;

E) in the case of a photocopy permission, no materials may be entered into electronic memory by User except in order to produce an identical copy of a Work before or during the academic term (or analogous period) as to which any particular permission is granted. In the event that User shall choose to retain materials that are the subject of a photocopy permission in electronic memory for purposes of producing identical copies more than one day after such retention (but still within the scope of any permission granted), User must notify CCC of such fact in the applicable permission request and such retention shall constitute one copy actually sold for purposes of calculating permission fees due; and

F) any permission granted shall expire at the end of the class. No permission granted shall in any way include any right by User to create a substantively non-identical copy of the Work or to edit or in any other way

modify the Work (except by means of deleting material immediately preceding or following the entire portion of the Work copied).

iv) Books and Records; Right to Audit. As to each permission granted under the academic pay-per-use Service, User shall maintain for at least four full calendar years books and records sufficient for CCC to determine the numbers of copies made by User under such permission. CCC and any representatives it may designate shall have the right to audit such books and records at any time during User's ordinary business hours, upon two days' prior notice. If any such audit shall determine that User shall have underpaid for, or underreported, any photocopies sold or by three percent (3%) or more, then User shall bear all the costs of any such audit; otherwise, CCC shall bear the costs of any such audit. Any amount determined by such audit to have been underpaid by User shall immediately be paid to CCC by User, together with interest thereon at the rate of 10% per annum from the date such amount was originally due. The provisions of this paragraph shall survive the termination of this License for any reason.

b) **Digital Pay-Per-Uses of Academic Course Content and Materials (e-coursepacks, electronic reserves, learning management systems, academic institution intranets).** For uses in e-coursepacks, posts in electronic reserves, posts in learning management systems, or posts on academic institution intranets, the following additional terms apply:

i) The pay-per-uses subject to this Section 14(b) include:

A) **Posting e-reserves, course management systems, e-coursepacks for text-based content**, which grants authorizations to import requested material in electronic format, and allows electronic access to this material to members of a designated college or university class, under the direction of an instructor designated by the college or university, accessible only under appropriate electronic controls (e.g., password);

B) **Posting e-reserves, course management systems, e-coursepacks for material consisting of photographs or other still images not embedded in text**, which grants not only the authorizations described in Section 14(b)(i)(A) above, but also the following authorization: to include the requested material in course materials for use consistent with Section 14(b)(i)(A) above, including any necessary resizing, reformatting or modification of the resolution of such requested material (provided that such modification does not alter the underlying editorial content or meaning of the requested material, and provided that the resulting modified content is used solely within the scope of, and in a manner consistent with, the particular authorization described in the Order Confirmation and the Terms), but not including any other form of manipulation, alteration or editing of the requested material;

C) **Posting e-reserves, course management systems, e-coursepacks or other academic distribution for audiovisual content**, which grants not only the authorizations described in Section 14(b)(i)(A) above, but also the following authorizations: (i) to include the requested material in course materials for use consistent with Section 14(b)(i)(A) above; (ii) to display and perform the requested material to such members of such class in the physical classroom or remotely by means of streaming media or other video formats; and (iii) to "clip" or reformat the requested material for purposes of time or content management or ease of delivery, provided that such "clipping" or reformatting does not alter the underlying editorial content or meaning of the requested material and that the resulting material is used solely within the scope of, and in a manner consistent with, the particular authorization described in the Order Confirmation and the Terms. Unless expressly set forth in the relevant Order Confirmation, the License does not authorize any other form of manipulation, alteration or editing of the requested material.

ii) Unless expressly set forth in the relevant Order Confirmation, no License granted shall in any way: (i) include any right by User to create a substantively non-identical copy of the Work or to edit or in any other way modify the Work (except by means of deleting material immediately preceding or following the entire portion of the Work copied or, in the case of Works subject to Sections 14(b)(1)(B) or (C) above, as described in such Sections) (ii) permit "publishing ventures" where any particular course materials would be systematically marketed at multiple institutions.

iii) Subject to any further limitations determined in the Rightsholder Terms (and notwithstanding any apparent contradiction in the Order Confirmation arising from data provided by User), any use authorized under the electronic course content pay-per-use service is limited as follows:

A) any License granted shall apply to only one class (bearing a unique identifier as assigned by the institution, and thereby including all sections or other subparts of the class) at one institution;

B) use is limited to not more than 25% of the text of a book or of the items in a published collection of essays, poems or articles;

C) use is limited to not more than the greater of (a) 25% of the text of an issue of a journal or other periodical or (b) two articles from such an issue;

D) no User may sell or distribute any particular materials, whether photocopied or electronic, at more than one institution of learning;

E) electronic access to material which is the subject of an electronic-use permission must be limited by means of electronic password, student identification or other control permitting access solely to students and instructors in the class;

F) User must ensure (through use of an electronic cover page or other appropriate means) that any person, upon gaining electronic access to the material, which is the subject of a permission, shall see:

- o a proper copyright notice, identifying the Rightsholder in whose name CCC has granted permission,
- o a statement to the effect that such copy was made pursuant to permission,
- o a statement identifying the class to which the material applies and notifying the reader that the material has been made available electronically solely for use in the class, and
- o a statement to the effect that the material may not be further distributed to any person outside the class, whether by copying or by transmission and whether electronically or in paper form, and User must also ensure that such cover page or other means will print out in the event that the person accessing the material chooses to print out the material or any part thereof.

G) any permission granted shall expire at the end of the class and, absent some other form of authorization, User is thereupon required to delete the applicable material from any electronic storage or to block electronic access to the applicable material.

iv) Uses of separate portions of a Work, even if they are to be included in the same course material or the same university or college class, require separate permissions under the electronic course content pay-per-use Service. Unless otherwise provided in the Order Confirmation, any grant of rights to User is limited to use completed no later than the end of the academic term (or analogous period) as to which any particular permission is granted.

v) Books and Records; Right to Audit. As to each permission granted under the electronic course content Service, User shall maintain for at least four full calendar years books and records sufficient for CCC to determine the numbers of copies made by User under such permission. CCC and any representatives it may designate shall have the right to audit such books and records at any time during User's ordinary business hours, upon two days' prior notice. If any such audit shall determine that User shall have underpaid for, or underreported, any electronic copies used by three percent (3%) or more, then User shall bear all the costs of any such audit; otherwise, CCC shall bear the costs of any such audit. Any amount determined by such audit to have been underpaid by User shall immediately be paid to CCC by User, together with interest thereon at the rate of 10% per annum from the date such amount was originally due. The provisions of this paragraph shall survive the termination of this license for any reason.

c) ***Pay-Per-Use Permissions for Certain Reproductions (Academic photocopies for library reserves and interlibrary loan reporting) (Non-academic internal/external business uses and commercial document delivery)***. The License expressly excludes the uses listed in Section (c)(i)-(v) below (which must be subject to separate license from the applicable Rightsholder) for: academic photocopies for library reserves and interlibrary loan reporting; and non-academic internal/external business uses and commercial document delivery.

i) electronic storage of any reproduction (whether in plain-text, PDF, or any other format) other than on a transitory basis;

ii) the input of Works or reproductions thereof into any computerized database;

iii) reproduction of an entire Work (cover-to-cover copying) except where the Work is a single article;

iv) reproduction for resale to anyone other than a specific customer of User;

v) republication in any different form. Please obtain authorizations for these uses through other CCC services or directly from the rightsholder.

Any license granted is further limited as set forth in any restrictions included in the Order Confirmation and/or in these Terms.

d) **Electronic Reproductions in Online Environments (Non-Academic-email, intranet, internet and extranet).** For "electronic reproductions", which generally includes e-mail use (including instant messaging or other electronic transmission to a defined group of recipients) or posting on an intranet, extranet or Intranet site (including any display or performance incidental thereto), the following additional terms apply:

i) Unless otherwise set forth in the Order Confirmation, the License is limited to use completed within 30 days for any use on the Internet, 60 days for any use on an intranet or extranet and one year for any other use, all as measured from the "republication date" as identified in the Order Confirmation, if any, and otherwise from the date of the Order Confirmation.

ii) User may not make or permit any alterations to the Work, unless expressly set forth in the Order Confirmation (after request by User and approval by Rightsholder); provided, however, that a Work consisting of photographs or other still images not embedded in text may, if necessary, be resized, reformatted or have its resolution modified without additional express permission, and a Work consisting of audiovisual content may, if necessary, be "clipped" or reformatted for purposes of time or content management or ease of delivery (provided that any such resizing, reformatting, resolution modification or "clipping" does not alter the underlying editorial content or meaning of the Work used, and that the resulting material is used solely within the scope of, and in a manner consistent with, the particular License described in the Order Confirmation and the Terms.

15) Miscellaneous.

a) User acknowledges that CCC may, from time to time, make changes or additions to the Service or to the Terms, and that Rightsholder may make changes or additions to the Rightsholder Terms. Such updated Terms will replace the prior terms and conditions in the order workflow and shall be effective as to any subsequent Licenses but shall not apply to Licenses already granted and paid for under a prior set of terms.

b) Use of User-related information collected through the Service is governed by CCC's privacy policy, available online at www.copyright.com/about/privacy-policy/.

c) The License is personal to User. Therefore, User may not assign or transfer to any other person (whether a natural person or an organization of any kind) the License or any rights granted thereunder; provided, however, that, where applicable, User may assign such License in its entirety on written notice to CCC in the event of a transfer of all or substantially all of User's rights in any new material which includes the Work(s) licensed under this Service.

d) No amendment or waiver of any Terms is binding unless set forth in writing and signed by the appropriate parties, including, where applicable, the Rightsholder. The Rightsholder and CCC hereby object to any terms contained in any writing prepared by or on behalf of the User or its principals, employees, agents or affiliates and purporting to govern or otherwise relate to the License described in the Order Confirmation, which terms are in any way inconsistent with any Terms set forth in the Order Confirmation, and/or in CCC's standard operating procedures, whether such writing is prepared prior to, simultaneously with or subsequent to the Order Confirmation, and whether such writing appears on a copy of the Order Confirmation or in a separate instrument.

e) The License described in the Order Confirmation shall be governed by and construed under the law of the State of New York, USA, without regard to the principles thereof of conflicts of law. Any case, controversy, suit, action, or proceeding arising out of, in connection with, or related to such License shall be brought, at CCC's sole discretion, in any federal or state court located in the County of New York, State of New York, USA, or in any federal or state court whose geographical jurisdiction covers the location of the Rightsholder set forth in the Order Confirmation. The parties expressly submit to the personal jurisdiction and venue of each such federal or state court.

Last updated October 2022

JOHN WILEY AND SONS LICENSE TERMS AND CONDITIONS

Apr 24, 2023

This Agreement between Dr. YOGESHWAR MORE ("You") and John Wiley and Sons ("John Wiley and Sons") consists of your license details and the terms and conditions provided by John Wiley and Sons and Copyright Clearance Center.

License Number 5535500689032

License date Apr 24, 2023

Licensed Content
Publisher John Wiley and Sons

Licensed Content
Publication Advanced Materials Interfaces

Licensed Content
Title Highly Stable and End-group Tuneable Metal–Organic Framework/Polymer Composite for Superior Triboelectric Nanogenerator Application

Licensed Content
Author Sujit K. Ghosh, Satishchandra Ogale, Minal Wable, et al

Licensed Content
Date Oct 6, 2022

Licensed Content
Volume 9

Licensed Content
Issue 34

Licensed Content
Pages 11

Type of use	Dissertation/Thesis
Requestor type	Author of this Wiley article
Format	Electronic
Portion	Full article
Will you be translating?	No
Title	Highly Stable and End-group Tuneable Metal–Organic Framework/Polymer Composite for Superior Triboelectric Nanogenerator Application
Institution name	Indian Institute of Science Education and Research, Pune
Expected presentation date	May 2023
Requestor Location	Dr. YOGESHWAR MORE Homi bhabha road pashan pune Pune, Maharashtra 411008 India Attn: Dr. YOGESHWAR MORE
Publisher Tax ID	EU826007151
Total	0.00 EUR

Terms and Conditions

TERMS AND CONDITIONS

This copyrighted material is owned by or exclusively licensed to John Wiley & Sons, Inc. or one of its group companies (each a "Wiley Company") or handled on behalf of a society with which a Wiley Company has exclusive publishing rights in relation to a particular work (collectively "WILEY"). By clicking "accept" in connection with completing this licensing transaction, you agree that the following terms and conditions apply to this transaction

(along with the billing and payment terms and conditions established by the Copyright Clearance Center Inc., ("CCC's Billing and Payment terms and conditions"), at the time that you opened your RightsLink account (these are available at any time at <http://myaccount.copyright.com>).

Terms and Conditions

- The materials you have requested permission to reproduce or reuse (the "Wiley Materials") are protected by copyright.
- You are hereby granted a personal, non-exclusive, non-sub licensable (on a stand-alone basis), non-transferable, worldwide, limited license to reproduce the Wiley Materials for the purpose specified in the licensing process. This license, **and any CONTENT (PDF or image file) purchased as part of your order**, is for a one-time use only and limited to any maximum distribution number specified in the license. The first instance of republication or reuse granted by this license must be completed within two years of the date of the grant of this license (although copies prepared before the end date may be distributed thereafter). The Wiley Materials shall not be used in any other manner or for any other purpose, beyond what is granted in the license. Permission is granted subject to an appropriate acknowledgement given to the author, title of the material/book/journal and the publisher. You shall also duplicate the copyright notice that appears in the Wiley publication in your use of the Wiley Material. Permission is also granted on the understanding that nowhere in the text is a previously published source acknowledged for all or part of this Wiley Material. Any third party content is expressly excluded from this permission.
- With respect to the Wiley Materials, all rights are reserved. Except as expressly granted by the terms of the license, no part of the Wiley Materials may be copied, modified, adapted (except for minor reformatting required by the new Publication), translated, reproduced, transferred or distributed, in any form or by any means, and no derivative works may be made based on the Wiley Materials without the prior permission of the respective copyright owner. **For STM Signatory Publishers clearing permission under the terms of the [STM Permissions Guidelines](#) only, the terms of the license are extended to include subsequent editions and for editions in other languages, provided such editions are for the work as a whole in situ and does not involve the separate exploitation of the permitted figures or extracts**, You may not alter, remove or suppress in any manner any copyright, trademark or other notices displayed by the Wiley Materials. You may not license, rent, sell, loan, lease, pledge, offer as security, transfer or assign the Wiley Materials on a stand-alone basis, or any of the rights granted to you hereunder to any other person.
- The Wiley Materials and all of the intellectual property rights therein shall at all times remain the exclusive property of John Wiley & Sons Inc, the Wiley Companies, or their respective licensors, and your interest therein is only that of having possession of and the right to reproduce the Wiley Materials pursuant to Section 2 herein during the continuance of this Agreement. You agree that you own no right, title or interest in or to the Wiley Materials or any of the intellectual property rights therein. You shall have no rights hereunder other than the license as provided for above in Section 2. No right, license or interest to any trademark, trade name, service mark or other branding ("Marks") of WILEY or its licensors is granted hereunder, and you agree that you shall not assert any such right, license or interest with respect thereto

- NEITHER WILEY NOR ITS LICENSORS MAKES ANY WARRANTY OR REPRESENTATION OF ANY KIND TO YOU OR ANY THIRD PARTY, EXPRESS, IMPLIED OR STATUTORY, WITH RESPECT TO THE MATERIALS OR THE ACCURACY OF ANY INFORMATION CONTAINED IN THE MATERIALS, INCLUDING, WITHOUT LIMITATION, ANY IMPLIED WARRANTY OF MERCHANTABILITY, ACCURACY, SATISFACTORY QUALITY, FITNESS FOR A PARTICULAR PURPOSE, USABILITY, INTEGRATION OR NON-INFRINGEMENT AND ALL SUCH WARRANTIES ARE HEREBY EXCLUDED BY WILEY AND ITS LICENSORS AND WAIVED BY YOU.
- WILEY shall have the right to terminate this Agreement immediately upon breach of this Agreement by you.
- You shall indemnify, defend and hold harmless WILEY, its Licensors and their respective directors, officers, agents and employees, from and against any actual or threatened claims, demands, causes of action or proceedings arising from any breach of this Agreement by you.
- IN NO EVENT SHALL WILEY OR ITS LICENSORS BE LIABLE TO YOU OR ANY OTHER PARTY OR ANY OTHER PERSON OR ENTITY FOR ANY SPECIAL, CONSEQUENTIAL, INCIDENTAL, INDIRECT, EXEMPLARY OR PUNITIVE DAMAGES, HOWEVER CAUSED, ARISING OUT OF OR IN CONNECTION WITH THE DOWNLOADING, PROVISIONING, VIEWING OR USE OF THE MATERIALS REGARDLESS OF THE FORM OF ACTION, WHETHER FOR BREACH OF CONTRACT, BREACH OF WARRANTY, TORT, NEGLIGENCE, INFRINGEMENT OR OTHERWISE (INCLUDING, WITHOUT LIMITATION, DAMAGES BASED ON LOSS OF PROFITS, DATA, FILES, USE, BUSINESS OPPORTUNITY OR CLAIMS OF THIRD PARTIES), AND WHETHER OR NOT THE PARTY HAS BEEN ADVISED OF THE POSSIBILITY OF SUCH DAMAGES. THIS LIMITATION SHALL APPLY NOTWITHSTANDING ANY FAILURE OF ESSENTIAL PURPOSE OF ANY LIMITED REMEDY PROVIDED HEREIN.
- Should any provision of this Agreement be held by a court of competent jurisdiction to be illegal, invalid, or unenforceable, that provision shall be deemed amended to achieve as nearly as possible the same economic effect as the original provision, and the legality, validity and enforceability of the remaining provisions of this Agreement shall not be affected or impaired thereby.
- The failure of either party to enforce any term or condition of this Agreement shall not constitute a waiver of either party's right to enforce each and every term and condition of this Agreement. No breach under this agreement shall be deemed waived or excused by either party unless such waiver or consent is in writing signed by the party granting such waiver or consent. The waiver by or consent of a party to a breach of any provision of this Agreement shall not operate or be construed as a waiver of or consent to any other or subsequent breach by such other party.
- This Agreement may not be assigned (including by operation of law or otherwise) by you without WILEY's prior written consent.
- Any fee required for this permission shall be non-refundable after thirty (30) days from receipt by the CCC.

- These terms and conditions together with CCC's Billing and Payment terms and conditions (which are incorporated herein) form the entire agreement between you and WILEY concerning this licensing transaction and (in the absence of fraud) supersedes all prior agreements and representations of the parties, oral or written. This Agreement may not be amended except in writing signed by both parties. This Agreement shall be binding upon and inure to the benefit of the parties' successors, legal representatives, and authorized assigns.
- In the event of any conflict between your obligations established by these terms and conditions and those established by CCC's Billing and Payment terms and conditions, these terms and conditions shall prevail.
- WILEY expressly reserves all rights not specifically granted in the combination of (i) the license details provided by you and accepted in the course of this licensing transaction, (ii) these terms and conditions and (iii) CCC's Billing and Payment terms and conditions.
- This Agreement will be void if the Type of Use, Format, Circulation, or Requestor Type was misrepresented during the licensing process.
- This Agreement shall be governed by and construed in accordance with the laws of the State of New York, USA, without regards to such state's conflict of law rules. Any legal action, suit or proceeding arising out of or relating to these Terms and Conditions or the breach thereof shall be instituted in a court of competent jurisdiction in New York County in the State of New York in the United States of America and each party hereby consents and submits to the personal jurisdiction of such court, waives any objection to venue in such court and consents to service of process by registered or certified mail, return receipt requested, at the last known address of such party.

WILEY OPEN ACCESS TERMS AND CONDITIONS

Wiley Publishes Open Access Articles in fully Open Access Journals and in Subscription journals offering Online Open. Although most of the fully Open Access journals publish open access articles under the terms of the Creative Commons Attribution (CC BY) License only, the subscription journals and a few of the Open Access Journals offer a choice of Creative Commons Licenses. The license type is clearly identified on the article.

The Creative Commons Attribution License

The [Creative Commons Attribution License \(CC-BY\)](#) allows users to copy, distribute and transmit an article, adapt the article and make commercial use of the article. The CC-BY license permits commercial and non-

Creative Commons Attribution Non-Commercial License

The [Creative Commons Attribution Non-Commercial \(CC-BY-NC\) License](#) permits use, distribution and reproduction in any medium, provided the original work is properly cited and is not used for commercial purposes.(see below)

Creative Commons Attribution-Non-Commercial-NoDerivs License

The [Creative Commons Attribution Non-Commercial-NoDerivs License \(CC-BY-NC-ND\)](#) permits use, distribution and reproduction in any medium, provided the original work is

properly cited, is not used for commercial purposes and no modifications or adaptations are made. (see below)

Use by commercial "for-profit" organizations

Use of Wiley Open Access articles for commercial, promotional, or marketing purposes requires further explicit permission from Wiley and will be subject to a fee.

Further details can be found on Wiley Online Library

<http://olabout.wiley.com/WileyCDA/Section/id-410895.html>

Other Terms and Conditions:

v1.10 Last updated September 2015

Questions? customercare@copyright.com.

JOHN WILEY AND SONS LICENSE TERMS AND CONDITIONS

Apr 24, 2023

This Agreement between Dr. YOGESHWAR MORE ("You") and John Wiley and Sons ("John Wiley and Sons") consists of your license details and the terms and conditions provided by John Wiley and Sons and Copyright Clearance Center.

License Number	5535491162502
License date	Apr 24, 2023
Licensed Content Publisher	John Wiley and Sons
Licensed Content Publication	Angewandte Chemie International Edition
Licensed Content Title	Hydrophobic Shielding of Outer Surface: Enhancing the Chemical Stability of Metal–Organic Polyhedra
Licensed Content Author	Sujit K. Ghosh, Myoung Soo Lah, Jianwen Jiang, et al
Licensed Content Date	Jan 2, 2019
Licensed Content Volume	58
Licensed Content Issue	4
Licensed Content Pages	5
Type of Use	Dissertation/Thesis
Requestor type	Author of this Wiley article
Format	Electronic
Portion	Figure/table
Number of figures/tables	1
Will you be translating?	No
Title	Hydrophobic Shielding of Outer Surface: Enhancing the Chemical Stability of Metal–Organic Polyhedra
Institution name	Indian Institute of Science Education and Research, Pune
Expected presentation date	May 2023
Portions	Graphical abstract
Requestor Location	Dr. YOGESHWAR MORE Homi bhabha road pashan pune Pune, Maharashtra 411008 India Attn: Dr. YOGESHWAR MORE
Publisher Tax ID	EU826007151
Total	0.00 EUR
Terms and Conditions	

TERMS AND CONDITIONS

This copyrighted material is owned by or exclusively licensed to John Wiley & Sons, Inc. or one of its group companies (each a "Wiley Company") or handled on behalf of a society with which a Wiley Company has exclusive publishing rights in relation to a particular work (collectively "WILEY"). By clicking "accept" in connection with completing this licensing transaction, you agree that the following terms and conditions apply to this transaction (along with the billing and payment terms and conditions established by the Copyright Clearance Center Inc., ("CCC's Billing and Payment terms and conditions"), at the time that you opened your RightsLink account (these are available at any time at <http://myaccount.copyright.com>).

Terms and Conditions

- The materials you have requested permission to reproduce or reuse (the "Wiley Materials") are protected by copyright.
- You are hereby granted a personal, non-exclusive, non-sub licensable (on a stand-alone basis), non-transferable, worldwide, limited license to reproduce the Wiley Materials for the purpose specified in the licensing process. This license, **and any CONTENT (PDF or image file) purchased as part of your order**, is for a one-time use only and limited to any maximum distribution number specified in the license. The first instance of republication or reuse granted by this license must be completed within two years of the date of the grant of this license (although copies prepared before the end date may be distributed thereafter). The Wiley Materials shall not be used in any other manner or for any other purpose, beyond what is granted in the license. Permission is granted subject to an appropriate acknowledgement given to the author, title of the material/book/journal and the publisher. You shall also duplicate the copyright notice that appears in the Wiley publication in your use of the Wiley Material. Permission is also granted on the understanding that nowhere in the text is a previously published source acknowledged for all or part of this Wiley Material. Any third party content is expressly excluded from this permission.
- With respect to the Wiley Materials, all rights are reserved. Except as expressly granted by the terms of the license, no part of the Wiley Materials may be copied, modified, adapted (except for minor reformatting required by the new Publication), translated, reproduced, transferred or distributed, in any form or by any means, and no derivative works may be made based on the Wiley Materials without the prior permission of the respective copyright owner. **For STM Signatory Publishers clearing permission under the terms of the STM Permissions Guidelines only, the terms of the license are extended to include subsequent editions and for editions in other languages, provided such editions are for the work as a whole in situ and does not involve the separate exploitation of the permitted figures or extracts**, You may not alter, remove or suppress in any manner any copyright, trademark or other notices displayed by the Wiley Materials. You may not license, rent, sell, loan, lease, pledge, offer as security, transfer or assign the Wiley Materials on a stand-alone basis, or any of the rights granted to you hereunder to any other person.
- The Wiley Materials and all of the intellectual property rights therein shall at all times remain the exclusive property of John Wiley & Sons Inc, the Wiley Companies, or their respective licensors, and your interest therein is only that of having possession of and the right to reproduce the Wiley Materials pursuant to Section 2 herein during the continuance of this Agreement. You agree that you own no right, title or interest in or to the Wiley Materials or any of the intellectual property rights therein. You shall have no rights hereunder other than the license as provided for above in Section 2. No right, license or interest to any trademark, trade name, service mark or other branding ("Marks") of WILEY or its licensors is granted hereunder, and you agree that you shall not assert any such right, license or interest with respect thereto
- NEITHER WILEY NOR ITS LICENSORS MAKES ANY WARRANTY OR REPRESENTATION OF ANY KIND TO YOU OR ANY THIRD PARTY, EXPRESS, IMPLIED OR STATUTORY, WITH RESPECT TO THE MATERIALS OR THE ACCURACY OF ANY INFORMATION CONTAINED IN THE MATERIALS, INCLUDING, WITHOUT LIMITATION, ANY IMPLIED WARRANTY OF MERCHANTABILITY, ACCURACY, SATISFACTORY QUALITY, FITNESS FOR A PARTICULAR PURPOSE, USABILITY, INTEGRATION OR NON-INFRINGEMENT AND ALL SUCH WARRANTIES ARE HEREBY EXCLUDED BY WILEY AND ITS LICENSORS AND WAIVED BY YOU.
- WILEY shall have the right to terminate this Agreement immediately upon breach of this Agreement by you.
- You shall indemnify, defend and hold harmless WILEY, its Licensors and their respective directors, officers, agents and employees, from and against any actual or threatened claims, demands, causes of action or proceedings arising from any breach of this Agreement by you.
- IN NO EVENT SHALL WILEY OR ITS LICENSORS BE LIABLE TO YOU OR ANY OTHER PARTY OR ANY OTHER PERSON OR ENTITY FOR ANY SPECIAL, CONSEQUENTIAL, INCIDENTAL, INDIRECT, EXEMPLARY OR PUNITIVE DAMAGES, HOWEVER CAUSED, ARISING OUT OF OR IN CONNECTION WITH THE DOWNLOADING, PROVISIONING, VIEWING OR USE OF THE MATERIALS REGARDLESS OF THE FORM OF ACTION, WHETHER FOR BREACH OF CONTRACT, BREACH OF WARRANTY, TORT, NEGLIGENCE, INFRINGEMENT OR OTHERWISE (INCLUDING, WITHOUT LIMITATION, DAMAGES BASED ON LOSS OF PROFITS, DATA, FILES, USE, BUSINESS OPPORTUNITY OR CLAIMS OF THIRD PARTIES), AND WHETHER OR NOT THE PARTY HAS BEEN ADVISED OF THE POSSIBILITY OF SUCH DAMAGES. THIS LIMITATION SHALL APPLY NOTWITHSTANDING ANY FAILURE OF ESSENTIAL PURPOSE OF ANY LIMITED REMEDY PROVIDED HEREIN.
- Should any provision of this Agreement be held by a court of competent jurisdiction to be illegal, invalid, or unenforceable, that provision shall be deemed amended to achieve as nearly as possible the same economic effect as the original provision, and the legality, validity and enforceability of the remaining provisions of this Agreement shall not be affected or impaired thereby.

- The failure of either party to enforce any term or condition of this Agreement shall not constitute a waiver of either party's right to enforce each and every term and condition of this Agreement. No breach under this agreement shall be deemed waived or excused by either party unless such waiver or consent is in writing signed by the party granting such waiver or consent. The waiver by or consent of a party to a breach of any provision of this Agreement shall not operate or be construed as a waiver of or consent to any other or subsequent breach by such other party.
- This Agreement may not be assigned (including by operation of law or otherwise) by you without WILEY's prior written consent.
- Any fee required for this permission shall be non-refundable after thirty (30) days from receipt by the CCC.
- These terms and conditions together with CCC's Billing and Payment terms and conditions (which are incorporated herein) form the entire agreement between you and WILEY concerning this licensing transaction and (in the absence of fraud) supersedes all prior agreements and representations of the parties, oral or written. This Agreement may not be amended except in writing signed by both parties. This Agreement shall be binding upon and inure to the benefit of the parties' successors, legal representatives, and authorized assigns.
- In the event of any conflict between your obligations established by these terms and conditions and those established by CCC's Billing and Payment terms and conditions, these terms and conditions shall prevail.
- WILEY expressly reserves all rights not specifically granted in the combination of (i) the license details provided by you and accepted in the course of this licensing transaction, (ii) these terms and conditions and (iii) CCC's Billing and Payment terms and conditions.
- This Agreement will be void if the Type of Use, Format, Circulation, or Requestor Type was misrepresented during the licensing process.
- This Agreement shall be governed by and construed in accordance with the laws of the State of New York, USA, without regards to such state's conflict of law rules. Any legal action, suit or proceeding arising out of or relating to these Terms and Conditions or the breach thereof shall be instituted in a court of competent jurisdiction in New York County in the State of New York in the United States of America and each party hereby consents and submits to the personal jurisdiction of such court, waives any objection to venue in such court and consents to service of process by registered or certified mail, return receipt requested, at the last known address of such party.

WILEY OPEN ACCESS TERMS AND CONDITIONS

Wiley Publishes Open Access Articles in fully Open Access Journals and in Subscription journals offering Online Open. Although most of the fully Open Access journals publish open access articles under the terms of the Creative Commons Attribution (CC BY) License only, the subscription journals and a few of the Open Access Journals offer a choice of Creative Commons Licenses. The license type is clearly identified on the article.

The Creative Commons Attribution License

The [Creative Commons Attribution License \(CC-BY\)](#) allows users to copy, distribute and transmit an article, adapt the article and make commercial use of the article. The CC-BY license permits commercial and non-

Creative Commons Attribution Non-Commercial License

The [Creative Commons Attribution Non-Commercial \(CC-BY-NC\) License](#) permits use, distribution and reproduction in any medium, provided the original work is properly cited and is not used for commercial purposes.(see below)

Creative Commons Attribution-Non-Commercial-NoDerivs License

The [Creative Commons Attribution Non-Commercial-NoDerivs License \(CC-BY-NC-ND\)](#) permits use, distribution and reproduction in any medium, provided the original work is properly cited, is not used for commercial purposes and no modifications or adaptations are made. (see below)

Use by commercial "for-profit" organizations

Use of Wiley Open Access articles for commercial, promotional, or marketing purposes requires further explicit permission from Wiley and will be subject to a fee.

Further details can be found on Wiley Online Library <http://olabout.wiley.com/WileyCDA/Section/id-410895.html>

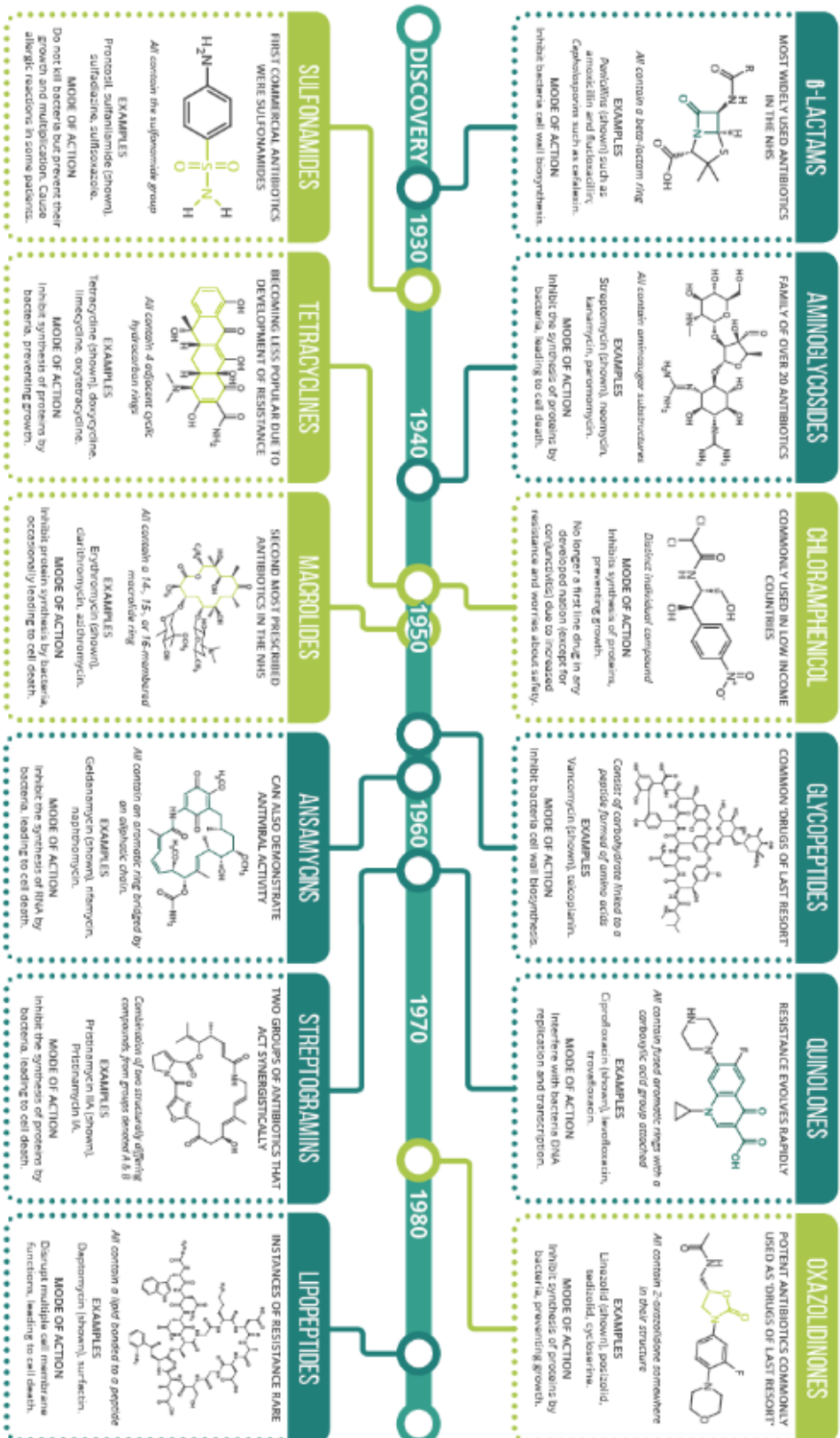
Other Terms and Conditions:

v1.10 Last updated September 2015

Questions? E-mail us at customer@copyright.com.

DIFFERENT CLASSES OF ANTIBIOTICS - AN OVERVIEW

Key: ● COMMONLY ACT AS BACTERIOSTATIC AGENTS, RESTRICTING GROWTH & REPRODUCTION ● COMMONLY ACT AS BACTERICIDAL AGENTS, CAUSING BACTERIAL CELL DEATH



JOHN WILEY AND SONS LICENSE TERMS AND CONDITIONS

Apr 24, 2023

This Agreement between Dr. YOGESHWAR MORE ("You") and John Wiley and Sons ("John Wiley and Sons") consists of your license details and the terms and conditions provided by John Wiley and Sons and Copyright Clearance Center.

License Number	5535500283402
License date	Apr 24, 2023
Licensed Content Publisher	John Wiley and Sons
Licensed Content Publication	Chemistry - An Asian Journal
Licensed Content Title	Stabilizing Metal–Organic Polyhedra (MOP): Issues and Strategies
Licensed Content Author	Samraj Mollick, Sahel Fajal, Soumya Mukherjee, et al
Licensed Content Date	Aug 23, 2019
Licensed Content Volume	14
Licensed Content Issue	18
Licensed Content Pages	13
Type of use	Dissertation/Thesis
Requestor type	University/Academic
Format	Electronic

Portion	Figure/table
Number of figures/tables	1
Will you be translating?	No
Title	Stabilizing Metal–Organic Polyhedra (MOP): Issues and Strategies
Institution name	Indian Institute of Science Education and Research, Pune
Expected presentation date	May 2023
Portions	Scheme 1
Requestor Location	Dr. YOGESHWAR MORE Homi bhabha road pashan pune Pune, Maharashtra 411008 India Attn: Dr. YOGESHWAR MORE
Publisher Tax ID	EU826007151
Total	0.00 USD

Terms and Conditions

TERMS AND CONDITIONS

This copyrighted material is owned by or exclusively licensed to John Wiley & Sons, Inc. or one of its group companies (each a "Wiley Company") or handled on behalf of a society with which a Wiley Company has exclusive publishing rights in relation to a particular work (collectively "WILEY"). By clicking "accept" in connection with completing this licensing transaction, you agree that the following terms and conditions apply to this transaction (along with the billing and payment terms and conditions established by the Copyright Clearance Center Inc., ("CCC's Billing and Payment terms and conditions"), at the time that you opened your RightsLink account (these are available at any time at <http://myaccount.copyright.com>).

Terms and Conditions

- The materials you have requested permission to reproduce or reuse (the "Wiley Materials") are protected by copyright.
- You are hereby granted a personal, non-exclusive, non-sub licensable (on a stand-alone basis), non-transferable, worldwide, limited license to reproduce the Wiley Materials for the purpose specified in the licensing process. This license, **and any CONTENT (PDF or image file) purchased as part of your order**, is for a one-time use only and limited to any maximum distribution number specified in the license. The first instance of republication or reuse granted by this license must be completed within two years of the date of the grant of this license (although copies prepared before the end date may be distributed thereafter). The Wiley Materials shall not be used in any other manner or for any other purpose, beyond what is granted in the license. Permission is granted subject to an appropriate acknowledgement given to the author, title of the material/book/journal and the publisher. You shall also duplicate the copyright notice that appears in the Wiley publication in your use of the Wiley Material. Permission is also granted on the understanding that nowhere in the text is a previously published source acknowledged for all or part of this Wiley Material. Any third party content is expressly excluded from this permission.
- With respect to the Wiley Materials, all rights are reserved. Except as expressly granted by the terms of the license, no part of the Wiley Materials may be copied, modified, adapted (except for minor reformatting required by the new Publication), translated, reproduced, transferred or distributed, in any form or by any means, and no derivative works may be made based on the Wiley Materials without the prior permission of the respective copyright owner. **For STM Signatory Publishers clearing permission under the terms of the [STM Permissions Guidelines](#) only, the terms of the license are extended to include subsequent editions and for editions in other languages, provided such editions are for the work as a whole in situ and does not involve the separate exploitation of the permitted figures or extracts**, You may not alter, remove or suppress in any manner any copyright, trademark or other notices displayed by the Wiley Materials. You may not license, rent, sell, loan, lease, pledge, offer as security, transfer or assign the Wiley Materials on a stand-alone basis, or any of the rights granted to you hereunder to any other person.
- The Wiley Materials and all of the intellectual property rights therein shall at all times remain the exclusive property of John Wiley & Sons Inc, the Wiley Companies, or their respective licensors, and your interest therein is only that of having possession of and the right to reproduce the Wiley Materials pursuant to Section 2 herein during the continuance of this Agreement. You agree that you own no right, title or interest in or to the Wiley Materials or any of the intellectual property rights therein. You shall have no rights hereunder other than the license as provided for above in Section 2. No right, license or interest to any trademark, trade name, service mark or other branding ("Marks") of WILEY or its licensors is granted hereunder, and you agree that you shall not assert any such right, license or interest with respect thereto
- NEITHER WILEY NOR ITS LICENSORS MAKES ANY WARRANTY OR REPRESENTATION OF ANY KIND TO YOU OR ANY THIRD PARTY, EXPRESS, IMPLIED OR STATUTORY, WITH RESPECT TO THE MATERIALS OR THE ACCURACY OF ANY INFORMATION CONTAINED IN THE MATERIALS, INCLUDING, WITHOUT LIMITATION, ANY IMPLIED WARRANTY OF MERCHANTABILITY, ACCURACY, SATISFACTORY QUALITY, FITNESS FOR

A PARTICULAR PURPOSE, USABILITY, INTEGRATION OR NON-INFRINGEMENT AND ALL SUCH WARRANTIES ARE HEREBY EXCLUDED BY WILEY AND ITS LICENSORS AND WAIVED BY YOU.

- WILEY shall have the right to terminate this Agreement immediately upon breach of this Agreement by you.
- You shall indemnify, defend and hold harmless WILEY, its Licensors and their respective directors, officers, agents and employees, from and against any actual or threatened claims, demands, causes of action or proceedings arising from any breach of this Agreement by you.
- IN NO EVENT SHALL WILEY OR ITS LICENSORS BE LIABLE TO YOU OR ANY OTHER PARTY OR ANY OTHER PERSON OR ENTITY FOR ANY SPECIAL, CONSEQUENTIAL, INCIDENTAL, INDIRECT, EXEMPLARY OR PUNITIVE DAMAGES, HOWEVER CAUSED, ARISING OUT OF OR IN CONNECTION WITH THE DOWNLOADING, PROVISIONING, VIEWING OR USE OF THE MATERIALS REGARDLESS OF THE FORM OF ACTION, WHETHER FOR BREACH OF CONTRACT, BREACH OF WARRANTY, TORT, NEGLIGENCE, INFRINGEMENT OR OTHERWISE (INCLUDING, WITHOUT LIMITATION, DAMAGES BASED ON LOSS OF PROFITS, DATA, FILES, USE, BUSINESS OPPORTUNITY OR CLAIMS OF THIRD PARTIES), AND WHETHER OR NOT THE PARTY HAS BEEN ADVISED OF THE POSSIBILITY OF SUCH DAMAGES. THIS LIMITATION SHALL APPLY NOTWITHSTANDING ANY FAILURE OF ESSENTIAL PURPOSE OF ANY LIMITED REMEDY PROVIDED HEREIN.
- Should any provision of this Agreement be held by a court of competent jurisdiction to be illegal, invalid, or unenforceable, that provision shall be deemed amended to achieve as nearly as possible the same economic effect as the original provision, and the legality, validity and enforceability of the remaining provisions of this Agreement shall not be affected or impaired thereby.
- The failure of either party to enforce any term or condition of this Agreement shall not constitute a waiver of either party's right to enforce each and every term and condition of this Agreement. No breach under this agreement shall be deemed waived or excused by either party unless such waiver or consent is in writing signed by the party granting such waiver or consent. The waiver by or consent of a party to a breach of any provision of this Agreement shall not operate or be construed as a waiver of or consent to any other or subsequent breach by such other party.
- This Agreement may not be assigned (including by operation of law or otherwise) by you without WILEY's prior written consent.
- Any fee required for this permission shall be non-refundable after thirty (30) days from receipt by the CCC.
- These terms and conditions together with CCC's Billing and Payment terms and conditions (which are incorporated herein) form the entire agreement between you and WILEY concerning this licensing transaction and (in the absence of fraud) supersedes all prior agreements and representations of the parties, oral or written. This Agreement may not be amended except in writing signed by both parties. This Agreement shall be binding upon and inure to the benefit of the parties' successors, legal representatives,

and authorized assigns.

- In the event of any conflict between your obligations established by these terms and conditions and those established by CCC's Billing and Payment terms and conditions, these terms and conditions shall prevail.
- WILEY expressly reserves all rights not specifically granted in the combination of (i) the license details provided by you and accepted in the course of this licensing transaction, (ii) these terms and conditions and (iii) CCC's Billing and Payment terms and conditions.
- This Agreement will be void if the Type of Use, Format, Circulation, or Requestor Type was misrepresented during the licensing process.
- This Agreement shall be governed by and construed in accordance with the laws of the State of New York, USA, without regards to such state's conflict of law rules. Any legal action, suit or proceeding arising out of or relating to these Terms and Conditions or the breach thereof shall be instituted in a court of competent jurisdiction in New York County in the State of New York in the United States of America and each party hereby consents and submits to the personal jurisdiction of such court, waives any objection to venue in such court and consents to service of process by registered or certified mail, return receipt requested, at the last known address of such party.

WILEY OPEN ACCESS TERMS AND CONDITIONS

Wiley Publishes Open Access Articles in fully Open Access Journals and in Subscription journals offering Online Open. Although most of the fully Open Access journals publish open access articles under the terms of the Creative Commons Attribution (CC BY) License only, the subscription journals and a few of the Open Access Journals offer a choice of Creative Commons Licenses. The license type is clearly identified on the article.

The Creative Commons Attribution License

The [Creative Commons Attribution License \(CC-BY\)](#) allows users to copy, distribute and transmit an article, adapt the article and make commercial use of the article. The CC-BY license permits commercial and non-

Creative Commons Attribution Non-Commercial License

The [Creative Commons Attribution Non-Commercial \(CC-BY-NC\) License](#) permits use, distribution and reproduction in any medium, provided the original work is properly cited and is not used for commercial purposes.(see below)

Creative Commons Attribution-Non-Commercial-NoDerivs License

The [Creative Commons Attribution Non-Commercial-NoDerivs License \(CC-BY-NC-ND\)](#) permits use, distribution and reproduction in any medium, provided the original work is properly cited, is not used for commercial purposes and no modifications or adaptations are made. (see below)

Use by commercial "for-profit" organizations

Use of Wiley Open Access articles for commercial, promotional, or marketing purposes requires further explicit permission from Wiley and will be subject to a fee.

Further details can be found on Wiley Online Library
<http://olabout.wiley.com/WileyCDA/Section/id-410895.html>

Other Terms and Conditions:

v1.10 Last updated September 2015

Questions? customercare@copyright.com.





Home



Help ▾



Live Chat



YOGESHWAR MORE ▾

Cation-Triggered Drug Release from a Porous Zinc–Adeninate Metal–Organic Framework



Author: Jihyun An, Steven J. Geib, Nathaniel L. Rosi

Publication: Journal of the American Chemical Society

Publisher: American Chemical Society

Date: Jun 1, 2009

Copyright © 2009, American Chemical Society

PERMISSION/LICENSE IS GRANTED FOR YOUR ORDER AT NO CHARGE

This type of permission/license, instead of the standard Terms and Conditions, is sent to you because no fee is being charged for your order. Please note the following:

- Permission is granted for your request in both print and electronic formats, and translations.
- If figures and/or tables were requested, they may be adapted or used in part.
- Please print this page for your records and send a copy of it to your publisher/graduate school.
- Appropriate credit for the requested material should be given as follows: "Reprinted (adapted) with permission from {COMPLETE REFERENCE CITATION}. Copyright {YEAR} American Chemical Society." Insert appropriate information in place of the capitalized words.
- One-time permission is granted only for the use specified in your RightsLink request. No additional uses are granted (such as derivative works or other editions). For any uses, please submit a new request.

If credit is given to another source for the material you requested from RightsLink, permission must be obtained from that source.

[BACK](#)

[CLOSE WINDOW](#)



A Water-Stable Cationic Metal–Organic Framework as a Dual Adsorbent of Oxoanion Pollutants

Author: Aamod V. Desai, Biplab Manna, Avishek Karmakar, et al

Publication: Angewandte Chemie International Edition

Publisher: John Wiley and Sons

Date: Feb 8, 2016

© 2016 WILEY-VCH Verlag GmbH & Co. KGaA, Weinheim

Order Completed

Thank you for your order.

This Agreement between Dr. YOGESHWAR MORE ("You") and John Wiley and Sons ("John Wiley and Sons") consists of your license details and the terms and conditions provided by John Wiley and Sons and Copyright Clearance Center.

Your confirmation email will contain your order number for future reference.

License Number 5535511188709

[Printable Details](#)

License date Apr 24, 2023

✓ Licensed Content

Licensed Content Publisher	John Wiley and Sons
Licensed Content Publication	Angewandte Chemie International Edition A Water-Stable Cationic Metal–Organic Framework as a Dual Adsorbent of Oxoanion Pollutants
Licensed Content Title	A Water-Stable Cationic Metal–Organic Framework as a Dual Adsorbent of Oxoanion Pollutants
Licensed Content Author	Aamod V. Desai, Biplab Manna, Avishek Karmakar, et al
Licensed Content Date	Feb 8, 2016
Licensed Content Volume	55
Licensed Content Issue	27
Licensed Content Pages	5

📄 Order Details

Type of use	Dissertation/Thesis
Requestor type	University/Academic
Format	Electronic
Portion	Figure/table
Number of figures/tables	1
Will you be translating?	No

📄 About Your Work

Title	A Water-Stable Cationic Metal–Organic Framework as a Dual Adsorbent of Oxoanion Pollutants
Institution name	Indian Institute of Science Education and Research, Pune
Expected presentation date	May 2023

📄 Additional Data

Portions	figure 1
----------	----------

📍 Requestor Location		📄 Tax Details	
Requestor Location	Dr. YOGESHWAR MORE Homi bhabha road pashan pune Pune, Maharashtra 411008 India Attn: Dr. YOGESHWAR MORE	Publisher Tax ID	EU826007151
\$ Price			
Total	0.00 EUR		

Would you like to purchase the full text of this article? If so, please continue on to the content ordering system located here: [Purchase PDF](#)
If you click on the buttons below or close this window, you will not be able to return to the content ordering system.

Total: 0.00 EUR

[CLOSE WINDOW](#) [ORDER MORE](#)